

PROCEEDINGS OF SPIE



SPIE—The International Society for Optical Engineering

F61775-98-WE 027

CSP 98-1028

Laser Optics '98

Superstrong Laser Fields and Applications

Alexander A. Andreev
Editor

22-26 June 1998
St. Petersburg, Russia

Organized by

Institute for Laser Physics, S.I. Vavilov State Optical Institute
General Physics Institute, Russian Academy of Sciences
P.N. Lebedev Physical Institute, Russian Academy of Sciences
Institute for Fine Mechanics and Optics, Technical University
Russian National Center of Laser Physics, St. Petersburg State University
Scientific Council on Coherent and Nonlinear Optics, Russian Academy of Sciences
SPIE—The International Society for Optical Engineering
SPIE Russia Chapter
OSA—Optical Society of America
EOS—European Optical Society
ROS—Rozhdestvensky Optical Society
Government of St. Petersburg

DISTRIBUTION STATEMENT A
Approved for Public Release
Distribution Unlimited



Volume 3683

19990702 017

DTIC QUALITY INSPECTED 4

AQ F99-10-1694



PROCEEDINGS OF SPIE

SPIE—The International Society for Optical Engineering

Laser Optics '98

Superstrong Laser Fields and Applications

Alexander A. Andreev

Editor

22–26 June 1998

St. Petersburg, Russia

Organized by

Institute for Laser Physics, S.I. Vavilov State Optical Institute • General Physics Institute, Russian Academy of Sciences • P.N. Lebedev Physical Institute, Russian Academy of Sciences • Institute for Fine Mechanics and Optics, Technical University • Russian National Center of Laser Physics, St. Petersburg State University • Scientific Council on Coherent and Nonlinear Optics, Russian Academy of Sciences • SPIE—The International Society for Optical Engineering • SPIE Russia Chapter • OSA—Optical Society of America • EOS—European Optical Society • ROS—Rozhdestvensky Optical Society • Government of St. Petersburg

Supported by

Ministry of Science and Technical Policy of Russia • Ministry for Economics of Russia • Ministry for Education of Russia • Russian National Foundation for Basic Research • SPIE—The International Society for Optical Engineering • Lawrence Livermore National Laboratory (USA) • USAF European Office of Aerospace Research and Development • OSA—Optical Society of America

Sponsored by

Technische Zentrum Nord (Germany)
Thomson-CSF (France)
JENOPTIK Technologie GmbH (Germany)

Published by

SPIE—The International Society for Optical Engineering



Volume 3683

SPIE is an international technical society dedicated to advancing engineering and scientific applications of optical, photonic, imaging, electronic, and optoelectronic technologies.



The papers appearing in this book comprise the proceedings of the meeting mentioned on the cover and title page. They reflect the authors' opinions and are published as presented and without change, in the interests of timely dissemination. Their inclusion in this publication does not necessarily constitute endorsement by the editors or by SPIE.

Please use the following format to cite material from this book:

Author(s), "Title of paper," in *Laser Optics '98: Superstrong Laser Fields and Applications*, Alexander A. Andreev, Editor, Proceedings of SPIE Vol. 3683, page numbers (1998).

ISSN 0277-786X
ISBN 0-8194-3157-5

Published by
SPIE—The International Society for Optical Engineering
P.O. Box 10, Bellingham, Washington 98227-0010 USA
Telephone 360/676-3290 (Pacific Time) • Fax 360/647-1445

Copyright ©1998, The Society of Photo-Optical Instrumentation Engineers.

Copying of material in this book for internal or personal use, or for the internal or personal use of specific clients, beyond the fair use provisions granted by the U.S. Copyright Law is authorized by SPIE subject to payment of copying fees. The Transactional Reporting Service base fee for this volume is \$10.00 per article (or portion thereof), which should be paid directly to the Copyright Clearance Center (CCC), 222 Rosewood Drive, Danvers, MA 01923. Payment may also be made electronically through CCC Online at <http://www.directory.net/copyright/>. Other copying for republication, resale, advertising or promotion, or any form of systematic or multiple reproduction of any material in this book is prohibited except with permission in writing from the publisher. The CCC fee code is 0277-786X/98/\$10.00.

Printed in the United States of America.

Contents

vii *Conference Committees*

SESSION 1 SUPERSTRONG LASER FIELDS AND APPLICATIONS

- 2 **Nonlinear dynamics of laser wake fields in underdense plasmas [3683-01]**
N. E. Andreev, High Energy Density Research Ctr. (Russia); E. V. Chizhonkov, M.V. Lomonosov Moscow State Univ. (Russia); L. M. Gorbunov, P.N. Lebedev Physical Institute (Russia)
- 9 **Computational model of short-pulse laser target interactions [3683-02]**
J. Limpouch, Czech Technical Univ.; A. A. Andreev, S.I. Vavilov State Optical Institute (Russia); L. Drška, Czech Technical Univ.
- 15 **First picosecond terawatt CO₂ laser [3683-03]**
I. V. Pogorelsky, I. Ben-Zvi, M. Babzien, K. Kusche, J. Skaritka, Brookhaven National Lab. (USA); I. K. Meshkovsky, A. A. Dublov, V. A. Lekomtsev, I. V. Pavlishin, Yu. A. Boloshin, G. B. Deineko, Optoel Co. (Russia); A. Tsunemi, Sumitomo Heavy Industries, Ltd. (Japan)
- 25 **Ionization processes by intense laser pulse interaction with solid targets [3683-04]**
N. E. Andreev, High Energy Density Research Ctr. (Russia); I. L. Beigman, P.N. Lebedev Physical Institute (Russia); V. V. Kostin, M. Ef. Veisman, High Energy Density Research Ctr. (Russia); A. M. Urnov, P.N. Lebedev Physical Institute (Russia)
- 33 **Temporal structure of a short powerful laser pulse under an operation of ionization processes [3683-05]**
M. V. Chegotov, High Energy Density Research Ctr. (Russia)
- 42 **Start in vacuum of fast electrons generated at oblique incidence of an ultrashort intensive laser pulse on a flat target [3683-06]**
A. A. Andreev, I. A. Litvinenko, K. Yu. Platonov, S.I. Vavilov State Optical Institute (Russia)
- 57 **Extremely intensive γ source with high spectral brightness [3683-07]**
A. A. Andreev, Yu. Rozhdestvensky, S.I. Vavilov State Optical Institute (Russia); K. Yu. Platonov, State Technical Univ. (Russia)
- 63 **Second-harmonics emission from short-pulse laser-irradiated solid targets [3683-08]**
J. Limpouch, Czech Technical Univ.; A. A. Andreev, K. Yu. Platonov, S.I. Vavilov State Optical Institute (Russia)
- 69 **Spatial and spectral parameters of superthermal particle extension in laser plasma experiments with a picosecond laser pulse [3683-09]**
V. M. Komarov, V. G. Borodin, A. V. Charukchev, V. N. Chernov, V. V. Il'yn, V. A. Malinov, V. M. Migel, N. V. Nikitin, S.I. Vavilov State Optical Institute (Russia)
- 75 **Focusing system of multiterawatt laser facility PROGRESS-P [3683-10]**
V. N. Chernov, V. G. Borodin, A. V. Charukchev, V. A. Malinov, V. M. Migel, N. V. Nikitin, I. G. Rozivika, S.I. Vavilov State Optical Institute (Russia)

- 79 **Initiation of laser-induced damage and ultimate light intensities in multilayer optical coatings with sublayered microstructure [3683-11]**
A. S. Gruzdeva, V. E. Gruzdev, S.I. Vavilov State Optical Institute (Russia)
- 90 **Generation performance of Cr:LiSAF new active medium for flashlamp-pumped tunable solid state lasers [3683-12]**
V. B. Gerasimov, SE SDB Granat (Russia); A. S. Kuznetsov, ELS Co. (Russia); A. A. Salnikov, V. O. Umnov, SE SDB Granat (Russia); A. V. Shestakov, ELS Co. (Russia)
- 96 **Surface studies using nonlinear spectroscopy with tunable picosecond pulses [3683-13]**
J. Löbau, A. Laubereau, Technische Univ. München (Germany)
- 108 **Precision laser ablation of wide-band-gap materials using VUV-UV multiwavelength excitation [3683-14]**
K. Sugioka, J. Zhang, S. Wada, H. Tashiro, K. Midorikawa, RIKEN—The Institute of Physical and Chemical Research (Japan)

SESSION 2 LASERS FOR FUSION

- 120 **Overview of the solid state laser projects for ICF applications at CAEP [3683-15]**
H. S. Peng, X. M. Zhang, X. F. Wei, W. G. Zheng, F. Jing, Z. D. Sui, X. D. Yuan, Institute of Nuclear Physics and Chemistry (China)
- 128 **High-power PROGRESS Nd:glass laser facility [3683-16]**
A. V. Charukhev, V. N. Chernov, V. A. Malinov, N. V. Nikitin, V. G. Borodin, V. M. Efanov, V. V. Iljin, V. M. Komarov, V. M. Migel, V. S. Popov, S. L. Potapov, S.I. Vavilov State Optical Institute (Russia)
- 138 **Soft x-ray plasma source pumped by an excimer laser: optimization and applications [3683-17]**
P. Albertano, Univ. degli Studi di Roma Tor Vergata (Italy); M. Belli, Istituto Superiore di Sanità (Italy) and INFN (Italy); S. Bollanti, P. Di Lazzaro, ENEA Frascati (Italy); A. Ya. Faenov, NPO VINIIFTRI (Russia); F. Flora, G. Giordano, ENEA Frascati (Italy); A. Grilli, INFN-LNF (Italy); F. Ianzini, Istituto Superiore di Sanità (Italy) and INFN (Italy); S. V. Kukhlevsky, Janus Pannonius Univ. (Hungary); T. Letardi, A. Marinai, A. Nottola, ENEA Frascati (Italy); L. Palladino, Univ. degli Studi dell'Aquila (Italy) and INFN (Italy); T. A. Pikuz, NPO VINIIFTRI (Russia); A. Reale, L. Reale, Univ. degli Studi dell'Aquila (Italy) and INFN (Italy); A. Scafati, Istituto Superiore di Sanità (Italy) and INFN (Italy); G. Schina, ENEA Frascati (Italy); M. A. Tabocchini, Istituto Superiore di Sanità (Italy) and INFN (Italy); I. C. E. Turcu, Rutherford Appleton Lab. (UK); K. Vigli-Papadaki, ENEA Frascati (Italy)
- 152 **Powerful thermonuclear neutron source with a double-pulse KrF laser [3683-18]**
I. G. Lebo, V. B. Rozanov, V. D. Zvorykin, P.N. Lebedev Physical Institute (Russia)
- 159 **Preliminary design of the spatial filters used in the multipass amplification system of TIL [3683-19]**
Q. H. Zhu, X. M. Zhang, F. Jing, Institute of Nuclear Physics and Chemistry (China)
- 164 **Preliminary design of the main amplification stage of Technical Integration Line (TIL) for the SG-III laser facility [3683-20]**
F. Jing, X. M. Zhang, Q. H. Zhu, Y. Z. Man, H. S. Peng, Institute of Nuclear Physics and Chemistry (China)

- 170 **Efficiency of thermonuclear burning in laser targets with spark ignition [3683-21]**
A. A. Andreev, S.I. Vavilov State Optical Institute (Russia); D. V. Il'in, A. A. Levkovskii,
V. E. Sherman, O. B. Vygovskii, St. Petersburg Institute of Machine Building (Russia)
- 179 **GARPUN KrF laser application to material studies at megabar pressures [3683-22]**
V. D. Zvorykin, V. G. Bakaev, V. Yu. Korol', G. V. Sychugov, P.N. Lebedev Physical
Institute (Russia)
- 186 **Development of the nonlinear optical element for light-beam apodization and large-aperture
laser amplifier decoupling [3683-23]**
L. M. Vinogradsky, S. K. Sobolev, Russian Federal Nuclear Ctr. VNIIEF; I. G. Zubarev,
M. V. Pyatakhin, Yu. V. Senatsky, P.N. Lebedev Physical Institute (Russia); V. M. Mizin,
State Scientific Ctr. of the Russian Federation NIOPIK; K. Ueda, Univ. of
Electrocommunications (Japan)

SESSION 3 DEVICES FOR ULTRAFAST OPTICS

- 196 **Optically detected carrier transport and capture in III/V semiconductor QW structures:
high-resolution experiments, model calculations, and applications in fast 1.55- μ m lasers
[3683-24]**
H. Hillmer, Deutsche Telekom (Germany); S. Marcinkevicius, Royal Institute of
Technology (Sweden)
- 208 **New approach to computer simulation of femtosecond pulse propagation in a nonlinear
medium [3683-25]**
V. A. Trofimov, M.V. Lomonosov Moscow State Univ. (Russia)
- 217 **Spatiotemporal filtration of ultrashort light pulses by one-dimensional nonlinear band gap
structures [3683-26]**
A. G. Smirnov, B.I. Stepanov Institute of Physics (Belarus)
- 225 **Stark-induced contribution to mode locking in cw solid state lasers with semiconductor
saturable absorber [3683-27]**
V. L. Kalashnikov, D. O. Krimer, I. G. Poloyko, V. P. Mikhailov, International Laser
Ctr. (Belarus)
- 233 *Author Index*

Conference Committees

Conference Honorary Chairs

Alexander M. Prokhorov, General Physics Institute, Russian Academy of Sciences
Charles H. Townes, University of California/Berkeley (USA)

Organizing Committee

Arthur A. Mak, *Chair*, Institute for Laser Physics, S.I. Vavilov State Optical Institute
Alexander A. Andreev, *Cochair*, Institute for Laser Physics, S.I. Vavilov State Optical Institute
Vladimir M. Arpishkin, *Cochair*, ROS—Rozhdestvensky Optical Society
E.I. Akopov, SPIE Russia Chapter
T. Fujioka, Tokai University (Japan)
O.D. Gavrilov, Institute for Laser Physics, S.I. Vavilov State Optical Institute
A.S. Gorshkov, Institute for Laser Physics, S.I. Vavilov State Optical Institute
V.B. Kryuchenkov, International Science Technology Center
H. Lowdermilk, Lawrence Livermore National Laboratory (USA)
E.I. Makurov, S.I. Vavilov State Optical Institute
V.B. Smirnov, St. Petersburg State University
E. Spitz, Thomson-CSF (France)
Yu.A. Straus, S.I. Vavilov State Optical Institute
B.S. Zykov, International Science Technology Center

Program Committee

Arthur A. Mak, *Chair*, Institute for Laser Physics, S.I. Vavilov State Optical Institute
Alexander A. Andreev, *Cochair*, Institute for Laser Physics, S.I. Vavilov State Optical Institute
Leonid N. Soms, *Scientific Secretary*, Institute for Laser Physics, S.I. Vavilov State Optical Institute
P.A. Apanasevich, B.I. Stepanov Institute of Physics (Belarus)
S.N. Bagaev, Institute of Laser Physics
N.G. Basov, P.N. Lebedev Physical Institute
V.I. Bespalov, Institute of Applied Physics
F.V. Bunkin, General Physics Institute
Yu.D. Golyaev, Polyus Research and Development Institute
V.M. Gordienko, M.V. Lomonosov Moscow State University
V.P. Kandidov, M.V. Lomonosov Moscow State University
Ya.I. Khanin, Institute of Applied Physics
O.A. Kocharovskaya, Institute of Applied Physics
N.I. Koroteev, M.V. Lomonosov Moscow State University
V.I. Kovalev, P.N. Lebedev Physical Institute

V.I. Kovalev, P.N. Lebedev Physical Institute
I.B. Kovsh, Laser Association
V.V. Lyubimov, Institute for Laser Physics, S.I. Vavilov State Optical Institute
A.A. Manenkov, General Physics Institute
Yu.T. Mazurenko, S.I. Vavilov State Optical Institute
A.P. Napartovich, TRINITI
A.N. Oraevsky, P.N. Lebedev Physical Institute
V.Ya. Panchenko, NICTL Laser Research Center
P.P. Pashinin, General Physics Institute
G.T. Petrovskiy, S.I. Vavilov State Optical Institute
L.A. Rivlin, Moscow State Institute of Radio Engineering, Electronics
 and Automation
N.N. Rosanov, Institute for Laser Physics, S.I. Vavilov State Optical Institute
A.S. Rubanov, B.I. Stepanov Institute of Physics (Belarus)
V.A. Serebryakov, Institute for Laser Physics, S.I. Vavilov State Optical Institute
I.A. Shcherbakov, General Physics Institute
V.E. Sherstobitov, Institute for Laser Physics, S.I. Vavilov State Optical Institute
A.P. Shkadarevith, Peleng (Belarus)
V.B. Smirnov, St. Petersburg State University
M.S. Soskin, Institute of Physics (Ukraine)
A.P. Sukhorukov, M.V. Lomonosov Moscow State University
V.I. Ustyugov, Institute for Laser Physics, S.I. Vavilov State Optical Institute
V.V. Valuev, GPO Almaz
E.A. Viktorov, Institute for Laser Physics, S.I. Vavilov State Optical Institute
G.M. Zverev, Polyus Research and Development Institute

American Local Committee

Howard Lowdermilk, *Chair*, Lawrence Livermore National Laboratory (USA)
Sherene Goulart, *Secretary*, Lawrence Livermore National Laboratory (USA)

Asian Local Committee

Sadao Nakai, *Chair*, Osaka University (Japan)
Tomoo Fujioka, *Cochair and Scientific Secretary*, Tokai University (Japan)

European Local Committee

Erich Spitz, *Chair*, Thomson SA (France)
Arnaud Brignon, *Scientific Secretary*, Thomson-CSF (France)
Henri Rajbenbach, *Scientific Secretary*, European Commission (Belgium)

SESSION 1

Superstrong Laser Fields and Applications

Nonlinear dynamics of laser wake fields in underdense plasmas

N.E. Andreev

High Energy Density Research Center of Russian Academy of Sciences,
Izhorskaya st. 13/19, 127412 Moscow, Russia
E-mail: andreev@laslab.ras.ru

E.V. Chizhonkov

Moscow State University, Moscow 119899, Russia

L.M. Gorbunov

P.N. Lebedev Physical Institute, RAS, Moscow 117924, Russia

ABSTRACT

Our new completely nonlinear hydrodynamic numerical code permits to study the temporal evolution of wake fields and a laser pulse in conditions quite near to the wavebreaking or cavitation. It is shown that a short narrow laser pulse of the relativistic intensity generates so strong plasma wave that the electron trajectories intersection can appear. In the case of longer laser pulses, those are undergone the self-modulation effect, the cavitation arises behind a laser pulse in the region of the wakefield even for the nonrelativistic pulse intensities.

1 INTRODUCTION

A short laser pulse, propagating in underdense plasmas, excites behind itself the plasma waves. The electromagnetic fields of such wave (so-called wakefield) is due to the separation of ion and electron charges and can be used for the electron acceleration up to high energies (see, for example,¹). There are a few different models, methods, and approximations in order to calculate the self-consistent evolution of a laser pulse and wake fields excited by a pulse in a plasma¹. In this paper to describe the plasma response and pulse evolution we use the set of

relativistic hydrodynamic equations for electrons which are averaged over high-frequency motion, and the equation for the envelope of a high-frequency laser field. On the base of this model we numerically investigate the nonlinear dynamics of wake fields as well as a laser pulse in 3-D axially symmetric case. The main our attention is focused on the extremely nonlinear wake fields when electron plasma density is quite near to zero or has the very high peaks. These states are quite near to the cavitation and wave-breaking or self-intersection of electron trajectories respectively.

2 A MODEL AND RESULTS

The set of hydrodynamic equations for a cold relativistic collisionless electron fluid and an envelope of a laser pulse has the form ²

$$\frac{\partial n}{\partial t} + \text{div}(n\mathbf{v}) = 0, \quad (1)$$

$$\frac{\partial \mathbf{p}}{\partial t} = e\mathbf{E} - mc^2 \nabla \gamma, \quad (2)$$

$$\frac{\partial \mathbf{E}}{\partial t} = -4\pi en\mathbf{v} - \frac{c^2}{e} \text{rot rot } \mathbf{p}, \quad (3)$$

$$\gamma = \left[1 + \frac{p^2}{m^2 c^2} + \frac{|a|^2}{2} \right]^{1/2}, \quad (4)$$

$$\left(\frac{2i\omega}{c^2} \frac{\partial}{\partial t} + 2ik \frac{\partial}{\partial z} - \Delta_{\perp} \right) a = \frac{\omega_{p0}^2}{c^2} \left(\frac{n}{n_0 \gamma} - 1 \right) a, \quad (5)$$

where e , m , and c are the charge and mass of an electron, and the velocity of light respectively; n , \mathbf{p} , and $\mathbf{v} = \mathbf{p}/(m\gamma)$ are the concentration, momentum, and velocity of electron fluid; a is the normalized complex amplitude of a laser field envelope, ω and k are the frequency and wave number of a laser pulse propagating along the OZ -axis; n_0 is the initial background electron concentration, $\omega_{p0} = (4\pi e^2 n_0 / m)^{1/2}$ is the plasma frequency; $\Delta_{\perp} = \frac{1}{r} \frac{\partial}{\partial r} \left(r \frac{\partial}{\partial r} \right)$ is the transverse part of the Laplace operator.

In the axially symmetric case all values depend only on variables z , r and t . We introduce the new dimensionless variables and functions

$$\eta = \frac{\omega_{p0}}{c}(z - ct), \quad \rho = \frac{\omega_{p0}}{c}r, \quad \theta = \omega_{p0}t, \quad (6)$$

$$\mathbf{q} = \frac{\mathbf{p}}{mc}, \quad \psi = q_z - \gamma, \quad \nu = \frac{n}{n_0}, \quad \varphi = \nu/\gamma. \quad (7)$$

In the quasistatic approximation when $\partial/\partial\theta \ll \partial/\partial\eta$ and $\varepsilon = \omega_{p0}/\omega \ll 1$ the basic equations (1)-(5) are reduced to the form³

$$\frac{\partial\beta}{\partial\eta} + \frac{1}{\rho} \frac{\partial}{\partial\rho} \rho \frac{\partial q}{\partial\eta} - \Delta_{\perp}\gamma + \varphi\gamma = 0 \quad (8)$$

$$q\varphi + \frac{\partial\beta}{\partial\rho} = 0, \quad (9)$$

$$\varphi\psi - \Delta_{\perp}\psi + 1 = 0, \quad (10)$$

$$2\gamma\psi + \psi^2 + q^2 + 1 + \frac{|a|^2}{2} = 0, \quad (11)$$

$$\frac{2i}{\varepsilon} \frac{\partial a}{\partial\theta} + \Delta_{\perp}a + (1 - \varphi)a = 0, \quad (12)$$

where $\beta = \partial\psi/\partial\eta$, $q \equiv q_r$, $\Delta_{\perp} = \frac{1}{\rho} \frac{\partial}{\partial\rho} \left(\rho \frac{\partial}{\partial\rho} \right)$. Here we suppose that a background plasma density is homogeneous. The case of inhomogeneous plasma (with a preformed plasma channel) as well as the method of numerical solution of equations (8)-(12) are described in Ref.³.

At the initial moment of time ($\theta=0$) we suppose the Gaussian form of a laser pulse

$$a(\rho, \eta) = a_0 \exp \left\{ -\frac{\rho^2}{\rho_0^2} - \frac{(\eta - \eta_0)^2}{l_0^2} \right\}, \quad (13)$$

where a_0 is the maximum value of the amplitude, and ρ_0, l_0 are the width and length of the pulse respectively; η_0 is the initial position of the pulse centre.

To examine our numerical code we calculate initially the nonlinear structure of a magnetic field generated by a laser pulse of a given form with the parameters of Ref.⁴. The agreement with the results of Ref.⁴, where PIC code was used, is very good that gives an indication of the applicability of our model for describing nonlinear wakefield dynamics.

As a first application of our numerical code we investigate the features of wake fields excited by the short and narrow laser pulse of a given form. The length and width of a pulse are taken to be $l_0 = 5.5$ and $\rho_0 = 2.3$, respectively. The last number corresponds to the laser pulse width of the order of 0.4 with respect to the plasma wavelength. The pulse centre is situated at the point $\eta_0 = 30.0$. Fig.1 shows the longitudinal velocity and electron density on the axis $\rho = 0$ as well as the radial velocity $w_{\rho}(\rho = 10^{-3})$ in the case of $a_0 = 1.75$. It is seen the sharp narrow peaks of the electron density separated by the deep holes. In the point of absolute maximum the electron density exceeds the background ion density more than 23 times, while in the point of absolute minimum the value of normalized electron density perturbation is $\Delta N_{\min} = -0.86$. The appearance of electron density maxima is mainly due to radial electron motion. This conclusion agrees with results of Ref.⁵ and follows from the Fig.1b where the radial electron velocity changes the sign approximately on the same scale length along the axis as the width of density maxima.

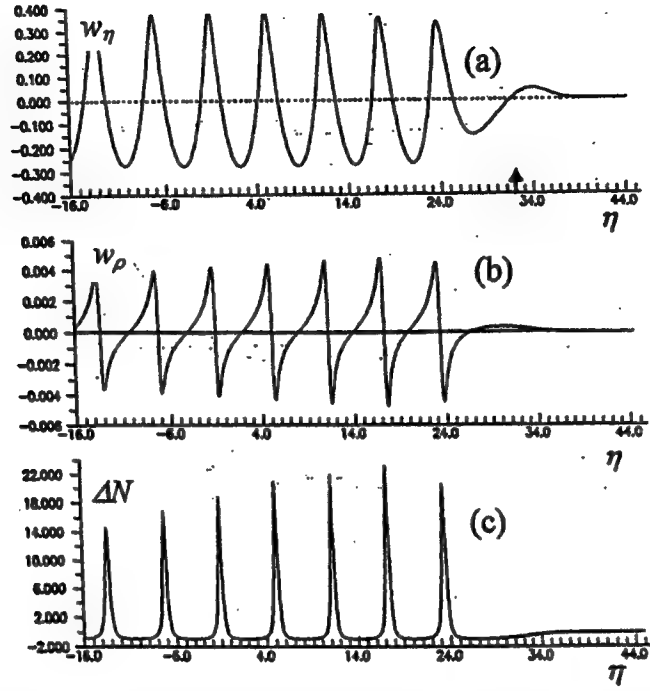


Fig. 1. The axial (w_η) and radial (w_ρ) components of a velocity and density (ΔN) of electrons in wake field excited by the short and narrow laser pulse. The arrow indicates the initial position of the laser pulse centre.

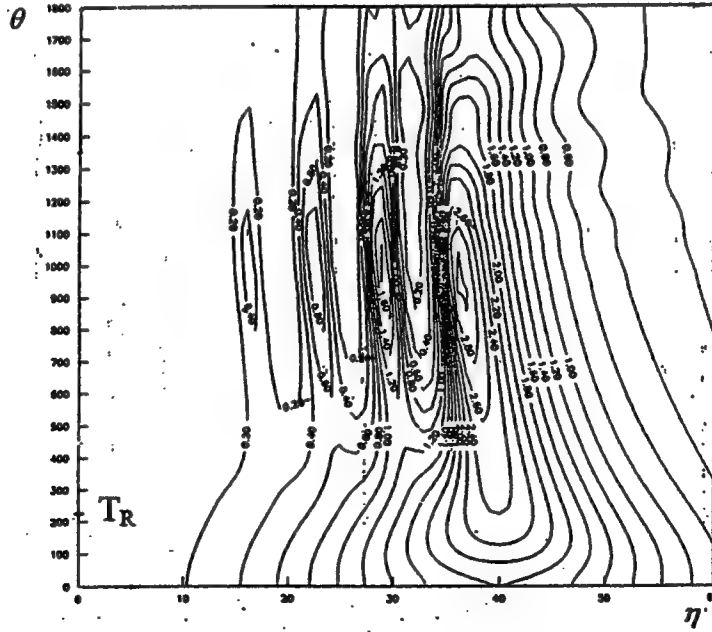


Fig. 2. The contour plots of the laser field amplitude on the plane (θ, η) for $\rho = 0$. The initial maximal amplitude is 0.27. T_R corresponds to the Rayleigh length.

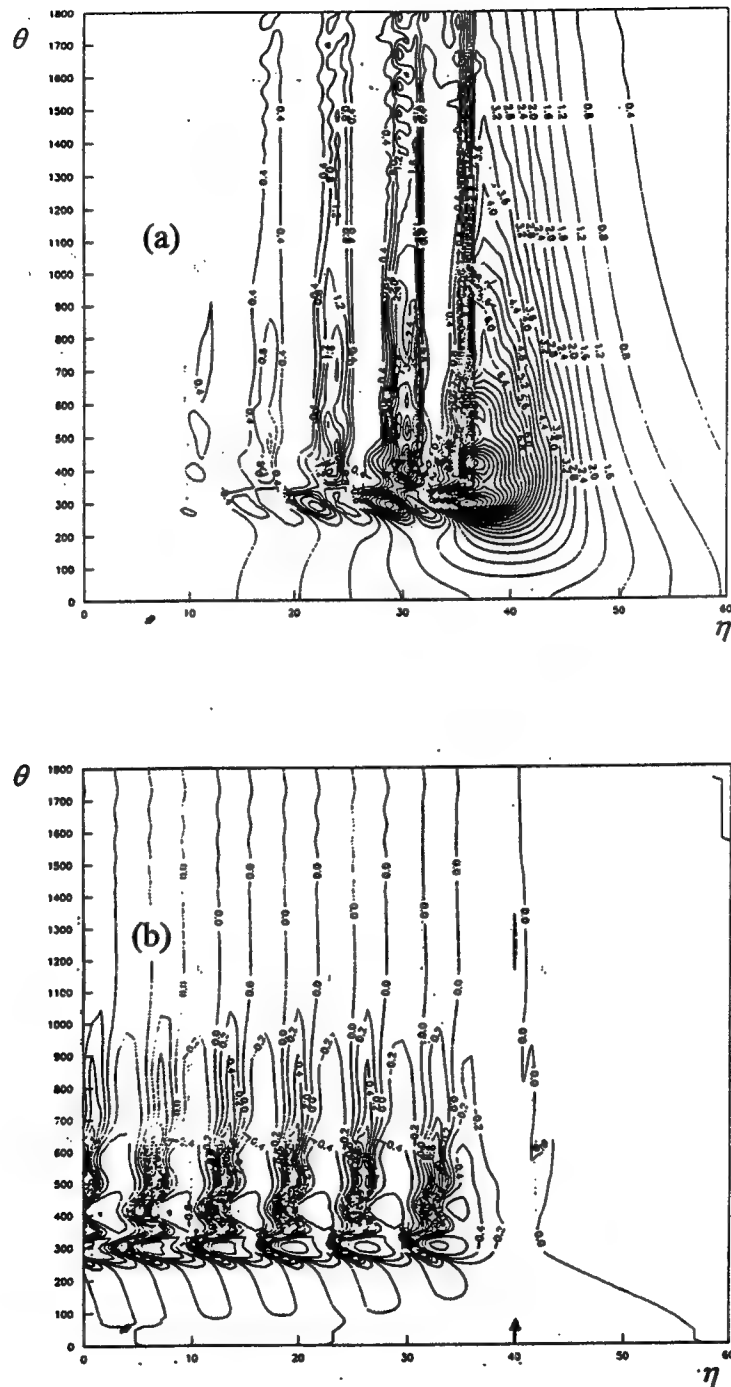


Fig. 3. The contour lines of the laser field amplitude (a) and electron density (b) on the plane (θ, η) for $\rho=0$. The initial maximal amplitude is 0.31. All other parameters are the same as in Fig.2.

The height of the maxima of electron density and the depth of its minima increase rapidly with the increase of the value a_0 . So, for $a_0 = 1.85$ we obtain $\Delta N_{\max} = 78.84$ and $\Delta N_{\min} = -0.9075$, while for $a_0 = 1.9$ the corresponding values are 133.8 and -0.9188 , respectively. It is possible to think that the further small increase of a_0 produces the self-intersection of electron trajectories or cavitation.

The second problem considered here is the dynamics of a self-modulation of laser pulses⁶⁻⁸. This process takes place for a laser pulse that length exceeds the wavelength of a plasma wave and its power is near to the critical one for relativistic self-focusing. As the first step we repeated the results of Ref.⁶ where the another numerical code was used. We obtained the fine agreement with Ref.⁶ where the following set of parameters characterizing the laser pulse at the initial moment of time was taken: $a_0 = 0.27$, $\rho_0 = 20$, $l_0 = 20$, $\eta_0 = 40$. Fig.2 shows the corresponding contour line of dimensionless laser field amplitude in the plane (θ, η) for $\rho = 0$ (on the axis). The analogous plot, as well as the plot of electron density are shown in Fig.3 for $a_0 = 0.31$ and the same other parameters as in Fig.2.

Comparing Figs.2 and 3 we conclude that a small variation of a pulse intensity influences very strongly on the self-modulation dynamics. By increase of the intensity all stages of the self-modulation (growth, saturation and erosion) start to be shorter. The amplitude of electron density variations increases especially. In Fig.3 the absolute maximum and minimum of normalized electron density are $\Delta N_{\max} = 3.717$ and $\Delta N_{\min} = -0.9144$ respectively. It is seen in Fig.3 that the positions of electron density extrema on the axis is not conserved. It means that phase velocity of the excited plasma wave varies in time.

We also performed the calculations for $a_0 = 0.33$. In this case the electron density cavitation appears at some distance behind the laser pulse.

3 SUMMARY

Thus, our new completely nonlinear hydrodynamic numerical code permits to study the temporal evolution of wake fields and a laser pulse in conditions quite near to the wavebreaking or cavitation. From considered examples we are able to conclude that a short narrow laser pulse of the relativistic intensity (the value a_0 is more than unit) generates so strong plasma wave that the electron trajectories intersection may appear. Mainly this effect is due to the electron motion in the radial direction. Qualitatively these conclusions agree with results of Ref.⁵. In the case of longer laser pulses, those are undergone the self-modulation effect, the cavitation arises for nonrelativistic pulse intensities (a_0 is less than unit). Opposite to the Ref.⁹ in our pattern the cavitation appears not inside a laser pulse but behind a pulse in the region of the wakefield. We also observe the temporal variation of the phase velocity of excited wakefield. Evidently, such effect can be undesirable for the wakefield acceleration because it produces the disorder of a phase between the accelerated particle and plasma wave.

Acknowledgments

This research was supported in part by the Russian Foundation for Basic Research under Grants No.97-02-16537 and 98-02-16263.

4 REFERENCES

- [1] E. Esarey, P. Sprangle, J. Krall, and A. Ting, IEEE Trans. Plasma Sci., V.24, p.252 (1996)
- [2] P. Mora and T.M. Antonsen, Jr., Phys. Plasma, V.4, p.217 (1997)
- [3] N.E. Andreev, E.V. Chizhonkov, and L.M. Gorbunov, Russian Journal of Numer. Analysis and Mathem. Modelling, V.13, No.1, p.1 (1998)
- [4] L. Gorbunov, P. Mora, and T.M. Antonsen, Jr., Phys. Rev. Lett., V.76, p.2495 (1996)
- [5] S.V. Bulanov, F. Pegoraro, A.M. Pukhov, and A.S. Sakharov, Phys. Rev. Lett., V.78, p.4205 (1997)
- [6] N.E. Andreev, L.M. Gorbunov, V.I. Kirsanov, A.A. Pogosova, and R.R. Ramazashvili, JETP Lett., v.55, p.571 (1992)
- [7] T.M. Antonsen, Jr., and P. Mora, Phys. Rev. Lett., V.69, p.2204 (1992)
- [8] P. Sprangle, E. Esarey, J. Krall, and G. Joyce, Phys. Rev. Lett., V.69, p.2200 (1992)
- [9] P. Mora and T.M. Antonsen, Jr., Phys. Rev. E, V.53, p.2068 (1996)

Computational Model of Short Pulse Laser Target Interactions

J. Limpouch^a, A.A. Andreev^b and L. Drška^a

^aFaculty of Nuclear Science and Physical Engineering, Czech Technical University,
Břehová 7, 115 19 Prague, Czech Republic

^bInstitute for Laser Physics, Vavilov State Optical Institute,
Birzhevaya line 12, Skt. Petersburg, Russia

ABSTRACT

A complex self-sustained 1D hydrodynamics model of interactions of ultrashort laser pulses with solid targets has been developed. The main application of the model is the interpretation of experiments through the comparison of the code results with output of various types of diagnostics. It can be also used in search of optimum experimental conditions for certain proposed applications of such systems.

Keywords: Ultrashort laser pulses, laser plasma interactions, hydrodynamics model, fast particles, x-ray emission and harmonics

1. INTRODUCTION

The development of T³ (terawatt table-top) lasers have opened up opportunities for extensive research of interactions of high intensity ($I \simeq 10^{14} - 10^{19} \text{ W/cm}^2$) short laser pulses ($\tau \simeq 100 \text{ fs} - 1 \text{ ps}$) with solid targets. The physics of this system is considerably different from conventional interactions of longer pulses as due to a short time scale hydrodynamic motion is no longer a dominant factor and high density plasmas are produced. The non-linear character of interaction is very apparent and a considerable part of energy is transferred to a group of very fast particles. Another advantage of T³ laser is relatively high repetition rate, which is usually several Hz, but it can be easily raised up to several kHz. A detailed review of experimental results and theoretical methods used for description of interaction of short laser pulses with solid target is presented in paper.¹

2. COMPUTATIONAL MODEL

The dynamics of plasma is described via one fluid two temperature Lagrangian hydrocode with electron and ion thermal conductivities, both natural and artificial ion viscosities, and ponderomotive force impact on plasma motion. Laser absorption, energy transport by fast electrons and energy losses via bremsstrahlung and recombination emission are included. Very fine spatial grid with typically 200 - 500 cells is used to model the shape of the density profile in the expanding plasma in detail so that the laser fields may be calculated properly.

The populations of all charge states Z in plasma are described via set of atomic rate equations, including collisional ionization, radiative and three body recombination.

Maxwell's equations are solved in the presented model both for s- and p-polarized laser radiation. The method of numerical solving of Maxwell's equations for p-polarized laser radiation in hot plasma, taking into account spatial dispersion and Landau damping, is described in.² Wavebreaking is described in a phenomenological way by introduction of an effective damping rate of plasma wave.

The acceleration of electrons at resonant absorption is treated in each time step via stationary electron diffusion³ in the velocity space. Electrons are accelerated preferentially in direction to the underdense plasma. The energy of fast electrons matches the difference between the overall laser absorption and integrated local collisional absorption, so that energy conservation is maintained. We assume here a Maxwellian distribution of electrons, entering the critical region from overdense plasmas, with local temperature T_e . A typical electron distribution function $f_{\text{accel}}(v)$ of the accelerated electrons at the vacuum side of the acceleration region is plotted in Fig. 1 at the maximum of laser pulse. We assume fast electrons only these electrons carrying the net increase in energy flux density, it means that

Other author information: J.L.: E-mail: limpouch@lilit.fjfi.cvut.cz
A.A.A.: E-mail: andreev@ilph.spb.su

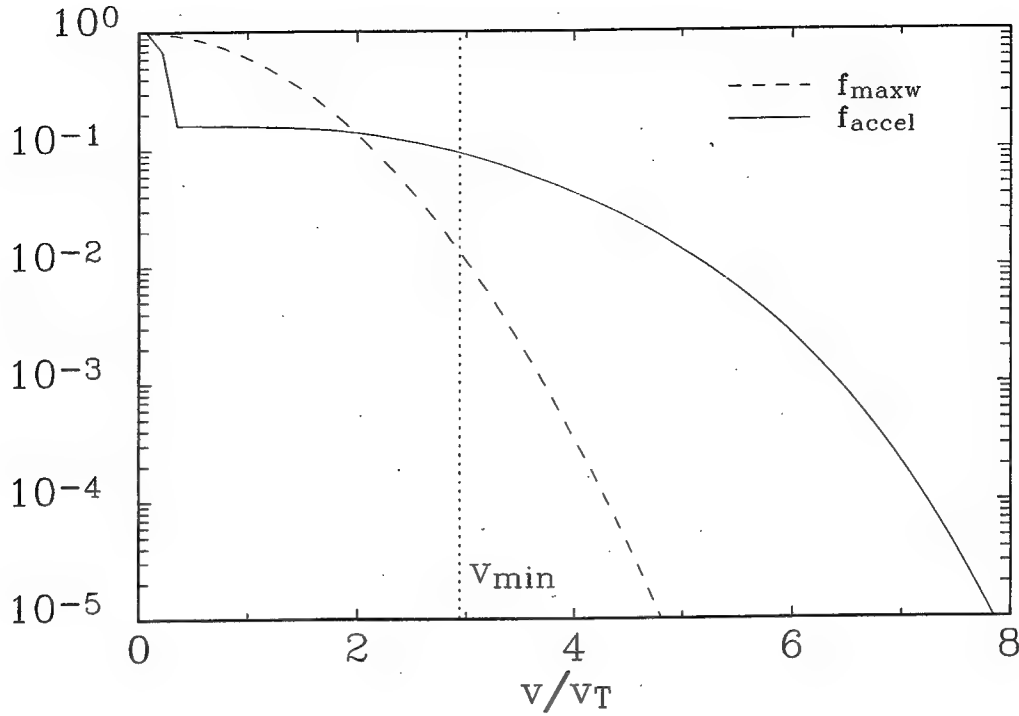


Figure 1. Velocity spectrum f_{accel} of electrons accelerated by resonance absorption, f_{maxw} is the spectra of electrons incident from overdense plasma. Velocity v_{min} is the minimum velocity of the distribution function of fast electrons. The spectrum is taken at the maximum of p-polarized Gaussian 400 fs FWHM Nd-laser pulse with peak intensity 10^{16} W/cm² incident at 45° onto a solid aluminium target.

there are no fast electron with velocity $v < v_{min}$ and the distribution function of fast electrons is $f_{accel} - f_{maxw}$ for $v > v_{min}$. These energetic electrons are then reflected back from the plasma-vacuum boundary losing a fraction η_i of their energy, so that the integral energy lost by fast electrons is equal to the energy gained by the energetic ions.

The distribution function of fast electrons reflected from plasma-vacuum boundary is then used as a boundary condition for solving the transport of energetic electrons into the solid target. The transport is described simply as continuous slowing down with the Bethe-Bloch stopping power. The time of flight of fast electrons inside the simulation box is neglected. The energy lost by fast electrons in a spatial cell leads to the heating of thermal electrons there.

Electrostatic acceleration of ions in the expanding plasma forming a double layer at the plasma-vacuum boundary is assumed. The spectrum of fast ions is found from the electron spectrum via model developed by Gurevich and Mescherkin.⁴ This model assumes quasineutrality and the time of fast electron roundtrip in corona small compared to the laser pulse. Then the electron distribution is symmetric in longitudinal velocity v and electron concentration is given by an electrostatic potential. The evolution of ion density and velocity is then described by collisionless hydrodynamics. Ion velocity distribution is expressed via transformation of variables.

Second harmonics (SH) emission is a very important diagnostics tools which can provide a detailed information about particularly important region of critical surface neighbourhood. We calculate the intensity and the phase of SH emission by solving of the Maxwell's equations for SH field. Spatial dispersion is not included for SH field, as it does not influence the intensity and phase of SH emission. We also neglect the influence of SH fields back on the basic harmonics, which limits the range of validity of the model to medium laser intensities, where the energy conversion to SH is small. The phase of SH emission is controlled mainly by the motion of the source of SH emission which is

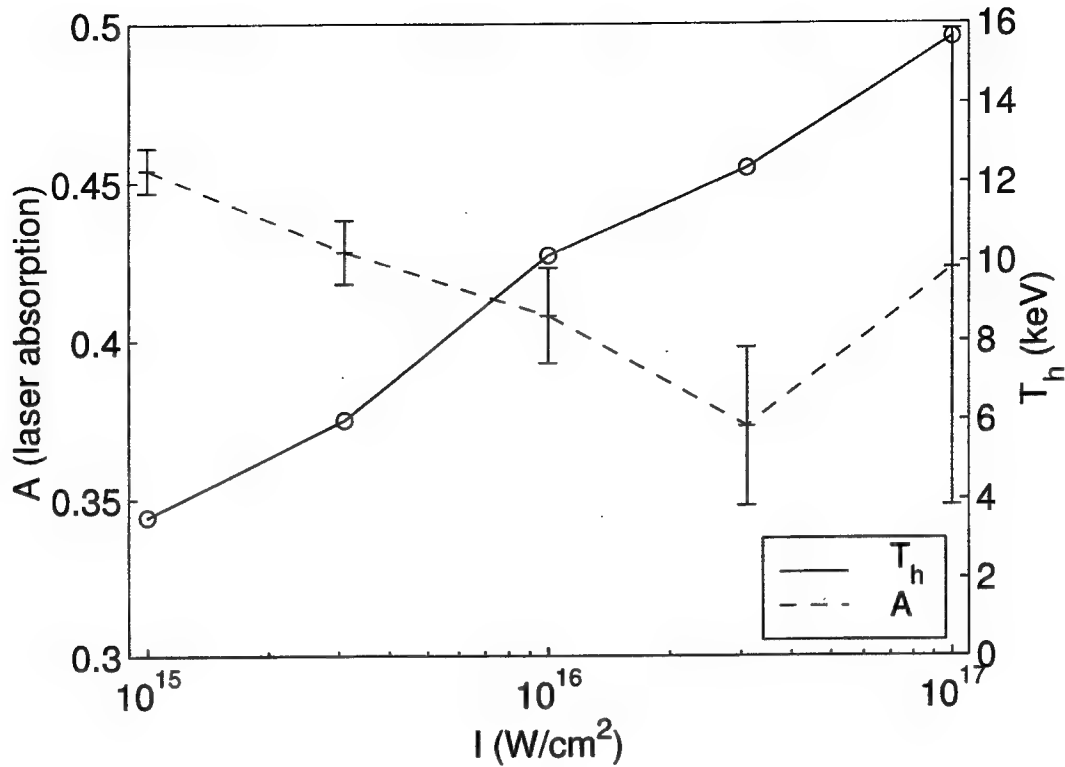


Figure 2. Laser absorption efficiency A and hot electron temperature T_h versus laser intensity. P-polarized Nd laser 1.5 ps FWHM Gaussian pulse is incident at 45° on solid Al target.

maximum in the neighborhood of the critical surface and thus the shift of SH spectra is near to the Doppler shift of radiation reflected from the moving critical surface.

Radiation transport in x-ray lines is modelled as a postprocessor to 1D hydrocode in planar geometry. The spectrum of K-shell line emission is calculated together with a self-consistent description of the excitation kinetics. In the implemented model for the simulation of non-equilibrium line transfer, the coupling is carried out by an iterative procedure, where the populations are obtained by linearization while the line transfer is computed within the core saturation approximation and with complete frequency redistribution.⁵ The core saturation concept is used, both for the acceleration of convergence and for description of the variation of the radiative intensity within each hydrodynamic cell. Voigt emission and absorption line profiles are presently assumed, taking into account natural, lifetime, electron impact Stark and Doppler broadening. Macroscopic Doppler shift is taken into account on a Lagrangian hydrodynamic grid. Ion correlation Stark broadening needs a more general line profile and will be incorporated later. Radiative transfer is solved together with the level populations only for potentially optically thick lines. As the transit time of radiation through plasma is negligible, radiative transfer is written in approximation of infinite speed of light.

3. SIMULATION RESULTS

Only a limited number of examples of simulation results can be shown here. Firstly, the dependence of laser absorption and hot electron temperature on laser intensity is presented. Laser absorption efficiency, plotted in Fig. 2, decreases slowly with laser intensity. The increasing density profile modification due to increasing ponderomotive force leads not only to decrease of collisional absorption, but in our case also to a slight reduction of resonance absorption. However, for the highest intensity assumed here, the dynamics of plasma corona is very complicated, there are periods when plasma density profile changes rapidly and cavitons are formed. In this case a significant dependence of

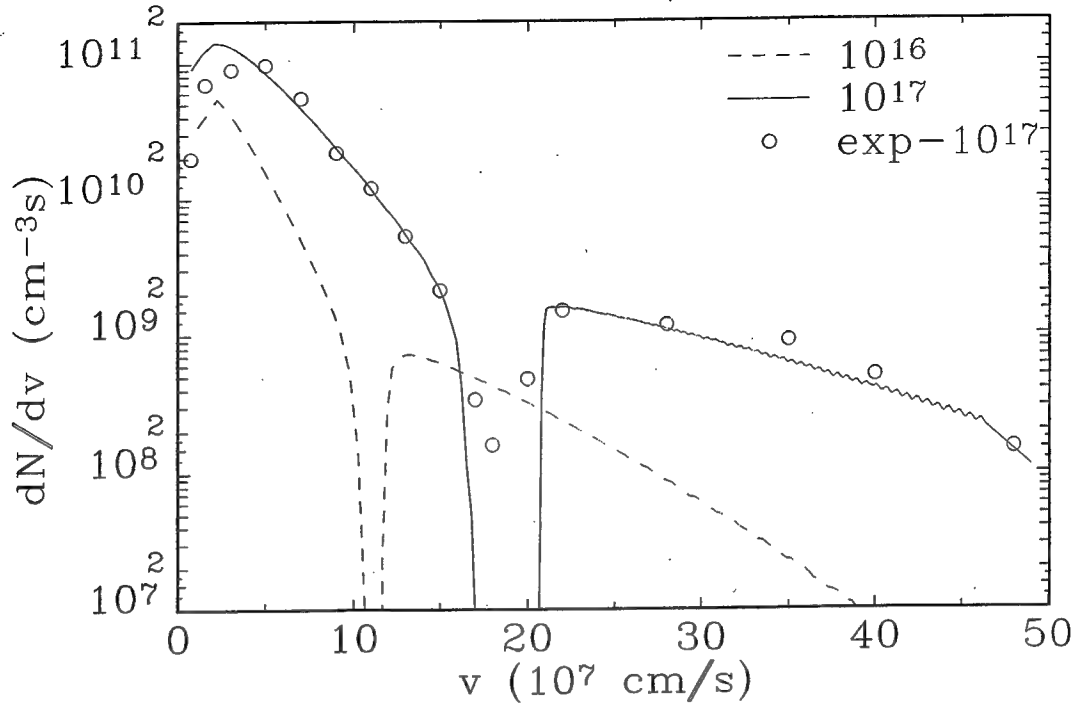


Figure 3. Velocity spectrum of ions at the interaction of 1.5 ps FWHM Gaussian pulse of p-polarized Nd laser radiation incident at 45° on solid Al target for two values of laser intensity.

the overall absorption efficiency on the detailed parameters of simulations is observed. This uncertainty in absorption efficiency is represented by error bars in Fig. 2.

Absorption efficiencies in our simulations are somewhat lower compared with experiments and some results of PIC code, see review paper.¹ Thus we deduce that it is rather difficult to account exactly for all absorption mechanisms of ultrashort laser pulses incident on solid targets in the frame of 1D hydrocode. The same figure depicts the rise of hot electron temperature with laser intensity. The deduced hot electron temperature is $T_h \sim I^\alpha$, where $\alpha \simeq 0.6$, which is in good agreement with scaling PIC simulations.⁶

We present the calculations for the conditions of recent experiments.⁷ Here, 1.5 ps FWHM pulse of p-polarized Nd-laser radiation was incident at 45° onto plane Al target. Laser intensity was varied between 10^{16} and 10^{17} W/cm², intensity contrast was $\sim 10^6 - 10^7$. The fast ion spectrum was measured in direction normal to the target. The ion spectrum is presented for the respective intensities in Fig. 3. As the experimental spectrum is not absolutely calibrated, i.e. the total energy of fast ions is not known, the experimental spectrum is normalized, so that the maxima of fast ion distributions are equal. An excellent agreement with measurement in fast ion energy and spectrum is obtained.

The formation of the minimum in ion velocity distribution is physically connected with a formation of a narrow layer inside the expanding plasma, where a strong electric field forms a region of fast acceleration of ions. In situations, when the ratio of fast to thermal electron temperature is high ($\gtrsim 10$), the assumption of quasineutrality does not hold in this region any more. Then the applied theoretical model of ion acceleration leads to formation of a discontinuity in the solution for the density and velocity profile of expanding plasma and thus the ion distribution $f_i(u) = 0$ is calculated inside the gap and thus the depth of the minimum of ion distribution is overestimated.

We skip here presentation of results for SH emission, as they are presented in a special paper in these proceedings.⁸ The emission from the target in x-ray lines is important both for diagnostics and possible applications. Here evolution of power emitted normally from the target in selected x-ray lines is presented in Fig. 4 for interaction of short laser

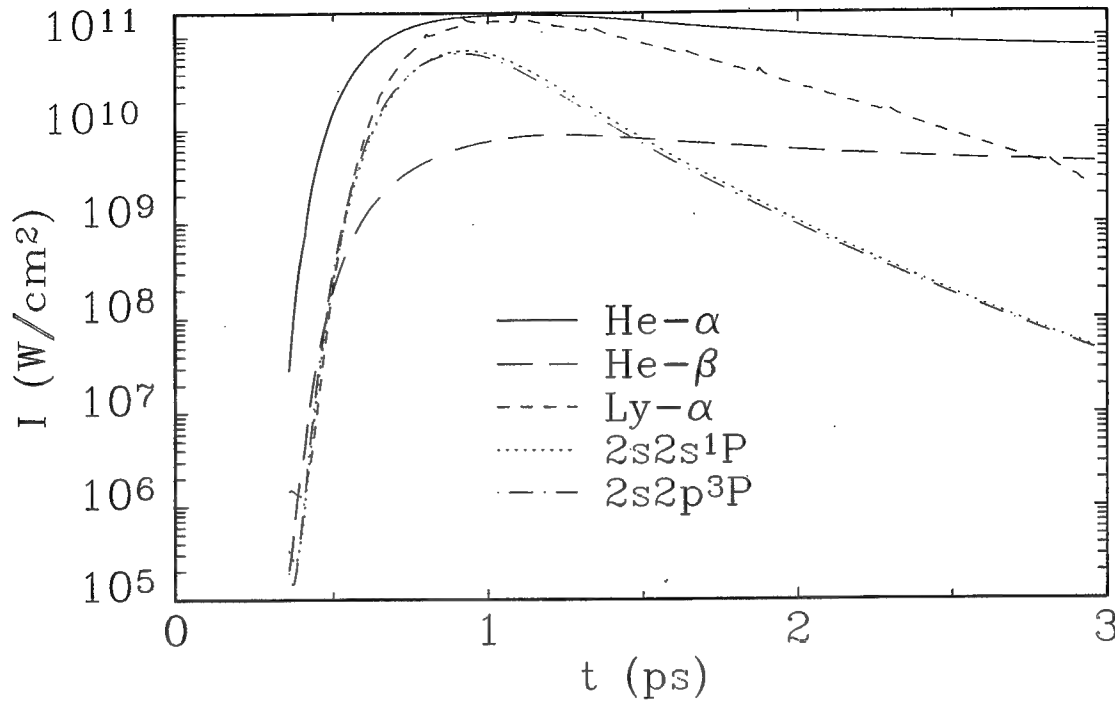


Figure 4. Evolution of power emitted normally from the target in selected x-ray lines: He- α , He- β , Ly- α and its dominant He-like satellites; 400 fs FWHM Gaussian, $I_m = 10^{16}$ W/cm 2 at $t_m = 0.6$ ps unpolarized, $\lambda = 0.256$ μ m, $\theta = 45^\circ$

pulse of moderate intensity with solid Al target. The emission of H-like lines starts with a delay compared to He-like lines due to delay in ionization of Al to H-like state. In spite of the fact that concentration of He-like ions is considerably larger than concentrations of H-like ions during the whole simulation run, the maximum intensity of Ly- α is comparable to He- α line due to very large optical thickness of plasma for He- α line. The decrease of He- α emission after the laser pulse is very slow, as the influence of recombination and de-excitation is partially compensated by decreasing of optical thickness of the source.

4. CONCLUSIONS

Self-contained 1D hydrodynamics model of interactions of short laser pulses with solid targets has been developed. Simulation results compare well with experiments in absorption efficiency, hot electron temperature, fast ion spectrum and SH emission intensity and spectra. Model may be used as a means of analysis of plasma dynamics and as an optimization tool for various output quantities, such as fast ion spectrum and x-ray yield.

Acknowledgements

Support by grant No. 202/97/1186 of the Grant Agency of the Czech Republic is gratefully acknowledged. The invitation of J.L. and A.A.A. to the series of "CECAM Workshops on Short Pulse Interactions", held in Lyon, France, are acknowledged together with the support of organizers and inspiring discussions at the meetings. The participation of J.L. at the Laser Optics conference has been partially sponsored by SPIE.

REFERENCES

1. P. Gibbon, and E. Förster, "Short-pulse laser-plasma interactions," *Plasma Phys. Control. Fusion* **38**, pp. 769–793, 1996.

2. J. Limpouch, L. Drska, M. Tagviashvili, and A. A. Andreev, "Resonance absorption and fast electrons in short-pulse laser-target interactions," in *Advances in Laser Interaction with Matter and Inertial Fusion*, G. Velarde, J. M. Martinez-Val, E. Minguez, J. M. Perlado, eds., pp. 621–624, World Scientific, Singapore, 1997.
3. N. E. Andreev, V. P. Silin, and G. L. Stenchikov, *ZhETF* **78**, pp. 1396–1403, 1980 (in Russian).
4. A.B. Gurevich, and A.P. Mescherkin, "Acceleration of ions in expanding plasma", *ZhETF* **80**, pp. 1810–1826, 1981 (in Russian).
5. O. Peyrusse, "A model for the simulation of non-equilibrium line transfer in laboratory", *Phys. Fluids* **B4**, pp. 2007–2011, 1992.
6. P. Gibbon, A. R. Bell, "Collisionless absorption in sharp-edged plasmas", *Phys. Rev. Letts* **68**, pp. 1535–1538, 1992.
7. V.A. Komarov *et al.*, in *Book of Abstracts, Laser Interactions and Related Plasma Phenomena*, Monterrey, 1997.
8. J. Limpouch, A. A. Andreev, and K. Yu. Platonov, "Second harmonics emission from short pulse laser irradiated solid targets," in *Proc. SPIE*, these proceedings, 1998.

The first picosecond terawatt CO₂ laser

Igor V. Pogorelsky^a, Ilan Ben-Zvi^a, Marcus Babzien^a, Karl Kutsche^a, John Skaritka^a,
Igor K. Meshkovsky^b, Andrey A. Dublov^b, Vasili A. Lekomtsev^b, Igor V. Pavlishin^b, Yuri A. Boloshin^b,
Gennady B. Deineko^b and Akira Tsunemi^c

^a Accelerator Test Facility, BNL, Upton, NY 11973, USA

^b Optoel Co., Sablinskaya 14, St. Petersburg, 197101 Russia

^c Sumitomo Heavy Industries Ltd., Japan

ABSTRACT

The first terawatt picosecond CO₂ laser, PITER I, is under commissioning at the Brookhaven Accelerator Test Facility. PITER I consists of a single-mode TEA oscillator, semiconductor optical switch, and two stages of the multi-atmosphere amplifiers. We report on design, simulation, and tests of the 10 atm final amplifier that allows multi-terawatt peak power extraction in a picosecond laser pulse.

Keywords: CO₂ lasers, high-pressure gas discharges, picosecond laser pulses

1. INTRODUCTION

Table-top terawatt (TW) picosecond and subpicosecond solid state lasers are the sources of the most intense electromagnetic radiation and strongest electric and magnetic fields available for laboratory research. However, progress in newly emerged strong-field physics applications, such as laser accelerators or Compton x-ray sources, toward high through-put instruments is impeded by the low average power of the TW lasers. This is primarily due to the inherently low efficiency of the thermal diffusion cooling of the solid active elements. Fast gas flow CO₂ lasers are potentially a rational complement to the solid state laser technology. This is not just because the absolute maximum average power has been demonstrated with these devices, but is also due to favorable wavelength scaling of fundamental light-matter interactions.

Typical for CO₂ lasers, a relatively long nanosecond pulse duration is the prime reason why they have not been utilized so far in a full manner for strong-field physics research. Kilojoules of laser energy are required to reach a terawatt peak power. This is still possible with CO₂ lasers and has been demonstrated previously [1, 2]. However, the nanosecond pulses are incompatible with many of the strong-field physics processes which are typically localized in very short time intervals. A picosecond and femtosecond pulse duration turns out to be a prerequisite for the successful use of lasers in high energy physics and many other advanced scientific applications.

The concept of picosecond terawatt CO₂ lasers has been proposed some time ago [3-6]. However, radical steps in this direction have not been taken until the project on the First Picosecond TERawatt (PITER I) CO₂ laser project initiated at the Brookhaven Accelerator Test Facility (ATF). Today, PITER I is close to completion and will become available for the ATF users in 1999. The system comprises: a hybrid single-mode CO₂ oscillator, semiconductor optical switch driven by a picosecond Nd-YAG laser, and two stages of multi-atmosphere CO₂ laser amplifiers.

We report here on design and study of PITER I. The ATF laser assembly and preliminary test results are described in Section 2. In Section 3, we address prospects for future progress in pico- and femtosecond CO₂ laser technology. The review of physical limitations and potential capabilities of the picosecond terawatt CO₂ laser technology [7] justifies a conclusion that moderate efforts may lead to development of CO₂ lasers of 10 kW average power, 10-50 J per pulse, and down to 100 fs pulse duration with the resulting peak power of 100 TW and higher. We discuss potential applications of such lasers in high energy physics projects based on using strong laser fields.

2. DESIGN AND STATUS OF PICOSECOND TERAWATT CO₂ LASER PITER I AT THE BNL ACCELERATOR TEST FACILITY

2.1 BNL Accelerator Test Facility Overview

The ATF is the US Dept. of Energy user's facility dedicated to the proposal-driven peer reviewed research in high energy physics and basic energy science. For this mission, the facility is equipped with high-power lasers and a high-brightness electron linear accelerator. Fig.1 shows the main ATF components: linac, Nd:YAG and CO₂ lasers.

A mode-locked solid state laser helps to slice a picosecond 10- μm pulse on a semiconductor optical switch. The same laser produces electron bunches at a photocathode gun which are accelerated by the RF linac to the 50 MeV energy. This permits automatic synchronization of the amplified CO₂ laser pulse with a picosecond electron bunch for interaction experiments including: laser acceleration, Compton scattering, etc. The optical diagram in Fig.1 shows the CO₂ laser setup. The system includes: oscillator, picosecond pulse slicer, regenerative amplifier, and large-aperture final amplifier.

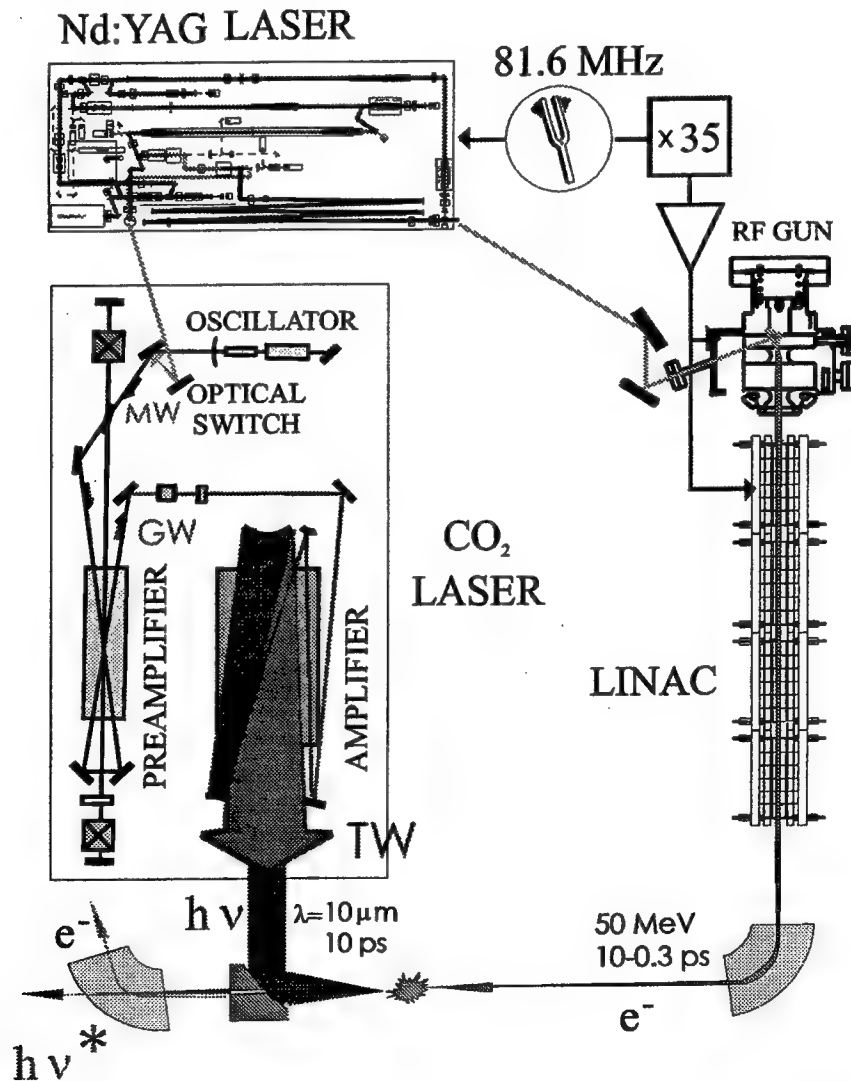


Fig.1 Principle diagram of the ATF laser system and linac synchronized to subpicoseconds for electron-photon interaction experiments

As shown in the floor plan in Fig.2, the system occupies two rooms in the ATF building. Positioning of the high-pressure laser amplifier in Room C1, and its 1-MV Marx generator behind the partition, helps to isolate these potential sources of the EM noise from the computer-interfaced control and diagnostics equipment located in Room C2. By means of an in-vacuum laser beam transport tube, the CO₂ laser system is optically connected with the control Nd:YAG laser located close to the linac front end. Room C2 accommodates the oscillator, picosecond pulse slicer, and preamplifier, all located on the same optical table.

The oscillator and semiconductor switch supply a seed pulse into the regenerative preamplifier with the active discharge volume of 1.2 liters (optical aperture 2×5 cm², discharge length 1.2 m). Extracted by a Pockels cell at several millijoules, the laser pulse is redirected for additional passes through the same discharge cell to acquire ~100 mJ energy. The preamplifier output is directed to the final amplifier stage with the active discharge volume of 10 liters (optical aperture 10 cm, discharge length 1 m). Amplified up to 30 J, picosecond CO₂ laser pulse will be transported to the ATF experimental hall for its use in experiments based on interaction with the relativistic electron beam.

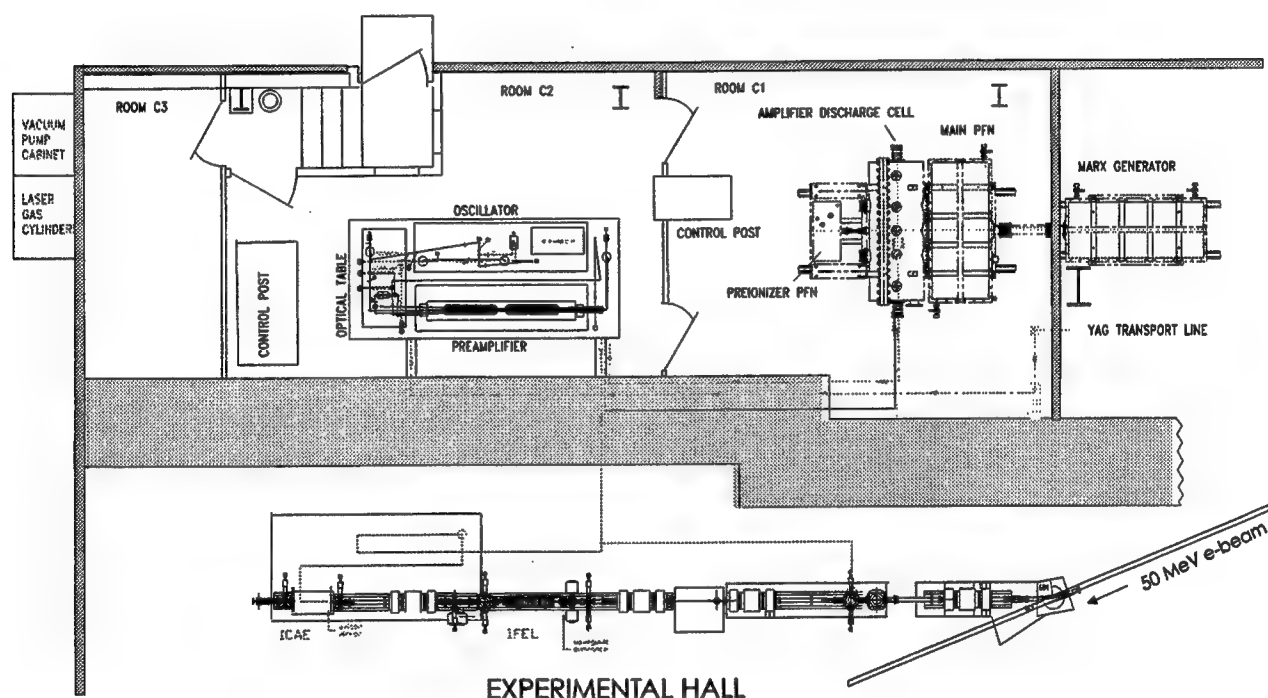


Fig. 2 Fragment of the ATF floor plan showing CO₂ laser rooms and a portion of the experimental hall

2.2 Oscillator

In PITER I, the 10- μ m beam is originated in the hybrid single-longitudinal zero-transverse mode TEA laser oscillator built in collaboration with LANL [6,8]. The oscillator is assembled on the optical table in Room C2. Block-diagram of this device is presented in Fig.3. Single-longitudinal-mode operation of the oscillator is due to a combination of a low-pressure auxiliary discharge tube, used to provide a narrow peak in the gain spectrum, and piezo-electric fine tuning of the oscillator cavity length. Such design permits generation of laser pulses with a smooth temporal envelope (without mode beating) that is needed for the reproducible picosecond slicing. A diffraction grating, used as the end reflector in the laser cavity, selects a predetermined line in the CO₂ rotational spectrum. When the diffraction grating is replaced by a copper mirror, the oscillator operates predominantly at the 10P(20) 10.59 μ m line.

The energy for a TEA discharge is supplied from the 25 kV Blumlein network. An automatic UV preionization is produced by branching a portion of the discharge current onto a preionizer structure inside the TEA discharge head. A separate low-pressure (18 torr) discharge tube is triggered 0.2 ms in advance of the main discharge.

The oscillator output pulse energy is ~150 mJ, about 50% of that is contained in the leading short pulse with the FWHM duration of 75-100 ns. The output beam has a Gaussian spatial profile with a 6 mm diameter at the $1/e^2$ level and the 1.2 mrad angular divergence.

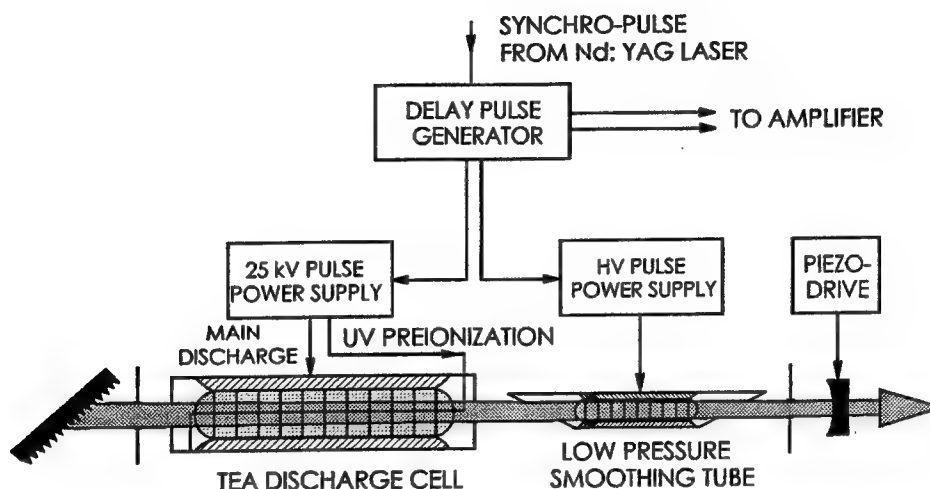


Fig.3 Block-diagram of the hybrid oscillator

2.3 Semiconductor Picosecond Optical Switch

Due to a discrete rotational structure of the gain spectrum, and for other physical and technical reasons, mode-locking techniques do not work for CO₂ lasers as well as for solid state lasers. However, alternative methods to produce picosecond and sub-picosecond CO₂ laser pulses have been developed. One of them is semiconductor optical switching [9].

Illustrated in Fig.4, the optical switching scheme works as follows. The 1 MW, 100 ns, $\lambda=10\ \mu\text{m}$ pulse generated by the CO₂ oscillator is combined with the 5 mJ, 20 ps, $\lambda=1\ \mu\text{m}$ Nd:YAG pulse by the dichroic ZnSe beamsplitter, and both are directed to the Ge Brewster window. Having a photon energy above the band gap of germanium, the Nd:YAG pulse creates a cold electron-hole plasma within the 1 μm surface layer. When the plasma reaches the critical density the refractive index becomes imaginary, and the Ge window, which is normally transparent to the 10- μm radiation, turns to a metal-like mirror. By this process, a 150 ps mid-IR pulse defined by the diffusion of the free-carriers into the bulk material is reflected from the Ge slab. In order to increase the contrast and sharpen the leading edge of the reflected pulse, the same process is repeated at the second reflection switch.

To define the trailing edge of the pulse, thereby shortening it to a few picoseconds, a complement to the reflection switching, transmission switching, is used for a third Ge stage. After a variable time-delay introduced by a prism, the Nd:YAG pulse is directed to the third Ge switch. It truncates the CO₂ laser pulse tail by means of both reflection and absorption.

The angle between the 1- μm and 10- μm beams is kept close to 1° to ensure that the sliced pulse front has a negligible tilt. The polarization rotation of the input Nd:YAG beam by $\lambda/2$ -plates provides the optimum redistribution of the control pulse energy between the reflection and transmission switches.

The reflection switches are placed on rotary stages of the 0.3 arc-sec accuracy. After precise angular adjustment to the Brewster angle, the signal-to-background contrast exceeding 1,000,000:1 has been obtained. A mirror placed on the same

stage as the Ge plate automatically conserves overall alignment of the slicing system during the reflection switch angular tuning.

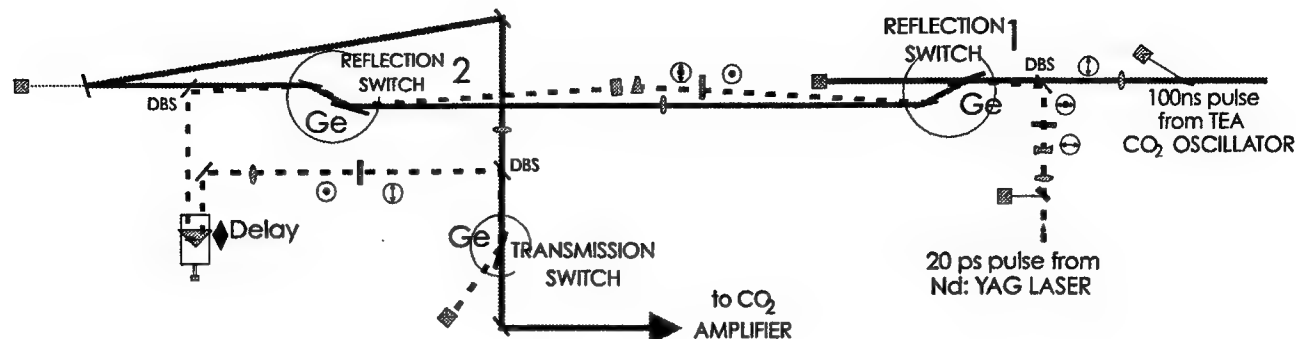


Fig.4 Three-stage semiconductor optical switch

2.4 Preamplifier

The peak power of the sliced CO₂ laser pulse is increased to the 1-10 GW level in a regenerative preamplifier (RP) (see optical scheme in Fig.1). The seed laser pulse is trapped inside the optical cavity by means of the Pockels cell, and is amplified during a predetermined number of round trips until it is kicked from the cavity in a similar manner as it has been trapped.

The operation sequence for the Pockels cells in the regenerative preamplifier is as follows. Linearly polarized seed pulse is introduced along the optic axis of RP by reflection from the surface of the polarizing Brewster beamsplitter. The beamsplitter is designed to reflect s-polarized light and transmit p-polarized light. After a double pass through the $\lambda/4$ -plate, the laser beam polarization is turned 90° and transmitted by the beamsplitter. While the amplified pulse is making its first round trip inside the RP cavity, a HV control pulse reaches the entrance Pockels cell that acts now as the $\lambda/4$ -retarder (7 kV is required for a 5 cm long CdTe crystal). Thus, when the amplified laser pulse reaches the entrance Pockels cell it gets an additional 90° polarization rotation that compensates action of the $\lambda/4$ -plate. That means that the amplified beam stays p-polarized and, hence, is trapped inside the RP cavity as far as the HV potential is kept at the electrodes of the entrance cell.

After the laser pulse is amplified in multiple trips up to the required energy, it shall be released from the RP cavity. We arrange it by activating the exit Pockels cell that, in double pass, rotates the laser polarization 90°. The RP output energy is limited primarily by the optical damage threshold of the Pockels cell crystal that, for picosecond CO₂ laser pulses, is 100 mJ/cm². Hence, the energy of ~20 mJ may be safely transmitted through the crystal of the 1x1 cm² aperture. A saturable absorber and a plasma shutter positioned in the preamplifier output beam serve to increase the signal-to-noise contrast and prevent self-excitation and parasitic ringing in the laser system.

The cross-section scheme of the preamplifier discharge cell is shown in Fig.5. Two 60 cm long high-voltage electrodes are positioned under the ground mesh electrodes. The 35-kV surface discharges, sliding along the sapphire tubes, serve as the sources of the UV ionization. UV photons penetrate through the ground mesh electrode into the discharge region producing initial ionization of the gas mixture. Energized with the 150 kV discharge, the preamplifier can operate at the 5 atm gas pressure. To amplify picosecond pulses, it will be filled with the isotopic gas mixture.

2.5 Amplifier

The terawatt power will be attained in the 10-atm, 10-liter final amplifier. The amplifier for PITER I has been designed and constructed by Optoel Co. The cross-section diagram, together with pictures taken at the test, stand are shown in Fig. 6-8. They illustrate the design and dimensions of the amplifier discharge cell that is the primary component of the amplifier.

Inside the high-pressure stainless steel amplifier discharge cell, there is a high-vacuum chamber of the 100 kV electron gun with the $10 \times 100 \text{ cm}^2$ explosive-emission cathode made with the carbon fibers. The electrons, accelerated up to 80 keV, are stopped at the 80 μm thick titanium foil window where they transfer the energy to the x-rays. The x-rays penetrate through the foil and the mesh ground electrode into the interelectrode space. The x-ray dose of 0.1 R is measured just after the mesh electrode. The x-ray dose drops several times over the 85 mm interelectrode primarily distance due to a geometric spread of the x-ray flux.

The 1 MV potential is applied to the discharge. We ensure that the 5 kJ energy load is delivered within a short time interval, because the uniform discharge breaks down to arcing after about 300 ns. To achieve a fast energy deposition, a low-inductance pulse-forming network (PFN) is installed between the discharge cell and a conventional 10-stage Marx generator. The PFN consists of two water capacitors with the commutation water spark gap. Immersed into water, stainless steel electrode plates of the PFN are adjustable to sharpen the leading front and shorten duration of the voltage pulse delivered to the amplifier discharge.

Further optimization of the amplifier configuration and gas mixture is under way. However, already achieved 3%/cm optical gain is the encouraging result never demonstrated previously in the x-ray preionized CO_2 lasers of such a big volume and a high pressure. The design parameters and results of preliminary tests of the amplifier are summarized in Table 1.

To simulate and optimize the optical design of PITER I, a special software package has been developed. This PC-based program solves a set of Kirchhoff-Fresnel and Franz-Nodvik equations permitting a reasonable prediction of the absolute energy gain and the intensity profile for a laser pulse propagating through the amplifier. The simulations correlate with the experimental results obtained with the ATF CO_2 laser preamplifier. The program helps to optimize the optical components and to reduce diffraction distortions of the laser beam. Fig. 9 demonstrates the result of such optimization. Similar approach used for modeling of the final amplifier permits to establish the optical setup free from parasitic reflections and the output beam distortions. In order to reduce energy losses due to the windows and absorption in the "cold" gas mixture, the folding convex mirrors of the four-pass amplifier are placed on adjustable fixtures inside the high-pressure discharge cell.

The peak power that may be achieved with PITER I depends to the great extent upon the duration of the input sliced pulse. For example for the 10 ps sliced pulse, that is the near term goal for the project, the 100 mJ input to the amplifier results in the 7 J output. With the 3 ps input laser pulse of the 100 mJ energy, the calculated output energy rises to 20 J equivalent to the 7 TW peak power. This higher output can be achieved due to the higher saturation fluence typical for the shorter laser pulse duration. For description of how the laser pulse duration affects the saturation in the picosecond CO_2 laser amplifier we address Ref. [4,10].

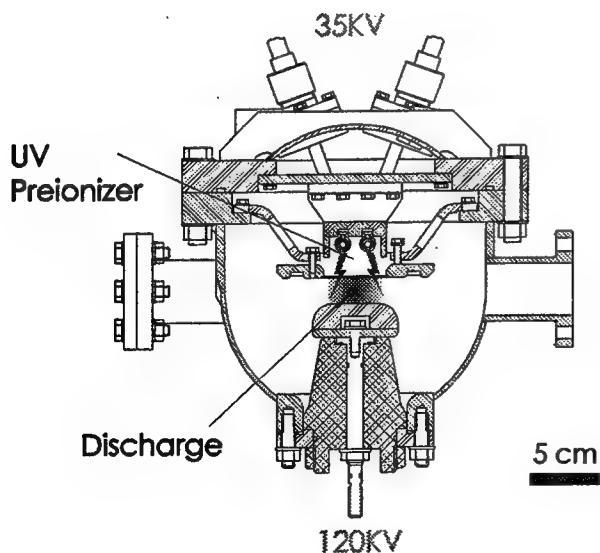


Fig. 5 Diagram of the preamplifier discharge cell

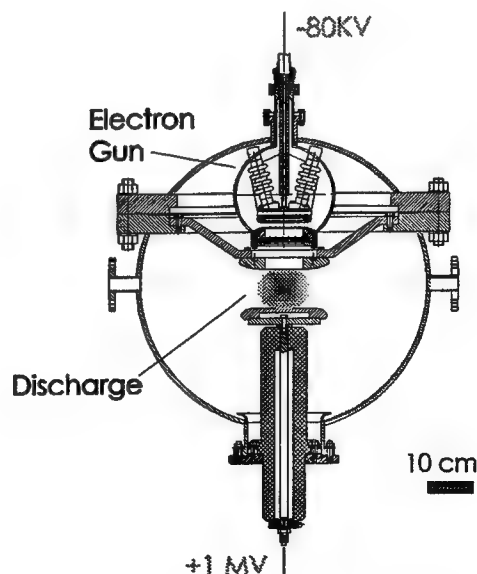


Fig. 6. Diagram of the amplifier cross-section

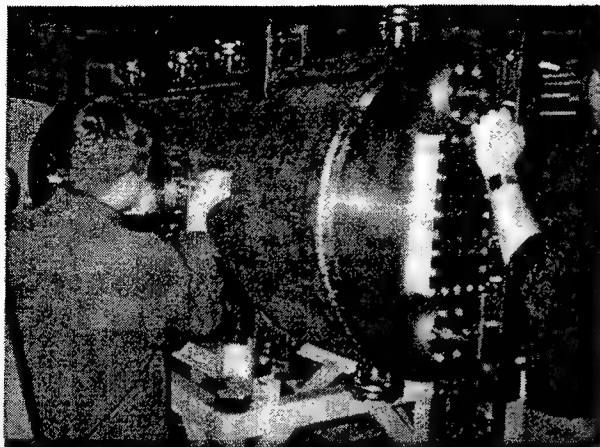


Fig.7 In preparation for pressure test of the amplifier

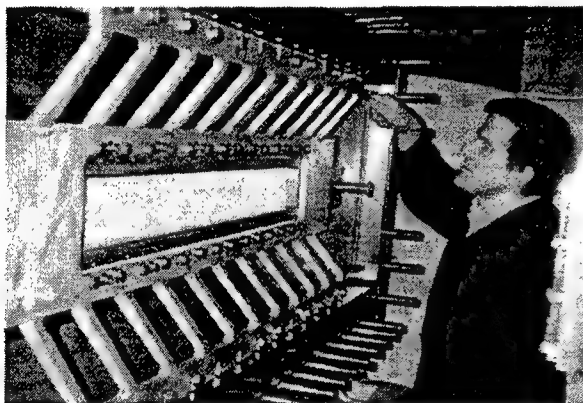


Fig.8 Alignment of ground mesh electrode in the amplifier discharge cell

TABLE 1.
Amplifier design parameters

Pressure	10 atm
Gas Mixture $\text{CO}_2\text{:N}_2\text{:He}$	1:0.5:8.5
Interelectrode Distance	8 cm
Electrode length	1 m
X-Ray Pulse Length	2 μs
X-Ray Dose	0.1 R
Discharge Voltage	1 MV
Stored Electric Energy	5 kJ
Discharge Peak Current	90 kA
Current Pulse FWHM	500 ns
Pulse Front	200 ns
Gain Coefficient	3%/cm
Saturation Energy	0.5 J/cm ²
Input Energy	30 mJ
Number of Passes	4
Output Aperture	80 cm ²
Output Energy	30 J
Laser Pulse Duration	10 ps
Peak Power	3 TW
Repetition Rate	0.1 Hz

The laser will deliver one pulse in several seconds limited primarily by the amplifier power supply and a slow gas circulation through the catalyst. That helps to keep the amplifier of a relatively compact size. As is seen on Fig.2, together with the pulsed power supplies, it occupies a space comparable to a regular size optical table.

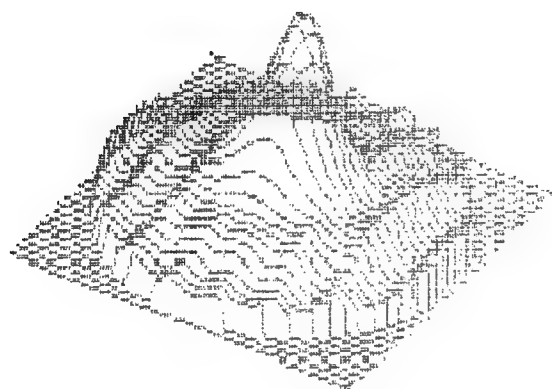
3. PROSPECTS OF PICOSECOND CO_2 LASER TECHNOLOGY AND POTENTIAL APPLICATIONS

3.1 Anticipated Progress of Picosecond CO_2 Laser Technology

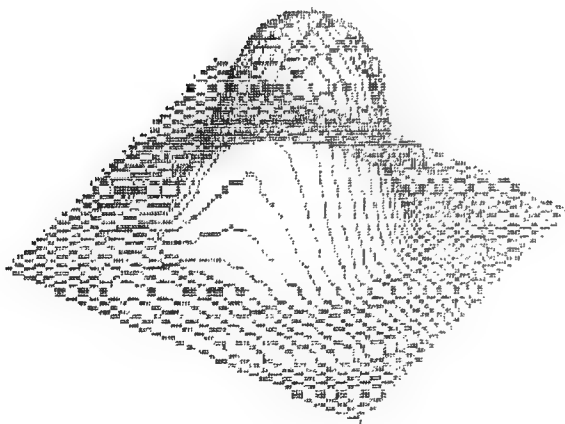
The minimum laser pulse duration sustained by the laser amplifier depends upon the amplifier spectral bandwidth. Smoothing of the rotational structure in the CO_2 spectrum via pressure broadening at about 10 atm permits the picosecond pulse amplification. An alternative way to achieve gain smoothing is to reduce the spectrum modulation period using a CO_2 gas mixture with a combination of the isotopes O^{16} and O^{18} [4,6]. Due to the isotopic shifts, the combined spectrum has 4-times denser rotational line structure than with a regular CO_2 molecule. That permits to reach gain smoothing at a significantly lower gas pressure. Theoretical limit to the pulse duration defined by the total 1 THz bandwidth of the 10P vibrational band of the CO_2 transition is 0.5 ps.

However, it is still not the bottom limit for CO₂ laser pulse shortening. Taking a combination of all available isotopes O^(16,18) and C^(12,13,14) a continuum can be produced that extends over the spectral region of the 7 THz bandwidth (see Fig.11). Then amplification of as short as 100 fs pulse becomes possible [5]. Another method of CO₂ laser pulse shortening uses ionization pulse chirping in a gas [5, 11]. Physics of this process is rather straightforward. Intense laser pulse propagating in a gas produces ionization. As a result the refractive index is nonuniform across the pulse envelope, and the tail of the pulse propagates at a higher speed catching up the front. After a propagation over a certain distance in a gas, or in the dispersive medium, the pulse will shorten. This effect has been observed already by P. Corkum inside the laser amplifier [11]. The CO₂ laser pulse chirping may be organized in a more controlled fashion inside a gas-filled hollow fiber [12]. Other important physical parameters demonstrated or feasible for the picosecond CO₂ laser technology are summarized in Table 2.

Note, that a gain cross-section is comparable to the number achievable with the solid state lasers. However, about ten times smaller concentration of CO₂ molecules in a gas than the active ions in a solid matrix results in a ten times lower gain. In addition, ten times lower photon energy makes the specific stored energy about hundred times less than in solid state lasers.



(a)



(b)

Fig. 9 Simulations of the laser beam distribution at the output of the CO₂ laser preamplifier; a) non-optimum case, b) after the optics optimization

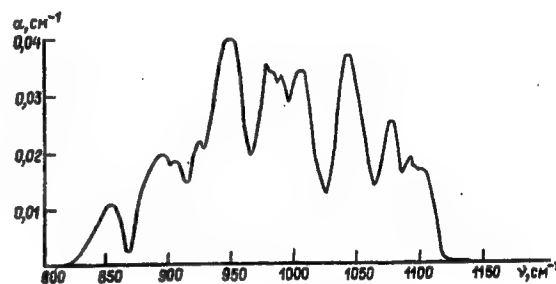


Fig.11 10-atm diluted mixture of CO₂ molecules composed of isotopes C¹², C¹³, C¹⁴, O¹⁶, O¹⁸ has a gain bandwidth (7 THz) sufficient to amplify 100 fs laser pulses [4].

Table 2. Demonstrated and prospective parameters of picosecond CO₂ lasers

Bandwidth (THz)	1-7
Minimum pulse length (ps)	0.5-0.1
Cross section (10 ⁻²⁰ cm ²)	5
Gain (%/cm)	3-4
Saturation energy (J/cm ²)	0.5
Stored energy (J/cm ³)	0.01
Active volume (cm ³)	10,000
Pulse energy (J)	10-100
Peak power (TW)	10-1000
Repetition rate (Hz)	100-1000
Average power (kW)	1-10

However, the big volume of a gas laser makes the total stored energy per CO₂ amplifier stage similar or higher than for a big-aperture slab solid state amplifier. Because of the ease of the heat removal by fast gas exchange in the CO₂ amplifier, it is potentially capable of high repetition rates that are difficult to attain with massive glass or crystal active elements. This is important for future advanced applications.

The prognosis about a possibility of picosecond CO₂ lasers with a kilowatt average power does not look over-optimistic if one recalls the prior achievements of this technology which is capable to the hundreds of kilowatt of the average laser power.

3.2 Prospective Application of Picosecond CO₂ Lasers for Lepton Accelerators and Colliders

T³ solid state lasers stimulated an abundance of new strong-field laser applications including: laser accelerators, ultra-bright x-ray sources, laboratory astrophysics, high excitation of atomic and molecular ions, etc. Emerging terawatt picosecond CO₂ lasers may provide an additional boost to such applications. This is based on the fact that the energy of oscillatory motion acquired by the electron from an electromagnetic wave, called ponderomotive potential, is quadratically proportional to λ ,

$$W_{osc} = e^2 E_L^2 / 2m\omega^2, \quad (1)$$

where e and m are correspondingly the electron charge and mass and ω is the laser frequency $\omega = 2\pi c/\lambda$.

Thus, any process, where the field-induced electron oscillation is paramount, is dramatically enhanced. The examples of such processes are: avalanche and tunneling ionization, plasma wave excitation, Thomson scattering, relativistic self-focusing, etc. Many of these processes are particularly relevant for electron acceleration in plasma.

Progress in the exploration of particle interactions relies upon the development of a new-generation of accelerators on a TeV energy scale. One of the prospective approaches is a linear e^-e^+ collider based on a high-gradient laser acceleration. The enthusiasm that drives research in this area is based on ultra-high electric fields attainable upon the tight focusing of terawatt laser beams. This may permit reduction of accelerator dimensions by orders of magnitude. Among the known laser acceleration techniques, the laser wakefield acceleration (LWFA) [13] is considered as the most promising. The LWFA method is based on the ponderomotive charge separation and a relativistic wake formation when a short laser pulse propagates in underdense plasma.

The amplitude of the accelerating field, E_a , due to the charge separation in a plasma wave is

$$E_a [V/cm] = \left(a^2 / \sqrt{1+a^2} \right) \sqrt{n_e} [cm^{-3}], \quad (2)$$

where n_e is electron density in plasma, and a is the dimensionless laser vector-potential

$$a = eE_L / mc\omega = 0.3E_L [TV/m] \lambda [\mu m]. \quad (3)$$

From Eqs.(2) and (3) we see that $E_a \propto \lambda^2$ for $a \ll 1$ and $E_a \propto \lambda$ for $a \gg 1$. Thus, a 10- μm CO₂ laser is capable of producing an accelerating gradient at least 10 times higher than the 1- μm laser of the same intensity. This is due to the stronger ponderomotive potential of plasma electrons oscillating in a lower-frequency electromagnetic field. For a more detailed discussion on this subject, see Ref. [14].

By Compton backscattering of the laser photons from the TeV electron beam, high brightness TeV photon beam can be created. It opens an opportunity to study a variety of interaction processes by colliding e^- , e^+ and γ beams in any combination and at independently controlled polarization.

The expression for the maximum gamma photon energy for linear (single photon) Compton backscattering is

$$\hbar\omega_\gamma = (x/x+1)E_e, \quad (4)$$

where E_e is the electron energy, and $x = 4E_e \hbar\omega / m^2 c^4$. At $x \gg 1$, the Compton photon energy approaches the electron energy, $\hbar\omega_\gamma \approx E_e$. For CO₂ laser, $x=1$ at $E_e=0.5$ TeV. Thus, the long wavelength of the CO₂ laser used for the $e^\pm \rightarrow \gamma$ converter at $E_e=2.5$ TeV does not degrade significantly ω_γ .

Another strong requirement to the laser wavelength is set by rescattering of gamma photons on the laser beam into pairs through the reaction $\gamma + \lambda \Rightarrow e^- + e^+$. This occurs when $\omega\omega_\gamma > m^2 c^4 / \hbar^2$. Based on this condition, the optimum laser wavelength is derived:

$$\lambda[\mu\text{m}] = 4.2 E_e[\text{TeV}]. \quad (5)$$

Then, for the 2.5 TeV collider the laser with $\lambda = 10.5 \mu\text{m}$ is the most optimum choice.

Lasers may be used also in polarized positron sources for e^-e^+ collider. Here, the backward Compton scattering serves as an intermediate process followed by pair production on a target or via two-photon rescattering. Polarization of the produced particles is easily controlled by the input laser beam. Capable of high average power and delivering ten times more photons than solid state lasers of similar energy, picosecond CO_2 lasers become the optimum choice for this application as well. The projected positron source for the Japan Future Collider at KEK [15] employs a hundred ~ 1 kW CO_2 lasers of 10 ps pulse duration. This project appears to become the biggest utilization of CO_2 lasers in fundamental science. It starts with the US-Japan Compton scattering experiment to be conducted at the BNL/ATF.

ACKNOWLEDGMENTS

Authors wish to thank Z. Segalov, T. Srinivasan-Rao, P. Corkum, F. Altrui, L. Smith, J. Sheehan, R. Cahill, G. Baranov, V. Kuchinsky and others who provided advice and assistance at the different stages of the project. This work was supported by the US Dept. Of Energy under the Contract DE-AC02-76CH00016. A partial support of SPIE provided for attending of the LASER OPTICS'98 Conference is appreciated.

REFERENCES

1. I.J. Bigio, S.V. Jackson, A. Laird, and J. Seagrave, "Beam diagnostics techniques for multiterawatt CO_2 lasers", *Appl. Opt.* **19**, 914-917 (1980); J. Jansen and T.S. Stratton, "A star is born in Los Alamos", *Laser Focus*, 76-84, Nov. 1980
2. V.A. Adamovich, V.N. Anisimov, E.A. Afonin, V.Yu. Baranov, V.L. Borzenko, S.M. Kozochkin, D.D. Malyuta, Yu.A. Satov, A.Yu. Sebrant, Yu.B. Smakovski, A.N. Starostin, A.P. Streltsov, V.M. Petryakov, and S.F. Chalkin, "TIR-1 carbon dioxide laser system for fusion", *Appl. Optics*, **19**, 919-923 (1980)
3. P.B. Corkum and C. Roland, "High energy picosecond 10 μm pulses", *High Intensity Laser Processes. SPIE 664*, 212-216 (1986)
4. V.T. Platonenko and V.D. Taranukhin, "Coherent amplification of light pulses in media with a discrete spectrum", *Sov. J. Quant. Electron.*, **13**, 1459-1466 (1983)
5. Z.A. Biglov and V.M. Gordienko, *Current Problems in Laser Physics 4*, Moscow 1991, 84-125 (in Russian)
6. T. Shimada, I.J. Bigio, N.A. Kurnit, and R.F. Harrison, "Large-volume high-pressure CO_2 laser for ultrashort pulse amplification", in *Proceedings of CLEO'88*, paper FD2, 422-423 (1988)
7. I.V. Pogorelsky, I. Ben-Zvi, M. Babzien, K. Kusche, J. Skaritka, I. Meshkovsky, A. Dublov, V. Lekomtsev, I. Pavlishin, and A. Tsunemi, "The first picosecond terawatt CO_2 laser at the Brookhaven Accelerator Tests Facility", *Proceedings of LASERS'97*, New-Orleans, LU, December, 1997 (to be published).
8. I.V. Pogorelsky, J. Fischer, K.P. Kusche, M. Babzien, N.A. Kurnit, I.J. Bigio, R.F. Harrison, and T. Shimada, "Subnanosecond multi-gigawatt CO_2 laser", *IEEE J. Quant. Electron.* **31**, 556-566 (1995)
9. A.J. Alcock and P.B. Corkum, "Ultra-fast switching of infrared radiation by laser-produced carriers in semiconductors", *Can. J. Phys.* **57**, 1280-1290 (1979)
10. I. Pogorelsky, I. Ben-Zvi, W.D. Kimura, N.A. Kurnit, and F. Kannari, "Picosecond CO_2 laser for relativistic particle acceleration", *Infrared Phys. Technol.* **36**, 341-354 (1995)
11. P.B. Corkum, "Amplification of picosecond 10 μm pulses in multi-atmosphere CO_2 lasers", *IEEE J. Quant. Electron.* **QE-21**, 216-232 (1985)
12. P.B. Corkum private communication
13. T. Tajima & J.M. Dawson, "Laser electron accelerator", *Phys. Rev. Lett.* **43**, 267-270 (1979)
14. I.V. Pogorelsky, "Prospects for Laser Wakefield Accelerators and Colliders Using CO_2 Laser Drivers", presented at the ICFA Workshop, Kyoto, Japan, July 14-18, 1997, to be published in *Nuclear Instrum. & Methods Phys. Res., A*
15. T. Okugi, Y. Kurihara, M. Chiba, A. Endo, R. Hamatsu, T. Hirose, T. Kumita, T. Omori, Y. Takeuchi, and M. Yosioka, "Proposed method to Produce a Highly Polarized e^+ Beam for Linear Colliders", *Jpn. J. Appl. Phys.*, **35**, 3677 (1996).

Ionization processes by intense laser pulse interaction with solid targets

N.E.Andreev^{1*}, I.L.Beigman², V.V.Kostin¹,
M.Ef.Veisman[†] and A.M.Urnov²

¹ High Energy Density Research Center,
Izhorskaya street 13/19, 127412 Moscow, Russian Federation;
² Lebedev Physics Institute,
Leninsky Prospect 53, 117924 Moscow, Russian Federation

ABSTRACT

The ionization dynamics of plasma, created on the surface of solid-state target irradiated by high power sub-picosecond laser pulses, is studied. The laser energy absorption, heating, expansion and ionization of the target matter are taken into account self-consistently.

We have employed and compared two different models of ionization: quasistationary (Saha) model and non-stationary model of average ion. Next, we have demonstrated the influence of ionization processes on plasma dynamics.

1 Introduction

We have studied the thermal ionization phenomena and its influence on the dynamics of heating of high-density hot plasma created on the surface of solid-state aluminum target, heated by intense (intensities $I_0 = 10^{15} - 10^{17} \text{ W/cm}^2$) short (durations $t_{FWHM} < 1 \text{ ps}$) laser pulses. The investigation is performed using 1-D Lagrangian computer code,¹ which was modified by taking into account ionization-recombination phenomena.

The ionization is described by the two means. The first one is quasistatic Saha model. The second one is nonstationary model, based on the Lotz expression for the rate of electron impact ionization² and shell model of average ion. This shell model assumes that only one kind of ions with continuously changing charge is available in plasma. In the case of quasistatic model we demonstrate, that the influence of the ionization on the dynamics of thermal wave propagation in the target matter can be taken into account in the form of additional "ionization thermocapacities". In the case of nonstationary calculations the shell model of the average ion makes it possible to use one equation for average ion charge instead of z_n equations (where z_n is the nuclear charge) for ions with charges $1 \dots z_n$ (if excited levels are disregarded).

It is demonstrated that in the region of dense high temperature plasma, the quasistatic ionization model can be

* e-mail:andreev@laslab.ras.ru

† e-mail:bme@hedric.msk.su

in a reasonable agreement with nonstationary one if the maximum ion charge is restricted by the value of $z_n - 2$ in the quasistatic case. This restriction is important at times less than $1ns$ due to long time, necessary to ionize the electrons in the most inner shell with very high ionization potentials. In the low-density layer of plasma corona the quasistatic ionization model overestimates the ionization rate. However, this circumstance does not lead to considerable overestimation of the rate of plasma heating because of the weak dependence of plasma temperature on the average ion charge.³

2 The ionization models

2.1 Equations for ion and electron concentrations

The ionization is described by the following equations for concentrations n_z of ions with charges z ($z = 0$ for neutral atoms) and electron concentration $n = \sum_{z=1}^{z_n} z n_z$ (quasineutrality is assumed):

$$\begin{aligned} \frac{\partial n_z}{\partial t} + \text{div}(n_z \mathbf{U}) &= S_z, \\ S_z &= W_z n_{z-1} + R_z n_{z+1} - (W_{z+1} + R_{z-1}) n_z, \\ S_0 &= R_0 n_1 - W_1 n_0, \quad S_{z_n} = W_{z_n} n_{z_n-1} - R_{z_n-1} n_{z_n}, \end{aligned} \quad (1)$$

$$\frac{\partial n}{\partial t} + \text{div}(n \mathbf{U}) = S = \sum_{z=1}^{z_n} z S_z = \sum_{z=0}^{z_n-1} (W_{z+1} n_z - R_z n_{z+1}), \quad (2)$$

where z_n is the nuclear charge; \mathbf{U} is the velocity of quasineutral plasma motion, equal to the ion fluid velocity; W_{z+1} and R_z are the ionization frequency for ions with charge z and recombination frequency for ions with charge $z+1$ respectively (indexes $z+1$ and z denote the charge of created ion).

The continuity equation for concentration of all ions, including neutral atoms, $n_i = \sum_{z=0}^{z_n} n_z$ reads as in the following case without ionization:

$$\frac{\partial n_i}{\partial t} + \text{div}(n_i \mathbf{U}) = 0. \quad (3)$$

The plasma created on the target surface is optically thin; therefore,

$$W_{z+1} = n K_{z+1}^{(i)}, \quad R_z = n^2 K_z^{(r)} + n (K_z^{(d)} + K_z^{(\nu)}), \quad (4)$$

where $K_{z+1}^{(i)}$ is the rate of ionization by electron impact, $K_z^{(r)}$, $K_z^{(d)}$ and $K_z^{(\nu)}$ are the rates of three-body, dielectron and radiative recombination respectively.

In the models, described below, we accept low population of excited levels.

2.2 Quasistationary ionization model

If the inequality

$$|W_{z+1} n_z - R_z n_{z+1}| \ll W_{z+1} n_z \text{ and } R_z n_{z+1}$$

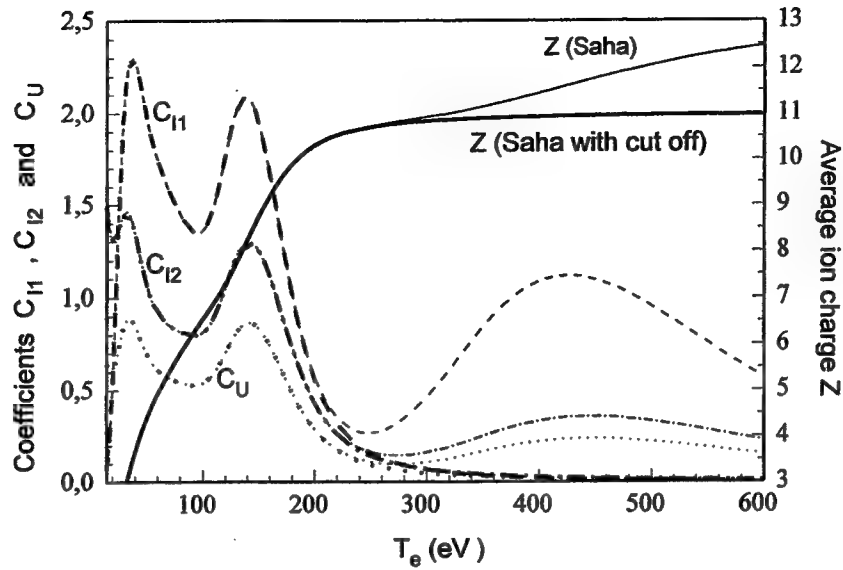


Figure 1: Average ion charge Z (solid lines), ionization thermocapacities C_{i1} (dashed lines) and C_{i2} (dash-dotted lines) and coefficient C_U (dotted lines) for solid-density aluminum plasma ($n_i = 610^{22} \text{ cm}^{-3}$). Thin lines stand for Saha model and thick lines represent the "Saha with cut off" model.

is fulfilled, then the quasistationary model of thermal ionization $n_z = n_z(T_e(t), n(t))$ can be employed (T_e is the electron temperature). In this case the ionization sources S_z in equations (1) can be written as

$$S_z \approx \frac{\partial n_z}{\partial T_e} \left(\frac{\partial}{\partial t} + \mathbf{U} \nabla \right) T_e + \text{div}(\mathbf{U}) \left(n_z - n_i \frac{\partial n_z}{\partial n_i} \right), \quad (5)$$

where concentrations n_z are obtained by equations $W_{z+1}n_z = R_z n_{z+1}$. We suppose that the plasma is sufficiently dense, so that $nK_z^{(r)} \gg K_z^{(d)} + K_z^{(\nu)}$. Then, the ionization equilibrium is described by Saha equations:

$$\frac{n_{z+1}}{n_z} = \frac{2g_{z+1}}{g_z} \frac{mT_e}{2\pi\hbar^2 n} \exp(-J_z/T_e), \quad (6)$$

where g_z is the statistical weight and J_z is the ionization potential of ions with the charge z .

He-like and H-like ions have very high ionization potentials and consequently, low ionization rates (the estimated characteristic ionization time is greater than 1 ns). Therefore, it is reasonable to restrict the maximum ion charge by the value of $z_n - 2$. This model is called further as the "Saha with cut off" model. The average ion charge $Z = n_i^{-1} \sum_{z=1}^{z_n} z n_z$, calculated by Saha and "Saha with cut off" models for solid-density aluminum plasma is shown on the Figure 1.

2.3 Nonstationary ionization model

The evaluation of the characteristic time of radiative recombination $\tau^{(\nu)} \sim [nK_z^{(\nu)}]^{-1}$ by the Seaton model⁴ shows that $\tau^{(\nu)} \gg 1 \text{ ps}$ for high temperature ($T_e \gg 1 \text{ eV}$) laser-produced plasma. Therefore, the account of $K_z^{(\nu)}$

is insignificant at the considered subpicosecond time intervals. The account of dielectron recombination is also not important for electron densities $n_e < 10^{24} \text{ cm}^{-3}$.² Hence, only the first term in the expression (4) for R_z should be considered.

With allowance made for a detailed balance principle, the following is an equation for the average ion charge $Z = n_i^{-1} \sum_{z=1}^{z_n} z n_z$:

$$\begin{aligned} \frac{\partial Z}{\partial t} + (\mathbf{U} \nabla) Z &= \frac{S}{n_i} = Z \left[1 - \frac{Z}{Z_{eq}} \right] \sum_{z=0}^{z_n-1} K_{z+1}^{(i)} n_z \\ &\approx Z n_i \left[1 - \frac{Z}{Z_{eq}} \right] K^{(i)}(Z), \\ K^{(i)}(Z) &= 6 \cdot 10^8 \frac{\text{cm}^3}{c} \sum_{k=1}^3 \xi_k(Z) e^{-J_k/T_e} \left(\frac{J_H}{J_k} \right) \left(\frac{J_H}{T_e} \right)^{1/2} \phi \left(\frac{J_k}{T_e} \right), \\ \xi_k(Z) &= 2k^2 q \left(\frac{z_n - P_{k-1} - Z}{2k^2} \right), \quad \phi(x) = -e^x \text{Ei}(-x), \\ J_k(Z) &= \left(z_n - P_{k-1} - \xi_k(Z) + 1 \right)^2 \frac{J_H}{k^2}, \end{aligned} \quad (7)$$

where Z_{eq} is the equilibrium average ion charge at the given temperature and density, which is determined from equations (6); ξ_k is the number of electrons on the k^{th} shell, $P_k = 0, 1, 2, 8, \dots$ for $k = 0, 1, 2, 3, \dots$; the function $q(x) = 0$ for $x < 0$, 1 for $x > 1$ and x for $0 \leq x \leq 1$; J_k is the ionization potential of k^{th} shell of the "average ion" and J_H is the ionization potential of Hydrogen.

In equations (7) we replace the sum $\sum_{z=0}^{z_n-1} K_{z+1}^{(i)} n_z / n_i$ by the function $K^{(i)}(Z)$ and explore semiempirical Lotz formula² for $K_{z+1}^{(i)}$ in the expression for $K^{(i)}(Z)$. The equation (7) for $K_{z+1}^{(i)}$ can be called as "The average ion approximation".

3 Equation for electron temperature

The common equation for electron temperature reads as⁵

$$\begin{aligned} \frac{3}{2} n \left(\frac{\partial T_e}{\partial t} + \mathbf{U} \nabla T_e \right) &= -\text{div } q_T + Q_L - n T_e \text{div } \mathbf{U} - Q_{e-i} \\ &\quad - \frac{3}{2} T_e S - Q_i, \end{aligned} \quad (8)$$

$$Q_i = \sum_{z=1}^{z_n} S_z \sum_{l=1}^z J_l. \quad (9)$$

The terms q_T , Q_L and Q_{e-i} denote the electron thermal flux, the density of absorbed power of laser radiation and the electron-ion energy relaxation power respectively (see⁵ for details). The term Q_i describes the losses on the thermal ionization.

In the case of nonstationary model (7) the term Q_i can be rewritten as the following:

$$Q_i = n_i^2 Z [1 - Z/Z_{eq}] K^{(i)}(Z) J_k(Z), \quad (10)$$

where $k(Z) = 3$ for $Z < z_n - 10$, $k(Z) = 2$ for $z_n - 10 \leq Z < z_n - 2$, $k(Z) = 1$ for $Z \geq z_n - 2$, and Z_{eq} is determined with the help of (6).

In the case of quasistatic ionization model the expression (5) allows to rewrite the equation (8) in the following form :

$$\left(\frac{3}{2} + C_{I1} + C_{I2}\right) n \left(\frac{\partial}{\partial t} + \mathbf{U} \nabla\right) T_e = -\operatorname{div} \mathbf{q}_T + Q_L \quad (11)$$

$$-(1 + C_U) n T_e \operatorname{div} \mathbf{U} - Q_{e-i},$$

$$C_{I1} = \frac{1}{n} \sum_{z=1}^{z_n} \frac{\partial n_z}{\partial T_e} \sum_{k=1}^z J_k, \quad C_{I2} = \frac{3T_e}{2n} \sum_{z=1}^{z_n} z \frac{\partial n_z}{\partial T_e},$$

$$C_U = -\frac{n_i}{Z} \sum_{z=1}^{z_n} \frac{\partial(n_z/n_i)}{\partial n_i} \left(\sum_{k=1}^z \frac{J_k}{T_e} + \frac{3}{2} z \right),$$

where coefficients C_{I1} and C_{I2} , shown on the Figure 1, can be treated as "ionization thermocapacities". The coefficient C_U is of minor importance since $\operatorname{div} \mathbf{U} \neq 0$ only at plasma surface, which is rapidly heated to temperatures, corresponding to the small values of C_U (see Figure 2).

Some difference in the shape of coefficients C_{I1} , C_{I2} and C_U , shown on the Figure 1 and in the ref.⁵ is connected with approximation $g_{z+1}/g_z = 1$ adopted in the ref.⁵. Though this approximation has noticeable effect on ionization thermocapacities, it does not practically change the value of $Z(T_e)$ and the dynamics of plasma heating.

4 Hydrodynamical equations and equation for ion temperature

The ionization does not change the form of continuity equation (3) and equation of motion of quasinutral plasma :

$$\frac{\partial \mathbf{U}}{\partial t} + \mathbf{U} \nabla \mathbf{U} = -\frac{\nabla [n_i Z T_e + P_i]}{n_i M} + \mathbf{F}_p, \quad (12)$$

where P_i is the ion fluid pressure and \mathbf{F}_p is the ponderomotive force (see ref.⁵ for details). The equation for ion temperature T_i is also unchanged:

$$n_i \left(C_i \frac{\partial T_i}{\partial t} + \mathbf{U} \nabla T_i \right) = -P_i \operatorname{div} \mathbf{U} + Q_{e-i}, \quad (13)$$

where C_i is the ion thermocapacity, the thermoconductivity of ions is neglected.

5 Simulation results

Figures 2 & 3 show the results of calculations of subpicosecond laser pulse (peak intensity $I_0 = 10^{17} \text{ W/cm}^2$, wavelength $\lambda_0 = 0.35 \text{ mkm}$ and duration $t_{FWHM} = 200 \text{ fs}$) with aluminum target. Solid lines show the results obtained by the nonstationary model of ionization (7), (8) and (10); dotted lines show the results for the nonstationary model, but without recombination (i.e., the factor $[1 - Z/Z_{eq}]$ in (7) is forced to be 1) and dashed lines show calculations with Saha model according to equations (11) & (6). Lines marked by the cycles show the results for unmovable (frozen) ions obtained with Saha (open cycles) and nonstationary (closed cycles) ionization models. It should be noted, that in the latter case the results obtained with and without account of recombination are practically identical.

One can conclude that quasistationary "Saha model with cut off" ensures satisfactory description of ionization in the dense and hot layer of plasma at the target surface (region between 0 and 100 nm on the Figure 3b). At the low-density corona region Saha model substantially overestimates the average charge of ions in plasma (compare dashed and solid curves on the figure 3b), that is connected with ion motion.

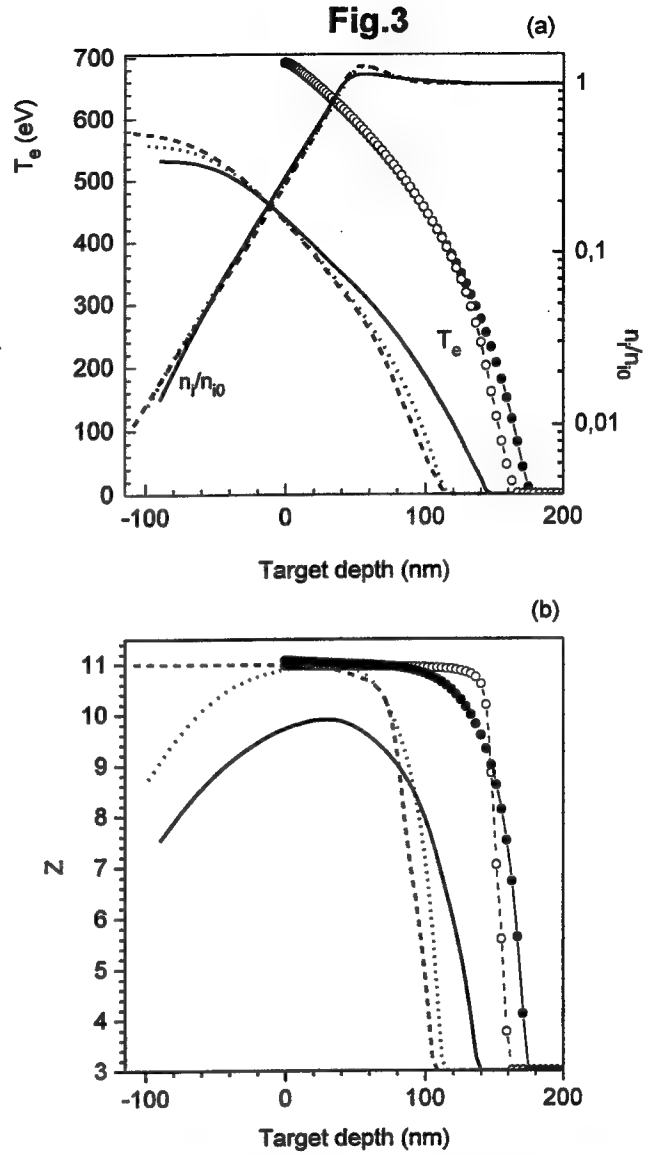
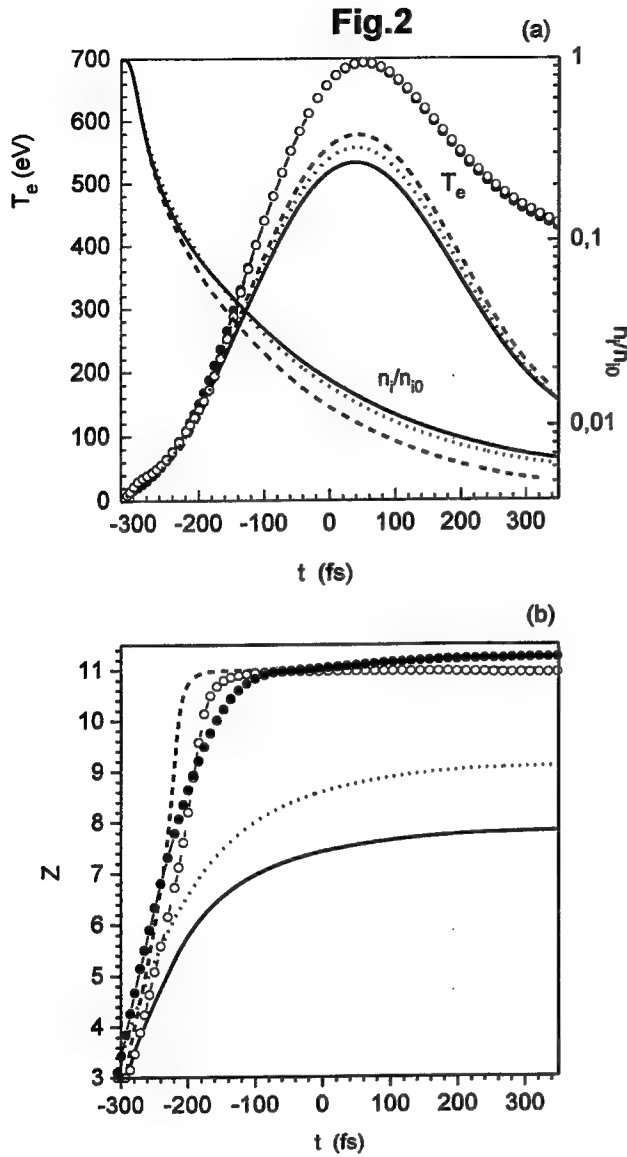


Figure 2: Time evolution of (a) electron temperature and ion concentration (normalized on the initial ion concentration $n_{i0} = 6 \cdot 10^{22} \text{ cm}^{-3}$) and (b) average ion charge at the target surface. Solid lines show results for nonstationary model of ionization. Dotted lines represent nonstationary model of ionization without three-body recombination, and dashed lines stand for Saha with cut off model of ionization. Lines marked by cycles show calculations in the case of "frozen" ions according to the Saha (open cycles) and the nonstationary (closed cycles) ionization models. Results are shown for Gaussian laser pulse with peak intensity $I_0 = 10^{17} \text{ W/cm}^2$, duration $t_{FWHM} = 200 \text{ fs}$ and wavelength $\lambda_0 = 0.35 \text{ mkm}$, normally incident on Aluminum target with $n_{i0} = 6 \cdot 10^{22} \text{ cm}^{-3}$.

Figure 3: Space distributions of (a) electron temperature and ion concentration and (b) average ion charge at time moment $t = 40 \text{ fs}$. The target surface is initially at $x = 0$. Designations and parameters are the same as on the Figure 2.

The ion motion leads to considerable decrease of the ion density at the target surface (see Figure 2a & Figure 3a). Therefore, ionization rate $K^{(i)}$ (7) decreases and becomes substantially lower, compared to one obtained with Saha model. As it is seen from the Figure 2b, at the target surface the average ion charge, obtained by the nonstationary model, achieves only the value ≈ 7.5 during the laser pulse action, while according to the Saha model, it achieves the value of $z_n - 2 = 11$ as soon as plasma temperature exceeds 200 eV (see Figure 1).

The account of recombination additionally reduces the average ion charge. The recombination, on the other hand, leads to the deeper propagation of thermal and ionization waves in the target material (compare solid and dotted curves on the Figure 3). The reason is that the recombination reduces the ionization losses, which, in turn, reduce the rate of the thermal wave propagation.⁵ The striking feature of the Figure 3 is that in the case of nonstationary ionization model the ionization front propagates deeper, as compared to the case of Saha model. This is connected, as was already mentioned above, with account of ionization losses, which are larger for Saha model due to higher ionization rate in this case (see Figures 2b & 3b). Larger ionization losses according to Saha model decrease the rate of the thermal and, consequently, ionization waves propagation (compare solid and dashed lines on the Figure 3a,b).

Despite of the mentioned discrepancies between nonstationary and Saha ionization models, the latter provides reasonable description of the rate of plasma heating (Figure 2a). This fact is connected with weak dependence of $T_e(t)$ on Z .³ The depth of the thermal wave propagation and the energy, stored in the electron component, are also described satisfactorily with the help of the Saha model (see Figure 3a).

6 Conclusions

1. For subpicosecond laser pulses the dynamics of plasma temperature and energy deposition are weakly dependent on the kind of employed ionization model (nonstationary or quasistatic).
2. In the low-density layer of plasma corona the Saha model substantially overestimates the ionization dynamics due to the plasma expansion. In the region of dense plasma (with the density closed to the solid-state one) the agreement between nonstationary and quasistatic models is better. However, nonstationary model provides deeper propagation of the thermal and ionization waves, as compared to Saha model, due to lower ionization losses in the former case.
3. The difference of ionization losses in two models is connected mainly with account of recombination in the nonstationary model, which substantially increase transient time.
4. Under approximation of immovable ("frozen") ions the results obtained with the Saha and the nonstationary ionization models are in a good agreement.

7 Acknowledgments

The work was supported by grant intas-RFBR 95 0875.

M. E. V. appreciates ISSEP for the financial support (grant no. a98-21-74).

8 REFERENCES

- [1] N.E.Andreev, V.E.Fortov, V.V.Kostin, M.E.Veisman, High Temperature **34**, 373 (1996).

- [2] D. Salzman, A. Krumbein, J. Appl. Phys. **49**, 3229 (1978)
- [3] Andreev, N.E. et al., Plasma Physics Reports **21**, 677 (1995).
- [4] M. Seaton, Mon. Not. of the Royal Astronom. Soc., **119** 81 (1959)
- [5] N.E.Andreev, V.V.Kostin and M.E.Veisman, Redistribution of energy in dense matter irradiated by short intense laser pulses, to be published in Physica Scripta (1998).

A temporal structure of a short, powerful laser pulse under an operation of ionization processes

M.V. Chegotov

High Energy Density Research Center, Joint Institute for High Temperatures
Russian Academy of Sciences, Izorskaya St., 13/19, Moscow 127412, Russia
E-mail: nloiko@sci.lebedev.ru

ABSTRACT

It is shown, that the essential laser pulse energy depletion due to ionization losses occurs at rather large distances only. The process of depletion is accompanied by a significant steepening of the temporal pulse form corresponding to the formation of a sharp ionization front of a medium density. The latter, in turn, becomes sharper, suffering an inverse influence of the steepening of a laser pulse temporal structure. The analysis of spatial and temporal evolution of magnitude of the laser pulse form steepening is carried out.

1 INTRODUCTION

In recent time a propagation of the short powerful laser in substance is under a great consideration. The reasons of the increased interest to this subject are according a wide range of applications, such as laser-plasma accelerators,¹ x-ray lasers,² laser-plasma channeling.³

The effect of laser pulse energy depletion because of the ionization processes during the pulse propagation in ionizing gas was mentioned earlier in the results of numerical solutions in.^{4,5}

Here the analytical model of a one-dimensional short powerful laser pulse propagation in ionizing medium is under consideration. In particular, it is shown, that the essential laser pulse depletion due to ionization losses occurs at rather large distances only. The process of depletion is accompanied by a significant steepening of the temporal pulse form corresponding to the formation of a sharp ionization front of a medium density. The latter, in turn, becomes sharper, suffering an inverse influence of the steepening of a laser pulse temporal structure. The analysis of spatial and temporal evolutions of magnitude of the steepening is carried out.

2 THE BASIC EQUATIONS

We consider a plane electromagnetic wave of frequency ω , incident from area $x < 0$ on the boundary $x = 0$ of homogeneous substance located in area $x > 0$. On the boundary $x = 0$ we consider a given intensity of an

electromagnetic wave:

$$I(x=0, t) = I_p(t) = c \frac{|E_p(t)|^2}{8\pi} . \quad (1)$$

Here c is the velocity of light, $E_p(t)$ the amplitude of an electrical field of an electromagnetic wave, so a full electrical field $\varepsilon(x, t)$ on the boundary $x = 0$ has a form $\varepsilon(x=0, t) = E_p(t) \cos(\omega t)$. As at rather small pressure of ionized gas the bremsstrahlung absorption of an electromagnetic energy of short, powerful laser pulse is less effective on a comparison with losses on ionization, we take into account only ionization losses. Then the equation describing spatial and temporal evolution of a laser radiation intensity in ionized substance has a form (compare with^{4,5})

$$\left(\frac{\partial}{\partial x} + \frac{1}{v_g} \frac{\partial}{\partial t} \right) I = - \sum_a \sum_k W_{a,k} \cdot n_{a,k} \cdot U_{a,k} . \quad (2)$$

Here $W_{a,k}$ ($n_{a,k}$) is the rate of ionization (density) of ions of substance a with ionization degree k and with a potential of ionization $U_{a,k}$; v_g the group velocity of laser pulse of intensity $I = c |E|^2 / 8\pi$. As shown in work^{4,6} the ionization of atoms and ions occurs on the tunnel mechanism in a rather wide range of parameters of a laser radiation in substance. Thereof the ionization rate $W_{a,k}$ we describe with the help of so-called ADK formulas⁷:

$$W_{a,k} = 6.66 \cdot 10^{16} \frac{(k+1)^2}{(M_{a,k})^{4.5}} \left[10.87 \frac{(k+1)^3}{(M_{a,k})^4} \frac{E_{at,u}}{E} \right]^{2M_{a,k}-1.5} \exp \left(- \frac{2}{3} \frac{(k+1)^3}{(M_{a,k})^3} \frac{E_{at,u}}{E} \right) \quad (3)$$

Here $W_{a,k}$ is measured in $1/sec$, $E_{at,u} = 5.142 \cdot 10^9 V/cm$, E the amplitude of an electrical field of an electromagnetic wave measured in V/cm , $M_{a,k} = (k+1) \sqrt{13.606/U_{a,k}}$, $U_{a,k}$ is measured in eV . Meaning, that characteristic times of recombination processes at small substance densities exceed duration of laser pulse, the equations for ion densities have the following form (compare with^{4,5})

$$\frac{\partial n_{a,k+1}}{\partial t} = -W_{a,k+1} n_{a,k+1} + W_{a,k} n_{a,k} , \quad (4)$$

the loss of a neutral atom density of substance a $n_{a,0}$ is described by the equation

$$\frac{\partial n_{a,0}}{\partial t} = -W_{a,0} n_{a,0} , \quad (5)$$

and the increase of a completely ionized atoms density of substance a with a charge of the kernel Z $n_{a,Z}$ is determined from the equation

$$\frac{\partial n_{a,Z}}{\partial t} = W_{a,Z} n_{a,Z-1} . \quad (6)$$

To the equation (2) it is necessary to add boundary (1), and to the equations (4) - (6) the initial conditions, which we consider homogeneous in space:

$$n_{a,k}(x, t = -\infty) = N_{a,k} . \quad (7)$$

3 AN ANALYTICAL MODEL

Starting the analysis of a system (1) - (7) we notice first of all that because of the rather large difference of potentials $U_{a,k-1}$, $U_{a,k}$, $U_{a,k+1}$ the processes of ionization of various atom envelopes of one substance appear to be carried in time in the same point of space and carried in space if the same instant is considered. It means, that in the given point of space during a defined time interval (time of ionization of the appropriate atom envelope) the only one term brings the basic contribution to the right side of the equation (2). Let, for a clarity, it will be a term proportional to $n_{a,k}$. Thus the equation for $n_{a,k}$ has the form

$$\frac{\partial n_{a,k}}{\partial t} = -W_{a,k} n_{a,k} . \quad (8)$$

At the same approach the equation for I looks as follows

$$\left(\frac{\partial}{\partial x} + \frac{1}{v_g} \frac{\partial}{\partial t} \right) I = -W_{a,k} \cdot n_{a,k} \cdot U_{a,k}. \quad (9)$$

As long as $W_{a,k}$ is determined by magnitude $|E| \propto \sqrt{I}$ only (see (3)), one has $W_{a,k} = W_{a,k}(I)$ and the system of two equations (8), (9) appears to be closed on itself. Further for a simplicity of the formulas we omit indexes a, k .

It is possible to transform the set of equations(8), (9) with initial-boundary conditions(1), (7) to one integral equation

$$\int_{I_p(u)}^I \frac{ds}{W(s)} + \int_{-\infty}^u I(u', x) du' + UNx = \int_{-\infty}^u I_p(t') dt', \quad (10)$$

where $u = t - x/v_g$ is the time in a frame, accompanying pulse, and $W(s)$ the ionization rate as function of intensity. Indeed, differentiating (10) in new variables u, x at first on u

$$\frac{1}{W(I)} \frac{\partial I}{\partial u} + I(u, x) = \frac{1}{W(I_p)} \frac{dI_p}{du} + I_p(u), \quad (11)$$

and then on x and, taking into account, that in new variable

$$n = -\frac{1}{UW} \frac{\partial I}{\partial x},$$

we obtain the equation

$$\frac{\partial n}{\partial u} = -Wn,$$

thus coming back to the system (8), (9). Adverting to the analysis of the equation (10) we notice, that the influence of ionization process to the ion density n (or neutrals at $k = 0$) will be evident, when for complete duration of pulse

$$\int_{-\infty}^{+\infty} W(I_p(t)) dt \geq 1. \quad (12)$$

Indeed, from the equation (8) one has at the boundary of substance entrance $x = 0$

$$n(x = 0, t) = N/G(t), \quad (13)$$

where $G(t) = \exp \left(\int_{-\infty}^t W(I_p(t')) dt' \right)$, so the significant modification of the density n can be expected, when the inequality (12) is satisfied only. Therefore further we consider, that the relation (12) is fulfilled.

As it is clear from the formula (13) the influence of ionization to the density n is essential at once on the entrance boundary of the substance at conditions (12). However action of ionization on laser pulse intensity appears to be negligible in the vicinity of the entrance boundary of the substance, when the following inequality is fulfilled

$$x \ll x_d = G(u_*) \cdot I_p(u_*) / (W(I_p(u_*)) \cdot N \cdot U). \quad (14)$$

Here u_* is the moment when function $D(u)$

$$D(u) = N \cdot U \cdot W(I_p(u)) / (I_p(u) \cdot G(u))$$

reaches a maxima. Thus $x_d = 1/D(u_*)$. At such penetration depths x we obtain from (10) for laser pulse depletion process

$$I(x, u) \approx I_p(u) (1 - x \cdot D(u)). \quad (15)$$

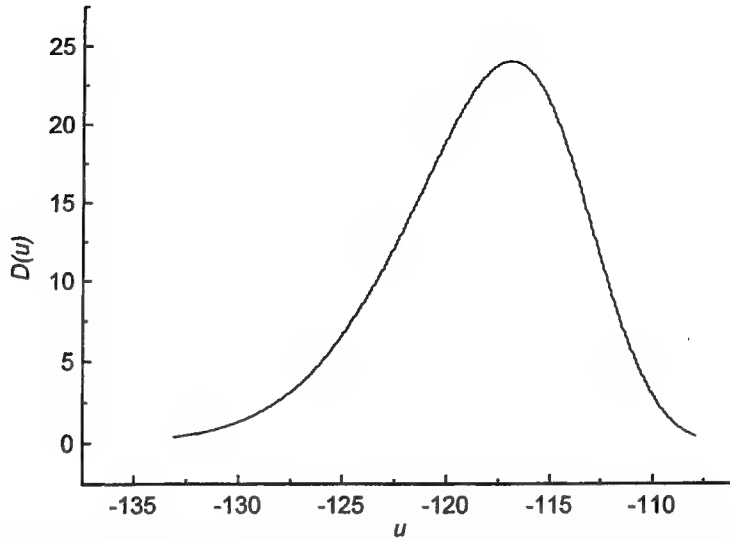


Figure 1: The dependence of D on u . D is measured in $1/cm$, u is in femtoseconds and is counted from a maxima of Gaussian laser pulse.

Thus, the essential influence of ionization to the laser pulse form can be expected on a rather large distance from the substance entrance only. If the thickness of the substance slab L appears less, than x_d , then according to (15), the influence of ionization of ions or neutrals on laser pulse will be negligible. If $L \geq x_d$, the intensity of the laser pulse is expected to complete depletion at distances $x \geq x_d$ in a neighborhood of time $u_* + x/v_g$. For example, for Gaussian pulse of 100 fsec FWHM, maximum intensity $I_{max} = 10^{16} W/cm^2$, wave length $1.06 \mu m$, propagating in hydrogen at pressure 1 atm and temperature $T = 293^0 K$, the function $D(u)$ has a form shown on Fig.1. $D(u)$ reaches a maxima at a moment $u_* = -117$ counted from a maxima of the pulse. The laser pulse intensity appropriate to this moment is equal to $I_p(u_*) = 2.26 \cdot 10^{14} W/cm^2$, and the depth x_d , according to (14), is equal to $420 \mu m$. Magnification of maxima pulse intensity up to $I_{max} = 10^{17} W/cm^2$ reduces x_d insignificantly: $x_d \approx 360 \mu m$ at the same remaining parameters. Increasing of laser pulse duration in 2 times (that is up to 200 fsec) at the same remaining parameters ($I_{max} = 10^{16} aW/cm^2$), leads to increasing of the length x_d up to $610 \mu m$.

Further we characterize a steepness of the laser pulse temporal form by derivative $\partial I(x, u)/\partial u$, and a steepening by the difference $\partial I(x, u)/\partial u$ from $dI_p(u)/du$. Then from the formula (15) a relation for a steepening is obtained

$$S(x, u) = \frac{\partial I(x, u)}{\partial u} - \frac{\partial I_p(u)}{\partial u} = -x \frac{d}{du} (I_p(u) D(u)) . \quad (16)$$

From Fig.1 it is clear, that $D(u)$ is sharp function in comparison with $I_p(u)$. The fast increase of $D(u)$ originates from the fact that W is sharply increasing function (3) of intensity I . However initial increase $D(u)$ for the account of $W(I_p(u))$ is replaced by sharper, exponential decrease of the factor $1/G(u)$. Thus, already at small x (see (14)) it is possible to expect an essential steepening of the pulse form (in scales of an initial steepness $dI_p(u)/du$). With magnification of x the steepening increases linearly according with (16).

With a deep penetration into substances pulse depletion increases. In turn, the approximation of a small deviation from the initial pulse form (15) becomes inapplicable. To make a qualitative picture of the spatial and temporal evolutions of intensity $I(x, t)$ and $n(x, t)$, we discuss at first corollaries of the simplified model of ionization process.

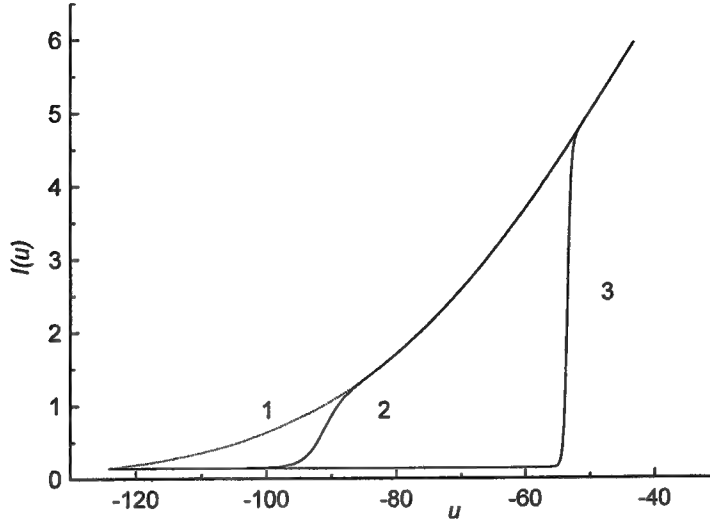


Figure 2: The dependence of $I(x, u)$ (in 10^{15} W/cm^2) on u (in femtoseconds) for three various depths of a penetration in substance: 1 - $x = 0$, 2 - $x = 0.169 \text{ cm}$, 3 - $x = 1.69 \text{ cm}$.

3.1 Linear approximation of the ionization rate W

Let's consider, that the ionization rate W in the equations (8),(9) is a linear function of I , if the intensity of a laser radiation has exceeded some ionization threshold of magnitude I_0

$$W = A \cdot (I - I_0) \cdot \theta(I - I_0), \quad (17)$$

Where θ is the Heaviside step-function. For magnitude I_0 it is possible to use a value $I_{th} = cU_{a,k}^4 / 128\pi(k+1)^2 e^6$ (e is a charge of an electron) predicted by the model of the threshold ionization.^{8,9} Then the equation (10) supposes an analytical solution:

$$I(x, u) = I_0 + \frac{(I_p(u) - I_0) \cdot G(u)}{G(u) + \exp(N \cdot A \cdot U \cdot x) - 1}, \quad (18)$$

$$n(x, u) = \frac{N \cdot \exp(N \cdot A \cdot U \cdot x)}{G(u) + \exp(N \cdot A \cdot U \cdot x) - 1}. \quad (19)$$

On Fig.2 the typical behavior of $I(x, u)$ (18), is presented at $I_0 = 1.4 \cdot 10^{14} \text{ W/cm}^2$, $A = 0.82 \text{ cm}^2/\text{J}$, density N , appropriate to hydrogen pressure of 1 atm at temperature $T = 293^0 \text{ K}$. Hydrogen is entered by Gaussian laser pulse of 100 fsec FWHM and maxima intensity $I_{max} = 10^{16} \text{ W/cm}^2$. Here $A = (\partial W / \partial I) |_{I=I_0}$, where $W(I)$ is determined by the ADK formula (3). It is clear, that as long as laser radiation penetrates in to the substance both the depletion of pulse energy and pulse steeping occur. With the help of formula (18) we can define, in what moment a steepening of the pulse form S reaches a maxima in the given point of space x :

$$S = \frac{G(u)}{G(u) + \exp(N \cdot A \cdot U \cdot x) - 1} \left\{ \frac{dI_p(u)}{du} + \right. \\ \left. [I_p(u) - I_0] W(I_p(u)) \frac{\exp(N \cdot A \cdot U \cdot x) - 1}{G(u) + \exp(N \cdot A \cdot U \cdot x) - 1} \right\} - \frac{dI_p(u)}{du}.$$

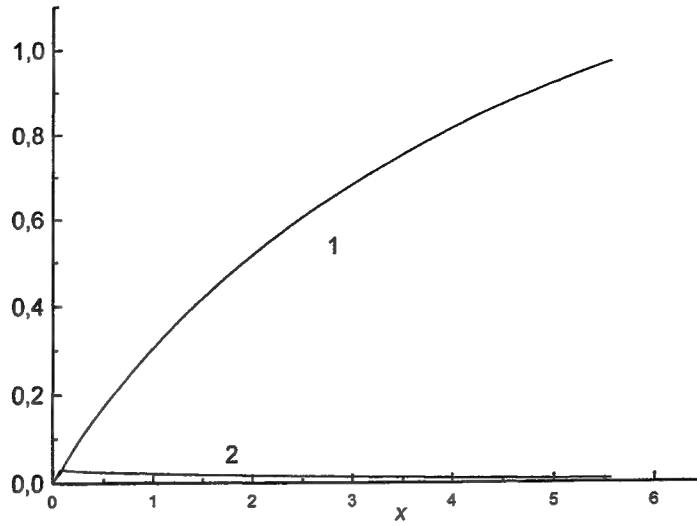


Figure 3: The dependence of $S_m(x)/I(x, u_m)$ (curve 1) and $|d \ln(I_p(u))/du|$ (curve 2) in terms of ω on x in cm .

The most fast varying function in this expression is G . It follows from here, that the moment u_m , when the steepening S reaches a maxima in the given point x , can be found approximately from the equation

$$G(u_m) = \exp(N \cdot A \cdot U \cdot x) - 1. \quad (20)$$

In turn, the maximum value of a steepening of the pulse form $S_m(x)$ in a point x is determined by the formula

$$S_m(x) = \frac{1}{2} \left\{ \frac{1}{2} [I_p(u_m) - I_0] W(I_p(u_m)) - (dI_p(u)/du) |_{u=u_m} \right\}, \quad (21)$$

Let's notice, that in a lack of ionization or in the vicinity of $x = 0$ we have $S = 0$. The formula (21) is obtained in conditions of rather deep penetration ($x \gg x_d$ (compare with (14))). At such large x it is possible to neglect unit in the equation (20). Then, taking into account the definition of A (17), the equation (20) accepts the following form

$$\int_{i_0}^{u_m} (I_p(t) - I_0) dt = N \cdot U \cdot x. \quad (22)$$

On Fig.3 $S_m(x)/I(x, u_m)$ is shown for values of parameters corresponding to Fig.2. From Fig.3 it is clear, that $S_m(x)/I(x, u_m)$ considerably exceeds $|d \ln(I_p(u))/du|$ practically at all values of x and increases with growth of x .

It is possible to look at relations (20), (22) look from the other point of view. First of all, substituting (20) in (19) and taking into account a smallness of unit term on a comparison with exponential one we obtain

$$n(x, u_m) = N/2, \quad (23)$$

So at the moment of the greatest increase of $I(x, u)$ in the given point of space x the ion density appears to be depleted till the half of initial one. Thus, substituting (20) in (18), one can obtain

$$I(x, u_m) = \frac{1}{2} [I_p(u_m) + I_0]. \quad (24)$$

It is possible to show (similar to $I(x, u)$), that at the same moment u_m the steepness $|\partial n(x, u)/\partial u|$ reaches the maxima in a point x .

The maximum magnitude of a steepening of the laser pulse form is reached, according with (21), in such point x and such appropriate moment u_m , when $I_p(u_m)$ reaches a maximum value of the I_{max} , and is equal

$$S_m^{max} = \frac{1}{4} (I_{max} - I_0) W(I_{max}) . \quad (25)$$

Such value of a steepening is reached, according with (22), at a penetration of ionization front to the depth

$$x_{max} = \frac{1}{N \cdot U} \int_{t_0}^{u_{max}} (I_p(t) - I_0) dt$$

Here u_{max} is the moment when $I_p(u_{max}) = I_{max}$.

3.2 An arbitrary dependence of the ionization rate W on intensity I

Let's notice, that the relation (22), expressing itself an energy conservation law, can be obtained from (10) at arbitrary sharp enough dependence W on I (for example (3)). Such dependence ensures a steep profile of ionization front $n(x, t)$ and $I(x, t)$. In turn a relation, similar to (22), can be obtained immediately from (8) and (9). Indeed, integrating of (8), (9) on x along all thickness of substance slab from 0 up to L and taking into account practically abrupt profiles of $n(x, t)$ and $I(x, t)$, we come to a relation

$$\int_{-\infty}^u (I_p(t) - I_0) dt = N \cdot U \cdot x , \quad (26)$$

similar to the equation (22). Here I_0 is the intensity of a laser radiation, at which the velocity of ionization W is not large, so the pulse profile has a time to deplete down to magnitude I_0 only. As it will be evident from further (see section 4), a good evaluation for I_0 is the value of threshold intensity of the threshold ionization model,^{8,9} used in section 3.1.

Meaning, that I_{max} can essentially exceed I_0 , the formula (25) predicts a significant steepening of the pulse form even at weak (linear, see (17)) dependence W on I . Though a sharp dependence W on I (3) does not change a qualitative picture of temporal and spatial evolutions of $I(x, t)$ and $n(x, t)$, however it leads to the much larger magnitude of a steepening of the pulse form than linear approximation (17).

Let's determine a maximum magnitude of the steepness of the pulse form $\partial I/\partial u$ in an arbitrary point u . For this purpose we differentiate the equation (11) on u , meaning, that the derivative $\partial^2 I/\partial u^2$ equals zero at the maxima of function $\partial I/\partial u$. As a result we obtain a system of two equations: (11) and

$$\left[I - I_p - \frac{I_p'}{W(I_p)} \right]^2 + \frac{W(I)}{W'(I)} \left(I - I_p - \frac{I_p'}{W(I_p)} \right) + \frac{1}{W'(I)} \left(I_p' - (I_p')^2 \frac{W'(I_p)}{W^2(I_p)} + \frac{I_p''}{W(I_p)} \right) = 0 , \quad (27)$$

Where $W'(I) = dW(I)/dI$, $I_p' = dI_p(u)/du$, $I_p'' = d^2 I_p(u)/du^2$. From the relation (27) it is possible to determine a value of pulse intensity I , appropriate to the largest value of a steepness $\partial I/\partial u$ at given u . In turn the value $\partial I/\partial u$ itself is determined by relation (11). Added to the equations (11), (27) the equation (26) gives an opportunity to define the magnitude of the largest pulse steepness as a function of penetration depth x of laser pulse into substance.

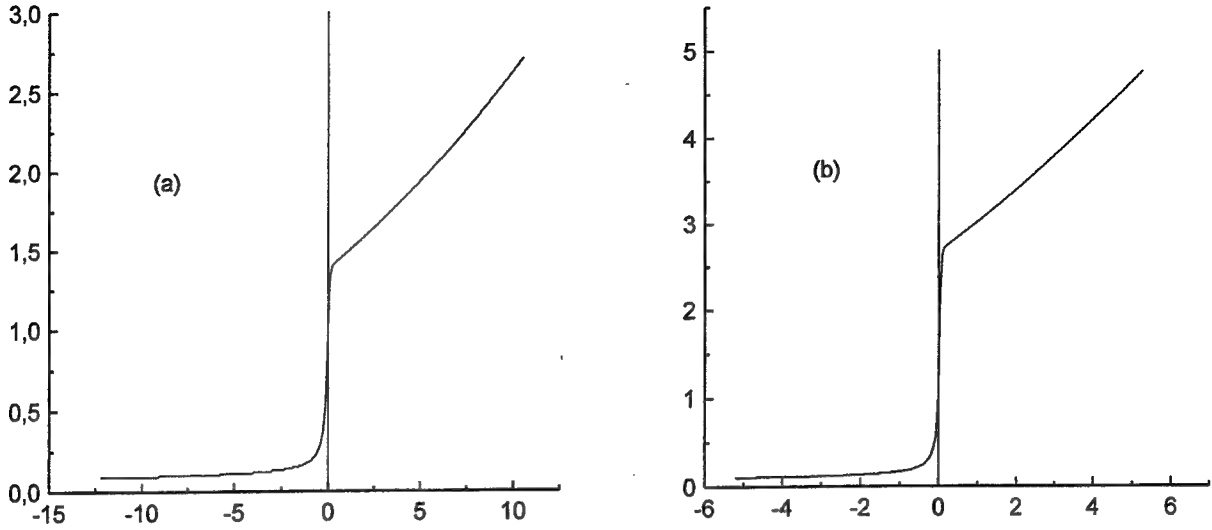


Figure 4: The dependence of I (in 10^{15} W/cm^2) on u (in fsec) for various penetration depths x : (a) - $x = 0.337 \text{ cm}$, (b) - $x = 0.675 \text{ cm}$.

4 OUTCOMES OF A NUMERICAL SOLUTION

The set of equations (2) - (6) was solved numerically together with boundary and initial conditions (1), (7) at Gaussian form of incident pulse. On Fig.4 the time dependence of I at various points x of atomic hydrogen taken at pressure $p = 1 \text{ atm}$ and temperature $T = 293^0 \text{ K}$ are presented. On that Figure the verticals display positions of ionization front defined by the equation (26) at $I_0 = 1.2 \cdot 10^{14} \text{ W/cm}^2$. It is evident, that these positions are in the vicinities of points, where $|\partial I(x, u)/\partial u|$ reaches a maxima at given x . Further on Fig.5 the dependence of a largest steepness $(\partial I/\partial u)_{max}$ on the penetration depth into substance x is presented. The dependence of $(\partial I/\partial u)_{max}$ on x , determined by formulas (26), (27), coincides with $(\partial I/\partial u)_{max}$ from the numerical solution if the value $I_0 = 1.2 \cdot 10^{14} \text{ W/cm}^2$ is substituted into the formula (26). This value of I_0 is rather close to the threshold intensity I_{th} for hydrogen.^{8,9} From Fig.5 one can see that linear approximation of $W(I)$ leads to $(\partial I/\partial u)_{max}$ which is much smaller in comparison with $(\partial I/\partial u)_{max}$ calculated at ADK dependence (3) of W on I .

5 CONCLUSIONS

A short high power laser pulse propagation in ionizing medium in a plane wave approximation is under investigation. The analytical model is based on the equations^{4,5,7} which describe the influence of ionization processes on the powerful laser pulse propagation in the ionizing medium. It is shown that the essential depletion of the laser pulse temporal profile could be expected only after a long enough distance propagation. The depletion leads to the local steepening of the laser pulse time form which corresponds to the sharp medium density ionizing front formation. In turn the latter becomes sharper by the backward influence of laser pulse form steepening. The spatial and time evolution of the laser pulse form steepening is evaluated. The ionization processes are expected to form rather sharp laser pulse temporal profile (about laser pulse high frequency period time scaling).

One of the really existing physical objects where the spatial diffraction is compensated by the pertinent

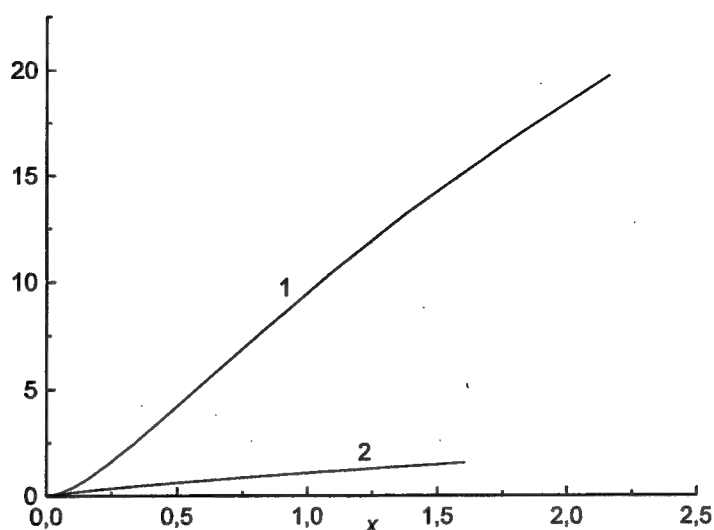


Figure 5: The dependence of $(\partial I/\partial u)_{\max}/I$ (in terms of ω) on x (in cm), obtained with use of tunnel ionization formula (curve 1) and its linear approximation (curve 2).

refraction index profile (and a plane wave approximation could be applicable) is an optically guiding long distance channel.³ The presence of ionizing gas inside the channel will lead to the laser pulse temporal profile steepening. Such kind of laser pulses are useful for laser-particle acceleration.¹⁰ Thus such large optical channels could be used not only for sharpening of the laser pulse form but for the direct laser-particle acceleration.

Supported by RFBR Grant 98-02-16263.

6 REFERENCES

- [1] E. Esarey, P. Sprangle, J. Krall, and A. Ting, *IEEE Trans. Plasma Sci.* **24**, 252 (1996).
- [2] C.J. Pawley et al. *Phys. Plasmas* **4**, 1969 (1993).
- [3] Y. Ehrlich et al., *Phys. Rev. Lett.*, **77**, 4186 (1996).
- [4] V.P. Kandidov, O.G. Kosareva, S.A. Shlenov, *Quantum electronics*, **21**, 971 (1994).
- [5] A.V. Bohrovsky, A.L. Galkin, *JETP*, **108**, 426 (1995).
- [6] F. Ilkov, J.E. Decker, and S.L. Chin, *J. Phys. B*, **25**, 4005 (1992).
- [7] M.V. Ammosov, N.B. Delone, V.P. Krainov, *JETP*, **91**, 2008 (1986).
- [8] R.R. Freeman, and P.H. Bucksbaum, *J. Phys. B*, **24**, 325 (1991).
- [9] J.H. Eberly, J. Javanainen, and K. Rzazewski, *Phys. Rep.* **204**, 331 (1991)
- [10] L.M. Gorbunov, V.I. Kirsanov, *Sov. Phys. JETP*, **66**, 290 (1987). P. Sprangle, E. Esarey, A. Ting, and G. Joyce, *Appl. Phys. Lett.*, **53**, 2146 (1988).

Start in vacuum of a fast electrons, generated at oblique incidence of an ultra short intensive laser pulse on a flat target

A.A.Andreev I.A.Litvinenko K.Yu.Platonov

Institute of Laser Physics "Vavilov State Optical Institute"
Russia, 199034, St.Petersburg, Birzhevaya line, 12

Abstract

In result of numerical and analytical consideration is shown, that the essential part electrons, having been in area undercritical density, under action of arising forces is formed in clots and takes off for vacuum in a direction, different from normal to a normal of a surface in a narrow interval of corporal corners. The received results prove an opportunity of laser electrons acceleration at reflection USLP from a flat target.

Keywords: ultra short laser pulse, electrons acceleration, superstrong laser fields, particles in a cell simulation (PIC-code)

Introduction

Development of laser engineering, allowing to generate powerful ($q \sim 10^{18}$ W/cm²) ultra short laser pulses (USLP) ~ 0.1 ps the program facilities [1], has resulted in that, former representations about mechanisms of interaction of such laser radiation with substance becomes unsufficiently for an explanation of the physical phenomena observable in experiments. In particular, in numerical and real experiments [2,3] data on angular distribution taking off from a target fast electrons were received at incident of a laser pulse. From the analysis of these data follows, that the basic part taking off from a target fast electrons moved along a direction of a reflected laser pulse. The possible reason of formation of such bunches is acceleration electrons taking off from laser plasma in electromagnetic fields of falling and reflected laser pulses. The present work is devoted to research of electrons dynamics in the field of fall and reflection USLP. It is supposed, that the laser plasma is collisionless, and the electrons movement is determined by an external electromagnetic field and ambipolar potential, caused by division of charges. For study of electrons dynamics we shall carry out analytical estimations and numerical decision of a problem. In the first paragraph a trajectory of a electron movement is analytically built, angle of a start and energy is estimated. It allows to

understand a physical picture of the phenomenon, and hereinafter to interpret data of the numerical account. In the second paragraph the same problem is solved numerically by a method of a PIC-code for specific parameters of a laser pulse and plasma. In the third paragraph results of the numerical account are discussed, comparison of analytical and numerical results will be carried out, received dependences are explained.

1. Analytical consideration of an electron start from a surface of a target

We shall consider incidence of a laser pulse with limited width R on a surface of a target.

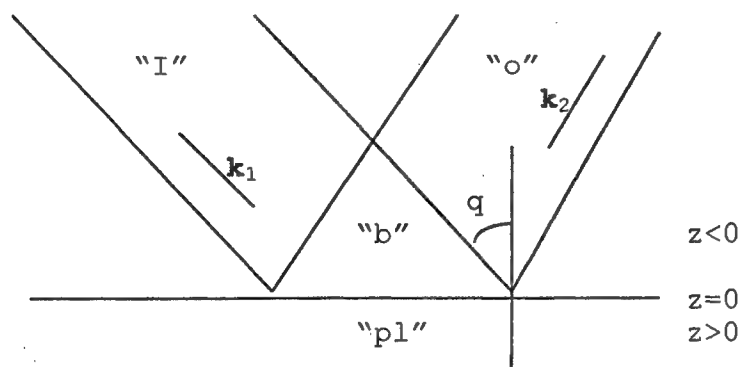


fig.1

The following obvious distribution of fields (Fig. 1) are formed: the area "i" contains a field of a falling wave, "o" - reflected, "b" - superposition of falling and reflected waves, "pl" - field inside plasma. Let's assume, that near to a surface of a target there is the small electron group, and the presence of this group has no an effect for distribution of fields in vacuum and in plasma. The origin of this group is explained as follows: in result pondermotive pressure WHETHER occurs sharpness of a structure of electron concentration, and the small part of electrons with concentration less critical remains in vacuum. The similar picture of distribution of electronic concentration turned out in result one dimension of numerical modeling [6], where the main attention was given to processes inside plasma. These electrons will be considered further. As width of a laser bunch makes tens of lengths of waves, we shall use for the description of electromagnetic fields 1D theory, applied in limits of the cross size of a laser beam.

We use the following system dimensionless variable: $t \Rightarrow \omega t$; $y, z \Rightarrow (w/c)y, z$; $E, B \Rightarrow eE/m\omega c, eB/m\omega c$; $A, f \Rightarrow eA/mc^2, ef/mc^2$; $v \Rightarrow v/c$. Fields E and B we shall assume unrelativistic $E, B < 1$. In linear on E and in approximation the system of the equations collisionless of hydrodynamics plasma and Maxwell equations gives the following

distribution of fields:

Area "i" $B_x = -E_0 \cos[z \cos \theta + y \sin \theta - t]; E_z = \sin q B_x; E_y = -\cos q B_x$

Area "o" $B_x = -h E_0 \cos[-z \cos \theta + y \sin \theta - t + a]; E_z = \sin q B_x; E_y = \cos q B_x$

Area "b" Here the field is a sum of fields in areas "i" and "o",
(h- factor of reflection of a laser wave, a - phase of a reflected wave, q- angle of incidence in relation to target normal).

Area "pl" $E_z = (\sin \theta / \epsilon(z)) B_x; E_y = \text{Re}\{(i/\epsilon)(\partial B_x / \partial z)\} = \text{Re}\{-i \int (\sin 2\theta / \epsilon - 1) B_x(z') dz'\}$, where $\epsilon(z)$ - dielectric constant of spatially of non-uniform plasma. For magnetic field B_x the known equation [8] is used:

$$\epsilon(z) (d/dz) [(dB_x/dz) / \epsilon(z)] + (\epsilon(z) - \sin^2 \theta) B_x = 0 \quad (1)$$

With a boundary condition $B_x \rightarrow 0$ ($z \rightarrow \infty$). Factor of reflection and the phase of a reflected wave are determined from a condition of a continuity of a magnetic field and its by derivative on border of areas "b" and "pl". For plasma with inhomogeneity scale smaller than laser wave length we use results of analytical accounts of fields and factor of absorption through an impedance of plasma, resulted in work [4].

Impedance z of plasma, agrees [4] looks like:

$$z = -1.38 i z^{1/6} (1 + z^{1/3} (0.72 - \sin^2 q (0.21 + 0.24 \ln z))) + p z^{1/2} \sin^2 q, \quad (1a)$$

Where $z = (wL/c)^2$ - small parameter. The parameters h and a , are connected to an impedance z :

$$h = |\cos q - z| / |\cos q + z|; a = \arg((\cos q - z) / (\cos q + z)) \quad (1b)$$

Scale of plasma inhomogeneity is estimated as product of duration of a laser pulse t_1 on ion sound speed, determining speed of expansion of a plasma clot in vacuum.

Thus, 1D model allows to find cross electromagnetic fields near to a surface of plasma. We shall note, the considered above distribution of fields on the basis of the hydrodynamic equations is fair only for a mode of normal skin-effect. In a mode of anormal skin-effect (ASE) h and a should be taken from numerical simulations. The similar numerical simulations are submitted for example in work [5,6].

We shall pass to the description of electron dynamics. In the equations of a movement instead of fields E_z, E_y, B_x conveniently to enter vector potential \mathbf{A} with components A_y, A_z ($\text{div } \mathbf{A} = 0$): $\mathbf{B} =$

$\text{rot} \mathbf{A}$; $\mathbf{E} = -\partial \mathbf{A} / \partial t$. We shall also consider nonrelativistic intensity of laser fields, that is $A \ll 1$, then the decision of the equations of a movement it is possible to carry out by a method of iterations on degrees A . In areas "I and "o", where there are the only running waves character of an electron movement is well known: oscillations in an electrical field and uniform rectilinear movement with speed $A^2/4$ along a direction of a wave vector. In area "b, where electrons are concentrated, taking off in vacuum the character of a movement is more combined. The law of conservation "y" components of a cross initial pulse gives the following expression for "y" to making electron speed:

$$\begin{aligned} v_y = & hE_0 \cos q \sin(-z \cos q + y \sin q - t + a) - E_0 \cos q \sin(z \cos q + y \sin q - t) + \\ & + E_0^2 \cos^2 q \sin q \{ h^2 \sin^2(-z \cos q + y \sin q - t + a) + \sin^2(z \cos q + y \sin q - t) - \\ & - 2h \sin(-z \cos q + y \sin q - t + a) \sin(z \cos q + y \sin q - t) \} / 2 + \quad (2) \\ & + \sin q v_z^2 / 2 \end{aligned}$$

On an axis z the equation of a movement looks as follows:

$$dv_z/dt = (\sin q - v_y) B_x \quad (3)$$

We shall solve system of the equations (2,3) method of iterations on degrees of a field E_0 . Such approach is equivalent an averaging on electron oscillations and transition to the average equations of a movement. In the first order on E_0 electron makes harmonic fluctuation in an electrical field of a wave, and the average force, working on it, is equal to zero. In the second order averaging on time of expressions (2) and (3) gives the following result:

$$\begin{aligned} \langle v_y \rangle = & \sin q E_0^2 (1 + h^2 - 2h \cos 2q \cos(2z_0 \cos q - a)) / 4 \\ d\langle v_z \rangle / dt = & -h E_0^2 \cos q \sin(2z_0 \cos q - a), \quad (4) \end{aligned}$$

Where z_0 - average electron coordinate. From (4) follows, that at a determined phase of a reflected wave and initial electron position the force, working on it, changes a mark at change of a mark of size $2z_0 \cos q - a$. Therefore electrons will be broken on two groups: moving in vacuum and in plasma the electron distribution is those, that in the beginning of a pulse $|z_0| < 1$. The force in the right part of the equation (4) corresponds to potential energy

$$U(z_0) = h E_0^2 \cos^2(z_0 \cos q - a/2). \quad (4a)$$

Electrons with energy it is less $h E_0^2$ under action of potential (4a) concentrate in points of minimum $U(z_0)$ (in basic in the minimum nearest to a surface) and surfaces in the party of a

reflected pulse move in parallel, where leave area, engaged in a field.

In the equation (4) there is not enough force working on electrons on the part of ions, i.e. ambipolar field. We shall emphasize, that this force also of the second order on E_0 , as ambipolar field compensates pondermotive pressure of laser radiation. For a presence ambipolar field, included in the right part of the equation (4), we shall consider the following model of charge distribution in system (see fig. 1a)

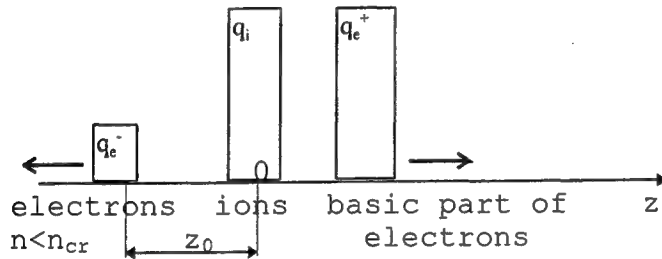


fig.1a

As already was spoken, we believe, that on the part of vacuum on plasma works pondermotive pressure of radiation, superseding the basic part of electrons deep into plasmas and not touching small area of plasma, laying in transparency area.

Without consideration influence of this small part to formation ambipolar field we have in area "pl" balance between pondermotive force and ambipolar field, created by basic part of electrons.

$$E_{am} = -(\sin q - v_y) B_x \quad z > 0. \quad (5)$$

Hence, volume charge density r , from ambipolar field, looks like

$$r = (1/4p) \partial E_{am} / \partial z \quad (6)$$

Charge density is nonzero only inside a skin-layer, i.e. in very narrow area near to a surface. For example in real conditions scale of a skin-layer about one tenth length of a wave of falling radiation. Therefore on distances from border of plasma of a wave comparable to length, but smaller, than width of a laser beam, the charge configuration (6) is equivalent to a plane with superficial charge density s equal

$$s = \int_{z=0}^{\infty} r \, dz = (1/4p) \left. E_{am} \right|_{z=0}^{\infty} = - (1/4p) (\sin q - v_y) B_x \quad (7)$$

Ambipolar field in vacuum, influencing on a start of particles, is possible to consider as a field of surface charge s : $E_{am}=4\pi s$. In result the average equation of a movement on an axis z with the account ambipolar field of signs a kind

$$d\langle v_z \rangle / dt = -hE_0^2 \cos q (\sin(2z_0 \cos q - a) + \sin a). \quad (8)$$

Thus, ambipolar field compensates pressure of light and resulting force differs from zero only because pondermotive force, working on electron, undertakes in a point z_0 , and ambipolar field (see fig. 1a) is determined by the same force of plasma taken on border at $z=0$. We shall note, that for short pulse duration inhomogeneous scale of plasma there is less length of a wave and $|z_0| < 1$ on an extent of a greater part of a pulse. Therefore on the initial stage of a movement электронов the equation (8) should be spreaded out on small z_0 :

$$dv_z / dt = -2hE_0^2 z_0 \cos^2 q \cos a \quad (8a)$$

Thus, model account arising ambipolar field results in reduction of amplitude accelerating force. In an offered way of the account ambipolar field are made following approximation:

a) In the equations decomposition on degrees E_0 is used, in result of action of a field was reduced to reduction of factor at E_0^2 in amplitude of force, working on electron;

б) One-partial equations of a movement are used, therefore ambipolar field has appeared not dependent from number taking off electrons, and latter from intensity of radiation;

в) Used theory is one dimensional, therefore the equation (8) is fair at $z_0 < (S/4\pi)^{1/2}$, where S - area of a laser stain on a target in λ^2 . On distances large $S/4\pi$ ambipolar field looks as a field dot charge $q=sS$, that is decreases with increase z_0 ;

Thus, the ambipolar field influence on electron movement электронов in the given analytical model is taken into account in some approximations and the results have qualitative character.

2. Numerical modeling of an electron movement

The analytical model of electron movement over a surface of plasma constructed in the previous section contains enough plenty approximations for the quantitative description of process of electron start from a surface. Accuracy of this model - multiplier about unit. The stricter consideration of the given problem requires the joint decision of the equations of electron movement and Maxwell equations in 2D geometry. This difficult computing problem will be solved hereinafter on the following technique. For its simplification we shall take h and a from (1a) and (1b), that

is cross fields over a surface of plasma ($z < 0$) we shall consider given. Ambipolar field and trajectories of an electron movement we shall calculate by a self-consistent way.

For calculation E and B in the field of crossing falling and reflected laser radiation a principle of a superposition is used. At $z > 0$ and outside of a beam all components of electrical and magnetic fields rely equal to zero. Ambipolar field is calculated in each moment of time with the help of the Puasson equation and develops with fields of a laser pulse.

We parameters of a laser pulse and shall take targets close to possible experiment. We shall consider a flat laser beam of width $R=10$ a micron, falling under the corner $q=30^\circ$ of degrees on a target (Fig. 1). We shall choose factor of reflection equal 0.8, phase $a=0$. It corresponds to estimations under the formulas (1a), (1b) for a laser pulse by duration 100 fs and intensity 10^{18} W/cm². We shall take frequency of laser radiation $\omega=1.8 \cdot 10^{15}$ s⁻¹. In culculations a few meanings of the maximum intensity of laser radiation 10^{16} , 10^{17} and 10^{18} W/cm² and various cross and temporary structures of a laser pulse were considered. The plasma of a target, on which laser radiation influences, in an initial moment of time has the following parameters: in electronic density $N_e(z)$ and average electron temperature, equal 0.1 keB. The dependence $N_e(z)$ undertakes from estimations of plasma dynamics under influence warming up picosecond laser prepulse. At $z > 0$ $N_e(z) = a N_{cr}$, and in area $z < 0$ $N_e(z) = a N_{cr} \exp(-z/z_c)$, where $N_{cr}=10^{21}$ cm⁻³ - critical concentration, $a=3$ the relation of maximal concentration to critical, $z_c=0.3$ micron - scale of inhomogenity in a critical point.

For the description of an electron movement of plasma a method "particles in a cell" (PIC-code) is used. 3D movement of particles are described by the relativistic equations in view of Lorence force.

Used differences scheme has the second order of approximation on space and time. For increase of accuracy of size of fields influencing on a particle, they are calculated for each particle on each temporary step separately. The number of steps was necessary 18000. The range of taken into account times was equalled $3t_i$. Amount of particles in each account makes 100000. All of them were injected in the field of a laser stain in an initial moment of time according to a structure of density and meaning of initial energy of target plasma. The further their movement proceeds up to a moment of the ending of a pulse and start from area of a stain. Spatial distribution of electron density for four moment of time during a laser pulse is fixed, evidently to present a picture of a movement of particles. After ending of laser pulse for each particle an angle of a start j it an angle between a pulse and normal to a surface on a moment of the ending of the account and energy is remembered. Summarizing on all particles the saved

information function $n_e(j)$ - density of a start electrons under a angle j is defined and average energy of electrons is calculated. The ions in the given model are also assumed driven. In an initial moment of time the ion structures and electronic concentration coincide, hereinafter the ions move under action of the same fields as electrons.

3. Results of numerical simulations and their analysis

The simulations are spent for meanings of peak capacity of laser radiation 10^{16} , 10^{17} , 10^{18} W/cm² with triangular on space and time by distribution of laser fields in a pulse. Separately account for intensity 10^{18} W/cm² and pulse of the rectangular form was spent. The complete duration made for pulses of the triangular form - 200 fs, rectangular -100 fs.

We shall begin consideration of results from the analysis of a pulse of the triangular form and intensity 10^{18} W/cm². On a Fig.2 spatial dependences of electron density for four moment of time are resulted: $t=0$, 40, 70, 308.9 fs. On an axis absciss on all diagrams of a Fig.2 in linear scale of adjourment coordinate z , varying from 4 microns up to 10 micron, on an axis of ordinates - y , varying from 12 micron up to 10 micron. The scales for definition of density are resulted in terms of number/cm³. The account shows, that laser radiation pushed electrons inwards plasmas already to 40 fs. Arising pondermotive potential pushed a part of electrons from a point $z \sim z_c$. Hereinafter this part under action of laser radiation and ambipolar potential is formed in two wide bunches and flies away to the right. Comparison of distributions on moment of time $t=70$ fs and 308,9 fs speaks that really from plasma undercritical density (there is the formation of a electron bunch, moving not on normal to a surface of a target. A Fig.3 - it is brightest illustrates. On it electron angular distribution with coordinates $z > 0$ on a moment of time $t=308,9$ fs $n_e(j)$ is resulted.

The analysis of Fig.3 speaks about presence of a electron bunch with energy 15 keV, flying under a angle-58° to normal, that a little bit differs from average meaning of energy - 18keV. For intensities 10^{16} and 10^{17} W/cm² the results of the appropriate accounts $n_e(j)$ are resulted on Fig.4,5. At decrease of intensity electron angular distribution taking off narrow (electron take off closer to normal), angular asymmetry of distribution (in the party of a reflected pulse) disappears, at intensity 10^{16} equal electron number takes off. The angular distribution has three characteristic peaks: central and two symmetric lateral. The central peak on the diagrams $n_e(j)$ (see fig. 3,4,5) has appeared in result of influence of numerical model, in which free ends of laser plasma are moving under action of a pulse. We shall note, that the electron energy taking off poorly depends on intensity of a laser pulse and makes

7,9 keV for 10^{17} W/cm² and 13 keV - for 10^{18} W/cm². This effect is connected to indemnification of accelerating force by ambipolar field.

The ions also leave a target, but, as against electrons, it is normal to a surface. Average energy of an ion about electronic (at $Z=1$). The reason of a movement of ions is ambipolar potential.

We shall pass to the analysis of account, where was used rectangular on space and on time of distribution of intensity of a laser pulse with the maximum meaning 10^{18} W/cm². The results of this account are submitted on Fig.6 four 2D pictures by dependences of electron density on moment of time 0fs, 40fs, 70fs, 200fs same, as for triangular distribution. On an axis абсшхсс on all diagrams of Fig.6 in linear scale coordinate $-z$, varying from -4 micron up to 10 micron, on an axis of ordinates y , varying from -12micron up to 10 micron is postponed. The scales for definition of density are resulted in terms of number/sm³. Account shows, that laser radiation "press" electron into inwards plasmas also to 40 fs. Arising pondermotive potential pushed a part of electrons from a point $z=z_c$. The hereinafter "rejected" part, as against a case of a pulse of the triangular form, gets in a minimum pondermotive potential and is kept in it during duration of a laser pulse, making fluctuation in a potential hole. The formed electronic clot has the cross size 0.2-0.4 microns and extend along the whole surface of a laser stain. The period of fluctuations of a particle in potential (4a) exceeds laser period. After ending a laser pulse (> 100 fs) formed electronic clot flies away from a target under a characteristic corner 34° with average energy 19 keV. As it is visible from comparison of results for identical intensity 10^{18} W/cm

² but various cross structure of a pulse the average energy electron is poorly sensitive to the form of a pulse but spatial distribution and the corners of a start electrons in vacuum much differ for rectangular and triangular distributions. Assuming that with increase of laser intensity the role ambipolar field will decrease we have carried out additional calculations of a range of corners of a start and энергий for triangular distribution intensities 10^{19} W/cm² and 10^{20} W/cm² without the account ambipolar field. The corners of a start thus make 42 - 51 and 48 - 57 degrees and energy 450 - 570 КэВ and 4600 - 5200 КэВ accordingly. From these data follows, that electrons take off in a narrow interval of corners between mirror direction and direction of an electrical field of a wave, and the electron energy grows proportionally to intensity of laser radiation in conformity with relativistic electron dynamics in a field flat monochromatic wave [7].

4. Comparison of numerical and analytical results

We shall carry out comparison of numerical and analytical results. We as the equations constructed in item 2 of a nonrelativistic movement shall carry out consideration for intensity 10^{17} W/cm² and pulse of the triangular form. Cross and the temporary structure of a laser pulse is possible to take into account, by entering in the formulas of section 2 dependence of amplitude E_0 on average electron coordinates (y_0, z_0) and time. By taking this dependence from the numerical account for intensity 10^{17} and pulse of the triangular form we shall receive the following equation of a movement on an axis z in area "b":

$$d\langle v_z \rangle / dt = -hE_0^2 F(t) (1 - |z_0 \sin q - y_0 \cos q| / 2pR) (1 - |z_0 \sin q + y_0 \cos q| / 2pR) \cos q \sin(2z_0 \cos q). \quad (11)$$

Where R - radius of a beam in terms of of lengths of waves (hereinafter $R=5$).

In (11) z_0 and y_0 are those, that $|z_0 \sin q \pm y_0 \cos q| < 1$ and phase of a reflected wave $a = 0$. Thus ambipolar field of ions is not taken into account, as on sharp border the force (5) does not work. The function $F(t)$ describes a temporary structure of a laser pulse. In a point $2z_0 \cos q = -p$ (we shall remind, that in vacuum $z_0 < 0$) z -component of force changes its sign: electrons with $2z_0 \cos q > -p$ fly in plasma; electrons with $2z_0 \cos q < -p$ in vacuum. Just such picture of a movement we notice in numerical experiment even for intensity 10^{18} (Fig.2) on times 0-40fs (point $2z_0 \cos q = -p$ corresponds to distance of 0.3 microns from a surface of plasma at $q=30^\circ$). As it is obvious, that the central part of a target will scatter more heavily, since there intensity of a field is higher. We shall note that initial electron concentration exponentially falls down from $z=0$ with 0.3 microns characteristic scale, so in an interval of lengths 0.3-0.6 microns the concentration of particles is sufficient great. As the amplitude of a field also falls down at distance from a surface a formed electronic clot will be moved together in the party of vacuum. The equation (11) corresponds to an electron movement in potential

$$U(z, y, t) = hE_0^2 F(t) (1 - |z \sin q - y \cos q| / 10p) (1 - |z \sin q + y \cos q| / 10p) \cos^2(z \cos q), \quad (12)$$

corresponding peaks with decreasing amplitude. For an estimation of speed v_z after ending a laser pulse, potential (12) is possible averaging on oscillations in space, that will result in replacement $\cos^2(z \cos q)$ on $1/2$. As the amplitude of a laser pulse depends on distance up to its axis, law of momentum conservation (2) will be unfair: besides average speed (4) occurs y -making forces, working on electron. At intensity $> 10^{16}$ W/cm² and given scale cross inhomogeneity of this force brings in the basic contribution to

acceleration electron on an axis y. Thus electron flying in area "b" occurs on the average under action of the following forces:

$$\begin{aligned} f_z &= hE_0^2 F(t) (\partial / \partial z) (1 - |z \sin q - y \cos q| / 10p) (1 - |z \sin q + y \cos q| / 10p) / 2 \\ f_y &= E_0^2 F(t) (\partial / \partial y) (1 - |z \sin q - y \cos q| / 10p)^2 / 4 + h^2 E_0^2 F(t) (\partial / \partial y) (1 - |z \sin q + y \cos q| / 10p)^2 / 4 \end{aligned} \quad (13)$$

In areas "I" and "o" potentials accordingly make

$$V(z, y, t) = E_0^2 F(t) (1 - |z \sin q - y \cos q| / 10p)^2 / 4 \quad \text{и} \quad U(z, y, t) = h^2 E_0^2 F(t) (1 - |z \sin q + y \cos q| / 10p)^2 / 4 \quad (14).$$

Thus, in vacuum will be formed potential profile, consisting of a central triangle (13) and contiguous to it triangular strips (14). Speed and corner of a electron start under action of the above-stated forces depend on an initial rule (situation) electron. Electron with $y > 0$ and $y < 0$ roll down from a triangular potential structure (13), get in potential of strips (14), roll down from it, coming back in plasma or taking off in vacuum and forming two lateral peaks on fig. 5. The time of a electron movement under action of forces (14) is much less than duration of a pulse, therefore electron will have time to pass all areas, engaged in a field. Hence $F(t)$ it is possible to consider constant during a electron movement. As height and spatial arrangement of potential barriers (13), (15) are known, easily to estimate speed of electron, moving in described potential structure.

For an example we shall estimate energy and corner of a electron start moving to the right from potential peak (13) from area «b» to area «o». In area «b» the particle collects speed with the following components $\Delta v_z = (E_0/2) (2\eta - \eta^2)^{1/2}$ and $\Delta v_y = (E_0/2)$. These speeds are initial at movement from following potential peak in area «o». There the particle in addition gets components of speed $\Delta v_z = (E_0/2) \sin q$ and $\Delta v_y = (E_0/2) \cos q$. In results estimating characteristic energy and corner of a start for intensity 10^{17} W/cm^2 we receive $\sim 10 \text{ kev}$ and 30° for electron taking off to the right.

We shall notice, that at increase of intensity the size y-components of speed (4) becomes comparable with speed, got under action of forces (14). In result the angular electron distribution will get asymmetry, and electrons will take a great interest in a reflected pulse. Thus at increase of intensity will occurs brodering of electron angular distribution and it's deformation in a direction of a reflected pulse (for a triangular structure pulse). For a rectangular structure of a pulse with intensity 10^{18} W/cm^2 the analytical theory allows qualitatively to explain

occurrence and deduction of an electronic clot in potential $V(z_0) = hE_0^2 \cos^2(z \cos q)$ (in a minimum, nearest to a surface), however used nonrelativistic approximation does not allow correctly to estimate electron dynamic parameters at intensity 10^{18} W/cm^2 .

5. The conclusion

Results received with use of analytical model and 2D PIC of a code, for collisionless fly of flat target plasma under action of falling and reflected laser radiation subpicosecond duration with density of a flow of energy $> 10^{16} \text{ W/cm}^2$ have shown, that electrons, having been in area undercritical density, under action pondermotive and ambipolar forces take off for vacuum in directions, different from normal to a surface of a target. The angular distribution flying electrons has the following peculiarities:

- a) At intensity (10^{17} W/cm^2) the angular distribution practically is symmetric rather normal, the characteristic corner of a start is determined by the cross form of a laser pulse and corner of fall.
- b) At increase of intensity occurs broadening and deformation of angular distribution. There is the appreciable share electrons, flying is closer to mirror direction. This effect is connected to enthusiasm electrons by a reflected pulse.
- c) At intensity $> 10^{17} \text{ W/cm}^2$ the energy taking off electrons is proportional to laser intensity, as the increase of accelerating force is not compensated ambipolar field.
- d) The ions take off from a target normally to a surface under action ambipolar field.

At nonrelativistic intensities of a laser field the energy and corner of a start electrons will be coordinated with the appropriate analytical estimations.

In the field of crossing a falling and reflected laser pulse formation of electronic clots in the field of a minimum of pondermotive potential is observed.

Received results allow to use a short intensive laser pulse for reception of clots accelerated electrons.

REFERENCES

1. Perry M., Mourou G. Science, **264**, 917 (1994).
2. Kruer W.L., Estabrook K. Phys. Fluids, **28**, 430 (1985).
3. Gauthier G.C., Bastiani S., et al. Proceeding of SPIE, Jule 97.
4. Andreev A.A., Semahin A.N. Proceeding of SPIE, Vol. 2097 Laser Applications (1993)/327.
5. Wilks S.C., Kruer W.L., Phys. Rev. Letts, **69**, 1383 (1992).
6. Ruhl H., Mulser P., Physics Letters A, **205** (1995), 388.
7. Landau L.D., Liphshitz E.M. Theory of field. "Science", 1973.
8. Ginzburg V.L. Electromagnetic wave propogation in plasma. "Science", 1967.

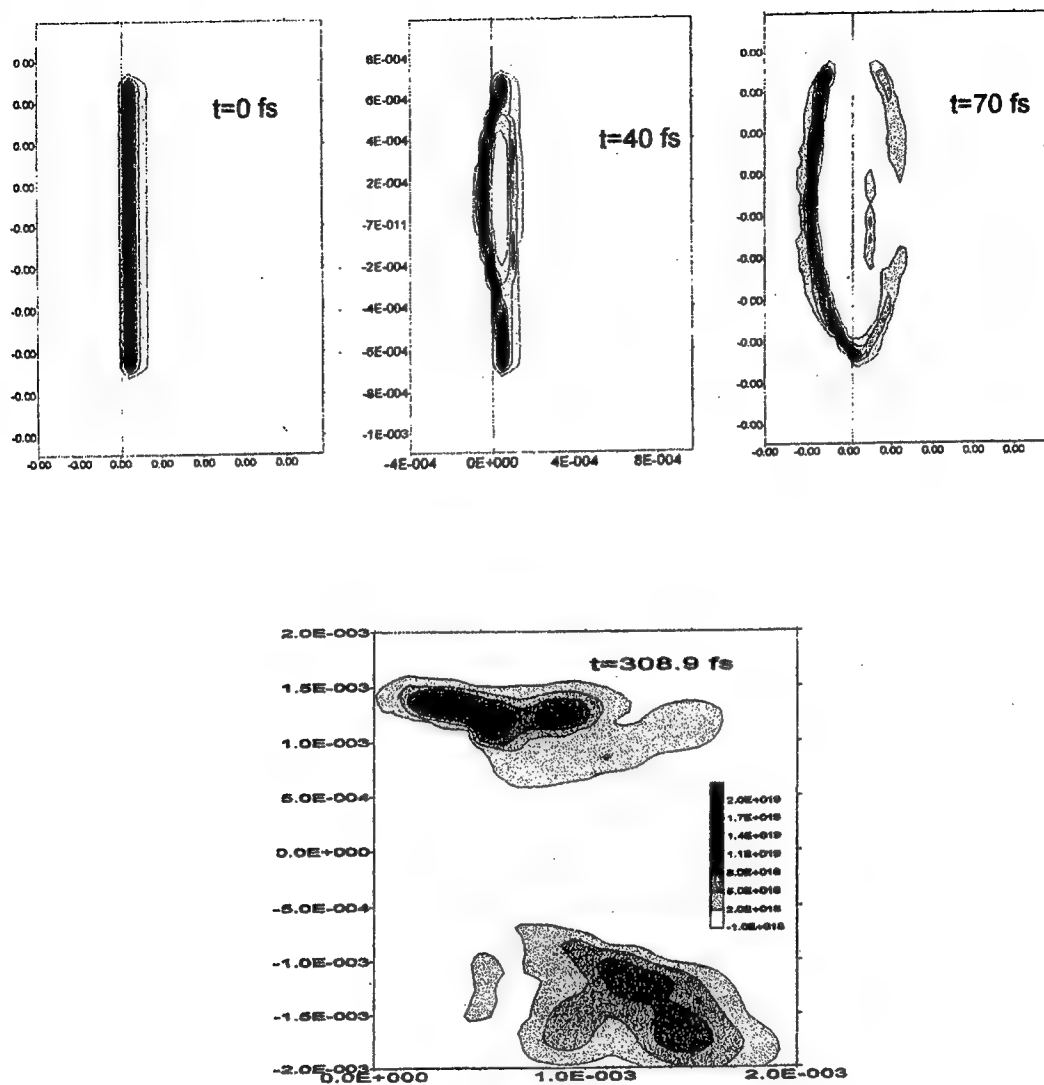


Fig.2.

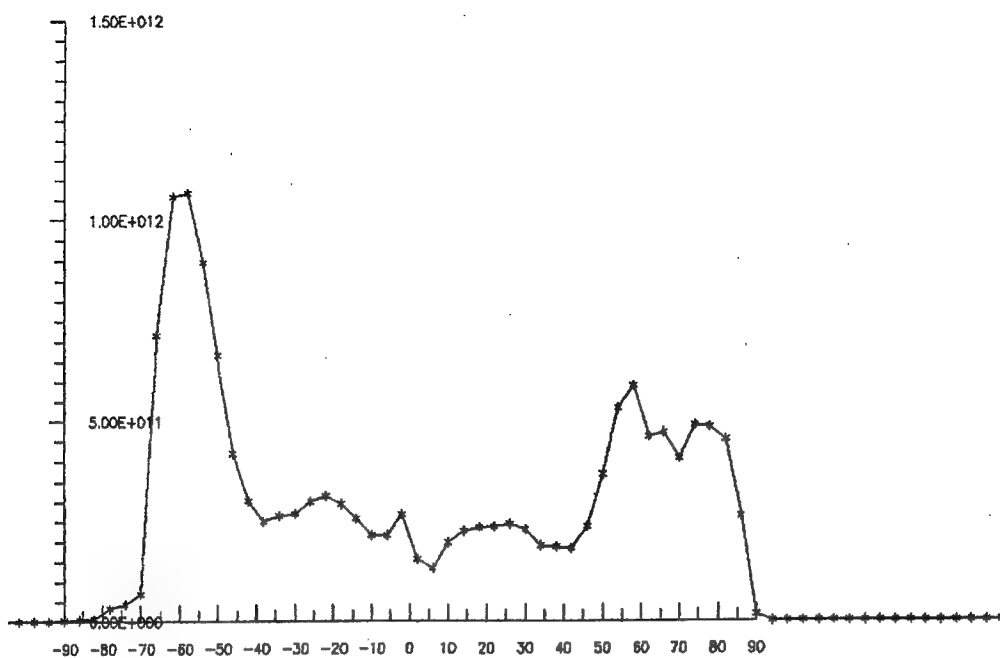


Fig.3.

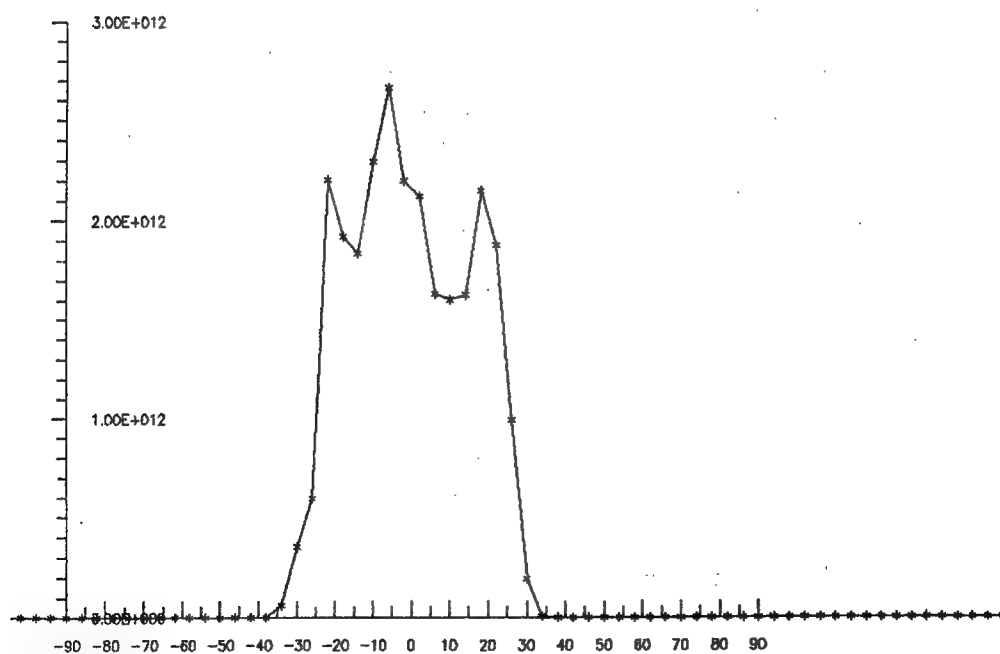


Fig.4.

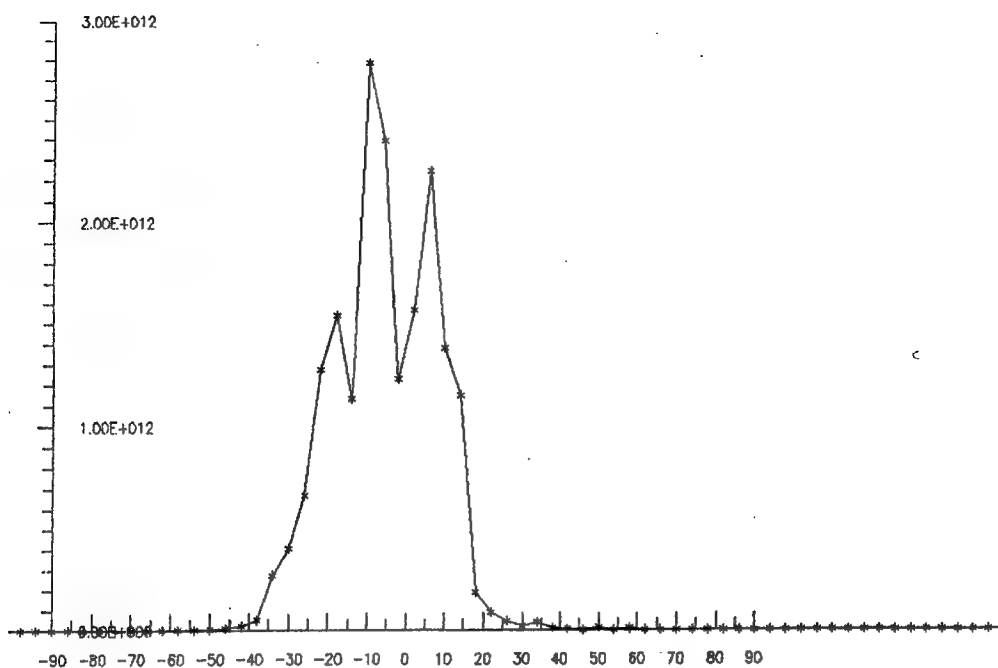


Fig.5.

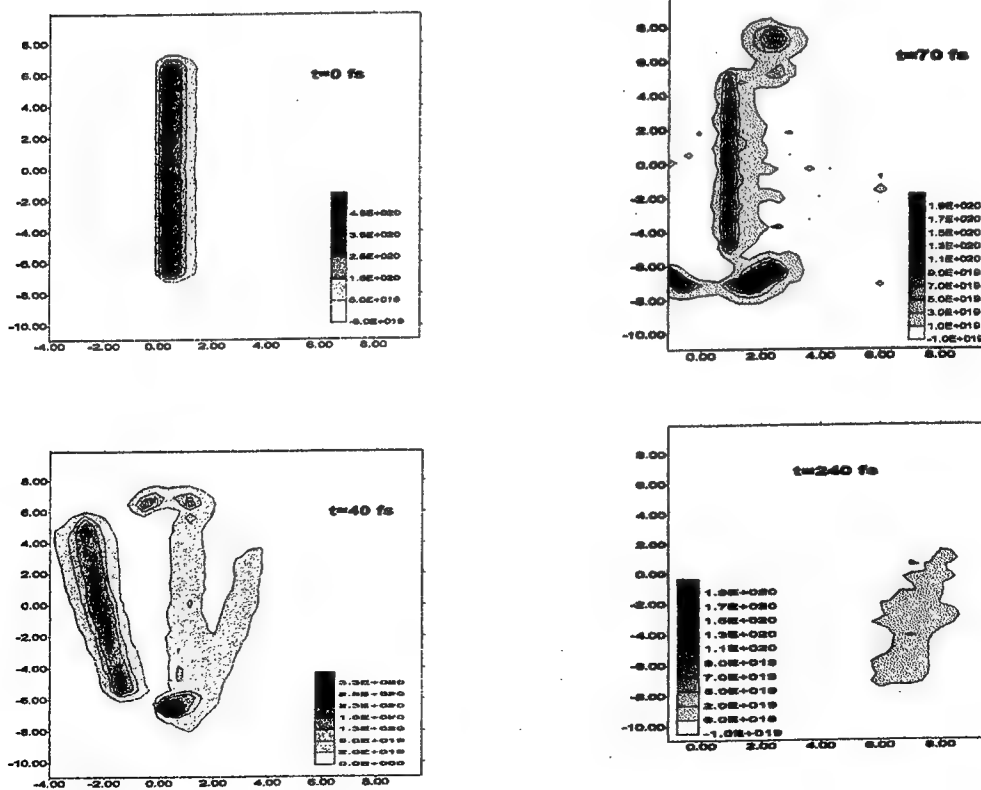


Fig..6.

Extremely Intensive γ -Source with High Spectral Brightness

A.Andreev, Yu.Rozhdestvensky

State Optical Institute, Institute of Laser Physics
199034, St.Petersburg, Birzhevaya Line 12, Russia
and

K.Platonov,

State Technical University, St.Petersburg, Russia

In this work we consider a possibility of pulse γ -source creation for atoms of nuclear isomers localized in a magnetic trap. It was shown, that in this case we can obtain a γ -radiation pulse duration of $10^2 - 10^3$ picosecond with a pulse energy about 10^{-3} J.

1. Introduction

At the present moment the significant number of physical problems requires for its successful solution of reformed incoherent sources of γ -radiation. Thus the area of these problems is really wide - of a non-destructive diagnostics in different condensed matters to medical investigations.

We have to point out, that in the present time the radioactive source intensity cannot be large than $10 - 10^2$ GBk while for many researches considerably large intensity is required. Usually as an intensive γ -source (with activity about 10^6 GBk) the synchrotron radiation is used. In this case the source power is determined by intensity of synchrotron radiation, and the rearrange of frequency is carried out by means of selection of required frequency from the continuous spectrum of the radiation. However, despite of significant success, using of synchrotron radiation as γ -source has a few essential lacks. E.g. obtaining of significant intensity of γ -radiation in required frequency range is not possible because the synchrotron radiation spectrum is continuous. As a result, with decreasing of the frequency range the power of such γ -source is decreasing as well in consequence of the frequency selective experiments with high power γ -source become impossible.

In the present paper we consider the possibility to use as intensive rearrange incoherent γ -source of the cold nuclear isomers localized in magnetic trap (*magnetic trap* - MT) [2,3]. The nuclei are prepared in the isomeric state (for example, by interaction of the nuclei

with neutrons) (Fig.1), and after that the cooled atoms are injected into magnetic trap **MT**. The space localization of the nuclei into **MT** arises by the magnetic force, which acts to atoms in the magnetic field with the spatial gradient. Naturally, before that all atoms with isomeric nuclei have to be optical pumped to electronic state with the needed magnetic moment occurs. Subsequent pumping of nuclei from ground isomeric state to excited isomeric state of active γ -transition (Fig.1) is carried out by X-ray radiation of laser plasma which is obtained by action of powerful laser pulse with duration \approx a few picoseconds on the solid-state target

We have to mark, that the incoherent X-ray pumping of nuclear γ -transition by radiation of laser plasma as well as approaching schemes of resonance levels in the isomeric nuclei have been considered earlier in [1,4,5] in the concept of γ -laser with two step pumping.¹

We shall mark, that using as the pulse γ -radiation source of an ensemble of cooled atoms of nuclear isomers which are trapped in **MT** allows already for small concentration of the isomeric nuclei about 10^{15} cm^{-3} to receive 10^{12} γ -photons during life time of the upper state $|3\rangle \rightarrow |2\rangle = (\Gamma_0)^{-1}$ (where $\Gamma_0 \approx 10^9 \text{ s}^{-1}$ - natural width of active γ -transition). Such activity can be compared only with the activity, which takes place through a minute after nuclear explosion $7 \cdot 10^{13}$ GBk. As a result the real possibility to simulate such intensive acting to different materials (including organic mediums that is really important for medical researches) in laboratory occurs.

At the same time such γ -source will have significant frequent selectivity, that opens new possibilities in selective γ -experiments. In the simplest case the frequent width of such γ -source can be determined as inhomogeneous γ -radiation width on account of a recoil of nuclei by emission of γ -photons. Accordingly the spectral brightness of such radioactive source, based on the isomeric nuclei in a magnetic trap, is also high $\approx 10^6$ GBk/Hz.

2. Basic idea of intensive γ -source

Now, let us consider the main idea of intensive γ -source which is based on using of isomer nuclei in **MT** (Fig.2). We will assume, that the pumping of active γ -transition $|3\rangle \rightarrow |2\rangle$ consists of two steps: the first step - atoms have to be prepared in nuclear isomer state $|1\rangle$ e.g. by interaction between the dense atom gas and intensive beam of thermal neutrons (Fig.2). After that all atoms with isomeric nuclei by means of optical pumping by laser radiation are transferred to electronic state with determined magnetic moment, which is necessary for consequent capture of isomeric atoms into **MT**. The space

¹The idea to use two step pumping of γ -resonance (when the isomeric nuclei are at first prepared, and only after that by means of X-ray or optical radiation the pumping of γ -transition occurs) has been offered in [1,4] and the possible schemes of γ -levels has been represented in [5]. Despite of the high efficiency of such method for creation of population inversion on the active γ -transition, our viewpoint is that the optimism of the authors [4,5] about the possibility to obtain the generation coherent γ -radiation with two step pumping is exaggerated. The fact is that for estimations of resonance γ -radiation amplification in [4,5], the line width of active γ -transition has been taken in an electro-dipole approximation. At the same time [7] in the nuclear system such type of transitions are suppressed very strongly (for considered scale of energies 20-100 keV in $10^4 - 10^6$ times). As a result, with taking into account of last circumstance an amplification of γ -radiation cannot be large then $10^{-4} - 10^{-5} \text{ cm}^{-1}$.

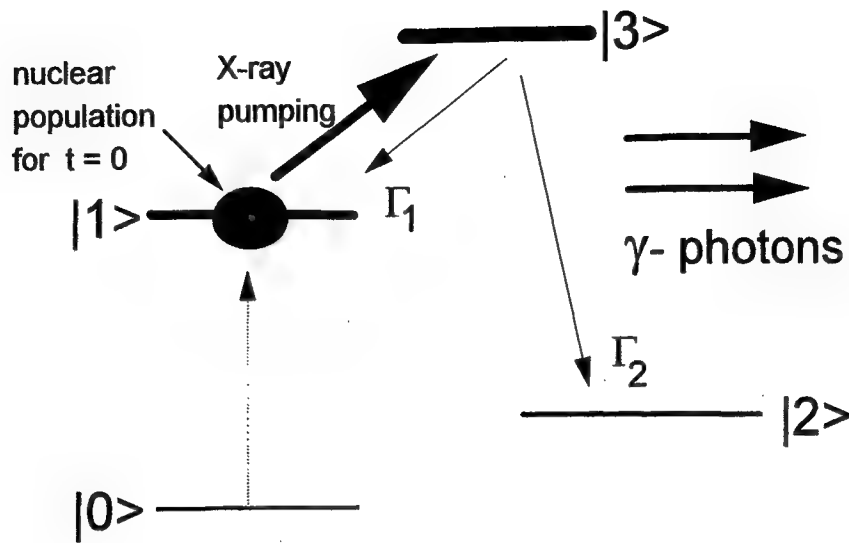


Fig.1 This is interaction level system. Here, the ground state is marked as $|0\rangle$, while the state $|1\rangle$ is an isomeric state. Initially, all nucleuses are in isomeric state $|1\rangle$. The nucleuses are transferred by X-ray pumping to an active state $|3\rangle$ which is decayed to the state $|2\rangle$ by spontaneous emission. $\Gamma_{1,2}$ are partial probabilities of spontaneous decay by channels $|3\rangle \rightarrow |1\rangle$, $|3\rangle \rightarrow |2\rangle$.

localization of the nuclei into **MT** arises by the magnetic force, which acts to atoms in the magnetic field having the spatial gradient. To keep atoms into **MT** with temperature $\approx 10^{-2}\text{K}$ (atom velocity $\approx 10^3\text{cm/c}$) the magnetic field about 100 Gauss is required. The second step of active γ -transition pumping uses X-ray radiation of laser plasma, obtained near of localization atom area by action of powerful laser pulse with duration \approx a few picoseconds on the solid-state target (Fig.1). Using in our case **MT** considerably increases the efficiency of X-ray pumping as for low concentration of the isomeric nuclei the X-radiation will be absorbed in whole volume the trap and not just in skin-area as it was at solid-state concentration \square . For example, X-ray absorption length for solid-state concentration $\approx 10^{23}\text{cm}^{-3}$ is 10^{-7}cm for the energy of X-photon equal to 1keV while for typical concentration $\approx 10^{15}\text{cm}^{-3}$ of atoms in **MT** X-ray absorption length is equal to 0.1cm that is corresponding to typical size of localization area for atoms in **MT**. As a result the number of atoms which can be transferred to state $|3\rangle$ for the case of **MT** considerably more than for solid-state concentration.

On the other hand, the number of the isomeric nuclei which is necessary for a loading of **MT** are not to much higher that is why the requirements to the efficiency of preparation of the isomeric nuclei have to be much lower than for solid-state concentration. Besides low velocities of cooled isomeric atoms in **MT** much increase spectral brightness of such γ -sources as the width of spectral line of γ -radiation will be determined by recoil effect of the nuclei at an absorption of quantum of X-ray pumping.

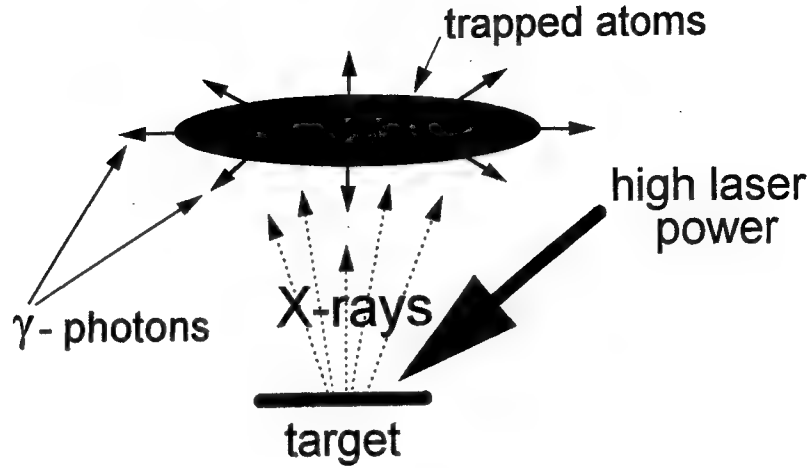


Fig.2 The scheme of γ -source setup.

3. X-ray pumping of the isomeric nuclei

In this section we shall discuss the efficiency of X-ray photon transformation from hot laser plasma to γ -photons for the isomeric nuclei localized in a magnetic trap. At the present time the X-ray pumping of such intensity (when the number of resonant X-ray photons at least is equal to one of the isomeric nuclei in MT) can be obtained only at acting of impulse of a laser radiation with the power about $10^{17} - 10^{18}$ W/cm² on the solid-state target. Originating at such action the hot plasma spot has the spectrum of a radiation close to a spectrum "black body". Let us now estimate the number of the isomeric nuclei, which can be activated in a magnetic trap at pumping by a X-radiation of laser plasma. The X-ray photons stream from unit of a surface of a hot plasma spot is equal to

$$\frac{dN_x}{dt d\omega_x dS} = \frac{\omega_x^2}{\pi^2 c^2} [e^{\frac{\hbar\omega_x}{T}} - 1]^{-1}, \quad (1)$$

where T - temperature of laser plasma, and ω_x and N_x - the frequency and number of X-ray photons accordingly. Assuming, that the plasma spot has the square S , and size of a cloud of the isomeric nuclei along direction of pump propagation is equal to a , it is possible to estimate a full section of pump X - ray resonant absorption by nucleus ensemble in a magnetic trap

$$\sigma_f = N_0 S a \sigma_x, \quad (2)$$

where $\sigma_x = 2\pi c^2 / \omega_x^2$ - the X-ray section of resonant absorption. Then during of laser pulse τ_i , on the upper active level $|3\rangle$ will pass N_S of the isomeric nuclei in volume of a magnetic trap

$$N_S = \frac{dN_x}{dt d\omega_x dS} \sigma_f \Gamma_0 \tau_i = \frac{2}{\pi} N_0 S a \Gamma_0 \tau_i, \quad (3)$$

where Γ_0 - natural width of the resonant γ -transition $|3\rangle \rightarrow |2\rangle$. As can see from (3) only small part of nuclei into **MT** can be activated e.g. for $\tau_i \approx 10^{-10}$, $\Gamma_0 = 10^9 \text{c}^{-1}$ the number of activated nuclei is about 10^{-3} from initial number N_0 .

Now we can estimate the power value of pulse γ -radiation when all isomeric nuclei into **MT** are pumped. We consider, that in the localization area of **MT** $\approx 10^{-3} \text{cm}^{-3}$ while the number of isomeric nuclei is $N_0 \approx 10^{12}$. Then the γ -radiation power, which can be obtained at pumping of all isomeric nuclei localized in a trap, is 10^{12} γ -photons during the lifetime $\tau(\Gamma_0)^{-1}$ of the upper excited state $|3\rangle$. The natural width of an excited state $|3\rangle$ Γ_0 can be obtained from an one-partial approximation as $\Gamma_0 \approx 10^9 \text{c}^{-1}$ for $\lambda_\gamma \approx 6 \cdot 10^{-9} \text{cm}$ ($\hbar\omega_\gamma = 20 \text{keV}$) and we have considered transition $|3\rangle \rightarrow |2\rangle$ as M1 []. The full energy of γ -radiation will be about $2 \cdot 10^{-3} \text{J}$. At the same time the width of γ -radiation spectrum, which can be obtained on the transition $|3\rangle \rightarrow |2\rangle$, is determined by Doppler effect because of the recoil at an absorption of **X**-ray pumping. For above mentioned values, width of a spectrum obtained γ -radiation $\Delta\omega_D = \hbar k_\gamma^2 / (A m_p) = 10^{14} \text{Hz}$, where k_γ - wave vector and γ -radiation correspondently, A -atom number, m_p -proton mass.

We shall underline, that (3) determines the number of the activated nuclei in a magnetic trap without any losses. To determine real concentration of the isomeric nuclei into **MT** N_γ it is necessary to take into account losses of the **X**-ray photons of two basic processes: a photoeffect in a continuous spectrum of **X**-ray pumping with the section

$$\sigma^{ph.eff.}(\omega) = \frac{32\pi^{1/2}\alpha^4 Z^5}{3} (e^2/(m_e c^2))^2 (m_e c^2/(\hbar\omega))^{7/2} \quad (4)$$

and by absorption of **X**-ray photons other nuclear and electron levels.

We shall mark, that the electron envelopes of atoms have sections of a resonance absorption considerably large than σ_x . Therefore it needs to take out a low-frequent part of the pump spectrum that can be done with using a filter, bounding the pump frequency lower than the frequency ω^* . As a result, the real concentration of the activated isomeric nuclei can be given by

$$N_\gamma = \frac{N_S}{1 + \sum_{i=1} \frac{\gamma_i(e^{\frac{\hbar\omega_x}{T}} - 1)}{\Gamma_0(e^{\frac{\hbar\omega_i}{T}} - 1)} + \int_{\omega^*} \sigma^{ph.eff.}(\omega) \frac{\omega^2}{2\pi c^2} \frac{e^{\frac{\hbar\omega_x}{T}} - 1}{e^{\frac{\hbar\omega}{T}} - 1} \frac{d\omega}{\Gamma_0}} \quad (5)$$

where in a sum on "i" are included as nuclear and electronic levels, which have the frequencies into spectral interval of pumping. Thus each such resonance has the of absorption section $\sigma_i = 2\pi c^2/\omega_i^2$ and width γ_i .

Now we shall choose the energy of pump photons $\hbar\omega_x > T, \hbar\omega_*$, then for all "i" $\omega_i > \omega_x$ ($\omega^* < \omega_x < \omega_i$ for $\forall i$) and the addends in a sum of a denominator of fraction (5) will be exponential are small. We shall estimate now losses of pump photons because of ionization. For this it is necessary to calculate an integral in a denominator of fraction (5). As a result the condition of small losses of activated atoms at ionization can be given by

$$7.4 Z^5 \alpha^6 (m_e c^2 / \hbar\omega^*)^{3/2} \frac{T}{\hbar\Gamma_0} (e^{\frac{\hbar\omega_x}{T}} - 1) e^{-\frac{\hbar\omega_x}{T}} \leq 1, \quad (6)$$

where $\alpha = \frac{1}{137}$ - constant of fine structures.

Substituting in (6) $\hbar\Gamma_0 = 10^{-3} \text{eV}$, $\hbar\omega_* = 511 \text{eV}$, $\hbar(\omega_x - \omega^*) < T$ and $T = 400 \text{eV}$, we

have to receive from (6) the estimate of a charge of the isomeric nuclei $Z \leq 10$. That is why to consider the nuclei with the charge much larger than $Z = 10$ it is necessary to increase the laser puls power to $10^{20} - 10^{21} \text{ W/cm}^2$.

4. Conclusion

Thus we have shown a possibility of creation of an impulse monochromatic γ -source with high activity by **X-ray** pumping of active γ -transition of the cooled isomeric nuclei into **MT**. In our case the **X-ray** pumping has been taken of laser plasma which is produced by interaction between very intensive laser optical pulse and target surface.

It is necessary especially to note, that such γ -source can be created already now and for its experimental realization there are not really difficulties. In experiments on observation such activity of nuclei into **MT** the nuclei of ^{58}Co , ^{84}Rb , ^{93}Mo or ^{152}Eu could be used as they have needed scheme of nuclear transitions [8]. For example, preferably for the first experiment to take ^{84}Rb nuclei because of both the laser pumping and trapping into **MT** such atoms known very well [3,4]. As a result into **MT** the concentration 10^{11} cm^{-3} [] can be easily obtained. Then during laser pulse such number of cooled nuclei allows to receive $\approx 10^6$ resonant γ -photons. At the same time the noise of a natural γ -activity can be eliminated by using time-selective registration of the signal. Thus the noise of natural γ -activity for the isomeric nuclei with a half-life 1 hour is corresponding $\approx 10^7$ of decompositions in a second at the pointed above number of nuclei. However, for times $\approx 10^{-6} \text{ s}$ the number of natural emitted γ -photons is ≈ 20 while one of γ -photons by **X-ray** pumping of active γ -transition will exceed 10^6 . Therefore a signal/noise ratio in such time-selective experiment amounts to 10^5 , that can easily be observed.

1. Recoilless gamma-ray lasers

Reviews of Modern Physics, v. **69**, N.4, 1085 (1997)

2. V.V.Vladimirsky **Zh.Sov.Teor.Exp.Fiz.**, **39**, 1062 (1960)

3. D.Boiron, C.Triche, D.R.Meacher, P.Verkerk, G.Grynberg
Phys.Rev.A, v. **52**, N.5, R3425 (1995)

4. C.B.Collins, F.W.Lee, D.M.Shemell, B.D.DePaola, S.Olariu, I.Iovitzu Popescu
J.Appl.Phys., **53**(7), 4645 (1982)

5. A.V.Andreev

Vest.Mosw.University 3, Physics and Astronomy 35, 28 (1994)

6. Izava Y, *Phys.Lett.B*, **88**, 59 (1989)

7. .Bor, B.Mottelson - **Atom nuclear structure**, .2,(1976)

8. **Nuclear Data Sheets**, 1989 - 1998.

Second Harmonics Emission from Short Pulse Laser Irradiated Solid Targets

J. Limpouch^a, A.A. Andreev^b and K.Yu. Platonov^b

^aFaculty of Nuclear Science and Physical Engineering, Czech Technical University,
Břehová 7, 115 19 Prague, Czech Republic

^bInstitute for Laser Physics, Vavilov State Optical Institute,
Birzhevaya line 12, Skt. Petersburg, Russia

ABSTRACT

Second harmonics intensity and spectra, emitted from solid Al target heated by obliquely incident p-polarized 1.5 ps Nd-laser pulse, are interpreted in the frame of 1D hydrodynamics model including resonance absorption, fast electron generation and transport and acceleration of ions. Second harmonics spectra reveal blue shift for laser intensity 10^{16} W/cm², while red shift is observed for laser intensity 10^{17} W/cm². It corresponds to a qualitative difference in the critical surface dynamics observed in simulations. A good agreement of simulation results with experiment is observed for the lower intensity while possible explanations of certain discrepancies for the higher intensity are proposed.

Keywords: Hydrodynamics model, resonance absorption, second harmonics emission, critical surface motion

1. INTRODUCTION

Second harmonics (SH) emission is a very important diagnostics tools which can provide a detailed information about particularly important region of critical surface neighbourhood. Parametric instabilities¹ and resonance absorption² are the well-known sources of SH emission in laser-produced plasmas. While parametric instabilities are unimportant in short-pulse interactions with solid targets due to submicron density scale length of plasma, resonance absorption of obliquely incident p-polarized laser radiation is often a dominant mechanism of laser absorption. Both energy conversion to SH and SH spectrum has been measured in short pulse experiments.³

In this paper we investigate the interaction of ultrashort laser pulses with a planar aluminium target in the frame of 1D hydrodynamics model. We focus our study on the dependence of critical surface motion on laser intensity and we compare the calculated SH intensity and spectra with results from experiments.⁴

2. THEORETICAL MODEL

The dynamics of plasma is described via one fluid two temperature Lagrangian hydrocode with electron and ion thermal conductivity, both natural and artificial ion viscosity and ponderomotive force impact on plasma motion. Very fine spatial grid with up to 500 cells is used to model in detail the shape of the density profile in the expanding plasma so that the laser electromagnetic fields may be calculated properly. The ionic populations in plasma are calculated via a set of atomic rate equations for the populations of charge states. The energy loss by bremsstrahlung and recombination radiation is taken into account.

Laser absorption and electromagnetic fields are calculated for p-polarized laser radiation by numerical solving Maxwell equations in hot plasma, taking into account spatial dispersion. The model includes collisional absorption, Landau damping and wavebreaking of the plasma wave. The acceleration of electrons by plasma wave damping is treated in each time step via stationary electron diffusion in the velocity space. The averaged diffusion coefficient $D(v)$ is calculated in the model of electron acceleration by resonant Fourier component F_k of longitudinal electric field.

The energetic electrons travelling to the plasma vacuum boundary are reflected there in a double layer and a part of their energy is transferred to a group of energetic ions. The transport of electrons into the target is then described

Other author information: J.L.: E-mail: limpouch@lilit.fjfi.cvut.cz
A.A.A.: E-mail: andreev@ilph.spb.su

in a simplified manner. Fast electrons penetrate deep into the target, where they preheat the solid density target material as a precursor to the thermal wave. A detailed description of the model can be found elsewhere.⁵

Here we have calculated the intensity and the phase of SH emission by solving of the Maxwell's equations for SH field. Spatial dispersion is not included for SH field, as it does not influence the intensity and phase of SH emission significantly. We have also neglected the impact of SH fields back on the basic harmonics, which limits the range of the validity of the model to medium laser intensities, where the energy conversion to SH emission is small. The equations for SH fields are written, as follows

$$\begin{aligned}\frac{\partial}{\partial x} E_{2y} - 2i \frac{\omega_0}{c\epsilon_2} (\epsilon_2 - \sin^2 \theta) B_2 &= \frac{4\pi \sin \theta}{c\epsilon_2} j_{2x} \\ \frac{\partial}{\partial x} B_2 - 2i \frac{\omega_0 \epsilon_2}{c} E_{2y} &= -\frac{4\pi}{c} j_{2y}\end{aligned}\quad (1)$$

where B_2 , E_{2y} are magnetic and transverse electric field of SH emission, ω_0 and θ denote laser frequency and angle of incidence, ϵ_2 is plasma dielectric constant for SH emission. The source of SH emission is the non-linear current \vec{j}_2

$$\vec{j}_2 = -i \frac{e}{4\pi m \omega_0} \left(\vec{E}_1 \operatorname{div} \vec{E}_1 + \frac{\omega_p^2}{4\omega_0^2} \nabla \vec{E}_1^2 \right) \quad (2)$$

where \vec{E}_1 is electric field at laser frequency.

The source of SH emission is maximum in the neighborhood of the critical surface, where also resonance conditions for the sum of laser and plasma wave with SH electromagnetic wave are fulfilled. The phase of SH emission is controlled mainly by the motion of the source of SH emission which is near to the critical surface and thus the shift of SH spectrum is near to the Doppler shift of radiation reflected from the moving critical surface.

When the density scale length L is small $L < \lambda_0$, the laser magnetic field B_r at resonance surface ($\operatorname{Re}(\epsilon) = 0$) is approximately equal to field at the plasma-vacuum boundary $B_r \simeq 2 B_0$, where B_0 is the field of incident laser wave in vacuum. Thus the terms with the maximum powers of ϵ , ϵ_2 in denominator dominate the SH source (the right side of eq.(1)) and the equation for SH magnetic field B_2 is transformed to the following form

$$\tilde{B}_2'' - \frac{\epsilon_2'}{\epsilon_2} \tilde{B}_2' + 4(\epsilon_2 - \sin^2 \theta) \tilde{B}_2 = \sin \theta \frac{\tilde{B} \tilde{B}'}{\epsilon^2} \left(2 \frac{\epsilon'^2}{\epsilon_2^2} + \frac{\epsilon' \epsilon_2'}{\epsilon \epsilon_2} \right) \quad (3)$$

where ' denotes $d/d\xi$, $\xi = k_0 x = \omega_0/cx$ and $\tilde{B} = eB/m\omega c$. The solution of eq.(3) that meets the following boundary conditions

$$\tilde{B}_2 \rightarrow 0 \quad (\xi \rightarrow 0) \quad \tilde{B}_2 = R_2 \exp(-2i\xi) \quad (\xi \rightarrow -\infty)$$

can be easily found using Green function of eq.(3). The amplitude R_2 of the emitted SH radiation can be expressed, as follows

$$|R_2| = \pi \frac{\sin^3 \theta}{\cos \theta} \frac{|\tilde{B}_0|^2}{\gamma^2} \quad (4)$$

Here a linear profile of plasma density was assumed in the vicinity of the critical surface, and parameter $\gamma = \nu_{eff}/\omega_0$ describes the damping rate of resonance peak of longitudinal laser electric field, which is dominated either by collisions or by propagation of plasma waves or by wavebreaking. The expression (4) differs only by a coefficient of order 1 from similar expression derived by Dragila.⁶ Thus a simple formula of the efficiency of laser energy conversion to SH emission reads

$$\eta_2 = I_{2\omega}/I_0 \simeq 4 I_{18} (\omega_0 L/c)^{4/3} \Phi^2(q)$$

where laser intensity $I_{18} = I/10^{18} \text{ W/cm}^2$, $\Phi(q)$ is the Ginzburg function and $q = (k_0 L)^{2/3} \sin^2 \theta$. This expression differs by the multiplier $2.5 (k_0 L)^{2/3}$ from the classical formula for long plasmas $k_0 L \gg 1$, derived in paper.²

It is important to note that in case of high intensities investigated here, the dominant mechanism of limitation of the longitudinal laser field is the wavebreaking mechanism and the density scale length L depends on laser intensity. When the formula from paper⁷ is used for $L(I)$, the conversion efficiency is expressed, as follows

$$\eta_2 \simeq 2.10^{-4} T_{keV}^4 I_{18}^{-1} \sin^2 \theta \quad (5)$$

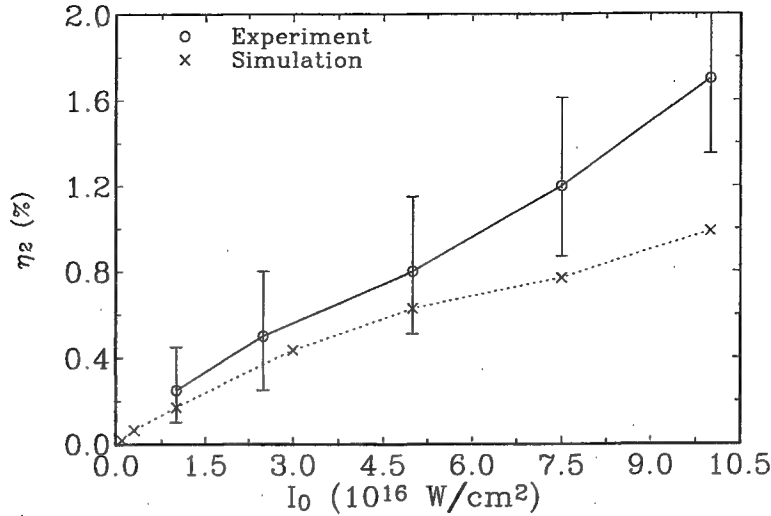


Figure 1. Efficiency $\eta_2 = I_2/I_0$ of laser energy transformation to SH emission from plasma versus peak laser intensity. P-polarized Gaussian 1.5 ps FWHM pulse of Nd-laser is assumed to be incident at 45° onto a solid aluminium target.

As the electron temperature rises with laser intensity $T \sim I^\alpha$, where $\alpha \gtrsim 0.3$, the transformation efficiency η_2 still grows with laser intensity, but the increase is slower than linear.

When the phase characteristics of second harmonics emission are investigated, it can be shown that the phase of the term in the Green function integral (product of the source and of the Green function) is negligible. Thus the frequency shift in the SH emission is given only by the motion of the critical surface and thus the influence of the plasma density profile may be neglected. Now, we shall consider generation of sidebands of SH emission due to the decay of plasma wave into plasma wave and ion sound wave, proposed by Cairns.⁸ As the propagation of ion sound normal to the critical surface, investigated in paper,⁸ is here inhibited due to sharp density profile, we assume sound waves propagating along the critical surface. From the phase condition of the parametric decay $\vec{k}_l = \vec{k}_{l'} + \vec{k}_s$ and $\omega_l = \omega_{l'} + \omega_s$, the frequency of the sound waves is given by

$$\omega_s \simeq 2 \frac{Z m_e}{M_i} \omega_l \quad (6)$$

As the amplitude of the plasma wave, generated by the decay, may be large, the plasma wave $\omega_{l'}$ can decay into plasma wave and ion sound again and a series of sidebands, shifted by $j\omega_s$, where $j=0,1,2,\dots$ may be formed in SH spectrum.

3. NUMERICAL RESULTS

Presented results have been obtained for the conditions of experiment,⁴ where 1.5 ps FWHM Gaussian pulse of Nd-laser was incident onto a flat Al target. The angle of incidence was 45° , the intensity contrast was 10^6 to 10^7 . The peak laser intensity I_0 was varied in range 10^{16} - 10^{17} W/cm 2 .

The overall efficiency of energy transformation to SH emission is displayed in Fig. 1 versus laser peak intensity. The experimental results are plotted together with the results of numerical simulations. When plasma electron temperature scales $T \sim I^{0.5}$, then according to the formula (5), the transformation efficiency grows linearly with the laser intensity $\eta_2 = I_2/I_0 \sim I_0$. This scaling is plausible for the experimental data. However, the computed transformation efficiencies are generally somewhat lower than the experimental values and they indicate a weaker dependence of transformation efficiency on laser intensity, especially for higher laser intensities $I \geq 5 \cdot 10^{16}$ W/cm 2 . For these intensities the simulation is very sensitive to the detailed conditions (e.g. the shape of laser pulse) due to enormous value of the ponderomotive force. Also many non-linear effects (wavebreaking, acceleration of fast

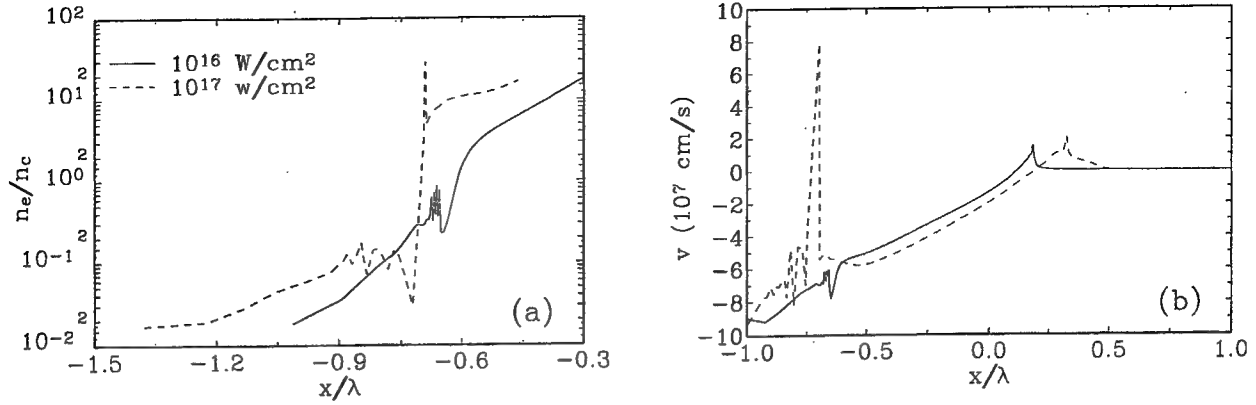


Figure 2. Spatial profiles of (a) electron density n_e (normalized on critical density n_c) and of plasma velocity v at the maximum of Nd-laser pulse and laser peak intensities $I_0 = 10^{16} \text{ W/cm}^2$ and $I_0 = 10^{17} \text{ W/cm}^2$. P-polarized Gaussian 1.5 ps FWHM pulse of Nd-laser is assumed to be incident at 45° onto a solid aluminium target.

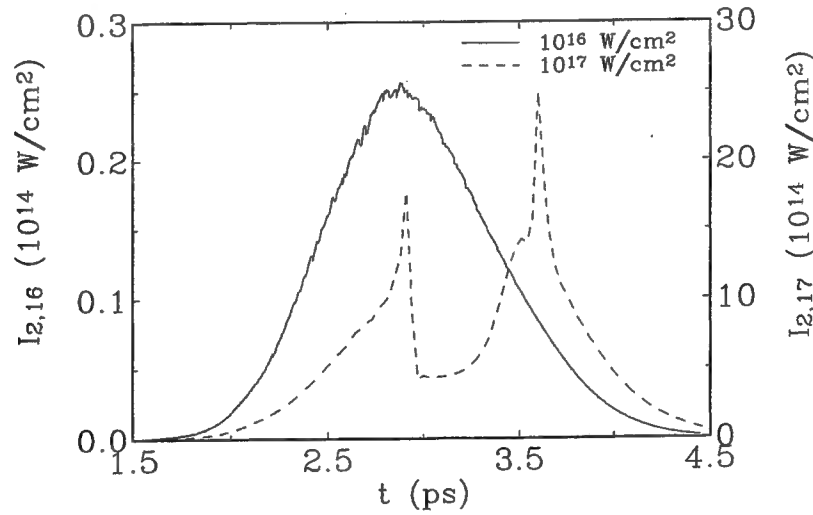


Figure 3. Evolution of intensity of SH emission for laser peak intensities $I_0 = 10^{16} \text{ W/cm}^2$ and $I_0 = 10^{17} \text{ W/cm}^2$ (left and right y axis are used for the lower and higher laser intensities, respectively). P-polarized Gaussian 1.5 ps FWHM pulse of Nd-laser is assumed to be incident at 45° onto a solid aluminium target.

electrons) are described only phenomenologically in the frame of hydrocode, and thus they may easily become a source of inaccuracy.

While blue shift $\Delta\lambda = -1.0 \pm 0.2 \text{ nm}$ of the SH spectrum was observed in experiment for laser intensity 10^{16} W/cm^2 , the situation changed qualitatively for the higher intensity 10^{17} W/cm^2 and red shift $\Delta\lambda = 0.8 \pm 0.2 \text{ nm}$ has been measured. It indicates a qualitative change in the motion of the critical surface. Our simulations really indicate a possibility of such variation in plasma dynamics in the studied laser intensity range. It is presented in Fig. 2, where plasma density and velocity profiles are plotted at maximum of laser pulse for the respective intensities. Fig.2b shows that at the higher intensity an period exists when the plasma motion in the vicinity of the critical surface is directed inwards the target. Then the critical surface moves also inwards and plasma density scale length is shortened. In our simulations this period is relatively short when a laser prepulse is absent.

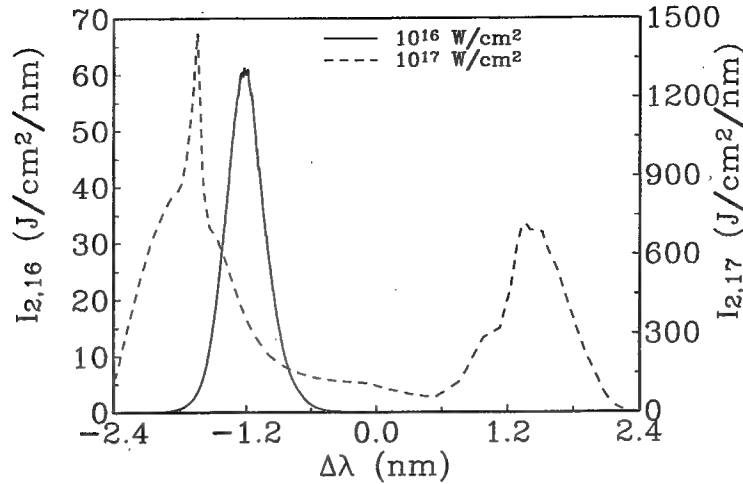


Figure 4. Computed integral spectra of SH emission for the same conditions as in previous figure.

The sensitivity of SH emission to plasma dynamics is demonstrated in Fig. 3, where the evolution of SH emission intensity is plotted for incident laser intensities $I_0 = 10^{16}$ W/cm² and $I_0 = 10^{17}$ W/cm², respectively. For the lower intensity the maximum of SH emission is approximately at the maximum $t = 2.9$ ps of the laser pulse. The smooth shape of the SH emission pulse is near to the shape of I_0^2 . The SH emission pulse is qualitatively different for the higher intensity when two peaks are formed and separated with a period when a very sharp plasma density profile is unfavorable for laser energy transformation to SH emission.

The comparison of the computed SH spectra for laser intensities $I_0 = 10^{16}$ W/cm² and $I_0 = 10^{17}$ W/cm² is presented in Fig. 4. Blue shift of the SH spectra for the lower intensity is caused by an outward motion of the critical surface. The magnitude of the blue shift of SH spectrum corresponds well to the critical surface velocity at the laser pulse maximum and it is in a good agreement with the experimental value. The model of SH emission underestimates SH line width as SH spectrum is computed assuming infinitely narrow laser line. As the experimental SH line width corresponds to broadening given by the laser spectral width for $I_0 = 10^{16}$ W/cm² and the calculated SH line width is narrower than in experiment, the simulations are not in contradiction with the experiment.

The spectrum in Fig. 4 is more complicated for the higher intensity. At the laser pulse maximum an inward motion of the critical surface is observed (Fig. 2a) and thus SH emission during the first temporal peak (Fig. 3) of SH intensity is red shifted. However, the inward motion of the critical surface lasts only part of the laser pulse duration and at the time of the second maximum of SH emission the critical surface moves in the outward direction. Thus blue shift of SH emission is obtained at the end of laser pulse and two peaks are observed in SH spectrum. Spectra with both blue and red shifted components have been occasionally observed in experiment.⁴

However, the typical experimental spectrum, that is measured for laser intensity 10^{17} W/cm², is plotted in Fig. 5. This spectrum contains only red shifted component, the magnitude of the red shift in experiment is less but comparable to the calculated value. A rather small broadening of SH spectrum compared to that corresponding to the width of laser spectrum indicates a rather stable motion of the critical surface inwards with velocity $v \sim 4 \cdot 10^7$ cm/s during the most intense part of SH emission.

The discrepancy in plasma dynamics may be caused by the non-linear character of laser-plasma interaction which is difficult to describe correctly in the frame of hydrodynamics model. The dynamics of the critical surface may be dominated also by two dimensional character of the interaction, as the motion of the critical surface inwards may be prolonged by radial ponderomotive force pushing plasma radially out of the focus. This idea is supported by the fact that the spectrum presented in Fig. 5 is emitted by the central part of the laser focus, while a blue shift is observed in SH emission from the edge of the focus. The discrepancy may be also explained by a possible laser prepulse. According to the experimental data the prepulse intensities are likely to be in range $10^{10} - 10^{11}$ W/cm², which can

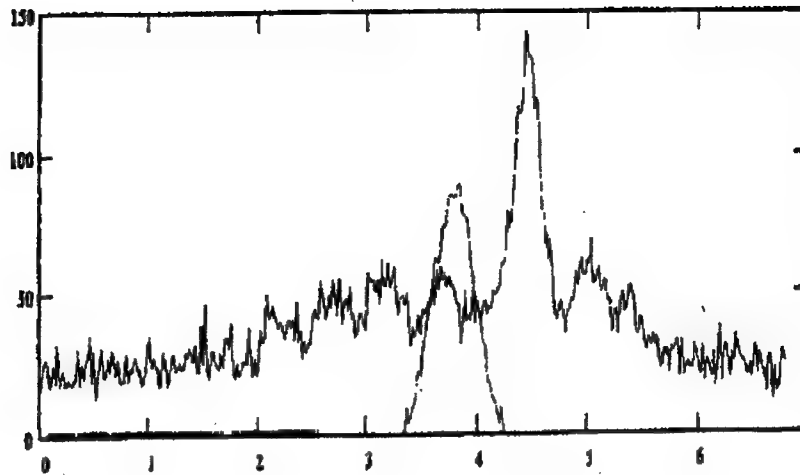


Figure 5. SH spectrum, measured at the axis of laser spot, when p-polarized Gaussian 1.5 ps FWHM pulse of Nd-laser with peak intensity $I_0 = 10^{17}$ W/cm² is incident at 45° onto a solid aluminium target. The shift of SH wavelength is measured from the plotted laser pulse (wavelength divided by 2), the wavelength axis scale is 1 nm.

lead to a significant evaporation of the target material. Then a larger density scale length of plasma could support a stable inward motion of the critical surface. A detailed study of laser prepulse impact on target dynamics and SH spectrum is being planned.

The motion of the critical surface cannot explain long sidebands in SH spectrum, observed in Fig. 5. We have presented here a proposal of the sidebands generation due to a decay instability, physically similar to paper,⁸ but with a different geometry. The shift of the j -th sideband is according to eq.(6) $|\Delta\lambda_j/\lambda_0| \simeq 2jZm_e/M_i \simeq 5 \cdot 10^{-4} j$, which is $\Delta\lambda_j \simeq 0.5 j$ nm. This is near to the distance of the secondary maxima, observed in Fig. 5.

4. CONCLUSIONS

SH emission from short pulse laser irradiated solid targets is calculated for conditions of experiment.⁴ The numerical results indicate a qualitative change in plasma dynamics, when incident laser intensity is increased from $I_0 = 10^{16}$ W/cm² to $I_0 = 10^{17}$ W/cm². This difference is indicated in SH spectrum by transition from a blue shift to a red shift of SH spectra. While the results for the lower intensity are in a good agreement with experiment, some discrepancies are observed for the higher intensity, where non-linear character of laser plasma interaction is apparent and SH spectrum containing both red and blue shifted component are calculated. Tentative explanations of this discrepancy are discussed. A decay instability mechanism is proposed to account for broad wings observed in SH spectrum.

REFERENCES

1. N.G. Basov *et al.*, *Kvantovaya elektronika* **6**, p. 1829, 1979.
2. N.E. Erokhin, S.S. Moiseev, and V.V. Mukhin, *Nuclear Fusion* **14**, pp. 333–339, 1974.
3. D. von der Linde, and H. Schüller, *Appl. Phys. Letts* **66**, p. 807, 1995.
4. A.A. Andreev, V.I. Bayanov *et al.*, *AIP Conference Proceedings* **426**, pp. 61–66, 1997.
5. J. Limpouch, L. Drska, M. Tagviashvili, and A.A. Andreev, in: *Advances in Laser Interaction with Matter and Inertial Fusion*, eds. G. Velarde *et al.*, World Scientific 1997, pp. 621–624.
6. R. Dragila, *Phys. Rev. A* **44**, p. 6828, 1991.
7. K. Estabrook, and W.L. Kruer, *Phys. Rev. Letts* **40**, pp. 42–45, 1978.
8. R.A. Cairns, *J. Plasma Phys.* **22**, pp. 149–156, 1979.

Spatial and spectral parameters of superthermal particle extension in laser-plasma experiments with picosecond laser pulse

V.M.Komarov, V.G.Borodin, A.V.Charukchev, V.N.Chernov V.V.Ilyin, V.A.Malinov, V.M.Migel, N.V.Nikitin,

Scientific Research Institute of Complex Testing
Sosnovy Bor, Leningrad region, 188537, Russia

ABSTRACT

On the PROGRESS laser facility the spectral and spatial characteristics of superthermal particles extension in experiments with flat targets and picosecond duration of heating laser pulse are investigated. The opportunity to use multiframe pulse interferometry for visualization of spatial and power parameters of superthermal particle extension alongside with traditional means of charged particle diagnostics with an irradiation of flat targets in an atmosphere of residual gas are considered.

The basic part of laser radiation ($\lambda = 1053 \text{ nm}$) with energy up to 20 J [1] and pulse duration 200 ps is directed to target chamber. A few part of a heated laser pulse amplified and compressed with Raman backscattering compressor [2] up to 10-20 ps with energy 20-30 mJ and wavelength 622 nm was used as optical diagnostic beam in multiframe interferometer. Series of experiments both with p and with the s-polarized radiation were carried out. On the basis of received interferograms the measurements of spectral parameters of fast particles by traditional methods with time-of-flight technique are carried out. This data are compared with spatial distribution of fast ions at picosecond (1.5 ps) laser-plasma experiments and laser intensity up to 10^{19} W/cm^2 on the PROGRESS-P laser.

1.INTRODUCTION

One of the important features of high power laser pulse - solid target interaction at intensity $10^{16} - 10^{19} \text{ W/cm}^2$ is superthermal charge particle generation. Now experimental data about spatial and spectral ion distribution are not sufficiently. Here we report about spatial and spectral ion distribution measurements as by optical diagnostic means so by using of charge particle collector array.

2.SCHEME OF OPTICAL MEASUREMENTS

Principal scheme of laser multiframe interferometer is shown in Fig.1 [1]. The main portion of laser pulse energy with pulse duration 200 ps enters the vacuum chamber where with $f/1.5$ focusing objective lens is focused on a solid state target covered of rarefied gas at pressure a few mm Torr. Spot size on a target (60% of laser energy) is $5 \mu\text{m} \times 7 \mu\text{m}$ and peak intensity on a target is up to 10^{17} W/cm^2 . A few portion of laser pulse energy ($< 10\%$) enters in diagnostic channel where at first one is converted to the second harmonics of the laser pulse with KDP-crystal and then one enters to Raman-compressor. In this compressor laser pulse is formed with $\lambda = 622 \text{ nm}$ and 20 ps pulse duration that extends to the back direction. This diagnostic beam is divided into two parts: smaller portion of laser energy enters to the optical interferometer and other portion enters to the optical delay line (ODL). ODL affords maximal delay 200 ns. Two beams removed from the ODL is injected into the interferometer too. To display a plasma jet on a film, $f/6$ -lens with a magnification of $10\times$ is used.

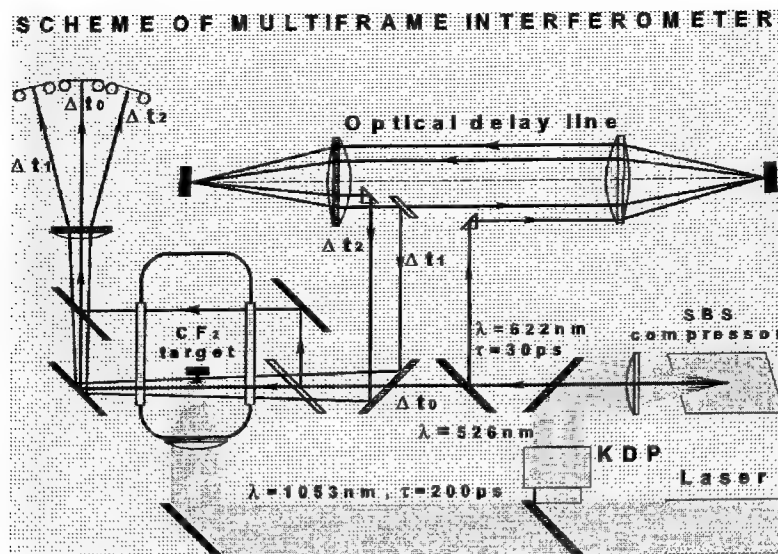


Fig. 1. Basic optical scheme of multiframe interferometer

In this scheme heating laser pulse is locked in step with diagnostic pulse with time spread up to ± 10 ps related to time spread in Raman backscattering compressor. In addition, it may be noted that diagnostic pulse wavelength is distinguished highly from heating pulse wavelength and its harmonics and it allows to suppress unwanted illumination from plasma on image plane. These factors in combination with short exposure allow to investigate the spatial distribution and to estimate the energy of suprathermal charge particles emitted from laser plasma visually.

2.1. EXPERIMENTAL RESULTS

In Fig. 2 the images of shock wave front in rarefied air at different time after shot and at laser intensity on a target $\approx 5 \cdot 10^{17}$ W/cm² is shown. Because of high spatial resolution (3-4 μ m) it can see fine structure of shock wave front and brief narrowed

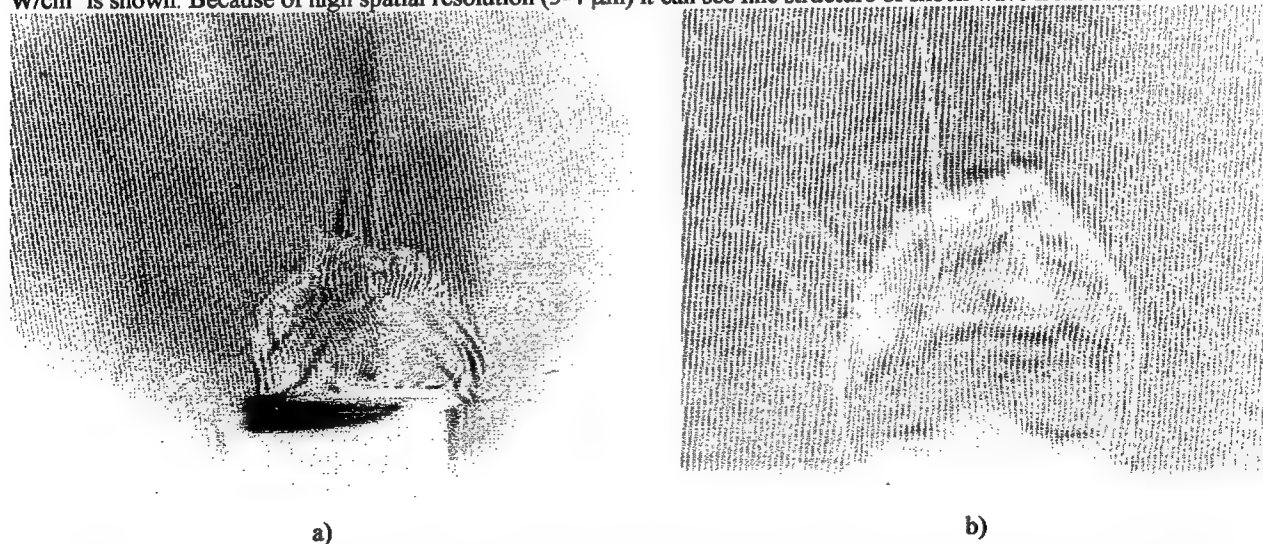


Fig. 2. Interferograms of shock waves in laser-plasma interaction at intensity on CF₂-target - $5 \cdot 10^{16}$ W/cm² (5 ns after shot)

jets with length more than basic front radius. These jets are track of charge particles emitted from plasma with suprathermal velocities. The direction of jet propagation is the direction of predominant suprathermal particle extension. In addition, visualization of suprathermal particle tracks allows to estimate characteristic ion energy in jet and then to carry out more detailed measurements of suprathermal ion spectrum with other diagnostic means.

The main part of our experiments demonstrates plasma jets are emitted along the target normal or at less than 20° with respect to a target normal and weak jets in specular direction with respect to the incident laser beam, see Fig.2a. This behavior was typical for two-third of the shots. In addition, usually, jets emitted in "specular" direction were shorter than jets emitted along the target normal. In one-third of the shots plasma jets is emitted at specular direction with respect to the incident laser beam so as along target normal. This situation is shown in Fig.2b.

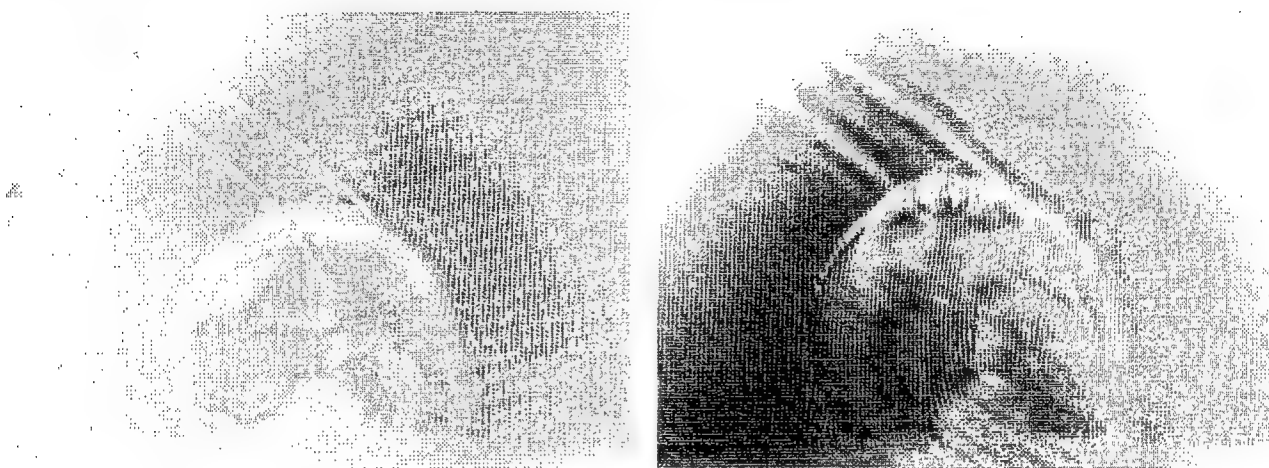


Fig.3. Interferograms of shock waves in laser-plasma interaction at intensity on CF_2 -target - $8 \cdot 10^{16} \text{ W/cm}^2$
a) 5 ns after short
b) 8 ns after short

It is interesting that in a few shots it can see crooked jets as superstrong magnetic field effect on the charge particle beam, see Fig.3..

3. FAST ION MEASUREMENTS

Using optical measurement we placed array of ion collectors so along predominant direction of jet extension as in other directions to get information about fast ion velocity distribution by a time-of-flight technique. Each charge collector was equipped with biased mesh (-80 V) and cylindrical cavity collecting electrode to suppress the emission of secondary electrons from the detector surface. The ion current detected by charge collectors was recorded with multichannel 60 MHz-digitizer. The distance from the target to the detectors, were fixed to be 45 cm throughout the experiments. The ion collectors were used either as an array of detectors for angularly resolved ion current trace measurements or as a detector for ion spectrometry to estimate ion charge state (Z/A) measurements. The ion charge Z is estimated by comparison of time integration value of ion kinetic energy from collector data and absorbed plasma energy measured with plasma calorimeter aligned near the collector [2].

In Fig.4 fast ion current output from the collectors fixed at different positions with respect to target normal in experiments with s and p-polarization is shown. Upper traces are ion currents along target normal and bottom traces are ion currents in specular direction.

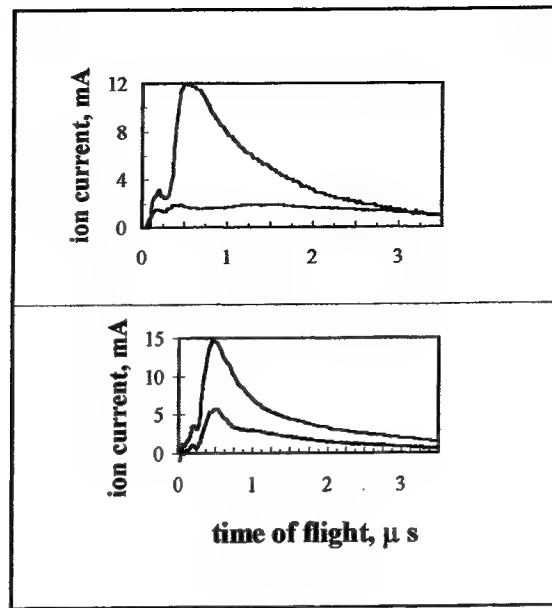


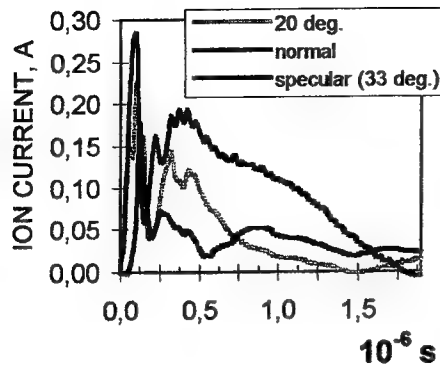
Fig.4. The fast ion current output from the collectors fixed at different positions with respect to target normal in experiments with s (top) and p-polarization (bottom). Laser intensity 10^{17} W/cm^2 .

It is seen that curves of ion currents (for p-polarization, in particular) are similar in form but not in amplitude and so fast ion extension is predominantly along target normal and at specular direction fast ion current is critically smaller. In addition, fast ion current at all other angles is smaller than at specular angle with slow decrease with increasing angle from the target normal. Comparison of maximum ion velocity put from a time-of-flight technique ($4 \cdot 10^6 \text{ m/s}$) and mean jet velocity ($3.5 \cdot 10^6 \text{ m/s}$) shows that jets are traces of fast ion extension. Of course, this time-of-flight technique did not measure peak velocities of fast ions. It would be necessary to use method [3] to do it, for example. But combination of time-of-flight technique and multiframe interferometer selects the direction and carries out preliminary adjustment.

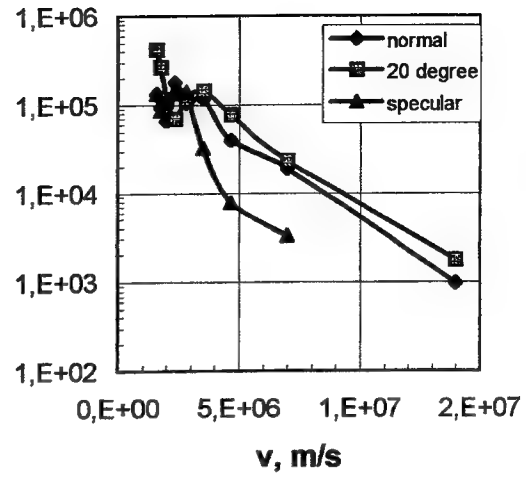
Now we are going to carry out spatial distribution experiments with 1.5 ps-pulse duration at laser intensity up to 10^{19} W/cm^2 and use CPA-pulse as probe in multiframe interferometer. However, we have carried out preliminary ion collector experiments to compare fast ion output to subnanosecond data. Position of ion collector array were so ones as at subnanosecond experiments.

PROGRESS-P Nd-glass laser system with $1.06 \mu\text{m}$ wavelength utilizing chirped-pulse amplification and compression up to 1.5 ps was used for these experiments. Laser energies up to 16 J are concentrated by axis parabola mirror with $f/1.1$ (laser beam diameter - 180 mm) into a focal spot (50 % of the laser energy) with a diameter of $7 \mu\text{m}$. Peak intensity on target was up to 10^{19} W/cm^2 . The main pulse is preceded by long ASE-prepulse of much lower intensity ($\leq 10^{-8}$). The "short" (with a duration of $\leq 10 \text{ ps}$) prepulse contrast with respect to main pulse was less than 10^{-3} . The laser was usually polarized in the plane of incidence (p-polarization) and incident on the planar optically polished metal (Al) target at 33° with respect to the target normal.

Fig.5(a) shows ion current traces of collectors for different angles with respect to the target normal at laser intensity 10^{19} W/cm^2 . The traces are similar in form and amplitude is decreased with increasing angles from the target normal so as at subnanosecond experiments. Fast ion velocity distribution is shown in Fig.5 (b).



a)



b)

Fig.5. Ion current traces (a) and ion velocity distribution (b) for different angles with respect to the target normal at laser intensity 10^{19} W/cm^2 .

Here, it is assume that fast ion emission is predominantly from protons with peak recorded velocity $1.8 \cdot 10^7 \text{ m/s}$. It is seen that picosecond and subnanosecond fast ion spatial distribution data is similar.

By integrating of fast ion current of collector array spatial distribution of fast ion energy have been obtained, see Fig.6.

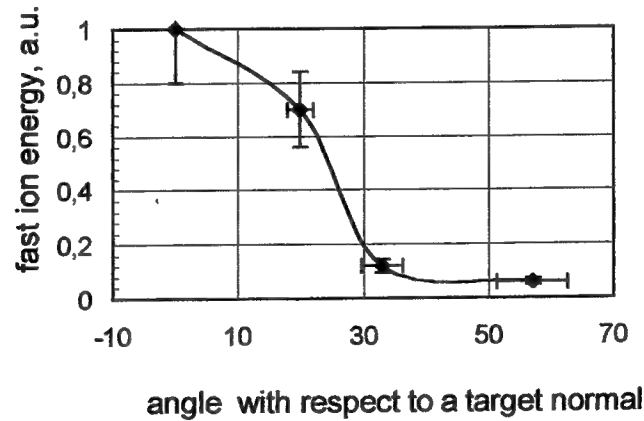


Fig.6. Fast ion energy spatial distribution at laser intensity 10^{19} W/cm^2 (angle of incident 33°).

4. CONCLUSION

Measurements of spatial fast ion components by interferometric method at subnanosecond laser-plasma interaction have carried out. This method get fast ion spatial distribution in observable form. At laser intensity 10^{19} W/cm² fast ion spatial distribution by time-of-flight technique have been measured. It is foundd that fast ion spatial distribution at subnanosecond and picosecond laser-plasma interactions is similar.

5. AKNOWLEDGMENTS

This work is supported by the International Scientific and Technology Center under Project # 107-94.

6. REFERENCES

1. V.G.Borodin et.al., V.A.Gorbunov, S.S. Gulidov, Izvestiya , т.53 № 8, 1467 1989.
2. A.A.Andreev, V.M.Komarov , A.G.Samsonov, A.N.Semakhin, "Characteristics of fast particles generated in a subnanosecond laser plasma", Kvantovaya Elektron., 19, № 7, 709, 1992.
3. A.P.Fews, P.A.Norreys,F.N.Beg, A.R.Bell, A.E.Dangor, C.N.Danson, P.Lee, S.J.Rose, "Plasma ion emission from high intensity picosecond laser pulse interactions with solid targets", Phys.Rev.Lett., v.37, № 13, 1801, 1994.

Focusing system of multiterawatt laser facility PROGRESS-P

V. N. Chernov, V. G. Borodin, A. V. Charukchev, V. A. Malinov, V. M. Migel, N. V. Nikitin
and I. G. Rozivika

Research Institute for Complex Testing of Optoelectronic Devices,
Research Center «S. I. Vavilov State Optical Institute», Sosnovy Bor, Leningrad region, 188537, Russia

ABSTRACT

Focusing of multiterawatt laser beams is of particular importance for superstrong field experiments. The parameters of focusing system of 30-TW Nd:glass laser facility PROGRESS-P with chirped pulse amplification and results of experimental investigations of laser beam propagation through this system are presented. Near diffraction-limited beam quality is obtained at output laser amplifier chain by use the low-thermal phosphate Nd:glass and high quality optical elements. Output 180 mm beam is compressed to 1.5 ps using two holographic gratings with dimensions 420x210 mm, injected in target chamber through the LiF-window with low nonlinear refractive index coefficient and focused to targets by means developed $f/1.1$ on-axis parabolic mirror with focal length of 200 mm. Over 50% energy is obtained in 6-7 μm focal spot in target chamber for low power beam. Determination of the focal spot dimensions for 10 TW beam from X-ray plasma image show that microspot diameter not exceeds 7 μm .

Keywords: laser beam, superstrong field, picosecond laser pulse, parabolic mirror, focusing.

1. INTRODUCTION

To achieve superhigh intensity in focusing multiterawatt ultrashort laser pulse generated by laser with chirped pulse amplification (CPA) it is necessary to prevent of nonlinear breakup of compressed high-intensity laser beam under propagation to target, to use of high optical quality focusing optics with minimum focal length and to obtain of near diffraction-limited beam quality on the output CPA-laser amplifier. In this work we present the parameters of focusing system of 30-TW CPA Nd:glass laser facility PROGRESS-P^{1,2} and results of experimental investigation of beam propagation through this systems.

2. CONFIGURATION OF FOCUSING SYSTEM

The pulse after propagation through rod amplifier chain with output 85-mm rod amplifier and expansion to 180 mm by output vacuum spatial filter is compressed in a single-pass air compressor on two gold-coated holographic diffraction gratings with dimensions of 420 mmx210 mm and 1600 lines/mm. The gratings have damage threshold of 260 mJ/cm² for 1-ps pulses. The grating separation is equal 2.8 m and compressor efficiency is over 80 %. To prevent the nonlinear breakup of compressed high-intensity pulse under propagation to vacuum target chamber we minimized path of compressed pulse in air up to 3 m and directed the beam in chamber through high optical quality 2-cm-thick LiF-window with low nonlinear refractive index coefficient $n_2 = 0.35 \cdot 10^{-13}$ esu and used on-axis parabolic mirror with focal length of 200mm for beam focusing to targets. The estimated B-integral accumulated after compression in air space and window is ~ 3 (limiting value) for 30-TW laser beam.

3. ON-AXIS PARABOLIC MIRROR CHARACTERISTICS

In focusing system it is preferable to use parabolic mirror for minimization of nonlinear aberrations of the focusing beam. We developed the on-axis parabolic mirror with diameter 220 mm for focusing the beam with diameter up to 200 mm at the wavelength of 1.053 μm . The technological process of forming the aspheric surface consists of three stages: (1) the initial forming of the surface by means of the mask tool; (2) the zonal retouch of the surface by a small-dimension tool, and (3) smoothing of small-scale roughnesses by a full-scale tool. The parabola quality was controlled by means of the installation

shown in Figure 1 for measurement of energy distributions of the almost ideal beam of the YLF:Nd laser ($\lambda = 1.053 \mu\text{m}$) and of the He-Ne laser ($\lambda = 0.63 \mu\text{m}$) and finally - by means of the Fizeau interferometer. The scheme for measurements of focal energy distributions provided increase of the focal spot dimensions by 2000 times. Figure 1 presents the results of measurements for one of the parabolas for 200 mm diameter incident beam. It follows from these data that only 25 % is in the diffraction-limited $2.5\text{-}\mu\text{m}$ -diameter spot for the 200-mm beam, and 50 % of the energy is concentrated in the spot with the diameter of $6\text{-}7 \mu\text{m}$. The interferogram of the wavefront of the He-Ne laser beam after double reflection from the parabola showed that the root-mean-square deformation of the wavefront does not exceed 0.5λ .

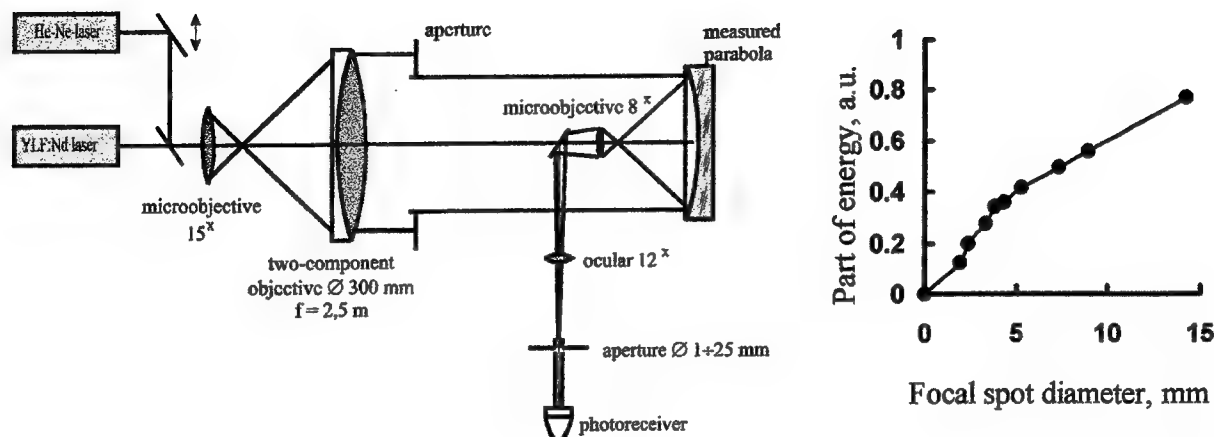


Figure 1. Scheme for measurements of radiation energy distributions ($\lambda=1.053 \mu\text{m}$ and $\lambda=0.63 \mu\text{m}$) in the focal plane of mirror parabolas and distribution of laser radiation energy $\lambda = 1.053 \mu\text{m}$ in the focal plane mirror parabola with the 200-mm focal length for 200 mm diameter beam.

4. BEAM PROPAGATION EXPERIMENTS

Laser pulse with energy 20-45 J and duration of 300 ps was obtained at output of amplifier chain. This pulse was compressed to 1.5 ps with spectral width of 1.5 nm. We investigated both far-field intensity distribution on the output amplifier chain and target chamber parabola microspot intensity distribution. Measurements were made using added optical systems and two-dimensional CCD-cameras as detectors. Optical system for the output amplifier far-field registration has 50-90 m equivalent focal length. Another optical system for registration of focusing microspot intensity distributions in target chamber has magnification of 300. We also determined of output amplifier far-field energy distribution by calorimeter measurements of the focusing laser energy passed through diaphragms of various diameter.

Figure 2 shows far-field intensity and energy distributions of the output amplifier laser beam with energy of 25 J. The distributions are presented in equivalent target plane for suitable comparison with final focusing system characteristics. The data demonstrate that the laser beam can be focused to spot with dimensions $2 \times 3 \mu\text{m}$ FWHM intensity (exceed the diffraction limit by two times) and more than 50% of energy is within a $5\text{-}\mu\text{m}$ diameter spot. This near diffraction-limited beam divergence was obtained by use in amplifier chain the low-thermal phosphate Nd:glass GLS22 and KGSS0180/18 and high quality optical elements.

The intensity distributions for laser beam focusing in target chamber by on-axis parabolic mirror are presented at Figure 3. At present, we investigated this beam spatial characteristics only for low power laser beam (about 50 GW) because of equipment damage limitation. Over 50% energy is obtained in $6 \mu\text{m}$ focal spot. Focal spot dimensions of high-power (up to 10 TW) beam are determined indirectly from 1.5 keV X-ray plasma image by use camera-obscure with $5 \mu\text{m}$ pinhole, 12.3x magnification and $5.5 \mu\text{m}$ spatial resolution. We determined from this X-ray plasma image that spot diameter not exceeds $7 \mu\text{m}$ and average power density about 10^{19}W/cm^2 is obtained with 10 TW focusing laser beam.

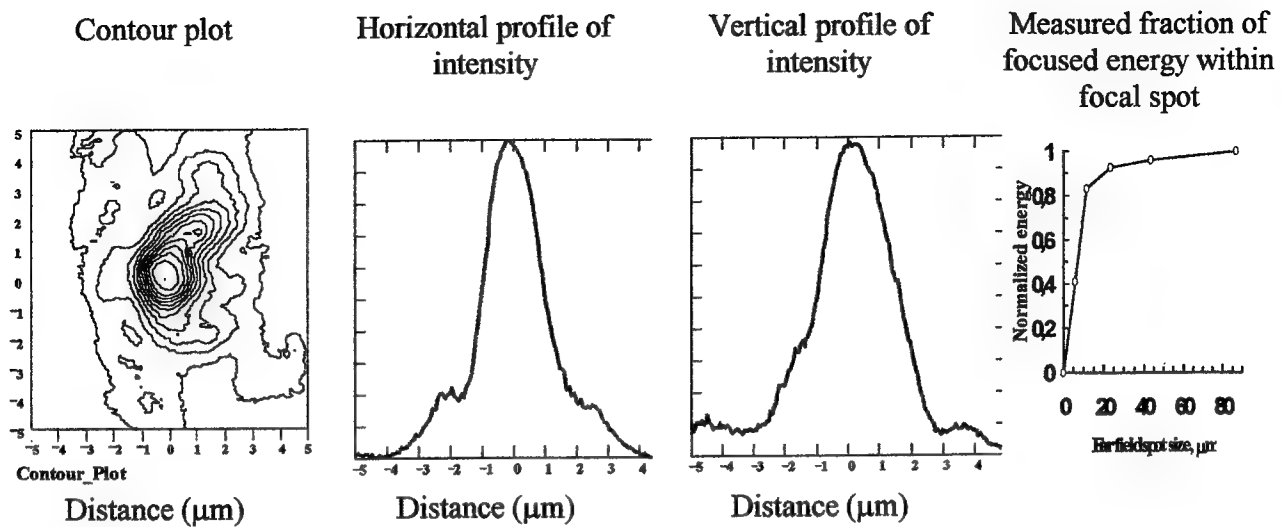


Figure 2. Far-field intensity and energy distributions of the output amplifier laser beam in equivalent target plane

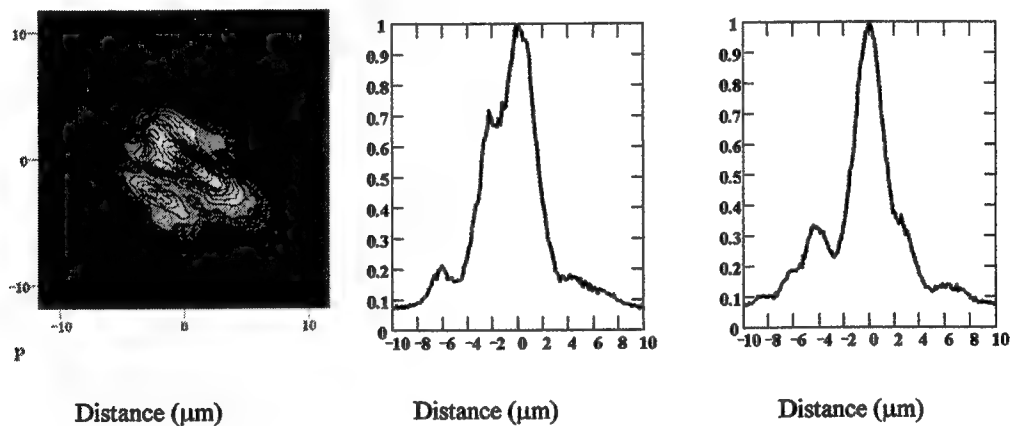


Figure 3. The intensity distributions for 180-mm laser beam focusing in target chamber by on-axis parabolic mirror with focal length 200 mm.

5. CONCLUSION

In conclusion, configuration of air grating compressor and 200 mm aperture parabolic mirror in vacuum target chamber with low nonlinear LiF window ensure the prevention of nonlinear breakup of compressed 200 mm diameter 30 TW laser pulse under propagation to target. The developed 200 mm diameter $f/1$ on-axis parabolic mirror concentrates 50% energy almost ideal beam in 6-7 μm diameter focal spot ($2.5\times$ diffraction limit). Use of the low thermal distortion phosphate Nd:glass in laser amplifier and optimization of its scheme enable us to produce uncompressed laser beam with $(1.5-2)\times$ diffraction limit. Direct optical measurements of low-power laser focal microspot radiation distribution in target chamber and indirect determination of high-power focal spot dimensions from X-ray plasma image show that microspot diameter not exceeds 7 μm and average power density about $10^{19}\text{W}/\text{cm}^2$ is obtained with 10 TW focusing laser beam.

6. ACKNOWLEDGMENTS

This work was supported by International Scientific and Technology Center under Project #107.

7. REFERENCES

1. E. G. Borodin, A. V. Charukchev, V. N. Chernov et al., "The PROGRESS-P 30 TW Picosecond Nd:glass Facility", *AIP Conference Proceedings*, vol. 406, "Laser Interaction and Related Plasma Phenomena", 13th International Conference, Monterey, USA, April 13-18, 1997, pp. 389-395, Woodbury, New York, 1997.
2. V. N. Chernov, E. G. Borodin, A. V. Charukchev et al., "Methods and means of superstrong field formation on multiterawatt laser facility PROGRESS-P", *AIP Conference Proceedings*, vol. 426, "Superstrong Fields in Plasmas", 1st International Conference, Varenna, Italy, August-September 1997, pp.450-453, Woodbury, New York, 1998.

Initiating of laser-induced damage and ultimate light intensities in multilayer optical coatings with sub-layered microstructure

Anastasia S.Gruzdeva^{*}, and Vitali E.Gruzdev^{*}

State Research Center "S.I.Vavilov State Optical Institute"
Birzhevaya Liniya, 12, St.-Petersburg 199034 Russia.

ABSTRACT

The problem of initiating of laser-induced damage (LID) and ultimate laser fluence for homogeneous and low-absorbing optical coatings is considered. It is shown that nonlinear electrodynamic processes of formation of shock electromagnetic waves is the ultimate mechanism of LID initiating in ideal coatings because of developing of super local field instability resulting from field disruptions accompanying the shock waves. Theoretical model of formation of shock electromagnetic waves is presented. In particular, two necessary conditions for shock wave formation are obtained. Computer modeling is used to investigate dynamics of shock-wave developing. Influence of coating parameters upon blow-up field instability is investigated. It is proposed a new design of multilayer optical coatings: each layer should include microlayers with similar refractive indexes and gradually varying nonlinear refraction. Such microstructure excludes sharp jumps of nonlinear optical refraction which are critical for increasing of field-instability threshold.

Keywords: nonlinear optics, optical coatings, computer modeling, blow-up field instability, laser-induced damage.

1. INTRODUCTION

The most important role in initiating of laser-induced damage of optical coatings has been supposed to be played by laser heating and thermal processes¹⁻⁴ rather than electrodynamic processes. But the effects should be taken account of in case of high-power lasers giving enough power to induce sufficient nonlinear variations of refractive index. Most probably the nonlinear effects dominate in initiating of LID in high-quality dielectric films and coatings with low absorption which makes heating small and of minor importance. This implies ultimate mechanisms of LID in low-absorbing and defect-free dielectric films and coatings to be determined by the nonlinear optical phenomena.

This problem is also connected with the question why are LID thresholds for multilayer coatings several times lower than those for bulk materials? In most cases it is connected with absorbing microinclusions¹⁻⁴. There is no doubt that it is true but modern technologies of optical-material manufacturing are being improved very fast resulting in decreasing of number of absorbing inclusions. Moreover, microstructure of the coatings is more homogeneous as compared with bulk materials due to less size of grains which coating layers consist of^{5, 6}. Thus, the problem of ultimate LID mechanisms is becoming actual. In particular, only investigations in this area can answer the question: can LID threshold for multilayer coating be of the same value as that for bulk material?

Slow progress in investigation of nonlinear optics of optical coatings is caused by complication of the problem what is connected with specific geometry of the coatings and complicated nonlinear equations. Exact analytical solution to the problem cannot be obtained practically. Widely used asymptotical approaches (for example, approximation of slowly-varying amplitudes) are not valid in that case because approximate methods can result in losing some important effects which can play major role in real situations. The ultimate mechanisms of LID can be revealed only by detailed investigation of exact solutions to exact equations describing developing of nonlinear electrodynamic processes in layered dielectric medium. Only numerical methods can help in this situation. In this connection computer simulation is used by the authors as a method allowing the most general approach to investigation of nonlinear processes and giving detailed information about local variations of acting electric field.

^{*} Tel. (812) 218 0231, e-mail: photophys@dost.beam.ifmo.ru

2. THEORETICAL MODEL

Characteristic features of optical coatings are small thickness of dielectric layers and multiple interfaces. So, both linear and nonlinear optical properties of dielectric varies several times within one radiation wavelength. There is a great question what nonlinear phenomena can take place in such medium. In particular, formation of field disruptions is likely to appear in such medium. Some analogy between electromagnetic and acoustic waves can be used to consider possible nonlinear self-influence of laser radiation in layered media. In particular, propagation of high-power acoustic waves is well known to be accompanied by formation of field disruptions resulting in fast field variations⁷. The disruption turns into high-frequency vibrations and can disappear in lossy medium after acoustic wave has passed some distance⁷. Something similar must happen to high-power laser field propagating through transparent dielectric. This process cannot be described with usual approximation of slowly-varying amplitude because scale of field variations must be less than radiation wavelength. This implies that general nonlinear wave equation should be considered to describe formation and developing of the disruptions. For example, the equation is as follows for 1-dimensional propagation of linearly polarized laser wave:

$$\frac{\partial^2 E}{\partial x^2} - \frac{1}{c^2} \frac{\partial^2 E}{\partial t^2} = \frac{4\pi}{\epsilon_0 c^2} \frac{\partial^2 P_{NL}}{\partial t^2}, \quad (1)$$

where c is light speed in the medium in linear case, ϵ_0 is linear dielectric permeability, and nonlinear response of the medium P_{NL} depends on electric field in the following way⁸: $P_{NL} = (6\chi_{1122} + 3\chi_{1221})E^2 E$. Accordingly, laser-induced variation of refractive index is given by⁸

$$\Delta n = n_2 |E|^2 = (2\pi/\epsilon_0)(6\chi_{1122} + 3\chi_{1221})E^2. \quad (2)$$

So, we consider propagation of monochromatic plane wave with linear polarization (equ. 1) in transparent isotropic lossless dielectric without dispersion and with nonlinear optical response (equ.2).

Exact solutions to equation (1) are rather difficult to be studied in details but rather simple estimations of threshold field amplitude resulting in disruption formation can be obtained using the following simple consideration of field propagation in nonlinear isotropic medium with positive nonlinear index n_2 .

Let us consider a part of instantaneous profile of electric field with amplitude E_0 , propagating in nonlinear medium (Fig. 1a). Field disruption appears if point 1 of the profile with field value $E_0 - \Delta E$ has overtaken profile's top 2. That is possible because laser-induced addition to refractive index is larger at point 2 than at point 1, so, profile maximum slows down itself. We consider not moving coordinate system which x-axis coincides with direction of wave propagation. If Δt is duration of moving of point 1 in nonlinear medium then coordinates of points 1 and 2 in the medium are respectively $x_1 = \Delta t u_1$ and $x_2 = \Delta x + \Delta t u_2$, where

$$u_2 = \frac{c_0}{n_0 + n_2 E_0^2}, \quad u_1 = \frac{c_0}{n_0 + n_2 (E_0 - \Delta E)^2}, \quad (3)$$

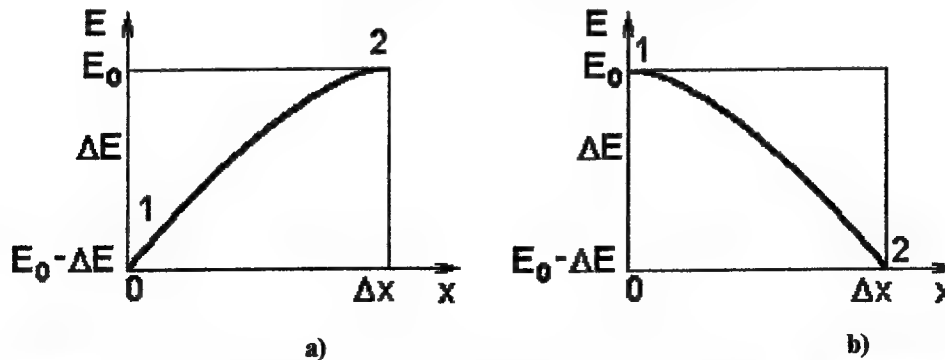


Fig.1 A part of instant profile of laser wave near its maximum at the beginning of disruption formation in nonabsorbing dielectric with positive nonlinear coefficient of refractive index (a) and negative one (b).

c_0 - is light speed in vacuum, $n_0^2 = \epsilon_0$. According to the mentioned above $u_1 = u_2 + \Delta u$ and $u_1 > u_2$. If field-induced addition to

refractive index is smaller than n_0 , we can derive the following formula from (3)

$$\Delta u = \frac{2n_2 E_0 \cdot \Delta E}{n_0 + n_2 E_0^2} \quad (4)$$

The coordinates of points 1 and 2 will be the same at some moment $t + \Delta t$: $x_1 = \Delta t \cdot u_1 = x_2 = \Delta x + \Delta t \cdot u_2$. Duration of disruption formation Δt can be estimated from the expression: $1/\Delta t = u/\Delta x$, which implies the following:

$$\frac{1}{\Delta t} = \frac{2n_2 E_0}{n_0 + n_2 E_0^2} u_2 \frac{\partial E}{\partial x}, \quad (5)$$

where $u_2 = c_0/(n_0 + \Delta n)$ - is speed of profile's maximum and $\Delta E/\Delta x \approx \partial E/\partial x$. Starting at moment t , the maximum will have passed distance $s = u_2 \Delta t$ in nonlinear medium by the moment $t + \Delta t$ that gives the following equation for E_0

$$E_0^2 \frac{n_2}{s} - E_0 \cdot 2n_2 \frac{\partial E}{\partial x} + \frac{n_0}{s} = 0. \quad (6)$$

Solution to the equation exists only if the following condition is satisfied

$$\left| \frac{\partial E}{\partial x} \right| \frac{s}{2} \geq \sqrt{\frac{n_0}{n_2}}. \quad (7)$$

This condition shows that field disruption cannot appear at arbitrary point of field profile, for example, at profile's top where derivative $\partial E/\partial x$ is about zero. At the same time the disruption cannot appear far from the top where field magnitude is too small.

Integrating of (6) gives the following estimation for threshold field-amplitude of disruption formation:

$$E_{th} \approx \sqrt{\frac{n_0}{n_2} \left(\exp\left\{ \frac{\Delta x}{s} \right\} - 1 \right)}, \quad (8a)$$

where $\Delta x \leq s$. It is interesting that this estimate is very close to that obtained by integrating (7):

$$E_{th}^* \approx \frac{2\Delta x}{s} \sqrt{\frac{n_0}{n_2}}. \quad (8b)$$

For example, disruption threshold is $E_{th} = 16.2 \cdot 10^6$ V/cm ($I_{th} = 6.95 \cdot 10^{11}$ W/cm²) for $s = 2\Delta x$, $n_0 = 1.41$ and $n_2 = 3.14 \cdot 10^{-10}$ (esu) while $E_{th}^* = 20.1 \cdot 10^6$ V/cm ($I_{th}^* = 1.07 \cdot 10^{12}$ W/cm²) for the same parameters.

Similar consideration is valid for negative nonlinear coefficient of refractive index. In this case top of field profile can overtake a part of the profile moving at distance Δx in front of the top, i.e., geometry of this problem is reversed with respect to that depicted in Fig.1 and point 1 corresponds to profile's. This implies the points 1 and 2 to move with the following speeds

$$u_1 = \frac{c_0}{n_0 - n_2 E_0^2}, \quad u_2 = \frac{c_0}{n_0 - n_2 (E_0 - \Delta E)^2}. \quad (9)$$

Similar consideration shows that disruption threshold can be estimated in the following way:

$$E_{th} \approx \sqrt{\frac{n_0}{n_2} \left(1 - \exp\left\{ -\frac{\Delta x}{s} \right\} \right)} \quad (10)$$

To describe evolution of field disruptions which have already appeared introducing of fast-varying amplitude according to the following seems to be reasonable

$$E(x, t) = E_f(x, t) \cdot \exp(i\omega t - ikx), \quad \left| \frac{\partial E_f}{\partial t} \right| \gg |E_f| \cdot \omega, \quad \left| \frac{\partial E_f}{\partial x} \right| \gg |E_f| \cdot k. \quad (11)$$

Substitution of (11) into (1) leads to the following equation:

$$\frac{\partial^2 E_f}{\partial x^2} - \frac{1}{c^2} \left(1 + \frac{4\pi\chi}{\varepsilon_0} |E_f|^2 \right) \frac{\partial^2 E_f}{\partial t^2} = 0. \quad (12)$$

Propagation of high-power field described by (12) is well known to result in appearing of field disruption after the field passes some distance in nonlinear medium^{7,9}. This means that secondary disruptions can appear after the first disruption has formed. What happens to the disruptions? How do they develop and what can they result in? Answering these questions by analytical solving of (1) or (12) is too much difficult. The only thing to be expected from analogy with acoustic waves is generation of higher harmonics. Computer simulation seems to be the most suitable tool to attack this problem and to get more detailed information.

3. SIMULATION MODEL

Computer calculations are widely used to investigate nonlinear processes because most nonlinear problems are very complicated and it is difficult to find appropriate analytical methods *a priori*. Numerical methods of solving nonlinear problems are the most popular in spite of some drawbacks they have. For example, numerical solution does not allow to see dynamical development of processes with transition periods and how various feedbacks work. Bearing in mind drawbacks of computer simulation nevertheless it is possible to say that it has advantage over numerical methods because it allows to see dynamics of nonlinear processes and work of feedbacks taking part in the process. This helps to understand mechanisms and physics of nonlinear phenomena and shows ways for developing analytical approaches.

Simulation method used by the authors to investigate 1-dimensional propagation of plane linearly-polarized monochromatic wave of high amplitude is based on dependence of field magnitude at fixed time-space point on field magnitudes at previous moments in neighboring points. It is very similar to well-known finite-difference time-domain (FDTD) technique^{10,11}. The dependence is derived from nonlinear differential wave equation (1) by reducing it to a finite-difference equation in traditional way¹⁰⁻¹³. So, the following updating finite-difference equation is obtained

$$E_x^t = 2E_{x-1}^{t-1} - E_{x-1}^{t-2} + \frac{(c_0 \cdot \Delta t)^2}{(n_0 \cdot \Delta x)^2} \left(E_{x+1}^{t-2} - 2E_x^{t-1} + E_{x-1}^t - \frac{4n_0^2 \pi \chi}{c_0^2} \left((E_{x-1}^{t-1})^3 - 2(E_x^{t-2})^3 + (E_{x+1}^{t-3})^3 \right) \right). \quad (13)$$

where $\chi = (6\chi_{1122} + 3\chi_{1221})$, Δx is period of regular spatial mesh, and Δt is corresponding time increment. The obtained dependence describes field evolution in medium with certain parameters if field source is given. Field evolution is observed in the form of animation which can be stopped at any appropriate time.

Outgoing waves are described by functions of the following type: $F(x-ct)$ at exit boundary of space grid and $E_s + F(x+ct)$ at entrance boundary. This allows to exclude artificial reflection and calculation mistakes at the boundaries. E_s is source field which is assumed to be as follows $E_s = E_0 \sin(2\pi t / \nu)$. This source describes normal incidence of plane linearly polarized monochromatic wave of amplitude E_0 and frequency ν onto plane surface of considered medium.

There are some reasons for 1-dimension (1-D) case to be considered. First, 1-D nonlinear propagation of plane wave is described by relatively simple equation (if nonlinear differential equation can be called simple). Some properties of solutions to the equation have already been investigated [for example^{7,9}], so, developed method can be verified by comparing of obtained data with previous results. Second, exact solutions of linear differential equation are well known¹² to satisfy finite-difference relation derived from the differential equation. That property of finite-difference relation and stability of calculation procedure make calculations more precise and obtained results more reliable. For stability of calculations to be obtained the calculation procedure is subjected to the following well known criterion¹³

$$c \cdot \Delta t < \Delta x, \quad (14)$$

where Δx - is space grid period, and Δt - is corresponding time increment. This allows to exclude increasing of calculation mistakes. Space resolution is selected to be 100 cells of spatial mesh per radiation wavelength in vacuum to give appropriate resolution. Development of field disruptions (see section 4) is investigated with resolution 200 cells per wavelength.

The developed simulation model has been tested in case of linear light propagation through boundary of two transparent dielectrics with different refractive indexes and plane dielectric plate (Fabri-Perout resonator). Results of calculations are in excellent agreement with well known theoretical results¹⁴ with an accuracy of ($\pm 1\%$). Obtained results for nonlinear case were difficult to be compared with theoretical results because the latter are absent, nevertheless, observed phenomena are in nice qualitative agreement with similar facts of theory of nonlinear acoustic waves⁷. In particular, modeling of

laser-field evolution in defect-free nonabsorbing nonlinear dielectric has shown possibility of disruption formation (Fig. 2) according to the analogy with acoustic waves: disruption appears after laser wave has passed some distance in the medium (point 1 in Fig. 2) and it turns into high-frequency variations (points 2-5). Corresponding laser-induced variations of dielectric permeability ϵ are also shown in Fig. 2.

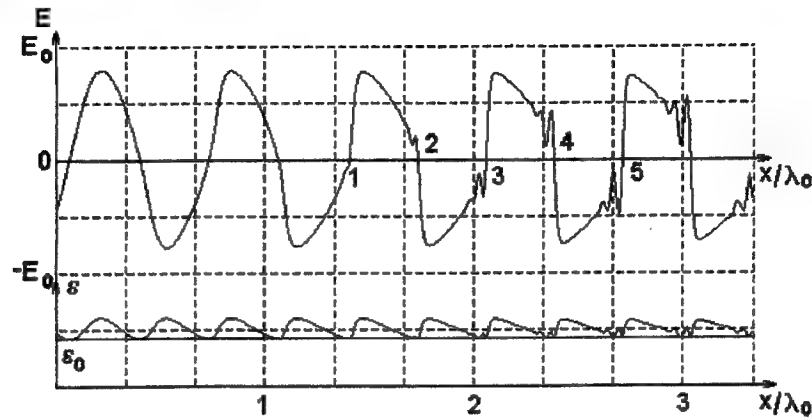


Fig. 2. Formation of field disruption in homogeneous transparent medium with positive addition to refractive index.

Expected threshold of field disruption formation for homogeneous dielectric can be obtained in the same way as it was done in section 2. For example, for the dielectric with $n = 1.50$ and $n_2 = 10^{-10}$ esu the threshold is $E_{th} = 10^8$ V/cm ($I_{th} = 2.65 \cdot 10^{13}$ W/cm²).

4. RESULTS OF SIMULATION

Single dielectric film on glass substrate and multilayer coatings are considered in the paper one after another. Investigation of single film allows to reveal nature and features of dynamical development of nonlinear field variations which should be similar for multilayer coatings.

4.1. Single layer on glass substrate

Plane nonabsorbing film on glass substrate is considered as initial model. Film thickness d is varied from 0.25 down to 0.1 of radiation wavelength λ_0 . The sizes are appropriate for the most layers in widely used optical coatings. Refractive index of the film and substrate is chosen in agreement with experimental results¹⁵⁻¹⁸ but the authors have met a difficulty with lack of experimental data on nonlinear optical properties of thin films. In particular, we had to choose nonlinear refractive index according to experimental results for bulk materials in spite of that properties of thin dielectric films are well known to differ great from those of bulk material. In many cases we have not got experimental data on nonlinear optical properties of widely used dielectric films. So, sometimes nonlinear parameters of the considered coatings are chosen in such a way as to make nonlinear electrodynamic processes within the investigated film more obvious and convenient for investigation of their physics because revealing of physics of nonlinear phenomena in thin layers is one of major aims of the present paper. In particular, single film refractive index (n_0) is a bit less than that of substrate ($n_0=1.50$) while film's nonlinear coefficient (n_2^D) is chosen to be more than that of the substrate ($n_2=3.14 \cdot 10^{-13}$ esu).

Formation of field disruptions accompanied by generation of higher harmonics has been observed. Fig 3 depicts consequent "snap-shot photos" of field profile to show stages of nonlinear evolution of laser radiation passing through the medium described above (upper curve depicts instantaneous space distribution of laser field) as well as laser-induced variation of refractive index (lower curve). Field disruption appears as soon as radiation with initial smooth field distribution (Fig. 3a, 3b) runs into thin film with rather large nonlinear index (Fig. 3c). Developing further, the disruption stays inside the film and high-frequency pulsations appear after laser radiation passes through the film (Fig. 3d). The disruption can be smoothed when moves into the substrate, turning into high-frequency pulsations and then disappearing,

but it can increase due to multiple reflections at boundaries of the film (Fig. 3d, 3e) giving rise to formation of super local

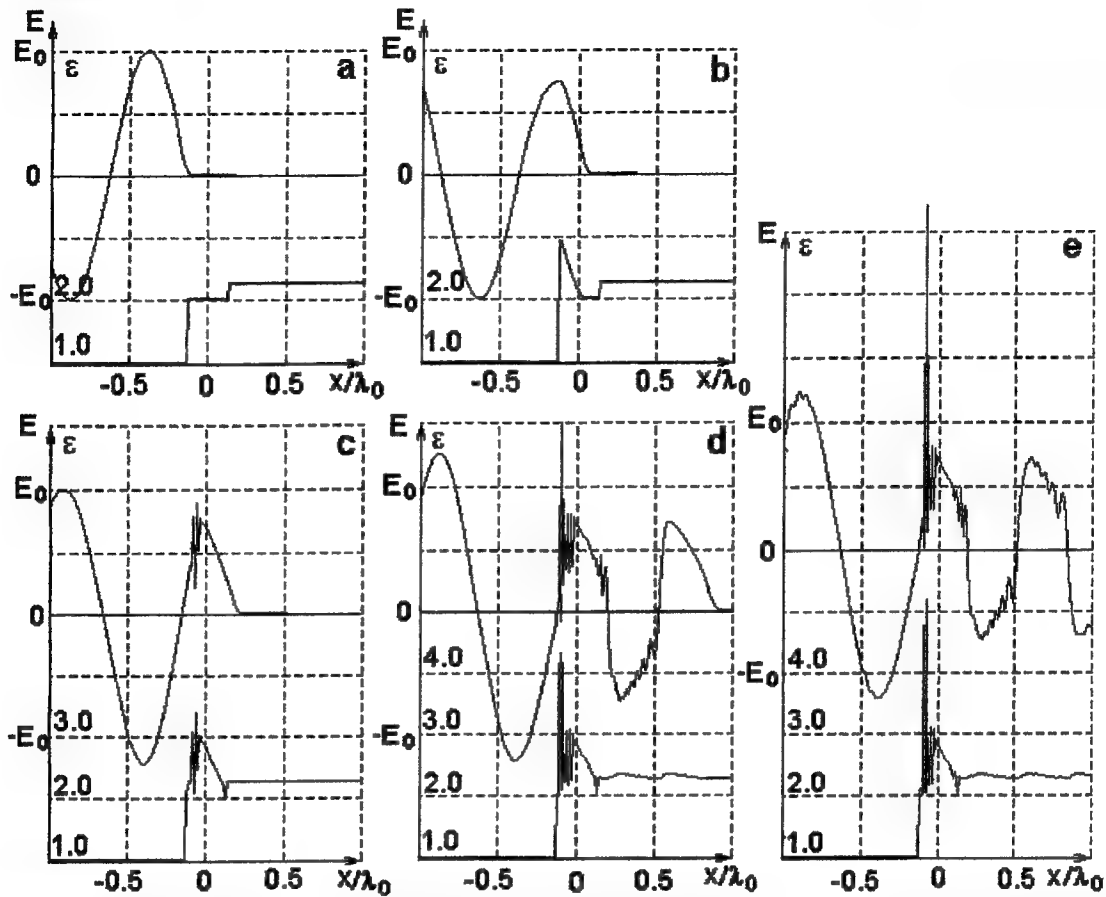


Fig. 3. Evolution of high-power laser plane wave and laser-induced addition to refractive index in single $\lambda_0/4$ -layer on glass substrate. Initial amplitude $E_0=3.65 \cdot 10^8$ V/cm, substrate refractive index $n_0=1.50$, layer refractive index $n_D=1.41$, nonlinear coefficient of refractive index for the substrate and layer are consequently $n_2=3.0 \cdot 10^{-13}$ and $n_2^D=3.14 \cdot 10^{-10}$ esu.

field maximum (Fig. 3e). Its size is less $0.1\lambda_0$ and its amplitude is some powers of magnitude more than that of incident field. If field disruption has appeared the maximum is formed very fast (within one tenth of laser-field period). It looks like field blow-up⁷, so the described process can be referred to as field blow-up instability. Maximum field magnitude is not limited by anything in the framework of the described model if there is no absorption in the medium. The observed fast blow-up should be accompanied by great positive feedback. Instantaneous profiles of laser-induced variation of refractive index accompany photos of instantaneous field distribution in Fig. 3 to investigate character and nature of the feedbacks. Threshold-like behavior of blow-up instability should be mentioned: it develops only if incident field amplitude exceeds some threshold value referred to as instability threshold. For example, blow-up instability threshold for single layer was $3.65 \cdot 10^8$ V/cm for the following parameters: layer size $d=\lambda_0/4$, refractive index of the substrate $n_0=1.50$, refractive index of the layer $n_D=1.41$, nonlinear coefficient of refractive index for the substrate and layer are correspondingly $n_2=3.0 \cdot 10^{-13}$ esu and $n_2^D=3.14 \cdot 10^{-10}$ esu.

Generation of higher harmonics has been observed for laser-field intensity close to instability threshold (Fig. 3 e). The harmonics appear in reflected radiation and their frequencies are 10 or more times higher than that of incident radiation. this harmonic generation is rather weak for single layer and much more stronger for multilayer coatings. That is why this issue is discussed in more details below.

Dependence of instability threshold on defect's parameters (nonlinear coefficient of refractive index (Fig. 4), size

parameter (Fig. 5), refractive index (Fig. 6),) was investigated for short (from femtosecond to picosecond) pulses. As it can be expected instability threshold depends on nonlinear coefficient in the most critical manner (Fig. 4). Dependence of the threshold on size parameter (i.e., ratio of defect thickness to radiation wavelength in vacuum) is practically absent for large values of nonlinear coefficient (Fig. 5) that is most unexpected, especially if one bears in mind well known resonant properties of plane layers for low radiation intensities¹⁴. Instability threshold depends on layer size parameter more actively when difference between nonlinear index of the film and that of the substrate is less than one power of magnitude.

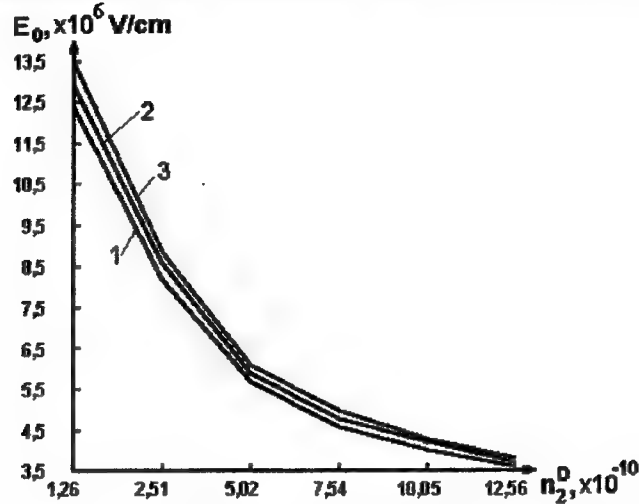


Fig. 4. Threshold of blow-up instability as a function of nonlinear coefficient of film refractive index for fixed size parameter $d/\lambda_0=0.25$, refractive index of the substrate $n_0=1.500$ and varied film refractive index $n_D=1.378$ (1), 1.414 (2) and 1.449 (3). Nonlinear coefficient of refractive index of the substrate is $n_2=3.14 \cdot 10^{-12}$.

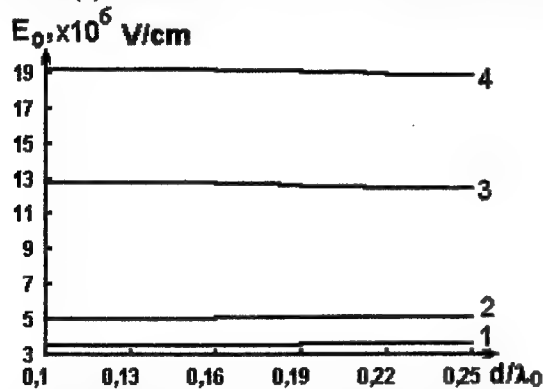


Fig. 5 Threshold of blow-up instability as a function of size parameter d/λ_0 for fixed refractive index of the dielectric film $n_D=1.378$ and substrate material $n_0=1.500$ and varied nonlinear coefficient of defect refractive index $n_2^D=3.14 \cdot 10^{-10}$ (1), $6.28 \cdot 10^{-11}$ (2), $1.25 \cdot 10^{-11}$ (3) and $6.25 \cdot 10^{-12}$ (4). Nonlinear coefficient of refractive index of the substrate is $n_2=3.14 \cdot 10^{-12}$.

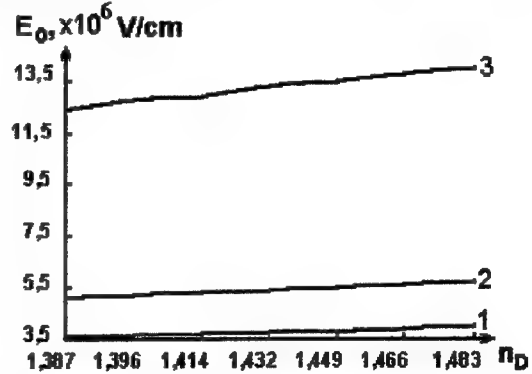


Fig. 6 Threshold of blow-up instability as a function of dielectric-film refractive index for fixed refractive index of substrate material $n_0=1.500$, size parameter $d/\lambda_0=0.25$ and varied nonlinear coefficient of refractive index of the film $n_2^D=3.14 \cdot 10^{-10}$ (1), $6.28 \cdot 10^{-11}$ (2) and $1.256 \cdot 10^{-11}$ (3). Nonlinear coefficient of refractive index of the substrate is $n_2=3.14 \cdot 10^{-12}$.

In the latter case size dependence changes its slowly decreasing character for slowly increasing. Instability thresholds increase linearly with increasing refractive index (Fig. 6).

4.2. Field evolution in multilayer coatings

Nonlinear field evolution in 4-layer AR coating was simulated and investigated. The coating included quarter-wavelength

layers with the following optical parameters: "low" refractive index $n_L = 1.414$, "high" refractive index $n_H = 1.563$, size parameters $d_L/\lambda_0 = 0.18$ and $d_H/\lambda_0 = 0.15$, nonlinear coefficients of refractive index $n^L_2 = 3,14 \cdot 10^{-10}$ esu, $n^H_2 = 3,14 \cdot 10^{-12}$ esu. The coating was considered to be deposited on glass substrate with parameters $n_s = 1.51$, $n^S_2 = 3,0 \cdot 10^{-12}$ esu. Blow-up instability took place within the first layer with high nonlinear index and its threshold was about $3,65 \cdot 10^8$ V/cm.

Influence of refractive index profile of multilayer coating on value of instability threshold was investigated also. For this purpose, radiation propagation through coating with sine-shaped variation of refractive index was simulated. Parameters of the coating were similar to those of AR coating: variation of refractive index from $n_L = 1.414$ up to $n_H = 1.563$ with space period $d/\lambda_0 = 0.32$, variation of nonlinear coefficient from $n^L_2 = 1,256 \cdot 10^{-9}$ esu to $n^H_2 = 1,256 \cdot 10^{-11}$ esu. Parameters of substrate were the same as in case of AR coating. Blow-up instability threshold was $3,71 \cdot 10^8$ V/cm.

Nonlinear evolution of laser radiation in 14-layered HR coating was simulated too. The coating consisted of quarter-wavelength layers with parameters: $n_H = 2.3$, $n_L = 1.414$, $d_H/\lambda_0 = 0.11$, $d_L/\lambda_0 = 0.18$, $n^H_2 = 3,14 \cdot 10^{-12}$ esu, $n^L_2 = 3,14 \cdot 10^{-10}$ esu. Substrate parameters were kept the same. Instability threshold was about $3,2 \cdot 10^8$ V/cm. Instability thresholds of 16-layered HR coating with parameters $n_H = 2.55$ (corresponds to TiO_2 film¹⁸), $n_L = 1.45$ (corresponds to SiO_2)¹⁹, $d_H/\lambda_0 = 0.10$, $d_L/\lambda_0 = 0.17$, $n^H_2 = 0,8 \cdot 10^{-10}$ esu¹⁸, $n^L_2 = 3,14 \cdot 10^{-12}$ esu¹⁹ was only $0,9 \cdot 10^8$ V/cm. Development of field instability started with small perturbations of field distribution in outer TiO_2 layer in both cases (Fig. 7). It took more than 120 periods of field vibrations for the instability to develop in HR coatings in contrary to AR coatings and single layer where blow-up instability develops within 1-8 periods of laser field. The largest part of the time (about 80%) was spent for quasi-linear field evolution which finished with formation of high-frequency pulsations with period about 1/10 of laser-field period (Fig. 7). Blow-up instability developed from the pulsations within 10-50 laser-field periods. So, long quasilinear stage was finished with short blow-up stage.

Investigation of coating with sine-shaped variation of refractive index and parameters similar to those of HR coating ($n_H = 2.3$, $n_L = 1.414$, $d/\lambda_0 = 0.15$, $n^H_2 = 1,256 \cdot 10^{-11}$ esu, $n^L_2 = 1,256 \cdot 10^{-9}$ esu), shown the developing of blow-up instability to be divided into two stages too - long quasilinear stage taking some tens of laser periods and short blow-up stage lasting from 1 up to 10 laser periods. Instability threshold was $1,9 \cdot 10^8$ V/cm.

In all the mentioned cases generation of higher harmonics (HH) was observed. The most interesting features of this generation are as follows. First, HH are high-frequency, in particular, generation of 14-th harmonic is depicted in Figs. 7d, e. Second, generation of single HH of rather high power is seen in reflected radiation while transmitted radiation contains many HH which generation is connected with formation of field disruptions. Third, HH appears in reflected radiation a few periods of radiation before field blow-up, so, pulses of HH are very short. Forth, the most intensive generation of HH was observed for HR coating with TiO_2 layers. This problem requires special consideration and it will be investigated in more details in one of our further papers.

5. DISCUSSION AND CONCLUSIONS

Nonlinear evolution of high-power laser field in layered media has been investigated. The simplest model of radiation (plane linearly-polarized monochromatic wave) and the media (dielectric nonabsorbing layers without dispersion) has been used for computer modeling. New mechanism of abrupt super local increasing of laser-field amplitude in dielectric coating has been described and investigated. The mechanism is referred to as blow-up field instability. The instability is shown to be threshold-like phenomenon. It can be one of important mechanisms of field localization which goes before thermal processes of LID in transparent dielectric.

The obtained estimations (8a), (8b) are in good agreement with results obtained by simulation of field propagation through single nonabsorbing layer. Disruption formation always precedes blow-up instability, so, its threshold must be higher than the value given by (8). Small difference between theoretical results and modeling shows that disruption formation is finished after wave has passed distance $s \approx 2\lambda \div 4\lambda$ in the layer. On the other hand, simulation results shows that appearing of disruption is not always followed by field blow-up and field discontinuity can smooth turning into high-frequency vibrations. A certain positive feedback between local field variations and laser-induced variations of refractive index is needed for blow-up instability to develop. If incident field amplitude is above instability threshold then

laser-induced abrupt local variations of refractive index near field disruption are enough for the feedback to be formed and field blow-up to develop. If incident field amplitude is a bit above instability threshold then the feedback is formed due to multiple reflections at defect boundary.

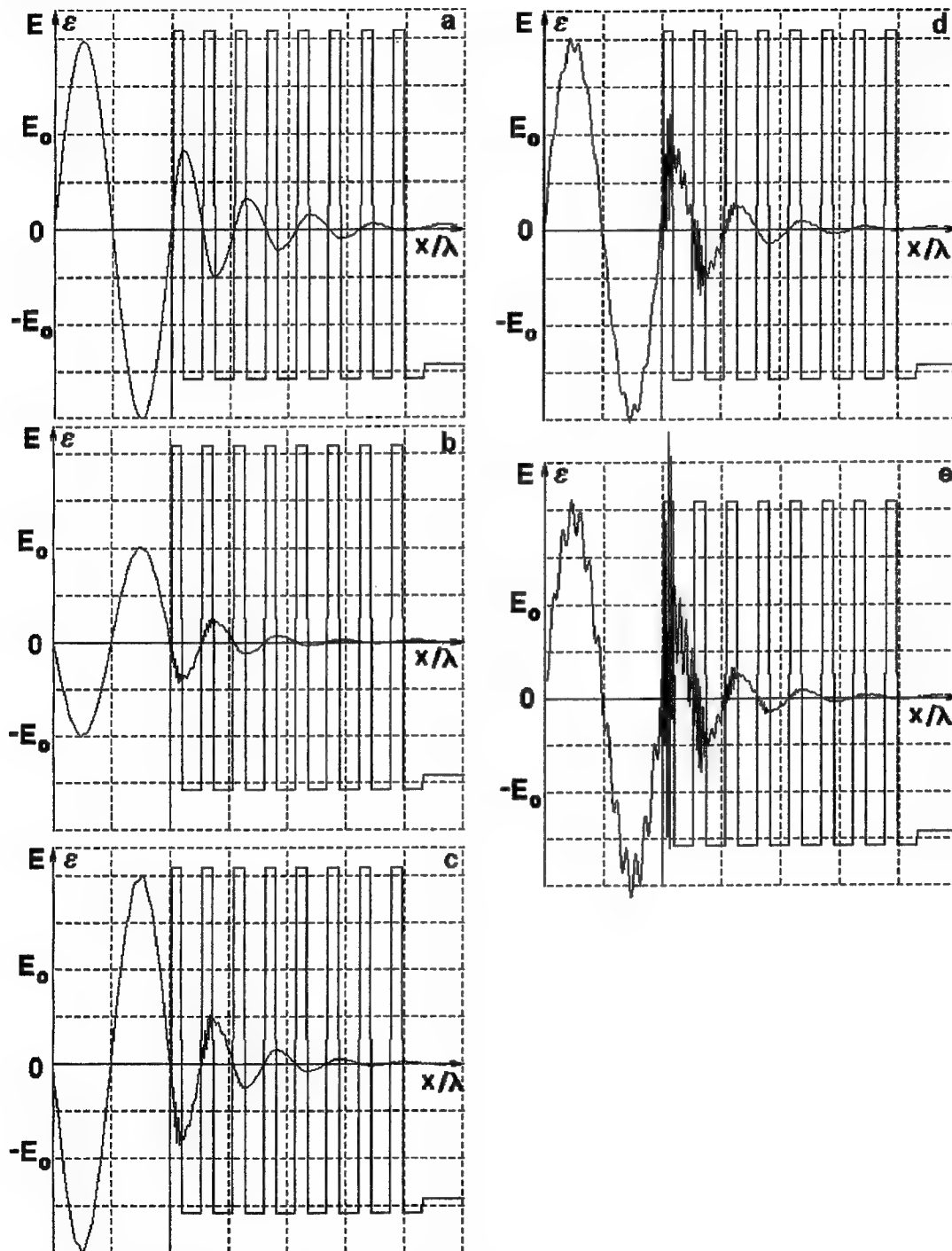


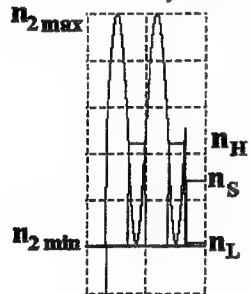
Fig. 7. Developing of blow-up field instability in HR coating with $\text{TiO}_2/\text{SiO}_2$ layers.

Estimations (8) imply strong dependence of threshold for disruption formation on nonlinear coefficient and weak dependence on refractive index. Thresholds (8a), (8b), and (10) do not depend on radiation wavelength and layer thickness. These facts are in surprisingly good agreement with results obtained by simulation (Fig. 4, 5, 6).

Calculated values of threshold field amplitude exceed well known experimental data^{2,5,6}. One important feature should be mentioned in this connection. Theoretical estimation of the threshold of field disruption formation for layered medium is lower (by factor of 2 in the presented calculations) than that for homogeneous dielectric. It is not difficult to show that it is true in general case because distortions of field profile in homogeneous dielectric must be high enough to move top of the profile by $\lambda/4$ while field disruption in layered medium appears if field profile is distorted a bit.

It should be mentioned that if incident field amplitude is just a bit above instability threshold then the feedback is formed due to multiple reflections at layer boundary. Instability threshold can be decreased much in multilayer coatings due to strong influence of multiple reflection on feedback formation.

Investigation of multilayer coatings have shown field blow-up instability to take place only within layers with large value of nonlinear coefficient. Instability thresholds for single layer are very similar to those of AR coatings. This can be connected with quenching of reflected waves resulting in general decreasing of light intensity in the coatings. Instability thresholds of layers with sine-shaped variation of refractive index do not differ much from those of similar AR coatings.



Obtained strong dependence of field-instability threshold on nonlinear refraction shows that it is the most sensitive to step-like variations of nonlinear refraction. In this connection it is reasonable to propose the following design of multilayer coatings which can result in increasing of ultimate LID threshold (Fig. 8.): sub-layers should be introduced into each layer so that variations of nonlinear refraction becomes rather smooth while linear refraction is kept the same as in linear approximation.

Fig. 8. Sublayer microstructure of optical coating with smooth variations of nonlinear refraction from $n_{2 \min}$ to $n_{2 \max}$.

Field blow-up is influenced great by sign of nonlinear coefficient what is illustrated well by the example with HR coatings consisting of $\text{TiO}_2/\text{SiO}_2$ layers. Field disruption always appear within TiO_2 layer not far from its boundary that corresponds to well known experimental results.

Investigation of field evolution in optical coatings has resulted in a general regularity: field instability develops fast in single layers and AR coatings and rather slowly in HR coatings. This implies dependence of field instability threshold on pulse duration. The obtained results can be applied to femtosecond and picosecond laser pulses only. Instability thresholds can be lower for 10-picosecond or longer pulses due to possibility for long pre-instability development of small disruptions. This problem is very important because it gives a key to do experimental checking of the model and ideas presented in this paper. In particular, it allows to prove which estimate (8a) or (8b) is correct because estimated instability thresholds depend on pulse duration in different ways. Unfortunately, it has not been investigated yet.

Generation of HH is one more interesting nonlinear process taking place in multilayer coatings under action of high-power radiation. This process can be of great importance for LID of optical coatings because the generated harmonics are of UV range and they can induce multiphoton absorption. The presented approach can also be used to model generation of HH in optical coatings but special paper should be devoted to investigation of this problem. Unfortunately, the authors have not got information about any experimental investigation of generation of such high-order harmonics.

6. REFERENCES

1. M.F.Koldunov, A.A.Manenkov, I.L.Pocitilo, // *Laser-Induced Damage in Optical Materials: 1993*, Proc. SPIE v. 2114, pp.469-487 (1993).
2. A.A.Manenkov, "Ultimate Laser Intensities in Transparent Solids", *Laser Physics*, v. 6 (3), pp. 501-505 (1996).

3. T.W.Walker, A.H.Guenther, P.E.Nielsen, "Pulsed Laser-Induced Damage to Thin-Film Optical Coatings - Part I: Experiment", *IEEE J. of Quant. Electron.*, v. **QE-17** (10), pp.2041-2052 (1981).
4. T.W.Walker, A.H.Guenther, P.Nielsen, "Pulsed Laser-Induced Damage to Thin-Film Optical Coatings - Part II: Theory", *IEEE Journal of Quant. Electron.*, **QE-17**(10), pp. 2053-2065 (1981)
5. M.Ohring, "Why are thin films different from the bulk?", *Laser-Induced Damage in Optical Materials: 1993*, Proc. of SPIE, v. **2114**, pp.624-639, 1994.
6. Z.Wo et al, "Optical and thermal characterization of barium titanate thin films prepared by metalorganic deposition", *Laser Damage in Optical Materials: 1993*, Proc. SPIE, v.**2114**, pp.251-261, 1993.
7. M.B.Vinogradova, O.V.Rudenko, A.P.Sukhorukov, *Theory of waves*, Moscow, Nauka Publ., 1990, Ch.IX (in Russian).
8. P.D.Maker, R.W.Terhune, "Study of Optical Effects Due to an Induced Polarization Third Order in the Electric Field Strength", *Phys. Rev.*, vol. **137**(3A), pp. A801-A818 (1965).
9. V.Ya.Arsenin, *Methods of Mathematical Physics and Special Functions*, Nauka Publ., Moscow, 1974, Ch. III (in Russian).
10. K.S.Yee, "Numerical solution of initial boundary value problems in isotropic media", *IEEE Transactions on Antennas and Propagation*, **AP-14**, p.302, 1966.
11. V.E.Gruzdev, A.S.Gruzdeva, "Computer simulation of light propagation through optical coatings with inhomogeneous microstructure", in *High-Power Laser Ablation*, Proc. SPIE, v. **3343**, 1998 (to appear).
12. W.E.Milne, *Numerical Solution of Differential Equations*, New York, 1953, Ch. VIII.
13. N.N.Kalitkin, *Numerical Methods*, Nauka Publ., Moscow, 1978, Ch. XIII (in Russian).
14. M.Born, E.Wolf, *Principles of Optics*, 4-th ed. Pergamon Press, N.Y.,1968, Ch.1.6
15. M.J.Weber, D.Milam, W.L.Smith, "Nonlinear Refractive Index of Glasses and Crystals", *Opt. Engineering*, v. **17**, p. 463 (1978).
16. R.Adair, L.L.Chase, S.A.Payne, "Nonlinear refractive-index measurements of glasses using three-wave frequency mixing", *Journal of the OSA B*, v. **4**, p. 875 (1987).
17. M.Bertolotti, A.Ferrari, C.Sibilia et al // *Appl. Phys.*, v. **27**, p. 1811 (1988).
18. Y.Watanabe, M.Ohnishi, T.Tsuchiya, "Measurement of nonlinear absorption and refraction in titanium dioxide single crystal by using a phase distortion method", *Appl. Phys. Lett.*, v. **66** (25), pp. 3431-3432 (1995).
19. M.J.Soileau, W.E.Williams, N.Mansour, E.W.VanStryland, "Laser-induced damage and the role of self-focusing", *Opt. Engineering*, v. **28** (10), p. 1133 (1989).

Generation performance of Cr: LiSAF new active medium for flashlamp pumped tunable solid-state lasers

Vyacheslav B. Gerasimov^a, Alexander S. Kuznetsov^b, Andrey A. Salnikov^a,
Vladimir O. Umnov^a, and Alexander V. Shestakov^b

^aSE SDB "Granat", 95 Volokolamskoe sh., Moscow, 123424 Russia

^bELS. Co, 3 Vvedenski street, Moscow, 117342 Russia

ABSTRACT

Free-running generation performance of a flashlamp-pumped Cr: LiSAF rod are presented. Laser average powers of 14 W at 10 Hz repetition rate, total laser and slope efficiencies of 3.5% and 5.1%, respectively, have been achieved. The laser was tuned from 810 to 910 nm (FWHM) with only one pair of broad band mirrors and a birefringent filter in the cavity.

A Cr³⁺: LiSrAlF₆ (Cr: LiSAF) broad band crystal laser medium may be used in prospective tunable coherent sources for various applications (generation in blue and UV spectral regions, efficient amplification of ultrashort pulses in a terawatt range, development of moving LIDAR systems, science and medicine research, and others). Cr: LiSAF has the best balance of the laser properties: the wide luminescent range (770-1000 nm); the high generation efficiency with different pumpage types (flashlamp, laser and diode); relatively long life time of the upper-state level; possibility to operate in free-generation mode, Q-switching and mode-locked regimes; relatively high spatial quality of the beam due to the negative and small values of thermal conductivity and refractive index time derivative on the c-axes; relatively high light strength and volume threshold of the optical damage (160-500 GW/cm²), small nonlinear refractive index ($n_2=0.55 \times 10^{-20}$ m²/W) and dispersion.¹ Unfortunately the fluoride hosts have an essential defect - their poor thermal performances restrict the value of repetition rate of the laser pulses necessary for such applications. So the thermal conductivity and the thermal figure of merit of Cr: LiSAF are 3.1 W/mK and 0.42 W/m^{1/2}, respectively.² These values are about one tenth of those for a Nd: YAG crystal. So far the published results on laser performances of the flashlamp-pumped Cr: LiSAF in different regimes demonstrate not more than a few Hz repetition rate.^{3,4,5,6}

Experiental results on the free-running flashlamp-pumped Cr: LiSAF are presented in this paper. The laser average powers of 14 W, the repetition rate of 1-10 Hz, the total laser and slope efficiencies of 3.5% and 5.1%, respectively, have been obtained. The laser was tuned from 810 to 910 nm (FWHM) with linewidth up to 3 nm with only one pair of broad band mirrors and a birefringent filter in the cavity.

In order to determine the pumping efficiency and to optimise the energy generation performance the 6.35×100 mm 1.5% Cr: LiSAF rod with BBAR coated end faces and about 0.0015 cm⁻¹ non-active absorption index on the wavelength of 1.064 mkm is optimal inserted in different duffuse and silver reflecting pump chambers with only one xenon flashlamp.

To cool the pump chamber the 50:50 mixture of ethylene glycol and distilled water was used.

Power supply of the pump lamp provides the pump energy range from 17.5 to 45.0 J for pulse duration of 100-150 mks (FWHM). The lamp operates in a simmer mode at repetition rates of 1, 5 and 10 Hz. The laser resonator with length 45 cm consists of two broad band mirrors. A HR mirror with the reflection coefficient of 99.5% for the wavelength region of 730-950 nm either flat or sphere with raduis of the curvature of 1492 mm is used. Flat output mirrors with the different transmission coefficients are used.

Further author information -

V.B.G., A.A.S., and V.O.U.: Telephone: 095 491-71-30; Fax: 095 491-50-21, 095 490-93-96
A.S.K., and A.V.S.: E-mail: avshest@ipolus.msk.su; Telephone/Fax: 095 334-86-40

In order to tune output wavelength of generation in the range from 0.8 to 0.95 μm threeplate birefringent wave selector with mkm roll device BF-03-450 (Tekhnoscan, Joint-Stock Company, Russia) was inserted into the optical resonator. The tuning of the wavelength in this range is fulfilled for the main peaks of the third or fourth orders of the transmission (the orders of the transmission for the thinnest plate) with instantaneous rolling all plates of the selector without change of their slopes. The roll angle of the selector determines the wavelength of the laser.

The fig. 1 shows the output pulse energy as a function of the flashlamp pump energy in non-selective flat-flat resonator for the different reflections of the output mirror for the wavelength 850 nm. It is seen that for these experimental conditions the best optimum output mirror should have reflection of 70%. Therefore all next spectral-energy curves were obtained for the 70% mirror.

Fig. 2 shows the Cr: LiSAF output pulse energy as a function of the pump energy for different types of laser pumping cavities and 1 Hz repetition rate.

The total laser and slope efficiencies of $\sim 3\%$ and $\sim 4\%$, respectively, were obtained using quartz silver monoblok as the laser pumping cavity with In_2O_3 coated one flashlamp to filter UV radiation. The similar results were observed with Ce-doped flashlamp (model ENP-5/90).

To avoid optical unstability of the optical resonator due to directed active medium thermal lens and to improve generation performance of the Cr: LiSAF laser at 10 Hz repetition rate the HR flat mirror was replaced by the spherical mirrors with radius of curvature of 1.5 m, 5 m and 10 m.

Fig. 3 shows the output energy as a function of the pump energy for different repetition rates and radii of the curvature of the HR mirror.

Maximum output energy of 1.6 J of Cr: LiSAF placed in the silver pump chamber at repetition rate of 1 Hz and radius of curvature of the HR mirror 1.5 m has been achieved and it was reduced only by 15% at repetition rate of 10 Hz. Maximum average power 14 W at 10 Hz repetition rate, total laser and slope efficiencies of 3.5% and 5.1%, respectively, have been achieved.

Dependence of threshold pump energy on reflectivity of the output mirror on 850 nm is shown in fig. 4. The crossing of the curve with X-axes defines the passive losses of the laser material. It is seen that Cr: LiSAF losses is less than 0.01 cm^{-1} .

We should underline here the active element generation characteristics are depended on crystal orientation. That is why we obtained in our experiments the totally linear-polarized output radiation.

The laser beam energy divergence for 45 J pump pulse does not depend on the wavelength selector in optical resonator and it was not more than 1.5-3 mrad at 10 Hz repetition rate.

It should be noted that the placing of the wavelength selector results in reducing of the pulse duration by 1.3 factor. The pulse duration for the non-selective resonator is 90 mks at 45 J pulse of pumping.

The wavelength dependence of the Cr: LiSAF output average power for selective resonator is shown on fig. 5. When the wavelength selector is installed in the optical resonator the average output power is reduced by factor 2 and it not larger than 4.5 W at wavelength of $847 \pm 3 \text{ nm}$. For the broad band resonator mirrors the laser was tuned from 810 to 910 nm (FWHM) with linewidth not more than 3 nm and not more than 6 nm in selective and non-selective resonator, respectively.

It should be noted that there are an angular range of the birefringent filter which corresponds to maximal energy characteristics and to smooth (without jumps) tuning. To extend the tuning range it is desirable to use instead of one broad band mirror the different narrow band mirrors with different reflectivity at the wavelength range considered.

Preliminary experimental results for the Q-switching Cr: LiSAF mode using the effect of the frustration of the Full Inner Reflection were obtained. The output energy more then 0.1 J at 10 Hz repetition rate and laser pulse duration 80 ns was achieved.

The results of the experimental research described in this article demonstrate that the flashlamp pumped Cr: LiSAF may efficiently operates in a tunable mode at 10 Hz frequency repetition which is the great importance for different applications.

REFERENCES

1. M. Richardson, M.J. Soileau, P. Beaud, Y.-F. Chen, R. DeSalvo, S. Gamov, D.J. Hagan, S. Klimentov, M. Sheik-Bahae, A.A. Said, E. Van Stryland, and B. Chai, "Self-focusing and optical damage in Cr: LiSAF and Cr: LiCAF", *SPIE*, vol. 1848, pp. 392-402, 1993.
2. S.A. Payne, L.K. Smith, R.J. Beach, B.H.T. Chai, J.H. Tassano, L.D. DeLoach, W.L. Kway, R.W. Solarz, and W.F. Krupke, "Properties of Cr: LiSrAlF₆ crystals for laser operation", *Appl. Opt.*, vol. 33, pp. 5526-5536, 1994.
3. M. Stalder, B.H.T. Chai, and M. Bass, "Flashlamp pumped Cr: LiSrAlF₆ laser", *Appl. Phys. Lett.*, vol. 58, pp. 216-218, 1991.
4. P. Beaud, Y.-F. Chen, B.H.T. Chai, and M.C. Richardson, "Gain Properties of LiSrAlF₆:Cr³⁺", *Opt. Lett.*, vol. 17, pp. 1064-1066, 1992.
5. H. Takada, K. Miyazaki, and K. Torizuka, "Flashlamp-Pumped Cr: LiSAF Laser Amplifier", *IEEE J. Quantum Electron.*, vol. 33, no. 12, pp. 2282-2285, 1997.
6. B.H.T. Chai, M. Bass, and M. Stadler, "Crystal Growth and Lasing Performance of Cr-Doped LiCaAlF₆ and LiSrAlF₆ Crystals", *OSA Proceedings on Advanced Solid State Lasers*, March 5-7, 1990.

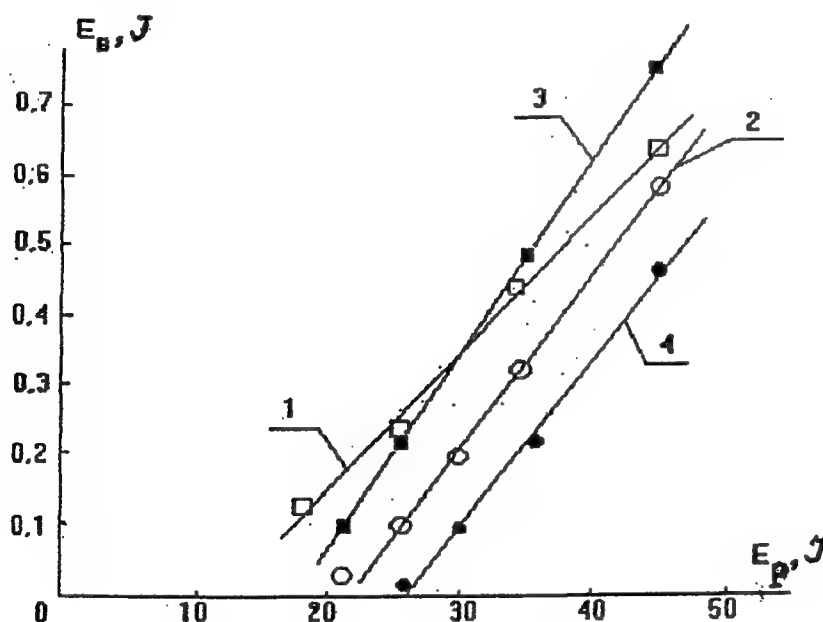


Fig. 1. Cr: LiSAF output pulse energy as a function of the flashlamp pump energy for different reflectivities on 850 nm R_{850} of the output mirror. One Ce-doped lamp (model ENP-5/90) In_2O_3 diffuse laser pump cavity, repetition rate of 1 Hz and duration of the pump pulse of 150 mks.

1 - $R_{850}=85\%$; 2 - $R_{850}=57\%$; 3 - $R_{850}=70\%$; 4 - $R_{850}=45\%$.

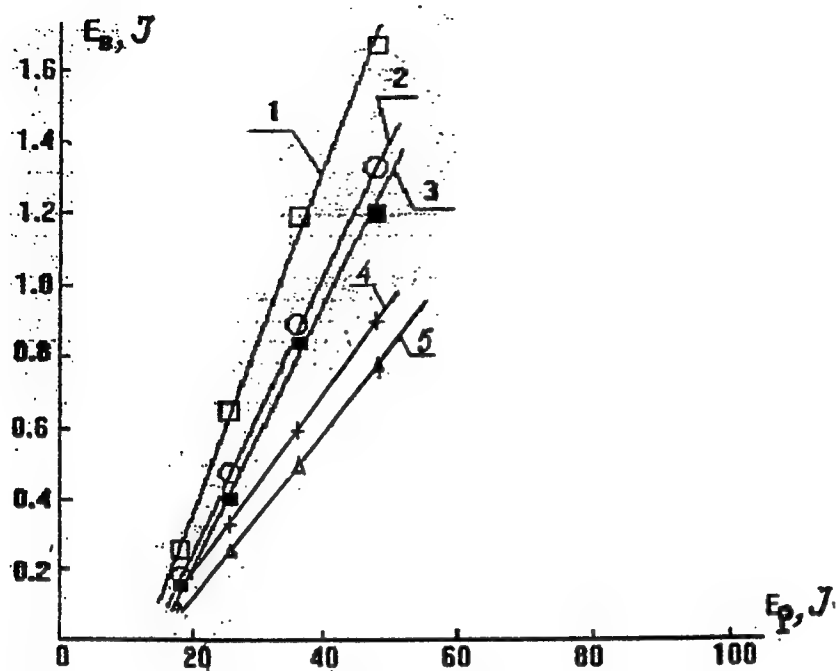


Fig. 2. Cr:LiSAF output pulse energy as a function of the flashlamp pump energy for different types of the laser pump cavities. Repetition rate of 1 Hz.

1 - quartz silver monoblok as laser pumping cavity with In_2O_3 coated one flashlamp (model ESP-600). Spherical HR mirror has radius of curvature of 1.5 m;

2 - similar conditions of part 1 with flat HR mirror;

3 - laser pumping cavity of part 1 with Ce-doped flashlamp (model ENP-5/90);

4 - diffuse glass reflector with In_2O_3 coated flashlamp (model ESP-600);

5 - diffuse Eu-doped quartz glass ZrO_2 reflector with Ce-doped flashlamp (model ENP-5/90).

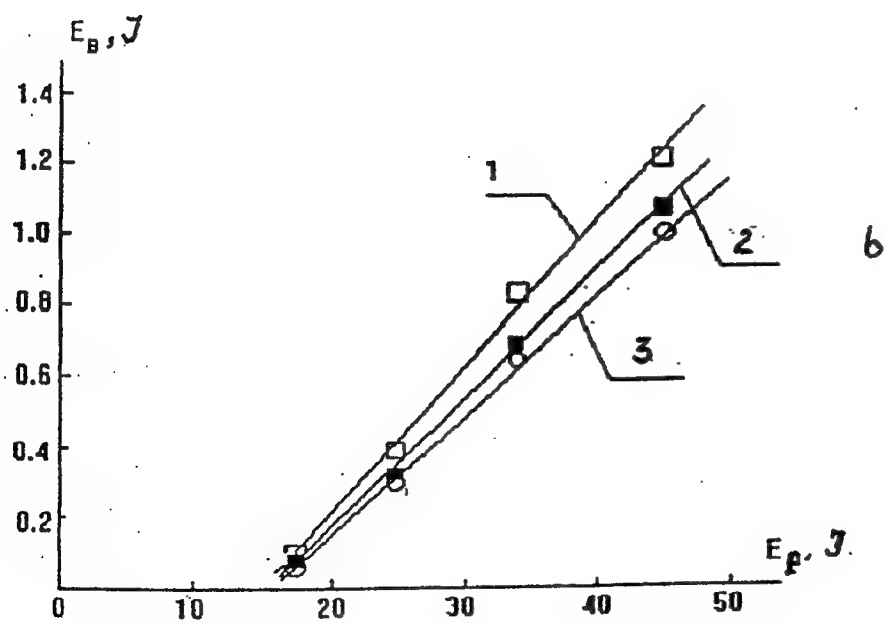
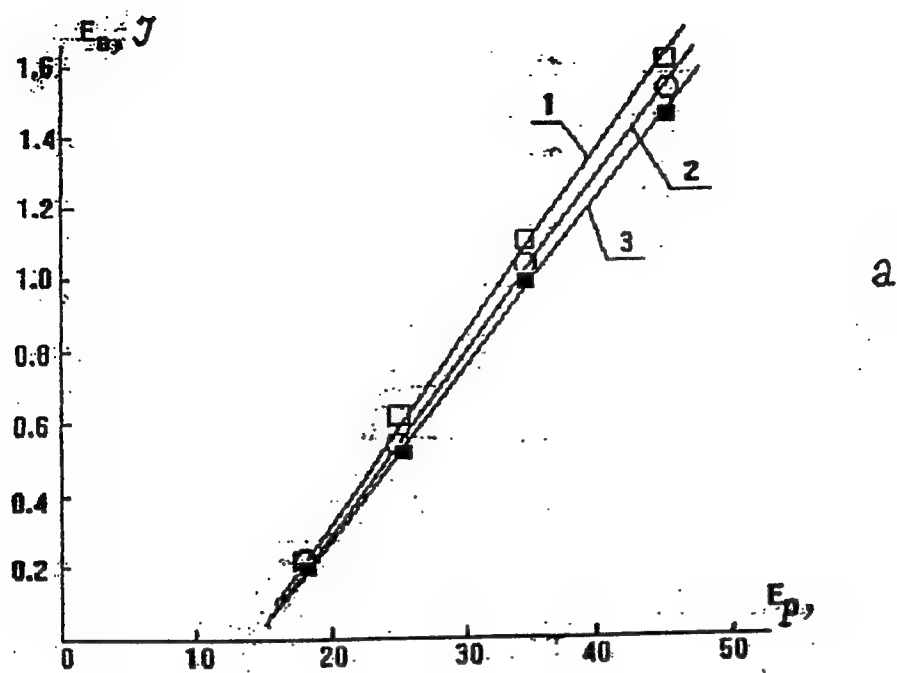


Fig. 3. Cr:LiSAF output pulse energy as a function of the flashlamp pump energy with silver pump cavity for different repetition rates and radii of curvature of HR mirror of 1.5 m (a) and 5 m (b).
1 - 1 Hz; 2 - 5 Hz; 3 - 10 Hz.

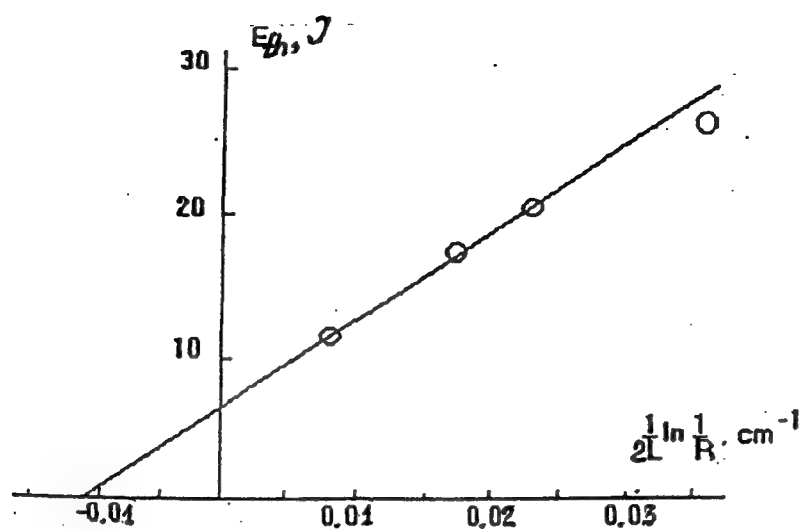


Fig. 4. Dependence of threshold pump energy on reflectivity of the output mirror for the 850 nm wavelength.

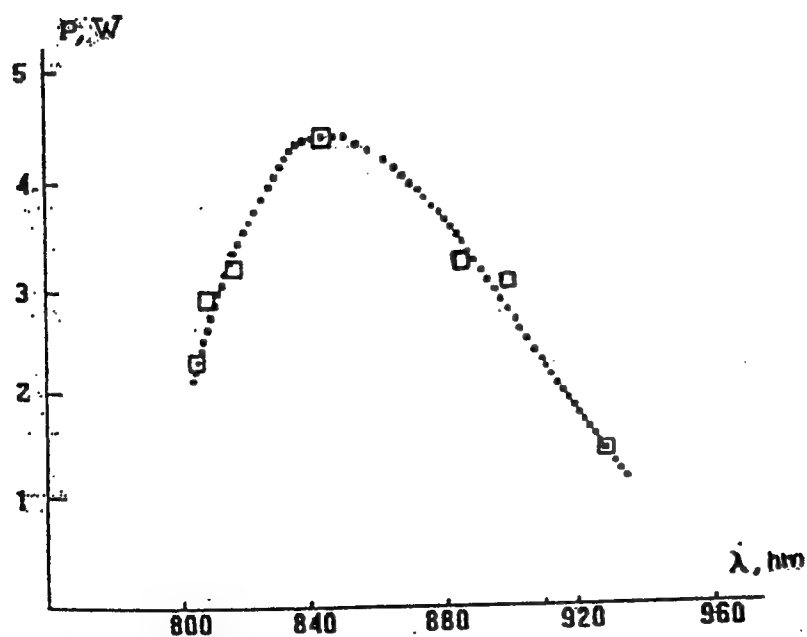


Fig. 5. Wavelength dependence of the Cr: LiSAF output average power for the selective resonator. Pump pulse energy of 34 J, repetition rate of 10 Hz and pump pulse duration of 150 mks.

Surface Studies Using Non-Linear Spectroscopy with Tunable Picosecond Pulses

J. Löbau and A. Laubereau

Technische Universität München, Physik-Department E11, James-Franck-Straße,
85748 Garching, Germany

ABSTRACT

Chemisorbed films of octadecyltrichlorosilane (OTS) and ethyltrichlorosilane (ETS) at the interface calcium fluoride:air have been studied by vibrationally resonant IR pump IR-vis probe sum-frequency (SF) spectroscopy. Using a total internal reflection geometry, a signal enhancement of more than two orders of magnitude compared to the conventional setup is achieved. This enhancement in combination with two independently continuously tunable infrared sources provide new insight in intramolecular energy flow processes and the corresponding relaxation times on dielectric surfaces. A fast energy exchange between the CH_3 -stretching modes detected by SF spectroscopy occurs within a few picoseconds. A two-exponential decay of the CH_3 -stretching modes is observed: The energy relaxation is fast with time constants in the picosecond range, while the ground state is repopulated in approximately 100 ps. Due to the fast energy exchange within the CH-stretching vibrations and their strong anharmonic coupling, bleaching of a SF-active mode can be achieved, even if the pumped mode does not directly contribute to the SF spectrum. This weakening of the selection rules in IR pump IR-vis probe SF spectroscopy is demonstrated for the methylene stretching vibrations of OTS.

Keywords: Sum-frequency spectroscopy, surfaces, energy relaxation, pump-probe vibrational spectroscopy, anharmonic coupling

1. INTRODUCTION

Since ultrashort laser pulses have become available, a lot of pump-probe experiments were carried out to determine time constants of various relaxation processes. This method was used successfully on both electronic and vibronic states in liquids,¹ polymers² and semiconductors.³ Due to the lack of suitable surface-sensitive investigation methods, only few measurements report relaxation times of molecular vibrations at interfaces.⁴⁻⁶ Thus little is known about the behavior of molecules adsorbed at interfaces, which is essential for many chemical reactions and biological processes.

The most promising way to realize pump-probe measurements with high time resolution is the use of ultrashort light pulses. Therefore, most of the common surface-sensitive techniques based on particle interaction with the surface (e. g. electron spectroscopy) are of little use to determine relaxation times in molecules. Successful approaches to adopt conventional pump-probe experiments on surfaces of small solid particles have been reported.^{4,5} However, the application of this method requires special conditions, e. g. a large ratio of surface to volume to increase the surface signal with respect to the perturbing bulk contributions. Another method to increase the surface signal is the use of a near-glancing incidence geometry in time-resolved infrared reflection absorption spectroscopy (IRRAS), e. g. on CO adsorbed on metal surfaces.⁶

A more versatile method to perform pump-probe measurements on surfaces is the use of inherent surface-sensitive methods like SF spectroscopy. Since its invention in the group of Shen,⁷ there have been many successful applications in surface spectroscopy.⁸⁻¹⁴ SF spectroscopy is a nonlinear optical technique, originating from the second-order nonlinear susceptibility $\chi_{ijk}^{(2)}(\omega_{\text{IR}})$. Since $\chi_{ijk}^{(2)}$ vanishes in the bulk of centrosymmetric media, only molecules at the surface contribute to the SF signal due to the symmetry breaking at the interface. The SF signal is enhanced by vibrational resonances of the adsorbed molecules; these lines can be bleached by pumping the modes with an

Correspondence: J. Löbau, Physikalisch-Technische Bundesanstalt, Fachlabor 5.23AZ, Bundesallee 100, 38116 Braunschweig, Germany. Phone (+49)-531-592-5259, Fax -5277, E-mail: joerg.loebau@ptb.de

additional infrared pulse. The optical method SF spectroscopy can be used on surfaces under a normal atmosphere and does not require vacuum conditions. Because it is even possible to study buried interfaces, a great number of systems becomes accessible to time-resolved measurements.

After the first pump-probe SF measurements by Harris and Levinos¹⁵ with only one single tunable IR frequency, further experiments on adsorbates at metal¹⁶ and semiconductor surfaces^{17,18} followed. In this paper, "two-color pump-probe SF spectroscopy" denotes the use of two independently tunable infrared pulses in addition to the upconversion pulse. Since the SF signal generated at metal or semiconductor surfaces is usually much stronger than the signal generated by adsorbed molecules on dielectric surfaces, the only two-color pump-probe SF experiments published so far have been performed on hydrogen-terminated silicon^{19,20} and diamond²¹ surfaces. In this paper we report two-color pump-probe SF measurements on chemisorbed molecules on dielectric surfaces, using a total internal reflection (TIR) geometry to increase the SF signal and, therefore, the signal-to-noise ratio. Compared to our preliminary relaxation times in the system OTS on calcium fluoride (CaF₂),²² an improved experimental setup with an enormous increase of the signal-to-noise ratio provides new insight in the energy transfer processes on surfaces.

Due to the selection rules for SF spectroscopy, SF spectra may differ considerably from IR-absorption spectra; it is possible for strong IR-active modes to vanish completely in the SF spectra. The combination of IR-vis SF probing after an IR excitation by a preceeding pump pulse has been demonstrated at an hydrogen-terminated silicon surface,¹⁹ we extend this technique to molecules adsorbed on dielectric surfaces. The IR pump pulse is absorbed according to the IR cross section of the pumped molecular vibration, and SF-active modes can be affected due to energy relaxation or anharmonic coupling to the pumped mode. Scanning the IR pump pulse while monitoring the SF signal of a SF-active molecular vibration, IR excitation spectra are obtained. We call this technique sum-frequency infrared absorption spectroscopy (SF-IRAS).

2. THEORY

A tunable probe wave $\vec{E}(\omega_{\text{IRpr}})$ in the IR with frequency ω_{IRpr} and a wave $\vec{E}(\omega_{\text{vis}})$ with fixed frequency ω_{vis} in the visible are coupled by $\chi_{ijk}^{(2)}(\omega_{\text{IRpr}})$ ⁸ (the indices i, j, k refer to the Cartesian coordinates):

$$P_i^{(2)}(\omega_{\text{SF}}) = \sum_{jk} \chi_{ijk}^{(2)}(\omega_{\text{IRpr}}) E_j(\omega_{\text{vis}}) E_k(\omega_{\text{IRpr}}) \quad (1)$$

The induced nonlinear polarization $P_i^{(2)}(\omega_{\text{SF}})$ radiates a wave at the sum-frequency $\omega_{\text{SF}} = \omega_{\text{vis}} + \omega_{\text{IRpr}}$, the corresponding SF signal is referred to as SFv-pr. Due to the symmetry of the $\chi^{(2)}$ -tensor, there are three commonly used polarization combinations for the SF generation process, referred to as ssp, sps and ppp.⁸ The three letters indicate the polarization with respect to the plane of incidence and refer to the SFv-pr, vis and IRpr pulses, respectively (cf. Sec. 3, Fig. 2). In pump-probe experiments, a fourth letter is necessary to denote the polarization of the IR pump pulse. In contrast to SF experiments on conductive surfaces which permit only electric fields perpendicular to the surface (p-polarized), on dielectric media electric fields parallel to the surface are not screened, allowing a variety of polarization combinations.

$\chi^{(2)}$ can be decomposed into two parts (Eq. (2)): A non-resonant χ_{ijk}^{nr} and a resonant contribution $\chi_{ijk,\nu}$ due to the ν -th vibrational mode with resonance frequency ω_ν and damping constant Γ_ν . The non-resonant part is important on metals and semiconductors, but on dielectric media it is small compared to the resonant contribution of the adsorbed molecules.

$$\chi_{ijk}^{(2)} = \chi_{ijk}^{\text{nr}} + \sum_{\nu} \chi_{ijk,\nu}^{(2)} \quad (2)$$

$$\text{with } \chi_{ijk,\nu}^{(2)} = \frac{A_{ijk,\nu}}{\omega_\nu - \omega_{\text{IRpr}} - i\Gamma_\nu/2} \quad (3)$$

The linestrength of the respective mode $A_{ijk,\nu}$ can be expressed in terms of the IR transition dipole moment $\mu_{k,\nu}$ and the Raman polarizability $\alpha_{ij,\nu}$. N is the number density of the adsorbed molecules:

$$A_{ijk,\nu} = N \langle \alpha_{ij,\nu} \mu_{k,\nu} \rangle (n_{0,\nu} - n_{1,\nu}) \quad (4)$$

Angular brackets indicate the average over the molecular orientations on the surface. $n_{0,\nu}$ and $n_{1,\nu}$ are the fractional populations of the ground and excited state, respectively.²³ Since the CH-stretching vibrations considered in this work are in the range of 3000 cm^{-1} , the thermal population of the excited states is in the order of 10^{-7} and, therefore, neglected. Without application of a pump pulse, the unperturbed populations are $n_{0,\nu} = 1$ and $n_{1,\nu} = 0$, leading to a corresponding SF signal S_0 . With I denoting the intensity of the respective pulse, the radiated SF signal is

$$S = I_{\text{SF}} \propto |P_i^{(2)}(\omega_{\text{SF}})|^2 \propto |\chi_{ijk}^{(2)}|^2 I_{\text{vis}} I_{\text{IRpr}} \quad (5)$$

In pump-probe measurements, a mode ν_{pu} is pumped with ω_{IRpu} , which reduces the population of the vibrational ground state of this mode and hence $A_{ijk,\nu_{\text{pu}}}$. The IR pump pulse arrives at the sample at a delay time t_D before the IR probe and upconversion pulse pair; the detected SF signal $S(t_D)$ generated by the IR probe pulse at ω_{IRpr} and the upconversion pulse is proportional to $|\chi_{ijk}^{(2)}|^2$ (Eq. (5)) and therefore proportional to $(n_{0,\nu_{\text{pr}}} - n_{1,\nu_{\text{pr}}})^2$. Thus, in analogy to conventional IR absorption pump-probe experiments, the properly normalized SF signal is²³

$$1 - \sqrt{\frac{S(t_D)}{S_0}} = 1 - (n_{0,\nu_{\text{pr}}}(t_D) - n_{1,\nu_{\text{pr}}}(t_D)) = \Delta n_{1,\nu_{\text{pr}}}(t_D) - \Delta n_{0,\nu_{\text{pr}}}(t_D), \quad (6)$$

which represents the pump-induced change of the population difference of the probed mode ν_{pr} . In the following, this is referred to as the differential signal.

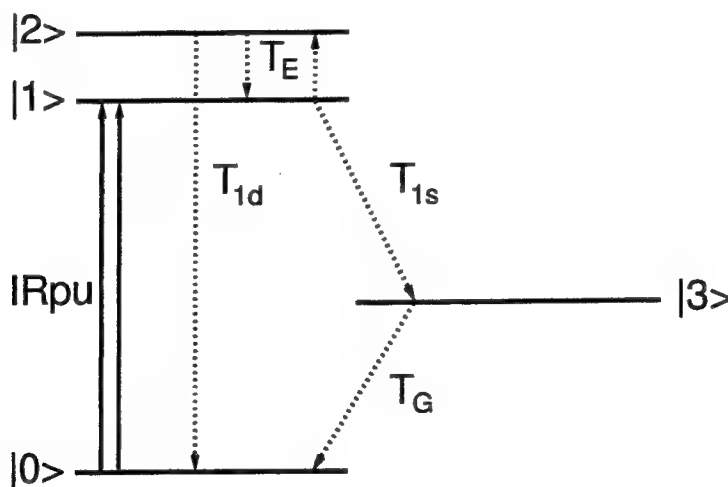


Figure 1. The four-level system used to fit the time-resolved data. After being pumped to level |1> (CH_3 -s stretching mode), the population decays to an intermediate level |3> (CH_3 -bending modes). Additionally, there is an energy exchange with time constant T_E and detailed balance between levels |1> and |2> (CH_3 -d stretching mode). This yields an effective life time of the s-mode T_{1s} . The population in level |2> decays with a lifetime T_{1d} to the ground state |0>. Additionally, level |0> is repopulated from the intermediate level |3> with the ground state recovery time T_G . The other two possible transitions $|2\rangle \rightarrow |3\rangle$ and $|1\rangle \rightarrow |0\rangle$ turn out to be negligible.

A four-level model (Fig. 1) is used to interpret the experimental data; the corresponding rate equations are integrated numerically to compute the evolution of the population for each level. An IR pulse with duration t_p pumps molecules from the ground state |0> to level |1>, the first excited state of the symmetric CH_3 mode. The population in level |1> decays within a time constant of T_{13} to an intermediate level |3>. An additional energy exchange with detailed balance and a time constant $T_E = T_{21}$ occurs between levels |1> and |2>, the first excited state of the degenerate CH_3 stretching mode. The energy difference of $\Delta E = 85\text{ cm}^{-1}$ and the higher statistical weight $g = 2$ of the antisymmetric d-mode due to the two-fold degeneracy have to be taken into account for calculating the

balance between the stretching vibrations, i. e. $T_{12} = T_E \times e^{\Delta E/kT}/g$. This yields a life time $T_{1s} = (1/T_{12} + 1/T_{13})^{-1}$. The population of level $|2\rangle$ with the life time $T_{1d} = (1/T_E + 1/T_{20})^{-1}$ decays with the time constant T_{20} to the ground state $|0\rangle$, additionally to the energy exchange with level $|1\rangle$. This decay to the ground state can be interpreted as energy transfer to a methylene stretching mode: When only a methyl stretching mode is excited, a fast energy transfer to the methylene modes of the molecule can occur. After the transfer of the vibrational quantum, the methyl group is in its ground state $|0\rangle$, while a methylene mode is still excited.

The common vibrational ground state of the CH_3 modes corresponds to the approximation that the anharmonic frequency shift of the combination tones of the two CH_3 modes is large compared to the line width, while the anharmonic frequency shift is neglected for the $\text{CH}_3\text{-CH}_2$ combination tones. The ground state $|0\rangle$ is repopulated from the intermediate level $|3\rangle$ with the ground state recovery time T_G . Level $|3\rangle$ in our model may be assigned to CH_3 bending modes. With respect to the experimental situation, pumping of level $|2\rangle$ instead of level $|1\rangle$ is also considered. The two time constants T_{23} and T_{10} for the possible transitions $|2\rangle \rightarrow |3\rangle$ and $|1\rangle \rightarrow |0\rangle$, respectively, are used as fit parameters but turn out to be long compared to the other relaxation times and can, therefore, be neglected.

The population dynamics is computed from the corresponding rate equations. The resulting SF signal at delay time t_D is calculated by convoluting the probe pulse pair with the respective population differences, assuming an equal pulse duration and a Gaussian shape for all three pulses. The relaxation times are fitted to the experimental data using a weighted least squares fit. The pulse duration t_p is known from cross correlation measurements but is used as a fit parameter to improve the fit quality.

The SF spectra shown in this paper are fitted to $|\chi_{ijk}^{(2)}|^2$ (Eqs. (3), (5)). To obtain a reliable fit, both the pumped and unpumped spectra are fitted simultaneously, assuming equal linewidths and frequency positions. Only the amplitude $A_{ijk,\nu}$ may vary between the two spectra. The line parameters obtained by this procedure yield a credible differential signal $1 - \sqrt{\frac{S(t_D)}{S_0}}$.

Because of the fast vibrational relaxation within the CH-stretching modes and their anharmonic coupling, an excitation of a mode ν_{pu} can rapidly affect the probed mode ν_{pr} . Therefore, scanning the pump frequency ω_{pu} and monitoring the SF signal generated by the IR-vis probe pulse pair at a fixed frequency ω_{pr} , information on the IR cross section of the pumped mode, the orientation of the transition dipole moment and the coupling to the probed vibration can be obtained. Since the IR absorption determines the differential signal, the excitation spectra measured in this way are fitted to a Lorentzian lineshape

3. EXPERIMENTAL

The preparation of OTS ($\text{CH}_3(\text{CH}_2)_{17}\text{SiCl}_3$) and ETS ($\text{CH}_3\text{CH}_2\text{SiCl}_3$) films chemisorbed on a CaF_2 surface is described elsewhere.^{24,25} We obtain a nicely hydrophobic sample surface, and the spectra shown in this work prove the film quality to be high.

Our 2-color pump-probe sum-frequency spectrometer is pumped by a Kerr-lens modelocked (KLM) Nd:YLF laser operated at a fundamental wavelength of $1.047\ \mu\text{m}$.²⁶ The laser generates pulse trains of several hundred pulses at a repetition rate of 60 Hz and a pulse duration of 2.7 ps. To generate two independently tunable infrared pulses, two identical two-stage parametric devices are used.^{11,27} In each branch, the amplified and frequency-doubled pulse train of the laser is used to pump an optical parametric oscillator (OPO). The pulses emitted by the OPO (tunable from $1.2 - 1.8\ \mu\text{m}$) are mixed with an amplified single-pulse at the laser fundamental wavelength in a LiNbO_3 parametric amplifier. The obtained difference frequency is tunable from 2400 to $4200\ \text{cm}^{-1}$ with an approximately Gaussian pulse shape and a duration of 2.7 ps, bandwidth of $6\ \text{cm}^{-1}$, and energy of $5\ \mu\text{J}$ for the probe and $20\ \mu\text{J}$ for the pump IR pulse. For the upconversion pulse at $523.5\ \text{nm}$, a duration of approximately 3 ps with $50\ \mu\text{J}$ energy is achieved by frequency-doubling of an amplified single laser pulse. The repeatability of the IR frequency is found to be $\pm 2\ \text{cm}^{-1}$ which is comparable to the absolute accuracy of our frequency calibration.

Before reaching the sample, the IR pump pulse passes a variable delay line to adjust its temporal position with respect to the IR probe and upconversion pulse pair. All three pulses are focused onto the surface of the sample to a spot diameter of approximately $200\ \mu\text{m}$ with angles of incidence of 52° for the upconversion and 58° for the IR pulses. The sample, a silane coated CaF_2 prism, is mounted in a TIR geometry, the configuration is shown in Fig. 2. Half-wave plates are used for adjusting the polarization of the incident beams. The TIR geometry is chosen because

of the great enhancement of the SF signal: A gain of more than two orders of magnitude compared to the regular external reflection geometry (i. e. laser pulses incident from the low-index side) is achieved.²⁸

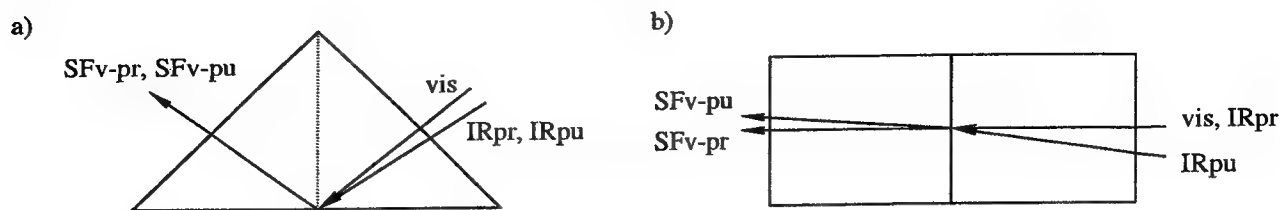


Figure 2. SF-generation on the hypotenuse of a silane coated CaF_2 prism in TIR geometry. (a) side view, (b) top view. The incident IR probe (IRpr) and upconversion (vis) pulse pair generates the usually detected SF-signal (SFv-pr). The SF-signal SFv-pu, generated by the IR pump (IRpu) and upconversion pulses near zero delay, is used to optimize the spatial overlap of the IR pump pulse and to determine zero delay. In the measurements shown in this paper, it is blocked by an aperture.

The SF signal (SFv-pr), generated by the upconversion (vis) and the IR probe (IRpr) pulse pair, is detected by a photomultiplier tube after passing a polarizer and suitable interference filters. As shown in Fig. 2, also by the upconversion and the IR pump (IRpu) pulse pair a SF signal (SFv-pu) is generated near zero delay. Due to different angles of incidence of IRpr and IRpu and the \vec{k} -matching condition, SFv-pu emerges under a slightly different angle compared to SFv-pr. It can therefore be blocked by an aperture during the measurements shown in this work. On the other hand, the SFv-pu signal can be used to determine zero delay and to optimize the spatial overlap between the IR pump and the visible pulse, enabling control of the IR pump-probe beam overlap. A chopper wheel which blocks every second IR pump pulse allows to record pumped and unpumped SF signals almost simultaneously. The measurements presented in this paper are averaged over 10 scans consisting of 50 pumped and unpumped measurements at each position. All experiments are made under normal atmospheric conditions at room temperature.

4. RESULTS AND DISCUSSION

4.1. SF Spectra

In Fig. 3a a SF spectrum of OTS on a CaF_2 surface in TIR geometry in ppp polarization is shown.* The filled diamonds in Fig. 3a indicate the unpumped SF signal. The spectrum is dominated by the three lines at 2875 cm^{-1} , 2933 cm^{-1} , and 2960 cm^{-1} . These peaks are attributed to the symmetric CH_3 -stretching (s) mode, the symmetric overtone of a methyl bending mode, intensified by Fermi-resonance with the symmetric stretching mode, and the degenerate CH_3 -stretching (d) mode, respectively.^{8,29-31} The maximum at 2860 cm^{-1} is caused by the symmetric methylene stretching vibration,⁸ while the peak at 2910 cm^{-1} is attributed to the antisymmetric methylene stretching mode. In perfectly ordered films, the CH_2 stretching modes vanish due to a local inversion symmetry in the monolayer.⁸ This behavior can be seen e. g. in OTS monolayers on glass,¹³ where no CH_2 contributions are visible. The weak methylene peaks in the SF spectra shown here indicate an ordered film with a few *gauche*-defects, causing an imperfect cancellation of the methylene modes. A quantitative analysis of the line amplitudes including spectra in ssp and sps polarization yields a tilt angle of about 33° to the surface normal for the symmetry axis of the terminal methyl group,²⁸ assuming a δ -distribution function.

An IR pump pulse with $\omega_{\text{IRpu}} = 2960\text{ cm}^{-1}$ which arrives at the sample 1 ps before the probe pulse pair generates the maximum differential signal, i. e. the SF signal with pump pulse is a minimum. The pumped SF signal is presented by the open circles in Fig. 3a, the corresponding normalized differential signal is shown in Fig. 3b. The solid line in 3b is calculated from the line parameters obtained from the fit to the SF spectra in 3a. Although only the d-mode is pumped, all visible CH-stretching modes are bleached simultaneously. The greatest pump-induced signal changes appear at the fundamental CH_3 -modes at 2875 cm^{-1} and 2960 cm^{-1} ; the differential signal at the overtone at 2933 cm^{-1} and at the methylene modes is smaller by approximately a factor of two. At 2807 cm^{-1} there is a hint to an excited state transition $v = 1 \rightarrow v = 2$, corresponding to a negative differential signal. Unfortunately,

*Since SF spectra of ETS look very similar, they are not presented in this paper.

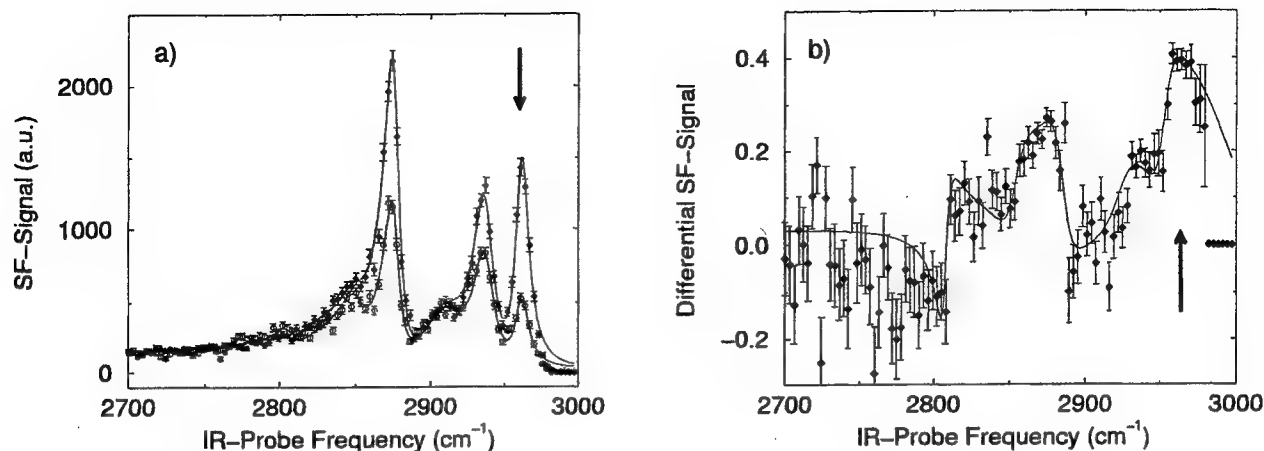


Figure 3. OTS on CaF_2 in TIR, $\omega_{\text{IRpu}} = 2960 \text{ cm}^{-1}$, pump frequency indicated by arrows, pppp polarization, $t_D = 1 \text{ ps}$. (a) pumped (open circles) and unpumped (solid diamonds) SF-spectra. (b) SF differential signal, the solid line represents the theoretical curve, calculated from the fit to the experimental data shown in (a).

the signal-to-noise ratio is not sufficient to determine the lifetime of the excited state $v = 1$. The frequency position of the excited state signal suggests that it belongs to the symmetric methyl stretching vibration, corresponding to a red shift compared to the fundamental mode of $68 \pm 6 \text{ cm}^{-1}$. This anharmonicity corresponds well to measurements of CH_3Cl in the gas phase: A red shift of the first overtone of the symmetric CH_3 -stretching mode in comparison to the fundamental mode of 61 cm^{-1} was found.³²

4.2. Time Resolved Measurements

In the time resolved measurements of the differential SF signal we focused on the s- and d-methyl stretching modes at 2875 cm^{-1} and 2960 cm^{-1} . Due to their large amplitudes in the SF spectra, a good signal-to-noise ratio can be obtained. Additionally, the interpretation of data concerning only the head group is less ambiguous than for the methylene modes of CH_2 -groups at different positions in the alkyl chain. The pump pulse in these measurements is p-polarized, and the combination for probing the s-mode is ssp and for the d-mode ppp, in short sspp and pppp, respectively. The polarizations are chosen to obtain maximum SF signals and, therefore, good signal-to-noise ratios.

Figure 4a and b show the temporal evolution of the SF signal when the same mode is pumped and probed. In Fig. 4a the decay of the CH_3 s-mode, and in 4b the relaxation of the CH_3 d-mode is shown. In order to get information on the coupling of the modes involved and the energy transfer between them, it is also necessary to pump one mode and probe the other one. This is shown in Fig. 4c for the CH_3 s-mode pumped and d-mode probed, while in Fig. 4d vice versa the d-mode is pumped and the s-mode is probed. The solid lines in Fig. 4 are obtained by simultaneously fitting the data of all four measurements to the four-level-model with one common set of parameters.

In all pump-probe measurements a rapid signal rise limited by the pulse duration can be observed. After reaching the maximum signal, the slower decrease is followed by a long-lived plateau. A striking difference between Figs. 4a and c, where the s-mode is pumped, and Figs. 4b and d with the d-mode pumped are the different signal amplitudes: Pumping the d-mode is more efficient by a factor of two compared to pumping the s-mode. This can be explained by the larger infrared cross section of the degenerate mode. The increased signal improves the signal-to-noise ratio in the d-mode pumped measurements. The theoretical curves in Fig. 4a, b and d describe the experimental points very well, while in c small deviations are visible, the calculated plateau for large delay time is too low. These deviations reveal the limits of our simple four-level-model. For a more realistic model, more modes of the molecule obviously have to be considered.

The time constants for OTS according to the four-level-model (Fig. 1) are obtained from the fit: The energy exchange time between level $|1\rangle$ and $|2\rangle$ is found to be $T_E = T_{21} = 2.6 \pm 1.5 \text{ ps}$, the energy decay time of the CH_3

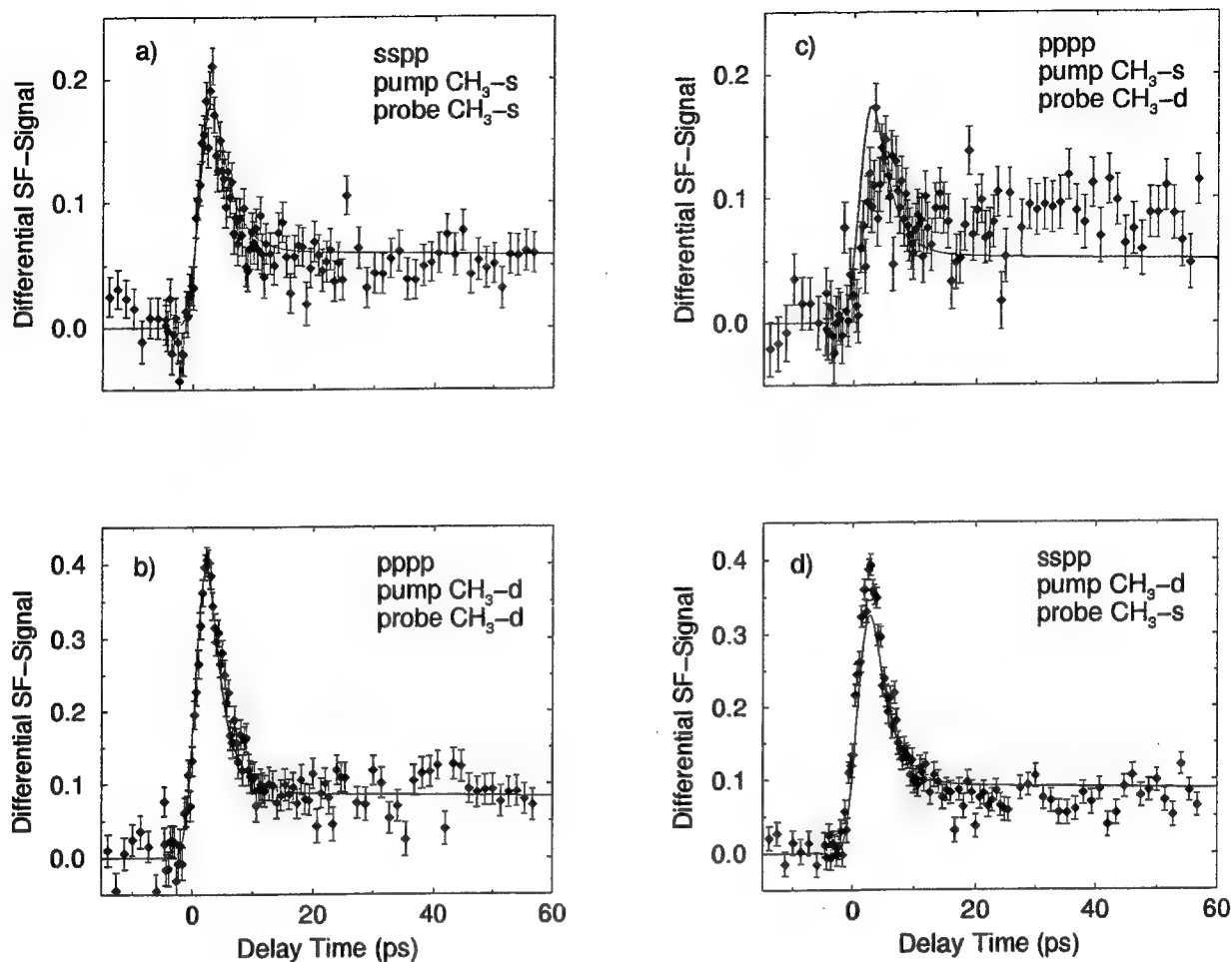


Figure 4. Temporal evolution of the differential signal of OTS on CaF₂ in TIR. (a) $\omega_{\text{IRpu}} = 2875 \text{ cm}^{-1}$, $\omega_{\text{IRpr}} = 2875 \text{ cm}^{-1}$; (b) $\omega_{\text{IRpu}} = 2960 \text{ cm}^{-1}$, $\omega_{\text{IRpr}} = 2960 \text{ cm}^{-1}$; (c) $\omega_{\text{IRpu}} = 2875 \text{ cm}^{-1}$, $\omega_{\text{IRpr}} = 2960 \text{ cm}^{-1}$; (d) $\omega_{\text{IRpu}} = 2960 \text{ cm}^{-1}$, $\omega_{\text{IRpr}} = 2875 \text{ cm}^{-1}$.

s-mode is determined to be $T_{1s} = 1.8 \pm 1.1 \text{ ps}$, and the life time of the d-mode is computed to $T_{1d} = 1.0 \pm 0.4 \text{ ps}$. The population of level $|3\rangle$ eventually decays within several hundred picoseconds, measurements over a larger time interval indicate $T_G > 150 \text{ ps}$ (data not shown).

The short relaxation times of the CH₃ stretching modes are consistent with energy relaxation via the CH₂ groups: The energy difference between the CH₃- and CH₂-stretching modes is small, suggesting an efficient relaxation channel for the CH₃-stretching modes in molecules with methylene groups. Moreover, due to the abundance of CH₂ groups in the chain of OTS, the statistical weight of the methylene modes is very high compared to the methyl modes: Besides three methyl stretching modes there are 34 methylene stretching modes in each OTS molecule.

For an ordered Langmuir-Blodgett film of cadmium stearate on a silver surface a lifetime of $T_{1s} = 2.5 \text{ ps}$ for the fast component and a ground state recovery time of $T_G = 165 \text{ ps}$ were reported for the symmetric methyl mode.¹⁵ These values agree fairly well with our data for OTS on CaF₂, the differences may be explained by the modified coupling to the substrate. For the system methyl thiolate on silver, Harris and coworkers have found relaxation times for the symmetric CH₃ stretching mode of $T_{1s} = 3 \text{ ps}$ and a temperature dependent T_G ranging from 49 ps at 110 K to 76 ps at 380 K.¹⁶ So the long relaxation component of our measurements tends to be longer than the times

determined by Harris for the two different systems, while our T_{1s} is somewhat shorter. The methyl group, coupled to a metal surface through a sulphur atom, obviously relaxes along different paths as compared to a methyl group separated from an insulator by a long alkyl chain containing 17 methylene groups.

Another possibility to explain the plateaus observed in the time resolved measurements (Fig. 4) should be mentioned: Due to the deposition of pump energy and the subsequent vibrational relaxation, a quasi-equilibrium among the vibrational modes of the adsorbate layer may be established at an elevated film temperature. The thermal population of excited states of low frequency modes with strong anharmonic coupling to the probed CH_3 stretching modes could, therefore, lead to the observed differential signal for large delay times. From our data it is impossible to distinguish unambiguously whether long-lived vibrational bottleneck states (e. g. CH_3 bending modes) are involved in the relaxation of the stretching modes, or if the temperature increase of the adsorbed monolayer accounts for the long lived signal amplitude in Fig. 4. In the latter case, T_G represents a cooling time of the adsorbate layer.

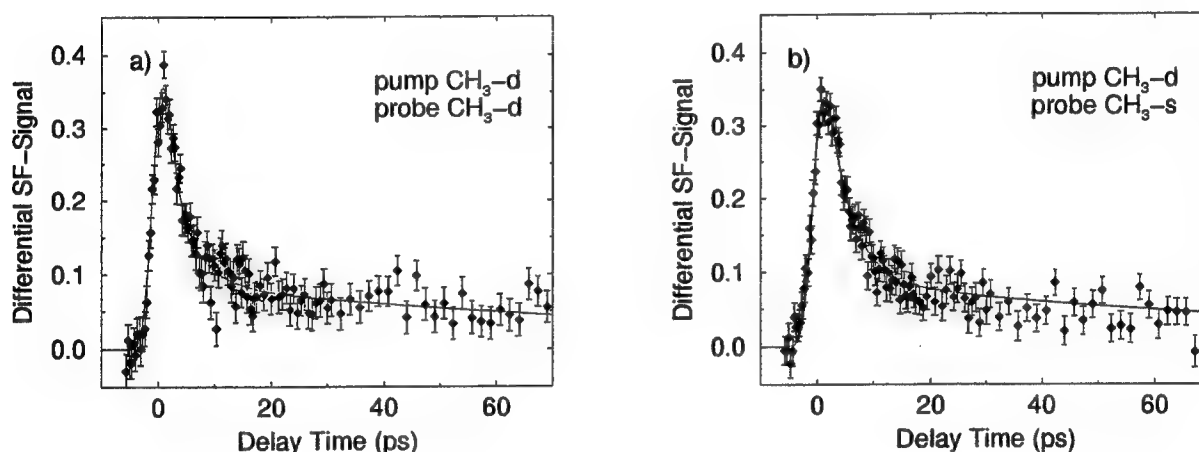


Figure 5. Temporal evolution of the differential SF signal of an ETS film (preliminary data). (a) $\omega_{\text{IRpu}} = 2960 \text{ cm}^{-1}$, $\omega_{\text{IRpr}} = 2960 \text{ cm}^{-1}$; (b) $\omega_{\text{IRpu}} = 2960 \text{ cm}^{-1}$, $\omega_{\text{IRpr}} = 2875 \text{ cm}^{-1}$.

Figure 5 shows the temporal evolution of the differential SF signal generated at an ETS film (preliminary data). In Fig. 5a the CH_3 d-mode is pumped and probed, in 5b the CH_3 d-mode is pumped and the s-mode is probed. The solid lines are once again obtained by simultaneously fitting the data to the four-level-model (Fig. 1). Although the figures look very similar to the OTS data in Fig. 4, the main difference is the absence of the long-lived plateau following the decrease after the maximum signal: The relaxation of the population in the intermediate level immediately sets in, leading to a ground state recovery time $T_G < 100 \text{ ps}$. The other relaxation times of ETS are found to be $T_E \approx 4 \text{ ps}$ for the energy exchange between the two CH_3 stretching modes, $T_{1s} \approx 3 \text{ ps}$ for the energy decay time of the CH_3 s-mode, and $T_{1d} \approx 1 \text{ ps}$ for the life time of the d-mode.

Thus in ETS T_{1d} is approximately the same as in OTS, while T_{1s} and T_E tend to be somewhat longer. This indicates a slightly different coupling of the modes involved due to the notably shorter alkyl chain. The shortened ground state recovery time suggests a stronger coupling of the methyl group to the substrate by the single methylene group in ETS compared to the 17 methylene groups in OTS.

4.3. Excitation Spectra

To demonstrate the new features obtainable by SF-IRAS, in fig.6 the differential SF signal for a fixed IR probe frequency and independently continuously tuned IR pump frequency is shown. The probe frequency ω_{IRpr} is fixed at 2875 cm^{-1} corresponding to the symmetric CH_3 -stretching vibration, and the IR pump pulse arrives at the sample 1 ps before the IR-vis probe pulse pair. Due to the close coupling of the CH stretching modes and the rapid energy

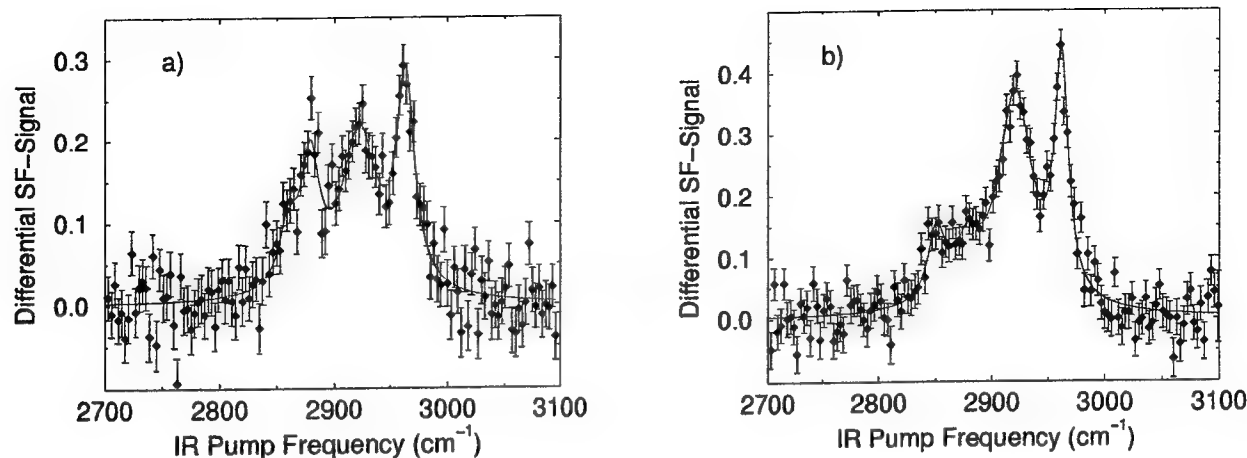


Figure 6. SF differential signal of the symmetric CH_3 -mode ($\omega_{\text{IRpr}} = 2875 \text{ cm}^{-1}$) of OTS on CaF_2 in TIR versus the IR pump frequency at a fixed delay time $t_D = 1 \text{ ps}$. Experimental points, fitted curves for (a) sspp- and (b) ssps-polarization combination.

transfer, the fractional population of the CH_3 -s stretching vibration is affected by the IR absorption of the pumped mode. Thus the SF-IRAS measurements resemble conventional IR absorption spectra of adsorbed monolayers.^{29,33}

In Fig. 6a and b the polarizations are set to sspp and ssps, respectively. The solid lines represent a fit to a Lorentzian lineshape. Four different lines can be resolved at 2849 cm^{-1} , 2875 cm^{-1} , 2917 cm^{-1} and 2960 cm^{-1} , although the line at 2849 cm^{-1} is just visible as a shoulder in Fig. 6a. As in the SF spectra (Fig. 3), we attribute the maxima at 2875 cm^{-1} and 2960 cm^{-1} to the CH_3 s- and d-mode, respectively. The line at 2849 cm^{-1} is assigned to the symmetric methylene mode, even though the frequency position is shifted about 11 cm^{-1} compared to the SF spectra. The line parameters are given in table 1.

The assignment of the maximum at 2917 cm^{-1} is more difficult since there is no corresponding line in the SF spectra at the same frequency. We attribute this line to the antisymmetric CH_2 -stretching mode which usually appears in the region of 2910 cm^{-1} in SF spectra. This interpretation is corroborated by the bigger frequency difference to the symmetric overtone of the CH_3 -bending mode located at 2933 cm^{-1} , and furthermore this mode should show only weak direct IR absorption. Additionally, the effect of pumping at 2917 cm^{-1} is more pronounced when the pump polarization is parallel to the surface (Fig. 6b). Since the alkyl chains of the adsorbate are nearly perpendicular,²⁸ the transition dipole of the antisymmetric CH_2 -stretching mode lies approximately parallel to the surface. This explains the higher differential signal when the pump pulse is s-polarized, while for the symmetric CH_3 -overtone the opposite behavior should be expected.

The same effect can be seen for the fundamental CH_3 -stretching modes: The s-mode at 2875 cm^{-1} with a dipole moment predominately perpendicular to the surface can be pumped more efficiently by a p-polarized pump pulse (Fig. 6a). In contrast, when the d-mode at 2960 cm^{-1} is pumped, the excitation is more effective for a s-polarized pump pulse (Fig. 6b), since the transition dipole moment of the d-mode lies almost parallel to the surface.

The slight frequency shift of the CH_2 stretching modes can be explained by the different environment of the methylene groups involved: In SF spectra, only the small fraction of CH_2 -groups at a *gauche*-defect in the alkyl chain can contribute to the SF signal. In the spectra shown in Fig. 6 — which are very similar to conventional IR absorption spectra^{29,33} — every methylene group in the chain can absorb energy from the pump pulse and contribute to the differential signal by energy transfer to the probed CH_3 s-stretching mode. Since the majority of methylene groups is highly oriented in an *all-trans* conformation, these groups dominate the antisymmetric CH_2 -peak in Fig. 6. Therefore, the maximum absorption is compatible with measurements in comparable bulk alkanes.³⁴ CH_2 -groups at a *gauche*-defect, which are probed by SF spectroscopy, are in a different environment and may therefore appear at a slightly different frequency. This interpretation and the frequency positions obtained from the SF-IRAS spectra

Table 1. Comparison of resonance frequencies and line widths for IR-vis SFS and SF-IRAS of OTS chemisorbed on CaF₂.

Mode ν	IR-vis SFS		SF-IRAS	
	$\omega_\nu(\text{cm}^{-1})$	$\Gamma_\nu(\text{cm}^{-1})$	$\omega_\nu(\text{cm}^{-1})$	$\Gamma_\nu(\text{cm}^{-1})$
CH ₂ -s	2860 \pm 4	20 \pm 6	2849 \pm 5	18 \pm 7
CH ₃ -s	2875 \pm 3	16 \pm 3	2875 \pm 4	20 \pm 5
CH ₂ -a	2910 \pm 4	25 \pm 6	2917 \pm 4	37 \pm 8
CH ₃ -OT	2933 \pm 4	21 \pm 4	—	
CH ₃ -d	2960 \pm 3	16 \pm 3	2960 \pm 4	19 \pm 4

in this work agree very well with spectroscopic investigations of OTS multilayers,³⁵ where also lines typical for CH₂-groups in *trans* conformation at 2849 cm⁻¹ and 2917 cm⁻¹ were found to dominate the spectra.

5. CONCLUSIONS

In this paper we report investigations on OTS and ETS monolayers chemisorbed on CaF₂-surfaces using 2-color pump-probe SF spectroscopy. An improved laser system combined with the signal enhancement in TIR geometry yields a significantly improved signal-to-noise ratio that allows to determine relaxation times more accurately than from preliminary data previously published.²² With two independently tunable IR pulses various combinations of tuning the probe or pump pulse and varying the temporal delay are possible.

A fast energy exchange between the CH₃-stretching modes is observed. Within our pulse duration of 2.7 ps all modes visible in the SF spectra in the CH-stretching region are bleached simultaneously. From the time-resolved data we obtain an energy redistribution time in the range of 3 ps, the life times of the CH₃ stretching modes are found to lie between 1 ps and 3 ps. Due to the larger infrared cross section of the CH₃ d-mode and the fast energy exchange, pumping the d-mode is more efficient than pumping the CH₃ s-mode, even when the excitation of the s-mode is monitored.

We also report novel investigations using sum-frequency infrared absorption spectroscopy (SF-IRAS). The symmetric CH₃ stretching mode is probed by SF spectroscopy, and the IR pump pulse is independently tuned. Due to the close coupling and the fast energy transfer from CH₂ and CH₃ stretching modes to the symmetric CH₃-stretching mode, the IR absorption of adsorbates can be studied. This technique combines the surface selectivity of SF spectroscopy with the advantages of conventional IR absorption spectroscopy, weakening the strict selection rules valid in SF spectroscopy. Thus surface selective spectra similar to conventional IR absorption measurements can be obtained. The comparison of SF-IRAS spectra with "conventional" SF spectra reveals significant differences: The line strengths of the CH stretching modes is altered, and the frequency position of the CH₂ modes are shifted. The frequencies of the CH₂ lines visible in the SF-IRAS spectra are found to be the same as in IR absorption spectra of OTS multilayers. This indicates that in SF-IRAS and in conventional absorption spectroscopy the methylene groups in *trans* conformation dominate the spectra, while in SF spectroscopy only the methylene groups at *gauche* defects contribute to the detected signal. The corresponding methylene modes have a slightly different resonance frequency.

Even modes invisible in SF spectra can be detected in the differential signal due to fast intramolecular energy transfer and anharmonic coupling of the pumped and probed modes. This offers the opportunity to detect molecular vibrations which are not Raman active or vanish in SF spectra due to symmetry reasons and, therefore, to extend this technique to new molecular systems.

ACKNOWLEDGMENTS

The authors are grateful to Martin Saß for acquisition of the ETS data.

REFERENCES

1. A. Fendt, S.F. Fischer, and W. Kaiser, "Vibrational lifetime and Fermi resonance in polyatomic molecules", *Chem. Phys.*, **57**, pp. 55-64, 1981.
2. H. Graener, T. Q. Ye, and A. Laubereau, "Transient-hole burning in the infrared spectrum of a polymer with intense picosecond pulses", *Phys. Rev.*, **B41**, pp. 2597-2600, 1990.
3. A. Laubereau, D. von der Linde, and W. Kaiser, "Direct Observation of the Lifetime of a Polariton Mode in Gallium Phosphide", *Opt. Comm.*, **7**, pp. 173-175, 1973.
4. J. D. Beckerle, M. P. Casassa, R. R. Cavanagh, E. J. Heilweil, and J. C. Stephenson, "Time resolved studies of vibrational relaxation dynamics of CO ($\nu=1$) on metal particle surfaces", *J. Chem. Phys.*, **90**, pp. 4619 - 4620, 1989.
5. M. Bonn, M. J. P. Brugmanns, A. W. Klein, and R. A. van Santen, "Enhancement of the vibrational relaxation rate of surface hydroxyls through hydrogen bonds with adsorbates", *Chem. Phys. Lett.*, **233**, pp. 309-314, 1995.
6. J. D. Beckerle, M. P. Casassa, R. R. Cavanagh, E. J. Heilweil, and J. C. Stephenson, "Ultrafast Infrared-Response of Adsorbates on Metal Surfaces: Vibrational Lifetime of CO/Pt(111)", *Phys. Rev. Lett.*, **64**, pp. 2090-2093, 1990.
7. X. D., Zhu, H. Suhr, and Y. R. Shen, "Surface vibrational spectroscopy by infrared-visible sum frequency generation", *Phys. Rev.*, **B35**, pp. 3047-3050, 1987.
8. P. Guyot-Sionnest, J. H. Hunt, and Y. R. Shen, "Sum-Frequency Vibrational Spectroscopy of a Langmuir Film: Study of molecular orientation of a Two- Dimensional System", *Phys. Rev. Lett.*, **59**, pp. 1597-1600, 1987.
9. M. Buck, "Organic Chemistry at Interfaces Studied by Optical Second-Harmonic and IR-Vis Sum-Frequency Generation", *Appl. Phys.*, **A55**, pp. 395-402, 1992.
10. D. Zhang, J. H. Gutow, K. B. Eisenthal, and T. F. Heinz, "Sudden structural change at an air/binary liquid interface: Sum frequency study of the air/acetonitrile-water interface", *J. Chem. Phys.*, **98**, pp. 5099-5101, 1993.
11. K. Wolfrum, H. Graener, and A. Laubereau, "Sum-frequency vibrational spectroscopy at the liquid-air interface of methanol:water solutions", *Chem. Phys. Lett.*, **213**, 41-46, 1993.
12. A. Tadjeddine, A. Peremanns, and P. Guyot-Sionnest, "Vibrational spectroscopy of the electrochemical interface by visible-infrared sum-frequency generation", *Surface Science*, **335**, pp. 210-220, 1995.
13. J. Löbau, A. Rumphorst, K. Galla, S. Seeger, and K. Wolfrum, "Adsorption of alkyl-trichlorosilanes on glass and silicon: a comparative study using sum-frequency spectroscopy and XPS", *Thin Solid Films*, **289**, pp. 272-281, 1996.
14. J. C. Conboy, M. C. Messmer, and G. L. Richmond, "Investigation of Surfactant Conformation and Order at the Liquid-Liquid Interface by Total Internal Reflection Sum-Frequency Vibrational Spectroscopy", *J. Phys. Chem.*, **100**, pp. 7617-7622, 1996.
15. A. L. Harris and N. J. Levinos, "Vibrational energy relaxation in a molecular monolayer at a metal surface", *J. Chem. Phys.*, **90**, pp. 3878-3879, 1989.
16. A. L. Harris, L. Rothberg, L. Dhar, N. J. Levinos, and L.H. Dubois, "Vibrational Energy relaxation of a polyatomic adsorbate on a metal surface: Methyl thiolate (CH_3S) on Ag(111)", *J. Chem. Phys.*, **94**, pp. 2438-2448, 1991.
17. P. Guyot-Sionnest, P. Dumas, Y. J. Chabal, and G. S. Higashi, "Lifetime of an Adsorbate-Substrate Vibration: H on Si(111)", *Phys. Rev. Lett.*, **64**, pp. 2156-2159, 1990.
18. P. Guyot-Sionnest, "Coherent Processes at Surfaces: Free Induction Decay and Photon Echo of the Si-H Stretching Vibration for H/Si(111)", *Phys. Rev. Lett.*, **66**, pp. 1489-1492, 1991.
19. K. Kuhnke, M. Morin, P. Jakob, N. J. Levinos, Y. J. Chabal, and A. L. Harris, "Vibrational energy transfer among adsorbate modes: Picosecond dynamics on stepped H/Si(111)", *J. Chem. Phys.*, **99**, pp. 6114-6125, 1993.
20. P. Guyot-Sionnest, P. H. Lin, and E. M. Hiller, "Vibrational dynamics of the Si-H stretching modes of the Si(100)/H:2x1 surface", *J. Chem. Phys.*, **102**, pp. 4269-4278, 1995.
21. R. P. Chin, X. Blase, Y. R. Shen, and S. G. Louie, "Anharmonicity and Lifetime of the C-H Stretch Mode on Diamond H/C(111)-(1x1)", *Europhys. Lett.*, **30**, pp. 399-406, 1995.

22. K. Wolfrum, J. Löbau, W. Birkhölzer, and A. Laubereau, "Vibrational sum-frequency spectroscopy of phase transitions in Langmuir-films and three-colour pump-probe studies of chemisorbed molecules", *Quantum Semi-class. Opt.*, **9**, pp. 257-267, 1997.
23. A. L. Harris and L. Rothberg, "Surface Vibrational Energy by sum frequency generation Five-wave mixing and coherent transients", *J. Chem. Phys.*, **94**, pp. 2449-2457, 1991.
24. J. Sagiv, "Organized Monolayers by Adsorption. 1. Formation and Structure of Oleophobic Mixed Monolayers on Solid Surfaces", *J. Am. Chem. Soc.*, **102**, pp. 92-98, 1980.
25. J. Löbau, K. Wolfrum, and A. Laubereau, "Relaxation and energy transfer of CH-stretching vibrations of octadecyl-trichlorosilane on surfaces, studied with 2-color pump-probe sum-frequency spectroscopy", submitted to *J. Chem. Phys.*
26. F. Lindemberger, R. Stöckl, R. Laenen, and A. Laubereau, "Kerr lens mode-locking of a pulsed Nd:YLF laser", *Opt. Comm.*, **117**, pp. 268-272, 1995.
27. K. Wolfrum, R. Laenen, and A. Laubereau, "Intense bandwidth- and diffraction-limited picosecond pulses with large tuning range", *Opt. Comm.*, **97**, pp. 41-46, 1993.
28. J. Löbau and K. Wolfrum, "Sum-Frequency Spectroscopy in Total Internal Reflection Geometry: Signal Enhancement and Access to Molecular Properties", *J. Opt. Soc. Am.*, **B14**, pp. 2505-2512, 1997.
29. F. J. Boerio and S. L. Chen, "Infrared Spectra of Adsorbed Films on Metal Mirrors", *J. Coll. Int. Sci.*, **73**, pp. 176-185, 1979.
30. N. Akamatsu, K. Domen, and C. Hirose, "SFG Study of Two-Dimensional Orientation of Surface Methyl Groups on Cadmium Arachidate Langmuir-Blodgett Films", *J. Phys. Chem.*, **97**, pp. 10070-10075, 1993.
31. C. Hirose, H. Yamamoto, N. Akamatsu, and K. Domen, "Orientation Analysis by Simulation of Vibrational Sum Frequency Generation Spectrum: CH-Stretching Bands of the Methyl Group", *J. Phys. Chem.*, **97**, pp. 10064-10069, 1993.
32. J. L. Duncan and M. M. Law, "A Study of Vibrational Anharmonicity, Fermi Resonance Interactions, and Local Mode Behavior in CH_3Cl ", *J. Mol. Spectrosc.*, **140**, pp. 13-30, 1990.
33. N. Watanabe, H. Yamamoto, A. Wada, K. Domen, C. Hirose, T. Ohtake, and N. Mino, "Vibrational sum-frequency generation (VSFG) spectra of n-alkyltrichlorosilanes chemisorbed on quartz plate", *Spectrochimica Acta*, **50A**, pp. 1529-1537, 1994.
34. R. G. Snyder and J. H. Schachtschneider, "Vibrational analysis of the n-paraffins - I Assignments of infrared bands in the spectra of C_3H_8 through $\text{n-C}_{19}\text{H}_{40}$ ", *Spectrochimica Acta*, **19**, pp. 85-116, 1963.
35. A. N. Parikh, M. A. Schivley, E. Koo, K. Seshadri, D. Aurentz, K. Mueller and D. L. Allara, "n-Alkylsiloxanes: From Single Monolayers to Layered Crystals. The Formation of Crystalline Polymers from the Hydrolysis of n-Octadecyltrichlorosilane", *J. Am. Chem. Soc.*, **119**, pp. 3135-3143, 1997.

Precision laser ablation of wide band-gap materials using VUV-UV multiwavelength Excitation

Koji Sugioka, Jie Zhang, Satoshi Wada, Hideo Tashiro, and Katsumi Midorikawa

The Institute of Physical and Chemical Research (RIKEN),
Wako, Saitama 351-0198, Japan

ABSTRACT

Novel ablation of wide band-gap materials such as fused quartz and GaN by multiwavelength excitation using a VUV-UV laser system is reviewed. Simultaneous irradiation of VUV and UV laser beams emitted from a VUV Raman laser presents great potential for precision microfabrication of the materials. The mechanism and the role of VUV beams in this process are made clear on the basis of band structure. The advantages of this technique are discussed in comparison with the conventional single wavelength ablation. Furthermore, another novel ablation of glass materials using a conventional UV laser, referred to as "laser-induced plasma assisted ablation (LIPAA)", is introduced. By LIPAA, a high quality micrograting structure is fabricated on fused quartz.

Keywords: VUV laser, precision ablation, wide band-gap material, fused quartz, multiwavelength excitation, laser-induced plasma assisted ablation

1. INTRODUCTION

Development of precision microfabrication technique of wide band-gap materials such as fused quartz, crystal quartz, sapphire, SiC, and GaN is strongly demanded in various industrial fields. For instance, fused quartz is one of the most important materials in optics and optoelectronics. Phase shift masks, optical waveguide devices, and integrated optoelectronic devices require sophisticated microfabrication technologies for the fused quartz¹. Reactive ion etching (RIE) provides a high resolution and low damage etching process of such materials; however, etch rate is low and a resist process based on photolithography is required for micropatterning.² Another scheme for the microfabrication is laser ablation, which has advantages of high etch rate and direct patterning without the resist process.⁴ Ablation of the fused quartz has been carried out by UV excimer lasers³ or a femtosecond excimer laser⁴. In these processes, microroughness, damage and cracks have been generated. Alternative way of laser ablation is use of vacuum ultraviolet (VUV) lasers possessing high photon energy and large absorption coefficient to the wide band-gap materials. Herman et al. have shown that an F₂ laser of a 157 nm wavelength is effective for the high quality ablation.⁵ But, a high photon cost, a short gas life time, and a low beam quality are generally pointed out as problems of the F₂ laser processing.

Recently, we have developed novel ablation technique of the wide band-gap materials such as fused quartz, sapphire, lithium niobate, SiC, and GaN by multiwavelength excitation using a VUV-UV laser system.⁶⁻¹⁴ In the present paper, precision microfabrication of fused quartz by simultaneous irradiation of VUV and UV laser beams is reviewed. The mechanism and the role of VUV beams in this process are made clear on the basis of a band structure. The advantages of this technique are discussed in comparison with the conventional single wavelength ablation. Furthermore, another novel ablation of glass materials using a conventional UV laser, referred to as "laser-induced plasma assisted ablation (LIPAA)", is introduced.

Further author information -

K.S.(correspondence): E-mail: ksugioka@postman.riken.go.jp, Telephone: +81-48-467-9495, Fax: +81-48-462-4682

2. CONCEPT OF MULTIWAVELENGTH EXCITATION PROCESS

Figure 1 shows a schematic illustration of the concept of multiwavelength excitation process. In this process, VUV and UV laser beams are directed to a substrate at the same time. The energy density of VUV laser is as small as several tens mJ/cm^2 , which is 1 - 2 orders lower in magnitude than that of single wavelength laser ablation using an F_2 laser. The energy density of simultaneously irradiated UV laser

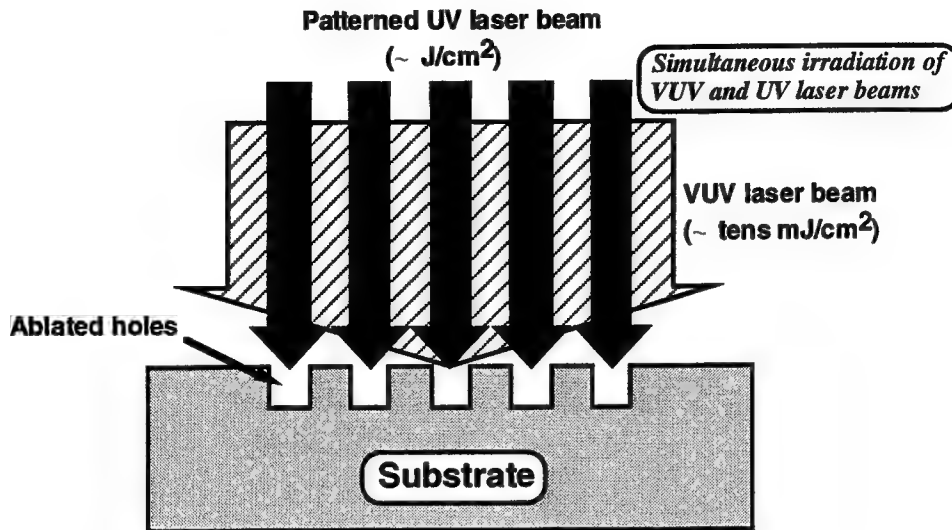


Fig. 1. Schematic illustration of concept of multiwavelength excitation process.

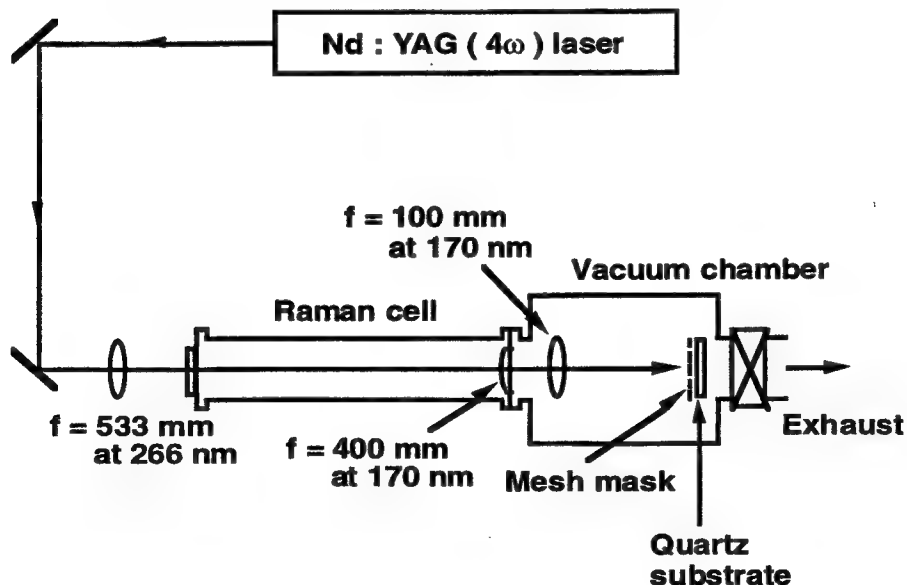


Fig. 2. Schematic illustration of experimental setup for multiwavelength ablation of wide band gap materials using the VUV Raman laser.

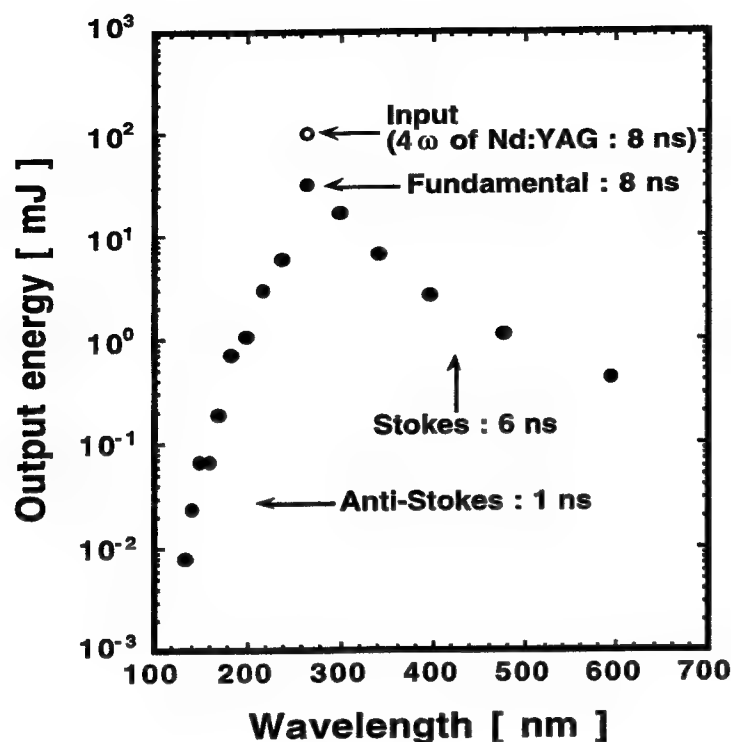


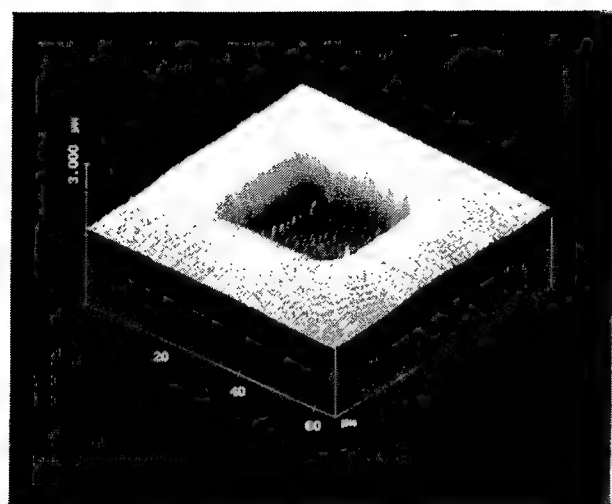
Fig. 3. Energy distribution of each wavelength emitted from the VUV Raman laser. The input energy of fourth harmonic of Nd:YAG laser is converted to 100 mJ.

has the order of 10^0 J/cm² which is comparable to that of single wavelength ablation. For micropatterning of solid surfaces by this process, the unpatterned VUV beams may be irradiated to a broad area and only the UV laser irradiation area should be localized, as shown in Fig. 2. The contrary scheme, i.e., patterned irradiation of the VUV beam with unpatterned irradiation of the UV beam, is also possible.

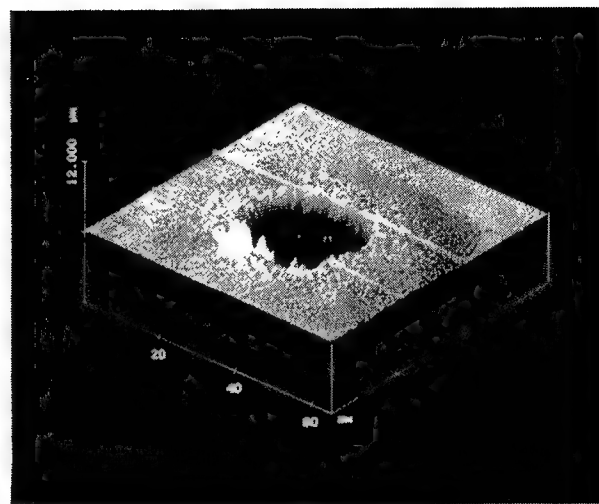
3. EXPERIMENT

The VUV Raman laser, using high-order anti-Stokes Raman scattering of a fourth harmonic of a Q-switched Nd:YAG laser (a 266 nm wavelength and an 8 ns pulse width) in a Raman cell filled with hydrogen gas at 4 atm., was used for ablation. Figure 2 shows a schematic illustration of experimental setup for multiwavelength ablation of the wide band-gap materials using the VUV Raman laser. Figure 3 shows output characteristics of the VUV Raman laser when a 100 mJ pulse of the fourth harmonic of Nd:YAG Laser is incident to the Raman cell. The VUV Raman laser simultaneously radiates fifteen discrete wavelengths from the 133 nm 9th-order anti-Stokes beam to the 594 nm 5th-order Stokes beam including the pump beam of a 266 nm wavelength whose energy is the largest and accounts for about 45 % of total energy of the output beams. The pulse energy of anti-Stokes lines exponentially decreases with increase of the order and drops to less than 1 mJ in the VUV region. The VUV beams has a tophat-like shape, although the 266 nm wavelength beam has a Gaussian-like shape.¹⁵ For the VUV Raman laser, the laser fluence was calculated by totaling pulse energy of each wavelength component.

In the experiment, all wavelength components emitted from the VUV Raman laser were directed to the fused quartz substrates placed in a vacuum chamber with pressure less than 8×10^{-5} Torr using a MgF₂ lens at the same time. In this case, a Ni mesh with $25 \times 25 \mu\text{m}^2$ apertures was put on the sample surface as a contact mask for the micropatterning. The irradiated area at the sample surface and the repetition rate of the laser pulses were set at about 1 mm in diameter and 1 Hz, respectively.



(a)



(b)

Fig. 4. AFM images of the samples ablated at 4.0 J/cm^2 and 60 pulses by (a) a VUV Raman laser and (b) a fourth harmonic of Nd:YAG laser (266 nm).

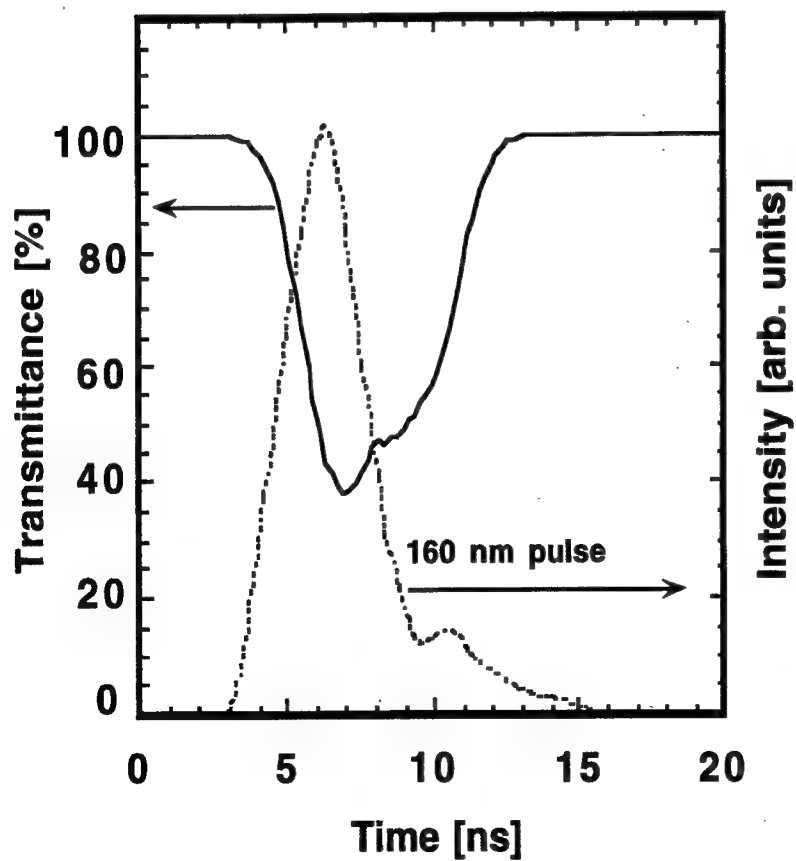


Fig. 5. Temporal variation of the transmittance of 266 nm beam during simultaneous irradiation of the VUV beams. For reference, a pulse form of the simultaneously irradiated 160 nm beam is also shown by the dashed line.

4. MICROPATTERNING OF FUSED QUARTZ

Figure 4 shows atomic force microscope (AFM) images of fused quartz ablated by (a) simultaneous irradiation of multiwavelength components emitted from the VUV Raman laser and (b) the only 266 nm wavelength beam. The laser fluence and number of laser pulses were 4.0 J/cm^2 (total of each wavelength component for the case of multiwavelength irradiation) and 60 pulses, respectively. For the sample ablated by the multiwavelength irradiation, a well-defined pattern corresponding to the contact mask pattern used was created. Neither cracks nor distortion took place at the edge region, and little debris was deposited on the circumference. A regular ripple pattern was observed on the ablated surface. This pattern was formed by diffraction of the laser beam at the edge of the contact mask. Therefore, the ablated surface structure reflected spatial energy distribution of the laser beam, indicating little thermal influence during the process. On the other hand, for the sample ablated by the only 266 nm beam, the ablated pattern was distorted, and the ablated surface showed irregular roughness. In addition, much debris was deposited on the circumference. In this process, the short wavelength components in the VUV region may play an important role in high-quality ablation, although each individual component has too small intensity to ablate fused quartz by itself.

5. MECHANISM OF MULTIWAVELENGTH EXCITATION PROCESS

In order to investigate the role of VUV beams, pulse forms of the 266 nm beam transmitted by fused quartz with and without simultaneous irradiation of the VUV beams were compared. In this case, the intensity of 266 nm beam was sufficiently enfeebled to avoid ablation. Ratio of the beam intensities of the both pulse forms at each time gives temporal variation of transmittance of the 266 nm beam. Figure 5 shows the transmittance variation as a function of time by the solid line. For reference, the pulse form of the simultaneously irradiated 160 nm beam is also shown by the dashed line. Although the transmittance is originally 100 %, it decreases as soon as fused quartz is irradiated by the VUV beams, and reaches a minimum value less than 40 %. Immediately after the VUV pulses, it recovers to almost 100 %. Therefore, the maximum absorption change caused by the VUV irradiation is estimated to be more than 60 %.

This phenomenon may be explained as the excited-state absorption (ESA) induced by coupling of the VUV and UV beams. In order to discuss ESA in the current case, the band structure of fused quartz¹⁶ is illustrated in Fig. 6. The energy gap and the electron affinity are about 9 and 0.9 eV, respectively.

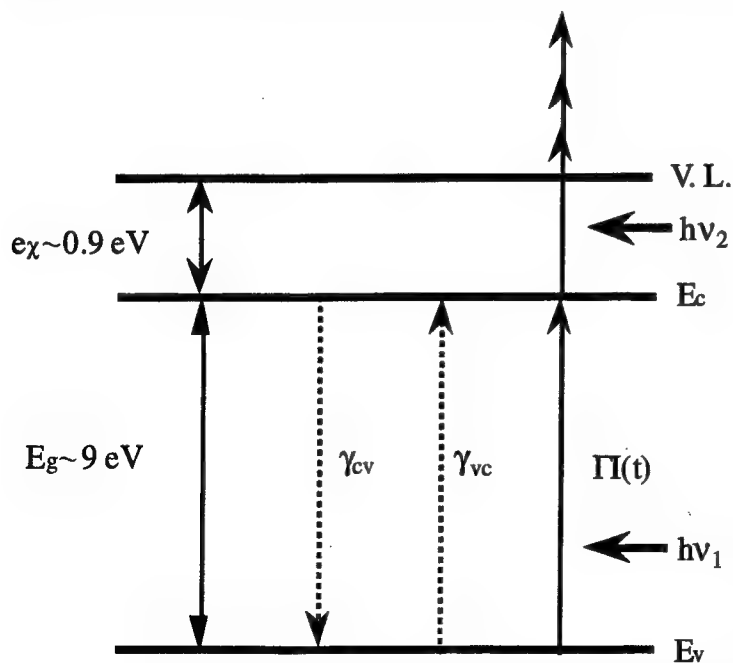


Fig. 6. Band structure of fused quartz. [V.L. : vacuum level, E_c : bottom of conduction band, E_v : top of valence band, E_g : band gap, e_χ : electron affinity].

When the incident light beams have photon energy more than 9 eV, corresponding to a wavelength of ~ 138 nm, electrons are excited from the valence band to the conduction band. The excited electrons are easily raised beyond the vacuum level by photons of more than 0.9 eV, which correspond to ~ 1.38 μm . Accordingly, the excited state may strongly absorb the 266 nm beam and then electron emission occurs. This cascade excitation process induces photoionization of constituent atoms and finally leads ablation. Assuming band-to-band excitation, formation of the excited state is possible only by a 133 nm beam in the VUV Raman laser beams. However, the absorption edge of fused quartz used is around 170 nm, which is ascribed to impurities and defects.¹⁷ The longer VUV beams may contribute excitation through such defect levels, although it is, so far, unknown which wavelength components play effective roles in the process. Thus, the band structure suggests that the ESA effect by the multiwavelength irradiation is responsible for high-quality ablation.

This novel ablation technique was applied to precise microfabrication of the other wide band-gap materials such as crystal quartz, sapphire, lithium niobate, SiC, and GaN.^{11, 12, 14} For every material, well-defined micropatterns with no cracks, no distortion, and little debris deposition were fabricated similarly to the case of fused quartz. Microanalysis using photoluminescence and Raman spectroscopy indicated that ablated surfaces of SiC and GaN had little deterioration of crystallinity.

6. ADVANTAGES OF MULTIWAVELENGTH EXCITATION PROCESS

The multiwavelength excitation process presented here has many advantages compared with the conventional single wavelength laser ablation. Comparison of features between the multiwavelength excitation and single wavelength processes is summarized in Table I. The role of the VUV beams in the multiwavelength excitation process is to form the excited-state, and then ablation takes place by deposition of energy of the UV beam in the excited regions. In this case, even extremely lower laser fluence of the VUV beams than that of single wavelength F_2 laser ablation can achieve high quality ablation by coupling it to large pulse energy of the UV laser beam, resulting in reduction of a photon cost and extension of a processing area. In the meanwhile, the excited-state region formed by the VUV beam irradiation extends over a whole substrate along the depth (substrate thickness : $0.6 \mu\text{m}$)¹³, while the effective absorption coefficient of the 266 nm beam to the excited region was estimated to be $3.4 \times 10^5 \text{ cm}^{-1}$.⁶ Accordingly, the most of energy of the 266 nm beam is absorbed in the shallow surface layer of

Table I. Comparison of features between the multiwavelength excitation and single wavelength processes

Process	Merits	Demerits
Single wavelength process	Simple setup	Large VUV pulse energy High photon cost VUV projection system
Multiwavelength excitation process	Small VUV pulse energy Low photon cost Large area processing UV projection system	Complicate setup

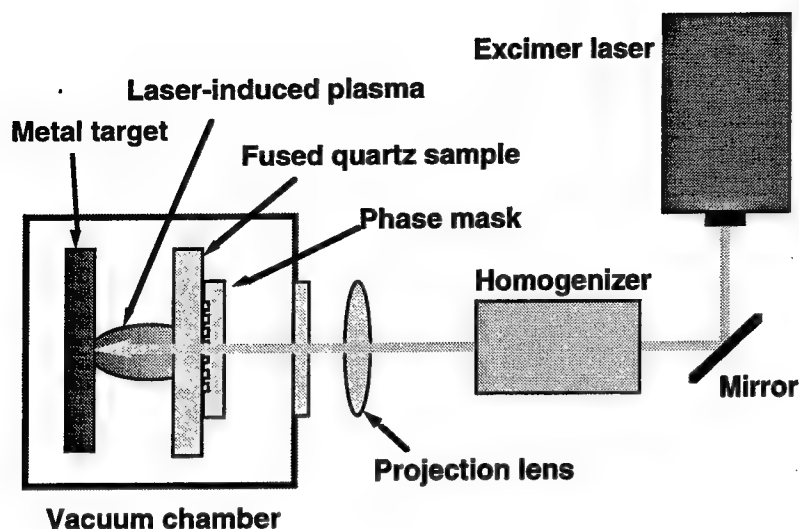


Fig. 7. Schematic illustration of the experimental apparatus for LIPAA. A phase mask with a $1.065\text{ }\mu\text{m}$ period designed for the KrF excimer laser beam is kept in contact with the front surface of substrate for direct microfabrication.

the excited region, so that the ablated structure may be determined by a beam pattern of 266 nm laser. Therefore, for direct microfabrication of the materials, the unpatterned VUV beams may be irradiated to a broad area and only the UV laser beam should be localized. For the localized irradiation of UV laser beam, a conventional mask projection system can be utilized. Comparatively, the VUV beam must be localized in the single-wavelength laser processing. The mask projection of UV beam is the well-developed technique and commercially available, while that of VUV beams has some difficulties mainly due to problems of optics at the present time.

7. LASER-INDUCED PLASMA ASSISTED ABLATION

The multiwavelength excitation process using the UV laser combined with the VUV laser has many advantages compared with the conventional single wavelength laser process as mentioned above. However, if the conventional UV laser can be utilized for microfabrication of fused quartz and the related glass materials, greater advantage is obvious for practical application. Recently, we have developed another microfabrication technique of the glass materials by laser-induced plasma assisted ablation (LIPAA)^{18, 19}. The most important feature of this technique is that the single conventional UV laser can lead to an effective ablation of the transparent materials by coupling to plasma generated from a metal target by the same laser.

Figure 7 shows a schematic illustration of the experimental apparatus for LIPAA. The KrF excimer laser of 248 nm wavelength and 34 ns pulse width is homogenized by using a couple of 5×5 microlens arrays (fly's eye type homogenizer). The homogenized beam is projected to the fused quartz substrate placed in the vacuum chamber using a single fused quartz lens. Since the fused quartz has no absorption in a UV range, the laser beam goes through the substrate and then is absorbed at a metal target surface (stainless steel 304) placed behind the substrate with a distance of $200\text{ }\mu\text{m}$. The repetition rate of laser irradiation is kept constant at 1 Hz . By interaction of plasma generated from the target and the laser beam, significant ablation takes place at the rear surface of substrate. In this experiment, a phase mask with a $1.065\text{ }\mu\text{m}$ period designed for the KrF excimer laser beam is kept in contact with the front surface of substrate for direct microfabrication. One of advantages of this technique is that the mask is not affected by debris deposition since ablation takes place at the reverse side of substrate. Additionally, it is noted that the mask has no damage by the laser irradiation, although a material of the mask is the same as the substrate. Because the laser beam may be only absorbed at the shallow surface of the fused quartz where the laser-induced plasma attacks.

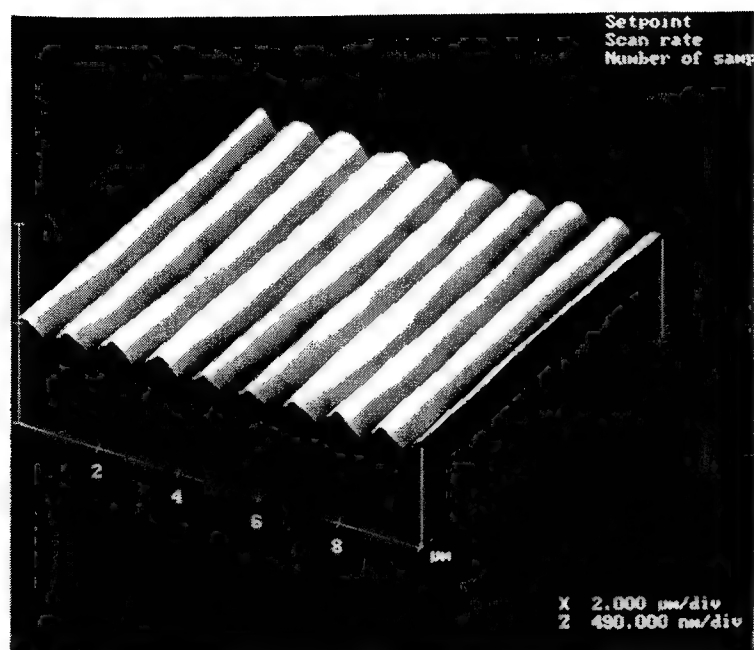


Fig. 8 AFM image of grating fabricated on the fused quartz substrate by LIPAA at the laser fluence of 1.3 J/cm^2 and 40 pulses. ($x : 2 \mu\text{m/div}$, $z : 490 \text{ nm/div}$)

Figure 8 shows an AFM image of grating fabricated on the fused quartz substrate at the laser fluence of 1.3 J/cm^2 and 40 pulses. Well-defined and clean micrograting structure was formed without any severe damage. A period of the grating is about $1.06 \mu\text{m}$, which well agrees with that of the mask used. The grating depth is estimated to be about 100 nm . Thus, the present technique is very attractive for precision microfabrication of fused quartz.

Although the mechanism of this technique is complicate and still unknown, we consider that ablation proceeds by combination of three processes, that is, influence of species in the plasma to the sample surface, plasma heating, and metal film deposition. We suppose the following two possibilities as the plasma direct interaction, i.e., (I) charge exchange between ions or electrons in the plasma and the sample surface, and (ii) transfer of kinetic or potential energy of the ions and radicals in the plasma to the sample surface. The plasma heating by an inverse bremsstrahlung (IB) absorption may be also possible, since it causes large change in optical properties of the substrate such as absorption coefficient. Another possibility is absorption of the laser beam to the metal thin film deposited on the substrate surface by laser ablation of the metal target. Further investigations on mechanism study suggested that the most dominant mechanism was the plasma interaction, and the detailed mechanism is discussed elsewhere¹⁸.

A visible laser can be also used for LIPAA instead of the UV laser. A second harmonic of Q-switched Nd:YAG laser (532 nm , 6 ns) fabricated micrograting on the fused quartz. In addition, it achieved high-speed hole drilling of fused quartz (0.5 mm thick) and Pyrex glass (1.5 mm thick).

8. CONCLUSIONS

High-quality ablation of fused quartz has been demonstrated by multiwavelength excitation using the VUV-UV laser system based on the VUV Raman laser. Simultaneous irradiation of the VUV and UV beams presents direct microfabrication of fused quartz with well-defined patterns, little debris deposition, and little thermal damage. The mechanism is attributed to the excited-state absorption, that is, ablation takes place by strong absorption of the 266 nm beam to the excited-state formed by the VUV beam irradiation. The novel ablation technique presented in this paper gives some advantages to precise microfabrication of not only fused quartz but also the other wide band-gap materials such as crystal quartz, sapphire, lithium niobate, SiC and GaN. The most featured point is that even low pulse energy of the VUV laser beams can achieve high quality ablation by coupling it to large pulse energy of the UV

laser beam, resulting in reduction of a photon cost, extension of a processing area, and applicability of a UV mask projection system. One of applications of this technique is selected area removal of SiO₂ films deposited on Al films for Si IC repair. As the other applications, fabrication of phase mask, microlens, optical waveguide, fiber grating and micromachine is expected. In the meanwhile, another novel ablation technique of glass materials, referred to as LIPAA in which the single conventional UV laser led to an effective ablation of the transparent materials by coupling to plasma generated from a metal target by the same laser, was demonstrated. LIPAA realized fabrication of micrograting and high-speed hole drilling for the glass materials. Thus, we conclude that ablation techniques using the multiwavelength excitation by the coupling of VUV and UV beams or laser-induced plasma have great potential for precision microfabrication of wide the band-gap materials.

9. REFERENCES

1. K. O. Hill, B. Malo, F. Bilodeau, D. C. Johnson, and J. Albert, "Bragg gratings fabricated in monomode photosensitive optical fiber by UV exposure through a phase mask", *Appl. Phys. Lett.* **62**, pp. 1035 - 1037 (1993).
2. I. Bennion, D. C. J. Reid, C. J. Rowe, and W. J. Stewart, "High-reflectivity monomode-fiber grating filters", *Electron. Lett.* **22**, pp. 341 - 343 (1986).
3. B. Braren and R. Srinivasan, "Controlled etching of silicate glasses by pulsed ultraviolet laser radiation", *J. Vac. Sci. Technol.* **B6**, pp. 537 - 541 (1988).
4. J. Ihlemann, B. Wolff, and P. Simon, "Nanosecond and femtosecond excimer laser ablation of fused silica", *Appl. Phys.* **A54**, pp. 363 - 368 (1992).
5. P. R. Herman, K. Beckley, B. Jackson, K. Kurosawa, D. Moore, T. Yamanishi, and J. Yang, "Processing applications with the 157-nm fluorine excimer laser", *SPIE Proc.* **Vol. 2992**, pp. 86 - 94 (1997).
6. K. Sugioka, S. Wada, A. Tsunemi, T. Sakai, H. Takai, H. Moriwaki, A. Nakamura, H. Tashiro, and K. Toyoda, "Micropatterning of quartz substrates by multi-wavelength vacuum-ultraviolet laser ablation", *Jpn. J. Appl. Phys.* **32**, pp. 6185 - 6189 (1993).
7. K. Sugioka, S. Wada, H. Tashiro, K. Toyoda, and A. Nakamura, "Novel ablation of fused quartz by preirradiation of vacuum-ultraviolet laser beams followed by fourth harmonic irradiation of Nd:YAG laser", *Appl. Phys. Lett.* **65**, pp. 1510 - 1512 (1994).
8. K. Sugioka, S. Wada, H. Tashiro, K. Toyoda, Y. Ohnuma, and A. Nakamura, "Multi-wavelength excitation by coupling of fourth harmonics of a Q-switched Nd:YAG laser with vacuum-ultraviolet beams for high-quality ablation of fused quartz", *Appl. Phys. Lett.* **67**, pp. 2789 - 2791 (1995).
9. K. Sugioka, S. Wada, Y. Ohnuma, A. Nakamura, H. Tashiro, and K. Toyoda, "Multiwavelength irradiation effect in fused quartz ablation using vacuum-ultraviolet Raman laser", *Appl. Surf. Sci.* **96-98**, pp. 347 - 351 (1996).
10. J. Zhang, K. Sugioka, S. Wada, H. Tashiro, and K. Toyoda, "Ablation of fused quartz by ultraviolet, visible or infrared laser coupled with VUV laser", *Jpn. J. Appl. Phys.* **35**, L1422 - L1425 (1996).
11. K. Sugioka, S. Wada, H. Tashiro, and K. Toyoda, "Ablation of wide band-gap materials by multi-wavelength irradiation using a VUV Raman laser", *Appl. Surf. Sci.* **109/110**, pp. 179 - 183 (1997).
12. J. Zhang, K. Sugioka, S. Wada, H. Tashiro, and K. Toyoda, "Direct photoetching of single crystal SiC by VUV-266 nm multiwavelength laser ablation", *Appl. Phys.* **A64**, pp. 367 - 371 (1997).
13. J. Zhang, K. Sugioka, S. Wada, H. Tashiro, and K. Toyoda, "Dual-beam ablation of fused quartz using 266 nm and VUV laser with different delay-times", *Appl. Phys.* **A64**, pp. 477 - 481 (1997).
14. J. Zhang, K. Sugioka, S. Wada, H. Tashiro, and K. Toyoda, "Precise microfabrication of wide band-gap semiconductors (SiC and GaN) by VUV-UV multiwavelength laser ablation", *Appl. Surf. Sci.* (in press).
15. H. Moriwaki, S. Wada, H. Tashiro, K. Toyoda, A. Nakamura, A. Kasai, and A. Nakamura, "Wavelength conversion of quadrupled Nd:YAG laser radiation to the vacuum ultraviolet by anti-Stokes stimulated Raman scattering", *J. Appl. Phys.* **74**, pp. 2175 - 2179 (1993).

16. B. E. Deal, E. H. Snow, and C. A. Mead, "Barrier energies in metal-silicon dioxide-silicon structure", J. Phys. Chem. Solids, **27**, pp. 1873 - 1879 (1966).
17. R. Brückner, "Properties and structure of vitreous silica. I", J. Non-Cryst. Solids **5**, pp. 123 - 175 (1970).
18. J. Zhang, K. Sugioka, and K. Midorikawa, "Direct fabrication of micrograting in fused quartz by laser-induced plasma assisted ablation using a KrF excimer laser", to be published.
19. J. Zhang, K. Sugioka, and K. Midorikawa, "Laser-induced plasma assisted ablation of fused quartz using fourth harmonic of Nd⁺:YAG laser", to be published.

SESSION 2

Lasers for Fusion

Overview of the solid state laser projects for ICF applications at CAEP

H.S.Peng, X.M.Zhang, X.F.Wei,
W.G.Zheng, F.Jing, Z.Sui and X.D.Yuan

China Academy of Engineering Physics
P.O.Box 501, Chengdu, China, 610003

ABSTRACT

The ICF Programs in China have made significant progress in solid state laser technology development and advanced laser facility designing with multilabs' efforts in the past years. The eight-beam SG-II laser facility is expected to complete for a 4.8-kJ output at $1.05\mu\text{m}$ and to operate for target experiments in a few months. A national project, SG-III laser facility, has been proposed to produce 60-kJ blue light for target physics experiments and is being conceptually designed. New laser technologies, including multipass amplification, large aperture plasma electrode switches, fast growth of KDP, laser glass with fewer platinum grains, long flash lamps and precision manufacturing of large optical components are being developed to meet the requirements of the SG-III Project. In addition, numerical simulations are being conducted for the optical design of the new facility. The Technical Integration Line (TIL) of 4×2 segmented array as a prototype module of SG-III with a chamber for laser beams measurements will be first built in the next few years.

Key words: Solid state laser, SG-III

1.INTRODUCTION

The inertial confinement fusion program was formally initiated by Prof. Ganchang Wang at China Academy of Engineering Physics in 1976(1). Since then, high power solid state laser technologies have been developed step by step according to the requirements of target physics in China. XG-1 laser facility was first built in 1984 and then upgraded to XG-II in 1993. SG-I laser facility was built in 1985 and the upgrade version, SG-II, is expected to complete in a few months. We have launched a more ambitious project to build a bigger solid state laser facility, SG-III, which is planned to deliver 60kJ at $0.35\mu\text{m}$ to targets(2). To meet the requirements on

technical performance and cost effectiveness, numerous projects to develop advanced laser technologies as used for the NIF in Lawrence Livermore National Laboratory (3) have been funded by the National ICF Committee for a number of years. To reduce technical risk for the SG-III construction, we have been working to first build the Technical Integration Line(TIL) for scientific and technical demonstration.

2. XG-II AND SG-II LASER FACILITIES

The XG-II laser facility is a single beam Nd-doped phosphate glass laser facility which was upgraded from XG-I in 1993 with an increased energy output. There are two oscillators in the front end to provide required pulse duration. The last two stages are 100-mm and 150-mm disk amplifiers. The technical specifications are listed in Table 1.

Table 1. XG-II Specifications

Laser pulse energy	260J / 1.054 μ m, 130J / 0.35 μ m
Beam number	1
Pulse duration	0.2-0.8, 1-5ns
Contrast ratio	$>10^7$
Beam divergence	0.2mrad

The XG-II facility is located in CAEP and mainly used for basic research on laser-plasma physics, x-ray laser experiments and diagnostic development.

The SG-II facility is now at the last moment of upgrading and expected to shoot for physical experiments soon. The facility is consisted of eight beams, each delivering 600J at 1.054 μ m or 240J at 0.35 μ m to targets. The eight beams are grouped into two double-pass amplifiers, each configured in a 2 x 2 segment array (4). The aperture of the beams in the amplifiers is 200mm and enlarged to 240mm by the spatial filters. The input laser pulse is injected into the amplifier laterally through the spatial filter at the focal plane by a 45⁰ mirror with a small central hole for beams separation.

The SG-II facility, located in the Joint Laboratory of High Power Laser and Physics, Shanghai, will be operated for experiments on laser-plasma interaction, hohlraum targets and direct-drive targets as well. Besides, x-ray laser and equation of state experiments will be conducted by using an additional target chamber, designed with a special configuration for beams arrangements.

Table 2. SG-II Specifications

Laser pulse energy	4.8kJ/1.054 μ m, 2.4kJ/0.35 μ m
Beam number	8
Pulse duration	20,100ps, 1-3ns
Beam energy balance	10% rms
Beam divergence	0.1mrad
Target chamber	2
Contrast ratio	$>10^7$

3. SG-III PROJECT

SG-III laser facility has been proposed to build, as the next step of high power solid state laser development in China. We have been working on the conceptual design of the facility for a couple of years. The requirements of target physics on the facility specifications are still being studied and Table 3 gives the primarily suggested criteria for the SG-III facility.

Table 3. Suggested Criteria for SG-III Facility

Laser pulse energy	60 kJ / 0.35 μ m
Pulse peak power	60 TW
Beam number	64
Pulse duration	1-5ns shaped (dynamic range > 10)
Beam power balance	$\leq 10\%$ rms
Beam pointing accuracy	$\leq 30\mu$ m rms
Shot rate	4 hours

The SG-III facility consists of a 64-beam Nd-doped phosphate glass laser, switchyard, target area and diagnostics housed in the main building with two laser bays. Technical support systems for construction, operation and maintenance of the facility are installed in an auxiliary building.

The 64 beams of the SG-III facility are grouped into 8 bundle. The amplifier module in each bundle is a 4 high x 2 wide array of Nd-doped phosphate glass slabs of 31.6 x 57.6 x 4 cm³, vertically stacked on edge at Brewster's angle to laser beam, as shown in Figure 1. The

hard aperture of 30cm x 30cm is just matched by the manufacturing capability of large aperture precision optics in China. Each laser bay contains 4 independent beamlines. The laser beams from the end window of transport spatial filters are transported to the switchyard and arranged there to enter the target chamber, after frequency conversion, either in a few beam cones for indirect drive hohlraum targets or in a spherically symmetrical distribution for direct drive illuminations of capsules, as depicted in Figure 2 and Figure 3. The target chamber is a 5-m-diameter sphere with many ports for both optical windows and diagnostic instruments mounting.

4. TECHNICAL INTEGRATION LINE

Conceptual design of the SG-III facility shows that many new laser technologies have to be used for performance and cost effectiveness. Some of them have not been examined on the existing facilities yet and others are even still under development. To reduce the risk, a technical integration line (TIL) as a prototype has been planned to build first in the next few years.

The TIL consists of six major systems which are front-end and preamplifier system, main amplifier system, beam control system, frequency conversion system, laser diagnostic system and integrated computer control system. The main amplifier of the TIL is actually a beamline amplifier module of the SG-III facility with Nd:glass slabs for only two apertures and dummy slabs for the rest six apertures. Respectively, all the systems are designed for 2-beam production and characterization.

Table 4. Designed Specifications for TIL

Laser pulse energy	1.5 kJ / 0.35 μ m
Beam aperture	25cm x 25cm(hard aperture 30 x 30cm ²)
Beam number	2 (6 apertures with dummy glass)
Pulse duration	1-3 ns shaped
Beam power balance	\leq 10% rms (for main pulse)
Beam pointing accuracy	\leq 30 μ m rms
Beam divergence	\pm 25 μ rad

Figure 4 shows the optical schematic of the TIL from pulse injection to final focus on target. The main amplifier stage has a cavity amplifier(A1) for four-pass amplification and a booster amplifier(A2) for energy extraction. The four-pass architecture is basically similar to that for NIF(3) and LMJ (5). The laser pulse (<10J) is injected into A1 at the focal plane of the cavity spatial filter for the first double-pass amplification, then directed into the optical chain of the beam reverser with a small aperture Pockels cell isolation switch and then re-injected for the second double-pass amplification by A1. The emerging pulse from A1 is finally amplified by A2 to the required output energy.

If the beam reverser can not function properly to suppress the ASE in the cavity and isolate the reflected beams effectively due to the damage of the pick-off mirror and some other technical issues , a full aperture Pockels cell will be placed between the mirror and glass slabs in A1. To relieve the difficulties in developing large Pockels cell with very high efficiency, we are planning to employ a combination architecture of small and large Pockels cells. The small one in the beam reverser is designed to turn on for isolating the optical path since the onset of the flashlamps' pumping until the arrival of the laser pulse to be amplified. While the large one in the cavity is designed to work for interstage isolation after the amplification of the laser pulse by A1. When the laser pulse travel through the Pockels cells, there is no voltage applied to them. To the laser pulse, the switches work in a static regime. A prototype plasma-electrode Pockels cell of 80mm x 80mm has been successfully developed at CAEP, while larger ones for the TIL still under development.

Numerical simulations are still being conducted for optical design and the results have shown that glass slabs' numbers of 9 for A1 and of 5 for A2 are preferred. The Nd-doped phosphate glass is newly developed (4) and has been put in pilot production.

An adaptive optics system was firstly tested on SG-I laser facility in Shanghai late in 1980's. Here again, we have designed an adaptive optical system, composed of a deformable mirror, Hartmann sensors, processor and wavefront controllor, to compensate for wavefront and thermal distortions. The deformable mirror will be installed prior to the injection of the laser pulse into A1 as in the Beamlet (6).

The power conditioning systems will also be modularized, each corresponding to a 4 x 2 x1 amplifier module. Capacitors using the self-healing, metallized dielectric technology are being developed by a number of vendors and a energy density of 0.5J/cc has been reached. Ce-doped quartz flashlamps 140-cm long, 3-cm in inner diameter are now under test and pilot production will soon begin. A few options of lager current switches are being considered and some of them are very promising.

Table 5. Nd-Doped Phosphate Glass (N₃₁)

Stimulated emission cross section	$4.5 \times 10^{-20} \text{ cm}^2$
Fluorescence lifetime	400 μ s (2.2%Nd ₂ O ₃)
Absorption coefficient (1.053 μ m)	0.1% / cm
Nonlinear refractive index	$1.2 \times 10^{-13} \text{ e.s.u.}$
Damage threshold (1.06 μ m,3ns)	$\geq 20 \text{ J / cm}^2$
Platinum grain	$\leq 0.2 \text{ / liter}$

As a part of the TIL project, we have started to build a amplifier laboratory to demonstrate that the designed amplifier module will function as projected. It will be a 4 x 2 x 3 amplifier-module assembly with respected power conditioning system, gas system, computer control system, light source and diagnostics.

5. ACKNOWLEDGMENTS

The work highlighted in this review was carried out by many of my colleagues in China Academy of Engineering Physics, Joint Laboratory of High Power Laser and Physics, National ICF Committee and contracted affiliations. Their contributions are highly appreciated.

6. REFERENCES

1. H.S.Peng, "ICF and Related Laser Programs in China", SPIE Vol.2096,33 (1993).
2. H.S.Peng, "Progress in the CAEP ICF Program", Laser Interaction and Related Plasma Phenomena, Vol.13, 76 (1997).
3. "National Ignition Facility Conceptual Design Report", UCRL-PROP-117093, NIF-LLNL-94-113, L-16973.
4. Z.Q.Lin,et.al., "SG-II Laser Elementary Research and Precision SG-II Program", IAEA TCM on Drivers and Ignition Facilities for Inertial Fusion, March 10-14, 1997, Osaka, Japan.
5. M.L.Andre, "Status of the LMJ Project", Solid State Lasers for Application to Inertial Confinement Fusion, 38(1996).
6. B.M.Van Wontergham,et.al., "Beamlet Pulse-generation and Wavefront-Control System", ICF Quarterly Report, Vol.5, No.1, 43 (1994).

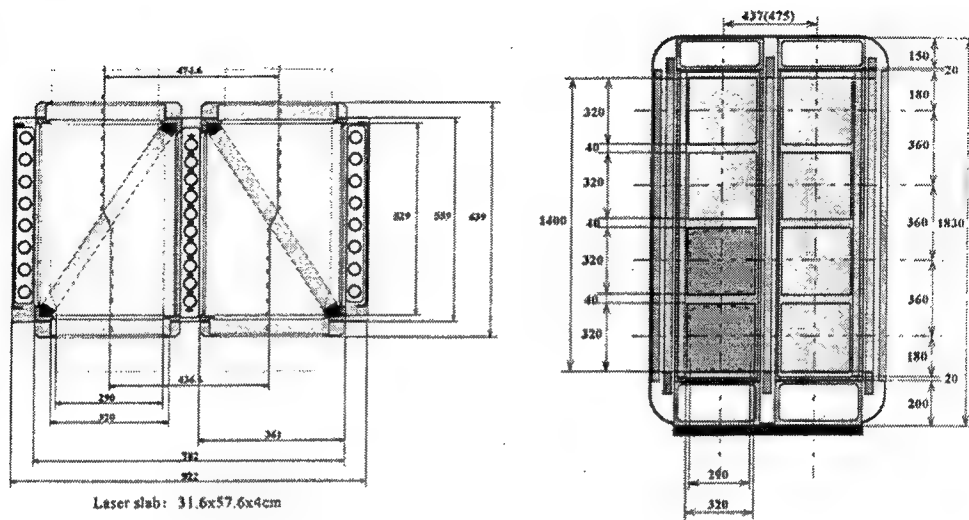


Figure 1. Schematic drawing of the 4 x 2 -segmented amplifier module

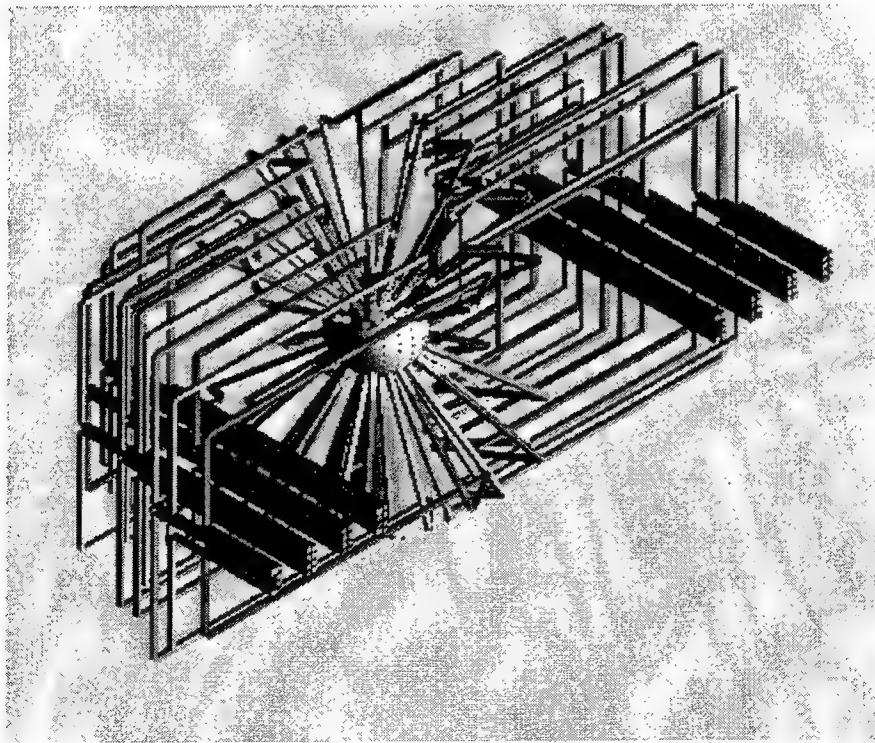


Figure 2. Isometric view of the target area for indirect drive targets

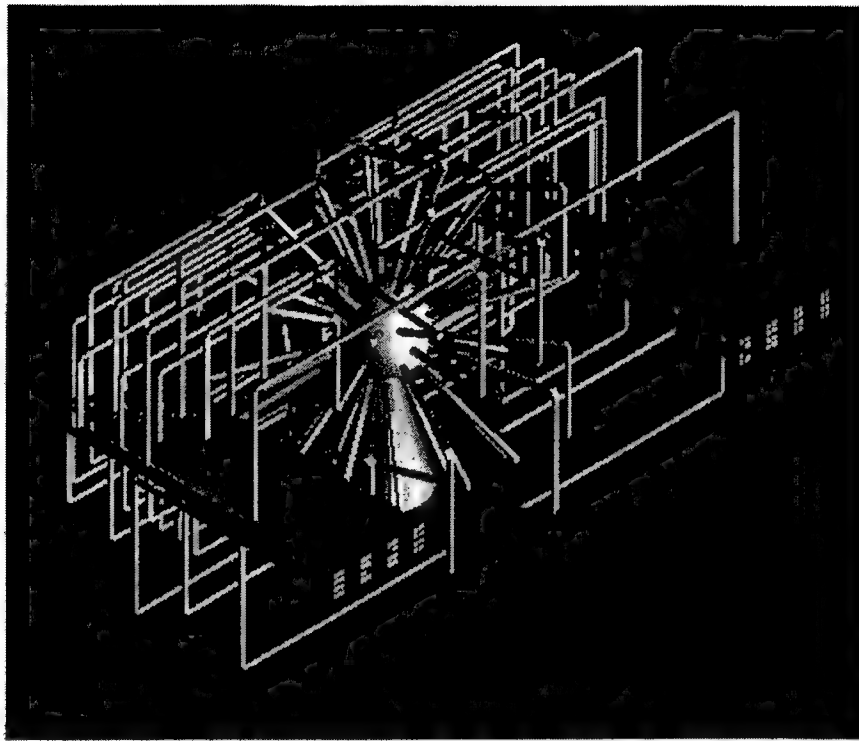


Figure 3. Isometric view of the target area for direct drive targets

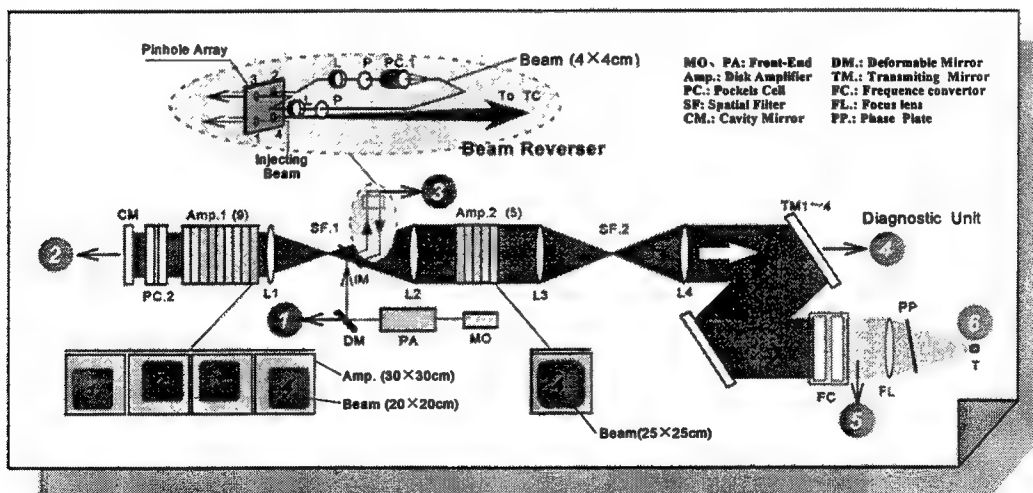


Figure 4. Schematic of the Technical Integration Line for SG-III laser facility

High power PROGRESS Nd: glass laser facility

Alexander V. Charukchev, Victor N. Chernov, Vladimir A. Malinov, Nikolai V. Nikitin,
Vladimir G. Borodin, Vladimir M. Efanov, Vladimir V. Iljin, Vladimir M. Komarov,
Vaycheslav M. Migel, Valentin S. Popov, Sergei L. Potapov

Scientific Research Institute for Complex Testing S.I. Vavilov State Optical Institute
Sosnovy Bor, Leningrad region, 188537, Russia

ABSTRACT

We present performance of PROGRESS Nd:glass laser facility which consists of a six beam phosphate Nd: glass laser, 30 TW PROGRESS-P picosecond YLF:Nd glass laser, which uses chirped pulse amplification (CPA) technique and target chamber. PROGRESS-M laser is capable to focus simultaneously at 1,054 μm the energy of 1.5 kJ in 1.5 ns and power of 3.5 TW in 200 ps on the fusion target. We report performance of a single beam 0.5 kJ PROGRESS-1M laser. This laser with output rod amplifier 14 cm is the prolongation of one of the beam of the multi-beam laser. PROGRESS-P CPA laser uses YLF:Nd oscillator, single mode optical fiber, Nd:glass rod amplifiers with output diameter of 85 mm. At the output, the chirped pulse with energy about 45 J is compressed up to 1.4 ps in the single-pass compressor on two holographic gratings, which produces power of 22 TW.

Keywords: Nd: glass, multi-beam, rod amplifier, multipass amplifier, chirp, laser facility, target.

1. INTRODUCTION

The PROGRESS facility has been operated since 1975 and concentrated on for fundamental experiments on ICF¹. For the past five years our efforts² have been devoted to forming superstrong fields on plasmas³.

2. MULTIPURPOSE RESEARCH LASER FACILITY PROGRESS

Multipurpose research laser facility PROGRESS is one of really of working Nd: glass lasers in Russia. The main directions of investigations are:

- laser fusion;
- superstrong fields in plasmas;
- power laser pulse propagation in air;
- laser engineering.

The scheme of PROGRESS multipurpose research laser facility is shown in the Fig. 1. It consists of a six beam PROGRESS-M phosphate Nd: glass laser, a single beam PROGRESS-1M laser, 30 TW PROGRESS-P picosecond YLF:Nd glass laser, which uses chirped pulse amplification (CPA) technique and target chamber with laser-plasma diagnostics. PROGRESS-M laser is capable to focus simultaneously at 1.054 μm the energy of 1.5 kJ in 1.5 ns and power of 3.5 TW in 200 ps on the fusion target. Now we have a single beam 0.5 kJ PROGRESS-1M laser with output rod amplifier 14 cm which is the prolongation of one of the beam of the multi-beam laser PROGRESS-M. The upgrade of PROGRESS-1M will include two disk amplifiers with 15 and 25 cm apertures and will provide energy 2.5 kJ in 1.5 ns. PROGRESS-P CPA laser uses YLF:Nd oscillator, single mode optical fiber, Nd:glass rod amplifiers with output diameter of 8,5 cm. At the output, the chirped pulse with energy about 45 J is compressed in the single-pass compressor on two holographic gratings and directed to target for laser-plasma interactions. We also have CPA 0.5 TW PROGRESS-1P laser with output rod amplifier 2 cm based on preamplifying stage of PROGRESS-P laser facility.

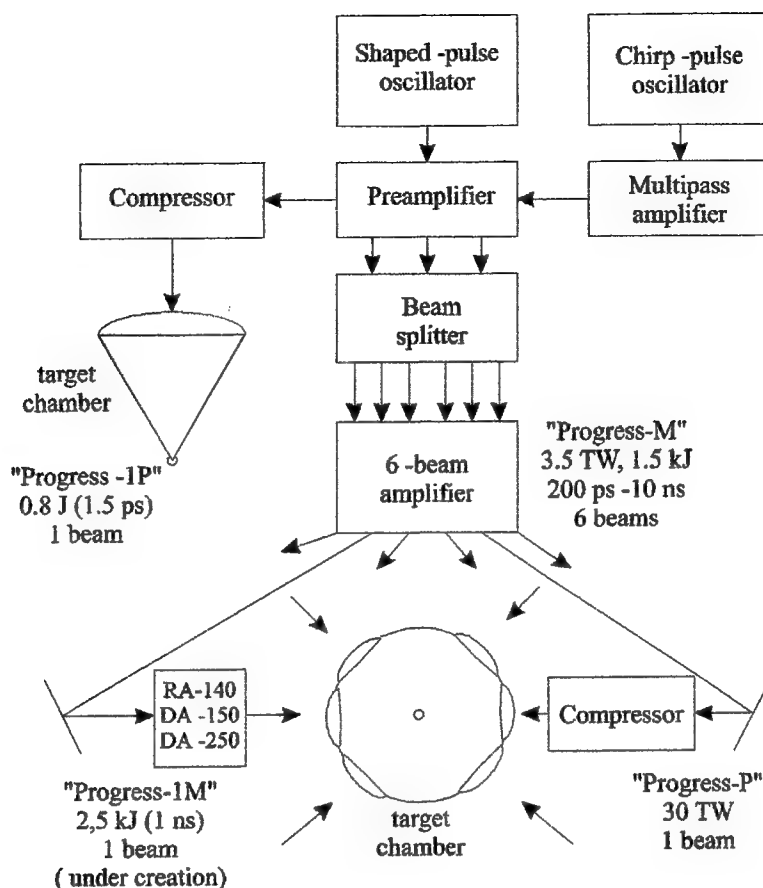


Figure 1. Multipurpose Research Laser Facility "PROGRESS"

3. THE PROGRESS-M PHOSPHATE GLASS LASER FACILITY

The scheme of PROGRESS-M laser facility and one of the beamline is shown in the Fig.2. It is a six beam laser system with an output aperture of 11 cm. Laser system consists of a small oscillator, a pulse formation system and six amplification chains. The output laser pulse from an oscillator is directed to the electrooptic deflector system, which temporally shapes laser pulse with duration of 0.2-10.0 ns, then the pulse is amplified by preamplifier, divided into three beams and then divided into two beams to make six amplifier beamlines based on the rod amplifiers. The output six beams are then directed by mirrors to target chamber.

The Q-switched phosphate glass oscillator produces smooth single-axial mode long laser pulses with 50-70 ns pulse duration. The first Pockels cell (PC-1) selects pulses with 10 ns duration from the long pulse oscillator output and decreases intensity level of the further optical elements. The pulse which passes through PC-1 is amplified by two 2 cm diameter x 46 cm-length amplifiers (RA-1 and RA-2) before being directed onto deflector system.

An optical system of deflector system (Fig.2) consists of two identical electro-optic deflectors (diverging EOD-1 and converting EOD-2 with LiNbO_3 crystals) and three air spatial filters (SF-3, DSF, SF-4). The spatial filters are spherical lenses with the focal length of all lenses equal 1000 mm and focal pinholes located at the focal planes of these lenses. The filters relay consecutively the image of the input hard aperture DHA of deflector system to its output. The diverging deflector deflects a focused beam in the focal plane of the "shaped" pinhole SP. The converting deflector compensates fully for this beam deflection. The axial propagation of the beam determines pulse peak power so that the pulse structure in space and time are governed entirely by the confinement and diffraction of the beam by the hard apertures and the form of the SP.

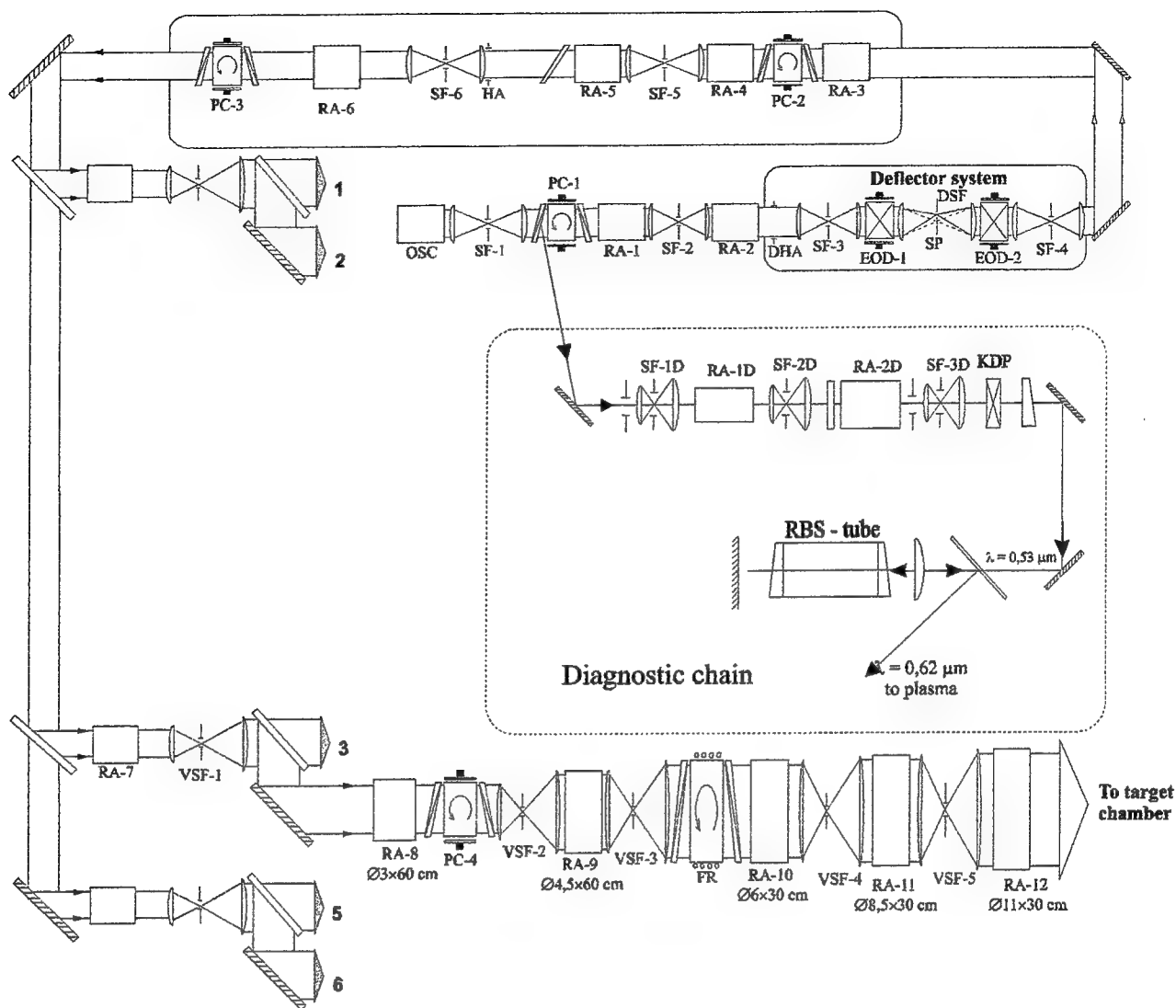


Figure 2. Scheme of laser system "Progress - M": OSC - oscillator, PC - Pockels cell, EOD - electrooptic deflector, SP - shaped pinhole aperture, DSF - deflector spatial filter, DHA - deflector hard aperture, HA - hard aperture, FR - Faraday rotator, SF - spatial filter, VSF - vacuum spatial filter, RA - rod amplifier, RBS - stimulated Raman backscattering in plasmas..

The pulse duration is determined mainly by velocity of beam scanning equal 3,75 mrad/ns, and by dimensions of the SP but its shape is determined by the profile of the SP. The off-axial passage determines the pulse contrast. Pulses with sharp leading edges can be generated if we suppress the long wings of the focal spot distribution of the laser beam in the focal plane DSF. It is also necessary to remove the diffraction scattering of a beam because of the clipping by hard apertures and the bulk scattering in the crystals. In our case the diffraction scattering of the beam is suppressed by the choice of the parameters SF-2, which transmits only the central maximum of the focused beam, which has the form Airy circle. The other air spatial filters in the preamplifier are also adjusted so that they transmit only the central maximum of the focused beam. Deflector system provides⁴ pulses 0.2-10 ns (FWHM) with high power contrast above 10^8 in 1 ns prior to main pulse (see Fig. 3, left) and

shaped pulses with a power drop up to a 10^3 by altering the shape and dimensions of the "shaped" pinhole SP (see Fig.3, right).

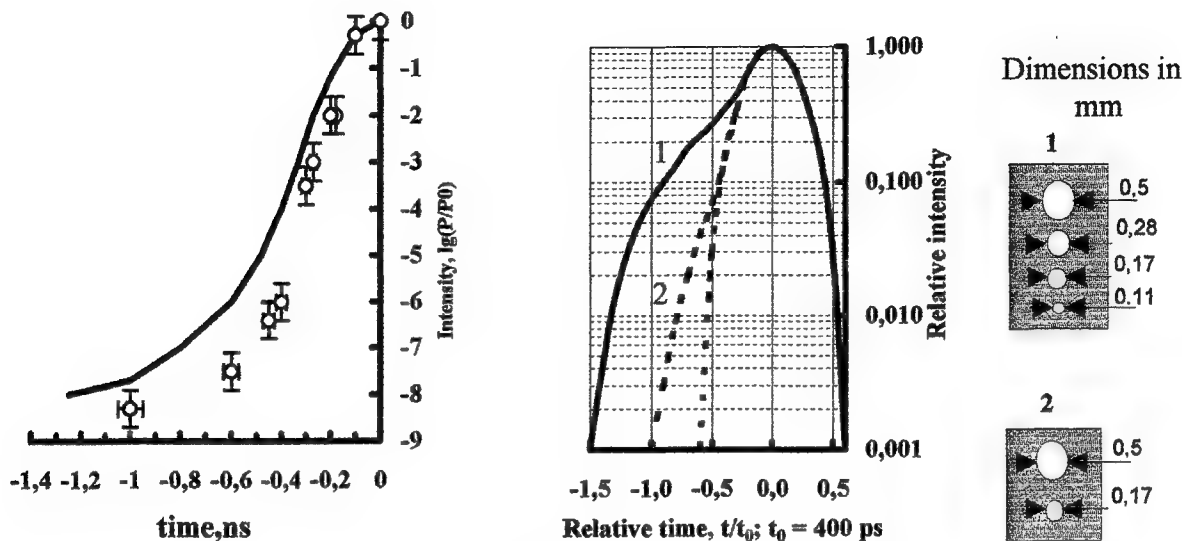


Figure 3. Pulse shaping by deflector system on "Progress - M" laser system.

For plasma diagnostics we design the diagnostic chain. After reflection from the output surface EOD-2, some of the energy is directed through RA-2, SF-2 and RA-1 and injected by input polarizer of PC-1 to the diagnostic chain. This part of the main pulse is selected with the stability of better than 10 ps respectively of the main pulse. Finally, the seed pulse is amplified by rod amplifiers RA-1D and RA-2D and converted in $0.53 \mu\text{m}$ by KDP crystal. After that, pulse is converted by Stimulated Raman backscattering (RBS) in tube into $0.62 \mu\text{m}$ and directed to plasma diagnostics.

By four 2 cm diameter rod amplifiers in preamplifier stage and then by one in the section where the beam is divided into three parts, the laser pulse is amplified up to 50-200 mJ on the input of each main amplifier chain.

Each of six beamlines consists of five rod amplifiers with increasing from 3 to 11 cm diameters, isolation elements (Pockels cell and Faraday rotator with 3 and 6 cm diameters correspondingly) and four high-power vacuum spatial filters (VSF). In the chain, rod stages from GLS22 glass and KGSS0180 with $\varnothing 3 \times 60\text{cm}$, $\varnothing 4.5 \times 60\text{cm}$, $\varnothing 6 \times 30\text{cm}$, $\varnothing 8.5 \times 30\text{cm}$ and $\varnothing 11 \times 30\text{cm}$ dimensions are used with small signal gains of 35, 25, 9.5, 4.9 and 3.7, respectively. Characteristics of large aperture rod amplifiers are presented in Table 1.

Table 1. Large aperture rod amplifiers parameters

\varnothing , cm	L , cm	L_p , cm	G_0	α_0 , cm^{-1}	α_r/α_0	W_p , kJ
6.0	30	25	9.5	0.091	1.10	22
8.5	32	25	4.9	0.064	1.15	40
11	32	25	3.7	0.052	1.18	70

\varnothing - clear aperture of amplifier, L - length of laser active element, L_p - pumped length, G_0 - small signal gain, α_0 - axis gain coefficient, α_r - edge gain coefficient, W_p - pumped energy

Both glasses were athermal with approximately the same stimulated-transition cross sections, but KGSS0180 had a considerably smaller (by factor of 1.5) nonlinear refractive index (10^{-13} cgs esu). VSF are used to expand the beam diameter and remove the fastest growing spatial frequencies out of laser beam cross section when passing through the amplifiers. In the chain relaying an image of the beam input hard aperture (HA) through the amplifier chain was used in order to obtain spatially uniform intensity distribution. This relaying scheme uses spatial filter SF-6, placed immediately after HA, and the following vacuum spatial filters. Besides retranslating VSF are also used to coordinate the diameter of the laser beam in the amplifier stage and forms the spatial beam profile close to rectangular with fill factor 0.8, which is close to maximum energy extraction from output aperture of the rod amplifier.

Calculations were made of amplification of the beam with the fill factor equal to 0.8, in the geometrical approximation, with account for saturation of the amplifier by means of the Frantz-Nodvick equation. The calculated and measured amplification performance of one of the main chains at a laser pulse width 200 ps and 1.6 ns as a function of the input energy to the chain is shown in Fig. 4. The output energy is close to 250 J under 1.6 ns duration. Under 200 ps duration of the pulse

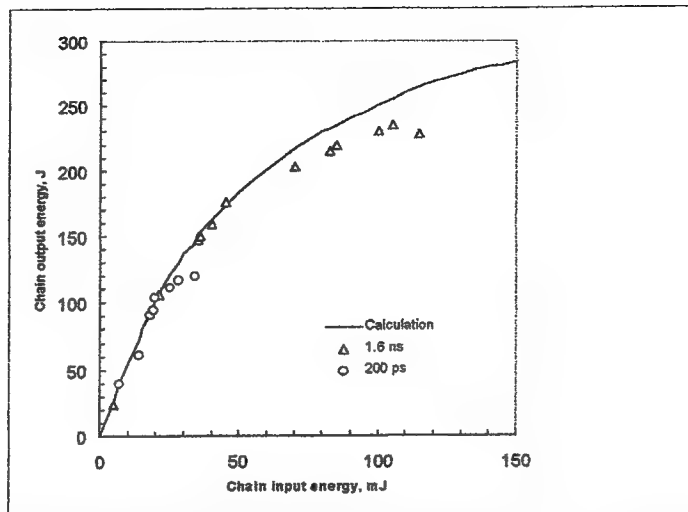


Figure 4. Output energy of one amplifier chain with output aperture 11 cm as a function of the input energy to the amplifier chain at the laser pulse duration of 200 ps and 1.6 ns. The solid curve is the result of simulation calculation.

there obtained a power of approximately 600 GW without noticeable small-scale self-focusing. This corresponds to focusable power 3.5 TW by six beams on the fusion target. The average firing rate, determined by thermal relaxation time of output 11 cm rod amplifier, is 1 shot/1 hour.

The target irradiation system consists of 18 mirrors with high reflectivity at the wavelengths of 1.054 and 0.53 μm . The target chamber has an inner diameter of 70 cm and is made of nonmagnetic stainless steel of 1.2 cm thickness. It is pumped to less than 10^{-6} torr.

The focusing optics of the target chamber consist of two classes of focusing lens designs of $f/1.3$ and the aperture diameter 130 mm. Three-element lenses with conventional spherical surfaces were made of TF-10 glass and focus the laser pulses with wavelength of 1.06 μm . The radii of surfaces were calculated to correct the spherical aberration. Nonlinear coefficient of TF-10 ($n_2 = 10^{-12}$ CGSE) is relatively high and thus limits the intensity of the focusing beam to be less than 4 GW/cm². Focus spot size of these lenses is less than 5 μm in diameter at the $1/e^2$ of peak intensity. The second design was planoconvex singlet with the convex side aspherized to give the spherical aberration correction. To correct a spherical aberration in the visible range there was added concentric meniscus. The glass taken was K-8, generally accepted as one of the best and cheapest materials. Using this design, spot sizes of 15 μm in diameter were obtained at the wavelengths of 1.06 and 0.53 μm . Because of its relatively smaller nonlinear refractive index the second design allows to focus the laser power to higher intensities.

We have reported on the development of a six beam PROGRESS-M phosphate - glass laser system with rod amplifiers up to 11 cm is created and output power of 3.5 TW in 200 ps and energy of 1.5 kJ in 1.5 ns with a power contrast more than 10^8 prior to the main pulse have been obtained

4. PERFORMANCE OF PROGRESS-1M FACILITY

In this section the main characteristics of design and experimental results of investigation of small signal gain of the 14 cm rod amplifier and a single beam PROGRESS-1M laser which is the prolongation of one of the chains of the six-beam laser PROGRESS-M are presented.

The laser rod with aperture 14 cm and length 47 cm dimensions was made of phosphate laser glass GLSS-22 with Nd₂O₃ concentration 5×10^{19} cm⁻³. The end surfaces were cut at the angle of 85° to the rod axis. The glass element was placed into a tube with output diameter 17.5 cm and thickness 0.7 cm made of Sm-glass which clipped pump light in the region 1.06

μm and was transparent in pumping region of laser rod. The rod was pumped by twenty xenon pulse flashlamps with inner diameter 16 mm. The flashlamps were surrounded by twenty silver-plated reflectors. The lamp pulse-forming network drove a pair of flashlamps in series with 1000 μF capacity and 100 μF inductor. Pumped pulse width on 0.35 amplitude level was equal to 800 μs .

For the large-aperture amplifiers the amplified spontaneous emission (ASE) becomes one of the factors limiting creation of the high level of the inversion density. The limit of the gain coefficient values rises with the decrease of the ratio between the pumping length of the laser rod l and its diameter d as well as a result of the rod outer surface antireflection.

The experiments⁵ conducted with the rod amplifiers with the apertures 10-60 mm, made of phosphate Nd: glass, have shown that when using distilled fluid as an index-matching the average gain coefficient α over the full aperture is limited by the value of $\alpha_{\text{lim}} = 1.1(l/d)^{-0.5}$. Using an index-matching solution, which refractive index is closer to the laser rod refractive index, instead of the distilled fluid allows us significantly increase the gain coefficient α .

The value of α_{lim} for 14 cm rod amplifier was estimated to be equal 0.045 cm^{-1} . In order to reduce ASE and increase the gain coefficient the active rod was surrounded by an index-matching solution with the refractive index equal to 1.54. Transmittance of 1 cm fluid layer is equal to 90+95% and 82% in the wavelength range 0.58-0.88 μm and 1.06 μm correspondingly. The energy experimental testing of the fluid has shown that the investigated fluid keeps its optical parameters invariable under the pulse energy loading up to 100 J/cm^2 .

Fig.5 shows experimental results of measuring the rod amplifier axial gain coefficient as a function of the energy stored in the capacity banks and gain profile for pumping energy 140 kJ. The rod amplifier axial gain coefficient was equal to 0.04 cm^{-1} .

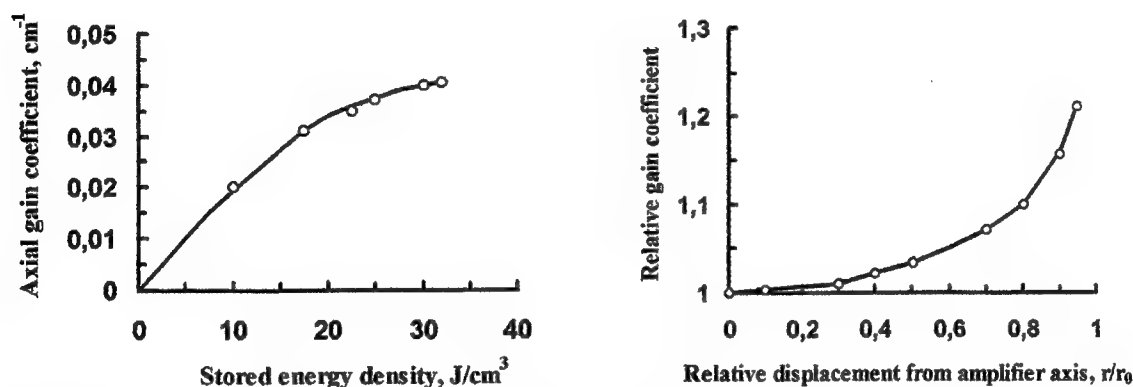


Figure. 5 Experimental results of measuring the rod amplifier axial gain coefficient and gain profile as a function of the energy stored in the capacity banks.

We placed this rod amplifier on the output of one of PROGRESS-M laser facility chains after an additional VSF, which expanded the beam coming from 11 cm rod amplifier to 14 cm. As a result of this design there was created a single beam PROGRESS-1M laser with output aperture of 14 cm. On the output of PROGRESS-1M we obtained 510 J laser energy at the pulse duration of 1.6 ns.

We have developed and created an effective 14 cm diameter rod amplifier with the gain coefficient close to those of 0.05 cm^{-1} obtained earlier in 11 cm diameter rod amplifiers. This amplifier was used in a single beam 0.5 kJ PROGRESS-1M laser. The created design is of definite scientific and practical interest for development of high power laser systems because of the importance of determining the rod amplifier limit dimensions.

5. CPA PROGRESS-P LASER FACILITY

A scheme of CPA laser system is shown in Fig. 6. It consists of four parts: the starting laser system, large amplifier chain, compression stage and focusing stage. Starting laser produces a chirped pulses with energy up to ~1 J and duration 300 ps at wavelength 1.053 μm . This pulses are used both to further amplification in large amplifier chain and to compression to ~1.5 ps duration by using of pair of two 1700 lines/mm holographic gratings for laser-plasma interaction experiments⁶ under

average intensity of $(2-4) \cdot 10^{17} \text{ W/cm}^2$. The chirped pulses are obtained by a cw mode-locked Nd:YLF oscillator generating a

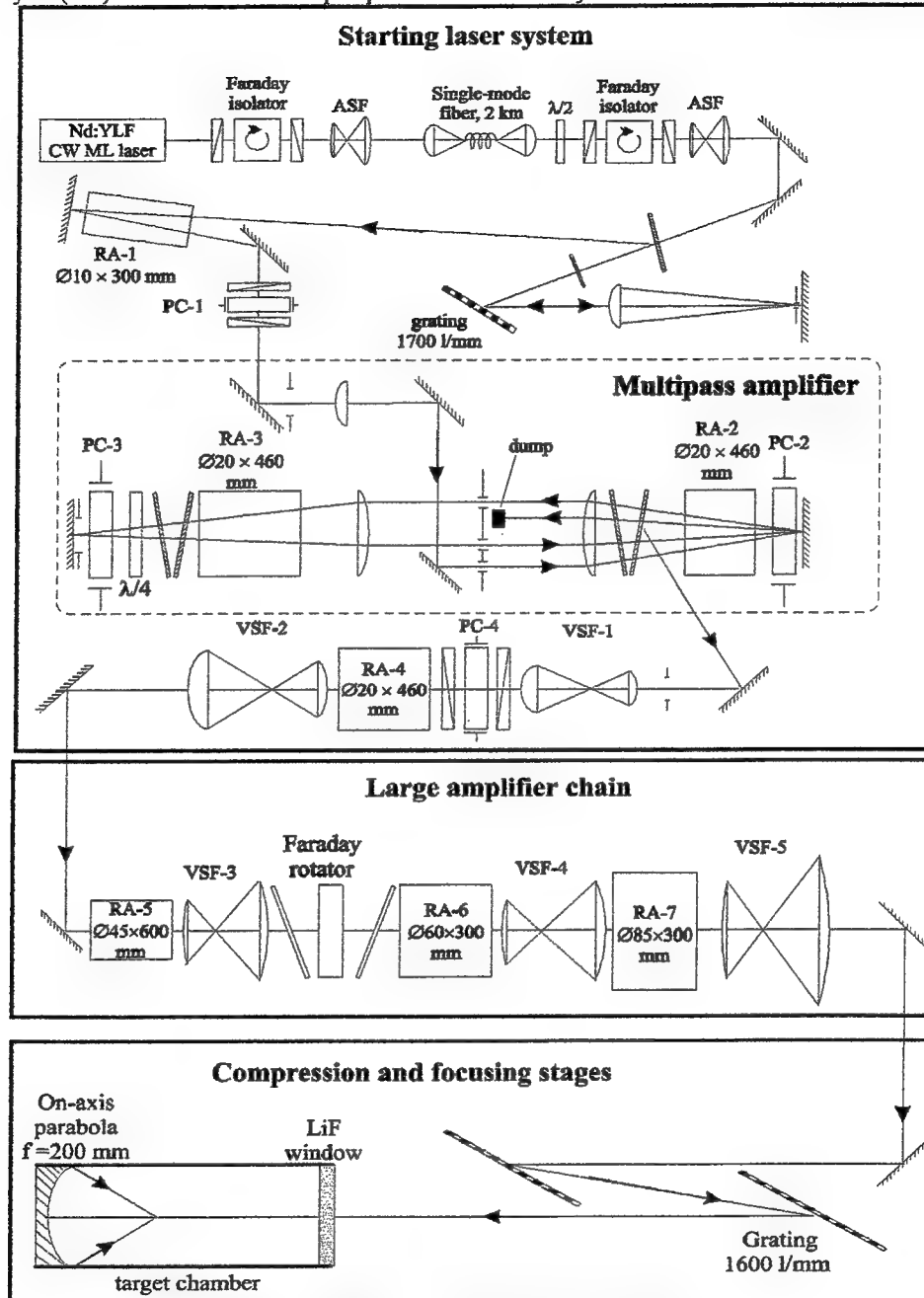


Figure 6. Scheme of laser system PROGRESS-P.

100-MHz train of 60 ps pulses with average power $\sim 2.5 \text{ W}$, 2 km single-mode optical fiber and four-pass stretcher with single 1700 lines/mm holographic grating. As a result of combined effects of group velocity dispersion and self-phase modulation, the pulse on output of fiber has been broadened to a 150 ps duration with spectrum of 3.0 nm FWHM. The stretcher has been passed only central part of spectrum $\sim 1.7\text{-}2.0 \text{ nm}$ FWHM for elimination of nonlinear chirp⁷ and expansion of laser pulse to 300 ps duration.

Amplification of pulse from 0.3 nJ to $\sim \text{J}$ level is performed in three rod amplifiers: two-pass, multipass and single-pass with output aperture of 2 cm. All the amplifiers contain phosphate Nd:glass GLS22 or KGSS0180 with maximum gain near

1.053 μm . A single laser pulse is selected and controlled through laser system by four Pockels cells which driving by high-voltage pulse generator based on the drift step recovery diodes⁸. The generators are produced 4-8 kV pulses with a FWHM of 5 ns and rise time ~ 1.5 ns (see Table 2). The main amplification of pulse (from 50 nJ up to 200 mJ) is carried out in

Table 2. High-Voltage Pulse Generators OG1-8 and OG2-5 based on the Drift Step Recovery Diodes (DSRD)		OG1-8	OG2-5
Output Voltage	at load 500 Ohm	+8 kV	+5 kV
Output Voltage	at load 50 Ohm	+5 kV	+3 kV
Pulse width at half maximum	at load 500 Ohm	5 ns	5 ns
Pulse width at half maximum	at load 50 Ohm	7 ns	7 ns
Maximum repetition rate	external. air cooling	1 kHz	1 kHz
Time stability (jitter)		< 50 ps	< 50 ps
Maximum delay time	sync/output pulse	150 ns	150 ns
Maximum delay time	first/second pulses		10 ns
Input triggering	at load 50 Ohm	+10 V	+10 V
Input D.C. voltage		+(0.6-1.0) kV	+(0.6-1.0) kV
Dimensions		42×78×94 mm	42×78×94 mm
Weight		0.25 kg	0.25 kg

developed multipass amplifier with net gain $\sim 4 \cdot 10^6$. Amplifier consists of two $\varnothing 20 \times 460$ mm Nd:glass rods with small signal gain up to ~ 50 . The optical scheme of multipass amplifier is disaligned conjugated resonator with relaying of end flat mirrors by use the 1.1 m focal length positive lens pair. In common focus of lenses in air is positioned three-pinholes system with 4-mm spacing between pinholes. The pulse is seeded into amplifier through one of pinholes and removed by Pockels cell. Optimization was made the pinhole diameter for producing the high-quality beam and reducing amplified spontaneous emission pedestal. The diameters of two front pinholes are chosen equal diffraction limited spot size ~ 0.5 mm for 6-mm amplifying beam and the last pinhole diameter is chosen equal 0.35 mm. Further amplification in single-pass amplifier $\varnothing 2.0 \times 46$ cm produces in excess of 1 J energy with nearly diffraction limited divergence of radiation.

To obtain the pulses with the power up to 30 TW we used a three-stage relay-imaged amplifier chain with rod amplifiers $\varnothing 4.5 \times 60$ cm, $\varnothing 6 \times 30$ cm and $\varnothing 8.5 \times 30$ cm dimensions, which is a part of the main amplifier chain of the PROGRESS-M facility. For output performance of the amplifier chain calculations were made also. This results show that the beam with the energy ~ 0.3 J obtained at the output of the starting laser should be applied to the input of the amplifier, to obtain the output beam with the required energy of about 55 J (with consideration for the losses in the compressor). For this regime the B-integral accumulating in section with aperture of 8.5 cm is equal ~ 1.3 . At the output, the beam is expanded by the vacuum spatial filter up to the diameter of ~ 200 mm to reduce the energy density in the compressor down to the value by 4 to 5 times lower than the damage threshold gold-coated holographic diffraction gratings equal to $\sim 200 \text{ mJ/cm}^2$. Fig. 7 shows a typical

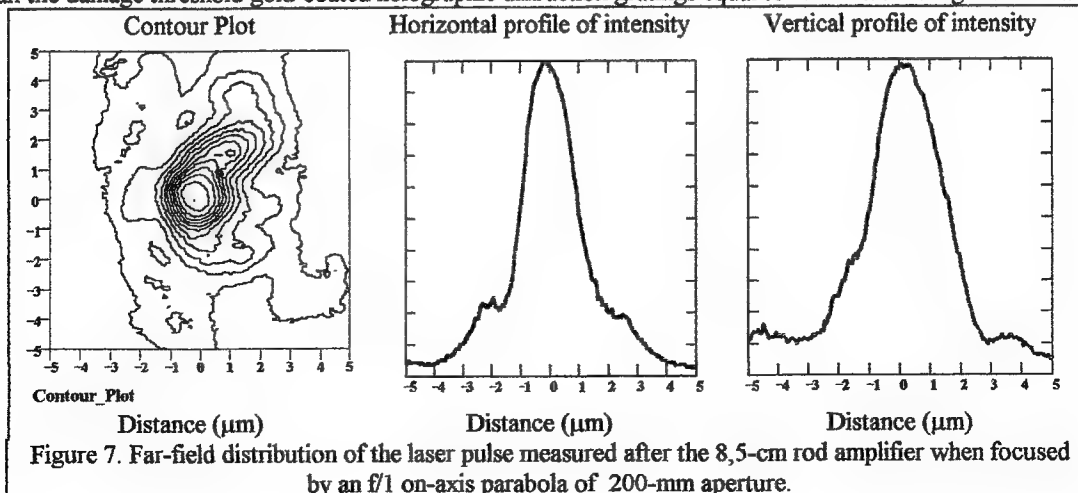


image and profile of intensities of far-field distribution of laser chirped pulse at 35-45 J measured using optical system with equivalent 60 m focal-length and a CCD camera. Images show a profile width $1/e^2$ width of 12 μm in plane when laser pulse focused by an $f/1$ on axis parabola of 200 mm aperture, corresponding to a 1.7-2 times diffraction limited beam. We measured that more than 50% of energy was within a 5- μm pinhole placed at this plane. The amplified spontaneous emission which passed through grating compressor as determined by the fast photo-diode and calorimeter are less than 10 μJ energy and 5 ns duration and makes the energy contrast ratio $\sim 10^5:1$ of laser pulse.

The pulse is compressed in the single-pass compressor on two gold-coated holographic diffraction gratings with dimensions of 420mm \times 210mm and 1600 lines/mm. The compressor efficiency is over 80 %. The duration of the compressed pulse for 200 mm beam was measured using a second-order single-shot autocorrelator. Measured autocorrelation trace and spectrum of the compressed pulse are shown in Fig.8. The FWHM of laser pulse is 1.5 ps and width of spectrum is 1.5 nm.

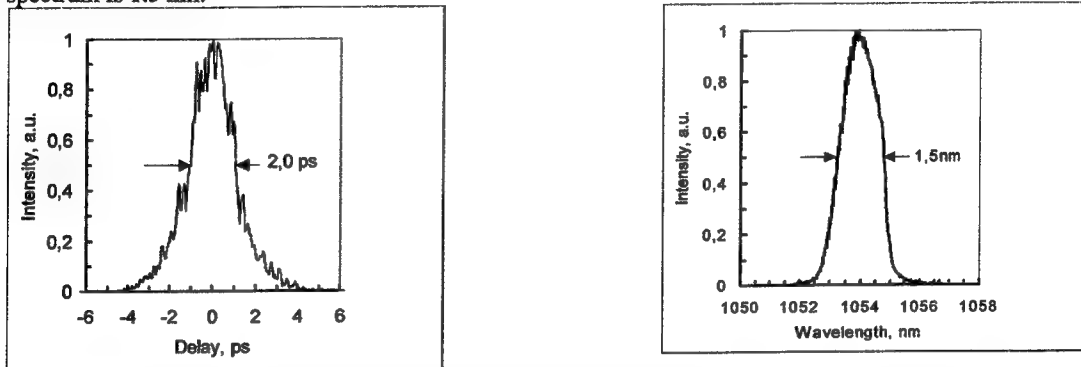


Figure 8. Single-shot autocorrelator trace and spectrum of the output laser pulse.

The beam is focused to the target by means of the on-axis mirror parabola with focal length of 200 mm. The parabola focuses $\sim 50\%$ of the energy of unaberrated beam of cw Nd:YLF laser with diameter of 200 mm in the 8 μm diameter spot (it exceeds the diffraction limited spot by 3 times). The beam is injected in the target chamber through the high optical quality LiF-window with low nonlinear refractive index coefficient. With the use of this means we achieve an intensity 10^{19} W/cm 2 .

In summary, we have demonstrated the generation of 22-TW near transform-limited 1.4-ps duration high-contrast laser pulses with a 1.7-2 times diffraction limited beam.

6. CONCLUSION

The main characteristics of PROGRESS laser facility are summarized in Table 3.

Table 3. Performance of laser facility "Progress"			
	"Progress-M"	"Progress-P"	"Progress-IM"
Number of beams	6	1	1
Energy	up to 1.5 kJ	45 J (chirped pulse)	510 J
Pulse Duration	200 ps - 10 ns (shaped)	1.4 ps	100 ps to 10 ns (shaped)
Power on the target	3.5 TW in 200 ps	22 TW	up to 2 TW in 100 ps
Focusing (energy)	80 % in 15 μm with $f/1.3$ focusing lenses	80 % in 10 μm with $f/1$ focusing lenses	
Contrast (ASE)	$\geq 10^8$	$< 30 \mu\text{J}$	$\geq 10^8$
Wavelength	1 μm , 0.5 μm	1 μm	1 μm
Output Beam Diameter	100 mm	180 mm	200 mm

We have reported on the development of a six beam PROGRESS-M phosphate - glass laser system with rod amplifiers up to 11 cm is created and output power of 3.5 TW in 200 ps and energy of 1.5 kJ in 1.5 ns with a power contrast more than 10^8 prior to the main pulse have been obtained. We have developed and investigated an effective 14 cm rod amplifier with the gain coefficient 0.04 cm^{-1} . We placed this rod amplifier on the output of one of PROGRESS-M laser facility chains and obtained energy of 510 J in 1.5 ns. CPA PROGRESS-P laser facility were created with power of 22 TW in 1.5 ps and high contrast ratio for laser-plasma experiments in ultrahigh irradiance on the target above 10^{19} W/cm^2 . As a result, the experiments will be performed on exposure of targets at the intensity over 10^{19} W/cm^2 . Laser-plasma experiments were carried out under intensities up to $4 \times 10^{18} \text{ W/cm}^2$. Diagnostics equipment was created for investigations of characteristics of laser radiation and plasma. We will be increased the output power PROGRESS-P facility up to 50-60 TW by using Ti: Sapphire master oscillator and plan to conduct laser-plasma experiments with simultaneous pico- and subpicosecond laser pulse effects on a solid target.

7. ACKNOWLEDGEMENTS

This work was supported by International Scientific and Technology Center under Projects #107 and 108.

8. REFERENCES

1. V. N. Alekseev, E. G. Bordachev, V. G. Borodin et al., "Six beam laser facility PROGRESS on Nd-phosphate glass", *Izv. Akad. Nauk SSSR, ser. phys.*, 48 (10), pp. 1477-1484.
2. E. G. Borodin, A. V. Charukchev, V. N. Chernov et al., "The PROGRESS-P 30 TW Picosecond Nd:glass Facility", In book "Laser Interaction and Related Plasma Phenomena" 13th International Conference, Monterey, CA, 1997 Editors George H. Milley and E. Michael Campbell, pp. 389-395, AIP Conference Proceedings 406, Woodbury, New York.
3. M. D. Perry and Gerard Mourou, "Terawatt to Petawatt Subpicosecond Lasers", *Science*, vol. 264, pp. 917-924, 1994.
4. V. A. Malinov and V. N. Chernov "Formation of laser pulses by deflector systems", *Kvantovay Electron. (Moscow)*, vol. 17, pp. 586-589, 1990.
5. V. I. Baynov, E. G. Bordachev, V. M. Volynkin et al., "Big- Aperture Rod Phosphate-Neodymium-Glass Amplifiers for High-Brightness", *Kvantovay Electron. (Moscow)*, vol. 13, pp. 1891-1896, 1990.
6. V. M. Komarov, V. G. Borodin, A. V. Charukchev et al., "Absorption and Fast Ion Generation in TW- Picosecond Laser-Plasma Experiments", In book "Laser Interaction and Related Plasma Phenomena" 13th International Conference, Monterey, CA, 1997 Editors George H. Milley and E. Michael Campbell, pp. 443-449, AIP Conference Proceedings 406, Woodbury, New York.
7. J. P. Heritage, R. N. Thurston, W. J. Tomlinson, A. M. Weiner, and R. H. Stolen "Spectral windowing of frequency-modulated optical pulses in a grating compressor", *Appl. Phys. Lett.* vol. 47, pp. 87-89, 1985.
8. V. A. Malinov, A. V. Charukchev, V. N. Chernov et al., "Methods for Shaping High-Power Picosecond Laser Pulses with a High- Contrast Ratio", In Abstracts International Conference on Superstrong Fields in Plasmas, Varenna, Italy, 1997.

Soft X-ray plasma source pumped by an excimer laser: optimisation and applications.

Patrizia Albertano^e, Mauro Belli^f, Sarah Bollanti^a, Paolo Di Lazzaro^a, Anatoly Ya Faenov^h,
Francesco Flora^a, Gualtiero Giordano^a, Antonio Grilli^g, Fiorenza Ianzini^f, Sergei V. Kukhlevsky^j,
Tommaso Letardi^a, Alessandro Marinai^b, Alessandro Nottola^b, Libero Palladino^c, Tatiana Pikuz^h,
Armando Reale^c, Lucia Reale^d, Anna Scafati^f, Giovanni Schina^a, Maria Antonella Tabocchini^f, I. C.
Edmond Turcuⁱ, Kostandia Vigli-Papadaki^b.

^a ENEA, Dept. INN, POBox 65, 00044 Frascati, Italy

^b ENEA guest

^c Univ. of L'Aquila, Dept. of Physics and INFN-LNGS, L'Aquila, Italy

^d University of L'Aquila, Dep. of Igiene e Sanità Pubblica, L'Aquila, Italy

^e University of Rome "Tor Vergata", Dept. of Biology 00133 Roma, Italy

^f Istituto Superiore di Sanità and INFN sez. Sanità, 00161 Roma, Italy

^g INFN-LNF, Via E. Fermi, 00044 Frascati, Italy

^h MISDC of NPO "VINIIFTRI", Mendeleevo, Moscow Region, Russia

ⁱ Rutherford Appleton Laboratory, Chilton, Didcot, Oxford, OX11 0QX, U.K.

^j Janus Pannonius University, Department of Physics, Ifjusag u. 6, Pecs H-7624, Hungary

ABSTRACT

A large volume excimer laser, HERCULES, has been successfully applied as pump for a soft X-ray plasma source. The laser pulse duration has been varied from the natural value of 120 ns down to 10 ns, reaching different emission spectra from the plasma which have resulted to be optimum for different applications of the plasma source itself.

Some experimental results on the applications of the source to different fields (X-ray microscopy, radio-biology, X-ray micro-lithography, basic plasma physics research) are presented; the choice of the best laser parameters in relation to the applications of the plasma source are also discussed.

Keywords: X-ray source, microscopy, radiobiology, spectroscopy, excimer laser

1. INTRODUCTION

A soft X-ray plasma source pumped by a large volume excimer laser (HERCULES) has been developed at ENEA laboratories in Frascati^{1,2}. The specific characteristic of this X-ray source is to be pumped by relatively long laser pulses (10-120 ns) so that, in spite of the high energy per pulse (2 and 7 J respectively), the laser beam intensity at the target is in the order of 10^{13} W/cm² when an $f^{\#}=3$ focusing triplet lens is used.

The low laser intensity allows the interaction chamber to be filled with helium without gas breakdown troubles: no reduction of the X-ray emission from target is observed when the helium pressure is risen up to atmospheric pressure.

The advantages of operating the X-ray source at atmospheric pressure lead to important results in different applications of the source, like X-ray contact microscopy or radiobiology, since any mechanical stress on the membrane which separate the specimen from the environment, can be avoided.

2. THE LASER SOURCE

The performances of the large volume excimer laser HERCULES, used for this X-ray source pumping, has been described widely elsewhere^{1,2}. It is a non-commercial ultraviolet system pumped by a self sustained electric discharge in a XeCl active medium (emission wavelength = 308 nm). When used as a positive branch unstable resonator, it emits a natural pulse duration of 120 ns with a pulse energy of 6-7 J. Alternatively it can be used as amplifier of a shorter (10 ns) and lower energy (30 mJ) pulse produced by a commercial XeCl laser. In this case the output energy of Hercules is 2 J but, because of the shorter pulse duration, the peak power results larger by a factor three.

For both optical configurations, Hercules is used as a pump for the X-ray plasma source. However, being the beam divergence almost the same in both cases, a different laser intensity is reached on the target ($\sim 1 \cdot 10^{13}$ and $3 \cdot 10^{13}$ W/cm² respectively) and consequently, a different plasma temperature is obtained: 135 and 200 eV respectively¹.

3. THE X-RAY SOURCE AND ITS CHARACTERISATION

After being focused by an $f^{\#}=3$ triplet lens, the laser beam reaches a waist of 15 μ m FWHM diameter on the target surface. The source's dimension of the re-emitted X-rays have been measured for 1-1.5 keV X-rays and for $h\nu=50$ -70 eV X-rays: it results to be ≈ 30 μ m and 45 μ m respectively, that is roughly the same value of the laser waist¹. The laser beam transportation efficiency from the Hercules output to the target is 65%.

The target used is a tape, moved by a step motor, and it is tilted by 45 degrees with respect to the laser direction so as to get a good X-ray flux also in the vertical direction; this is very important for many applications like the microscopy and the radiobiology, as it will be shown in the following.

The X-ray emission has been measured in three different spectral intervals each of which corresponds to different applications:

S_{70} : $40 < h\nu < 70$ eV (for imaging microlithography)

S_{ww} : $300 < h\nu < 500$ eV (for contact microscopy)

S_{1k} : $0.8 < h\nu < 1.6$ keV (for radiobiology or contact microlithography)

In Fig.1.a the penetration depth as a function of the energy of the X-rays is shown for water and proteins. As one can see, the penetration depth is in the order of few cm in the 100 keV region (hard X-rays), the one used in hospitals for irradiating human bodies. In the soft X-ray region, where our plasma source is emitting, the penetration depth becomes in the order of few microns; but right for this reason these X-rays allow applications completely different from the hard X-rays. As mentioned before, this soft X-ray region could be divided into three parts, depending on the application. In the water-window (S_{ww}), microscopy applications are allowable, since in this interval the difference in the absorption coefficient between water and proteins is considerable as it can be seen from Fig.1.a. In particular, soft X-ray contact microscopy results are going to be discussed later. In the S_{1k} interval, X-rays are sufficiently transmitted by biological material to allow a rather uniform irradiation through a penetration depth of 1-10 μ m, which is comparable with a mammalian cell thickness. For this reason this X-rays can be used for radiobiology applications. Also, some other interesting applications of the S_{1k} X-rays are contact microlithography and micro-radiology of insects as it can be seen later. Finally the S_{70} spectral interval is interesting for imaging microlithography, since at these wavelengths multilayer mirrors have a good reflectivity.

Fig.1.b shows the X-ray pulse energy obtained, in the three spectral regions, for the 120 ns and the 10 ns laser pulse configurations, when the target is placed at best focusing. In the 70 eV region, the highest conversion efficiency is obtained with the 120 ns configuration, 12% against 5% (for the calculation of the energy conversion efficiency, the optical transmission of 65% from the laser to the target has been taken into account), whilst in the water-window and in the 1 keV region, the highest conversion efficiencies are obtained with the 10 ns configuration. That is because with the latter one, the intensity on the target increases by a factor 3 and thus the generation of higher energy X-rays is favoured by a higher plasma temperature.

Thus, for each application, the laser configuration plus the target material is chosen in advance so as to obtain the highest conversion efficiency in the desired X-ray region.

The measurement of the X-ray flux in the different intervals is obtained by using fast PIN-diodes with suitable filters ($3\text{ }\mu\text{m Al}$, $0.5\text{ }\mu\text{m V}$ and $10\text{ }\mu\text{m Al}$ for the S_{70} , S_{ww} and S_{1k} spectral intervals respectively, with a 5 degrees grazing reflection on a Cu mirror to cut the harder X-rays for S_{70} and S_{ww}).

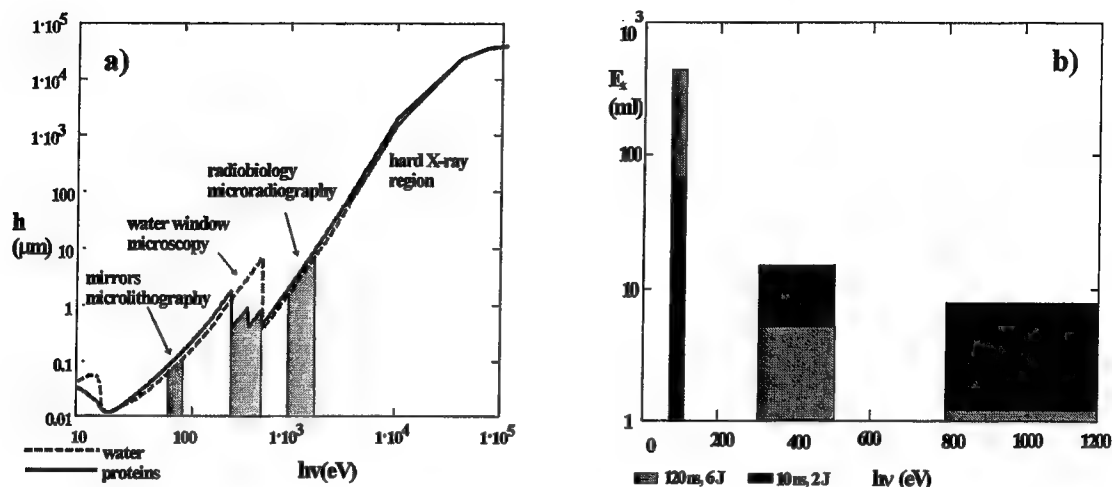


Fig.1: a): Thickness of water and proteins for transmission of 50% in various spectral regions.
b): X-rays pulse energy (target in focus) in the three spectral intervals with Cu target

Also the X-ray pulse duration is different for the three spectral intervals above mentioned, as shown in fig. 2a. For the S_{ww} and S_{70} spectral intervals the pulse duration (as well as the pulse energy) increases if we move the target out of focus by 0.5 mm and 1 mm respectively (see for example fig. 2b), both using the long or the short laser pulse.

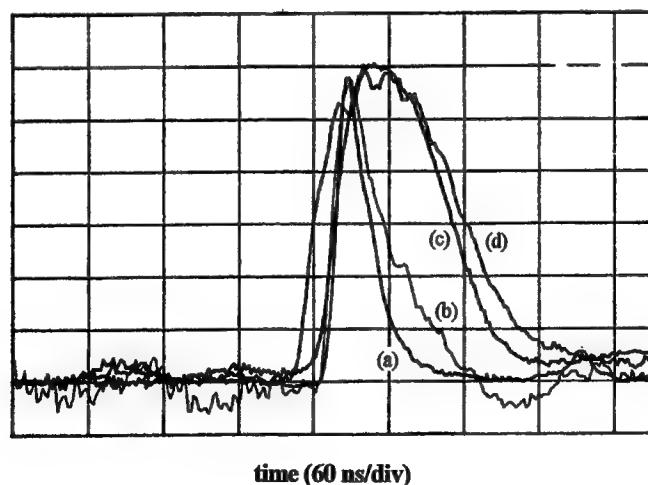


Fig. 2a: Time evolution of the X-ray pulse in the S_{1k} , S_{ww} and S_{70} (curves a, b and c respectively) spectral regions and of the laser pulse (curve d) for the 120 ns laser pulse. Vertical scale: arbitrary units. Target: 100 μm thick Cu tape.

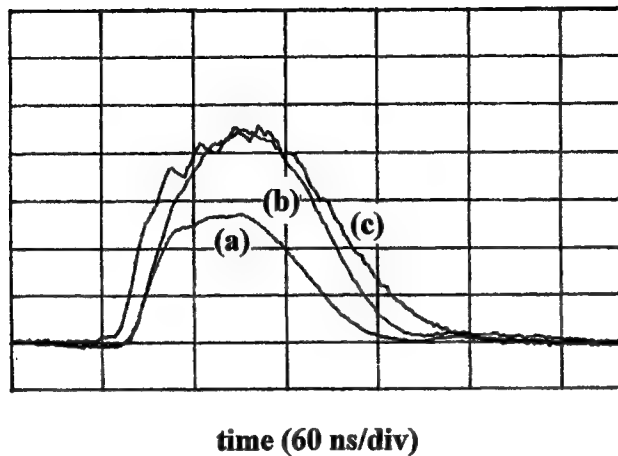


Fig. 2b: Time evolution of the 120 ns laser pulse (curve c) and of the X-ray pulse in the S_{70} spectral region when the target is at beam waist (curve a) and at +1mm from the beam waist (curve b). Vertical scale: arbitrary units (curves a and b have the same units). Target: 100 μm thick Cu tape. The FWHM for curves a and b are 103ns and 109ns respectively.

In particular, at 1 mm distance from best focus, the conversion efficiency in the S_{70} region reaches 20% for the 120 ns laser pulse and 11% for the 10 ns laser pulse. Hence, even for an optimised laser intensity, the conversion efficiency in the very low photon energy range is still significantly higher for the natural laser pulse duration than for the shortened one. In Fig. 2b the time evolution of the S_{70} X-rays, with the target being at best focus and at 1 mm from it, is compared for the 120 ns laser pulse. At the beginning the two pulses follow the same behaviour but then a higher emission is reached for a target position out of focus.

The interpretation of these results is not immediate. For the emission in the S_{70} range a rather simple explanation could be found in a rough black-body model: out of focus the laser intensity is lower and so the lower plasma temperature fits well for the 70 eV emission. For example, at the experimental peak of emission, at 1 mm from the beam waist, the laser spot diameter is roughly 250 μm , the laser intensity is 10^{11} W/cm^2 and so the estimated target temperature (according with a simple thermal equilibrium condition) is 30 eV. At this low temperature the corresponding black-body peak emission is very close to 70 eV. But for the water-window range another explanation should be found, since a temperature at the laser beam waist of 135 eV is just enough for a good emission. An interesting explanation, proposed by E. Turcu, is based on the relation between the laser spot diameter and the plasma expansion: at the early stage the plasma expands mainly normally to the target but later, after the expansion exceeds the laser spot diameter, it becomes isotropic, that is it changes from one-dimensional to three-dimensional with a consequent temperature fall. This fall reduces little the 70 eV emission but has a strong effect on the harder X-rays. The wider the laser spot, the longer the duration of the one-dimensional expansion and hence of the S_{ww} (and S_{ik}) X-rays emission. This explanation can justify not only the increased X-ray pulse duration when the target is at 1 mm from beam waist, but also the different duration at $z=0$ of the X-rays in the three different spectral regions.

Another effect which might contribute to these two phenomena, besides the three-dimensional expansion, is the laser defocusing by target ablation^{1,2}: during the long laser pulse, the target surface moves back by ablation and goes far from the beam waist. This causes a temperature fall that reduces the emission for S_{ww} and S_{ik} X-rays. The smaller the laser spot, the higher the laser intensity and the quicker the consuming of the target by ablation. A further investigation is needed to understand better which of these effects is the most important one.

As it can be noted in Fig. 2b, both in and out of best focusing the X-ray emission at 70 eV lasts more than 100 ns and this, in our knowledge, is a record.

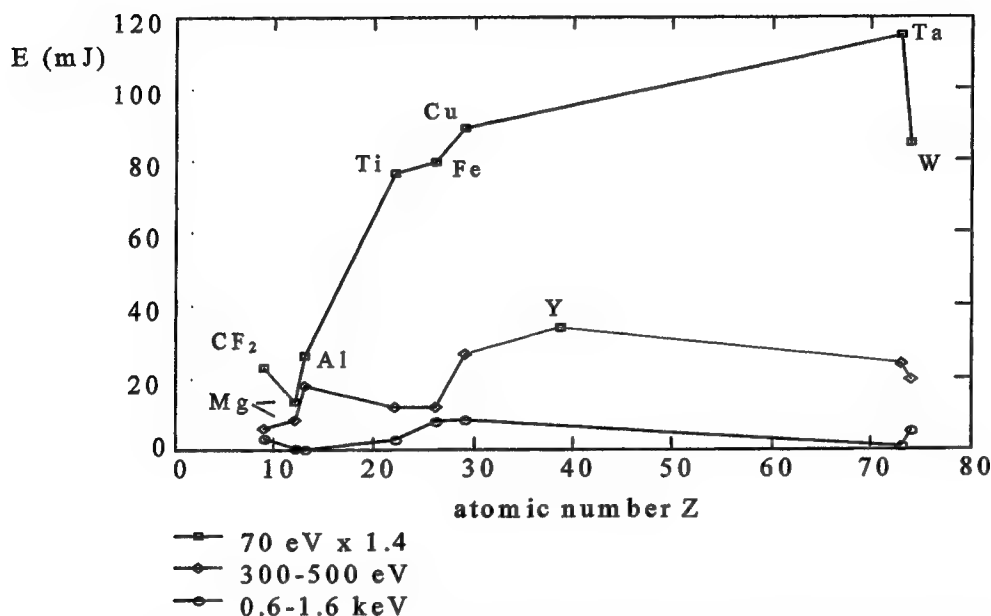


Fig. 3: X-ray pulse energy in the S_{70} , S_{ww} and S_{1k} spectral intervals for different target materials (laser: 10 ns, 2 J).

Up to here we discussed the comparison between long and short laser pulses using a copper target (which is one of the best for a good conversion efficiency in the S_{70} and S_{1k} intervals) but, of course, other target materials can be used in order to optimise the emission in the spectral interval of interest³. For example for X-ray microscopy applications other materials like yttrium or tantalum can reach a good efficiency in the S_{ww} interval, see Fig. 3, while minimising the emission at 1 keV (a large contribution of 1 keV photons might worsen the image contrast, being the transmission of both water and proteins high, as shown in 1.a).

The spatial distribution of the X-ray emission has been measured for the S_{ww} spectral interval when a Tantalum target is placed at best focus ($z=0$). A $\cos^{0.75}(\theta)$ distribution has been found, where θ is the angle with respect to the normal to the target.

The source can be operated in a repetitive mode up to 10 Hz (actually limited to 3 Hz by the power supply) and hence an average power of few watts can be reached in the S_{70} interval.

A typical problem of X-ray plasma sources is the debris emission from target. In our case, as mentioned in ref.^{1,2}, for a 100 μm thick Cu target quite large size debris (10-100 μm) are emitted and their spatial distribution is not isotropic: the emission is strongly peaked at the direction specular with respect to the laser incidence one, as if the laser could push the debris. By reducing the target thickness to 30 μm , the spatial distribution remains similar to the previous case but the debris size is much smaller, so that thin membranes, like 0.1 μm of Si_3N_4 or 1 μm Al, can survive for hundreds shots at few centimetres from the plasma. This is very important for microlithography applications: a multilayer mirror, placed close to the plasma, could be protected from debris bombardment simply by a thin Al filter which is periodically replaced by a new one (see also section 4.4). Anyway our work is still in progress about this point.

4. APPLICATIONS

4.1 Atmospheric pressure soft X-ray contact microscopy (SXCM)

As it has been mentioned above, the most important application of the S_{ww} spectral interval is the X-ray microscopy. For our source, we have developed a contact X-ray microscopy system (SXCM). The biological samples were placed *in vivo* in aqueous medium between a thin X-ray transparent window (100nm thick Si_3N_4 window made by FasTec Ltd., UK, with a transmission of approximately 60% at an X-ray energy of 400 eV) and a PMMA resist with a separation gap between the window and the resist being in the range of 5-15 μm . This sandwich was placed at 5 mm distance from the plasma, considering the optimum combination for obtaining an adequate X-ray flux, whilst minimising the penumbra. After development, the resists are analysed by an atomic force microscope. A more detailed description of the technique is reported in ^{4,5,6,7}.

As it is well known, the X-rays in the water window are highly absorbed by air. For this reason, the interaction chamber is held in vacuum, having the Si_3N_4 window to bear the atmospheric pressure of water. The elapsed time from initially loading the cells in the environmental holder, insertion into the chamber, evacuation and subsequent X-ray exposure is typically 15-30 minutes. Various materials were used as targets; among them yttrium and tantalum were giving the highest ratio between X-ray emission inside and outside the water-window. In Fig. 4.a an image of a green alga, *Leptolyngbya*, obtained using an yttrium target with this method, is shown. The flux in the S_{ww} spectral interval was 30 mJ/cm². The spatial resolution is ≈ 100 nm.

The new method for obtaining X-ray microscopy images is based on the use of a helium filled interaction chamber held at atmospheric pressure (Fig.5). This is possible since the transmission of helium at the water-window through the 5mm separation between the plasma and the Si_3N_4 window is more than 80%. The insertion of the sample is simply done through a pipe (Fig.5) while a small helium flux prevents the air to enter inside. In this case, no chamber evacuation is needed. Furthermore, with this method the size of the Si_3N_4 window is not limited by pressure effects.

The first image obtained in the helium filled chamber was of *Leptolyngbya* and can be seen in Fig.4.b. The image was obtained using a tantalum target with an X-ray flux in the water window of 25 mJ/cm². The quality of the image was limited by resist contamination (this factor though, had no connection with the applied method to obtain the image). Finally, an important point to be mentioned is that in helium environment the bombardment of debris emitted by the plasma is significantly slowed down.

A drawback of this new technique is the propagation of the shock-wave emitted by the plasma in the helium, but in our experience this does not damage the PMMA photoresist, when the specimen is in water and the thickness is 8-10 μm .

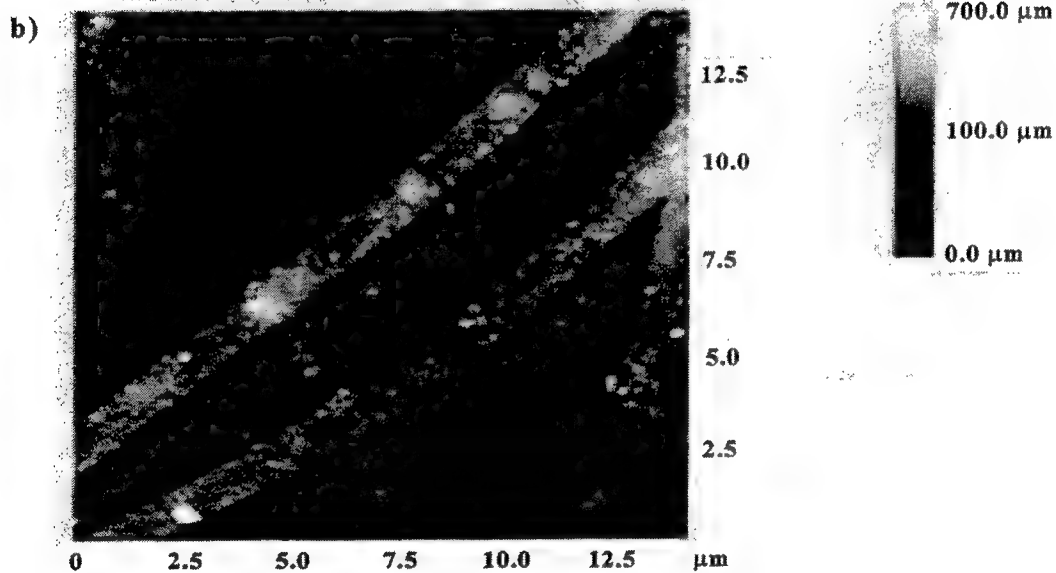
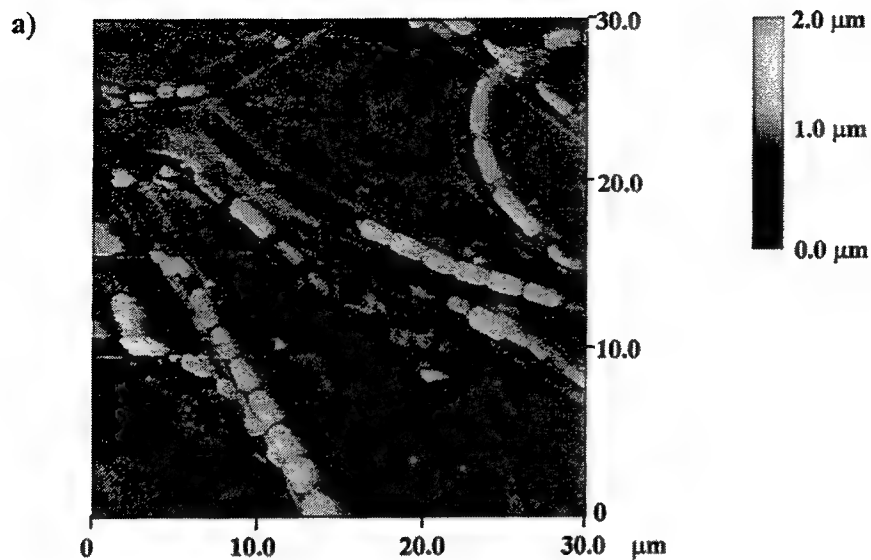


Fig. 4: a) X-ray microscopy image of *Leptolyngbya* obtained in vacuum (Yttrium target, 10 ns laser, X-ray fluence $F \approx 30 \text{ mJ/cm}^2$).

b) Image of *Leptolyngbya*, obtained at atmospheric pressure (Tantalum target, 10 ns laser, X-ray fluence $F \approx 25 \text{ mJ/cm}^2$).

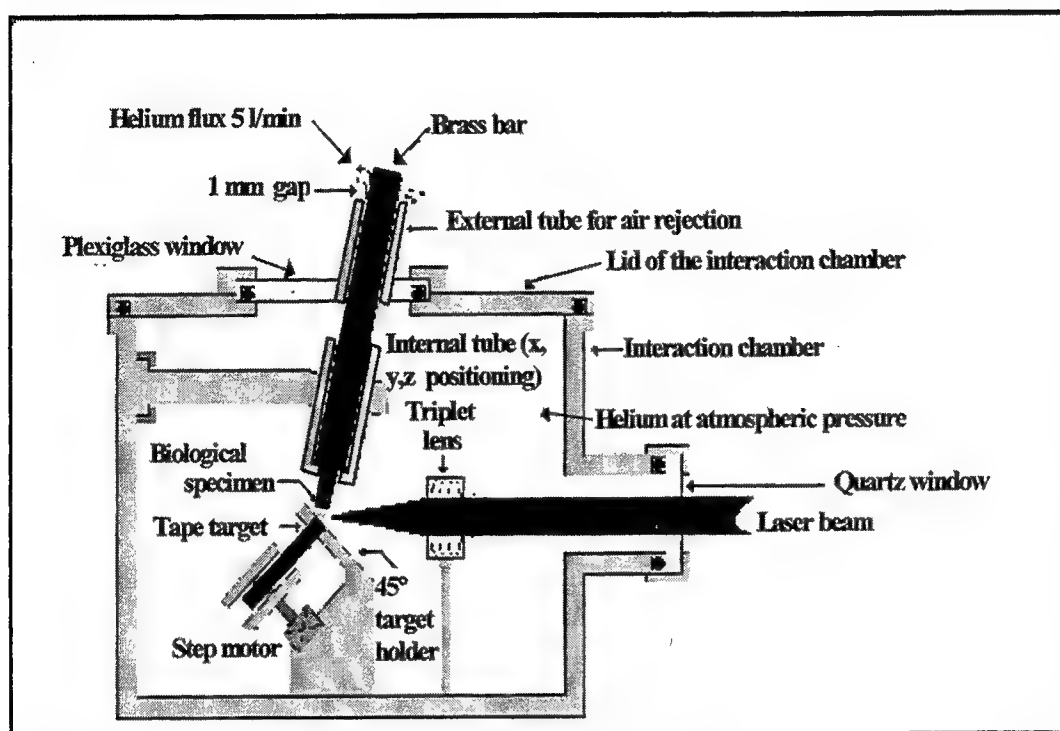


Fig. 5: Experimental apparatus for atmospheric pressure SXCM.

4.2 Micro-radiography

This application is very similar to the one used in hospitals for irradiating human bodies. Only that in this case, 1 keV radiation is being used and the irradiated bodies are considerably smaller. In our case, small insects were being used. The experimental set-up can be seen in Fig. 6. The insect was placed at a distance of 20-30 cm away from the plasma, whilst the whole chamber was at atmospheric pressure helium environment, that allowed the irradiation with only 1 keV X-rays and did not attenuate them more than 85%. This allowed the specimen to be put in air and alive, closed within two thin foils of Mylar (4 μm). After this sandwich (mylar foils and insect) an Aluminium filter was placed in front of the photographic film to cut off the UV and visible light and to select the 0.8-1.6 keV spectral window. The film was either a standard photographic film or DEF (more sensitive to the X-ray radiation).

An example of a microradiography image, obtained in DEF film (sensitivity > 1000 ASA) with this method, is shown in Fig. 7a. Interesting details of the insect internal structure can be observed. The main factor that is limiting our resolution is the film grain ($\approx 10 \mu\text{m}$). By reducing the film sensitivity and increasing the x-ray fluence by two orders of magnitude (in this case the sample was dead and dehydrated) we could improve the resolution to $\approx 2\text{-}3 \mu\text{m}$, as can be seen in fig 7b.

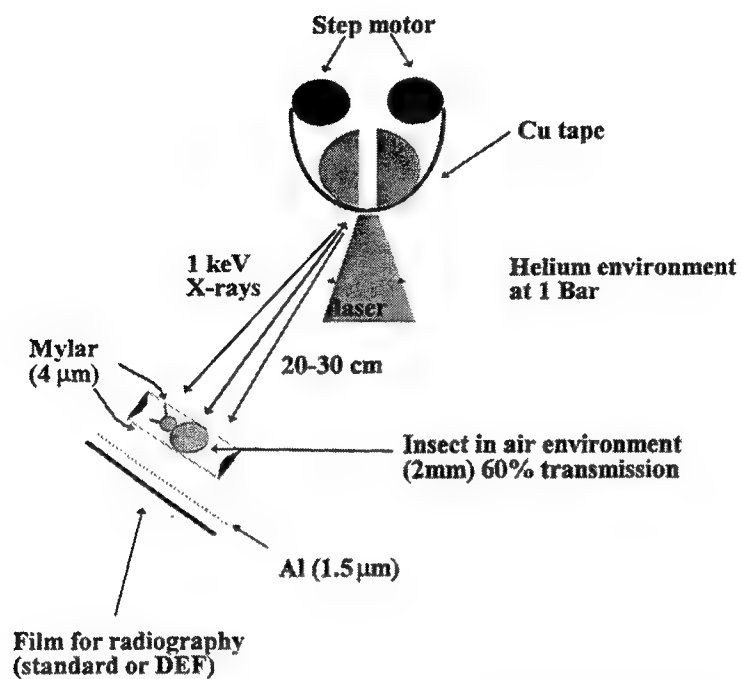


Fig. 6: Experimental apparatus for microradiography applications.

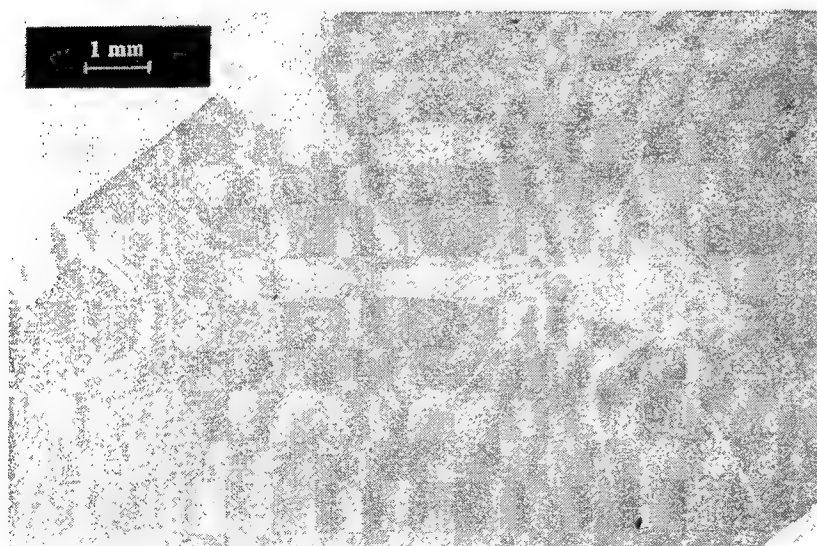


Fig.7a: Radiographic image of a small insect (libelluloidea). X-ray source: Cu tape, 10 ns laser pulse, 1 shot. Film: DEF (>1000 ASA) placed at 2 mm from the insect. Distance from the X-ray source: 35 cm. X-ray fluence=20 nJ/cm².

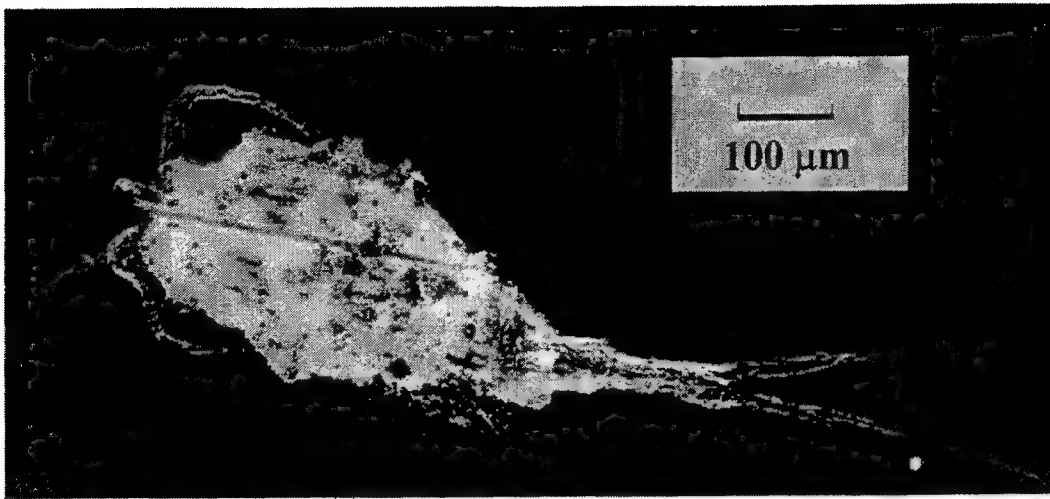


Fig. 7b: Radiographic image of a small insect (libelluloidea). X-ray source: Cu tape, 10 ns laser pulse, 180 shots. Film: AGFA ORTHOCHROMATIC FILM (10 ASA) placed at 1 mm from the animal. Distance from the X-ray source: 35 cm. X-ray fluence= $2 \mu\text{J}/\text{cm}^2$.

A theoretical limit for the spatial resolution, both for the X-ray microscopy and the micro-radiography, is given by the X-ray fluence in terms of statistical noise: in order to detect an object (for example a cube) having a size δ illuminated with a fluence F , the number of photons $N_1 = \delta^2 F e^{-\mu\delta} / h\nu$ which reach the detector (that is the film) under the object has to differ from the number $N_0 = \delta^2 F / h\nu$ of photons which reach the detector in other places (of the same area δ^2) by at least more than the statistical noise⁵ (where μ is the linear absorption coefficient of the object):

$$N_0 - N_1 \geq 2\sqrt{N_0} + 2\sqrt{N_1}$$

which gives a relation between the minimum X-ray fluence F and the spatial resolution δ :

$$F = h\nu \cdot \frac{4}{\delta^2} \cdot \left(\frac{1 + \sqrt{e^{-\mu\delta}}}{1 - e^{-\mu\delta}} \right)^2$$

So the requirements on the X-ray fluence scale as δ^2 when $\delta > 1/\mu$ or as δ^4 when $\delta \ll 1/\mu$. This equation is obtained assuming to have a transparent environment all around the object; else case the same equation still can be applied just by substituting μ with the difference $\Delta\mu$ between the object and the environment linear absorption coefficients.

In fig. 8 we have plotted F vs δ for a biological object (proteins) at two photons energies: $h\nu = 400 \text{ eV}$ (in the S_{ww}) and $h\nu = 1.2 \text{ keV}$ (in the $S_{1 \text{ keV}}$), for which $\mu = 2 \mu\text{m}^{-1}$ or $0.3 \mu\text{m}^{-1}$ respectively (see fig 1a, being $\mu = \ln(2)/\lambda$). As we can see, both for the images obtained in the water window (that is figs. 4a,b) at 1.2 keV (that is figs 7a,b) the theoretical resolution limit is just a factor 2 lower than the measured one and, in any case, very large fluences (up to kJ/cm^2 at 1.2 keV) are required for extremely good resolutions ($\delta \approx 10 \text{ nm}$). By moving the biological sample very close to the plasma source (2 cm) and by substituting the film with a PMMA photoresist (like for the contact microscopy technique used for images 4a,b) we reached at 1.2 keV a fluence 3 orders of magnitude larger than that of fig 7b on the same type of biological sample, as shown in fig. 9. But in this case the resolution has been limited to just $1 \mu\text{m}$ (that is 4 times the theoretical limit), mainly because of the penumbra blurring and by the diffraction (note the interference effect on the border of the animal structure).

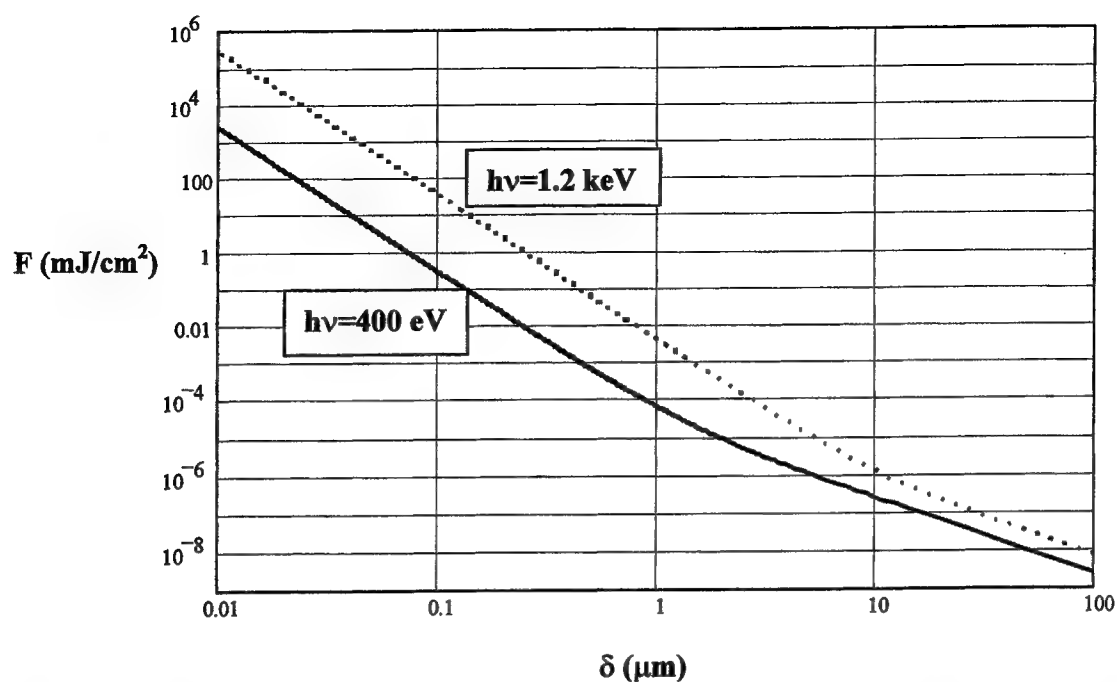


Fig.8: Minimum X-ray fluence vs the spatial resolution, according with the statistical noise theory, for a radiation propagating in proteins material; calculated for a photon energy $h\nu=400$ eV (solid line) and for $h\nu=1.2$ keV (dashed line).

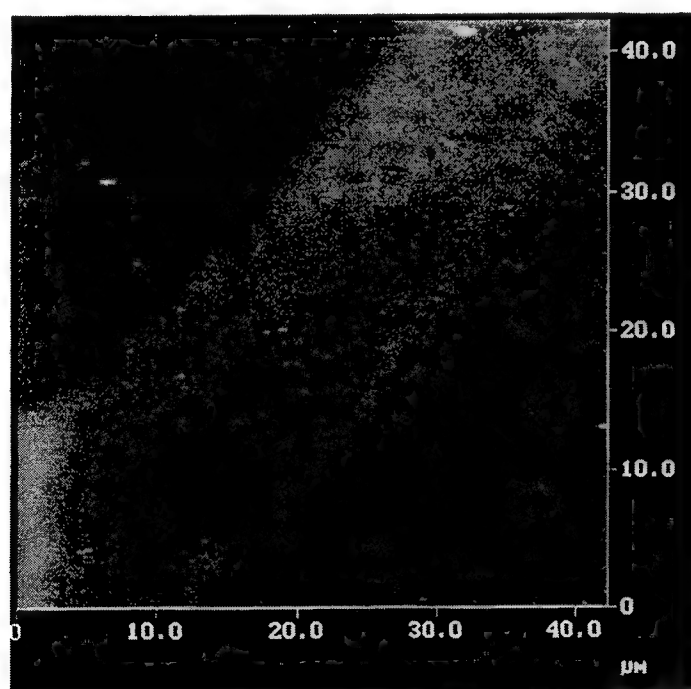


Fig9: Detail of the tail of a "copepod" like that of fig. 7b (right side of fig.7b) placed at 0.4 mm from a photoresist. Target: Cu tape (28 μm thick); Spectral range: $h\nu=0.8-1.6$ keV (10 μm Al filter), Photoresist: PMMA, distance from the plasma source = 2 cm, number of shots= 800; X-ray fluence= 2.5 mJ/cm^2 .

4.3 Radiobiology

At the typical energies of soft X-rays ($h\nu < 10$ keV), the photons are absorbed by the cells by photoelectric effect and the energy of the photoelectrons is released over dimensions comparable with those of the DNA (few nm). This causes very localised damage on the DNA, in contrast with the hard X-rays that damage a larger area, since the absorption process is mainly dominated by the Compton effect. Thus, irradiation with soft X-rays allowed to analyse the biological effects of very localised energy deposition events in cultured mammalian cells.

As far as it regards the X-ray photon energy choice, the S_{1k} region represents a good compromise for a small spatial range of energy deposition and a sufficient uniformity of the X-ray dose over a typical cell thickness (see fig. 1.a).

The X-ray fluxes appropriate for this study (few $\mu\text{J}/\text{cm}^2$) were obtained with few tens of laser shots on a copper tape target moved by a step motor. The experimental set-up was very similar to the one of the SXCM (Fig. 5), only that in this case the sample was placed at a distance of 20 cm, so as to allow uniform irradiation of the cells (grown as a monolayer on a 7 μm mylar foil of some squared centimetre area representing the basis of a special designed Petri dish). Even for this application the high transmission of the atmospheric pressure helium for the S_{1k} spectral region is being utilised.

The first results on the inactivation of the LN12 mouse cells are shown in Fig. 10. Work is in progress to achieve an accurate dose calibration in order to extract the relevant radiobiological parameters.

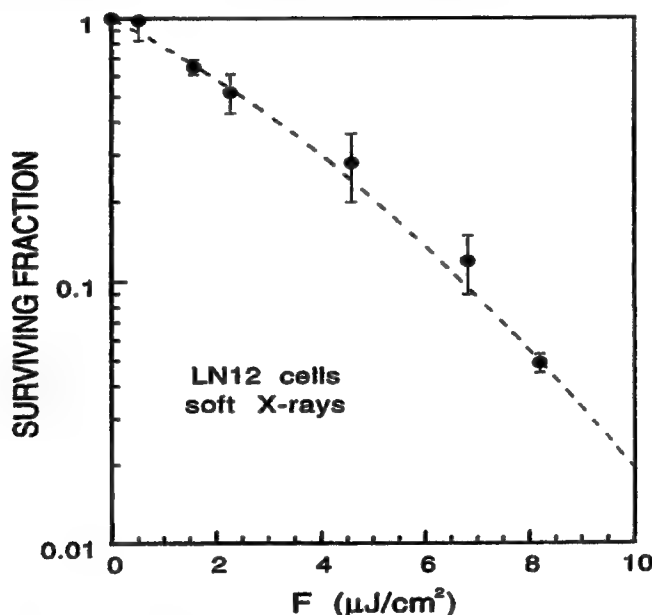


Fig. 10: Surviving fraction versus X-ray flux for LN12 cells.

4.4 Basic plasma research

The operation of the X-ray source in atmospheric pressure helium allows important applications to be undertaken in basic plasma research also. For example, it is possible to investigate the interaction between the plasma and a cold gas (helium) by measuring the X-ray emission versus the distance from the target. This has been done by using special spectrometers^{1,6} (based on spherical mica crystals, made by NPO VNIIFTRI Institute of Moscow) that give not only the spectrum but also a one-dimensional image of the X-ray source. In Fig. 11, the X-ray spectra obtained from a magnesium target at different values of helium pressure are shown. The spectrometer was aligned so as to obtain the sources image in the direction normal to the target. As it can be seen, the higher the helium pressure, the shorter the spatial length of the X-ray emission, but also the higher the emission for short distances. These results are still under investigation. A more detailed description can be found in⁸.

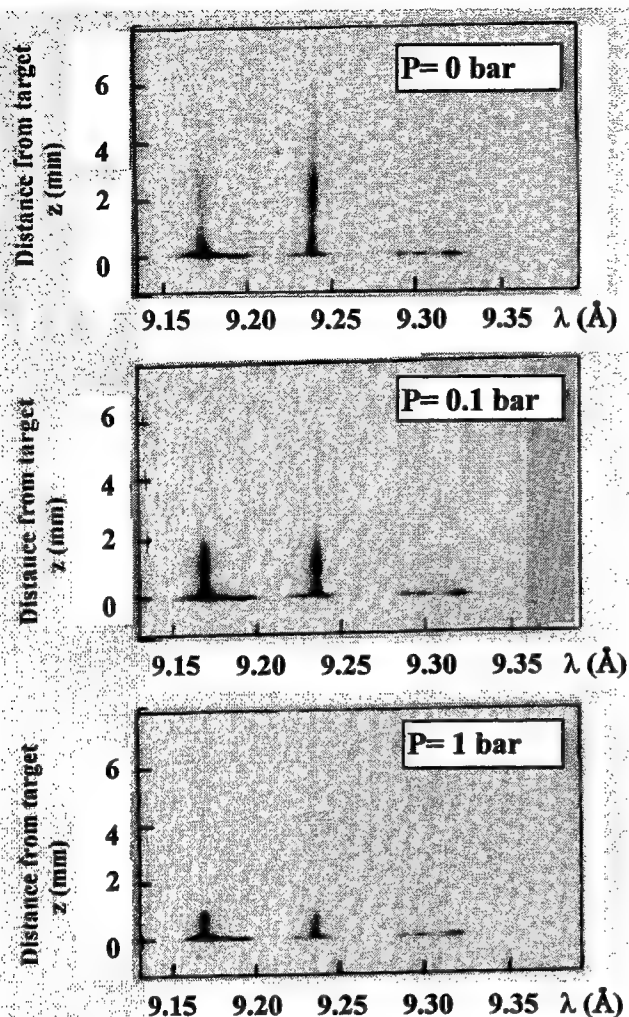


Fig. 11: Spectrum of Magnesium for different helium pressure values. Target: Mg 175 μm thick. Spectrometer: spherical mica crystal ($R=15\text{ cm}$) in 1-Dimensional imaging configuration. Laser configuration: 10 ns pulses, incidence normal to the target.

4.6 Near future experiments in microlithography

We are now approaching the imaging microlithography. A world-wide decision is to use for the imaging microlithography the $h\nu=100\text{ eV}$ photon energy range ($\lambda \approx 130\text{ Å}$), both because at this wavelength multilayer mirrors can reach considerably high reflectivity values (up to 70%) and because thin Beryllium filters can be used exploiting the K-edge spectral window. In our case, we exploited the L-edge window of Aluminium filters (50-72 eV) to avoid the use of toxic elements like Beryllium.

Using a multilayer mirror produced by the P. N. Lebedev Physical Institute (X-ray Optics Group) of Moscow we did our first experiment toward microlithography. Of course for this experiment we used the source configuration that maximises the emission in the S_{70} region, that is we used the 120 ns laser pulses with a Cu target placed at 1 mm from the laser beam waist (see Fig. 2b). After the reflection from the mirror protected by a $0.7\text{ }\mu\text{m}$ Al filter we measured, at the target normal, an X-ray flux of 2 mJ per steradian per shot in the spectral interval 64-72 eV. Considering the mirror spectral bandwidth (10%), the peak reflectivity (30%) and the Al filter transmission (20%), this flux is in good agreement with the data of Fig. 1.b and corresponds to a total emitted energy (in 10% bandwidth and 2π solid angle) of 0.1 J (assuming a $\cos^{0.75}(\theta)$ distribution of the X-rays).

CONCLUSIONS

Different applications of soft X-rays obtained from a plasma source pumped by an excimer laser were presented. In the water window spectral interval, a newly developed technique for SXCM is here proposed. With this new method, the use of a helium filled interaction chamber at atmospheric pressure enables a straightforward insertion of the samples in the chamber. As such, the long evacuation time needed for each sample to be imaged was successfully avoided. As it has been mentioned above, it is evident that the advantages of this new method are significant, with its potentials in need for further investigation. Moreover, the irradiation set-up of the plasma source has been successfully applied for radiobiological studies and microradiography experiments. The first results obtained with this method were satisfactory and work is being planned in this direction. Future research on the field is planned by utilising the phase contrast effect to obtain the images. Also experimental work on the shortening of the laser pulse to increase the conversion efficiency from laser energy to the S_{ww} and S_{1k} X-rays pulse energy and hence to enhance the X-ray flux is being currently carried out. This will allow a reduction of the bandwidth $\Delta\lambda/\lambda$ to 10% in the radiobiology application by cutting part of the S_{1k} range and thus will enable a more accurate relation between X-ray flux and dose to be achieved. Our first experiment toward imaging microlithography in the S_{70} interval gave excellent results and is well promising to reach a reliable X-ray source competitive with synchrotron storage rings.

ACKNOWLEDGEMENTS

We would like to thank the European Commission for the financial support for one of the researchers (K. Vigli-Papadaki) and for partly financing this project under the frame of the European Network "X-ray Microscopy". We also would like to thank Mr. Luigi Rossi for his essential contribute in designing and machining some mechanical components of the experimental set-up for the atmospheric pressure microscopy.

REFERENCES

1. S. Bollanti, R. Cotton, P. Di Lazzaro, F. Flora, T. Letardi, N. Lisi, D. Batani, A. Conti, A. Mauri, L. Palladino, A. Reale, M. Belli, F. Ianzini, A. Scafati, L. Reale, M.A. Tabocchini, P. Albertano, A.Ya. Faenov, T. Pikuz, A. Oesterheld, "Development and Characterisation of an XeCl Excimer Laser-Generated Soft-X-Ray Plasma Source and its Applications", *Il Nuovo Cimento* **18D**, *11*, pp.1241-1255, 1996.
2. S. Bollanti et al., "Characteristics of a soft X-ray plasma source for different pumping laser configurations and spectral analysis", *SPIE's 40th Annual meeting on Applications of Laser Plasma Radiation II*, S. Diego (Ca), USA, 9-14 July 1995, Vol. **2523**, p. 70, 1995.
3. M. Chaker, H. Pépin, V. Bareau, B. Lafontaine, I. Toubhans, R. Fabbro, B. Faral, "Laser- plasma X-ray sources for microlithography", *J. Appl. Phys.* **63**, p. 892, 1988.
4. R. Cotton et al., "X-ray contact microscopy using a plasma source generated by long and short (120 ns and 10 ns) excimer laser pulses", *SPIE's 40th Annual meeting on Applications of Laser Plasma Radiation II*, S. Diego (Ca), USA, 9-14 July 1995, Vol. **2523**, p. 184, 1995.
5. P. Albertano, L. Reale, L. Palladino, A. Reale, R. Cotton, S. Bollanti, P. Di Lazzaro, F. Flora, N. Lisi, A. Nottola, K. Vigli-Papadaki, T. Letardi, D. Batani, A. Conti, M. Moret, A. Grilli, "X-ray contact microscopy using an excimer laser plasma source with different target materials and laser pulse durations", *Journal of Microscopy* **187**, Pt.2, pp.96-103, Aug.1997.
6. S. Bollanti et al., "Long duration soft X-ray pulses by XeCl laser driven plasmas and applications", *Journal of X-ray science and technology*, vol. **5**, p. 261-277, 1995.
7. R. Cotton, J.H. Fletcher, C.E. Webb, A.D. Stead and T.W. Ford, "A Comparison of Laser Generated Plasma X-ray Sources for Contact Microscopy", *Proc. SPIE Conference on Application of Laser Plasma Radiation*, No **2015**, p. 86, 1993.
8. F.B. Rosmej, A. Ya. Faenov, T.A. Pikuz, I.Yu. Skobelev, A.E. Stepanov, A. N. Starostin, V.S. Rerikh, V.A. Makhrov, F.Flora, S. Bollanti, P. Di Lazzaro, T. Letardi, K. Vigli-Papadaki, A. Nottola, A. Grili, L. Palladino, L. Reale, A. Scafati, L. Reale, "Dominant role of dielectronic satellites in the radiation spectra of a laser plasma near the target surface", *JEPT Lett.*, v **65**, N *9*, 10 May 1997.
9. A. Reale, "Soft X-rays: Sources and Applications", *Proc. of the XXI Int. Conf. on "Phenomena in ionized gases"*, Ruhr Universitat, Bochum 19-24 September 1993.
10. B. Godard, P. Murer, M. Stehle, J. Bonnet, D. Pigache, "First 1 kW XeCl laser", *Proc. Int. Conf. on Lasers '93*, pp. 506-511, ed. by V. J. Corcoran, T.A. Goldman, STS Press, McLean, VA, 1994.

The power thermonuclear neutron source with double pulse KrF-laser.

1. G. Lebo, V. B. Rozanov, V.D.Zvorykin

Lebedev Physical Institute, Leninski pr.53, Moscow, Russia, 117924

ABSTRACT

Here we are discussing the feasibility to produce a powerful thermonuclear neutron source on the basis of double (long&short) pulses of KrF laser.

Keywords: KrF-laser, double (long&short) pulse, conical target

2. INTRODUCTION.

High efficiency and scalability of e-beam pumped KrF lasers, a large bandwidth and short UV wavelength of their radiation [1-3] as well as the potentiality for lasing with a pulse repetition frequency of several hertz [4] are very attractive to use such laser as a driver in laser fusion investigations. Moreover, a UV wavelength and a wide radiation spectrum are favorable for efficient absorption in plasma and suppression of plasma instabilities [5].

A small lifetime of the excited state of the KrF molecule ($\tau_c \sim 2\text{ns}$) gives no way of energy accumulation in an amplifier in a typical pump time $\tau_p = 100 - 500\text{ ns}$. Because of this it is common to use angular multiplexing of pulses with a desired duration ($\tau \sim 5\text{ ns}$) and a quasi-continuous amplification of the resulting train. In this case separate pulses travel through an amplifier in their own directions and then, after their path differences are counterbalanced, are simultaneously gathered at a single point on a target. Since the number of amplified pulses may reach several hundreds, such schemes contain a large number of mirrors and other optical elements considerably increasing the price of a set-up. (It is likely that a decrease of the number of beams by way of pulse summation on the basis of stimulated Raman scattering holds promise for tailoring special sharply edged time profiles of pulses which are required for adiabatic target compression) [2].

The hybrid (fusion-fission) system is a very promising approach for nuclear power plant [7-13]. As shown in [14,15], a KrF laser with a long ($\tau \sim 100\text{ ns}$) sharpened pulse can, in principle, be used to accelerate thin layers ("shock layers") in conical targets to the velocities of about 400 km/s (or two "shock layers" in two-sided conical targets flying toward one another with velocities of 200 km /s). In this case, a strike against a target containing the DT fuel might produce temperatures as high as 5-6 keV

and initiate a considerable neutron yield ($10^{16} - 10^{17}$ neutrons per pulse). The production of this neutron source is of interest for the studies in laser thermonuclear fusion (as a driver for hybrid nuclear-thermonuclear reactors) and various applied problems.

3. CONCEPT.

In [16] the scheme for separate heating and compression of fuel in conical targets was discussed. In recent years, the feasibility of separate compression of a thermonuclear fuel in spherical targets to high densities and heating it at a final stage has been discussed in the literature [17, 18]. This might, in principle, decrease the energy required to initiate thermonuclear reactions by a factor of 5-10. However, the question of a practical realization of this idea has not yet been solved.

We propose to accelerate thin envelopes and compress the fuel in conical targets with long pulses of a UV laser and subsequently heat the fuel and initiate thermonuclear reactions with short high-power pulses [19]. Moreover, we analyze the possibility of a simultaneous amplification of composite pulses (a long pulse -&- a short pulse) in a wide-aperture KrF amplifier. The feasibility of experimental tests of the given approach with the "GARPUN" KrF laser installation [20] is discussed.

A. Principles of formation of a composite pulse in a high-power KrF laser.

The amplification of long ($\tau \gg \tau_c$) pulses in the active medium of a KrF laser is described by three main parameters: the weak-signal gain g_0 , unsaturated absorption coefficient α , and saturation intensity I_s [1, 21]. The quantities g_0 and α are proportional to the specific pump power W in a unit volume of an active medium, whereas their ratio $\langle g_0/\alpha \rangle$ has only a weak dependence on W and ranges from 10 to 20. For the pump conditions that are typical of large-size amplifiers, $I_s \cong 1 \text{ MW/cm}^2$. The product $g_0 I_s$ determines the specific excitation power for the upper laser state of the KrF molecule, and the ratio $g_0 I_s/W = \eta_p \cong 0.25$ determines the excitation efficiency. The maximum efficiency of laser power extraction from the active medium is given by the expression $\eta_{\text{ext}} = [1 - (\alpha/g_0)^{0.5}]^2$, and therefore the laser efficiency $\eta = \eta_p \eta_{\text{ext}}$ is achieved for the radiation intensity $I_{\text{opt}} = I_s [(g_0/\alpha)^{0.5} - 1]$. For pulses with duration $\tau = 100 \text{ ns}$ and the range mentioned above for the ratio g_0/α , the optimum values of energy density $E_{\text{opt}} = I_{\text{opt}} \tau$ are equal to 220 - 350 mJ/cm^2 for $\eta_{\text{ext}} = 46 - 61\%$ and the efficiency of pump power conversion into radiation is $\eta = 12 - 15\%$.

In case of incoherent amplification of short pulses ($\tau < \tau_c$), the population of the excited state of a KrF molecule has no time to be restored by the pump, and the parameter I_s is replaced with the saturation energy density $E_s = I_s \tau_c \cong 2 \text{ MJ/cm}^2$ [2]. The optimum energy density $E_{\text{opt}} = E_s \ln(g_0/\alpha) = 4.6 - 6.0 \text{ MJ/cm}^2$ provides the highest efficiency of energy extraction from the active medium, which is given by the expression $\eta_{\text{ext}} = 1 - (\alpha/g_0)[1 + \ln(g_0/\alpha)] = 67 - 80\%$. Here, η_{ext} is the ratio between the radiation power increment on a unit amplifier length and the specific energy accumulated in a unit volume of the active medium. A single pulse takes down the inversion accumulated in a finite time τ_c . Because of this, the efficiency with respect to the total pump power that passed via the upper laser levels is low: $\eta_{\text{ext}} = (\tau_c/\tau_p) \eta_{\text{ext}}$.

In the case of amplification of a train of short pulses separated from one another by the interval Δt , which is comparable to τ_c , each subsequent pulse is amplified in a medium where inversion is not yet completely restored after the passage of a previous pulse. As a result, the gain is lower than that for a single pulse [22]. However, the efficiency of the laser energy extraction from the active medium is equal

$$\text{to } \eta_{ext} = \frac{1}{\Delta t / \tau_c} \left\{ \frac{[1 - \exp(-\Delta t / \tau_c)][1 - \exp(-\varepsilon)]}{1 - \exp(-\varepsilon)\exp(-\Delta t / \tau_c)} - \frac{\alpha \varepsilon}{g_0} \right\} \text{ and is higher due to a more complete use of the}$$

amplifier pump. Here $\varepsilon = E/E_s$ is the relative energy density in a separate pulse. The maximum efficiency is achieved for the energy density $E_{opt} = E_s \ln\{2\exp(-\Delta t / \tau_c) + (g_0/\alpha)[1 - \exp(-\Delta t / \tau_c)]^2\}$. For $\Delta t = \tau_c$, $E_{opt} = 3.1 - 4.3 \text{ mJ/cm}^2$ and $\eta_{ext} = 38 - 48\%$. In view of the fact that inversion still remains in the medium in the process of a long pulse amplification, one can use it for simultaneous amplification of short pulses. The expressions for optimum energy densities and intensities in this case can be obtained with allowance for the gain saturation with a long radiation pulse with the intensity of $I = I_{opt}$. This gives $g = (g_0 \alpha)^{0.5}$. Short pulses, in their turn, will modulate the gain of a medium and their radiation intensity in a long pulse. For single pulses, $E_{opt} = 0.5 E_s \ln(g_0/\alpha) = 2.3 - 3 \text{ mJ/m}^2$, $\eta_{ext} = (\alpha/g_0)^{0.5} \{1 - (\alpha/g_0)^{0.5} [1 + 0.5 \ln(g_0/\alpha)]\} = 10\%$. For a train with $\Delta t = \tau_c$ one obtains $E_{opt} = 1.4 - 1.8 \text{ mJ/m}^2$ and $\eta_{ext} = 5.4\%$. The simplest system is obtained provided a combination of a long pulse (100 ns) and a short pulse (10 - 100 ps) is amplified in final amplifier stages and focused onto a target along a single direction. In an active medium saturated with long pulses, amplified spontaneous emission, which determines the limiting amplifier size, is suppressed [4]. Moreover, the problem of contrast of short pulses, which imposes strong limits on the total gain of the whole laser system [2], becomes insignificant. Using beam multiplexing, one can transmit 10 such composite pulses through one large-size amplifier with an output aperture $\sim 10 \text{ m}^2$ and a pump pulse duration $\sim 1 \mu\text{s}$ [4] and obtain total energies of 220 - 350 kJ and 2.3 - 3.0 kJ in long and short pulses, respectively. To increase the fraction of energy contained in short pulses, one can decrease to a certain extent the radiation intensity in long pulses or use trains of short pulses that are preliminarily amplified in separate beams and thereafter combined with long pulses into a desired composite pulse.

B. Estimates of the parameters of a conical target.

Using 1D "Diana"-code simulations [23] we have shown earlier [19,24], that it would be possible to reach the velocity of high density plasma layer up 200-300 km/s into a cylindrical or conical channel with a help of long ($\tau \sim 100 \text{ ns}$) UV laser pulse. In [19] there has been considered double shell (or layers). conical target. An outer laser-accelerated layer ("shock layer") moves along a conical channel with the length of the order of 1 cm. A layer of DT ice (or a porous material filled with a DT liquid) is found at the top of the cone. A shock wave formed by the "shock layer" produces preliminary heating and compression of the fuel. As the "shock layer" flies closer, the fuel compression increases and the cone walls become deformed. An additional fuel heating by the second part of a composite pulse ($E_2 \approx 10 \text{ kJ}$) makes it possible to increase the neutron yield by 5-10 times in such systems. The 1D numerical simulation has shown that the neutron yield is up $10^{16} - 10^{17}$ for the laser energy of 0.3-0.5 MJ and DT-mass $\sim 50 - 100 \mu\text{g}$. The maximum fuel density exceeded 10 g/cm^3 , the average density was about $3 - 5 \text{ g/cm}^3$ and the fuel temperature $\approx 4 - 6 \text{ keV}$.

Note that an additional energy supply to the fuel through dense layers of the shell and stable acceleration of the shell in conical channels are the problems that have not yet been solved for the system under study.

4. Parameters of experimental installation "GARPUN" and the results of 2D numerical simulations of laser plasma accelerations through the channels.

Really, we have a KrF-laser system "GARPUN" with the following parameters:

Gas mixture	Ar/Kr/F2=(90-95)/(5-10)/(0.1-0.3)
Total pressure	1.25-1.75 atm
Active volume	16x18x100 cm
e-beams current density	2x50 A/cm ²
Acceleration voltage	350 kV
Pumping energy	2 kJ
Laser beam peak power	1 GW
Lase pulse duration	100 ns
Intensity in focal spot	5×10^{12} W/cm ²
Diameter of focal spot	150 μ m

The laser energy in a long pulse is $E_1 \approx 100$ J, and it would be possible to get $E_2 \approx 3-5$ J in a short pulse (with $\tau_2 \sim 10-50$ ps).

Using 2D Euler code "NUTCY" [25] in cylindrical coordinates (r, z, t) we have made a series of numerical simulations modeling the acceleration of thin CH-film (thickness $d = 50$ μ m, initial density 1 g/cm³) through the cylindriical channel (radius $r_d = 80$ μ m and length $L = 1.5$ mm). The copper wall had the initial density 8.93 g/cm³, and thickness 0.4 mm. The laser flux $q(t, r) = q_1(t) * q_2(r)$. $q_1(t)$ had a linear growth up to 100 ns and laser energy was 120 J.

In variant 2_01(Gaussian distribution in the focal spot): $q_2(r) = \exp(-(r/R_f)^2)/C$, $C = 0.5 * R_f^2 * (1 - \exp(-R_0/R_f)^2)$. R_0 is the right boundary; in variant 2_02 ("ideal focal spot"): $q_2(r) = 1/C$ if $r \leq 80$ μ m, $C = 0.5 * R_f^2$; and $q_2 = 0$ if $r > 80$ μ m. Fig.1a (left side) illustrates the isodensity lines of shell at the moment 27.4 ns (variant 2_01). The uper part of the wall is deformed as the result of the high pressure and temperature of the plasma in corona . In the right side of Fig.1b,c there are shown the density distributions of plasma along the axis at the moments $t = 22.4$ ns and $t = 27.4$ ns. To the moment $t = 27$ ns the CH-layer is destroyed, and laser beams come through the plasma.

Fig.2 illustrates the results of 2D simulations of CH-layer acceleration for the variant 2_02. The high density layer comes through the channel with an average velocity of about 30 km/s. The velocity of high density layer ($\rho > 0.1$ g/cm³) is about 50 km/s to the moment 47.5 ns (when the layer come out from the channel) (see Fig.2 c,d).

Thus, our first 2D simulations shows, that it is possible to accelerate the thin layer through the channel using "ideal focus" of laser beam. Really, it is a very difficult problem, and it requires a subsequent theoretical and experimental investigation.

5. Conclusion.

In conclusion, we note that several questions of principal importance for the system under consideration can be tested with the "GARPUN" KrF laser installation. The questions of primary importance are the simultaneous amplification of the long and short pulses, the feasibility of stable acceleration of thin layers in cylindrical and conical channels up to the velocities of the order of 100 km/s, and the interaction of short pulses with a dense plasma.

REFERENCES

1. A. G. Molchanov, "Theory of active media of excimer lasers", Trudy Fiz. Inst. im. P. N. Lebedeva AN SSSR, vol. 171, p. 54, (1986).
2. M. J. Shaw, Laser and Particle Beams, vol. 9, p. 309, (1991).
3. J. A. Sullivan, G. R. Alien, R. R. Berggren, et al., Laser and Particle Beams, vol. II, p. 359, (1993).
4. V. N. Smiley, Proc. SPIE, vol. 2, p. 1225, 1990
5. M. J. Shaw, R. Bailly-Salins, B. Edwards, et al., Laser and Particle Beams, vol. II, p. 331, (1993)
6. S. P. Obenschain, S. E. Bodner et al. Phys. Plasmas, v. 3, p. 2098, (1996)
7. L. P. Feoktistov, E. N. Avrorin et al. Sov. J. Quantum Electron., 8, 201, 1978
8. N. G. Basov, A. E. Sheindlin et al., Izv. Akad. Nauk SSSR, Energ. & Transport, (2) 3, (1979)
9. N. G. Basov, R. R. Grigoriantz et al., Preprint N214, Moscow, Lebedev Phys. Inst., Academy of Sciences of USSR, (1983).
10. N. G. Basov, N. I. Belousov et al. Sov. J. Quantum Electron, 15, 380, (1985)
11. N. G. Basov, N. I. Belousov et al. Sov. J. Quantum Electron., 17, 1324, (1987)
12. E. O. Adamov, N. G. Basov et al. Preprint N72. Moscow: Lebedev Phys. Inst., Academy of Sciences of the USSR, (1988)
13. N. G. Basov, V. I. Subbotin, L. P. Feoktistov Vestn. Ross. Akad. Nauk, 63, 878, (1993)
14. L. P. Feoktistov, I. G. Lebo, V. B. Rozanov, and V. F. Tishkin, Proc. SPIE, vol. 2770, p. 190, (1995).
15. N. G. Basov, I. G. Lebo, et al. Sov. J. Quantum Electron., 28, 316, (1998)
16. L. P. Feoktistov, Horizons of Laser Thermonuclear Fusion, in Future of Science [in Russian], Znanie, Moscow, (1985).
17. N. G. Basov, S. Yu. Gus'kov, and L. P. Feoktistov, J. Sov. Laser Research, vol. 13, p. 390, (1992).
18. M. Tabak, J. Hammer, M. E. Glynsky, W. L. Kruer, et al., Phys. Plasmas, vol. I, p. 1636, (1994).
19. V. D. Zvorykin, I. G. Lebo, V. B. Rozanov Bull. of Lebedev Phys. Inst. N9, 15, (1997), Allerton Press, Inc., NY
20. V. D. Zvorykin, High-power multistage KrF laser system ^GARPUN^. Technical Digest of 8th Laser Optics Cent., St Peterburg, p. 144, (1995).
21. Excimer Lasers, ed. C. K. Rhodes [Russian translation], Mir, Moscow, (1981).
22. C. J. Hooker, I. N. Ross, and M. J. Shaw, Annual Report of Rutherford Appleton Laboratory RAL-87-041, p. 226, (1987).

- 23 N. V. Zmitrenko, V. Ya. Karpov, A. P. Fadeev, and G. V. Shpatakovskaya, in Problems of Atomic Science and Engineering., ser. Methods and Programs of Numerical Solution of Problems of Mathematical Physics [in Russian], vol. 2, p. 38, (1982).
24. I. G. Lebo, V. B. Rozanov, G. V. Shpatakovskaya., V. D. Zvorykin, J. Russ. Laser Research, 18,147, (1997)
25. I.G.Lebo, V.B.Rozanov, V.F.Tishkin, V.V.Nikishin, In Proc. of 6-th Workshop on The Physics of Compressible Turbulent Mixing, Institut Universitaire des Systemes Thermiques Industriels, Marseille, 18-21 June 1997, France, p.312

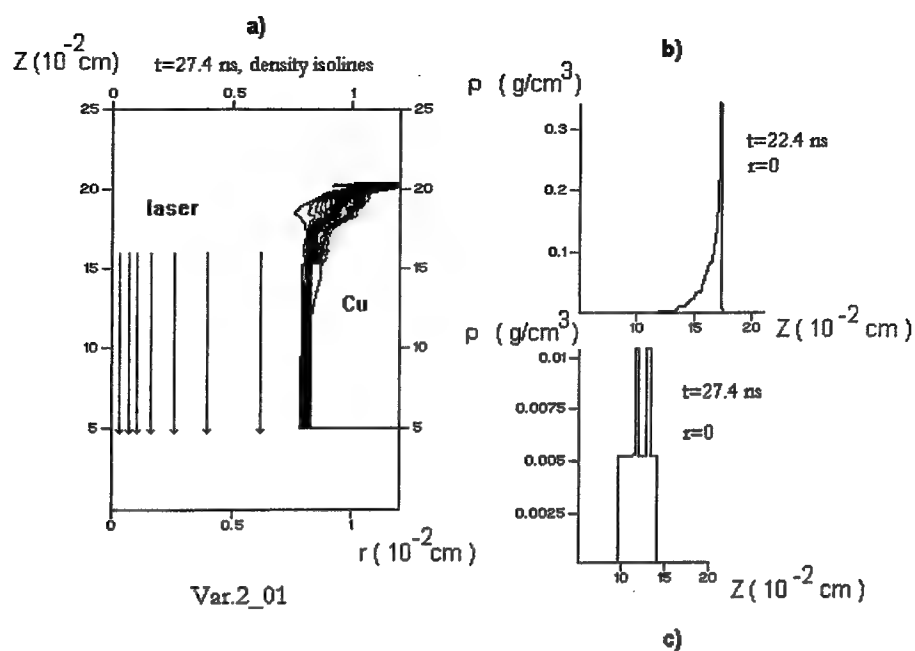


Fig.1

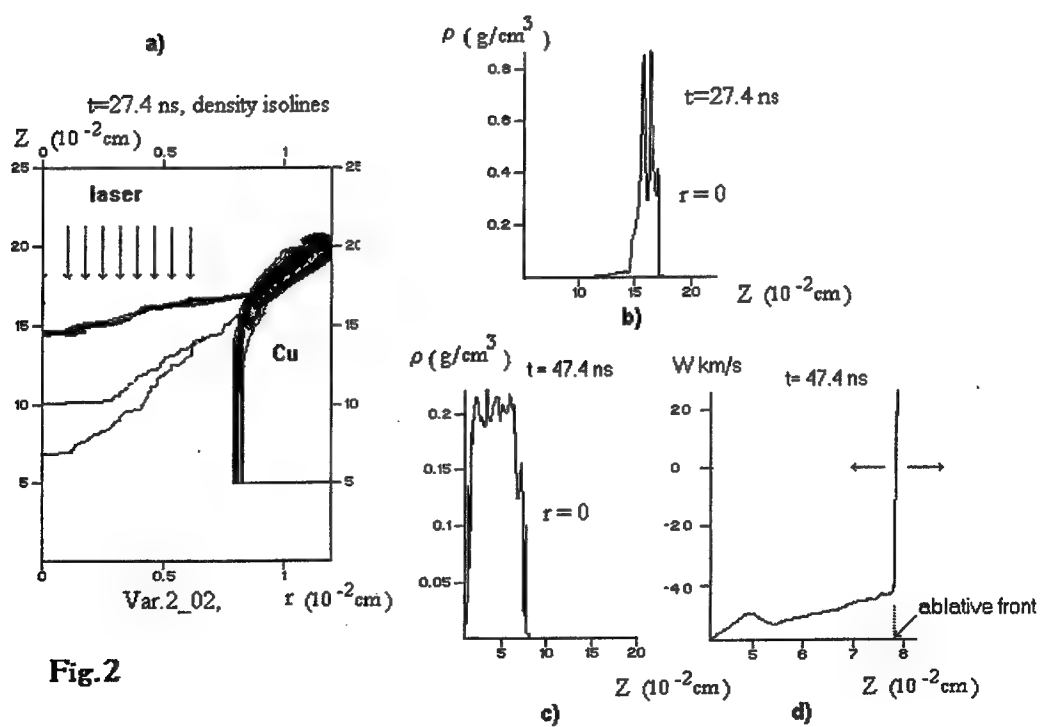


Fig.2

Preliminary Design of The Spatial Filters Used in The Multi-pass Amplification System of TIL

Zhu Qihua, Zhang Xiaomin and Jing Feng

Laboratory for Laser Fusion
Institute of Nuclear Physics and Chemistry
China Academy of Engineering Physics
(P.O.Box 525-80, Chengdu 610003, China. Fax: 86-816-2271598)

Abstract

The spatial filters are used in Technique Integration Line (TIL), which has a multi-pass amplifier, not only to suppress parasitic high spatial frequency modes but also to provide places for inserting a light isolator and injecting the seed beam, and to relay image while the beam passes through the amplifiers several times. To fulfill these functions, the parameters of the spatial filters are optimized by calculations and analyses with the consideration of avoiding the plasma blow-off effect and components damaging by ghost beam focus. The " ghost beams " are calculated by ray tracing. A software was developed to evaluate the tolerance of the spatial filters and their components, and to align the whole system on computer simulantly.

Key words: spatial filters, plasma blow-off effect, ghost beams, tolerance, system alignment

1. Introduction

The spatial filters used in Technique Integration Line (TIL), which has a multi-pass amplifier, are now being designed. The spatial filters can not only suppress parasitic high spatial frequency modes but also relay image while the beam passes through the amplifiers several times. They are used to enlarge the diameter of the beam and to provide places for inserting a light isolator and injecting the seed beam. Figure 1 is a simplified diagram showing the layout of TIL. There are two spatial filters in the main amplifying stage. The seed beam is injected from the cavity spatial filter near its focus.

So far, the design of the spatial filters has not fulfilled. In this paper, several aspects considered during the design of the spatial filters will be simply introduced.

Schematic of the Technical integration Line (TIL)

Amp.: Disk Amplifier module
 CM: Cavity Mirror
 SF: Spatial Filter
 PA: Pinhole Array
 CH: Collimating Hole
 SM0: Sampling Mirror
 FC: Frequency converter
 TC: Target chamber
 T: Target

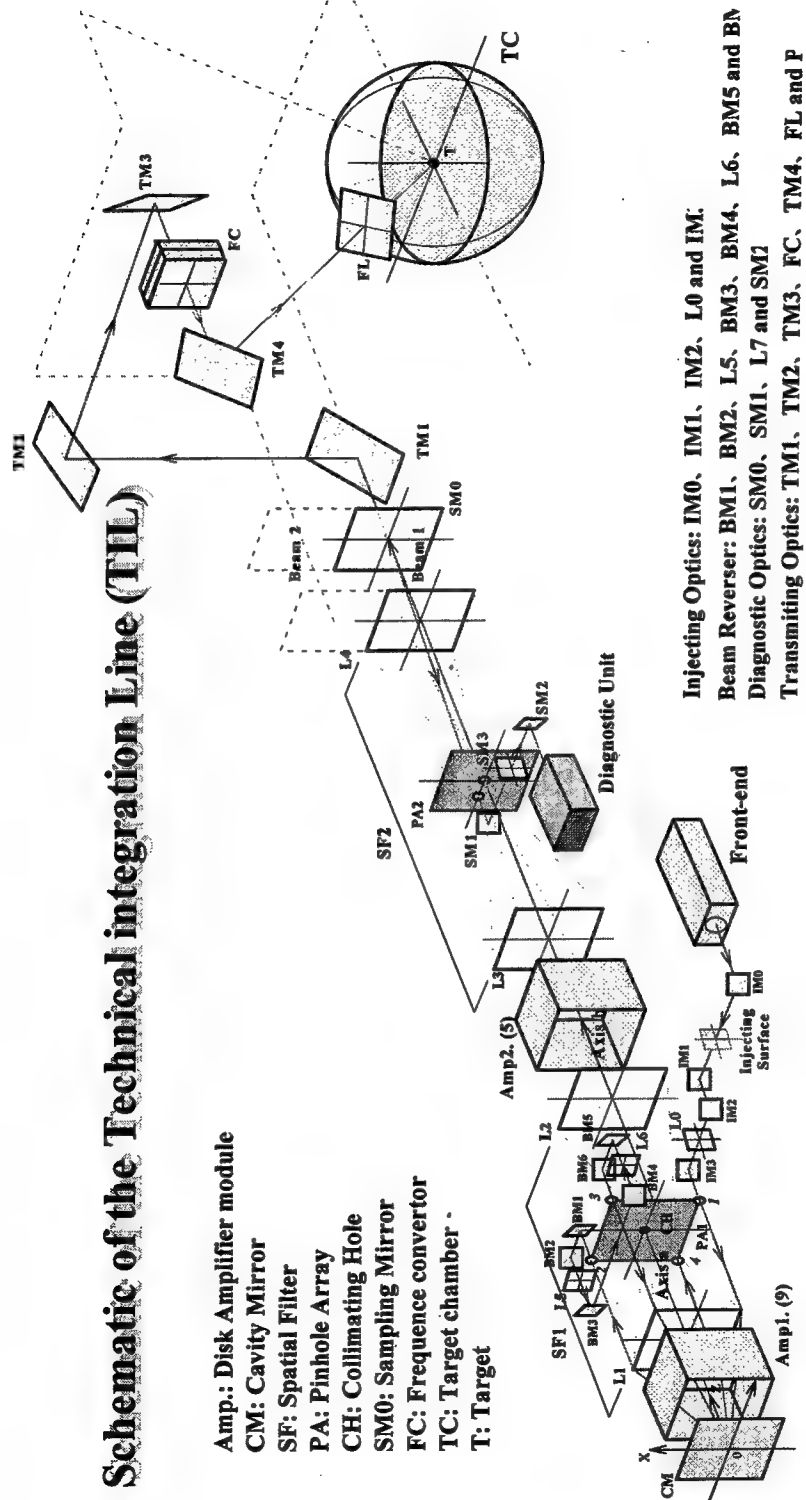


Figure 1. The Schematic Layout of TIL

2. Determining The Diameters of the Pinholes

The diameters of the pinholes will directly influence the filtering effect. The cut-off frequency of a pinhole is

$$\nu_{cut} = \pi d / (\lambda f) \quad (2.1)$$

where ν_{cut} is the cut-off frequency of the pinhole, d is the diameter of the pinhole, λ is the wavelength of the beam and f is focus length of the lens.

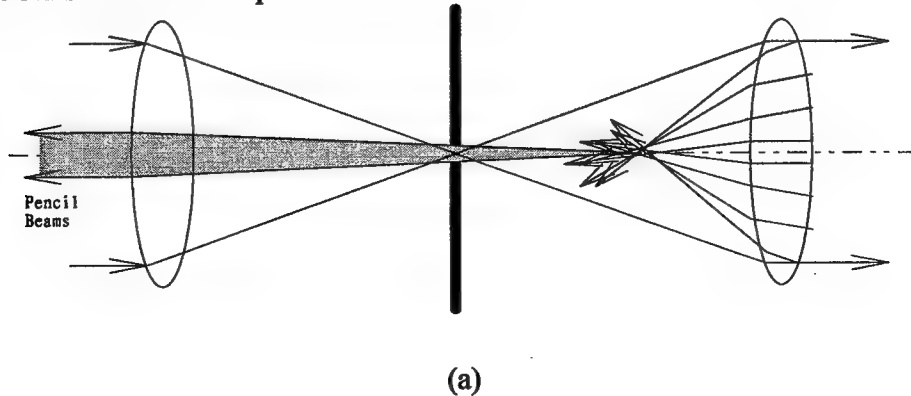
The intensity of the beam at the pinhole region is very high, any kind of pinhole material will generate a plasma, which expands into the pinhole and will refract and absorb the light significantly. It will introduce spatial modulation and will make the transmission efficiency lower. A reported velocity of the plasma ranges from 0.1 to 0.5 mm/ns^{1,2}.

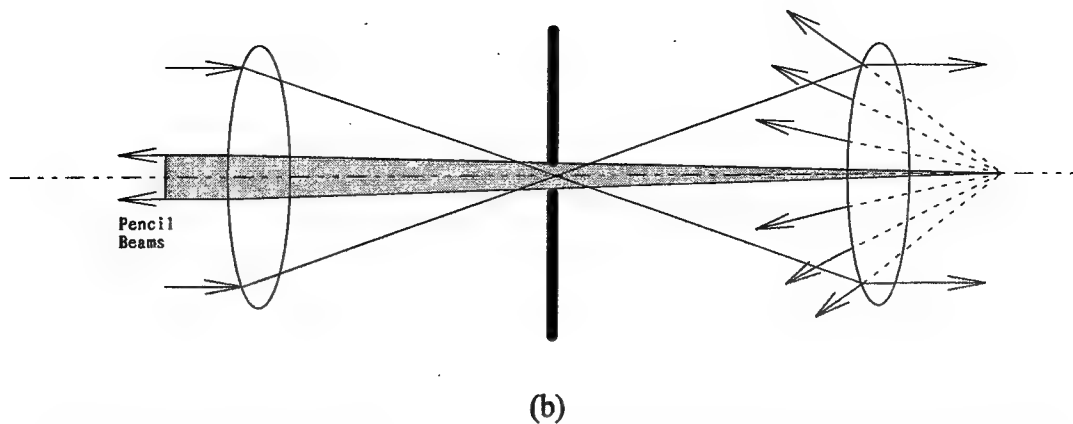
With the velocity (use the largest velocity 0.5mm/ns) and the time width of the beam, the minimum diameter of the pinhole can be determined. In fact, the real diameter is larger, because refraction occurs before complete closure. The diameter of the pinhole is selected so that the transmitted near-field beam profile will not be changed significantly.

After determining the diameters of the pinholes, the cut-off frequency of the spatial filter can be calculated from formula 2.1.

3. Calculation of The Ghost Beams And Elimination of The Pencil Beams

Ghost beams are the reflected beams from the surface of the spatial filter lens. The energy of the focus of these beams is high enough to damage the optic components. Clipping by the spatial filter pinholes, these beams form pencil beams. Figure 3.1 shows how the pencil beams formed.





(b)

Figure3.1 Pencil Beams Formed from The Reflected Beams from The Surface of The Spatial Filter Lens

Pencil beams pass through the system, their energy will be amplified for several times. On the one hand, the foci of them will damage optic components, on the other hand, the pencil beams may form pre-pulse which reaches the target before the main pulse. This will do great harm to the target and so the pencil beams must be eliminated.

The ghost beams are ray-traced through the system in order to determine the position of their foci, and to know which of the ghost beams will form pencil beams.

With the help of ray tracing, the ghost beam foci can be kept away from the optic components by changing the parameters of the spatial filter lens. The best way to eliminate pencil beams is to tilt the spatial filter lens for a small angle though this will cause some aberrations. After a tilting angle is selected, the ghost beams must be traced to see whether the pencil beams have been eliminated, and the aberrations caused by lens tilting must be evaluated.

4. Evaluating The Tolerance

When the spatial filter lens are fabricated, there exist some errors. The parameters of the fabricated lenses can not be exactly what we want. When the spatial filters are built, there will also exist some errors. So, before the spatial filters are built, the tolerances of each optic component must be first given out. The tolerance should better to be given out according to the manufacturing level of China in order to make the costs lower. But the tolerance must be evaluated, so that it meets our needs.

For this purpose, we developed a software named SG-III/4P. This program was developed not only for spatial filters but also for any other optic systems. It can be used to trace rays. For an optic system, given the position and direction of the input beam, the program can output the position and direction of the beam at any plane along the optic axis. It allows the optic components to shift in three dimensions and to rotate around the three axes. It can also give out random tolerances for each component which makes the simulation more accurate.

So, this program can be used to evaluate whether the tolerances we gave are reasonable. And, we plan to revise the interfaces of this program so that it is more convenient to use, and to enhance its functions so that we can easily use it to align the spatial filters especially the main amplifying stage simultaneously on computer. This will be very useful especially on the stage of research and design of system alignment.

5. Conclusions

The spatial filters used in the multi-pass amplification system of TIL are now being designed. During the design of them, the plasma blow-off effect of the pinholes are considered, the ghost beams and their foci are calculated with ray tracing, pencil beams are eliminated by tilting the spatial filter lenses for small angles, a code was developed to evaluate the tolerance of the spatial filters and their components and it can also be used to align optic system on computer simultaneously.

6. References

1. J.S.Pearlman, J.P.Anthes, " Closure of pinholes under intense laser radiation " , Applied Optics 16,8,8/77,2328-31.
2. J.M.Auerbach, N.C.Holmes, J.T.Hunt, G.J.Linford, " Closure phenomena in pinholes irradiated by Nd laser pulses " , Applied Optics 18,14,7/15/79,2495-99.

Preliminary design of main amplification stage of Technical Integration Line (TIL) for SG-III laser facility

F. Jing, X.M. Zhang, Q.H. Zhu, Y.Z. Man and H.S. Peng

Laboratory for Laser Fusion
Institute of Nuclear Physics and Chemistry
(P.O.Box 525-80, Chengdu 610003, China.)

ABSTRACT

Technical Integration Line(TIL) is the full scale two-beam prototype for Shenguang-III laser facility(SG-III). A four pass amplifier system with small aperture beam reverser has been designed as the main amplification stage for TIL, which will produce 1 kJ of UV radiation on the target from each beam in 1~3 nanoseconds shaped pulses. Two schemes were considered in the preliminary design, one of them employed only small aperture Pockels cell in the reverser, and the other used another larger plasma electrode Pockels cell(PEPC) in the main beam line. Simulated by a fast-running lumped-element computer code, the configuration of baseline scheme for TIL was settled. The basic requirements for optical elements were raised during simulation processing.

Key words: Nd:glass lasers, ICF drivers, SG-III laser facility

1. INTRODUCTION

Technical Integration Line(TIL) laser system which is the prototype for Shenguang-III laser facility(SG-III), the next generation driver for Inertial Confinement Fusion(ICF) in China, has been designed to adopt a four-pass amplification system with a beam reverser^[1]. By the requirement of the total design for TIL, each beam should have the ability to produce approximately 3.0kJ output energy in fundamental frequency in a 1~3ns pulse. In TIL, the 4×2 array amplifiers will be adopted in the main amplification stage to demonstrate all technologies which will be applied to SG-III. In the scheme, the amplifiers will be grouped in two parts, which are four-pass amplifiers and booster amplifiers, respectively. This configuration decision was made according to the results of preliminary cost evaluation among several main amplifier stage schemes. As a backup scheme, a moderate aperture PEPC will be adopted in the place near the reflective mirror and the booster amplifiers.

2. DETERMINATION OF BASIC PARAMETERS

According to the total design requirement for TIL, each beam should have the ability to produce 3.0 kJ energy in pulse with fundamental frequency. Take into account the damage threshold for large aperture optical elements in China was limited to 5 J/cm^2 in 1 nanosecond pulse, the output beam aperture should be more than 600 cm^2 . So the beam aperture in final stage amplifier was set to $25 \times 25 \text{ cm}^2$, thus required the aperture of amplifiers no less than $30 \times 30 \text{ cm}^2$ if the thermal distortion in the edges of Nd:glass slabs and alignment allowance and vignette allowance were considered. This choice was also coinciding with the optics processing ability in China today.

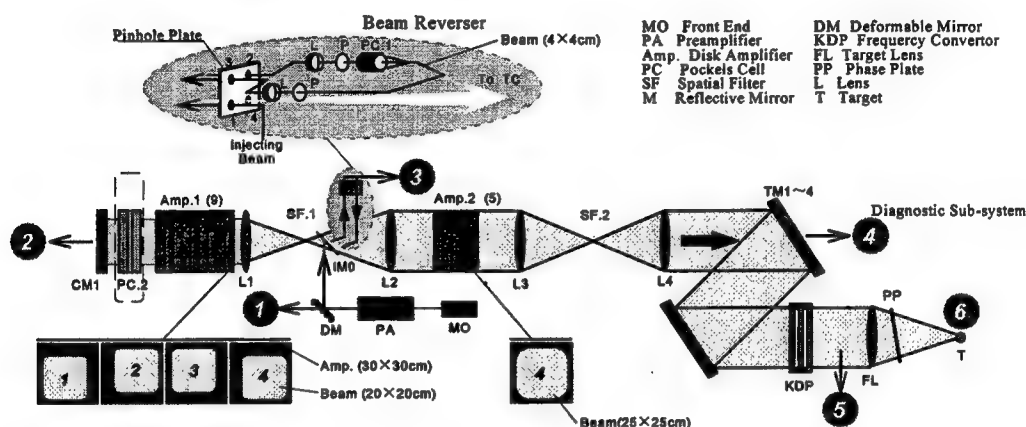


Figure 1. Optical layout of TIL

The optical layout diagram of TIL is depicted in Figure 1. The scheme we choose is a LMJ-like^[2] but have several merits. The filling factor of the booster amplifier is promoted by injecting the seed beam through the spatial filter in the four-pass amplifier(SF1). This change of injection place will rise the requirement for the input energy, but decrease the risk of self-lasing because of the lower total gain of the system. The axes of amplifiers and spatial filters in the system are parallel for an easy system alignment. The design also decreases the number of large aperture reflective mirrors and polarizers, and thus saves the cost.

The moderate aperture($24 \times 24 \text{ cm}^2$) PEPC will be placed into the four-pass amplifier when further experiments show that the small aperture Pockels cell in the beam reverser is not enough to isolate the whole system from parasitical oscillation. In this case, two characteristics of the system performance should be specified. At first, beam apertures on the PEPC is only $20 \times 20 \text{ cm}^2$ and it works under static conditions that decreases the requirement for the PEPC development. In the second, the insertion of the PEPC dose not affect the performance characteristics obviously except

for a little energy loss, which can be compensated by increasing of injecting energy. So we did not pay more attention to this scheme, and all discussions were based on the scheme with only a small aperture Pockels cell.

3. DETERMINATION OF SYSTEM CONFIGURATION

The optimization of main amplifier stage is the key point to make the design with a very good cost/performance ratio. The design optimization in present time is to configure the main amplifier stage. By simulations, the reasonable configuration was chosen and system performance was analyzed. These results will rise the requirement for the optical components or elements which will be employed in main amplifier stage of TIL.

To complete this work, two sets of computer codes were development in LLF. One code is a fast-running lumped-element program. This code does not include any detailed spatial information of beam and amplifiers, but can give the B-integral for each optical element. Amplifiers were taken as the Frantz-Nodvik types, and the gain recovery effect of amplifiers was also included^[3]. A two-dimensional code was also developed for simulation the beam propagated through saturated amplifiers and the other optical elements with phase distortion that cause the intensity modulations in the beam cross section and wave front distortion that decrease the frequency conversion efficiency and the energy focused on the target. After preliminary estimation, the conclusion was made that 12 ~14 slabs had enough stored energy for extraction of about 3000 Joules in fundamental frequency.

Cost evaluation was done firstly for the laser system used a simple model which dealt with the final stage of amplifier in the same type and same aperture. For different schemes, the requested drive pulse energy is varied to have the identical output for the facility and thus the cost of drive stage is quite different. In comparison with a MOPA system, double-pass and four-pass configurations needed smaller drive stages. The configuration of the system means a type of the arrangement of the slab numbers in the four-pass amplifier and booster amplifier with their specifications. A four-pass configuration with 12 slabs was the most economic one, and then in the second was the configuration with 14 slabs. So our further simulations will focus on the schemes of four-pass amplifier with 12 or 14 slabs.

To eliminate the gain nonuniformity caused by leaking of the pump light at the ends of amplifiers, odd-numbered slabs were placed both in the four-pass amplifiers and booster amplifiers. So we got 5 basic configurations for further evaluation : S1(9-5), S2(7-7), S3(11-3), S4(9-3), S5(7-5).

During the simulation process, several design parameters were fixed. The parameters of the phosphate neodymium-doped glass was not changeable. Beam aperture in four-pass amplifiers and booster amplifiers were fixed at $20 \times 20 \text{cm}^2$ and $25 \times 25 \text{cm}^2$, respectively. The loss coefficients for all types of the optical elements were fixed, too. The parameters of amplifiers, such as the thickness of the Nd:glass slabs and the stored energy density were assumed to be known and were adjustable among several sets of fixed values. The arrangement of the components or position of the main

elements was fixed. The focal lengths of input lens and output lens of SF1 were 900cm and 1125cm, respectively. The small signal gain coefficient was set to 0.05cm^{-1} when thickness of the slabs was set to 4 cm. Beam intensity modulations control were limited to a peak/average ratio no more than 1.5:1 and beam intensity used for calculation of the B-integral was 1.5 times the average value.

Following constraints were obeyed during simulations:

1. Output energy was 2.8kJ (1 ω) in 3ns rectangular pulse;
2. Increments of B-integral between pinholes of spatial filters meet the requirement of $\Delta B \leq 2$;
3. Damage thresholds of optical elements(1 ω , 1ns rectangle) were set as follows: Large aperture elements($30 \times 30\text{cm}^2$) $\sim 5.0\text{J/cm}^2$, and small aperture element ($\Phi 10\text{cm}$) $\sim 10.0\text{J/cm}^2$.

To produce square pulses from the amplifier system, shaped pulses are needed at the injection place. In TIL scheme, quasi-rectangular output pulses can be obtained by injecting pulses in exponential shapes.

The simulation results for the fluency distribution of all 5 configurations with 3 nanoseconds pulses are in Figure 2. Figure 3 shows the B-integral increments between pinholes of spatial filters for each configuration. All the results are listed in Table 1. The denoted figures indict the performance parameter of the scheme which are out of the above-mentioned constraints.

The simulation results show that S1(9-5) and S2(7-7) configurations are the possible arrangements for TIL, because they have smaller ΔB to avoid running the risk of filamattention and energy damage to the elements in beam reverser. Further simulations for analysis of parameter sensitivity show that S1 has much better characteristics for power balance, and it need less injection energy and has a smaller fluency at the beam reverser. So S1 has been chosen as the baseline scheme for TIL.

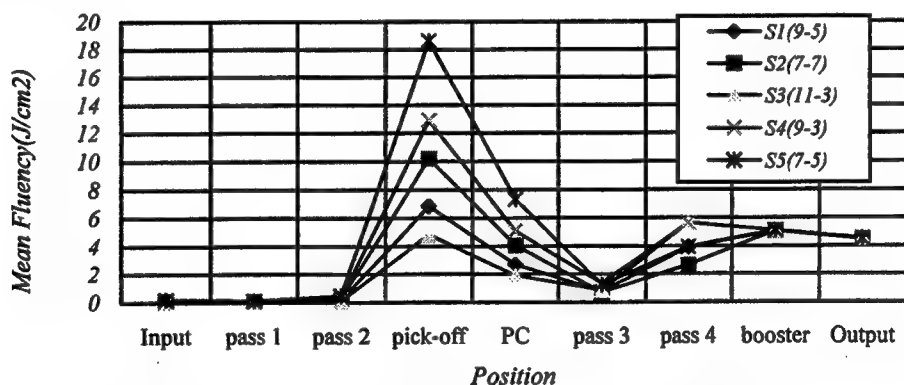


Figure 2. Fluency distributions for different configurations

Simulations have been done for S1 with a 1 ns pulse. Unfortunately, risk of filamattention limits the output energy to no more than 2 kJ. So thinner slabs are required for short pulses performance. The simulation results show when the thickness of the slabs decreases to 3.2cm, the output energy can increase about 20%.

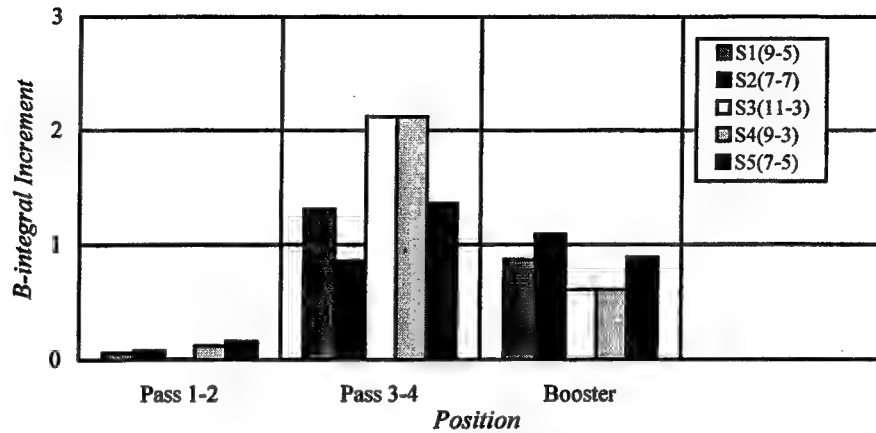


Figure 3. B-integral increments between pinholes for different configurations

Table 1. Simulation results of 5 schemes for 3ns square pulses

Scheme	$E_{in}(J)$	Input CR	$E_{out}(J)$	Fluency at reverser (J/cm^2)	ΔB at 3 rd - 4th passes	ΔB at Booster
S1(9-5)	1.41	0.27	2796	6.84	1.31	0.87
S2(7-7)	5.25	0.28	2798	★10.2	0.86	1.09
S3(11-3)	0.4	0.22	2822	4.83	★2.12	0.61
S4(9-3)	2.7	0.22	2813	12.9	★2.12	0.61
S5(7-5)	9.8	0.25	2810	★18.6	1.36	0.89

Two-dimensional beam propagation code was used to analyze the performance of the system and some beam parameters were determined. These parameters included the width of beam edge soften length, pre-shaping for the beam spatial distribution to compensate the nonuniformity of the beams caused by gain distribution of the amplifiers, etc. The results showed that the effect of the gain distribution of the amplifiers was not so remarkable as that on Beamlet^[4] because of the lower total gain, but the soften length at least 5% of the aperture was necessary to suppress the hard aperture diffraction.

Further simulations are still being done, which include the transmission phase distortions of the optical elements.

4. CONCLUSION

In the TIL scheme of four-pass amplifier with a beam reverser and booster amplifier, S5(7-5) with 12 Nd:glass slabs is the cheapest configuration but has a largest fluency at the place of beam reverser. S1(9-5) is little more cost than S5, but is preferable in performance, so we choose it as the baseline design of TIL.

The performance of TIL under short pulses(1 ns) will be further optimized.

5. REFERENCES

1. X.Zhang, et al, "Preliminary Design of Technical Integration Line (TIL) for SG-III Laser Facility," see this proceedings.
2. M.L.Andre, "Status of the LMJ project," *Proceedings of SPIE*, Vol. 3047, pp.38-42, 1996
3. W.H.Lowdermilk and J.E.Murray, "The multipass amplifier: Theory and numerical analysis," *J. Appl. Phys.* 51(5), pp.2436-2444, 1980.
4. B.M.Van Wonterghem, et al, "System description and initial performance results for Beamlet," *LLNL ICF Quarterly Report*, Vol.5, No.1, pp.1-17,1994

Study of efficiency of the thermonuclear burning in laser targets with spark ignition.

A.A. Andreev ^a, D.V. Il'in ^b, A.A. Levkovskii ^b, V.E. Sherman ^b, and O.B. Vygovskii ^b

^a S.I. Vavilov State Optical Institute, 12, Birzhevaya, St.-Petersburg, 199034, Russia

^b St.-Petersburg Institute of Machine Building, Department of Physics, 14, Polustrovsky St.-Petersburg 195108, Russia.

ABSTRACT

Numerical simulation of thermonuclear flash with isobaric ignitor for laser spherical targets with different dimensions and temperatures are performed and the target energy gain as a function of ignitor parameters is obtained. As a result the requirements for ignitor parameters are elaborated under which the spark ignition provides an essential increase in the gain as compared with volume ignition. Calculations are carried out with the use of TERA code based upon self-consistent solution for system of kinetic equations for thermonuclear particles and radiation, obtained by the Monte Carlo method, and of hydrodynamic equations.

Keywords: laser target, spark ignition, thermonuclear burning, energy gain

1. INTRODUCTION

To elaborate the requirements for laser pulse parameters in laser confinement fusion plants it is necessary to know the required parameters of thermonuclear (TN) target reached under target implosion. It is well known that the volume ignition of TN burning in homogeneously heated and pressed target is resulted with relatively low energy gain. The spark ignition of target^{1,2} by possible generation of a TN burn wave from a relatively small region of high temperature (ignitor) can substantially increase the burning efficiency. By means of this mechanism relatively cold targets may be ignited and as a result the laser pulse energy may be decreased essentially.

To produce the supersonic TN burn wave during the target lifetime, the ignitor temperature and dimension should be not too low. The relationship between the ignitor parameters and target burning efficiency was considered in our previous papers^{3,4} in the frame of semianalytical approaches (the list of references concerning the analytical, semianalytical and numerical calculations of TN burn wave in different approximations is given in these papers as well). The principal availability of ignition was studied in^{3,4} rather than numerical value of energy gain. The increase in ignitor temperature T_f ³ or, more generally, in ratio T_f/T_a ⁴ at initial conditions was chosen as the criterion of spark ignition (here and all through the report index f corresponds to the ignitor, index a - to the surrounding fuel).

As it was mentioned in^{3,4} this increase is a sufficient, but not a necessary condition. Numerical calculations in^{5,6} show that under for certain initial conditions a burn wave goes through two stages. The initial «subsonic» stage is characterised by a dropping or slightly rising temperature behind the wave front. This stage creates the conditions for the second «supersonic» stage of intense burning which give rise to TN flash. As a consequence the above mentioned criterion for high efficiency burning is too rigid: it is quite enough if the «subsonic» stage duration would be essentially less than the target hydrodynamic lifetime.

The process of «subcritical» ignition was studied for the case of the cold fuel³. The results were given in the form of a curve which separates determines the corresponding ignitor region on the $(\rho R_f, T_f)$ plane. Analytical evaluations³ of energy transport mechanisms and of target lifetime gives only the qualitative estimation of TN burning efficiency. In this paper, numerical methods are applied to the problem to obtain quantitative results for energy gain.

The mathematical simulation of target ignition processes is based on the self-consistent solution of kinetic equations system for fast TN particles and plasma hydrodynamic equations system because TN reactions give the main contribution to the burn wave propagation. The kinetic processes on this stage are characterized by sharp gradients of density and temperature with the scales of the order of TN particle ranges, by substantial anisotropy of particles spatial distribution, by complicated energy dependence of charged particles energy loss, and by presence of a set of correlated channels of primary and secondary thermonuclear reactions. Under the conditions the Monte Carlo (MC) method for the kinetic processes simulation seems to be more suitable convenient than other standard computational schemes. The TERA code⁵⁻⁸ based on MC simulation of nuclear reaction products and photons for each time step of a proper difference non-stationary scheme for medium equations is used.

The relationship between target gain and ignitor parameters is investigated in detail by means of a set of TERA simulations of burning the target with various parameters of isobaric ignitor at fixed fuel parameters. The regions of ignitor parameters are obtained which provide an efficient target burning.

2. PHYSICAL-MATHEMATICAL MODEL

2.1. The equations system

Mathematical model of the TN burning of inhomogeneous spherical target is described by equations system of motion, energy balance, continuity, state and quasistationary kinetic equations for fast TN particles⁹. Applying Lagrangian frame m, t : $dm = \rho(r)r^2 dr$, where $\rho(r)$ - plasma density, one obtains Eulerian equation of motion for two-temperature, single-fluid hydrodynamics in the form

$$\frac{\partial u}{\partial t} = -r^2 \frac{\partial P}{\partial m} + VF \quad (1)$$

where u is local speed of plasma, $P = P_i + P_e$ is total pressure by ions and electrons, F is the force of pressure by fast TN-particles of the j -th kind and $V = 1/\rho$ is the specific plasma volume.

Taking into consideration burning out, thermalization and leaving out of the TN reaction products the mass transfer is described by following equation of continuity⁹:

$$\frac{\partial V}{\partial t} = \frac{\partial}{\partial m} (r^2 U) + V^2 S \quad (2)$$

In the equation (2) S stands for generalized source responsible for mass changing due to TN fuel depletion and thermalization of TN reaction products:

$$S = \sum_{i,k} n_i n_k \langle \sigma_{ik} v \rangle (m_i + m_k) + \sum_i N_i m_i \quad (3)$$

where σ_{ik} is the TN reaction cross section of nuclei of the j -th and k -th kinds, N_i is changing the numbers of TN reaction products of the i -th kind as the result of thermalization in the units of time and volume, m_i , n_i are mass and particles concentration of the i -th kind.

The energy balance equations for electrons and ions in single-fluid two-temperature hydrodynamics approximation has the form⁹:

$$\begin{aligned} c_e \frac{\partial T_e}{\partial t} + P_e \left(\frac{\partial V}{\partial t} - V^2 S \right) + \frac{\partial q_e}{\partial m} + \frac{T_e - T_i}{\rho \tau} &= Q_e + Q_f \\ c_i \frac{\partial T_i}{\partial t} + P_i \left(\frac{\partial V}{\partial t} - V^2 S \right) + \frac{\partial q_i}{\partial m} - \frac{T_e - T_i}{\rho \tau} &= Q_i \end{aligned} \quad (4)$$

where T_i and T_e are ion and electron temperature, respectively, C_i and C_e are heat per unit of ions and electrons, respectively, q_i, q_e are ionics and electronics heat flows, respectively, τ is the characteristic time for ion-electron energy exchange,

Q_i and Q_e are energy per unit that fast particles transfer to ions and electrons, respectively, Q_f is the energy transport of radiation generated in the plasma.

At known distribution function of particles $f_j(v, r, \mu)$ and of photons $I_v(r, \mu)$ dissipation speeds (flux divergences) of fast particles energy Q_e, Q_i, Q_f , momentum F and particle numbers N_j may be obtained from equalities:

$$\begin{aligned} Q_{e,i} &= 2\pi m \int \left(\frac{\partial v}{\partial t} \right)_{e,i} f v^3 d\mu dv \\ Q_f &= 2\pi c \int \kappa_v I_v dv d\mu \\ F &= 2\pi m \int a f v^2 \mu dv d\mu \\ N_j &= 2\pi \lim_{v \rightarrow 0} (a_e + a_i) v^2 \int f_j d\mu \end{aligned} \quad (5)$$

In formulas (5), μ is the cosine of the angle between the radius vector and the particle velocity, a_i and a_e are the drag coefficient of a fast charged particle slowing down by ions and electrons, κ_v is the spectrum coefficient of photon bremsstrahlung absorption, m is the mass of the particle, c is the speed of light.

For spherically symmetric plasma the kinetic equations for fast charged particles f , neutron f_n and photon I distribution functions in quasy stationary approximation take the form ⁷:

$$\begin{aligned} v \left(\mu \frac{\partial}{\partial r} + \frac{1-\mu^2}{r} \frac{\partial}{\partial \mu} \right) f + \frac{\partial}{v^2 \partial v} (v^2 a f) &= W_0 + W_s - v f \sum_k n_k \sigma_k \\ v \left(\mu \frac{\partial}{\partial r} + \frac{1-\mu^2}{r} \frac{\partial}{\partial \mu} \right) f_n &= W_0 + W_{ns} - v f_n \sum_k n_k \sigma_{nk} \\ \left(\mu \frac{\partial}{\partial r} + \frac{1-\mu^2}{r} \frac{\partial}{\partial \mu} \right) I_v &= \kappa_v I_{vp} - (\kappa_v + \kappa_{vs}) I_v \end{aligned} \quad (6)$$

where $W_0(\rho, T, v)$; $W_s, W_{ns}(r, v, \mu, \{f_n, f\})$ are generalized sources of TN particles by primary fusion reactions and by neutron elastic scattering, $\sigma_k(r, v)$, $\sigma_{nk}(r, v)$ are fast particles and background plasma secondary TN reactions cross sections, κ_{vs} is the spectrum coefficient of photon scattering, I_{vp} is the Plank distribution function.

The closed-loop equations system (1) - (6) gives the possibility to simulate the dynamics of laser target's TN burning. In present paper the kinetic equations (6) are solved by straight stochastical modeling of the kinetic processes at given plasma parameters by the Monte Carlo method ⁵⁻⁸ while the single-fluid, two-temperature hydrodynamic equations (1)- (4) are solved by well-known difference scheme ⁹,

2.2. Initial parameters of target plasma

While spark ignition of laser target is studied, i.e. the target at the moment of implosion is supposed to be homogeneous with the exclusion fore a relatively small central hot spark - ignitor. We intend to obtain the thermonuclear gain as a function of ignitor dimension R_f , density ρ_f , and temperature T_f at different target parameters ρR_0 , T_0 . Taking

into account that the target at the instant of maximum pressure is approximately isobaric two independent ratios $\Delta_t = T_f / T_0 = \rho_0 / \rho_f$, $\Delta_r = R_f / R_0$ may be introduced as the main ignitor parameters.

In our previous report⁴ it was pointed out that possible values of temperature inhomogeneity Δ_t lie within the limits $2 < \Delta_t < 10$. The greater values are hardly to be reached under the target implosion. The case of lesser values is of no interest because it corresponds to volume not spark ignition in fact (the value $\Delta_t = 1$ relates to homogeneous target). The same reasons impose inequalities for ignitor dimension: $0.1 < \Delta_r < 0.5$.

As for target parameters ρR_0 , T_0 , we suppose that there is no TN flash in homogeneous target. In the opposite case the concept of spark ignition has no physical meaning. Preliminary calculations carried out for different homogeneous targets make it possible to establish the upper bound for target temperature and dimension.

3. THE NUMERICAL CALCULATIONS RESULTS.

3.1. Thermonuclear burning of homogeneous target.

The general measure of target TN burning efficiency is the TN gain $G = E_{tn} / E_0$, where E_{tn} is the released TN energy, E_0 is the target thermal energy at the moment of implosion. The results of TERA calculations of the gain for shellless homogeneous target with different ρR_0 , T_0 are presented in figure 1.

The sharp increase in the gain within narrow interval of target temperature T_0 corresponds to generation of self-sustaining TN burning. The TN flash may occur possible for relatively large targets only ($\rho R_0 > 1 \text{ g/cm}^2$). If the TN flash takes place the released energy depends weakly on the initial temperature T_0 , so that the gain diminishes as $1/T_0$. The values of parameters ρR_0 , T_0 corresponding to maximum gain coincide with the desired bound separating the volume and the spark ignition regions. The corresponding curve is presented in figure 2.

It is interesting to consider energy gain of volume ignited targets as a function of ρR_0 , T_0 in details. When temperature dependence of TN fusion rate in the range of active TN burning is neglected, one obtains:

$$G = E_{tn} / E_0 = \langle \sigma v \rangle \rho \Delta t / T_0 \quad (7)$$

where Δt is a characteristic time of target destruction.

This characteristic time may be approximated by the ratio of target radius, and mean speed of sound $v \sim \sqrt{T}$: $\Delta t \sim R_0 / \sqrt{T}$. The characteristic temperature of burning target T in its turn is determined by TN energy released: $T \sim E_{tn} \sim G T_0$. As a result, the energy gain may be presented in the form:

$$G = F(\rho R_0, T_0) \cdot \rho R_0^{2/3} / T_0 \quad (8)$$

where the coefficient F depends weakly on ρR_0 , T_0 .

The function $F(\rho R_0, T_0)$ is obtained from the data presented in figure 1 (see figure 3). It is seen that the value of coefficient F is approximately constant with the accuracy of 10 - 20% provided that the conditions of volume ignition are satisfied ($G \gg 1$). If the domain of target parameters at the moment of implosion lie above the solid curve given in figure 2, the TN energy gain may be evaluated as:

$$G = 370 \rho R_0^{2/3} / T_0 \quad (9)$$

In eq. (9) T_0 and ρR_0 are measured in keV and g/cm^2 , respectively.

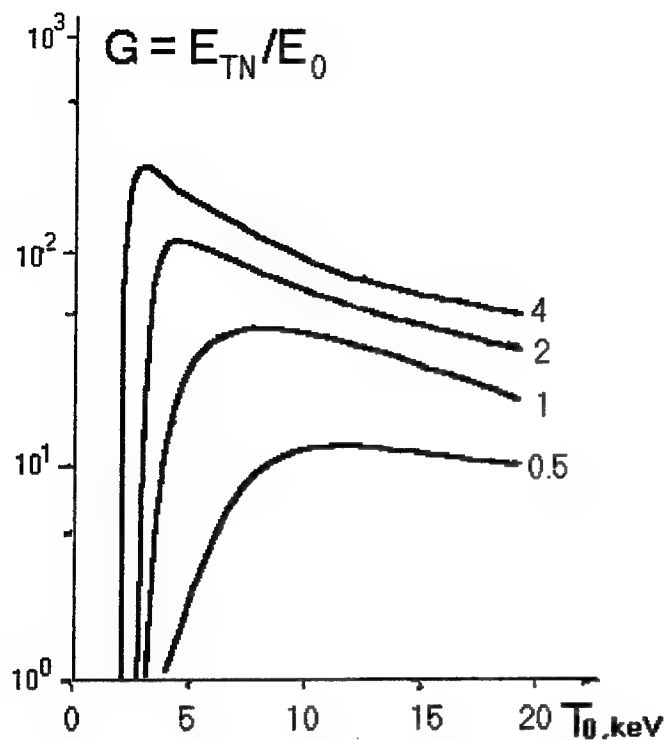


Fig. 1

The energy gain of homogeneous shellless target as a function of temperature T_0 at different ρR_0 . The curves are marked by corresponding values of ρR_0 in g/cm^2 .

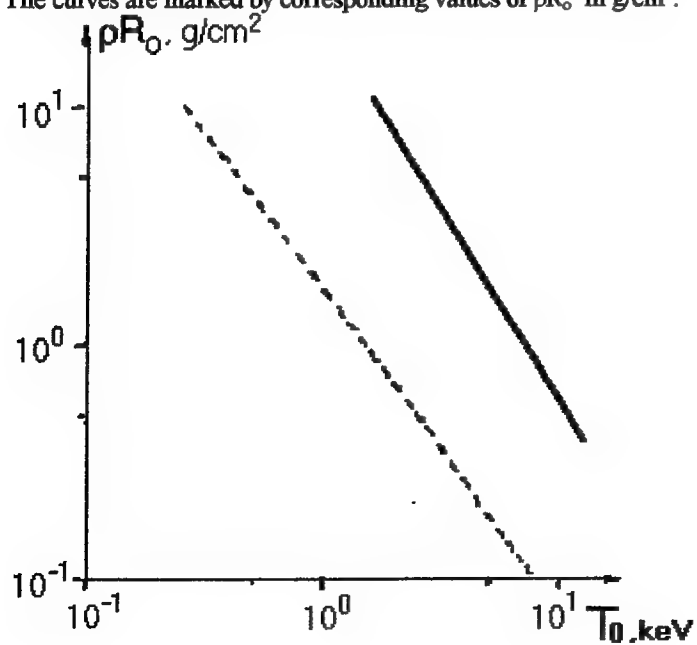


Fig. 2

Regions of possible target parameters for an isobar spark ignition. Above solid curve - region of volume ignition. Below dashed curve - region in which the spark ignition is impossible.

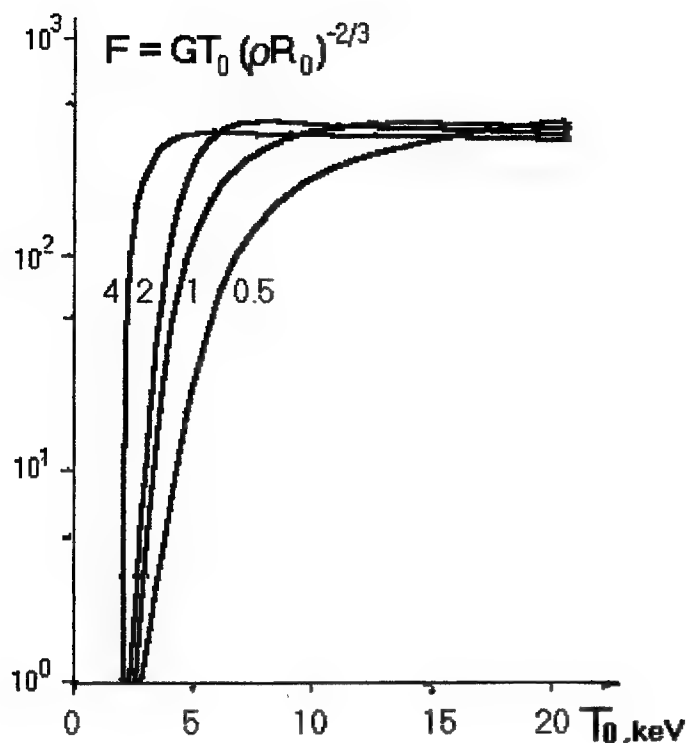


Fig. 3

Normalized energy gain F as a function of temperature T_0 at different ρR_0 . The curves are marked by corresponding values of ρR_0 in g/cm^2 .

3.2. Thermonuclear burning of inhomogeneous target with spark ignition.

The TN burning of a number of laser targets with different values of temperature T_0 , dimension ρR_0 , and ignitor parameters Δ_t , Δ_r is simulated by means of TERA code to obtain the energy gain G for each case. To present the results of calculations in observable form it is worthwhile to propose some preliminary reasons concerning the target ignition.

It was mentioned above that in rather small homogeneous targets ($\rho R_0 < 1 \text{ g/cm}^2$) the effective TN burning is impossible at any temperature T_0 . That is why the spark ignition in such targets is impossible as well. For large targets the upper bound of dimension and temperature to allow for spark ignition is given by the solid curve in figure 2. It is obvious that the restrictions imposed on ignitor parameters $\Delta_t < 20$, $\Delta_r < 0.5$ set a lower bound for the target temperature T_0 at each value of ρR_0 . This lower bound obtained by numerical calculations is presented in figure 2 as well.

If the target parameters are in the region described above, the possibility of ignition is determined by the ignitor parameters Δ_t , Δ_r . It may be expected that if the target ignition takes place the released TN energy is practically independent on ignitor parameters, and is close to that for homogeneous high-temperature target of the same dimension. It is a consequence of the facts that the target destruction time in this case depends not on initial temperature distribution but on the high temperature of TN flash, and that TN fusion reaction rate depends weakly on temperature in high-temperature limit ($T > 20 \text{ keV}$). So the relation (9) for homogeneous target energy gain is supposed to be approximately valid for the spark ignited targets, too.

As a whole, the above statements are in good agreement with the results of numerical calculations. To eliminate the gain typical dependence on target parameters, it is reasonable to present the results in the form of normalized energy gain: $F = GT_0 (\rho R_0)^{-2/3}$. The calculations of the normalized energy gain are carried out for target with various ρR_0 .

For given ρR_0 the values of temperature T_0 are fixed in the region below the solid curve in figure 2 and for each temperature the set of target with central isobaric ignitors with parameters $0.1 < \Delta_r < 0.5$, $1 < \Delta_t < 20$ is analyzed.

As an illustration the normalized energy gain dependencies $F(T_0, \rho R_0; \Delta_t, \Delta_r)$ for two targets with ρR_0 of 2 g/cm^2 and of 4 g/cm^2 are presented in figures 4, 5 respectively. The sharp increase in the gain within relatively narrow range of Δ_r corresponds to the target ignition. (For comparison with the case of the volume ignition see figure 1). Up to the critical ignitor parameters the minimum value F_{\min} corresponds to the burning of homogeneous target with temperature T_0 :

$F_{\min} = F(T_0, \rho R_0)$ and depends weakly on ignitor parameters. The further increase in Δ_t, Δ_r leads to the change in the gain which in the limit of large Δ_t, Δ_r tends to F_{\max} close to the value given by eq.(9). Choosing the condition $F = 0.5F_{\max}$ as the spark ignition criterium the curves on (Δ_t, Δ_r) plane can be obtained which separates the regions of spark ignition parameters. The curves corresponding to the shellless targets with different $T_0, \rho R_0$ are presented in figure 6

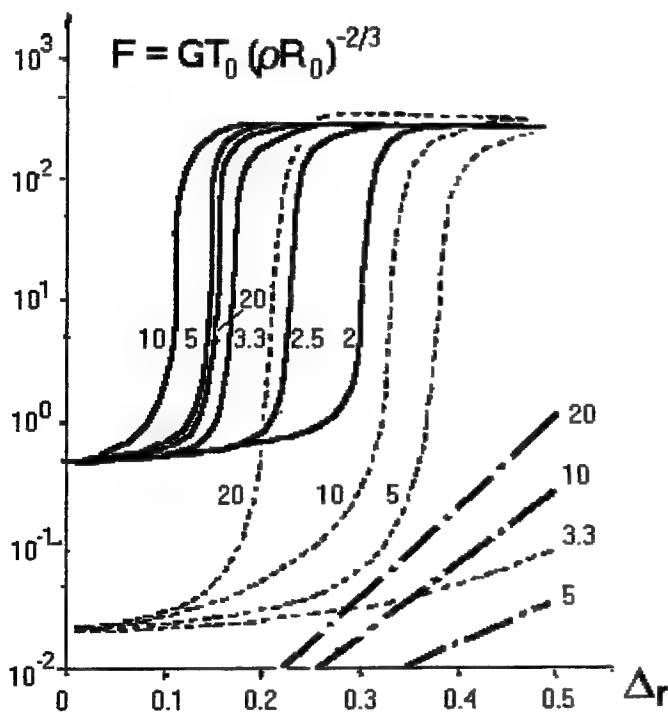


Fig. 4

Dependencies of normalized energy gain F on relative ignitor dimension Δ_r at different Δ_t (indicated in the figure) for isobar target with $\rho R_0 = 4 \text{ g/cm}^2$. Solid, dashed, and dash-dot lines correspond to $T_0 = 2, 1$, and 0.5 keV respectively

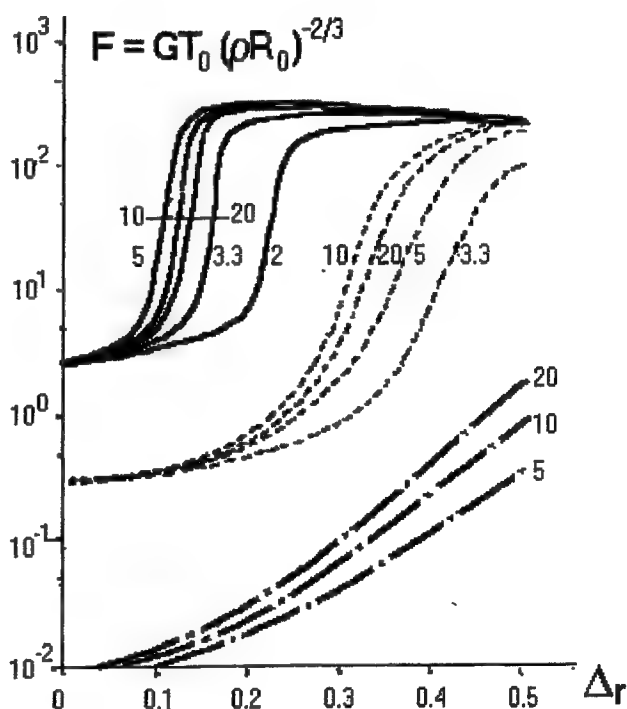


Fig. 5

Dependencies of normalized energy gain F on relative ignitor dimension Δ_r at different Δ_t (indicated in the figure) for isobar target with $\rho R_0 = 2 \text{ g/cm}^2$. Solid, dashed, and dash-dot lines correspond to $T_0 = 3, 2$, and 1 keV respectively

4. CONCLUSIONS.

Summing up the results it should be emphasized the following features of laser target TN burning with central isobaric ignitor:

- Because the ignitor temperature varies within several limits related to the target temperature, the spark ignition is possible only for rather hot target. The corresponding curve separating spark ignition region is presented in figure 2.
- If the spark ignition is possible, there are the critical ignitor dimension and temperature providing high efficiency of TN burning, when the target destruction time is essentially more than the time of TN burn wave generation and propagation. The corresponding regions of ignitor parameters for different shellless targets are presented in figure 6.
- For shellless target TN burning with high efficiency is possible only for rather large targets with $\rho R_0 > 1 \text{ g/cm}^2$. In the opposite case energy gain don't exceeds 20 -30 (see figure 1).
- In the case of ignition the energy gain may be evaluated with the reasonable accuracy by the simple relation: $G=370(\rho R_0)^{2/3}/T_0$. This relation is valid both for volume and spark ignition.

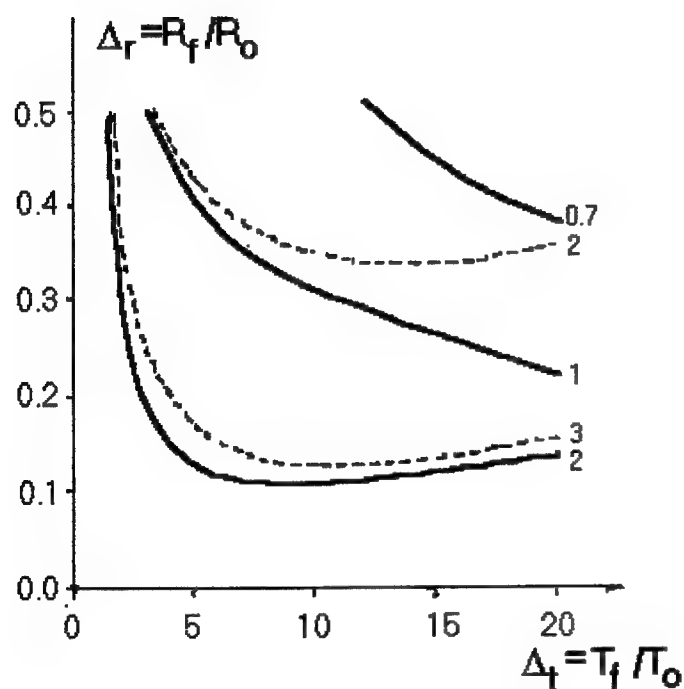


Fig. 6

Boundaries of isobar ignitor parameters, above which a TN flash is possible, for target with different T_0 and ρR_0 . The curves are marked by corresponding values of T_0 in keV. Solid and dashed lines correspond to $\rho R_0 = 4$ and 2 g/cm^2 respectively.

5. ACKNOWLEDGEMENTS

We are grateful to V.B.Rozanov, S.Yu.Gus'kov, I.G. Lebo for stimulating discussions.

This work is supported in part by the Russia Dept. of Education under Grant "Thermonuclear and nuclear reactors-1997"

6. REFERENCES

1. Yu. V. Afanas'ev, N. G. Basov, P. P. Volosevich et al., « Laser initiation of thermonuclear reaction in inhomogeneous spherical targets,» *Pis'ma Zh. Eksp. Teor. Fiz. (JETP Lett.)*, **21**, pp.150-155, 1975. (in Russian)
2. Yu. V. Afanas'ev, N. G. Basov, P. P. Volosevich et al., « Theoretical investigations of shall target compression and burning,» *Preprint FIAN 55*, Moscow, 1979. (in Russian)
3. O. B. Vygovskii, S. Yu. Gus'kov, D. V. Il'in, A. A. Levkovskii, V. B. Rozanov, and V. E. Sherman, « Criterion of formation of a thermonuclear burn wave in deuterium-tritium targets,» *J. Sov. Las. Research*, **14**, pp.85-91, 1993.
4. S. Yu. Gus'kov, D. V. Il'in, A. A. Levkovskii, V. B. Rozanov, and V. E. Sherman, «Study of ignition criteria in inhomogeneously heated laser target,» *Proc. SPIE-Int. Soc. Opt. Eng. (USA)*, **2770**, pp.182-189, 1996. (Laser Optics'95 and ICONO'95 Superintense Laser Fields, St.-Petersburg, Russia, 27 June - 1 July 1995.)
5. A. A. Levkovskii, «Mathematical simulations of thermonuclear flash in laser target,» *Preprint FIAN 73*, Moscow, 1990. (in Russian)
6. S. Yu. Gus'kov, N. V. Zmitrenko, D. V. Il'in, A. A. Levkovskii, V. B. Rozanov, and V. E. Sherman, «Physics of a two-temperature thermonuclear burning wave in an inertially confined plasma,» *Zh. Eksp. Teor. Fiz.*, **106**, pp.1069-1088, 1994. (in Russian); Engl. transl., *JETP*, **79(4)**, pp.581-590, October 1994.
7. D. V. Il'in, A. A. Levkovskii, V. B. Rozanov, and Yu. N. Starbunov, «Effect of X-ray transport processes on the laser target burn dynamics,» *Preprint FIAN 34*, Moscow, 1991. (in Russian)
8. V. A. Burtzev, S. Yu. Gus'kov, D. V. Il'in, A. A. Levkovskii, V. B. Rozanov, V. E. Sherman, Yu. N. Starbunov and N. V. Zmitrenko, «Mathematical modeling of the thermonuclear burning in the DHe3-targets with DT-ignition,» *Laser and Part. Beams*, **11**, pp.669-677, 1993.
9. J. J. Duderstadt & G. A. Moses, *Inertial Confinement Fusion*, John Wiley & Sons, New York, 1982.

GARPUN KrF laser application to material studies at megabar pressures

Vladimir D. Zvorykin, Valerii G. Bakaev, Vyacheslav Yu. Korol', Gleb V. Sychugov

P. N. Lebedev Physical Institute, Russian Academy of Sciences,
Leninsky pr. 53, 117924 Moscow, Russia

ABSTRACT

The advantages of a high-power KrF laser system "GARPUN" generating UV radiation of 248 nm wavelength, 100 J energy and 100 ns pulse duration for the production of megabar range ablation pressures are demonstrated. The scaling law for the pressure dependence on laser intensity reaching $5 \cdot 10^{12}$ W/cm² was established and compared with other wavelengths. High-pressure material investigations were carried out with the emphasis on a shock wave dynamics and equation of state studies. Pressure-induced transformation of the pyrolytic graphite into a diamond-like phase was observed for the first time in laser-target interactions.

Keywords: KrF laser, megabar ablation pressure, shock-wave dynamics, graphite-diamond phase transformation.

1. INTRODUCTION

A number of advanced technologies for the material modification, as well as new opportunities for fundamental investigations in solid state physics are based on the matter compression by very high pressures. Static method of a sample loading between diamond anvils can produce pressures at the level of tens kilobars. The dynamic methods using explosives or explosive-accelerated plane flyers pressurize the examined material by hundreds kilobars, but heat up the matter significantly by a shock wave generated. If a phase transition occurs during the sample loading, a high post-shock temperature will sufficiently influence a new phase.

Laser irradiation of targets produces ablation pressures in a multi-megabar range, and parameters of the matter compressed in such laser-induced shock wave may be determined¹. Graphite-diamond transformation, which begins in the pressure range of 200-400 kbar is of particular interest for a laser initiation^{2,3}. By means of time profiling of the laser pulse or using an appropriate target design with additional ablating layers one could compress the graphite gradually (close to adiabatic) to avoid an extra heating of the sample and to diminish the reverse process of diamond graphitization. The laser intensity of about 10^{12} W/cm² is necessary to reach the megabar pressure, the shorter radiation wavelength being favorable for higher pressures⁴. Pulse duration has to be compared with phase transition time, which is at least tens nanoseconds⁵. The spot diameter on a target has to exceed the extension of a compressed region defined by a product of the shock front velocity in a specimen and pulse duration, otherwise lateral unloading will reduce the pressure attained. By combining these values one can obtain for a few hundred microns spot the necessary laser energy of about several hundred joules.

So far graphite-diamond transformation hasn't been achieved in laser-driven shock experiments with nanosecond Nd:YAG laser pulses⁶. In our previous experiments⁷ at high-power KrF laser installation "GARPUN"^{8,9} we have observed by using micro-Raman spectroscopy technique the appearance of diamond-like phase in the pyrolytic graphite samples arranged in multi-layer targets irradiated by 100 ns laser pulses. Here we present new evidences of such a transformation obtained while investigating shock wave dynamics in planar graphite targets (see also¹⁰). This paper describes a performance of 100 J-class KrF laser system "GARPUN" intended for target shooting experiments by long-duration pulses with a controllable space-time intensity distribution in a focal spot. The dependence of the ablation pressure on laser intensity, radiation wavelength, and target material was measured. The hydrodynamic flow and shock wave propagation in condensed matter

Further author information-

V.D.Z. (correspondence): E-mail: zvorykin@sci.lebedev.ru; Tel.: (095)-132-6739, Fax: (095)-132-0425

were investigated for irradiances up to $5 \cdot 10^{12}$ W/cm². The application of GARPUN laser for studying of the equation of state and phase transitions in megabar-pressure matter was demonstrated.

2. GARPUN LASER PERFORMANCE FOR TARGET SHOOTING EXPERIMENTS

The setup of laser-target experiments is shown schematically in Fig. 1. The installation consists of electron-beam-pumped large-aperture module GARPUN, discharge-pumped master oscillator EMG 150 TMSC, target chamber and diagnostic technique. GARPUN module has an active volume dimensioned $16 \times 18 \times 100$ cm, which is pumped by two lateral counter-propagating electron beams of the area 12×100 cm and current density 50 A/cm². To avoid pinching of the beams and diminish the losses arising due to electrons scattering in a gas mixture and titanium foil windows of accelerators there was used the longitudinal pulsed magnetic field of about 1 kG produced by two solenoids. The pulses of 350 kV voltage and 100ns duration are delivered to a pair of electron accelerators by four water-filled Blumlein forming lines with 7.6 Ω wave impedance. A 7-stage Marx generator having 14 kJ initial storage energy charges them. The total pumping energy and specific pumping power reach 2 kJ and 0.8 MW/cm³, respectively, at 1.5-1.75 atm pressure of Ar/Kr/F₂ working gas mixture.

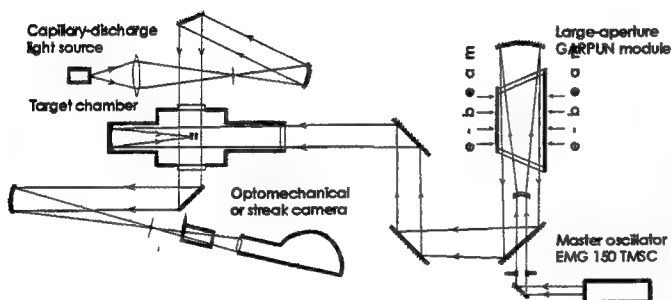


Fig. 1. Layout of laser-target experiments.

scheme described elsewhere^{10,11} enabled to diminish the divergence of laser beam up to 0.1 mrad and to increase the axial power of output radiation up to 1.6×10^{17} W/sr. An output beam was made slightly convergent by moving the unstable resonator mirrors apart their nominal position in order to reduce a cross section to 10×10 cm along the passage to the target chamber (~ 10 m) and to match to the focusing mirror aperture. The distribution of radiation fluence in a focal spot was measured by means of photographic films in a large dynamic range of 10000. For a spherical mirror with 40-cm focal length about 75% of total energy was contained inside a spot of 150 μ m dia. In order to examine a temporal dependence of far-field-zone intensity distribution a laser beam was strongly attenuated and focused onto a photo cathode of a streak camera. In contrast to a free-running regime, when a strong evolution was observed, the injection of seed radiation into the unstable resonator formed a quasi-steady distribution from the very beginning of oscillations. For a trapezoidal laser pulse-form with 20 ns rise time, 50 ns flat top, and 30ns droop, a peak intensity in the middle of the spot reached $q = 5 \times 10^{12}$ W/cm². It fell to less than 0.1 of the maximum value outside 150 μ m dia. Laser energies were varied up to 60 J to achieve different target irradiation.

An impulse associated with the ablation of a target material was measured with the help of a ballistic pendulum. A peak pressure was then derived using a dependence of the impulse on laser energy and intensity distribution across the focal spot. Evaporation time was supposed to be equal to laser pulse duration, the actual waveform being taken into account. The plasma and condensed matter flows were investigated with the help of high-speed optomechanical and streak cameras in different time scales. In both cases the slit scanning of the images and schlieren or shadow schemes were used. A collimated probe beam was formed by a pulsed capillary discharge source, and it was passed through an examined region near a target perpendicular to the laser beam.

3. EXPERIMENTAL RESULTS

3.1. Scaling law for ablation pressure

The ablation pressures acting on a front surface of the target in the middle of irradiated spot for different materials versus peak intensity are presented in Fig. 2. Within a measurement accuracy the pressure did not depend on the target material and

was changed up to 4 Mbar in the range of $q=10^{11}$ - $5 \cdot 10^{12}$ W/cm² in accordance with the power law $P = 45.3 \times (q/10^{14})^{0.79}$ where P is expressed in Mbar, and q in W/cm². The dependence for KrF laser is similar to another one, obtained for Nd:YAG laser of 0.53 μ m wavelength and 3 ns pulse duration⁶, but exceeds it by a factor of 1.7. Our results are in good quantitative agreement with a scaling law $P = 11.9 \times (q/10^{14})^{2/3} (\lambda)^{-2/3}$, where radiation wavelength λ is expressed in μ m, established for $q \geq 10^{13}$ W/cm² on the basis of numerous earlier experiments with planar targets⁴. The scaling $P = 20 \times (q/10^{14})^{7/9} (\lambda)^{-2/9}$ established for lower $q=10^{11}$ - $4.5 \cdot 10^{12}$ W/cm² coincides qualitatively to a present

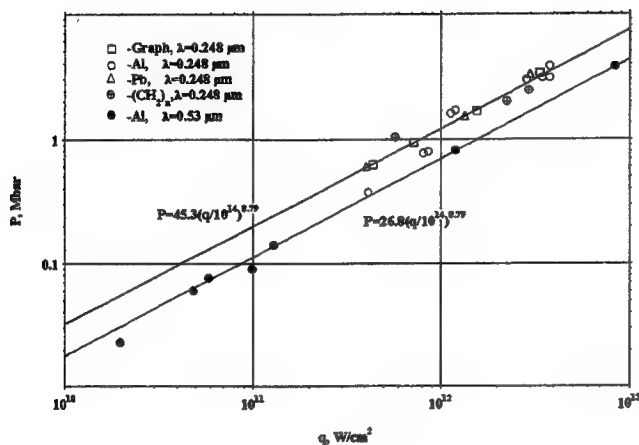


Fig. 2. Dependence of peak pressure on peak intensity.

intensity dependence, but differs in wavelength dependence, and also gives lower pressures by a factor of 1.6. It should be noted that mean pressures averaged across a focal spot of 150 μ m dia are 2 times lower than the peak values shown in Fig. 2.

3.2. Hydrodynamic flow investigation

Typical time dependent records of hot self-luminous laser-heated plasma and cold non-luminous ejected target material obtained by means of optomechanical and streak cameras are shown in Fig. 3 (a,b), where (b) is a reversed image. Plasma

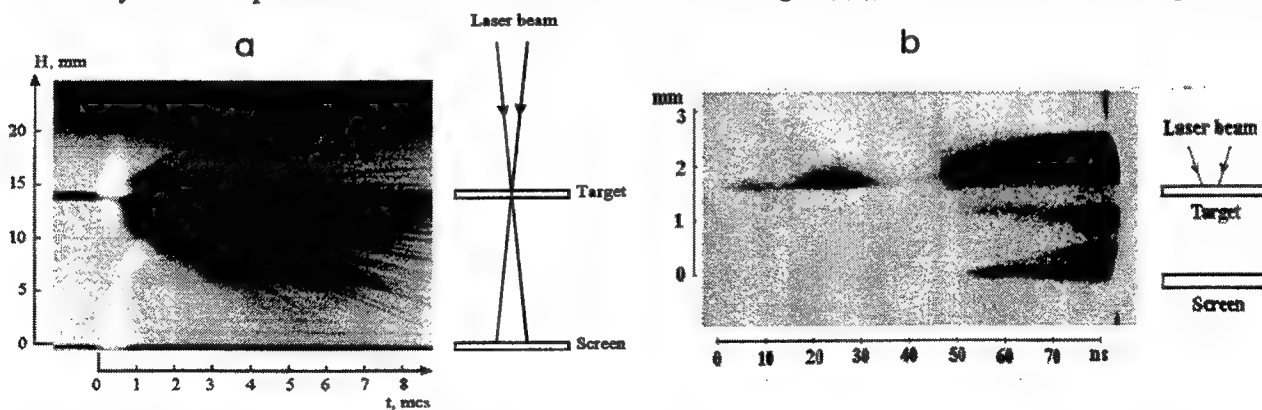


Fig. 3. Time-resolved records of laser-target interaction: a- shadow photography by optomechanical camera; b- self-luminescence registration by streak camera (reversed image).

produced at the irradiated target surface went away towards the incident laser radiation with a velocity 50-100 km/s. With a delay dependent on target thickness and laser intensity the plasma would appear at the backside of a target and also at the surface of a screen, which was placed behind to indicate that radiation penetrates through the target. The two plasmas expanding with comparable velocities formed a well-defined shock wave after their collision. The dependence of burn-through time on target thickness was measured for aluminum and graphite by using streak camera records (b). Burn-through

velocities were then determined revealing a large discrepancy in comparison with the previous ablation velocity measurements⁴. For example, laser pulses of 30 J energy, corresponding to a peak intensity $q=3.5 \times 10^{12}$ W/cm² penetrated through aluminum targets with thickness as large as $d=330$ μ m, thus exceeding by an order of magnitude the usual mass ablation rate. The reason for such an effect was two-dimensional character of the hydrodynamic flow of compressed target matter in present experimental conditions when a shock wave propagated along a distance sufficiently exceeding a spot diameter, especially its central region. Two-dimensional numerical simulations, which accounted for the actual temporal and spatial laser beam profiles¹⁰, confirmed this demonstrating a good agreement of burn-through times both calculated and measured. In contrast to one-dimensional conditions typical for nanosecond laser pulses^{4,6}, where a burn-through time is determined by an ablation rate of target material, for 100 ns laser pulses a radial squeezing out of the matter contributes, mainly, to a hole burning of a target.

Conical or semi-spherical profiles of shock waves are evidently seen in Plexiglas, which was placed in acoustic contact behind an aluminum target (Fig. 4). These time-integrated pictures were obtained by transmitting the Plexiglas samples in copper-vapor laser projection –microscopy scheme. An extended crater was created in the matter suffered a high ablation pressure due to its plastic deformation. Side-lobe perturbations of crater surface evidence about Kelvin-Helmholtz instabilities, which were arising because of tangential moving in the compressed matter. Numerical simulations¹⁰ showed that shock velocity at the vertex of a cone-shaped front was adjusted by itself to be equal to the velocity of ablating surface resulting in their joint quasi-steady propagation.

The small particles of the condensed material, which are clearly seen in Fig. 3(a) as shadow traces flew apart with velocities of about several km/s. Apparently, this ejection would take place under unloading of compressed matter, whenever the shock wave reached a back surface of the target. It should be noted that the main ejection occurred normally to the target.

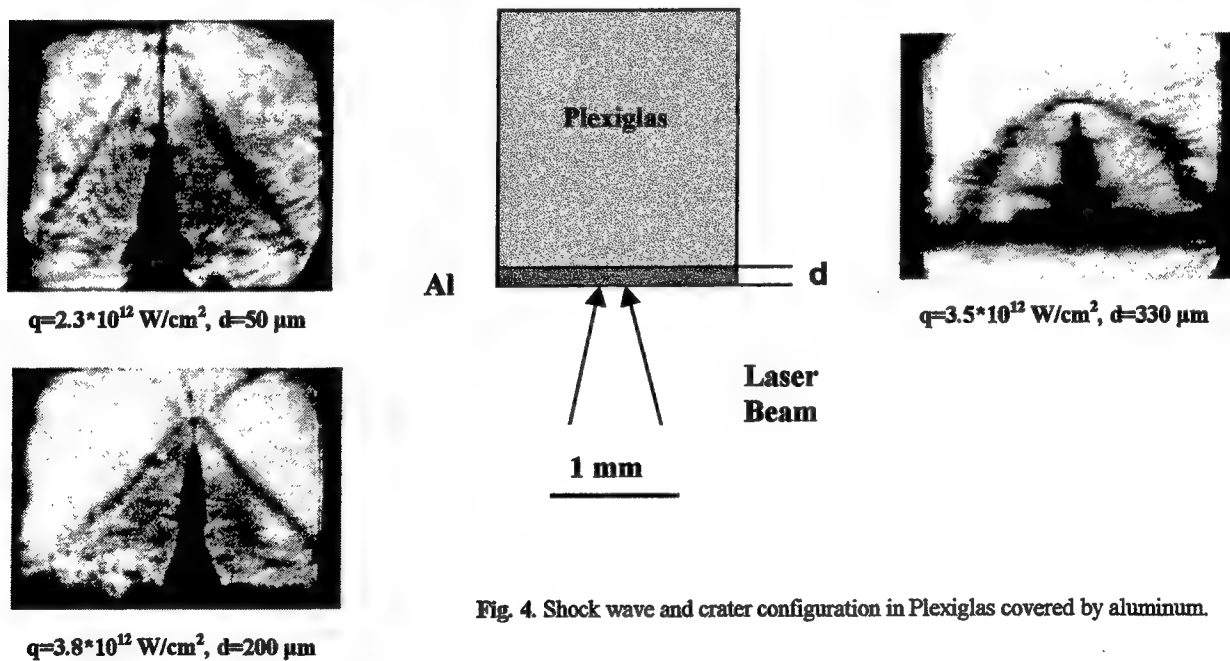


Fig. 4. Shock wave and crater configuration in Plexiglas covered by aluminum.

3.4. Hugoniot adiabat reconstruction

In conventional explosive or laser-driven planar shock-wave experiments the pressure, density and energy of compressed matter may be determined by using the conservation laws for mass, momentum and energy if at least two parameters of a shock wave are measured^{1,12,13}. This couldn't be applied to our two-dimensional hydrodynamic case. The ablation pressure generated at a front surface of a target might be sufficiently reduced by a lateral unloading, whilst a shock front reaching the backside ejected target matter. Using aluminum as a standard material with well-known Hugoniot adiabat^{13,14}, we took into

account these two-dimensional effects. The measurements of fly velocities were carried out for aluminum foils of different thickness, and the dependence of mass velocity versus shock pressure was plotted. Mass velocities in a shock wave were determined in assumption that they were half fly velocities of the condensed material from the backside of a target under unloading. It is true within an accuracy to several percent for the pressure range up to Mbar¹². Pressures were calibrated in comparison with the data of explosive experiments¹³, numerical approximations (solid line)¹⁴, and also Nd:YAG laser results⁶ (Fig.5a). They appeared to be 5.5 times below the peak pressures measured at the front target surface by the ballistic pendulum (see Fig.2).

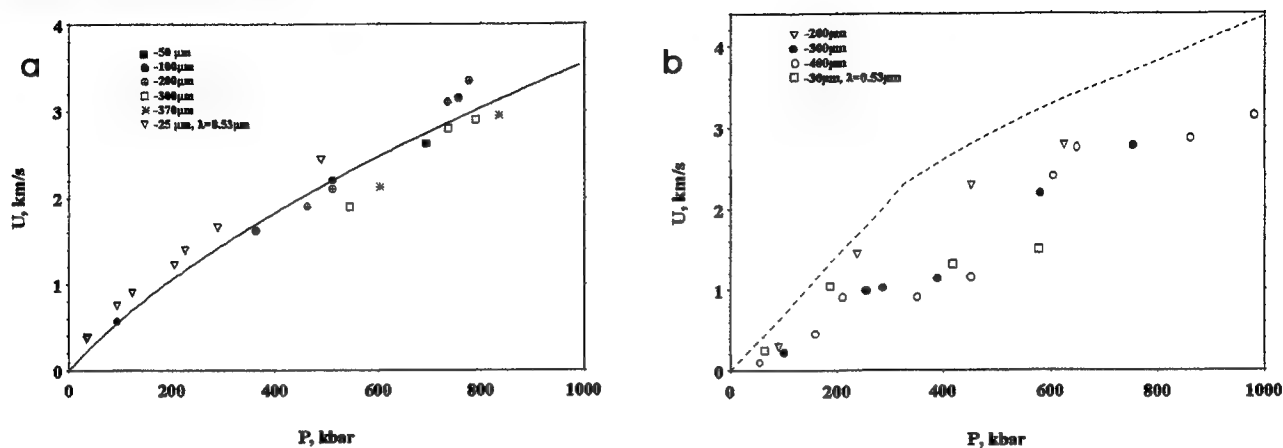


Fig. 5. Dependence of mass velocity on pressure for aluminum (a) and graphite (b).

These correction procedures to pressure values were used further when plotting the same dependence for the pyrolytic graphite (a quasi-single crystalline form) by initial density 2.20 g/cm³. The experimental data for both KrF and Nd:YAG lasers are compared in Fig. 5b with the calculated carbon Hugoniot adiabat (dashed line) assuming graphite and diamond phases¹⁴. In contrast to aluminum there was the saturation of velocities at the level of 1 km/s, which was observed in the pressure range of 200–400 kbar for the targets of 300–400 μm thickness. At elevated pressures up to 600 kbar velocities rose rapidly up to 2.5–3.0 km/s, which are rather below the calculated ones. Such a behavior may be explained by the bifurcation of a shock wave propagating in the specimen into two waves if the phase transformation would occur. Then two-step profile of shock pressure and mass velocity would appear¹². The first step compresses graphite into a state of incipient phase transition, and the second one includes the transformation in itself and compresses diamond into a terminal state. A shock speed of the first step and also amplitudes of pressure, density and mass velocity behind the front are independent of applied pressure. The similar parameters of the second step increase with pressure, and as a result it overtakes the first step at certain pressure. If the phase transition time is longer than a laser pulse the second step will not appear at all. It was the case of Nd:YAG lasers with a 3 ns pulse duration. The unloading after laser pulse termination might also reduce the amplitude of the second step. As the speed of a rarefaction wave, which is equal to a sound speed in matter, is much higher in compressed diamond than in graphite, the unloading might be the cause of velocity saturation for thicker targets in Fig. 5b, and not appear for a thin target. All these effects have not been considered in calculations¹⁴, and diamond phase formation at pressures $P \geq 330$ kbar is indicated only as a point of inflection on the curve.

The dynamics of two-step shock structure has been investigated carefully in experiments⁵ with explosive-driven flyers, where highly oriented pyrolytic graphite was transformed into a diamond-like phase through the martensitic mechanism. The transition onset pressure ~ 200 kbar, mass velocity behind the first step ~ 1 km/s, pressure ~ 400 kbar and corresponding velocity ~ 2.6 km/s (when the transition is overdriven to a single wave) were measured in those experiments, and are very close to the present values. In addition, the phase transition time was determined by the second step rise time, and it appeared to be several tens of nanoseconds that is just between the present laser pulses of 3 and 100 ns.

3.5. Target design

For the conservation of laden part of a graphite sample, which was usually broken due to unloading, the complicated targets were designed with additional layers from the material with higher acoustic impedance. By using one-layer or multi-layer constructions consisting of aluminum, tantalum or molybdenum foils it was possible to prolong the pressure pulse in

graphite by 2-3 times and to profile it in order to approach the load mode to the adiabatic one. This would reduce a post-shock temperature in the graphite. Only plastic deformation of graphite took place in this case in the pressure range of several hundred kilobars, sufficient for the phase transformation. Graphite samples after loading inside sophisticated targets were treated in concentrated mixture of acids at elevated temperature in order to extract the diamond phase, and then analyzed by means of micro-Raman-scattering technique. A line centered near $\nu=1320\text{ cm}^{-1}$ in the RS spectrum (Fig. 6) was observed additionally after the sample loading. It corresponds to the crystalline diamond line $\nu=1330\text{ cm}^{-1}$, which is shifted by 10 cm^{-1} . Such a shift indicates that a diamond-like phase exists in a dispersed state with diamond particle sizes of several nanometers¹⁵.

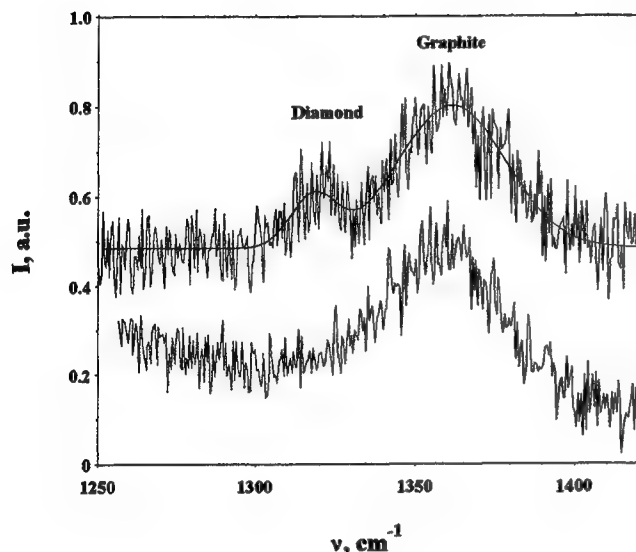


Fig. 6. Raman Scattering spectrum of graphite before (lower curve) and after (upper) laser irradiation.

4. CONCLUSIONS

The injection-controlled operation mode of high-power KrF laser GARPUN ensured target shooting by 100 ns laser pulses with a quasi-steady intensity distribution in a focal spot of $150\text{-}\mu\text{m}$ dia and peak intensity up to $5\cdot 10^{12}\text{ W/cm}^2$. The ablation pressure up to 4 Mbar generated a shock wave, which compressed the target material and produced its modification. A cone-shaped shock wave being essentially two-dimensional propagated in a self-regulated manner together with the ablation front, resulting in a radial squeezing out the solid matter and producing tangential moving of compressed layers. Such conditions are favorable for graphite-diamond phase transformation by martencitic mechanism, which was observed for the first time in laser-driven shocks by means of both dynamical (mass velocity versus pressure dependence) and RS methods. Using a standard material with well-known Hugoniot adiabat (i.e. aluminum) it was possible to reconstruct the equation of state for the tested material despite of the lateral unloading.

5. ACKNOWLEDGEMENTS

The authors are grateful to V.B. Rozanov and A.G. Molchanov for the statement of this work, I.G. Lebo for numerical simulations and helpful discussions, N.N. Mel'nik, G.E. Metreveli and O.F. Yakushev for the assistance in experiments. This work was supported by the International Science and Technology Center under Project No. 030-94 and also by Russian Foundation of Basic Research under Project No. 98-02-16993.

6. REFERENCES

1. Laser and particle induced shock waves. Special section in *Laser and Particle Beams*, 14, No. 2, pp. 109-236, 1996.

2. L.P. Feoktistov, V.V. Klimov, A.L. Feoktistov "Harnessing laser radiation for production of synthetic diamonds". *Bulletin of the Lebedev Physics Institute*, No. 9, pp. 1-3, 1992.
3. N.V. Zmitrenko, A.I. Nikanorov, V.B. Rozanov, S.A. Shumskii "Synthesizing Diamonds by Pressure Pulses". *Preprint of P.N. Lebedev Physical Institute*, No. 60, Moscow, 1992.
4. F. Dahmani and T. Kerdjia "Measurements and laser-wavelength dependence of mass-ablation rate and ablation pressure in planar layered targets". *Laser and Particle Beams*, 9, No. 3, pp.769-768, 1991; F. Dahmani and T. Kerdjia "Laser-intensity and wavelength dependence of mass-ablation rate, ablation pressure, and heat-flux inhibition in laser-produced plasmas". *Phys.Rev.A*, 44, No. 4, pp. 2649-2655, 1991.
5. D.J. Erskine and W.J. Nellis "Shock-induced martensitic transformation of highly oriented graphite to diamond". *J. Appl. Phys.*, 71, No. 10, pp. 4882-4886, 1992.
6. V.P. Avtonomov, Yu.G. Geondjian, V.Yu. Korol' V.Ya. Kuznetsov "Methodology of experiments in megabar pressure range produced by a laser". *Preprint of P.N. Lebedev Physical Institute*, No. 37, Moscow, 1993.
7. V.G. Bakaev, Yu.G. Geonjian, S.Yu. Gus'kov et al. "KrF-laser system for investigation on physics of megabar pressures, equation of state and phase transformations" in *Proc. Int. Conf. "Lasers'95"*, Charleston, SC, USA, December 4-8, 1995, V.J. Corcoran & T.A. Goldman Editors, pp. 426-431, STS Press, McLean, VA, 1996.
8. N.G. Basov, V.G. Bakaev, E.A. Grigor'yants et al. "Wide-aperture electron-beam-pumped excimer KrF laser with an output power of 1 GW". *Sov. J. Quantum Electron.*, 21, No. 8, pp. 816-817, 1991.
9. N.G. Basov, V.G. Bakaev, A.V. Bogdanovskii et al. "E-beam pumped "GARPUN" broadband KrF laser with ~1GW pulsed lasing power". *J. Sov. Laser Res.*, 14, No. 5, 1993.
10. V.G. Bakaev, V.Yu. Korol', I.G. Lebo et al. "Laser-target interections on KrF "GARPUN" facility". *Preprint of P.N. Lebedev Physical Institute*, No. 69, Moscow, 1997.
11. N.G. Basov, A.D. Vadkoovskii, V.D. Zvorykin et al. "Injection control of the parameters of radiation emitted by a high-power KrF laser pumped by an electron beam". *Quantum Electron.*, 24, No. 1, pp. 13-16, 1994.
12. Ya.B.Zeldovich and Yu.P. Raizer. *Physics of Shock Waves and High-Temperature Hydrodynamic Phenomena*. Academic, NY, 1967.
13. M.H. Rice, R.G. McQueen, J.M. Walsc "Compression of solids by strong shock waves". *Solid State Physics*, 6, pp. 1-64, 1958.
14. S.Yu. Gus'kov, V.B. Rozanov, M.A. Rumyantseva "Equations of state for metals (Al, Fe, Cu, Pb), polyethylene, carbon, and boron nitride as applied to problems of dynamical compression". *J. Russian Laser Res.*, 18, No. 4, pp. 311-342, 1997.
15. M. Yoshikawa, Y. Mori, H. Obata et al. "Raman scattering from manometer-sized diamond". *Appl. Phys. Lett.*, 67, No. 5, pp. 694-696, 1995.

Development of the nonlinear optical element for light beams apodization and large aperture laser amplifier decoupling

Leonid M. Vinogradsky*, Serge K. Sobolev*, Iosif G. Zubarev**, Mikhail V. Pyatakhin**,
Yury V. Senatsky**, Vitaly M. Mizin***, and Ken-ichi Ueda****

* Russian Federal Nuclear Center - VNIIEF, Sarov, Nizhny Novgorod region, Russia

** P.N. Lebedev Physical Institute of the Russian Academy of Sciences, Moscow, Russia

*** State Scientific Center of the Russian Federation - NIOPIK, Moscow, Russia

**** Institute for Laser Science, University of Electrocommunications, Tokyo, Japan

ABSTRACT

Dye-cell "soft" diaphragms for apodization of powerful laser beams are investigated. A cell design with a meniscus lens spacer is proposed to compensate thermal phase distortions in the transmitted laser beam. Laser shot-blasted "soft" aperture technology is discussed. The obtained results have revealed a feasibility to create a wide-aperture nonlinear optical decoupling element - apodizer for application in powerful iodine, neodymium and excimer lasers.

Keywords: laser beam apodizer, dye cell, meniscus spacer.

The light beam apodizers ("soft" diaphragms) have become rather widely used devices for the optical channels in the modern high-power laser facilities. The apodizers serve to smooth the intensity spatial distribution in the light beams, as their application allows one to suppress the sharp intensity spikes which may appear in the aperture of the beam diffracted by an ordinary "hard" diaphragm. So, the application of "soft" diaphragms improves the stability of high-power laser beams relative to self-focusing. It becomes also possible to optimise filling factor of the laser beam to increase the laser output of the active medium, to improve the efficiency of the laser radiation transformation into high-frequency harmonics¹⁻⁵.

Despite of a large number of the proposed methods and technologies for the formation of "soft" apertures, just a few types of apodizers have found practical application in the optical channels of high-power lasers. These apodizers are typical of high damage threshold to the laser radiation (1-5 J/cm²) and high contrast ratios, $K=10^2-10^3$, (K is the ratio between the radiation transmission coefficients at the axis and periphery of the beam). Among them note the so-called serrated-aperture apodizers cut from metal⁵, the diaphragms based on partially grained dielectric plates⁶, the diaphragms based on multilayered dielectric coatings, and some others.

One of the first proposed diaphragm represented a cell with a profiled liquid layer absorbing the laser radiation² (Fig. 1a). In order that a laser beam with homogeneous intensity distribution incident onto such a cell had the intensity distribution at the output described by a super-Gaussian function, the transmission coefficient of the diaphragm $T(r)$ had to be given by the function:

$$T(r) = T(0) \exp[-6.9(r/a)^N],$$

The profile of the optical elements limiting the absorbing liquid layer should be, generally speaking, aspherical. Or, thickness of a liquid layer, h , must be:

$$h(r) = h_0 + \frac{6.9}{k} (r/a)^N$$

Here $T(0)$ is the transmission coefficient at the diaphragm axis, a , the diaphragm radius at which $T(r)$ is reduced by 1000 times, $N=6-10$ is the diaphragm rigidity index, and k is the absorption coefficient of the dye solution. When a highly concentrated dye solution is used in a cell, the contrast of such a diaphragm can easily reach $K>10^3$. However, for cells of

Fig.1 type it is necessary to match, with high precision, the equality of refractive indexes of the liquid filling the cell, n_1 , and of the material of a cell window with curved surface, n (Fig.1a), or the lens-like spacer (Fig.1b). Estimations show that for diaphragms with about 100 mm aperture the admissible difference in the refractive indexes $\Delta n = n - n_1$ should not exceed 10^{-5} . In this case phase distortions in the beam, which had passed the "soft" diaphragm, will be within the diffraction angle of $\sim 10^{-5}$ rad. This condition dictates, obviously, strict requirements to the temperature control for a device of this type. In fact, the temperature coefficient β_1 of the refractive indexes for the most organic solvents of dyes used in lasers with wavelengths λ in the visible and near infrared ranges is $(-2) - (-5) \cdot 10^{-4}/K^7$. And for the most glasses and crystals, which can be used in the cell design, for the same wavelengths range the temperature coefficient β is $10^{-6} - 10^{-7}/K^8$. Thus, the main reason for the destruction of the immersion condition in the cell will be the variations in n_1 due to small variations in a cell temperature. In order to maintain immersion condition in a cell it is necessary to control the temperature in the cell with an accuracy of $\Delta t \sim 0.1/K$. These features of the soft diaphragms of Fig.1 type with profiled liquid layer complicate, of course, their practical usage.

At the same time, there may be a necessity in devices of such a type. As an example, the powerful iodine laser "Iskra 5" (Sarov) has 12 operating optical channels, each using several cells-decouplers bleachable under laser radiation at the wavelength $\lambda = 1.315 \mu m$. These cells with flat-parallel windows at the deep optical contact with apertures up to 400 mm are filled with dye solution with initial transmission $T(0) \sim 1\%$, and are located between amplifier's cascades. Each cascade represents a module filled with C_3F_7J gas pumped by an open discharge plasma radiation. The experience in iodine laser operation shows that the disturbances caused by the open discharge at the module periphery can produce distortions of intensity distribution profile in a laser beam propagating through the amplifier medium, thus reducing its parameters and deteriorating the focusing conditions at the target. These experimental observations have been the reason for the ISTC Project proposal to investigate the possibility of combining in one dye-cell optical element the characteristics of the bleaching decoupler and, at the same type, "soft" aperture properties - in order to suppress the distortions on the periphery of the laser beams propagating in the laser facility. This report informs of some results achieved at Feasibility Study of the ISTC Project N 651-98.

There are two approaches under study to the solution of the above formulated task. One approach suggests the use of a flat parallel layer of liquid in a cell decoupler. Under this condition the "soft" aperture has to be fabricated in one of the windows of the cell. For this fabrication a new technology is proposed, the laser shot-blasted processing of a transparent dielectric plate surface. The method is illustrated in Fig.2, where the laser-energy dissipation region with a specified transmission profile is formed by processing of a plate surface by the focused laser radiation. Note that the dissipation region may be formed also by a single (or several) layers inside of a plate volume (Fig.3). The main dimensional parameters of the plate and the processed region are illustrated in Fig. 3a. The specific feature of the proposed "soft" aperture formation is the appearance of a boundary distance L_{min} for receiving a smooth spatial intensity distribution in a laser beam after the diaphragm (Fig.3b). This parameter, as well as an admissible processing depth Δl , are connected with a dimensional parameters of the diaphragm by the following relations:

$$\sqrt{\lambda \Delta l} < \Delta r_c < \frac{L_{min}}{2r_0}$$

Here Δr_c is the dimension of a single scatterer, and r_0 is the diaphragm radius. At the distances $0 < L < L_{min}$ the spatial intensity profile of the beam after the diaphragm would be disturbed by a high contrast speckle-pattern connected with the interference of the radiation having passed the region of small scattering centers. However, at $\Delta r_c \leq 20 \mu m$, $\lambda = 1 \mu m$, $L_{min} \leq 20$ cm. Besides, as soon as for many practical applications the "soft" apertures are used in a combination with image-relaying systems, including spatial filters, high-frequency harmonics in spatial intensity distribution in a laser beam are effectively suppressed.

The essence of the second approach for the creation of a cell apodizer is illustrated in Fig.4. Here a cell is shown with flat-parallel windows and an inner spacer in the form of a meniscus lens made of a transparent material which divides the cell volume into two parts. The liquid layer absorbing the laser radiation is formed between one of the windows of the cell and the surface of the meniscus. The second (buffer) volume contains a clear solvent which does not absorb laser radiation. The optical power of the meniscus lens⁹ with refractive index n immersed into the medium with the refractive index $n_1 \approx n$ is very small. That is why the construction of the cell with meniscus spacer is expected to have considerably lower demands to the admissible difference in the refractive indexes of liquid and spacer, and accordingly, to the admissible

variations of the cell temperature. The deviation angle ψ for a ray having been passed through cell with equi-thickness (H) meniscus (Fig. 5b) is described by:

$$\psi(r) = (n^*-1)^2 H h'(r) h''(r) n$$

Here $n^*=n/n_1$ is the relative refractive index for the meniscus-liquid (window/liquid) interface, and n is the refractive index for the window/air interface. To compare, the same angle of deviation ψ_1 for the cell with a lens-type window (Fig. 5a) is described by:

$$\psi_1(r) = (n^*-1) n \cdot h'(r)$$

Thus, an application of a meniscus spacer in a cell may provide the improvement in the angle of deviation of the order of

$$\psi/\psi_1 = H h''(r) (n^*-1)$$

As the estimations show this improvement may be of 3-4 orders of magnitude. The obtained ratios are valid for small deviation angles, $h'(r) \ll 1$.

The calculations have shown that the application of meniscus spacers in cells can provide the operation of such devices as the "soft" diaphragms under rather mismatched refractive coefficients of the liquid and spacers (windows), up to $\Delta n \approx 0.1$. This means that such cells are practically insensitive to the temperature variation within several degrees. Moreover, there opens up a possibility to find some new materials for the cell liquids and windows among many media transparent in the near UV, visible, and near IR spectral range (for example, optical plastics). An application in such cells of nontoxic and non-aggressive solvents, such as water, for example, may be of interest.

The obtained results have revealed a feasibility to solve the problem of creation of a wide-aperture nonlinear optical element- apodizer formulated in frames of the ISTC Project N 651-98. It should be noted that the novel methods and technologies to be elaborated during the work on the Project and aimed at the formation of "soft" apertures may be of practical interest for high-power pulsed iodine, neodymium and excimer lasers, as well as for the lasers used in industry, medicine, and communication lines.

ACKNOLEGMENTS

This work is supported by the ISTC in frames of the Project N 651-98.

REFERENCES

1. Baranova N.B., Bykovsky N.E., Zeldovich B.Ya., Senatsky Yu.V. "Diffraction and self-focusing of radiation in high-power light pulse amplifier". *Kvantovaya Elektron.*, vol.1, N 11, pp.2435-2458, 1974.
2. Costich V.R. and Johnson B.C. "Apertures to shape high-power beams". *Laser Focus*, , pp.43-46. September 1974
3. Lukishova S.G., Krasiuk J.K., Pashinin P.P., Prokhorov A.M. "Light beams apodization as a technique for brightness increase in Nd:glass laser facilities". *Proc. of the General Physics Inst. of Acad. of Sciences of the USSR*, vol.7, pp.92-147. M."Nauka", 1987.
4. Mak A.A. et al. "Nd:glass lasers" M., "Nauka", 1990.
5. Van Wouterghen B.M., Murray J.R., Campbell J.H. "Performance of a prototype for a large-aperture multipass Nd:glass laser for inertial confinement fusion", *Appl.Optics*, 36, 21, 4932-4953, 1997.
6. Rizvi N., Rodkiss D., Panson C. "Apodizer development", *Rutherford Appleton Lab., Ann.report*, RAL-87-041, pp.113-114, 1987.
7. Schelyubsky V.I. "Control of glass homogeneity and composition level". M. "Stroyizdat" (1990).
8. "Physical quantities", Handbook, ed. by Grigoriev J.S. and Meilikov E.Z. M. "Energoatomizdat" (1991).
9. Maksutov D.D. "Astronomical optics", Leningrad, "Nauka" (1979).

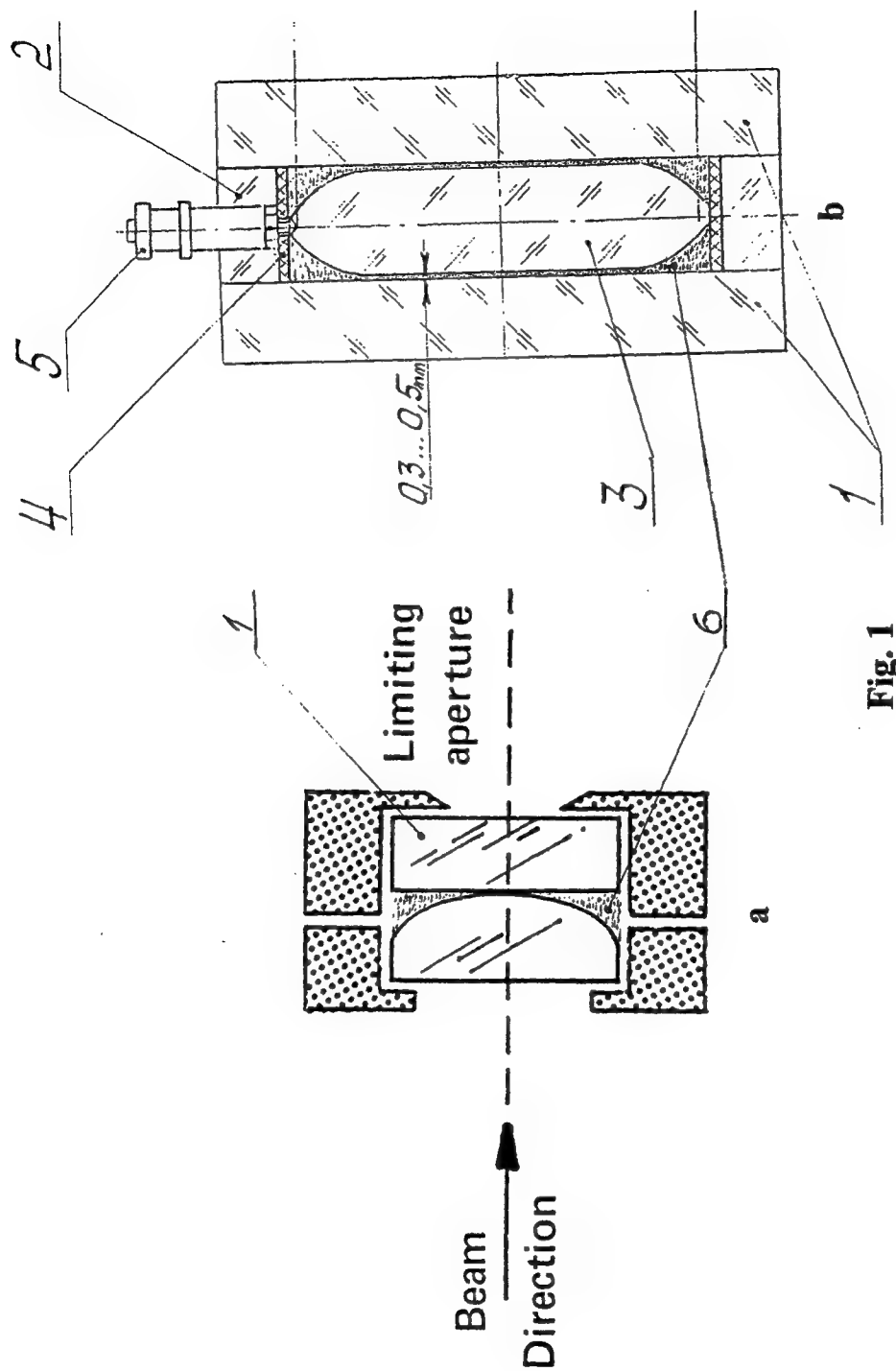


Fig. 1

1. Dye-cell apodizers: (a) without spacer, (b) with transparent spacer. Varying thickness of the absorber shapes the transmitted beam: 1 - cell windows, 2 - o-ring plate, 3 - transparent spacer, 4 - o-ring seal, 5 - filling neck, 6 - dye solution.

LASER SHOT-BLASTED SOFT APERTURE

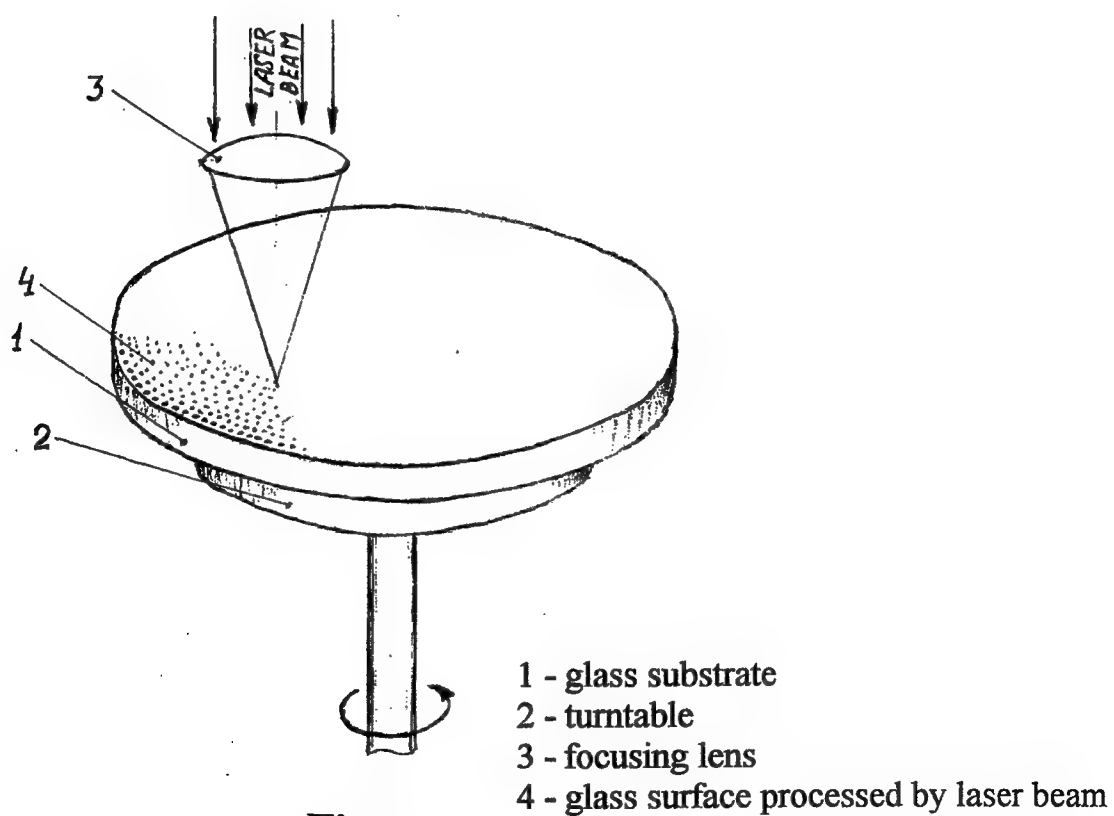


Fig. 2

2. Illustration to the proposed method of laser shot-blasted soft aperture manufacturing.

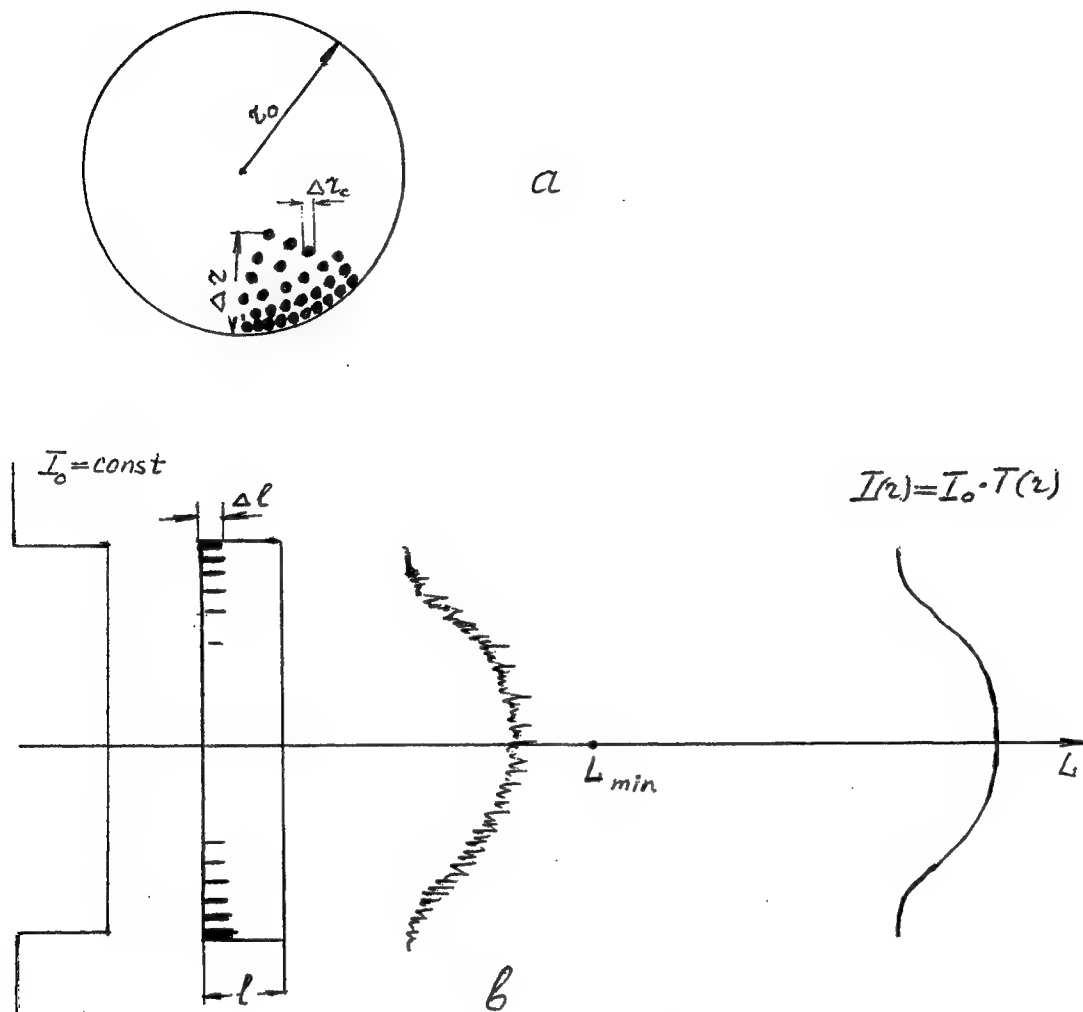


Fig. 3

3. Designation of the main dimensions in a laser-produced soft-aperture (a) and illustration to the formation of the profile of a laser beam by this soft aperture (b).

CONFIGURATION OF A DYE-CELL WITH SOFT APERTURE

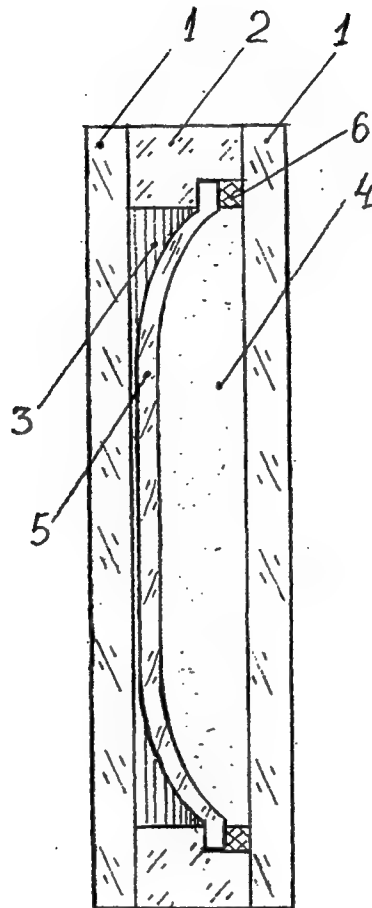


Fig. 4

- 1 - cell windows (glass, silica)
- 2 - "o"-ring cell frame
- 3 - absorbing liquid layer
- 4 - non-absorbing liquid layer
- 5 - meniscus lens spacer
- 6 - "o"-ring seal

4. Configuration of a dye cell apodizer with a meniscus spacer.

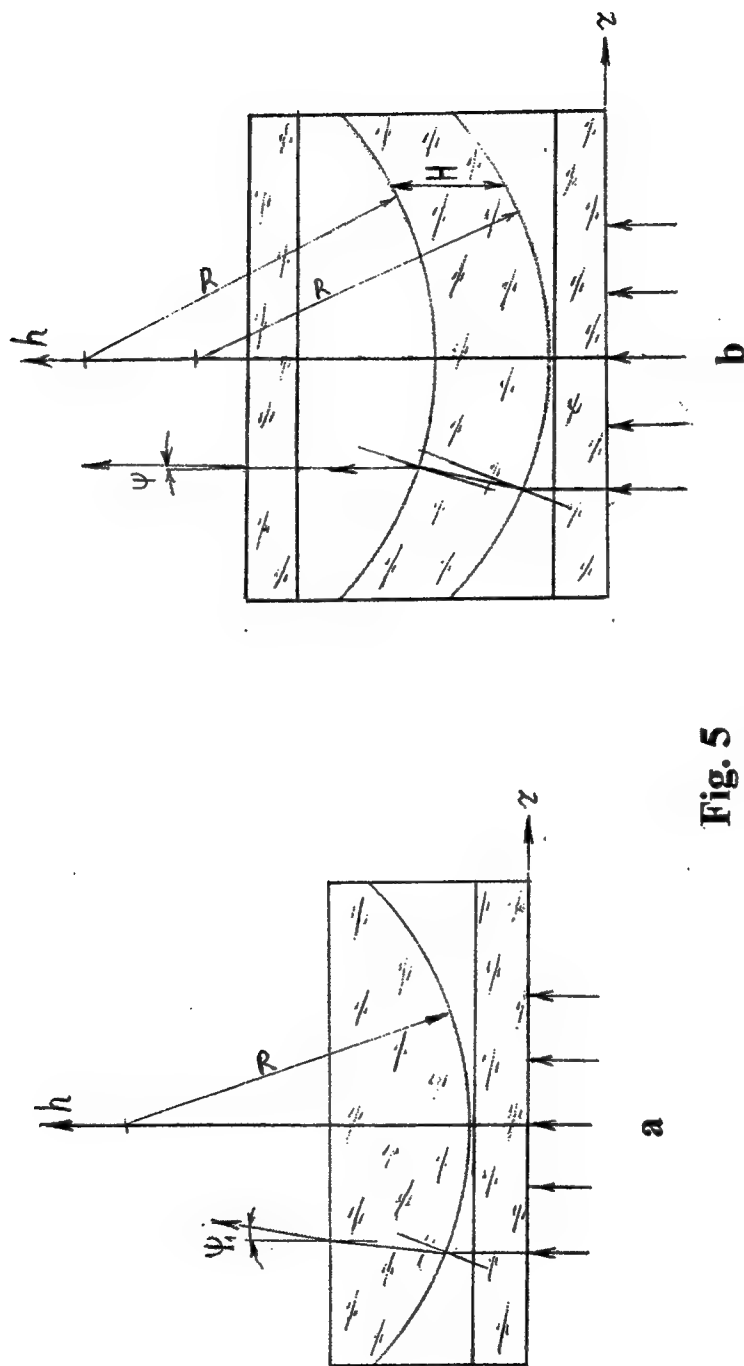


Fig. 5

5. Ray tracing for the beams propagating through the cell-apodizers with a lens-like window (a) and with a meniscus spacer (b).

SESSION 3

Devices for Ultrafast Optics

Optically detected carrier transport and capture in III/V-semiconductor QW structures: high resolution experiments, model calculations and applications in fast 1.55 μ m lasers

H. Hillmer^a and S. Marcinkevicius^b

^aDeutsche Telekom, Technologiezentrum, P.O.Box 100003, 64276 Darmstadt, Germany

Tel: +49 6151 83 3062, Fax: +49 6151 83 4912, e-mail: hillmer@tzd.telekom.de

^bDepartment of Physics II, Royal Institute of Technology, S-10044 Stockholm, Sweden

Keywords: Laser structures, carrier dynamics, quantum wells, transport, capture

ABSTRACT

Optically detected carrier dynamics in III/V semiconductor quantum well (QW) heterostructures perpendicular to the interfaces is studied. Photoluminescence (PL) emission originating from different semiconductor layers are recorded time-resolved to probe the carrier dynamics between these layers. High spatial and temporal resolution is obtained experimentally, partly even in the nm and sub-ps ranges, respectively. Using several specially tailored semiconductor heterostructures enable the following individual dynamic effects to be studied and separated: transport in extended unquantized layers, capture into the QWs, relaxation in the QWs, tunneling between the QWs and thermal reemission from the QWs. These basic physical effects have to be studied and understood to design and implement modern high-speed semiconductor laser devices. AlGaInAs and GaInAsP heterostructures are compared with respect to interwell transfer efficiencies and problems in technological implementation. This paper proceeds from basic research to applications in high-speed laser devices.

1 INTRODUCTION

For high-speed optoelectronic semiconductor devices, carrier dynamics of electrons and holes is very important. To obtain a fast dynamic response of the optical signal under high-speed current modulation in QW laser structures, an efficient and fast carrier transfer from the contact layers to the active QW layers is required, involving several physical processes: transport, capture, relaxation, tunneling and thermal reemission. The approach to isolate the effects involved is based on optical detection of the carrier dynamics by probe layers. A characteristic emission is attributed unambiguously to each of these probe layers which are placed purposefully at spatial positions in the heterostructure. The experiments and the corresponding model calculations are based on the optical detection of carrier dynamics since optical methods provide the highest spatial and temporal resolutions. Also the carrier generation is performed optically, except in the last study.

In a laser device several fundamental phenomena interact: (i) carrier transport, capture, relaxation, tunneling and thermal reemission lead to carrier densities varying from well to well, (ii) photon, carrier and injection current densities are longitudinally inhomogeneous, (iii) varying doping and band discontinuities cause band bending and internal electric fields, (iv) counteracting demands exist concerning thickness, composition and doping of the confinement layers, i.e. electrical and optical confinement as well as an efficient carrier capture into the active QW layers are desired simultaneously.

First, some mechanisms involved in direct modulation of laser diodes and important aspects of carrier dynamics will be shown. The temporal injection current variation (Fig.1 top) carries the information (bit pattern) to be translated into an intensity variation of the laser emission (Fig.1 bottom). To achieve highest bit rates, the bits have to follow each other at maximum speed, i.e. the laser should translate the current transients as fast and precisely as possible into the corresponding light intensity transients. This requires an efficient and fast carrier transfer from the contact layers to the active QW layers.

The retardation of the transfer originates from the following mechanisms (Fig.2):

- | | |
|--|--|
| 1: hole transport in the p-sided confinement layer (p-CL), | 2: electron transport in the n-sided confinement layer (n-CL), |
| 3: electron capture into the conduction band QW | 4: hole capture into the valence band QW |
| 5: thermionic emission of holes | 6: thermionic emission of electrons |
| 7: tunneling of holes | 8: tunneling of electrons |
| 9: capture of holes from the n-CL | 10: capture of electrons from the p-CL |
- and, finally, the relaxation processes inside the wells which are indicated by the vertical arrows.

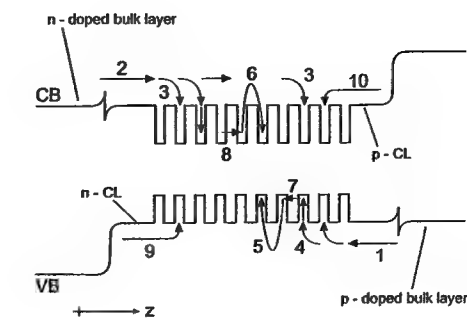
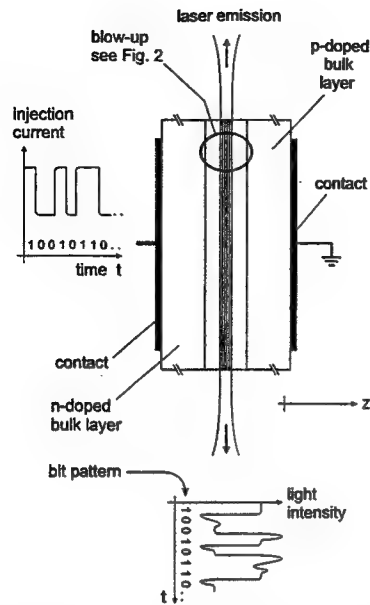


Fig. 2 Schematic of carrier dynamic processes in a MQW laser structure, blow-up of a detail shown in Fig. 1

Fig. 1 schematic of a directly modulated laser

"n-" and "p-" in front of CL indicate the position, relative to the QWs not the doping. The bulk layers are higher doped, thus, showing smaller dielectric relaxation times than the CLs. Small dielectric relaxation times in the bulk layers lead to a negligible influence of retardation effects in these layers caused by carrier transport. To visualize this problem, a tube should be imagined which is entirely filled by ping-pong balls (corresponding to a highly doped semiconductor transport distance). Inserting another ball at one end of the tube leads to an ultrafast response at the opposite end, i.e. to the emission of the last ball. Semiconductor transport distances of low doping correspond, in our model, to a tube which only contains a few ping-pong balls. In the latter case, the inserted ball has to travel part of the whole distance before a ball is emitted at the opposite end. Consequently, a noticeable retardation of the response occurs. Thus, retardation effects caused by carrier transport in the CLs (lower doping, slower dielectric relaxation) are much more pronounced than those attributable to carrier transport in the bulk layers (higher doping, faster dielectric relaxation).

Recently, carrier dynamics in semiconductor heterostructures (multiple QWs or superlattice structures) were studied. Ultrathin QWs with modified material compositions or varied well widths intended to emit a characteristic PL signal were inserted purposefully as spatial probe layers [1-22] at spatial positions in heterostructures. An enlarged QW was inserted inside or at the end of a superlattice structure to detect the arrival of carriers at the enlarged QW [1,2,4,5,7-10,14,17]. Heterostructures including QWs of different widths and, thus, specific emissions have been used to study the carrier transport in the barriers [3,6,11-13,15-17,23-25] additionally investigating carrier capture [6,11,17-22]. On the other hand carrier capture into QWs [6,11,17-24,27-77], carrier relaxation in QWs [78-84] and the interplay between capture and thermal reemission [15,67-73] were studied much more.

2 EXPERIMENTALLY MONITORED INTERWELL TRANSFER - COMPARISON: AlGaInAs vs. GaInAsP

Homogeneous carrier distributions from well to well are of major importance for the efficient operation of MQW lasers. However, modelling [88-93,19,21,22] has shown that, for MQW laser structures, the hole population differs from well to well for both continuous or time-varying current injection due to a slow interwell hole transport. Here an experimental verification is given for GaInAsP [19,21,22] and AlGaInAs [20,22] MQW structures by optical methods completed by corresponding model calculations.

Each sample contains a number N_{QW} of identical wells and a single QW probe layer of different well width or well composition terminating the sequence. The probe QW emits a PL well separated in the spectrum at lower energies from the PL of the N_{QW} wells. For each system (GaInAsP, AlGaInAs) a set of samples has been grown differing in N_{QW} (see Table 1). Fig.3 schematically shows a typical AlGaInAs structure. The four studied structures include $N_{QW}=1, 2, 4$ or 8 $Ga_{0.3}In_{0.7}As$ QWs of 3nm thickness and a terminating enlarged probe well of 7nm width. The corresponding 300K transition energies between the energetically lowest well levels are 0.79eV and 0.67eV, respectively. The QWs are separated by 10nm AlGaInAs barriers ($E_g = 1.02$ eV). The 12nm $Al_{0.48}In_{0.52}As$ blocking layer, grown close to the wide well, is used to prevent carriers, photogenerated on the right-hand side of the wide well, from being collected into the QW region. The thickness of the cap AlInAs layer with the band gap of 1.43 eV was 300nm, comparable to the absorption length of the laser light.

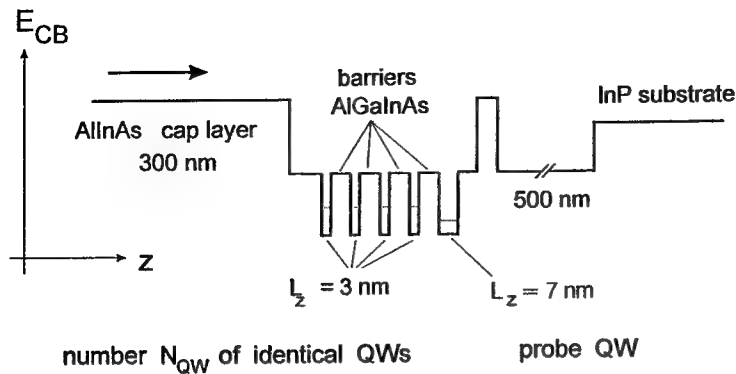


Fig. 3
Schematic of the conduction band (CB) structure of a AlGaInAs MQW structure to study interwell transfer. N_{QW} identical QWs are included and a terminating probe QW of lower band gap with either modified well width (as shown here for AlGaInAs samples) or well composition (as used for the GaInAsP samples).

material system	GaInAsP			AlGaInAs		
N_{QW}	1	2	4	2	4	8
cap layer τ_{dec}	40	40	44	13	13	13
probe QW τ_{rise}	52	67	88	18	21	32
$\tau_{dec} - \tau_{rise}$	12	27	44	5	8	19

Table 1:

Characteristic times from simple exponential profiles fitted to the experimental PL transients of AlGaInAs MQWs, N_{QW} =number of identical wells, dec=decay

The 3 studied GaInAsP structures include $N_{QW}=1, 2$ or 4 GaInAsP QWs ($L_z=8\text{nm}$) and a terminating 7nm probe QW of lower band gap energy using a different alloy composition. The corresponding 300K transition energies between the energetically lowest well levels are 0.95eV and 0.8eV, respectively. The QWs are separated by 12nm GaInAsP barriers ($E_g=1.15\text{eV}$). For both material systems the energy differences between barrier transitions and well transitions are similar (0.23eV for AlGaInAs, 0.20eV for GaInAsP) which allows the experimental results obtained for both sets of structures to be compared.

Time-resolved PL measurements were performed by an upconversion set-up [24] based on a self-mode-locking Ti:sapphire laser (central $\lambda=780\text{nm}$, repetition frequency 96MHz, pulse duration 100fs). Experimental temporal resolution was 200fs. Average excitation intensities used in the experiments range from 1 to 8mW corresponding to average carrier densities between $3 \cdot 10^{16}$ and $2 \cdot 10^{17}\text{cm}^{-3}$. Carrier density saturation inside the QWs is avoided by appropriate excitation densities.

Most carriers are generated in the cap layer (Fig.3). Some of these carriers undergo surface recombination but the majority diffuses towards the QWs. The temporal evolution of the cap layer PL reflects carrier dynamics in this layer (left transients in Figs. 4 and 5). For the GaInAsP samples the decay time τ_{dec} of this emission is mainly determined by the carrier transfer into

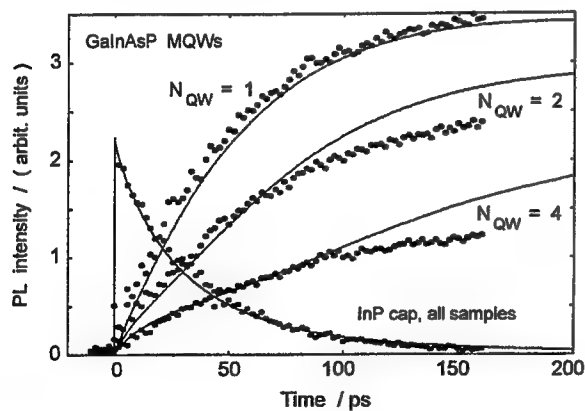


Fig. 4
Experimental PL transients (symbols) of an AlGaInAs MQW structure containing N_{QW} identical QWs and a terminating probe QW of enlarged width. The left profile corresponds to the AlInAs cap layer, the other to the probe QW. The full lines show fits obtained by model calculations.

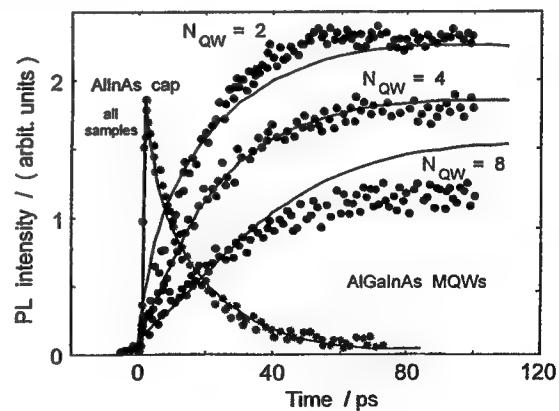


Fig. 5
Experimental PL transients (symbols) of a GaInAsP MQW structure containing N_{QW} identical QWs and a terminating probe QW of modified well composition. The data are taken from Fröjdh et al. [19]. The left profile corresponds to the InP cap layer the other to the probe QW. The full lines show fits obtained by model calculations.

the MQW region. For the AlGaInAs samples the emission decay time τ_{dec} is shorter since it is additionally influenced by surface recombination. τ_{dec} is found to be rather similar for all samples within a set (Figs. 4, 5 and Table 1). Before reaching the probe QW, these carriers pass the N_{QW} identical wells. Since optical transitions in different layers of a structure are spectrally separated, the characteristic times of the interwell carrier transfer can be evaluated from the dynamics of the PL measured at different energies. Experimental PL transients of the probe QW are shown by the symbols in Figs. 4 and 5 for the AlGaInAs and GaInAsP structures, respectively. With increasing number N_{QW} of identical wells, the increase of the PL intensity of the probe QW PL grows. In a first approximation $I_{PL} \sim (1 - \exp(-t/\tau_{rise}))$ for the probe QW intensity was fitted to the measured transients. The transport time across the N_{QW} identical wells can be approximated by the difference between the probe QW PL rise time and the cap layer PL decay time as shown in Table 1. Comparing the case $N_{QW}=4$ for both materials, the interwell transfer between the AlGaInAs MQWs seems to be faster than for GaInAsP MQWs (8ps versus 44ps). In the following, this will be modelled more precisely basis using a self-consistent solution of the continuity and Poisson equations.

3 MODEL CALCULATIONS: MECHANISMS DOMINATING CARRIER DYNAMICS COMPARISON OF THE AlGaInAs AND GaInAsP MATERIAL SYSTEMS

Interwell carrier transport is a more complicated process as transport in bulk layers. The model [94] used to calculate time- and spectrally-dependent PL signals self-consistently solves the time-dependent continuity and Poisson equations including: The interwell carrier transport is assumed to proceed via subsequent capture and thermionic emission to and from the QWs (processes 5 and 6 in Fig.2), tunneling processes between the wells (processes 7 and 8 in Fig 2) and by drift-diffusion in the CLs. Carrier transfer at the heterointerfaces is assumed to proceed via thermionic emission [95] and tunneling. For the carrier transport in the barriers, several approaches were examined: (i) a "classical" model describing carrier transport as a drift-diffusion with a specific capture probability into a QW [96] and (ii) a ballistic model considering 3D ballistic carrier transport across a QW including specific probabilities for a carrier to be transmitted, reflected, scattered and captured [95]. Comparing the calculated data with the experimental results shows that the first approach considering the precise widths of the barriers provides better agreement. Therefore, the first approach is used in the following. Most probably this is because high carrier densities in the barriers decrease the coherence lengths and, thus, quantum-mechanical aspects of the transport become less important. The PL signal was calculated from time-dependent electron and hole densities in various structure layers. To calculate carrier capture and emission, the thermionic emission model [97,98] was used. The net capture current to each QW was taken as the difference between capture and escape currents [19,98] including the quasi-Fermi levels for the unconfined 3D carriers and the confined 2D carriers in the QW. Electron and hole masses were calculated for both material systems [99], and electron and hole mobilities and diffusivities in the CLs were measured in separately grown layers for AlGaInAs [100] and taken from literature for GaInAsP [101]. The model the temporal variation of band bending in the QW region is included by self-consistently calculating the wave functions of confined states and using them to determine the QW carrier distributions. Different carrier densities in individual wells lead to non-uniform carrier distributions also in the barriers and internal electric fields. Band gap renormalisation and valence band nonparabolicity is also considered. Carrier generation in all layers of the structure is considered using respective absorption values. Carrier recombination is included in the rate equations using experimentally determined carrier lifetimes.

One of the major problems in a model including thermionic emission and capture is to chose the size of the neighbouring region of a QW (the distance on both sides of the QW in z-direction) from which efficient capture into the QW occurs. For the wide GaInAsP wells ($L_z=8\text{nm}$) the best agreement between the calculated and the measured transients is obtained if this capture distance equals L_z . For the thin AlGaInAs wells ($L_z=3\text{nm}$) the capture distance was treated as an adjustable parameter since the the capture distance equal to L_z provides a poor description of the experimental results. The best agreement between simulated and measured data was found for a width of the capture region of 6nm. In a first approximation, the capture distance can be taken as the squared carrier QW wave function according to [102]. For our 3nm AlGaInAs QWs the squared electron wave function gives 5.5nm (close to the determined capture width of 6nm). The calculated PL transients for the cap layer and the QWs are shown by full lines in Figs. 4 and 5. Taking into account that no fit parameters are included in the calculated transients except the capture width of 6nm for AlGaInAs QWs, experimental and calculated data are in good agreement. Additional insight into the relative importance of the processes interacting in carrier dynamics (Fig.2) can be obtained by varying some literature values used as parameters in the calculations: The simulation is much less sensitive to electron than hole parameters, confirming that hole dynamics determines interwell carrier transfer in QW laser structures. Besides, barrier carrier transport does not affect the overall interwell transfer significantly. Tunnelling of both electrons and holes has a minor influence because of the wide barriers and the band bending shifting the energy levels in the wells out of resonance. Thus, hole thermionic emission dominates the rate of the overall interwell carrier transfer process.

Finally, the large difference in the interwell transfer efficiency between the two materials will be discussed with respect to material band discontinuities. Fig.6 schematically displays two MQW heterostructures populated from the left-hand side by light absorption. In the following 'Gedankenexperiment' (Fig.6) we assume (i) identical well widths and capture probabilities

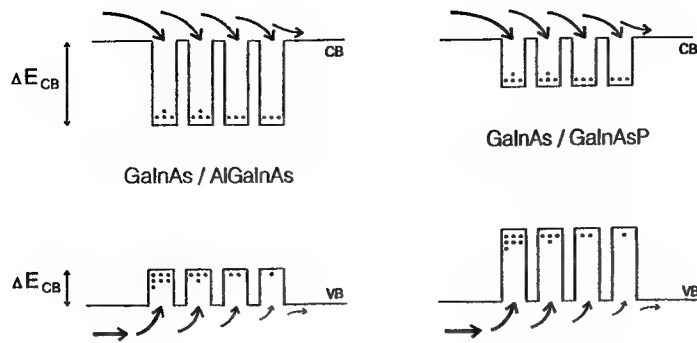


Fig. 6
Schematic band structure in space for ternary GaInAs wells embedded between either AlGaInAs or GaInAsP barriers, illustration of capture processes into the QWs of carriers injected from the left-hand side. The inhomogeneous carrier distribution from well to well is schematically indicated by a different number of dots in the QWs

for electrons in the AlGaInAs and GaInAsP wells and (ii) also for the holes the same well widths and capture probabilities in both systems. The capture rate of holes into the QWs is about five times more efficient than that of electrons [48]. Due to this asymmetry and the large hole effective masses, the carrier population inside the wells is considerably more inhomogeneous for valence band (VB) wells than for conduction band (CB) wells. The band discontinuity $\Delta E_{CB}/\Delta E_{VB}$ describing the relative depth of CB and VB wells is about 70/30 [103–106] in GaInAs/AlGaInAs heterostructures for Al contents present in our structures. $\Delta E_{CB}/\Delta E_{VB}$ is about 40/60 [107] for unstrained GaInAsP/GaInAsP heterostructures. The electrons having small effective masses can easily transfer from well to well by thermionic emission or tunneling and, thus, even high barriers as in AlGaInAs heterostructures do not markedly reduce the interwell transfer speed. The holes, however, having large effective masses suffer from high barriers during thermionic emission or tunneling. Note that tunneling processes do not participate markedly to the overall interwell transfer in our structures as mentioned above. Thus, hole interwell transfer is considerably slower in GaInAsP than in AlGaInAs. Therefore, the inhomogeneities in hole densities from well to well continue to be pronounced. Moreover, p-doping of the active region, again, due to the strong hole confinement, does not increase the interwell carrier transfer rate [21].

This shows that the depth of the VB QWs is a critical parameter for a fast interwell carrier transport. Literature values reported for band-discontinuities vary considerably, but the general trend towards considerably deeper electron wells in AlGaInAs than in GaInAsP is too evident to be overlooked. Note that the depths of the hole potential wells can be even more reduced at the expense of the electron wells by using compressively strained wells and tensile strained barriers. This improves the interwell transfer rates in both material systems. From a physical point of view, the AlGaInAs material system seems to be superior to GaInAsP. This is in agreement with experimental and theoretical studies of the differential gain, nonlinear gain factor [90] and optical gain [106]. In optoelectronics, however, GaInAsP still dominates over AlGaInAs due to a technology which, in many cases, is considerably more difficult or includes many drawbacks if Al is involved.

4 OPTICAL STUDY OF THE CARRIER TRANSPORT IN LASER STRUCTURE CONFINEMENT LAYERS

Now, MQW laser structures will be investigated, including 10 identical QWs, highly doped bulk regions and CLs of lower doping levels. We will focus on the optically detected transport in the CLs of laser structures after optical fs-pulse excitation by recording the time-resolved PL. The insets in Fig. 7 schematically show the active region and the neighbouring CLs of the three studied structures (A, B and C). Two structures with compressively strained $\text{Ga}_{0.3}\text{In}_{0.7}\text{As}$ QWs ($E_g=0.8\text{eV}$ at $T=300\text{K}$) and unstrained $\text{Al}_{0.47}\text{Ga}_{0.53}\text{As}$ barriers with $z=0.23$ (0.20) corresponding to $E_g=0.96\text{eV}$ (1.02eV) for the structure A (B) were investigated. Structure C is strain-compensated containing compressively strained $\text{Al}_{0.09}\text{Ga}_{0.91}\text{As}$ QWs and tensile strained $\text{Al}_{0.21}\text{Ga}_{0.79}\text{As}$ barriers ($E_g=1.02\text{eV}$). Lattice-matched $\text{Al}_{0.23}\text{Ga}_{0.77}\text{As}$ CLs of different widths (doping level $5 \cdot 10^{18}\text{cm}^{-3}$) embed the active region. The laser structures have been deposited on a $1\mu\text{m}$ p- $\text{Al}_{0.48}\text{In}_{0.52}\text{As}$ buffer layer grown on p-InP substrates. For further details see Table 2. Average excitation intensities between 10 and 130mW were used, corresponding to photoexcited carrier densities: $2 \cdot 10^{17}\text{cm}^{-3}$ - $2 \cdot 10^{18}\text{cm}^{-3}$ (averaged over absorption length and excitation area).

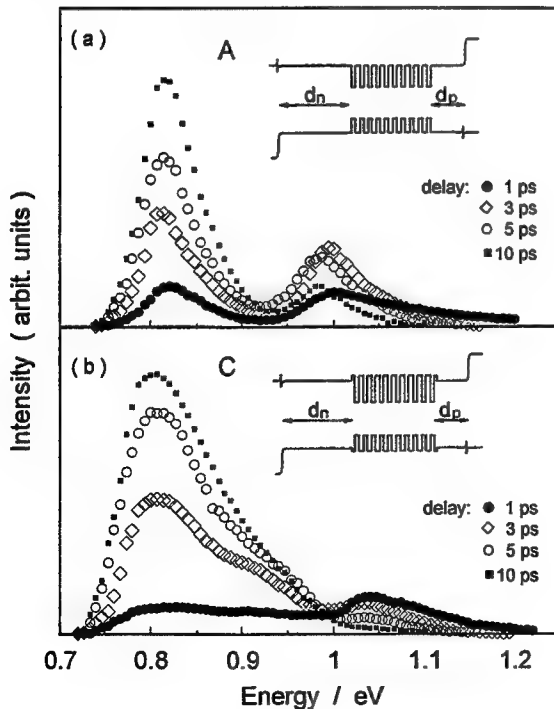
Figure 7a shows PL spectra for structure A measured at different delays after the pulsed optical excitation. While for a 1ps delay the PL peak at $\sim 1\text{eV}$ resulting from the radiative transitions in the barriers and the CLs is more intense, already 3ps after the pulse the PL from the QWs is stronger than from the CLs and barriers. The spectra show that carrier relaxation inside the wells is very fast, since the peak of the QW PL, even for the shortest time delays, does not show any considerable spectral shift with respect to the band gap energy. Although the spectra were measured under a rather high average excitation intensity of 40mW (carrier density in the wells $\approx 6 \cdot 10^{18}\text{cm}^{-3}$), we observe an efficient carrier collection into the QWs: at longer time delays the PL signal coming from the barriers is much weaker than that from the QWs. This is very different from GaInAsP/InP QW laser structures where much lower carrier densities have been sufficient to fill the conduction band QWs in a similar experiment [63]. This is attributed to the electron confinement which is better in the AlGaInAs than in the GaInAsP

system (see Fig.6). Fig.7b shows PL spectra measured for structure C at an excitation intensity of 130mW. Also in this case, the spectra reveal fast relaxation and even more efficient carrier capture since the QW-related PL peak shows a fast increase. At a time delay as short as 10ps, the peak of the barrier and confinement PL is barely seen, demonstrating more efficient carrier capture than in Fig.7a. Due to larger carrier density in the wells, the QW PL peak in Fig.7b is broader than in Fig.7a. For any time delays, we observe no inversion of the QW PL spectrum, confirming that intersubband carrier relaxation in the QWs is in the sub-ps range [108].

For a fixed detection wavelength the barrier PL transient consists of a fast rise which is determined by carrier relaxation in the barriers and the CLs, and a decay which is due to carrier transfer into the wells. Since hole relaxation and capture is much faster than those of electrons [109,102] the relaxation and capture times determined in present experiments should be attributed to the electrons. The increase of the barrier PL intensity is approximated by $I_{PL} \sim [1 - \exp(-t/\tau_{br})]$ with $\tau_{br} = 0.8 \pm 0.1$ ps for all samples. The barrier PL decay is single-exponential (barrier decay time τ_{bd}) for sample C at all excitation powers and for the other two samples in the case of lower excitations (br = barrier rise, bd = barrier decay, wr=well rise, where "the b for barrier" includes barriers and CLs).

The increase of the transient QW PL can be well fitted by $I_{PL} \sim [1 - \exp(-t/\tau_{wr})]$. The well rise time τ_{wr} includes: relaxation of carriers photoexcited in the QWs, capture of carriers generated in the barriers, and transport as well as capture of carriers excited in the CLs. Since the barriers and wells are thin compared to the CLs, τ_{bd} and τ_{wr} can mainly be attributed to carrier transport in the CLs and capture into the QWs (evaluated time constants in Table 2). τ_{wr} is found not to deviate much from τ_{bd} (Table 2) indicating that the difference may be mainly attributed to carrier relaxation in the QWs.

In a first approach, according to the last paragraph, a single effective time constant was used, describing the carrier transport in the n-sided and p-sided CLs in combination. In a second approach two time constants were used, corresponding to carrier transport from the n-sided and in the p-sided CLs separately. However, the transport time related to the n-sided CL is found to be very similar to the single effective time constant used in the first approach. Since the n-sided CL is several times wider than the p-sided CL in all the structures (Table 2), the single effective time constant mainly reflects carrier transport in the n-sided CL. These transport times show a linear dependence on the squared width of the n-sided CL and can be described by an ambipolar diffusivity of $D_{amb} = 3 \text{ cm}^2/\text{s}$ [66]. These results are in good agreement to the data obtained below, where somewhat wider CLs (see Table 4) allow to determine two separate time constants for the n-sided and p-sided CLs. All these studies show a clear increase of τ_{wr} with increasing transport distances in the CLs. Summarizing some important points: electrons and holes show different mobilities and capture efficiencies into QWs which has initiated the development and design of laser structures of asymmetric confinement where d_n is not equal to d_p .



structure	n - sided CL d_n / nm	barrier width L_B / nm	well width L_z / nm	number of QWs N_{QW}	p - sided CL d_p / nm	barriers/CLs PL decay time τ_{bd} / ps	PL rise time of QWs τ_{wr} / ps
A	130	6	3	10	50	5.1	5.8
B	112	8	3	10	25	4.1	5.0
C	85	6.4	7.2	10	25	2.5	3.0

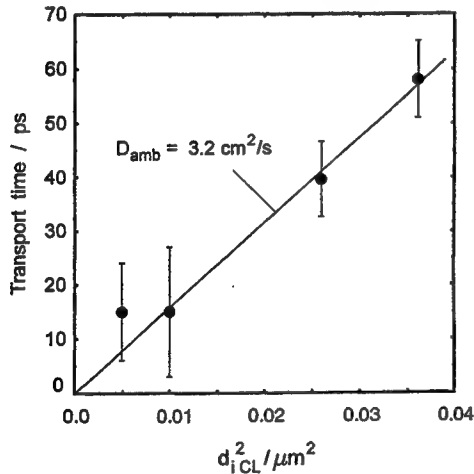
Table 2:
Characteristic times from simple exponential fits and structural parameters of AlGaInAs MQW structures

← Fig. 7
PL spectra at different times after the excitation pulse for (a) structure A containing ternary $\text{Ga}_{0.3}\text{In}_{0.7}\text{As}$ wells and unstrained AlGaInAs barriers and for (b) the strain-compensated structure C with quaternary AlGaInAs wells and barriers. The insets schematically show the corresponding band structure.

5 CARRIER TRANSPORT IN BIASED LASER DEVICES MONITORED BY OPTICAL METHODS

Now, relaxation oscillations present after short optical pulse excitation, in electrically cw-biased MQW laser devices are studied time-resolved recording of the emitted laser light. Two laser devices (D, E) are compared including 10 compressively strained $\text{Ga}_{0.3}\text{In}_{0.7}\text{As}$ QWs ($E_g=0.8\text{eV}$ at $T=300\text{K}$), unstrained $\text{Al}_{0.21}\text{Ga}_{0.44}\text{In}_{0.35}\text{As}$ barriers ($E_g=1.02\text{eV}$) and asymmetric confinement, i.e. the n-sided CL width d_n unequals the p-sided CL width d_p (see Table 3). In this experiment, an optical modulation method [110,111] is used which is parasitic-free in contrast to electrical laser device modulations. For each of the measurements, the lasers are cw-biased by an individual injection current generating a corresponding photon density profile along the laser resonator. This continuous state is disturbed by 5ps Nd:YAG laser pulses ($\lambda=1.064\mu\text{m}$) focussed in a stripelike way homogeneously along the whole resonator length by a cylindrical lense. The light, entering from the n-side is absorbed partly in the QWs and barriers but mainly in the CLs. The relaxation oscillations in the emitted laser light are recorded by a fast photodiode/sampling oscilloscope. Taking the Fourier transform of the measured relaxation oscillations provides the intrinsic modulation response [110,111].

To fit the experimental modulation response profiles, coupled carrier and photon rate equations [110,111] were used including the transport times $\tau_{i\text{CL}}$ with $i=n$ or p , which correspond to CL widths d_n and d_p . For each of the laser devices two different times $\tau_{n\text{CL}}$ and $\tau_{p\text{CL}}$ were determined (see Table 3) due to the asymmetric CLs, the times being independent of the bias current within the experimental error. In the following, the transport in the p-sided and n-sided CLs is approximated to be purely diffusive with the ambipolar diffusivity D_{amb} . Using the diffusion equation with appropriate boundary conditions in a small-signal solution allows the transport times to be identified as $\tau_{n\text{CL}}=d_n^2/2D_{\text{amb}}$ and $\tau_{p\text{CL}}=d_p^2/2D_{\text{amb}}$. This implies a square dependence of $\tau_{i\text{CL}}$ on d_i . Fig.8 displays the experimental values from Table 3, confirming these approximative relations within the experimental error. The straight line yields a diffusivity of $3.2\text{cm}^2/\text{s}$. This agrees well with the ambipolar diffusivity $D_{\text{amb}}=3.3\text{cm}^2/\text{s}=2(1/D_e+1/D_h)^{-1}$, calculated from the experimental mobilities $\mu_e=2600\text{Vs}/\text{cm}^2$ and $\mu_h=65\text{Vs}/\text{cm}^2$ for electrons and holes in the quaternary CLs [100] using the Einstein relation.



laser device	d_n / nm	L_B / nm	L_z / nm	N_{QW}	d_p / nm	$\tau_{n\text{CL}}$ / ps	$\tau_{p\text{CL}}$ / ps
D	160	6	3	10	70	40	15
E	100	11	3	10	190	15	58

Table 3: Transport times from a diffusion model and structural parameters of AlGaInAs MQW laser devices, nCL=n-sided CL, pCL=p-sided CL.

Fig. 8 Effective transport times from the n- and p-sided CLs versus the squared widths of the corresponding CLs of AlGaInAs laser devices. The data are taken from Zimmermann et al. [111]. The straight line yields an ambipolar diffusivity of $3.2\text{cm}^2/\text{s}$.

6 CARRIER AND PHOTON DYNAMICS IN HIGH-SPEED LASER DEVICES

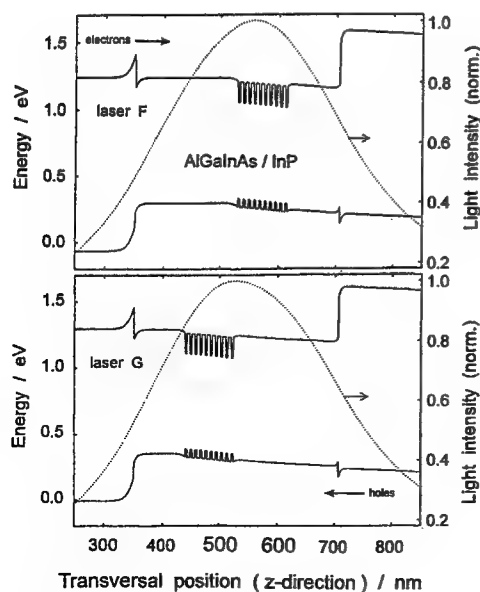
Theoretical and experimental studies of carrier and photon dynamics of laser devices have received great attention in recent years since these lasers rank among the key-components for high-speed communication systems (Fig.1). Recently, it has been found that modulation properties of MQW lasers are not only determined by the 2D character of the carriers in the active layers (QWs) but, in addition, essentially by the carrier dynamics in the CLs and barriers as well as the interwell transfer (Fig.2). Thus, the modulation properties of MQW lasers are determined by many complicated interacting processes. Two examples will be given in the following of counteracting demands which are imposed on the geometric and compositional parameters of high-speed laser structures by these interacting processes. (i) CL widths have to be as thin as possible to enable a fast carrier transport of the injected carriers to the QWs. On the other hand, however, a proper optical confinement requires sufficiently thick CLs on both sides of the QWs between the low refractive index bulk n- and p-doped layers. (ii) CLs should

be highly doped to reduce the dielectric relaxation times and, thus, the transport times. On the other hand, they should contain a low doping to reduce reabsorption losses.

Simulations [100] of laser dynamics were performed using a drift-diffusion model for electrons and holes using the Poisson and continuity equation. The carrier recombination includes radiative processes such as Shockley-Read-Hall and Auger recombination as well as spontaneous and stimulated recombination. Furthermore, a rate equation is considered including the confinement factor, the photon lifetime, the spontaneous emission factor and a stimulated emission term. We neglect carrier heating and hot phonon effects, which may result in a slight overestimation of stimulated recombination. The simulation focusses on transport processes of carriers to the active regions and not on the explicit dynamics inside the QWs. These equations are used to simulate the intensity modulation response in a small signal (linear) regime. As an initial condition a stationary operation above threshold was taken. Changing the boundary conditions for the Poisson equation the system exhibits relaxation oscillations before entering the new stationary state. The Fourier transform of these oscillations results in the amplitude modulation response.

Since electrons and holes have different mobilities [100] and capture probabilities into the QWs [95,121], lasers with asymmetric CLs (Figs. 7 and 9) were developed and studied [100,134,118,158,121,95,159]. If $d_p \ll d_n$ is chosen, the less mobile holes have to travel a shorter distance at the expense of the more mobile electrons. But this asymmetry also provides a faster carrier transfer into the QWs due to another reason: electrons are captured less efficiently by the QWs which causes a larger accumulation of electrons transmitted across the QWs to the p-sided CL, but a smaller accumulation of uncaptured holes into the n-sided CL. Due to the asymmetry the population capacity of the accumulation region d_p with uncaptured electrons can be shrunk. This reduces the influence of the electron capture process from the accumulation region d_p (process 10 in Fig.2). Since the holes are captured more efficiently, the region d_n will not be populated by many holes and, thus, may have a larger extension. Therefore, the influence of the hole capture process from the accumulation region d_n (process 9 in Fig.2) will not increase markedly.

Different geometrical, compositional and doping conditions in the CLs are considered in the model calculations. In contrast to [134], our structures have different bulk layers (InP and AlInAs) embedding the CLs as well as, in many cases, a DFB grating. Therefore, we are able to remain close to the transverse maximum of the guided light field in optimized and implemented structures as shown below, in contrast to the structures reported in [134]. The variation of d_n and d_p in these asymmetric structures is useful for studying the influence of carrier transport and carrier capture on modulation bandwidth, since electrons and holes have considerably different capture times and mobilities. For our first comparison we select two structures (laser structures F and G in Table 4) with a nearly identical optical confinement factor $\Gamma=6\%$ and the same total thickness of the CLs d_n+d_p , but different positions of the MQW stack: either asymmetrically n-side shifted ($d_n=90\text{nm}$, $d_p=180\text{nm}$) or p-side shifted ($d_n=180\text{nm}$, $d_p=90\text{nm}$) which is illustrated in Fig.9. The calculations include electron and hole mobilities measured as a function of doping in the related quaternary AlGaInAs and ternary AlInAs materials at 300K [100].



laser device	d_n / nm	L_B / nm	L_z / nm	N_{QW}	d_p / nm
F	180	8	3	10	90
G	90	6	3	10	180
H	112	8	3	10	25
I	110	5.8	7.2	10	25

Table 4:
Structural parameters, AlGaInAs MQW laser devices,
nCL=n-sided confinement layer, pCL=p-sided CL.

Fig. 9
Calculated transversal band structures (full lines) and
corresponding guided optical fields (dotted lines) of
the AlGaInAs laser devices described in Table 4.

The required material parameters such as the mobilities [100] are used to calculate the transversal variation of the band edges solving the above mentioned equations self-consistently for the stationary case. The band edges are depicted in Fig.9 for both structures. Next, dynamic calculations are performed comparing the amplitude modulation response of both structures. Effects like the low and high frequency rollofts in the linear response of the system are identified by spatial transport. For a photon density of $14 \cdot 10^{15} \text{cm}^{-3}$ the laser with the long p-sided CL shows a -3dB frequency of 22GHz and the laser with the short p-sided CL shows 28GHz. This laser still reveals a distinct resonance, i.e. an inherent potential to reach still higher bandwidths for increasing bias (rising photon densities). The structure with short p-sided CL (Fig. 9a) shows an enhanced modulation performance due to (i) a faster transfer of less mobile holes to the QWs due to the reduced d_p and (ii) an enhanced preventive measure against the consequence of the less efficient electron capture and noticeable amount of electron transmission across the QWs, since the electron accumulation in the p-sided CL is reduced by a smaller d_p . [134] also includes an experimental comparison between a symmetric structure and an asymmetric structure with shorter n-sided CL showing a -3dB frequency of about 10GHz and 7GHz, respectively (the confinement factor also changed and, unfortunately, the selected asymmetric structure was the less favorable of both possibilities).

Now, structural data of laser devices F and G are given in addition to those included in Table 4. Between the p-doped AlInAs buffer ($>2 \cdot 10^{18} \text{cm}^{-3}$ Be) and the active MQW stack, the "p-sided" p-doped AlGaInAs ($5 \cdot 10^{17} \text{cm}^{-3}$ Be) CL of width d_p is located. On the opposite side, between the DFB grating and the MQWs, the "n-sided" p-doped AlGaInAs ($5 \cdot 10^{17} \text{cm}^{-3}$ Be) CL is located. The DFB grating is covered by an n-doped InP top layer ($>2 \cdot 10^{18} \text{cm}^{-3}$ Si). Since the AlInAs and InP bulk layers are highly doped, the respective dielectric relaxation times are very small in these layers, leading to a very small influence of these layers on the modulation properties. The modelled structure includes: QW active region, CLs, AlInAs and InP bulk layers. The influence of these highly doped regions on the modulation properties is found to be negligible due to the small dielectric relaxation times. However, the AlGaInAs CLs are given a lower doping to reduce optical free carrier reabsorption losses of the guided optical field, but this implies a decrease in high-frequency properties due to transport in the CL. By varying d_n and d_p , these asymmetric structures become very useful for studying the influence of carrier transport and carrier capture into the QWs on modulation bandwidth, since electrons and holes differ considerably in mobilities and capture times.

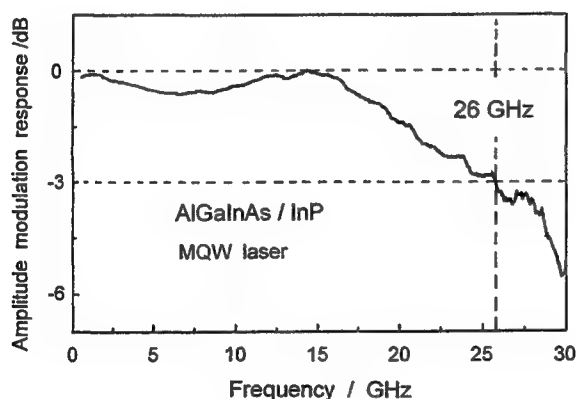


Fig. 10

Experimental amplitude modulation response of laser H at 120mA

The modelling results are also experimentally confirmed [160,118,111] for the implemented laser devices D and E (Table 3) showing also a difference between the two lasers in the -3dB frequency of 5-6 GHz, although at lower absolute values due to electrical parasitics. This result demonstrates the importance of geometry and doping of the laser structures for optimized high-frequency behaviour. After further optimizations using structures of reduced $d_p=25\text{nm}$ and $d_n=112\text{nm}$, we obtained 26GHz in the experimental modulation bandwidth (Fig.10) of distributed feedback (DFB) laser. This is a record value for the pure AlGaInAs material system at $1.55\mu\text{m}$ to the best of our knowledge. The calculated maximum bandwidths are even higher, probably due to, e.g., remaining parasitics, leakage currents, ohmic heating, non-isothermal transport and hot phonon effects. We believe that we do not approach the inherent bandwidths mainly due to the fact that our lasers suffer from leakage currents at the interface between the CLs/MQWs and the semi-insulating InP. The bandwidth of 26GHz was obtained for both, compressively strained ternary GaInAs QWs embedded between unstrained AlGaInAs barriers (deviceH, Table 4) and strain-compensated structures including compressively strained quaternary AlGaInAs QWs embedded between tensile strained AlGaInAs barriers (device I, Table 4). Recently the record value in the widely applied GaInAsP/InP has been improved from 26GHz to 30GHz [161,162]. Laser structures combining these two material systems (GaInAsP wells, AlGaInAs barriers) have also recently reached 30GHz [164]. These bandwidths correspond to laser devices emitting around $1.55\mu\text{m}$. Lasers with shorter wavelength close to 980nm recently have reached a bandwidth of 40GHz [164-166].

7 CONCLUSIONS

We studied optically detected carrier dynamics in various strained and unstrained (Al)GaInAs(P) QW structures perpendicular to the interfaces. The time-resolved PL from specific probe layers was recorded to monitor the carrier dynamics between these layers. The experimental methods enable high resolutions, partly even in the nm and sub-ps rang. Self-consistent solutions of the continuity, Poisson and rate-equation(s) are used to evaluate the experimental data. Using specially tailored heterostructures, the following individual dynamic effects are isolated and studied: transport, capture, relaxation, tunneling and thermal reemission. This paper starts from several basic physical effects and simple basic structures to finally approach real laser applications in high-speed laser devices. Asymmetric laser structures with short p-sided CLs can counteract the slower hole transport towards the QWs at the expense of the more mobile electrons travelling through a wider n-sided CLs. Interwell transfer is shown to be limited by hole thermionic emission.

We wish to thank A.Hangleiter, M.Zimmermann and S.Krämer for optically detected modulation experiments, K. Fröjd, T.Kuhn, A.Greiner and for model calculations, R.Lösch and W.Schlapp for MBE, C.Silfvenius, B.Stalnacke and G.Landgren for MOCVD, F.Steinhagen, E.Kuphal, B. Hübner, R.Göbel, and B.Kempf for technological support, financial support from the Swedish Council for Engineering Sciences.

8 REFERENCES

1. A. Chomette, B. Deveaud, J. Y. Emery, A. Regreny, and B. Lambert, *Solid State Commun.* 54, 75 (1985).
2. K. Fujiwara, J. L. de Miguel, and K. Ploog, *Jap. J. Appl. Phys.* 24, L405 (1985)
3. H. Hillmer, G. Mayer, A. Forchel, K. S. Löchner, and E. Bauser, *Appl. Phys. Lett.* 49, 948 (1986).
4. A. Nakamura, K. Fujiwara, Y. Tokuda, T. Nakayama, and M. Hirai, *Phys. Rev. B* 34, 9019 (1986)
5. B. Deveaud, J. Shah, T.C. Damen, B. Lambert, and A. Regreny, *Phys. Rev. Lett.* 58, 2582 (1987).
6. D. J. Westland, D. Mihailovic, J. F. Ryan, and M. D. Scott, *Appl. Phys. Lett.* 51, 590 (1987).
7. J. Benhlal, P. Lavallard, C. Gourdon, R. Gruosson, M.L. Roblin, A.M. Pougnet, R. Planel, *Journal de Physique Col.* C5, 471 (1987).
8. B. Deveaud, J. Shah, T.C. Damen, B. Lambert, A. Chomette, and A. Regreny, *IEEE J. of Quant. Electron.* 24, 1641 (1988).
9. B. Lambert, B. Deveaud, A. Chomette, A. Regreny, and B. Sermage, *Superl. and Microstruc.* 5, 565 (1989).
10. B. Lambert, B. Deveaud, A. Chomette, A. Regreny, and B. Sermage, *Semicond. Sci. Technol.* 4, 513 (1989).
11. H. Hillmer, A. Forchel, T. Kuhn, G. Mahler, H. P. Meier, *Phys. Rev.* 43, 13992 (1991).
12. G. Ambrazevicius, S. Marcinkevicius, T. Lideikis, and K. Naudcius, *Semicond. Sci. Technol.* 6, 41 (1991)
13. G. Ambrazevicius, S. Marcinkevicius, T. Lideikis, and K. Naudcius, *Semicond. Sci. Technol.* 7, 818 (1992)
14. T. Amand, J. Barrau, X. Marie, N. Lauret, B. Dareys, M. Brousseau, *Phys. Rev. B* 47, 7155 (1993).
15. G. Bacher, C. Hartmann, H. Schweizer, T. Held, G. Mahler, and H. Nickel, *Phys. Rev. B* 47, 9545 (1993).
16. H. Hillmer, T. Kuhn, A. Greiner, S. Hansmann, H. Burkhard, *Optical and Quantum Electron.* 26, S691 (1994).
17. P. A. Evans, P. Blood, and J. S. Roberts, *Semicond. Sci. Technol.* 9, 1740 (1994).
18. S. Marcinkevicius, U. Olin, C. Silfvenius, et al., in *Hot Carriers in Semicond.*, p. 575, K. Hess ed., Plenum Press, New York, (1996).
19. K. Fröjd, S. Marcinkevicius, U. Olin, C. Silfvenius, B. Stalnacke, and G. Landgren, *Appl. Phys. Lett.* 69, 3695 (1996).
20. S. Marcinkevicius, K. Fröjd, H. Hillmer, R. Lösch, and U. Olin, *Materials Science and Engineering*
21. N. Tessler, S. Marcinkevicius, U. Olin, C. Silfvenius, et al., G.L., *IEEE J. Selected Topics of Quantum Electronics* 3, 315 (1997).
22. S. Marcinkevicius, H. Hillmer, R. Lösch, K. Fröjd, and U. Olin, *Phys. Stat. Sol.* (1997)
23. S. Marcinkevicius, K. Fröjd, and K. Naudcius, *J. of Luminescence* 54, 89 (1992).
24. S. Marcinkevicius, U. Olin, J. Wallin, K. Streubel, and G. Landgren, *Appl. Phys. Lett.* 65, 2057 (1994).
25. S. Marcinkevicius, U. Olin, J. Wallin, K. Streubel, and G. Landgren, *Appl. Phys. Lett.* 66, 2098 (1995).
26. M. S. Skolnick, J. J. Finley, J. W. Cockburn, R. J. Teissier, R. Grey, G. Hill, and M. A. Pate, *Phys. Stat. Sol.* (1997).
27. E. O. Göbel, H. Jung, J. Kuhl, and K. Ploog, *Phys. Rev. Lett.* 51, 1588 (1983).
28. D. Bimberg, J. Christen, A. Steckenborn, G. Weimann, and W. Schlapp, *J. Lum.* 30, 562 (1985).
29. J. A. Brum, and G. Bastard, *Phys. Rev. B* 33, 1420 (1986).
30. J. A. Brum, T. Weil, J. Nagle, and B. Vinter, *Phys. Rev. B* 34, 2381 (1986).
31. J. Feldmann, G. Peter, E.O. Göbel, K. Leo, H.-J. Pollard, K. Ploog, K. Fujiwara, T. Nakayama, *Appl. Phys. Lett.* 51, 226 (1987).
32. B. Deveaud, F. Clerot, A. Regreny, K. Fujiwara, K. Mitsunaga, and J. Ohta, *Appl. Phys. Lett.* 52, 1886 (1988).
33. B. Deveaud, J. Shah, T. C. Damen, and W. T. Tsang, *Appl. Phys. Lett.* 52, 1886 (1988).
34. H.-J. Pollard, K. Leo, K. Rother, K. Ploog, J. Feldmann, G. Peter, E.O. Göbel, K. Fujiwara, et al., *Phys. Rev. B* 38, 7635 (1988).
35. B. Deveaud, J. Shah, T. C. Damen, and W. T. Tsang, *Appl. Phys. Lett.* 55, 2646 (1989).
36. D. Y. Oberli, J. Shah, J. L. Jewell, and T. C. Damen, *Appl. Phys. Lett.* 54, 1028 (1989).
37. P. Blood, E. S.-M. Tsui, and E. D. Fletcher, *Appl. Phys. Lett.* 54, 2218 (1989).
38. A. Weller, P. Thomas, J. Feldmann, G. Peter, and E.O. Göbel, *Appl. Phys. A* 48, 509 (1989).
39. U. Cebulla, G. Bacher, A. Forchel, D. Schmitz, H. Jürgensen and M. Razeghi, *Appl. Phys. Lett.* 55, 933 (1989).
40. T. Kuhn and G. Mahler, *Solid-state Electron.* 32, 1851 (1989).
41. B. Deveaud, F. Clerot, A. Regreny, K. Fujiwara, K. Mitsunaga, and J. Ohta, *Appl. Phys. Lett.* 55, 2646 (1989).
42. R. Kersting, X. Q. Zhou, K. Wolter, D. Grützmacher and H. Kurz, *Superlatt. Microstruc.* 7, 345 (1990).
43. P. W. M. Blom, J. E. M. Haverkort, and J. H. Wolter, *Appl. Phys. Lett.* 58, 2767 (1991).

44. S. Weiss, J. M. Wiesenfeld, D. S. Chemla et al., *Appl. Phys. Lett.* 60, 9 (1992).
45. R. Kersting, R. Schwedler, K. Wolter, K. Leo, and H. Kurz, *Phys. Rev. B* 46, 1639 (1992).
46. S. C. Kan, D. Vassilovski, T. C. Kan and K. Y. Lau, *Appl. Phys. Lett.* 61, 752 (1992).
47. K. R. Lefebvre, and N. G. Anderson, *Appl. Phys. Lett.* 61, 282 (1992).
48. S. C. Kan, D. Vassilovski, T. C. Kan and K. Y. Lau, *IEEE Phot. Technol. Lett.* 4, 428 (1992).
49. P. W. M. Blom, C. Smit, J. E. M. Haverkort, and J. H. Wolter, *Phys. Rev. B* 47, 2072 (1993).
50. D. Morris, B. Deveaud, A. Regreny, and P. Auvray, *Phys. Rev. B* 47, 6819 (1993).
51. P. W. M. Blom, J. E. M. Haverkort, P. J. van Hall, and J. H. Wolter, *Appl. Phys. Lett.* 62, 1490 (1993).
52. B. Deveaud, A. Chomette, D. Morris, and A. Regreny, *Sol. State Commun.* 85, 367 (1993).
53. M. R. X. Barros, P. C. Becker, D. Morris, B. Deveaud, A. Regreny and F. Beisser, *Phys. Rev. B* 47, 10951 (1993).
54. Y. Lam and J. Singh, *Appl. Phys. Lett.* 63, 1874 (1993).
55. P. Sotirelis, and K. Hess, *Phys. Rev. B* 49, 7543 (1994).
56. B. K. Ridley, *Phys. Rev. B* 50, 1717 (1994).
57. J. M. Wiesenfeld, S. Weiss, D. Botkin, D. S. Chemla, *Optical and Quantum Electronics* 26, S731 (1994).
58. B. Deveaud, D. Morris, A. Regreny, M. R. X. Barros, P. Becker, J. M. Gerard, *Optical and Quantum Electronics* 26, S679 (1994).
59. P. W. M. Blom, J. Claes, J. E. M. Haverkort, and J. H. Wolter, *Optical and Quantum Electronics* 26, S667 (1994).
60. P. W. Blom, J. Caes, J. E. M. Haverkort, and J. H. Wolter, *Optical and Quantum Electronics* 26, S667 (1994).
61. R. Kersting, R. Schwedler, A. Kohl, K. Leo, and H. Kurz, *Optical and Quantum Electronics* 26, S705 (1994).
62. L. Davis, Y. L. Lam, Y. C. Chen, J. Singh, and P. K. Bhattacharya, *IEEE J. Quantum Electron.* 30, 2560 (1994).
63. S. Marcinkevicius, U. Olin, J. Wallin, and G. Landgren, *Appl. Phys. Lett.* 66, 3164 (1995).
64. K. Muraki, A. Fujiwara, S. Fukatsu, and Y. Shiraki, *Phys. Rev. B* 53, 15477 (1996).
65. O. Heller, and G. Bastard, *Phys. Rev. B* 54, 5629 (1996).
66. S. Marcinkevicius, H. Hillmer, R. Lösch and U. Olin, *Appl. Phys. Lett.* 69, 1101 (1996).
67. G. Bacher, H. Schweizer, J. Kovac, A. Forchel, H. Nickel, W. Schlapp, and R. Lösch, *Phys. Rev. B* 43, 9312 (1991).
68. M. Gurioli, J. Martinez-Pastor, M. Colocci, C. Deparis, B. Chastaingt, and J. Massies, *Phys. Rev. B* 46, 11 (1992).
69. Chin-Yi Tsai, L. F. Eastman, Y.-H. Lo, and Chin-Yao Tsai, *IEEE Phot. Technol. Lett.* 6, 1088 (1994).
70. S. Weber, W. Limmer, K. Thonke, R. Sauer, K. Panzlaff, G. Bacher, H. P. Meier, P. Röntgen, *Phys. Rev. B* 52, 14739 (1995).
71. Chin-Yi Tsai, Chin-Yao Tsai, Y.-H. Lo, and L. F. Eastman, *IEEE Photon. Technol. Lett.* 7, 599 (1995).
72. R. Paiella, G. Hunziker, and K. J. Vahala, *Appl. Phys. Lett.* 69, 4142 (1996).
73. M. Abou-Khalil, M. Goano, A. Champagne, and R. Maciejko, *IEEE Phot. Technol. Lett.* 8, 19 (1996).
74. E. H. Reihlen, A. Persson, T. Y. Wang, K. L. Fry, and G. B. Stringfellow, *J. Appl. Phys.* 66, 5554 (1989).
75. M. Preisel, J. Mork, and H. Haug, *Phys. Rev. B* 49, 14478 (1994).
76. M. Preisel, and J. Mork, *J. Appl. Phys.* 76, 1691 (1994).
77. L. F. Register, and K. Hess, *Appl. Phys. Lett.* 71, 1222 (1997).
78. C. V. Shank, R. L. Fork, R. Yen, J. Shah, B. I. Greene, A. C. Gossard, and C. Weisbuch, *Solid State Commun.* 47, 981 (1983).
79. J. F. Ryan, R. A. Taylor, A. J. Turberfield, A. Angela, M. Maciel, J. M. Worlock, A. C. Gossard, et al., *Phys. Rev. Lett.* 53, 1841 (1984).
80. K. Leo, W. W. Rühle, and K. Ploog, *Phys. Rev. B* 38, 1947 (1988).
81. J. Shah, *Superlattices and Microstructures* 6, 293 (1989).
82. T. Elsässer, R. J. Bäuerle, W. Kaiser, H. Lobentanzer, W. Stolz and K. Ploog, *Appl. Phys. Lett.* 54, 256 (1989).
83. U. Cebulla, A. Forchel, G. Bacher, D. Grützmacher, W. T. Tsang, and M. Razeghi, *Phys. Rev. B* 40, 10009 (1989).
84. Chin-Yi Tsai, Chin-Yao Tsai, Y.-H. Lo, and L. F. Eastman, *IEEE J. Quantum Electron.* 31, 2148 (1995).
85. B. Nag, *Electron Transport in Compound Semicond.*, Vol. 11 of Springer Series in Solid-State Sciences (Springer, Berlin, 1980).
86. P. A. Markowich, C. A. Ringhofer, and C. Schmeiser, *Semiconductor Equations*, (Springer, Wien, 1990).
87. T. Kuhn, and G. Mahler, *Phys. Rev. B* 40, 12147 (1989).
88. R. Nagarajan, T. Fukushima, S. W. Corzine, and J. E. Bowers, *Appl. Phys. Lett.* 59, 1835 (1991).
89. R. Nagarajan, M. Ishikawa, T. Fukushima, R. S. Geels and J. E. Bowers, *IEEE J. Quant. Electron.* 28, 1990 (1992).
90. A. Hangleiter, A. Grabmaier, and G. Fuchs, *Appl. Phys. Lett.* 62, 2316 (1993).
91. N. Tessler, and G. Eisenstein, *Appl. Phys. Lett.* 62, 10 (1993).
92. N. Tessler and G. Eisenstein, *Optical and Quantum Electronics* 26, S767 (1994).
93. C. H. Lin, C. L. Chua, Z. H. Zhu, and Y. H. Lo, *Appl. Phys. Lett.* 65, 2383 (1994).
94. K. Fröjd, P. Holström, and U. Olin, Technical Report TR 310, Institute of Optical Research, Stockholm (1996).
95. M. Grupen and K. Hess, *Appl. Phys. Lett.* 65, 2454 (1994).
96. N. Tessler, and G. Eisenstein, *IEEE J. Quantum Electron.* 29, 1586 (1994).
97. K. Horio and H. Yanai, *IEEE Trans. Electron Devices* 37, 1093 (1990).
98. H. Schneider and K. v. Klitzing, *Phys. Rev. B* 38, 6160 (1988).
99. H. Hillmer, H. Burkhard, S. Hansmann, "valence-band masses", German Telekom, Technical Report 65 TB 29 E, p. 1-17 (1991).
100. H. Hillmer, A. Greiner, F. Steinhagen, T. Kuhn et al, *SPIE Proc.* 2693, "Physics and Simulat. of Optoelectr. Devices IV", p. 352 (1996).
101. R. J. Heyes, A. R. Adams, P. D. Greene, in T. Pearsall, Editor, *GaInAsP Alloy Semiconductors*, Wiley, New York, p. 189 (1982).
102. R. Kersting, R. Schwedler, K. Wolter, K. Leo, and H. Kurz, *Phys. Rev. B* 46, 1639 (1992).
103. Y. Sugiyama, T. Inata, T. Fujii, Y. Nakata, S. Muto, and S. Hiyamizu, *Jap. J. Appl. Phys.* 25, L848 (1986).
104. J. Thompson, R. M. Ash, N. Maung, A. J. Moseley and D. J. Robbins, *J. Electron. Mat.* 19, 349 (1990).
105. J.-C. Harmand, T. Matsuno, and K. Inoue, *Jap. J. Appl. Phys.* 29, L233 (1990).
106. O. Issanchou, J. Barrau, E. Idart-Alhor, and M. Quillec, *J. Appl. Phys.* 76, 3925 (1995).
107. S. Adachi, *Physical properties of III-V Semiconductor Compounds*, Wiley, New York, (1992).

108. M.C. Tatham, J.F. Ryan, C.T. Foxton, Phys. Rev. Lett. 63, 1637 (1989); G. Weber, A.M. dePaula, Appl. Phys. Lett. 63, 3026 (1993).
109. X. Q. Zhou, K. Leo, and H. Kurz, Phys. Rev. B 45, 3886 (1992).
110. A. Grabmaier, M. Schöffthaler, and A. Hangleiter, C. Kazmierski, M. Blez, A. Ougazzaden, Appl. Phys. Lett. 62, 52 (1993).
111. M. Zimmermann, S. Krämer, A. Hangleiter, F. Steinhagen, H. Hillmer, and H. Burkhard, Appl. Phys. Lett. 69, 2324 (1996).
112. Chin-Yi. Tsai, Chin-Yao Tsai, Y-H. Lo, R. M. Spencer, L. F. Eastman, IEEE J. of Elec. Topics in Quant. Electron. 1, 316 (1995).
113. T. C. Wu, S. C. Kan, D. Vassilovski, and K. Y. Lau, Appl. Phys. Lett. 63, 441 (1993).
114. N. Tessler, and G. Eisenstein, IEEE Phot. Technol. Lett. 5, 291 (1993).
115. R. F. Nabiev, E. C. Vail, and C. J. Chang-Hasnain, IEEE J. Selected Topics in Quantum Electron. 1, 234 (1995).
116. R. F. Nabiev, E. C. Vail, and C. J. Chang-Hasnain, SPIE proceedings Vol. 2382, "Laser diode and applications", p. 143 (1995).
117. A. G. Plyavenek, SPIE proceedings Vol. 2399 "Physics and simulation of optoelectronic devices III", p. 317 (1995).
118. H. Hillmer, A. Greiner, F. Steinhagen, R. Lösch, W. S., E. Binder, T. Kuhn, et al., Techn. Digest IX Int. Conference on hot carriers in semiconductors, Chicago, USA, 1995.
119. A. Greiner, T. Kuhn, H. Hillmer, S. Hansmann, H. Burkhard, NATO ASI on "Quantum transport in ultrasmall devices" 1994, Ed. D. K. Ferry, (1995).
120. M. Alam and M. Lundstrom, SPIE proceedings Vol. 2399 "Physics and simulation of optoelectronic devices III", p. 292 (1995).
121. M. Alam and M. Lundstrom, IEEE Photon. Technol. Lett. 6, 1418 (1995).
122. M. Grupen, K. Hess, L. Rota, SPIE proceedings Vol. 2399 "Physics and simulation of optoelectronic devices III", p. 468 (1995).
123. H. Hirayama, Y. Miyake, and M. Asada, IEEE J. Quant. Electron. 28, 68 (1992).
124. H. Hirayama, and M. Asada, Optical and Quantum Electronics 26, S719 (1994).
125. H. Hirayama, J. Yoshida, Y. Miyake, and M. Asada, IEEE J. Quant. Electron. 30, 54 (1994).
126. R. F. Kazarinov, and M. R. Pinto, IEEE J. Quantum Electron. 30, 49 (1994).
127. A. D. Sadvnikov, X. Li, and W.-P. Huang, IEEE J. Quant. Electron. 31, 1856 (1995).
128. J.E.A. Whiteaway, A.P. Wright, B. Garrett, G.H.B. Thompson et al., Optical and Quantum Electron. 26, S817 (1994).
129. H. Wenzel, and G. Erbert, SPIE proceedings Vol. 2693 "Physics and simulation of optoelectronic devices IV", 2693-47 (1996).
130. R. Nagarajan, T. Fukushima, M. Ishikawa, J.E. Bowers, R.S. Geels, and L.A. Coldren, IEEE Photon. Technol. Lett. 4, 121 (1992).
131. R. Nagarajan, M. Ishikawa, and J. E. Bowers, Electron. Lett. 28, 846 (1992).
132. R. Nagarajan, R.P. Mirin, T.E. Reynolds, and J.E. Bowers, IEEE Phot. Technol. Lett. 4, 832 (1992).
133. M. Ishikawa, R. Nagarajan, T. Fukushima, J. G. Wasserbauer, and J. E. Bowers, IEEE J. Quant. Electron. 28, 2230 (1992).
134. R. Nagarajan, R.P. Mirin, T.E. Reynolds, and J.E. Bowers, Electron. Lett. 29, 1688 (1993).
135. T. Fukushima, R. Nagarajan, M. Ishikawa, and J. Bowers, Jpn. J. Appl. Phys. 32, 70 (1993).
136. R. Nagarajan, Optical and Quantum Electronics 26, S647 (1994).
137. M. Ishikawa, R. Nagarajan, and J. E. Bowers, Optical and Quantum Electronics 26, S805 (1994).
138. W. Rideout, W. F. Sharfin, E. S. Koteles, M. O. Vassell, and B. Elman, IEEE Phot. Technol. Lett. 3, 784 (1991).
139. C. B. u, J. Eom, C. H. Lange, C. B. Kim, R. B. Lauer, W. C. Rideout, and J. S. LaCourse, IEEE J. Quant. Electron. 28, 118 (1992).
140. M. O. Vassell, W. F. Sharfin, W. C. Rideout and J. Lee, IEEE J. Quant. Electron. 29, 1319 (1993).
141. Y. L. Lam, and Y. Singh, Optical and Quantum Electronics 26, S757 (1994).
142. H. Yamazaki, M. Yamaguchi, M. Kitamura, and I. Mito, IEEE Phot. Technol. Lett. 4, 396 (1993).
143. C. Y. Tsai, L. F. Eastman and Y. H. Lo, Appl. Phys. Lett. 63, 3408 (1993).
144. T. Odagawa, K. Nakajima, K. Tanaka, H. Nobuhara, T. Inoue, N. Okazaki, and K. Wakao, Appl. Phys. Lett. 63, 2996 (1993).
145. T. Odagawa, K. Nakajima, K. Tanaka, H. Nobuhara, T. Inoue, and K. Wakao, IEEE J. Quantum Electron. 29, 1682 (1993).
146. L. V. T. Nguyen, A. J. Lowery, P. C. R. Gurney, and D. Novak, IEEE J. Select. Topics in Quant. Electron. 1, 494 (1995).
147. N. Tessler, R. Nagar, and G. Eisenstein, IEEE J. Quant. Electron. 28, 2242 (1992).
148. N. Suzuki, and M. Ishikawa, IEEE Phot. Technol. Lett. 5, 767 (1993).
149. N. Suzuki, and M. Ishikawa, Optical and Quantum Electronics 26, S789 (1994).
150. M. Quillec, SPIE Proceeding. Vol. 1361, p. 34 (1990).
151. L. F. Lester, and B. K. Ridley, J. Appl. Phys. 72, 2579 (1992).
152. J.E.A. Whiteaway, A.P. Wright, B. Garrett, G.H.B. Thompson, et al., Optical and Quantum Electron. 26, S817 (1994).
153. A. P. Wright, B. Garrett, G. H. B. Thompson, and J. E. A. Whiteaway, Electron. Lett. 28, 1911 (1992).
154. G. W. Taylor, and P. R. Claisse, IEEE J. Quantum Electron. 31, 2133 (1995).
155. B. Zhao, T. R. Chen, Y. Yamada, Y. H. Zhuang, N. Kuze, and A. Yariv, Appl. Phys. Lett. 61, 1907 (1992).
157. V. I. Tolstikhin, and M. Willander, IEEE J. Quantum Electron. 31, 814 (1995).
158. F. Steinhagen, H. Hillmer, R. Lösch, W. Schlapp, H. Walter, R. Göbel, E. Kuphal, H. L. Hartnagel and H. Burkhard, Electron. Lett. 31, 274 (1995).
159. D. Vassilovski, T.-C. Wu, S. Kan, K. Y. Lau and C. E. Zah, IEEE Phot. Techn. Lett. 7, 706 (1995).
160. F. Steinhagen, H. Hillmer, S. Hansmann et al., Technical digest IOOC'95, paper FB2-6 (Hong Kong) p.52 (1995).
161. P.A. Morton, T. Tanbun-Ek, R.A. Logan, N. Chand, K.W. Wecht, A.M. Sergeant, P.F. Sciortino, Electron. Lett. 30, 2044, (1994).
162. O. Kjebon, R. Schatz, S. Lourduoss, S. Nilsson, B. Stalnacke, and L. Bäckbom, Electron. Lett. 33, 488 (1997).
163. Y. Matsui, H. Murai, S. Arahira, S. Kutsuzawa, and Y. Ogawa, IEEE Phot. Technol. Lett. 9, 25 (1997).
164. J.D. Ralston, S. Weissner, K. Eisele, R.E. Sah, E.C. Larkins, J. Rosenzweig, J. Fleissner et al., IEEE Phot. Technol. Lett. 6, 1076 (1994).
165. S. Weissner, E. C. Larkins, K. Czotcher et al, Proceedings 21th Eur. Conf. on Opt. Comm. p. 1015, Th.B.3.3, Brussels (1995).
166. D. Klotzkin, X. Zhang, P. Bhattacharya, C. Caneau, and R. Bhat, IEEE Phot. Technol. Lett. 9, 578 (1997).

New approach to computer simulation of femtosecond pulse propagation in nonlinear medium

Vyacheslav A. Trofimov

Lomonosov Moscow State University, Department of Calculation Mathematics & Cybernetics
Vorobyovy Gory, Moscow 119899, Russia

ABSTRACT

The propagation of femtosecond light pulse in nonlinear medium is described by nonlinear Schrodinger equation with temporal derivation from nonlinear response. Properties of this equation are investigated and obtained invariants of the femtosecond pulse propagation in nonlinear medium (including nonlinear absorption medium). The transformation of this equation to a more convenient form is proposed. Various problems of nonlinear optics (second harmonic generation, self-action of laser pulse, interaction of counter propagating pulses, modulation instability of laser pulse) are considered with the aim of applying of proposed transformation. The transformation of Schrodinger equation allows creating of conservative differences schemes for computer simulation of an interaction of femtosecond laser pulse with matter. These schemes make available to control of numerical calculation accuracy. The transformation allows to formulate new approach of finding of soliton solution of nonlinear Schrodinger equation with temporal derivation from nonlinear response.

Keywords: laser pulse, femtosecond, nonlinear interaction, invariant, transformation.

1. INTRODUCTION

As it is known, at the present time a problem of an interaction of femtosecond light pulse with matter is one of the more modern problem of laser physics. It is a consequence of exceptional possibilities opening with creation of laser systems generating laser pulses with such duration¹⁻⁵. Mathematically the interaction is described by so-called generalized Schrodinger equation². This equation is different from one investigating early in laser physics by presence of a derivative of nonlinear response to time.

Despite on wide using of computer simulation of femtosecond pulse propagation in nonlinear medium (mainly, in problems of nonlinear fiber optics) during last ten years a basis of using difference methods is absent in papers. It should be noticed that properties of so-called generalized Schrodinger equation and its invariants did not be investigated practically too. However, using of generalized Schrodinger equation for numerical simulation has some difficulties as is written in reference¹. At the present time the main way of an estimation of a reliability of computer simulation results is constancy of these results under the condition of decreasing of mesh step one-second of one's value for example. On my opinion, this way gives very rough estimation of numerical solution validity. Hence finding of invariants of femtosecond pulse propagation in nonlinear medium is an important problem since they allow creating of conservative difference schemes⁶. Consequently we can realize an effective control over numerical calculation

It is necessary also to emphasize that finding of invariants has an independent interest since characteristics regimes of optical radiation propagation can be analyzed with the help of invariants and without using of computer simulation or laboratory experiments. As it is known integral characteristics of laser pulses and beams can be also expressed in terms of invariants. Invariants define soliton regimes of pulse propagation too. Despite on these circumstances an information of femtosecond pulse propagation invariants is absent in the literature until recently. The reason of this condition includes in a complicate form of the equation for which ordinary way of finding of the invariant is not available. These invariants are constructed in our papers⁷⁻¹⁷, which allowed to fill a gap being available in knowledge.

It is essentially to emphasize that the main idea for finding of invariants concludes in a transformation of so-called generalized Schrodinger equation to more convenient form failing to involve a temporal derivative from nonlinear response of medium^{7,9}. In this case there is a possibility to solve problems of femtosecond laser optics with the help of well-known conservative difference schemes which are mathematically validated and are multiply applied for solution of various nonlinear optics problems describing by ordinary nonlinear Schrodinger equation. It is necessary also to mention that the proposing approach allows to obtain new quality results under investigation of a problem of very short light pulse modulation instability.

In given paper the idea of transformation of so-called generalized Schrodinger equation and some results obtained with the help of the transformation are shortly discussed. We consider a self-action of femtosecond light pulse, an interaction of counter propagating laser pulses, a problem of second harmonic generation by femtosecond pulse.

2. Basic equations

A process of a femtosecond laser pulse propagation with allowance of temporal dispersion of nonlinear response of medium under the condition of axial symmetry of light beam is described by the following dimensionless generalized Schrodinger equation

$$\begin{aligned} \frac{\partial A}{\partial z} + \nu \frac{\partial A}{\partial t} + iD_2 \frac{\partial^2 A}{\partial t^2} + D_3 \frac{\partial^3 A}{\partial t^3} + iD_r \Delta_{\perp} A + \\ + \mathcal{E}_{nl} A - i\gamma \frac{\partial (\mathcal{E}_{nl} A)}{\partial t} = 0, \\ 0 < t < L_t, 0 < z, 0 < r < R, \end{aligned} \quad (1)$$

with the following initial and boundary conditions

$$\begin{aligned} A|_{z=0} = A_0(r, t), \quad A|_{t=0, L_t} = \frac{\partial A}{\partial t}|_{t=0, L_t} = 0, \\ A|_{r=R} = \frac{\partial A}{\partial r}|_{r=0} = 0. \end{aligned} \quad (2)$$

Here $A(z, r, t)$ is the amplitude of the slowly varying complex envelope of the electromagnetic field⁴

$$\mathcal{E} = A \exp \left(i \bar{\omega} t - i \bar{k} z \right) + k.c.. \quad (3)$$

Above symbol k.c. denotes complex conjugation, $\bar{\omega}, \bar{k}$ are dimensionless frequency and wave number of light beam correspondingly. The slowly varying complex amplitude is normalized on its initial maximum value, z is longitudinal coordinate measured in units of diffraction length (in this case $D_r = 1$) or dispersion one (in this case $D_2 = \pm 1$). Using of one of these units is defined by investigating problem. Coefficients D_2, D_3 describe dispersion effects of the second order and the third one correspondingly, ν is equal to a ratio of the length on which the longitudinal coordinate is normalized to a length passed by pulse during characteristic time in which units time are measured. Time of medium state change or the time of pulse shape change is chosen as the characteristic time of normalizing. Δ_{\perp} is the transverse Laplace operator which is written as $\frac{1}{r} \frac{\partial}{\partial r} \left(r \frac{\partial}{\partial r} \right)$ in the symmetric axial case, r is a transverse coordinate measured in units of initial beam

radius, R denotes the maximum value of a transverse coordinate. L_t is equal to time interval during which the propagation of femtosecond pulse is analyzed. Parameter γ describes the dispersion of nonlinear response of medium. Function \mathcal{E}_{nl} describes a perturbation of medium dielectric constant. For example this function is represented in the form

$\mathcal{E}_{nl} = i\alpha P + \delta_0 n$, α is equal to a ratio of initial optical power to characteristic power of pulse self-action, δ_0 characterizes light energy absorption on a length of normalizing of longitudinal coordinate. Functions $P(z, r, t)$ and $n(z, r, t)$ are defined by the following set of dimensionless equations

$$\tau \frac{\partial P}{\partial t} + P = |A|^2, \quad \frac{\partial n}{\partial t} = q \delta(n) |A|^2 - n / \tau_p. \quad (4)$$

Here τ is equal to a ratio of relaxation time of medium perturbation to the characteristic time of normalizing. A parameter q characterizes the initial optical beam power, $\delta(n)$ is a nonlinear dependence of medium absorption coefficient on the function n which under the analysis of light pulse propagation in semiconductor characterizes an electron concentration in conductivity band, τ_p is dimensionless free-electrons relaxation time. Perturbations of medium characteristics are equal to zero at the initial time

$$P|_{t=0} = n|_{t=0} = 0. \quad (5)$$

It is significant that the complex amplitude is a finite function. Hence beyond the time interval $(0, L_t)$ amplitude A is equal to zero. Consequently the following conditions take place

$$\frac{\partial^2 A}{\partial t^2} \Big|_{t=0, L_t} = \frac{\partial A}{\partial t} \Big|_{t=0, L_t} = 0. \quad (6)$$

3. Transformation of equation

First of all we consider the case $v=0$ for simplicity. Let introduce new function by the following rule^{8,9}

$$E(z, r, t) = \int_0^t A(z, r, \eta) \exp(i(\eta - t) / \gamma) d\eta. \quad (7)$$

It is easily to can be shown that this function satisfies an equation

$$\frac{\partial E}{\partial t} + \frac{i}{\gamma} E = A. \quad (8)$$

Applying the transformation to equation (1) we rewrite it in the form

$$\frac{\partial E}{\partial z} + iD_2 \frac{\partial^2 E}{\partial t^2} + D_3 \frac{\partial^3 E}{\partial t^3} + iD_r \Delta_\perp E - i\gamma \varepsilon_{nl} A = 0 \quad (9)$$

As a result of the introduction of $E(z, r, t)$ one can write the following initial and boundary conditions for it

$$E|_{z=0} = E_0(r, t), \quad E|_{t=0} = \frac{\partial E}{\partial t} \Big|_{t=0} = \frac{\partial^2 E}{\partial t^2} \Big|_{t=0} = 0, \quad (10)$$

$$E|_{r=R} = \frac{\partial E}{\partial r} \Big|_{r=0} = 0, \quad \left(\frac{\partial E}{\partial t} + \frac{i}{\gamma} E \right) \Big|_{t=L_t} = \frac{\partial}{\partial t} \left(\frac{\partial E}{\partial t} + \frac{i}{\gamma} E \right) \Big|_{t=L_t} = 0.$$

In (10) E_0 is defined by the initial distribution of complex amplitude calculated with the help of formula (8).

Thus a process of a femtosecond pulse propagation is described by equations (9), (8), (4) with the initial and boundary conditions (10). Obviously the equation (9) is more convenient for numerical simulation and for other analysis since it does not contain a derivative from nonlinear response of medium. This equation contains only derivatives from function E with unchanged coefficients. Consequently the differential operator is a line one in these variables.

It should be noted that the case $v=0$ considered above does not restrict the generality. Since for the case $v \neq 0$ taking place for a case of second harmonic generation or of an interaction of counter propagating beams the transformation (7) is valid. In some cases it is convenient introduce the next function according to the rule

$$E(z, r, t) = \tilde{E}(z, r, t) \exp(i\beta t), \quad (11)$$

The transformation (11) results in the following equation

$$\frac{\partial \tilde{E}}{\partial t} + i(\beta + \frac{1}{\gamma})\tilde{E} = \tilde{A}, \quad \tilde{A} = A \exp(-i\beta t). \quad (12)$$

In this case the equation with respect to \tilde{E} is written in the form

$$\begin{aligned} \frac{\partial \tilde{E}}{\partial z} + \frac{\partial \tilde{E}}{\partial t}(\nu - 2\beta D_2 - 3\beta^2 D_3) + i \frac{\partial^2 \tilde{E}}{\partial t^2}(D_2 + 3\beta D_3) + D_3 \frac{\partial^3 \tilde{E}}{\partial t^3} + \\ + iD_r \Delta_{\perp} \tilde{E} - i\gamma \epsilon_{nl} \tilde{A} + i\tilde{E}\beta(\nu - D_2\beta - D_3\beta^2) = 0 \end{aligned} \quad (13)$$

Choosing suitable value of parameter β one can remove one of terms of equation (13). The initial and boundary conditions (10) may be generalized very simplicity.

Principal consequence of the transformation is a possibility of invariant creation of various processes of femtosecond pulse interaction with matter. Below we write some examples of obtained invariants. For simplicity we consider a propagation of wide aperture beam ($D_r = 0$) since diffraction effects do not change the procedure of invariants deduction. Hence transverse structure of a laser beam we do not take into account.

4. INVARIANT OF SELF-ACTION

4.1 Transparent medium

A propagation of femtosecond light pulse in a transparent medium with Kerr-like nonlinear response ($\epsilon_{nl} = i\alpha P$) is described by the equation (1). After a corresponding transformation to $E(z, t)$ for a case of $v=0$ the equation (1) is written in the form

$$\frac{\partial E}{\partial z} + iD_2 \frac{\partial^2 E}{\partial t^2} + D_3 \frac{\partial^3 E}{\partial t^3} + \alpha\gamma P A = 0. \quad (14)$$

It should be noted that the case of $v=0$ means going to coordinate system moving together with light pulse. This equation has some laws of conservation^{7,14}, which are constant at the propagation of pulse. For example we write the following laws

$$I_1(z) = |E(z, L_t)|^2 = const, \quad I_2(z) = \int \left\{ i |E|^2 - \gamma \left\{ E \frac{\partial E^*}{\partial t} \right\} \right\} dt = const. \quad (15)$$

They allow to create conservative difference schemes which have a high accuracy and allow to control phase relations of laser pulse interaction with matter.

4.2 Nonlinear absorption medium

In the case of laser pulse propagation in nonlinear absorption medium $\varepsilon_{nl} = \varepsilon_0 n(z, t)$ (pure amplitude gratings of refractive index perturbations) for writing of invariants two new functions need to be constructed in the next manner

$$\tilde{A} = A e^{it/\gamma}, \quad \tilde{P} = \int_0^t A e^{it'/\gamma} d\eta = \int_0^t \tilde{A} d\eta. \quad (16)$$

After some algebra we can write the next conservation law¹⁰

$$\int_0^{L_t} A(z, \eta) e^{i\eta/\gamma} d\eta = \int_0^{L_t} A_0(\eta) e^{i\eta/\gamma} d\eta e^{iz/\gamma^2} \\ I_3(z) = I_3(0) e^{iz/\gamma^2} \quad (17)$$

Thus, in the process of femtosecond pulse interaction with matter a Fourier harmonic of complex amplitude with frequency $\omega = 1/\gamma$ oscillates along a direction of propagation with spatial frequency $k = 1/\gamma^2$. From statement (17) the very important conclusion follows for numerical simulation of femtosecond pulse propagation. If we use FFT algorithm at numerical simulation of equation (1) it is necessary that a series into which a solution is expanded contains the Fourier harmonic with frequency $\omega = 1/\gamma$. If this harmonic does not contain into the series a numerical solution does not take into account the properties of given equation.

Consequently a practice of a reliability estimation of computer simulation results obtained with the help of decreasing of mesh step one-second of one's value is not correct since numerical solutions obtained on two sequence meshes may not contain the harmonic with frequency $1/\gamma$.

The second statement concludes in choosing of the longitudinal mesh steep. It has not to be greater than value of γ^2 . Hence a value of the longitudinal mesh steep in the case of computer simulation of femtosecond pulse propagation depends on two spatial scales. The first scale is dispersion length and the second one is a length that is proportional to the square of coefficient γ that is equal to the product of light frequency by pulse duration.

Thus, it is necessary to choose the longitudinal mesh step taking into account a value of coefficient γ to obtain the correctness results of computer simulation of femtosecond pulse propagation with regard to influence of dispersion of nonlinear response. At using of FFT method one needs to take into account the presence of harmonic with frequency $1/\gamma$ in the series of functions.

5. COUNTER PROPAGATING FEMTOSECOND PULSES

As it is known the process of an interaction of counter-propagating pulses without regard to the third order dispersion which does not influence on the form of invariants written below is described by the following dimensionless equations

$$\frac{\partial A_+}{\partial t} + \frac{\partial A_+}{\partial z} + iD_2 \frac{\partial^2 A_+}{\partial t^2} + i\alpha(A_+ \varepsilon_+) + \gamma\alpha \frac{\partial}{\partial t}(A_+ \varepsilon_+) = 0, \\ \frac{\partial A_-}{\partial t} - \frac{\partial A_-}{\partial z} + iD_2 \frac{\partial^2 A_-}{\partial t^2} + i\alpha(A_- \varepsilon_-) + \gamma\alpha \frac{\partial}{\partial t}(A_- \varepsilon_-) = 0 \quad 0 < z < 1 \quad (18)$$

with initial and boundary conditions

$$A_{\pm} \Big|_{z=0,1} = A_{\pm 0}(t), \quad A_{\pm} \Big|_{t=0,L_t} = \frac{\partial A_{\pm}}{\partial t} \Big|_{t=0,L_t} = 0, \quad 0 < t < L_t$$

Here A_{\pm} are complex amplitudes of counter propagating waves measured in their initial maximum value, z is normalized on length a medium. Other notations correspond to ones mentioned above.

If all gratings induced by laser pulses have the same relaxation time then perturbations of refractive index for counter propagating waves are equal to the following values $\mathcal{E}_{\pm} = 2 |A_{\mp}|^2 + |A_{\pm}|^2$ correspondingly.

Let definite the two pairs of new functions for complex amplitudes of waves propagating in both directions as they are written in (16). In this case it is easy to obtain the law of changing of Fourier component along the longitudinal coordinate

$$I_2(z) = \int_0^{L_t} \sum_{\pm} \tilde{A}_{\pm}(z, t) \exp\left(\frac{it}{\gamma}\right) dt, I_2(z) = I_2(0) \exp\left(i\left(\frac{1}{\gamma^2} + \frac{1}{\gamma}\right)z\right). \quad (19)$$

Hence, the optical harmonic on a frequency $1/\gamma$ oscillates along the longitudinal coordinate with two spatial frequencies that are equal to $1/\gamma^2$ and $1/\gamma$ correspondingly. The presence of last harmonic is caused by finite quantity of light velocity. It is necessary to note that the interaction of counter propagating pulses is described by equations without temporal derivative from nonlinear medium response if we use new function according to (8).

6. SECOND HARMONIC GENERATION (SHG) OF FEMTOSECOND PULSE

Process of SHG of femtosecond pulse with allowance of a self-action, dispersion of first and second order and dispersion of nonlinear response can be described by the following set of dimensionless equations

$$\begin{aligned} \frac{\partial A_1}{\partial z} + iD_1 \frac{\partial^2 A_1}{\partial \eta^2} + \gamma \left\{ iA_2 A_1^* + \frac{1}{\omega} \frac{\partial}{\partial \eta} (A_2 A_1^*) \right\} e^{-i\Delta k z} + \\ + \alpha \left\{ iA_1 (|A_1|^2 + 2|A_2|^2) + \frac{1}{\omega} \frac{\partial}{\partial \eta} A_1 (|A_1|^2 + 2|A_2|^2) \right\} = 0, \quad 0 < z \leq 1, \\ \frac{\partial A_2}{\partial z} + \nu \frac{\partial A_2}{\partial \eta} + iD_2 \frac{\partial^2 A_2}{\partial \eta^2} + \gamma \left\{ iA_1^2 + \frac{1}{2\omega} \frac{\partial}{\partial \eta} (A_1^2) \right\} e^{i\Delta k z} + \\ + 2\alpha \left\{ iA_2 (2|A_1|^2 + |A_2|^2) + \frac{1}{2\omega} \frac{\partial}{\partial \eta} A_2 (2|A_1|^2 + |A_2|^2) \right\} = 0 \end{aligned} \quad (20)$$

with initial and boundary conditions ($j=1, 2$)

$$A_j(0, \eta) = A_{j0}(\eta), \quad A_j(z, 0) = A_j(z, L_t) = 0, \quad \frac{\partial A_j}{\partial \eta} \Big|_{\eta=0, L_t} = 0. \quad (21)$$

For simplicity we do not above take into account the third order dispersion. This condition does not restrict our analysis.

Here A_j is dimensionless complex amplitude of j -th pulse propagating along longitudinal coordinate z , η is time measured in coordinate system moving with the laser pulse, time is normalized on a pulse duration. Parameter γ is coefficient of nonlinear coupling of waves, α is a ratio of initial pulse energy to characteristic energy of self-action, ν characterizes the difference between group velocities of first and second harmonics, dimensionless parameter ω in (20) is the product of pulse duration by pulse frequency of basic harmonic. Coefficients D_1, D_2 describe broadening of pulse. In contrast to the case of a laser pulse self-action considered above notations in (20) are changed with the aim of applying of notations accepted at an investigation of SHG process.

To simplify the initial set of equations of (20) it is advantageous to make the new functions as

$$\frac{\partial E_j}{\partial \eta} + i j \omega E_j = A_j, \quad j = 1, 2. \quad (22)$$

From transformed set one can obtain a series of invariants of SHG process^{12,13}. Below the more important among them are written. So in the case of SHG without regard of a pulse self-action ($\alpha = 0$ in (20)) there are the following conservation laws. The first invariant $I_1(z)$ is the one of energy conservation. The second law is written as

$$I_2(z) = \int_0^{L_i} \left\{ \text{Im} \left(E_1 \frac{\partial E_1^*}{\partial \eta} + 2 E_2 \frac{\partial E_2^*}{\partial \eta} \right) - \omega (|E_1|^2 + 4|E_2|^2) \right\} d\eta = \text{const}. \quad (23)$$

It contains an information on phase of propagating pulse and displacement of a central frequency of pulse spectrum from its initial value.

If the SHG occurs under the condition of missing of phase synchronism the following law takes place also

$$\begin{aligned} I_3(z) = \int_0^{L_i} & \left\{ i(-D_1 F_1 - D_2 F_2 + \omega^2 D_1 J_1 + 4\omega^2 D_2 J_2) + \omega \left(D_1 \left| \frac{\partial E_1}{\partial \eta} \right|^2 + 2 D_2 \left| \frac{\partial E_2}{\partial \eta} \right|^2 \right) - \right. \\ & - \Delta k (i(J_1 + J_2) + \omega (|E_1|^2 + 2|E_2|^2)) + \nu \left(\left| \frac{\partial E_2}{\partial \eta} \right|^2 + 2i\omega J_2 \right) + \frac{\gamma}{2\omega} (A_2 (A_1^*)^2 e^{-i\Delta k z} + \\ & \left. + A_2^* A_1^2 e^{i\Delta k z}) \right\} d\eta = \text{const}, \quad F_j = i \text{Im} \left(A_j \frac{\partial A_j^*}{\partial \eta} \right), \quad J_j = i \text{Im} \left(E_j \frac{\partial E_j^*}{\partial \eta} \right), \quad j = 1, 2.. \end{aligned} \quad (24)$$

In the case of SHG process with allowance of pulse self-action ($\alpha \neq 0$ in (20)) the third invariant transforms to the form

$$I_3^\alpha(z) = I_3(z) + \frac{\alpha}{\omega} \int_0^{L_i} (0.5|A_1|^4 + 0.5|A_2|^4 + 2|A_1|^2|A_2|^2) d\eta = \text{const}. \quad (25)$$

But the law of (23) does not change.

7. MODULATION INSTABILITY OF FEMTOSECOND PULSE

In this section of paper an evolution of modulation instability of temporal perturbations of a light pulse is considered in brief. Complex amplitude of such pulse depends only on coordinates (z, t) and the derivative with respect to transverse coordinate is absent in equation (1). We consider a propagation of femtosecond pulse in transparent Kerr-like medium ($\mathcal{E}_{nl} = i\alpha |A|^2$). Since the third order dispersion does not influence on frequency interval of a growth of perturbations¹⁹ then in the later analysis it is not taken into account.

7.1 Analysis based on the equation (1)

Using a plane wave solution with the help of usual algebra of linear analysis of small perturbation development it is easily to obtain the following condition on frequency interval at which perturbations increase exponentially²⁰

$$\omega^2 < \frac{\alpha |A_0|^2}{D_2^2} (2D_2 - \gamma^2 \alpha |A_0|^2) . \quad (26)$$

From (26) the condition on parameters of a laser pulse interaction with the medium can be written as

$$\left| \alpha / D_2 \right| < 2 / \gamma^2 |A_0|^2 . \quad (27)$$

In (26), (27) A_0 is amplitude of unperturbed wave. From these formulas one follows that the dispersion of nonlinear response decreases the frequency interval.

7.2 Analysis based on the transformed equation

With the aim of an analysis of perturbation development function E is written in the form

$$E = (E_0 + \delta E) \exp(-i \alpha |A_0|^2 z), \quad E_0 = \frac{\gamma}{i} A_0 , \quad (28)$$

Applying of the transformed equation (14) is very important for an analysis of modulation instability in the frame work of linear approach since a perturbation and a derivative from it in general case can have various orders infinitesimal. Perturbations of complex amplitude and defined function E are connected each other by a relation

$$\delta E = \frac{\delta A}{i \left(\omega + \frac{1}{\gamma} \right)}, \quad \omega \neq -1/\gamma , \quad (29)$$

After uncomplicated transformations one can obtain that the frequency interval at which amplitude perturbations increase is defined by the following inequality

$$\omega^2 < \frac{\alpha |A_0|^2}{D_2^2} 2D_2 (1 + \gamma \omega) \quad (30)$$

Comparing formula (26) with (30) one can make two important conclusions. The first, a dispersion of nonlinear response results in increasing of frequency interval of modulation instability defined by expression (30). The second, for real light pulse with a central frequency ω_0 the high frequency domain of pulse spectrum and its low frequency domain are non-symmetric about a condition of appearing of modulation instability. The frequency interval of its development increases for frequencies greater than ω_0 . But for the opposite frequency relation this interval decreases. It should be noted that the general well-known property of a non-symmetric transformation of pulse spectrum shows in the modulation instability problem too under the action of dispersion of nonlinear response.

On my opinion, distinguish between (26) and (30) is caused by various procedure of linear approach in both cases. The temporal derivative from nonlinear response is present in the equation (1). Hence at the moment of perturbation growth an influence of the derivative maybe equal to (or greater than) one of nonlinear response. Consequently these terms in (1) have various orders infinitesimal. But in the transformed equation (14) an influence of nonlinear response is described only by the single term

8. ACKNOWLEDGMENTS

This work was supported by the Russian Foundation "Universities of Russia - fundamental investigations" (grant N5142).

9. CONCLUSION

The approach developing in this paper of mathematical modeling of femtosecond pulse interaction with matter is universal and can be applied to various problems of femtosecond laser optics. It allows to create invariants of a femtosecond pulse interaction with matter. Using these invariants one can write conservative differences schemes for computer simulation and control an accuracy of it. Invariants allow to formulate new quality results under investigation of a problem of very short light pulse modulation instability.

10. REFERENCES

1. G.P. Agrawal, *Nonlinear fiber optics*, 320 p., Academic press, Inc, London, 1989.
2. S.A.Akhmanov, V.A.Vysloukh, A.S.Chirkin, *Optics of femtosecond laser pulses*, 340 p., Nauka publishers, Moscow, 1988.
3. N.I.Koroteev, I.L.Shumay, *Physics of high-power laser radiation*, 310 p., Nauka publishers, Moscow, 1991.
4. A.P.Sukhorukov, *Nonlinear wave interactions in optics and radio-physics*, 231 p., Nauka publishers, Moscow, 1988.
5. S.A.Akhmanov, "High intensity light fields in nonlinear optics, plasma physics, technique of X-rays sources", *Modern problems of laser physics*, Ed. S.A.Akhmanov, V. 4, pp.5-17, Viniti publishers, Moscow, 1991.
6. A.A. Samarskii. *Theory of difference schemes*, 614 p., Nauka publishers, Moscow, 1983.
7. V.A. Trofimov. "On invariant of nonlinear propagation of femtosecond pulses," *Izvestiya Vuzov. Radiofizika*. (In Russian) **35** (6-7), 618-621 (1992).
8. V.A. Trofimov and I.G.Zakharova, "On the role of dispersion of the nonlinear response of a medium in the formation of high-absorption domain in cavity-free optical bistable systems," *BRAS. Physics. Supplement / Physics of Vibrations* **60** (4), 209-217 (1996).
9. V.A. Trofimov, "On new approach of modeling of nonlinear propagation of super short laser pulses," *J. of Calculation Mathematics & Mathematical Physics (In Russian)* **38** (5), 835 - 844 (1998).
10. V.A. Trofimov, "Invariant of a propagation of femtosecond pulses in nonlinear absorption medium," *J. of Calculation Mathematics & Mathematical Physics (In Russian)* **39** (12), 0 - 0 (1998) (will be published).
11. V.A. Trofimov, "Nonlinear wave equation of laser optics of femtosecond pulses," *Differential equations (In Russian)* **34** (7), 3 - 6 (1998).
12. S.A. Varentsova and V.A. Trofimov, "Lagrangean of SHG process by femtosecond light pulses," *Differential equations (In Russian)* **34** (7), 0 - 0 (1998).
13. S.A. Varentsova and V.A. Trofimov, "Invariants of process of SHG by femtosecond pulses," *Vestnik Moskovskogo universiteta. Seria vicheslitel'naya matematika i kibernetika. (In Russian)* **4**, 0 - 0 (1998) (will be published).
14. V.A. Trofimov, "Invariants of propagation of femtosecond pulses," *Izvestiya Vuzov. Radiofizika*. (In Russian) **41**, (1998) (will be published).
15. V.A. Trofimov, "Numerical methods for problems of femtosecond laser optics," *5 International conference Mathematics, computer, education*, p.202, Moscow University publishers, Moscow, 1998.
16. V.A. Trofimov, "New approach to computer simulation of femtosecond pulse propagation in nonlinear medium," *XXV ECLIM. Abstract of reports*, Th/P/10, Formia, Italy, 1998.
17. V.A. Trofimov, "New approach to computer simulation of femtosecond pulse propagation in nonlinear medium," *Technical Program of 9th Laser Optics Conference*, p.69, St.-Petersburg, Russia, 1998.
18. Yu.N.Karamzin, A.P.Sukhorukov, V.A. Trofimov, *Mathematical modeling in nonlinear optics*, 159 p., Lomonosov Moscow State university publishers, Moscow, 1989.
19. M. J. Potasek, "Modulation instability in an extended nonlinear Schrodinger equation," *Optics Letters* **12** (11), 921-923 (1987).
20. P.K.Shukla, J. Juul Rasmussen, "Modulation instability of short pulses in long optical fibers," *Optics Letters* **11** (3), 171 - 173 (1986).

Spatially-temporal filtration of ultrashort light pulses by one-dimensional nonlinear band gap structures

A.G. Smirnov

Stepanov Institute of Physics,
National Academy of Sciences of Belarus,
70 F. Scaryna Ave., 220072, Minsk, Belarus,
E-mail: andr@dragon.bas-net.by

ABSTRACT

It is shown that an interaction of ultrashort optical pulse with a deep modulated one-dimensional periodic structure with cubic nonlinearity is followed either by an optical switching, compression or reshaping of a reflected pulse depending on its duration, intensity and detuning of a carrier frequency from an edge of a forbidden gap. It is found out that a gap structure with a metal cover on a back edge possesses a considerably smaller intensity threshold to attain a compression at pulse reflection.

Keywords: band gap structures, ultrashort pulses, optical limiting, compression, self-oscillation

1. INTRODUCTION

In recent times there is a substantial interest in studying various dynamic effects in photonic crystals taking into account both material nonlinearity and crystal dispersion. Such phenomena as self-oscillation¹, self-phase modulation, solitons formation and pulse compression in transmission^{2, 3} were predicted and experimentally confirmed for nonlinear weakly modulated waveguides. It was found out that periodical structures with a large depth of modulation exhibit optical limiting for ultrashort light pulses⁴ and bistability⁵. Nevertheless the correlation between pulse duration and relaxation of nonlinear processes caused by structural organization of a gap crystal and its influence on dynamics of interaction hasn't been clarified.

In this paper the results of a detailed numerical study of ultrashort pulse transmission through and reflection off one-dimensional deeply modulated gap structure possessing Kerr type of nonlinearity with an instantaneous response of a medium are presented for wide range of pulse and crystal parameters and three regimes of interaction are established and investigated. The possibility of pulse compression in fully dielectric and partially metallized crystals is discovered and the necessary requirements for its realization are discussed.

2. NONLINEAR INTERACTION DYNAMICS

2.1 Basic relations and model assumptions

Band-gap structure under consideration is arranged as a stack of two sorts of dielectric layers with dielectric constants ε_1 , ε_2 and thickness d_1 , d_2 , besides $d = d_1 + d_2$, here d is a period of a structure. Such a one-dimensional crystal is implied to possess Kerr nonlinearity with an instantaneous response of a medium

$$\varepsilon(z, t) = \varepsilon_{lin}(z) + \chi(z)|E(z, t)|^2 \quad (1)$$

where $\chi(z)$ is cubic nonlinear coefficient taking χ_1 or χ_2 value for each sort of layers, $E(z, t)$ - electric field varying both in space and time inside a medium. It is assumed that light pulse with Gaussian distribution of its amplitude

$$E(t)|_{z=0} = E_0 \exp[-(t/2\tau)^2] \exp[i\omega_0 t] \quad (2)$$

and carrier frequency ω_0 propagates collinearly to a crystal axis coinciding with z-axis of coordinates system. It is well known that such periodic structure in linear regime exhibits a set of forbidden gaps of frequency that cause a significant reflection of radiation within gap spectral interval⁶. As numerical estimations demonstrate spectral bandwidth of forbidden gap $\Delta\omega_{gap}$ is significantly wider than bandwidth of a pulse spectrum $\Delta\omega \sim 1/\tau$ for pulse duration $\tau \sim 10^2/\omega_0$ and gap-structures with deep modulation $\Delta\varepsilon = 2|\varepsilon_1 - \varepsilon_2|/|\varepsilon_1 + \varepsilon_2| \sim 30-50\%$, at the same time $\Delta\omega$ is compatible in magnitude with a spectral width of adjacent maximas and minima in reflection spectrum (the insert on Fig. 1).

A perturbation of dielectric permittivity $\delta\varepsilon(t, z)$ arising at nonlinear interaction of light pulse with periodic structure causes the dynamic shift of a gap edge⁴ (let's define $\omega^-(t)$ as a red instant frequency of gap edge and $\omega^+(t)$ as a blue one) which occurs not instantaneously since light pulse needs a certain time to occupy the interior of a crystal. It is obvious that a dynamic edge shift rate $d\omega^\pm/dt$ depends on distribution of electric field inside a lattice and group velocity of a pulse that determines an energy flow through a crystal. Pulse group velocity varies via detuning of light carrier frequency from gap edge that is why nonlinear modulation of crystal lattice is more pronounced in the case of ω_0 being tuned in a band of relatively high transmission near gap edge, in contrast tuning within forbidden gap leads to excluding of main impulse energy from interaction zone due to its reflection. Besides one should take into account the fact that dynamic shift of band edge frequency occurs effectively in the case of primary concentration of electric field in crystal layers possessing nonlinearity, thus it is known that pulse tuning near red (blue) edge is accompanied with electric field concentrating in crystal layers with larger (smaller) value of dielectric permittivity.

2.2 Optical limiting dynamics

Let's consider the case of pulse detuning near red frequency ω^- and selffocusing nonlinearity $\chi > 0$ in crystal layers with higher ε , namely, $\chi_1 > 0$, $\chi_2 = 0$, $\varepsilon_1 > \varepsilon_2$. Since a gap edge red shift occurs due nonlinear interaction an initial detuning $\beta = \omega_0 - \omega^-(0)$ of a pulse carrier frequency may be compensated in a while, one may write this as follows $\omega_0 = \omega^-(\tau_c)$, here τ_c value differs for various structures parameters, duration and peak intensity of a pulse. It's worth to investigate three regimes of interaction: 1) $\tau > \tau_c$, 2) $\tau \sim \tau_c$, 3) $\tau < \tau_c$.

It is obvious that in the case of very short pulses when a set of pulse Fourier components lying inside a gap are excluded from interaction or low level of pulse intensity when $\delta\varepsilon(t, z)$ is too negligible to produce a sufficient gap shift a τ_c value may be much greater than pulse duration thereby no significant reflection takes place. On the contrary when pulse spectrum lies inside a transmission band that corresponds to longer pulses and intensity I_0 is sufficient one may obtain a crystal transition from transmitting to reflective state.

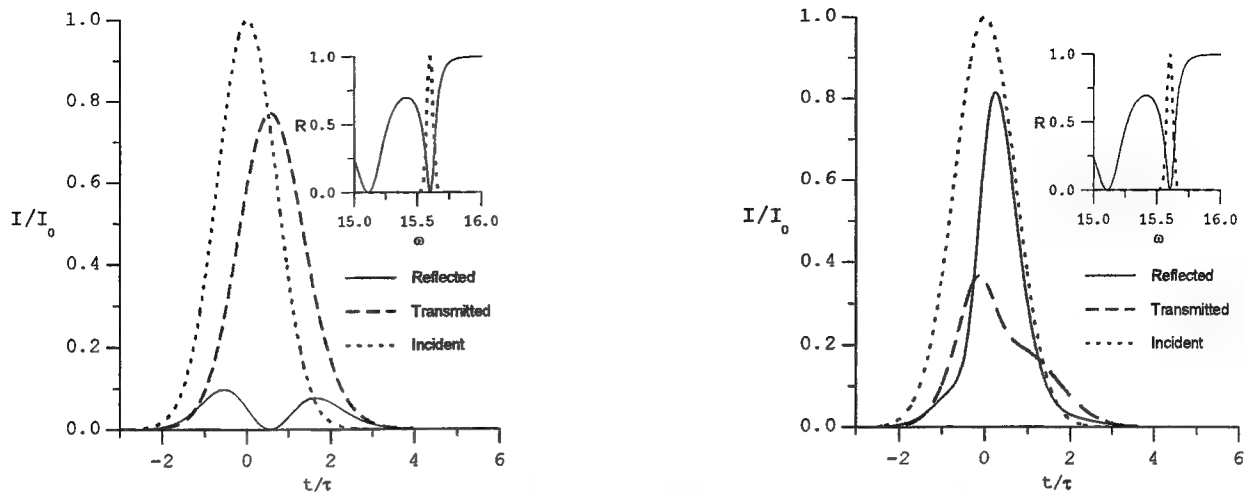


Fig.1. Normalized incident Gaussian, the transmitted and reflected pulses at $I_0=1$: $\tau=300$ fs. The inserts show incident pulse spectrum (dot line) and reflective spectrum of gap-structure (solid line), ω in 10^{14} Gz. Crystal parameters: $\epsilon_1=1.9881$, $\epsilon_2=1.$, $d_1=0.2$, $d_2=0.25$ μm , $L=20d$, a) $\chi_1=\chi_2=0$, b) $\chi_1=0.01$, $\chi_2=0$.

It can be seen from Fig. 1b, that reflected pulse in this case is shorter than an incident one since a leading part of a pulse passes through a crystal without reflection, at the same time a normalized peak intensity of a reflected pulse is not greater than unity for any level of incident intensity. To explain that fact one should recover that an amplitude of electric field inside a structure being at reflective state decays along crystal length (Fig. 2b) and an energy flow inside a crystal reduces in comparison with the case of transmitting state (Fig. 2a). Therby a competition process of inverse crystal transition into transmitting state prevents total reflection.

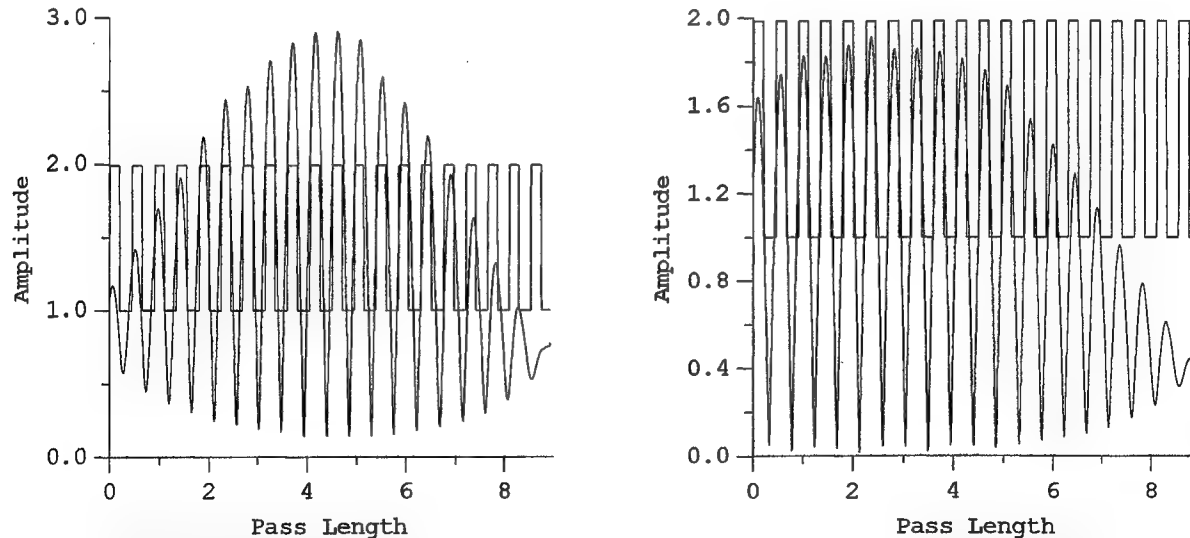


Fig. 2. The distribution of normalized electric field amplitude inside dielectric structure at a) transmitting and b) reflective states of a crystal.

The direct and inverse transitions may cause an oscillation of reflected pulse intensity in the case of continuous incident pulse with a period being proportional to τ_c , unfortunately these oscillations are negligible for ordinary dielectric gap structures since much energy flows outside through a crystal back edge. Fig. 3a depicts optical limiting dynamics for the case of continuous incident pulse in $\tau > \tau_c$ regime, it can be seen that a crystal produces a modulated reflected pulse with normalized peak intensity $^RI_{\max}$ exceeding unity (it should be pointed out that although $^RI_{\max} > I_0$ total pulse energy $W_{\text{total}} \sim \int |E|^2 dt = \int |E|^2 dt + \int |E|^2 dt$ remains constant). Such enlargement of peak intensity is caused by summing in time of a backward Bragg wave and rereflected leading part of incident pulse off metal mirror. From above it can be easily concluded that if $\tau \sim \tau_c$ condition is fulfilled one may obtain a single pulse with duration being shorter than initial one and peak intensity exceeding unity Fig. 3b. Such regime has all marks of true compression.

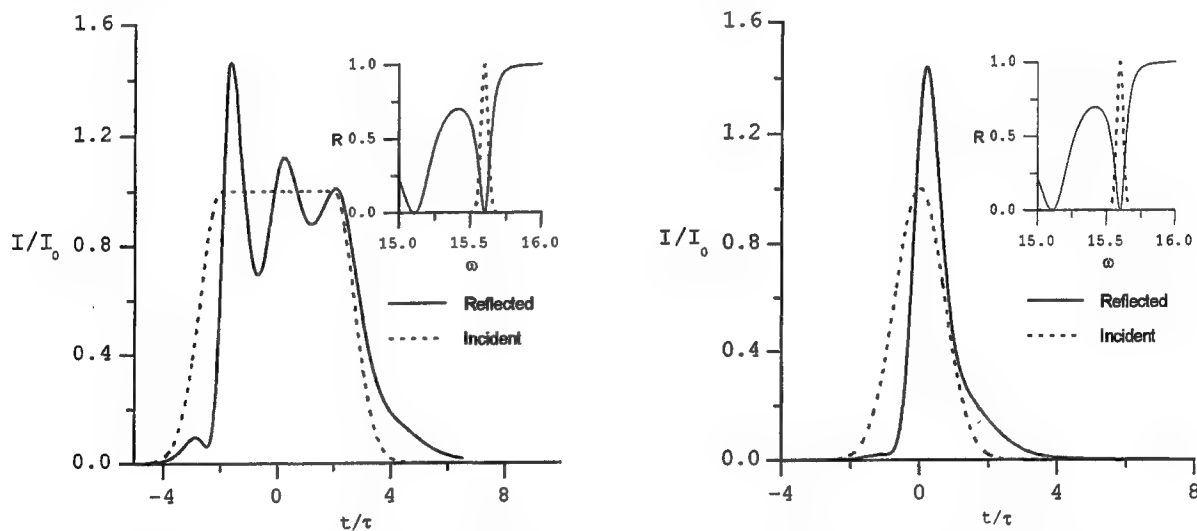


Fig. 3a, b. Normalized incident a) continuous b) Gaussian and reflected pulses at $I_0=0.5$; $\tau=300$ fs for gap crystal with a metalized back edge.

Let's underline three fundamental factors leading to compression: 1) relatively sharp switching of a crystal between transmittive and reflective states causing a leading and trailing parts of an incident pulse being cut from a main volume, that may be called a temporal filtration 2) accumulation and delay of energy of leading part with simultaneous transformation of direct wave into backward one and 3) synchronization of pulse duration with a time of compensation of detuning $\tau \sim \tau_c$. The necessary restrictions on crystal and pulse parameters to attain a compression effect are: 1) deep modulation of crystal lattice together with sufficient number of periods ~ 20 of a structure to provide a pronounced forbidden gap and dispersion 2) tuning of pulse spectrum $\Delta\omega \sim 1/\tau$ in transmission band near gap edge to diminish incident peak intensity I_0 at a fixed pulse duration, i.e. a certain relation between crystal length L and pulse duration $\tau \sim 10L/c$ should be satisfied 3) appropriate choice of type of nonlinearity, selffocusing or defocusing, in accordance with red or blue gap edge frequency chosen. Pay attention that if pulse bandwidth is too wide in comparison with transmission band or I_0 is too low $\tau < \tau_c$ may be observed, then simple optical limiting occurs when incident pulse is reflected mainly but no compression takes place since no detuning synchronization is supported.

2.3 Quasi-soliton formation and pulse compression

The results of this chapter demonstrate the existence of quasi-soliton formation and pulse compression in transmission for deeply modulated structures. That phenomenon was theoretically discovered earlier by Winful^{1, 3} and experimentally confirmed by Eggleton² et al for weakly sinusoid modulated waveguides ($\delta n \sim 10^{-4}$, $L \sim 55$ mm, $\tau \sim 50-90$ ps) and was explained as a result of interplay between a gap-structure dispersion and self-phase modulation. As it can be seen such regimes needs $\tau \sim 0.1L/c$ relation to be satisfied. The numerical simulations carried out for photonic crystals with large depth of modulation confirm an existence of a similar effects with a certain scaling in time and space, i.e. since the necessary level of dispersion is attained for crystals with $\delta n \sim 0.2-0.5$ at $L \sim 20d-40d$, $d \sim 0.5-1$ μm , required pulses duration lies within 30-100 fs for infra-red spectral range, $\lambda \sim 1$ μm . These regimes are attained for the case of pulse detuning near blue frequency ω^+ (red frequency ω^-) and selffocusing (defocusing) nonlinearity in crystal layers with lower (higher) ε (Fig. 4).

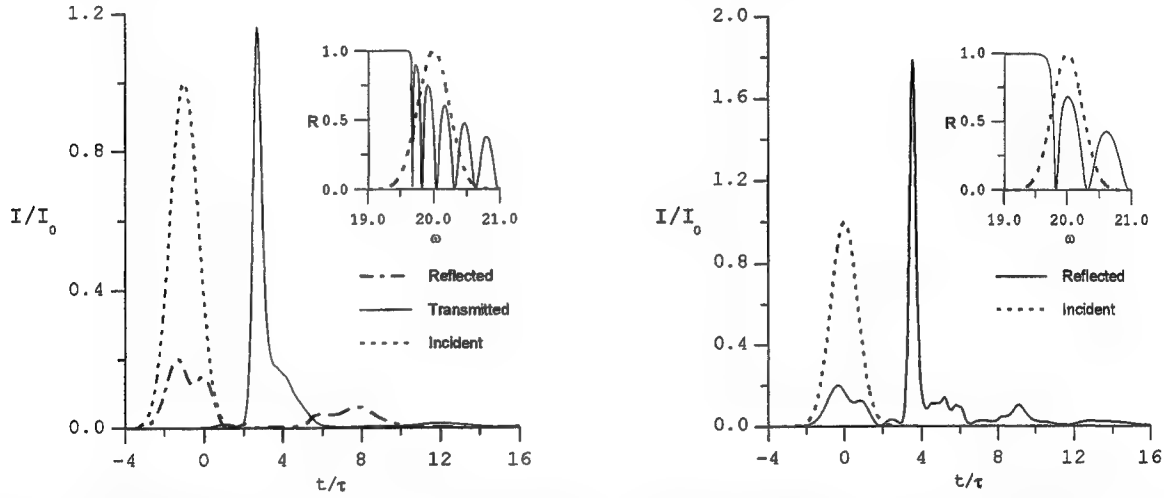


Fig. 4. Normalized incident Gaussian, the transmitted and reflected pulses at $I_0=4$: $\tau=30$ fs for a) ordinary, $L=40d$ and b) metalized, $L=20d$ gap crystals. Crystal parameters: $\varepsilon_1=1.9881$, $\varepsilon_2=1.$, $d_1=0.2$, $d_2=0.25$ μm , $\chi_1=0.$, $\chi_2=0.01$.

As simulations shows the increase of pulse duration in comparison with $\tau \sim 0.1L/c$ relation leads to a formation of a multiple quasi-soliton envelopes propagating along the structure almost with a constant shape Fig. 5. These solitons were referred to Bragg solitons² since the majority of pulse Fourier components lies outside a forbidden gap.

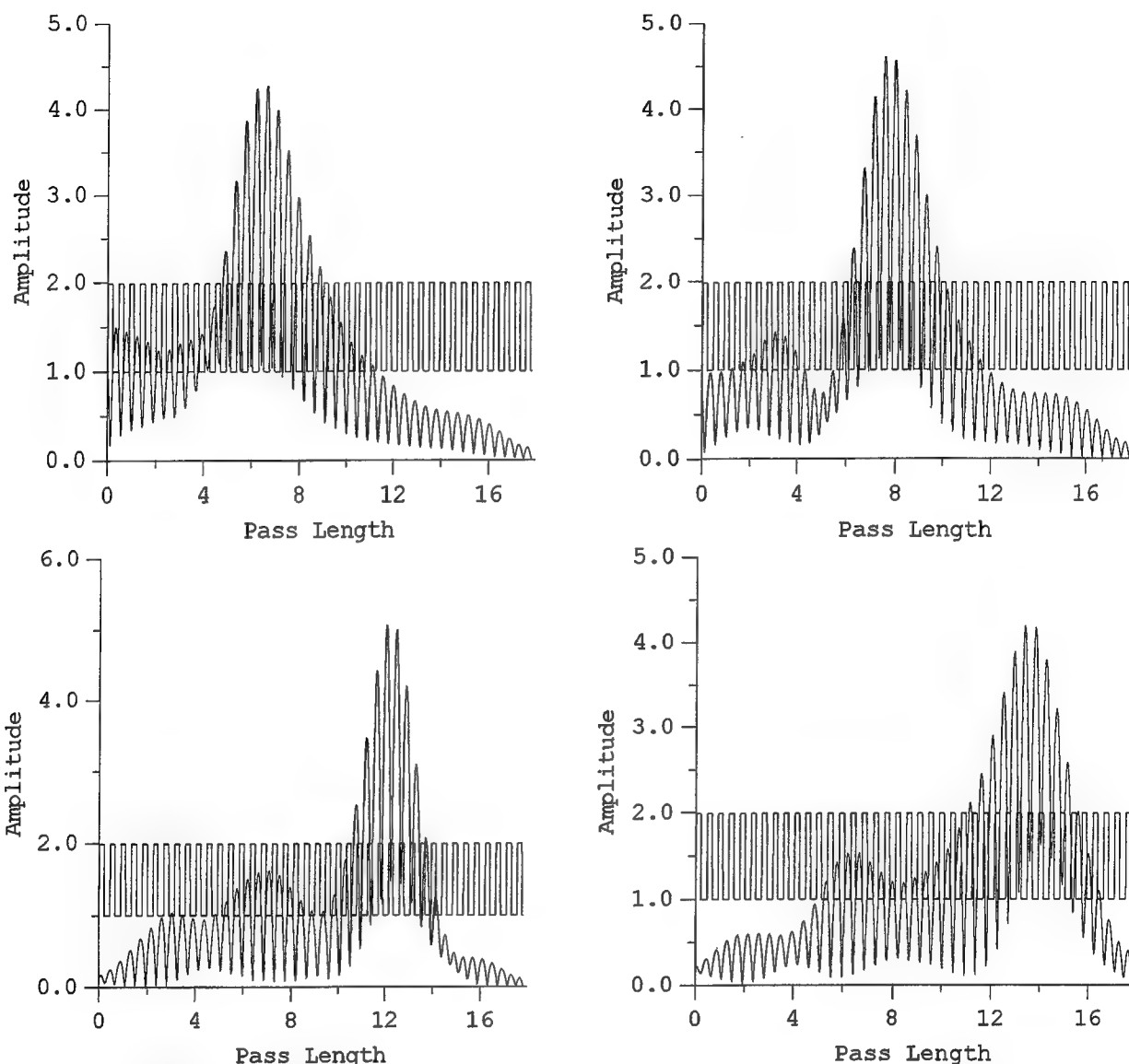


Fig 5. The evolution of distribution of electric field amplitude inside dielectric structure at quasi-soliton regime. Pulse and structure parameters correspond to Fig. 4a.

For the case of continuous incident pulse a photonic crystal produces a permanent self-oscillation of output pulse intensity with a period depending on input intensity and structural parameters (Fig. 6a). A covering of a crystal back edge with a metal mirror is a simple method enabling a twofold increase of interaction length and reduction of crystal length almost to several tens of periods. It seems fascinating that for the case of continuous pulse when a set of quasi-solitons interfere with each other at the same space and time location no envelope truncation occurs at the output of the system (Fig. 6b). That fact can be considered as an evidence of soliton behavior of light in photonic crystals.

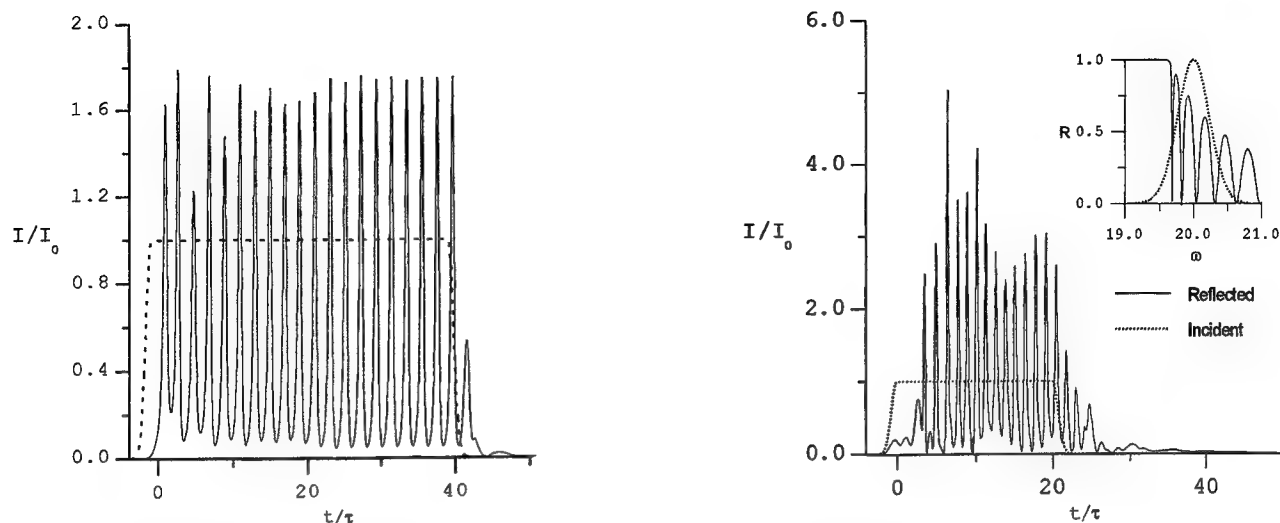


Fig. 6. Normalized incident continuous, a) the transmitted and b) reflected pulses at $I_0=4$: $\tau=30$ fs for a) ordinary, $L=40d$ and b) metalized, $L=20d$ gap crystals. Crystal parameters: $\epsilon_1=1.9881$, $\epsilon_2=1.$, $d_1=0.2$, $d_2=0.25 \mu\text{m}$, $\chi_1=0.$, $\chi_2=0.01$.

2.4 Distinguishing peculiarities of compression in reflection and compression in transmission

It is worth to give a short summary of the distinguishing features of two compression regimes described at chapter 2.2 and 2.3.

Table 1.

<i>Compression Regime</i>	<i>Physical Mechanism</i>	<i>Gap Edge & Nonlinearity Type</i>	<i>Time&Space Scaling</i>	<i>Metal Mirror Presence</i>	<i>Continuos Pump Response</i>
Optical Limiting Reflection	Gap edge shift, temporal filtration, $\tau \sim \tau_c$ synchronization	red & selffocusing blue & defocusing	$\tau \sim 10L/c$	Required	Decaying Oscillation
Quasi-soliton Formation	Phase self-modulation and geometry dispersion interplay	red & defocusing blue & selffocusing	$\tau \sim 0.1L/c$	Optional	Permanent Oscillation

3. CONCLUSIONS

In this report an interaction of ultrashort pulse with 1-D band-gap structure possessing Kerr type of nonlinearity is considered. It is found out that a simple pulse shortening takes place in an ordinary dielectric structures at optical limiting regime while the covering of crystal back edge with a metal may lead either to oscillation of reflected pulse intensity decaying in time or pulse compression. Quasi-soliton

formation referred as Bragg solitons are discovered in deeply modulated photonic crystals and effective pulse compression and permanent self-oscillation are demonstrated for femtosecond pulse duration and micron crystal length.

4. ACKNOWLEDGEMENTS

The author would like to thank V.N. Belyi and B.B. Sevruck for helpful discussion and encouragement of his researches.

5. REFERENCES

1. H. G. Winful, *Appl. Phys. Lett.*, **46** (1985) 527
2. B. J. Eggleton, R. E. Slusher, G. Martijn de Sterke, P. A. Krug, J. E. Sipe, *Phys. Rev. Lett.*, **76** (1996) 1627
3. H. G. Winful, R. Zamir and S. Fieldman, *Appl. Phys. Lett.*, **58** (1991) 1001
4. M. Scalora, J. P. Dowling, C. M. Bowden, M. J. Bloemer, *Phys. Rev. Lett.*, **73** (1994) 1368
5. B. E. Little, *IEEE J. Quant. Elec.*, **30**, 2589 (1994)
6. P. Yeh, A. Yariv, 1988, *Optical Waves in Layered Media* (New York: Wiley)

Stark induced contribution to mode locking in cw solid-state lasers with semiconductor saturable absorber

V. L. Kalashnikov, D. O. Krimer, I. G. Poloyko and V. P. Mikhailov

International Laser Center, 65 Skorina ave., Bld. 17, Minsk 220027, Belarus, Tel/Fax: /375-0172/ 326-286

ABSTRACT

It is shown, that the fast saturable absorber effect due to the Stark shift of the excitonic resonance in the quantum-confined semiconductor can contribute to ultra-short pulse formation and stabilize the pulses with extremely short duration at the below band-gap excitation, i. e. in the presence of the Stokes mismatch between gain band center and excitonic line. This mechanism is strong enough to provide self-starting over the full region of the cavity stability.

Keywords: solid-state laser, mode locking, optical Stark effect, semiconductor, saturable absorber

2. INTRODUCTION

Recently, a considerable progress has been made in self-starting femtosecond lasers using semiconductor structures¹. This allows the pulses as short as 6.5 fs to be generated directly from the resonator². The laser systems with semiconductor absorbers combine the advantages of the Kerr-lens mode locked system, the self-starting ability and the cavity alignment insensitivity³. The most striking feature of semiconductor absorbers used in the experiments is a long recovery time T (hundreds of fs) as compare with pulse duration. To explain an extremely-short pulse generation a soliton mode-locking mechanism was proposed⁴. This mechanism involves the stabilization of the Schrödinger soliton against laser continuum (noise) due to noise decaying within the positive net-gain window, which is much longer than the pulse duration. This decaying is the result of the dispersion spreading of the noise and the difference between the noise and pulse group velocities. However, as well as semiconductor loss saturation and slow change of the refractivity, other nonlinear effects, in particular, ac Stark-effect can contribute to mode-locking and produce a strong self-amplitude modulation (see, for example⁵). It was shown, that the intracavity intensities in the real solid-state lasers are high enough to produce an ultrafast nonlinear response due to ac Stark effect at below resonance excitation⁶ and thus has to be taken into account.

Here we present a simple model for mode-locking mechanism in the presence of the quadratic blue Stark shift of the excitonic resonance at below resonance excitation. One should note the difference with⁷, where an external signal driven antiresonant Fabry-Perot modulator based on quantum-confined Stark-effect in multi-quantum well semiconductor structure was used to actively mode-lock a diode-pumped Nd: YLF laser. In our case the mode-locking mechanism is purely due to the pulse self-action which is a power dependent and can self-start an ultrashort pulse operation.

3. MASTER EQUATIONS

The ac Stark shift $\Delta\omega$ which is due to the influence of nonresonant transitions on excitonic resonance is proportional to the polarizability difference between ground and excited states $\Delta\alpha$ ⁸: $\Delta\omega = |\Delta\alpha| \times |E|^2/\hbar$, where E is the field strength. The typical values of $|\Delta\alpha|$ for semiconductors are of order $10^{-19} \div 10^{-21} \text{ cm}^3$ (see ref.⁹), that corresponds to the Stark shift coefficient $\zeta = 8\pi|\Delta\alpha|/(n\hbar) = 1.26 \times 10^5 \div 10^3/n \text{ cm}^2 \text{ J}^{-1}$, where n is the index of refractivity.

The evolution of the complex field envelope $a(t)$ in the laser system containing the gain medium, saturable absorber, frequency filter and dispersive element obeys nonlinear operator's equation: $a^{k+1}(t) = AGDa^k(t)$, where k is the

round trip number, t is the local time. The Lorentian gain band is described as $G = \exp\left(\frac{gL_g}{1 + L_g t_g \frac{\partial}{\partial t}}\right)$, where

$L_g = \frac{1}{1 + i(\omega_l - \omega_g)t_g}$, ω_l is the pulse carrier frequency, ω_g is the gain band center, t_g is the inverse gain bandwidth (we assumed $t_g = 20$ fs for the Cr: forsterite laser with modulator based on PbS quantum-dot doped glass³), g is the saturated gain. $D = \exp\left(id \frac{\partial^2}{\partial t^2}\right)$ is the second-order group velocity dispersion operator, where d is the dispersion coefficient.

Neglecting the population of higher energy levels of the semiconductor and for weak exciton-exciton, exciton-phonon bound approximation, one can describe the interaction between laser field and quantum-confined absorber by the generalized two-level model⁸. The evolution of the off-diagonal element of the density matrix π and the population difference between ground and excited states η obey the differential equation set:

$$\frac{d\pi}{dt} + (t_a^{-1} - i(\omega_l - \omega_a - \Delta\omega))\pi = \frac{i}{h} \wp \eta,$$

$$\frac{d\eta}{dt} + \frac{\eta - \eta_0}{T} = -\frac{4}{h} \text{Im}(\pi \wp^*),$$

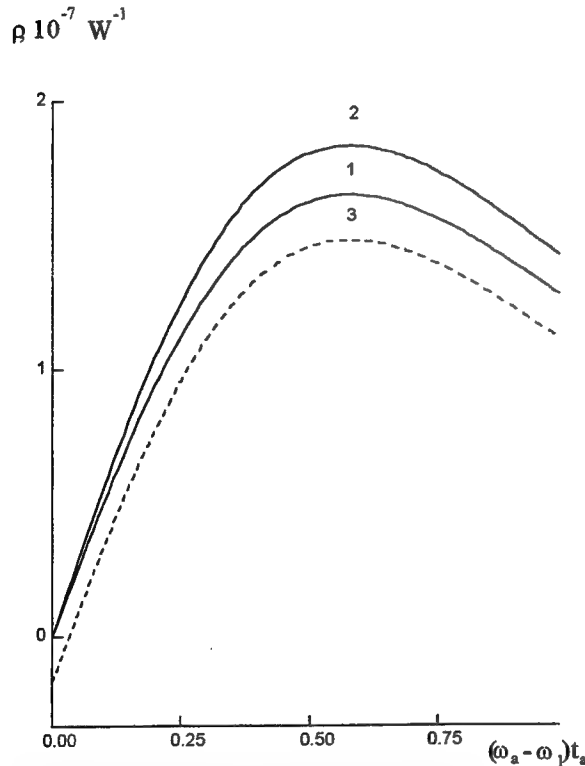


Fig. 1. Coefficient of self-amplitude modulation ρ versus normalized frequency mismatch from the excitonic resonance. $\Gamma = 0.05$ (1, 3), 0.1 (2); coefficient of two-photon absorption is $23 \text{ cm GW}^{-1} (3)^{15}$.

(justified later) as well as other high-order intensity dependent effects. We normalized all times on t_g , frequencies on t_g^{-1} , dispersion coefficient on t_g^2 , the intensities on U_a/t_g .

Using the expression for A one may obtain the instant intensity transmission:

where t_a is the inverse bandwidth of the absorption line, ω_a is the resonance frequency, \wp is the matrix element of the interaction, η_0 is the equilibrium population difference. The Stark shift which is possible only in generalized two-level model, in quasi-monochromatic approximation, i. e. when one neglects the cross-modulation between different pulse spectral components is proportional to $\wp |a(t)|^2$. In the incoherent approximation, the combined effects of saturable absorption and the Stark-effect contribution are contained in the operator

$$A = \exp\left\{ -\frac{\gamma L_a \exp\left[-\frac{\text{Re}(L_a)}{U_a} \int_{t_0}^t |a(t')|^2 e^{-\frac{t-t'}{T}} dt'\right]}{1 + L_a t_a \frac{\partial}{\partial t}} - r \right\},$$

where $L_a = \frac{1}{1 + i[\omega_l - (\omega_a + \wp |a(t)|^2)]t_a}$, U_a is the

saturation energy, γ is the saturated loss at the time t_0 corresponding to the pulse peak, r is the unsaturable loss. Integral in A accounts for the ordinary slow saturable absorption with recovery time T . We have assumed a Lorentian profile for the excitonic resonance and neglected the two-photon absorption (TPA)

$$M(|a(t)|^2) = \exp \left[\frac{-2\Gamma}{1 + \omega^2 \tau^2 - 2\omega \tau^2 \chi |a(t)|^2} \right] \quad (1)$$

where t is the local time, $\tau = t_g/t_g$, Γ is the nonsaturated loss, $\omega = \omega_l - \omega_a$, $\chi = U_a \zeta / t_g$, $\chi = 13$ used in our calculations corresponds to absorber saturation fluency $U_a = 390 \mu\text{J cm}^{-2}$. It is seen, that for the below resonance excitation with $\omega < 0$ (i. e. for the red shift of the pulse carrier frequency from the excitonic resonance) the expression of Eq. (1) describes the power-dependent loss saturation. The fast saturable absorber action results from "pushing out" of the excitonic resonance from the red-shifted pulse spectrum due to intensity-dependent blue Stark shift. The corresponding parameter of self-

amplitude modulation $\rho = \frac{\mu}{M} \frac{\partial M}{\partial |a|^2} \bigg|_{|a|^2 \rightarrow 0}$ is plotted in Fig. 1 (laser mode cross-section in absorber $\mu = 30 \mu\text{m}$) depending

on the mismatch between pulse carrier frequency and excitonic resonance. One can see, that ρ is of order of 10^{-7} W^{-1} that is close to corresponding parameter typical for Kerr-lens mode locked systems¹⁰, but in contrast to the latter is cavity alignment insensitive.

An expansion of the laser operator equation in series in t , local field energy and intensity, provided that the pulse duration is much shorter than T , gives the following laser dynamical equation similar to the generalized Landau-Ginzburg equation (a similar equation for the other physical situation was solved in ref.¹¹):

$$\begin{aligned} \frac{\partial a(k, t)}{\partial t} = & [c_1 + ic_2 \frac{\partial}{\partial t} + (c_3 + ic_4) \frac{\partial^2}{\partial t^2} + (c_5 + ic_6) |a(k, t)|^2 + \\ & (c_7 + ic_8) \varepsilon + (c_9 + ic_{10}) \frac{\varepsilon^2}{2} + (c_{11} + ic_{12}) \varepsilon \frac{\partial}{\partial t}] a(k, t), \end{aligned} \quad (2)$$

where $\varepsilon = \int_{t_0}^t |a(k, t')|^2 dt'$, $c_1 = gJ_g - \gamma J_a - r$, $c_2 = 2g\Omega J_g^2 - 2\gamma\omega\tau^2 J_a^2$, $c_3 = (1 - 3\Omega^2)J_g^3 - \gamma(1 - 3\omega^2\tau^2)J_a^3\tau^2$, $c_4 = g(\Omega^3 - 3\Omega)J_g^3 - \gamma(\omega^3\tau^3 - 3\omega\tau)J_a^3\tau^2 + d$, $c_5 = -2\gamma\omega\tau\chi J_a^2$, $c_6 = -\gamma\chi(1 - \omega^2\tau^2)J_a^2$, $c_7 = \gamma J_a^2$, $c_8 = -\gamma\omega\tau J_a^2$, $c_9 = -\gamma J_a^3$, $c_{10} = \gamma\omega\tau J_a^3$, $c_{11} = -\gamma(1 - \tau^2\omega^2)J_a^3\tau$, $c_{12} = 2\omega\gamma\tau^2 J_a^3$, $J_a = \frac{1}{1 + \omega^2\tau^2}$, $J_g = \frac{1}{1 + \Omega^2}$, $\Omega = \omega_l - \omega_g$. Here, the term $-2\chi\gamma J_a^2\omega\tau |a(k, t)|^2 a(k, t)$ is responsible for the fast saturable absorption.

4. LASER QUASI-SOLITON

The Eq. (2) has quasi-soliton solution $a(k, t) = a_0 \text{sech}^{1+i\psi} [(t - k\delta) / t_p] e^{i\phi}$, where t_p is the pulse duration, a_0 is the amplitude, ψ is the chirp, δ and ϕ are the time and phase delay after the full round-trip, respectively. Pulse duration and frequency shift for chirp-free solution and group velocity dispersion predicted by such a solution are presented in Fig. 2. It is seen, that the minimal pulse durations (close to the limit defined by t_g) are provided by normalized absorber-gain lines mismatch $(\omega_a - \omega_g) / t_g \approx 0.3 \div 0.7$. The increase of nonsaturated loss Γ shortens the pulse (curve 3 in compare with 1 in Fig. 2, a), that corresponds to growth of ρ (curve 2 in Fig. 1). The minimum of the pulse duration on mismatch $\omega_a - \omega_g$ corresponds approximately to the maximum of ρ in Fig. 1. Using the absorber with smaller U_a increases t_p (curve 2) because the absorber operates in the regime of strong saturation. Strong saturation introduces an additional blue shift from the gain band center (curve 2 in Fig. 2, c, for the mechanism of this shift see ref.¹²). Thus, the stronger saturation does not favor the Stark-induced mode locking. Strong self-phase modulation due to ac Stark effect, which is described by coefficient c_6 requires the negative dispersion for chirp compensation (Fig. 2, b). When the absorber band width is narrower than the band width (curve 4), the region of $\omega_g - \omega_a$, where chirp-free pulses exist, reduces, which is explained by bad overlapping of the pulse spectrum and excitonic line. However, for $t_a > t_g$ the generation of chirped pulses with

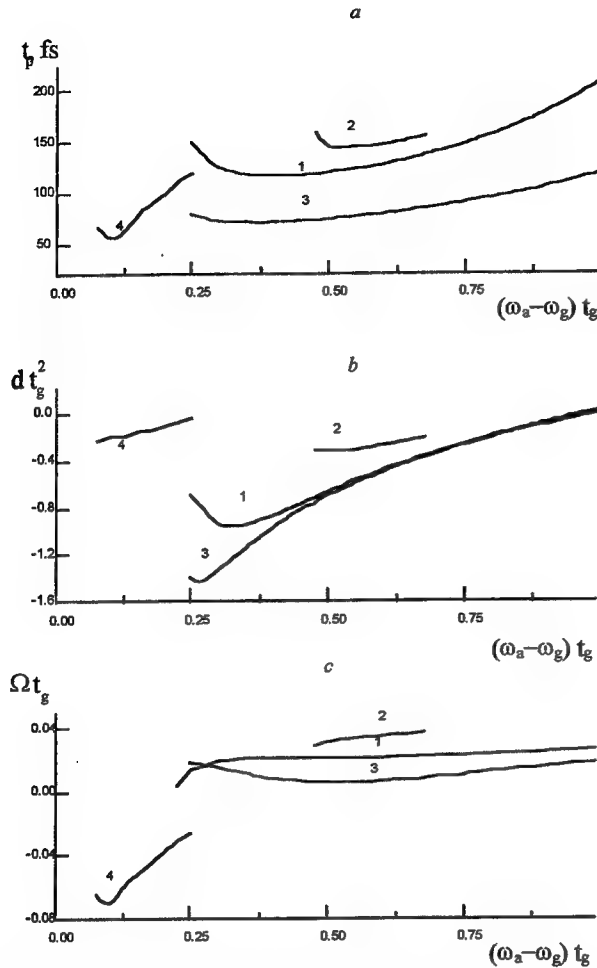


Fig. 2. Duration t_p (a), normalized second order group velocity dispersion dt_g^2 (b) and normalized frequency mismatch from excitonic resonance Ω_g (c) for chirp-free solution versus normalized mismatch between gain and loss resonances. $\chi = 13$ (1, 3, 4), 8 (2), $\Gamma = 0.05$ (1, 2), 0.1 (3, 4), $\tau = 1$ (1 - 3), 3 (4), $g - r = 0.01$.

the absorption recovery time.

To investigate the self-starting ability of the laser analyzed the stability of cw-regime. As the self-starting criterion the condition of modulational destabilization of cw operation and setting up of pulsations with the repetition rate correlated with the laser repetition rate¹⁴ was chosen. A cw-solution of Eq. (2) is $N = N_0 \exp(ik\xi)$, where real amplitude N_0 and phase ξ satisfy the equations:

$$\frac{\alpha_{\max} J_g}{1 + \sigma N_0^2 J_g} - \frac{\Gamma J_a}{1 + N_0^2 J_a} = 2\Gamma \chi J_a^2 \tau \omega N_0^2, \quad (3)$$

$$\xi = \phi + (1 - \omega^2 \tau^2) \chi J_a^2 N_0^2.$$

duration close to t_g is possible (Fig. 3). The large τ requires positive dispersion d for pulse existence (curve 2 in compare to 1), which may be explained by change of the sign of self-phase modulation coefficient in c_6 . However, for large τ , i. e. for the absorption line much narrower than the gain line, it would be necessary to account for the coherent nature of pulse-semiconductor interaction, which may cause new effects, for example self-induced transparency¹³ and may transform mode-locking dynamics essentially.

The described dependence of the pulse parameters on the frequency shift from excitonic resonance is confirmed by experimental results presented in ref.⁵. It was shown, that the resonance interaction with quantum-confined semiconductor structure does not favor an ultra-short pulse formation (fig. 2, a). Relatively small Stokes shift of the laser frequency from the excitonic resonance causes fs-pulse operation, while the increase of the Stokes shift brings the pulse duration into picosecond region.

5. ULTRA-SHORT PULSE STABILITY

In order to perform the stability analysis we calculated the net-gain Σ behind the pulse tail. Σ is the sum of saturated gain in active medium, loss in absorber and unsaturable loss. Evidently, the pulse would be unstable, if $\Sigma > 0$ for some frequency ω_n within the noise spectrum. Fig. 4 shows Σ calculated for five selected values of ω_n (curves 1 - 5 in Fig. 4). It is seen that the decrease of Γ (Fig. 4, a in compare with c), or, equally, decrease of U_a (Fig. 4, a, $U_a = 390 \mu\text{J cm}^{-2}$, in compare with $U_a = 240 \mu\text{J cm}^{-2}$ in Fig. 4, b) or growth of τ (Fig. 4, d) destabilizes the chirp-free pulse, but the suitable detuning between absorber and amplifier lines $\omega_a - \omega_g$ and suitable absorbers parameters τ and U_a allow for the generation of stable pulses with short duration, which is much shorter than

Here, all parameters have the same meaning as in Eq. (2), σ is the ratio of the loss saturation energy to the gain saturation energy ($\sigma=10^{-3}$). The cw power is normalized to the loss saturation power, $\alpha_{\max}=1$. We investigated the stability of cw solution against complex perturbation $v=v_0 \exp(\lambda k)$. The self-starting occurs when $\text{Re}(\lambda) > 0$ and $\text{Im}(\lambda) = \pm l$, l is the natural number (nondecaying oscillations set up with repetition rate which is multiply of inverse cavity round-trip). The linearization of eq. (2) and summing up with complex conjugated gives the equation for eigen values of perturbation:

$$\lambda = gJ_g - \kappa J_a + \left[\frac{\varepsilon_a N_0^2 J_a}{1 - i\omega T_c^a} - \frac{\varepsilon_g \sigma N_0^2 J_g}{1 - i\omega T_c^g} \right] [1 + \Re] - \omega c_2 - \omega^2 c_3 + i\omega^2 c_4 + (c_5 - ic_6) N_0^2 [2 + \Re], \quad (4)$$

where

$$\Re = \frac{\lambda + \kappa J_a - gJ_g + \frac{\varepsilon_g \sigma N_0^2 J_g}{1 - i\omega T_c^g} - \frac{\varepsilon_a N_0^2 J_a}{1 - i\omega T_c^a} + \omega c_2 + \omega^2 c_3 - i\omega^2 c_4 - 2(c_5 - ic_6) N_0^2}{\frac{\varepsilon_a N_0^2 J_a}{1 - i\omega T_c^a} - \frac{\varepsilon_g \sigma N_0^2 J_g}{1 - i\omega T_c^g} + (c_5 - ic_6) N_0^2}, \quad T_c^a = \frac{T}{1 + N_0^2 J_a},$$

$$T_c^g = \frac{T^g}{1 + \sigma N_0^2 J_g}, \quad T^g \text{ is the gain-medium upper state life time,}$$

$$\varepsilon_g = \frac{\alpha_{\max}}{(1 + \sigma N_0^2 J_g)^2}, \quad \varepsilon_a = \frac{\Gamma}{(1 + N_0^2 J_a)^2}.$$

The dependence of $\text{Im}(\lambda)$ versus $\text{Re}(\lambda)$ is shown in Fig. 5 for three different mismatches between gain and loss lines. One can see, that the cw regime is unstable for all three cases, but self-mode locking is possible only for the case 1, where the condition $\text{Im}(\lambda)=1$ is satisfied and self-amplitude modulation coefficient ρ (see Fig. 1) is close to its maximum.

Now we will check the validity of approximation that neglected the contribution of TPA in compare to one-photon absorption made in the beginning of the article. Comparing curves 3 and 2 in Fig. 1, plotted for the situation with and without TPA, one may conclude, that in our case the TPA contribution is small and we may neglect it.

In conclusion, we have analyzed the mode-locking mechanism in cw solid-state laser with semiconductor saturable absorber in the presence of the Stark shift of the excitonic resonance. Calculations showed that it is strong enough to self-start and maintain an ultra-short pulse generation.

6. REFERENCES

1. I. D. Jung, F. X. Kärtner, N. Matuschek, D. H. Sutter, F. Morier-Genoud, V. Scheuer, M. Tillich, T. Tschudi, and U. Keller, "Semiconductor saturable absorber mirrors supporting sub-10-fs pulses", *Appl. Phys.*, Vol. B 65, p. 137, 1997.
2. I. D. Jung, F. X. Kärtner, N. Matuschek, D. Sutter, F. Morier-Genoud, G. Zhang, U. Keller, V. Scheuer, M. Tilsch, and T. Tschudi, "Self-starting 6.5-fs pulses from a Ti:sapphire laser", *Opt. Lett.*, Vol. 22, p. 1009, 1997.

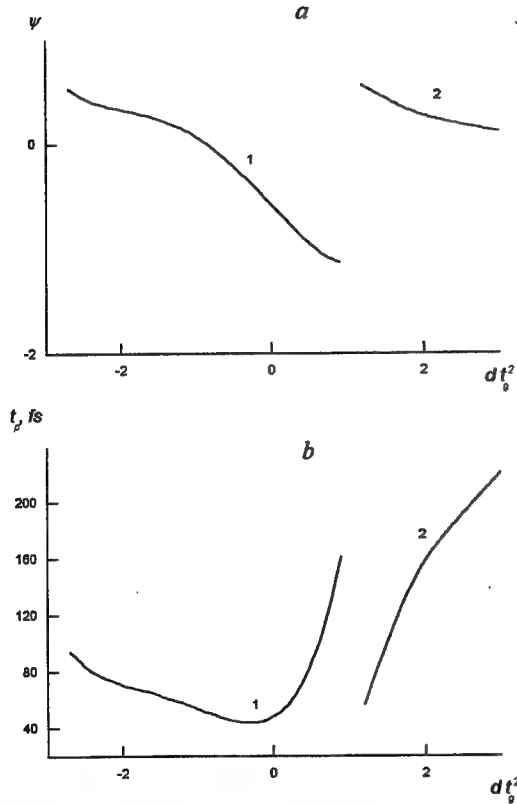


Fig. 3. Chirp ψ (a) and duration of the pulse t_p (b) versus normalized group velocity dispersion. $\tau = 1$ (1), 30 (2), $(\omega_a - \omega_g) t_g = 0.5$ (1), 0.2 (2); $\chi = 13$, $\Gamma = 0.1$, $g = r = 0.001$.

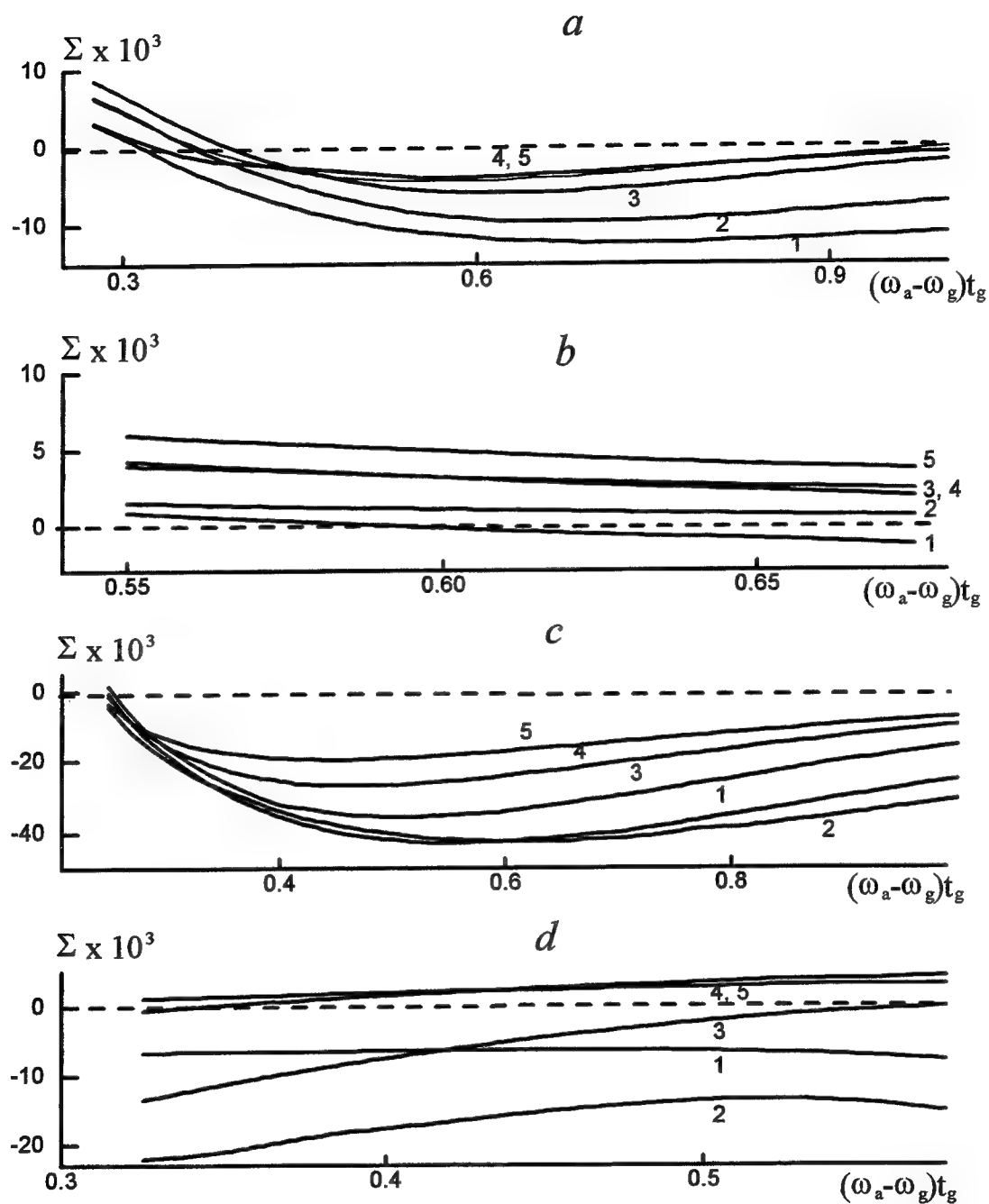


Fig. 4. Net-gain Σ behind the pulse tail for five selected noise frequencies $(\omega_n - \omega)t_g = 1$ (curve 1), 0.5 (2), 0 (3), -0.5 (4), -1 (5). $\chi = 13$ (a, c, d), 8 (b), $\Gamma = 0.05$ (a, b), 0.1 (c, d), $\tau = 1$ (a, b, c), 3 (d).

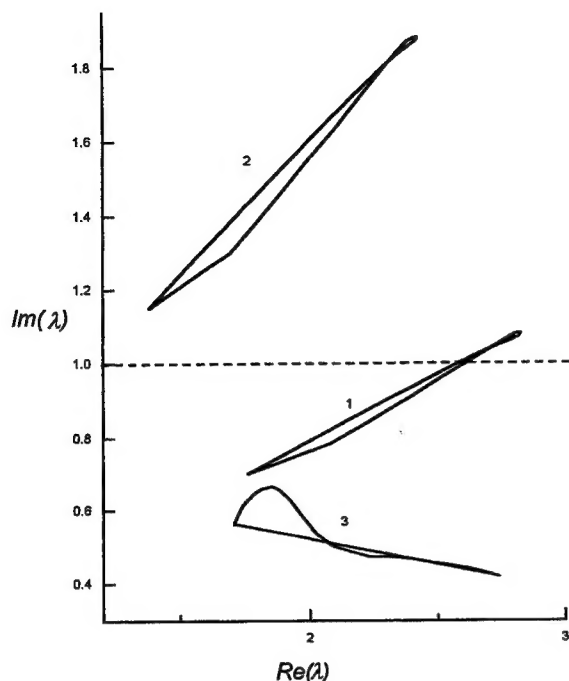


Fig. 5. Complex increment λ of cw perturbation to cw-solution. $\chi = 13$, $\Gamma = 0.1$, $\tau = 1$, $g-r = 0.01$, $(\omega_a - \omega_g) t_g = 0.7$ (1), 0.5 (2), 1 (3).

FIAN, Vol. 166, p. 15, 1986.

10. J. Herrmann, "Theory of Kerr-lens mode locking: role of self-focusing and radially varying gain", *J. Opt. Soc. Am.*, Vol. B11, p. 498, 1994.
11. J. C. Chen, H. A. Haus, E. P. Ippen, "Stability of lasers mode locked by two saturable absorbers", *IEEE J. Quantum Electr.*, Vol. QE-29, p. 1228, 1993.
12. V. L. Kalashnikov, V. P. Kalosha, I. G. Poloyko, and V. P. Mikhailov, "Ultrafast-pulse-formation mechanism by slow-loss saturation and self-phase modulation in solid-state lasers", *J. Opt. Soc. Am.*, Vol. B14, p. 2112, 1997.
13. V. D. Taranukhin, M. Yu. Pogosbekyan, "Influence of optical Stark effect on amplification of powerful pulses in resonance media", *Kvant. Elektron.*, Vol. 20, p. 823, 1993.
14. C.-J. Chen, P. K. A. Wai, and C. R. Menyak, "Self-starting of passively mode-locked lasers with fast saturable absorbers", *Opt. Lett.*, Vol. 20, p. 350, 1995.
15. E. W. van Stryland, W. A. Woodall, H. Vanherzeele, and M. J. Soileau, "Energy band-gap dependence of two-photon absorption", *Opt. Lett.*, Vol. 10, p. 490, 1985.

3. P.T. Guerreiro, S.Ten, E. Slobodchikov, Y.M. Kim, J.C. Woo, N. Peyghambarian, "Self-starting mode-locked Cr:forsterite laser with semiconductor saturable Bragg reflector", *Optics Commun.*, Vol. 136, p. 27, 1997.

4. F. X. Kärtner, I. D. Jung, and U. Keller, "Soliton mode locking with saturable absorbers: theory and experiments", *IEEE J. Selected Topics in Quant. Electr.*, Vol. 2, p. 540, 1996.

5. W. H. Knox, D. S. Chemla, D. A. B. Miller, J. B. Stark, S. Schmitt-Rink, "Femtosecond ac Stark-effect in semiconductor quantum wells: extreme low- and high-intensity limits", *Phys. Rev. Lett.*, Vol. 62, p. 1189, 1989.

6. S. Tsuda, W. H. Knox, S. T. Cundiff, W. Y. Jan, and J. E. Cunningham, "Mode-locking ultrafast solid-state lasers with saturable Bragg reflectors", *IEEE J. Selected Topics in Quant. Electr.*, Vol. 2, p. 454, 1996.

7. L. R. Brovelli, M. Lanker, U. Keller, K. W. Goossen, J. A. Walker, and J. E. Cunningham, "An antiresonant Fabry-Perot quantum well modulator to actively mode-lock and synchronize solid-state lasers", *Electron. Lett.*, Vol. 31, p. 381, 1995.

8. V. S. Butilkin, A. E. Kaplan, Yu. G. Chronopulo, E. P. Jakubovich, *Rezonansnie vzaimodejstviya sveta s veschestvom*, p. 38, Nauka, Moscow, 1977.

9. P. G. Elyseev, A. P. Bogatov, "Phenomena in semiconductor lasers connected with nonlinear refraction and influence of carriers on refractivity index", *Trudi*

Author Index

- Albertano, Patrizia, 138
 Andreev, Alexander Alexeevich, 9, 42, 57, 63, 170
 Andreev, N. E., 2, 25
 Babzien, Marcus, 15
 Bakaev, Valerii G., 179
 Beigman, I. L., 25
 Belli, Mauro, 138
 Ben-Zvi, Ilan, 15
 Bollanti, Sarah, 138
 Boloshin, Yuri A., 15
 Borodin, Vladimir G., 69, 75, 128
 Charukchev, Alexander V., 69, 75, 128
 Chegotov, M. V., 33
 Chernov, Victor N., 69, 75, 128
 Chizhonkov, E. V., 2
 Deineko, Gennady B., 15
 Di Lazzaro, Paolo, 138
 Drška, Ladislav, 9
 Dublov, Andrey A., 15
 Efanov, Vladimir M., 128
 Faenov, Anatoly Y., 138
 Flora, Francesco, 138
 Gerasimov, Vyacheslav B., 90
 Giordano, Gualtiero, 138
 Gorbunov, L. M., 2
 Grilli, Antonio, 138
 Gruzdev, Vitali E., 79
 Gruzdeva, Anastasia S., 79
 Hillmer, Hartmut, 196
 Ianzini, Fiorenza, 138
 Il'in, D. V., 170
 Il'yn, V. V., 69
 Iljin, Vladimir V., 128
 Jing, Feng, 120, 159, 164
 Kalashnikov, Vladimir L., 225
 Komarov, Vladimir M., 69, 128
 Korol', Vyacheslav Y., 179
 Kostin, V. V., 25
 Krimer, D. O., 225
 Kukhlevsky, Sergei V., 138
 Kusche, Karl, 15
 Kuznetsov, Alexander S., 90
 Laubereau, Alfred, 96
 Lebo, I. G., 152
 Lekontsev, Vasili A., 15
 Letardi, Tommaso, 138
 Levkovskii, A. A., 170
 Limpouch, J., 9, 63
 Litvinenko, I. A., 42
 Löbau, J., 96
 Malinov, Vladimir A., 69, 75, 128
 Man, Y. Z., 164
 Marcinkevicius, Saulius, 196
 Marinai, Alessandro, 138
 Meshkovsky, Igor K., 15
 Midorikawa, Katsumi, 108
 Migel, Vaycheslav M., 69, 75, 128
 Mikhailov, Victor P., 225
 Mizin, Vitaly M., 186
 Nikitin, Nikolai V., 69, 75, 128
 Nottola, Alessandro, 138
 Palladino, Libero, 138
 Pavlishin, Igor V., 15
 Peng, Han Sheng, 120, 164
 Pikuz, Tatiana A., 138
 Platonov, K. Y., 42, 57, 63
 Pogorelsky, Igor V., 15
 Poloyko, Igor G., 225
 Popov, Valentin S., 128
 Potapov, Sergei L., 128
 Pyatakhin, Mikhail V., 186
 Reale, Armando, 138
 Reale, Lucia, 138
 Rozanov, V. B., 152
 Rozhdestvensky, Yuri, 57
 Rozivika, I. G., 75
 Salnikov, Andrey A., 90
 Scafati, Anna, 138
 Schina, Giovanni, 138
 Senatsky, Yury V., 186
 Sherman, V. E., 170
 Shestakov, Alexsander V., 90
 Skaritka, John, 15
 Smirnov, A. G., 217
 Sobolev, Serge K., 186
 Sugioka, Koji, 108
 Sui, Z., 120
 Sychugov, Gleb V., 179
 Tabocchini, Maria Antonella, 138
 Tashiro, Hideo, 108
 Trofimov, Vyacheslav A., 208
 Tsunemi, Akira, 15
 Turcu, I. C. Edmund, 138
 Ueda, Ken-ichi, 186
 Umnov, Vladimir O., 90
 Umov, A. M., 25
 Veisman, M. Ef., 25
 Vigli-Papadaki, Kostandia, 138
 Vinogradsky, Leonid M., 186
 Vygovskii, O. B., 170
 Wada, Satoshi, 108
 Wei, X. F., 120
 Yuan, Xiao Dong, 120
 Zhang, Jie, 108
 Zhang, Xiao Min, 120, 159, 164
 Zheng, Wan Guo, 120

Zhu, Qi Hua, 159, 164
Zubarev, Iosif G., 186
Zvorykin, Vladimir D., 152, 179